LBNL-41995
CONF-980559

ERNEST ORLANDO LAWRENCE
BERKELEY NATIONAL LABORATORY

Proceedings of the TOUGH Workshop '98

Karsten Pruess, Editor
Earth Sciences Division

May 1998

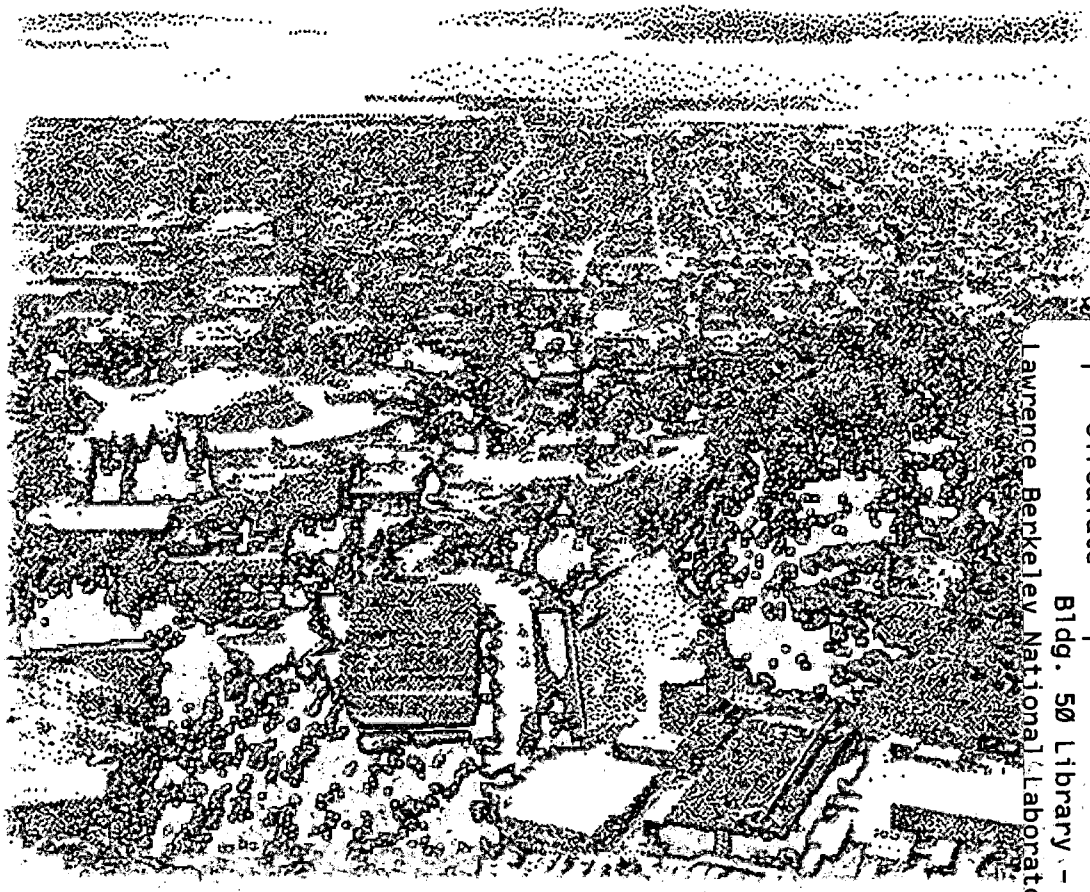

DISCLAIMER

LBNL-41995
CONF-980559

PROCEEDINGS OF THE TOUGH WORKSHOP '98

LAWRENCE BERKELEY NATIONAL LABORATORY
BERKELEY, CALIFORNIA

MAY 4 - 6, 1998

Karsten Pruess, Editor

Earth Sciences Division, Lawrence Berkeley National Laboratory
University of California, Berkeley, California 94720

May 1998

This work was supported by the Assistant Secretary for Energy Efficiency and Renewable Energy, Geothermal Division, of the U.S. Department of Energy under Contract No. DE-AC03-76SF00098.

ABSTRACT

The TOUGH Workshop '98, like its predecessors in 1990 and 1995, focused on applications and enhancements of the TOUGH/MULKOM family of numerical simulation programs for complex flows in permeable media, including multiphase, multicomponent, non-isothermal, and variable-density flows. The workshop program included eleven technical sessions and drew over 80 registered participants from 12 countries. The topical areas covered included geothermal reservoir engineering, nuclear waste isolation, environmental remediation, vadose zone hydrology, mining engineering, and simulation methods.

This volume features the extended summaries of papers that were presented at the workshop. The technical program and lists of authors and registered participants are included in appendices.

TABLE OF CONTENTS

Preface ix

Geothermal Reservoir Engineering 1

M.J. O'Sullivan, D.P. Bullivant, S. Follows, and W.I. Mannington, Dept. of Engineering Science, U. of Auckland, NEW ZEALAND. "Modelling of the Wairakei-Tauhara Geothermal System" 1

Omar Sigurdsson and Valgardur Stefansson, Orkustofnun, Reykjavik, ICELAND. "Use of TOUGH2 in Studying Reinjection Strategies" 7

C.M. Oldenburg and K. Pruess, LBNL. "Higher-Order Differencing for Front Propagation in Geothermal Systems" 13

M.C. Suárez A. and F. Samaniego V, CFE/PEMEX, Morelia, MEXICO. "FITH2 - A Set of FORTRAN Interfaces to Process TOUGH2 Information, Data and Results" 19

S.P. White, R.M. Young, and W.M. Kissling, IRL, Wellington, NEW ZEALAND. "Using ITOUGH2 to Improve Geothermal Reservoir Models" 25

J. Quijano, Comisión Ejecutiva Hidroeléctrica del Rio Lempa (CEL), EL SALVADOR. "Transmissivity Distribution at the Ahuachapán-Chipilapa Geothermal Field in El Salvador" 30

D. Bullivant and M.J. O'Sullivan, Dept. of Engineering Science, U. of Auckland, NEW ZEALAND. "Graphics and TOUGH2" 36

K. Osato, T. Sato, and S. Yokomoto, GERD, Ltd., Tokyo, JAPAN. "The Modeling Study Using TOUGH2 and the Micro-Gravity Change in Yanaizu-Nishiyama Geothermal Field" 41

T. Sato, K. Osato, S. White, J. Burnell, and S. Yokomoto, GERD/IRL, Ltd., Tokyo, JAPAN. "Development of an Integrated Reservoir Modeling System for the Modeling Study Using TOUGH2" 47

D. Bullivant and M.J. O'Sullivan, Dept. of Engineering Science, U. of Auckland, NEW ZEALAND. "Inverse Modelling of the Wairakei Geothermal Field" 53

G. Garcia-Estrada, CFE, Morelia, MEXICO. "Thermal Evolution of Hydrothermal Systems From a Geologic Perspective Using TOUGH2: Los Azufres, Mich., Mexico" 59

A.V. Kiryukhin, M.D. Lesnykh, A.Y. Polyakov, and E.G. Kalacheva, Institute of Volcanology, Petropavlovsk-Kamchatsky, RUSSIA. "TOUGH Applications to Analysis of the Pressure Transient Data of Verkhne-Mutnovsky Site, Mutnovsky Geothermal Field, Kamchatka" 65

Nuclear Waste Isolation 71

M. Reeves, D.G. Fryar, W.H. Statham, and M.K. Knowles, Duke Engineering & Services, Austin, TX. "Assessing Seal Performance and Parameter Sensitivity with a Full-Shaft Model" 71

V. Javeri, GRS, Köln, GERMANY. "Combined Gas and Nuclide Transport in a Two-Dimensional Repository Considering Variable Rock Convergence" 77

R. Senger, P. Marschall, and C. Bühler, Duke Engineering/NAGRA/Solexperts, SWITZERLAND. "Gas Tracer Transport in Two-Phase Flow Field: Numerical Simulations and Field Experiments at the Grimsel Test Site (GTS), Switzerland" 83

Y.S. Wu and K. Pruess, LBNL. "Several TOUGH2 Modules Developed for Site Characterization Studies of Yucca Mountain" 89

A.J.B. Cohen and C.M. Oldenburg, LBNL. "Effects of Faulted Stratigraphy on Saturated Zone Flow Beneath Yucca Mountain, Nevada" 95

G.A. Freeze, G.J. Ruskauff, T.L. Christian-Frear, and S.W. Webb, Duke Engineering & Services /Sandia, Albuquerque, NM. "Modeling the Effect of Excavation-Disturbed Zone Porosity Increase on Groundwater Inflow to an Underground Repository" 101

M. Jobmann, DBE, Peine, GERMANY. "Modification and Application of the TOUGH2 Code for Modeling of Water Flow Through Swelling Unsaturated Sealing Constructions" 106

P. Gribi, M. Niemeyer, R. Senger, and P. Zuidema, Colenco/Duke Engineering/NAGRA, Baden, SWITZERLAND. "Preliminary Investigation of Radionuclide Release under Two-Phase Conditions from a Proposed L/ILW Repository in Switzerland" 112

J.T. Birkholzer and Y.W. Tsang, LBNL. "Numerical Analysis of Thermal-Hydrological Conditions in the Single Heater Test at Yucca Mountain" 118

Environmental Remediation 124

S.W. Webb, S.A. Finsterle, K. Pruess, and J.M. Phelan, Sandia/LBNL, Albuquerque, NM. "Prediction of the TNT Signature from Buried UXO/Landmines" 124

M.J. Lupo and K.W. Brown, KW Brown Environmental, College Station, TX. "Distinguishing the Contributions of Multiple Sources from a Gasoline Release" 130

R.A. Hodges, R.W. Falta, and S. Finsterle, Clemson University/LBNL, Clemson, SC. "Three-Dimensional Simulation of DNAPL Transport at the Savannah River Site" 136

G.J. Moridis, Y.S. Wu, and K. Pruess, LBNL. "EOS9nT: A TOUGH2 Module for the Simulation of Flow and Solute/Colloid Transport" 142

J. Rossabi and R.W. Falta, Savannah River/Clemson University, SC. "The Behavior of Volatile Organic Contaminants in the Vadose Zone with Respect to Barometric Pumping and the Estimate of Residual Mass and Mass Removal Using T2VOC" 148

M. Nastev, R. Lefebvre, R. Therrien, and P.J. Gélinas, Soprin-ADS/NRS, Quebec, CANADA. "Numerical Modeling of Landfill Gas Production and Migration with a N2-CO2-CH4-H2O System and a Production Function" 154

A. Battistelli, A. Chersicla, C. Ferragina, G. Matarrese, and M. Pieroni, Aquater S.p.A., S. Lorenzo in Campo, ITALY. "Simulation of the Transport of Aromatic Amines in the Unsaturated Zone for the Evaluation of an Environmental Remediation Project" 160

P. Kroopnick, Fluor-Daniel, Kent, WA. "Numerical Modeling of JP-8 Remediation by Steam Injection into Artificial Fractures in a Clay Matrix" 166

M.J. Lupo, G.J. Moridis, and K.W. Brown, KW Brown Environmental/LBNL, College Station, TX. "Predicting the Fate of Trichloroethylene and its Daughters in a Heterogeneous Environment" 172

P.J. Schwind and E.C. Miller, Parsons Engineering/Lockheed Martin, Cincinnati, OH. "T2VOC Simulation and Optimization of SVE System Pulse Pumping of Vadose Zone Carbon Tetrachloride Contamination at the Idaho National Engineering and Environmental Laboratory" 178

R.W. Falta, J.S. Gierke, and G.L. Hein, Clemson University/Michigan Tech, Clemson, SC. "Using T2VOC to Model Kinetic Interphase Mass Transfer During Air Sparging" 186

Vadose Zone Hydrology 192

S.W. Webb, Sandia, Albuquerque, NM. "Using TOUGH2 to Model Capillary Barriers" 192

T.S. Liou, K. Pruess, and Y. Rubin, LBNL/UC Berkeley. "Numerical Simulation Experiments on Water Seepage in Unsaturated, Heterogeneous Fractures" 198

A.L. James, C.M. Oldenburg, and S. Finsterle, LBNL. "Analysis of Uncertainty for 2-D Fracture Flow and Seepage into an Excavated Drift" 205

C. Doughty, LBNL. "Numerical Modeling of Field Tests in Unsaturated Fractured Basalt at the Box Canyon Site" 210

C.K. Ho and S.W. Webb, Sandia, Albuquerque, NM. "The Effects of Heterogeneities and Wavy Interfaces on Capillary Barrier Performance" 216

C.F. Ahlers, S. Finsterle, and G.S. Bodvarsson, LBNL. "Characterization and Prediction of Subsurface Pneumatic Pressure Variations at Yucca Mountain, Nevada" 222

Mining Engineering 228

R. Lefebvre, J. Smolensky, and D. Hockley, INRS/SRK Inc., Quebec, CANADA. "Modeling of Acid Mine Drainage Physical Processes in the Nordhalde of the Ronnenburg Mining District, Germany" 228

T. Xu, K. Pruess, and G. Brimhall, LBNL/UCB, Berkeley, CA. "Introducing Reactive Chemical Transport to TOUGH2: Application to Supergene Copper Enrichment" 234

S.P. White, T. Xu, and K. Pruess, IRL/LBNL, Wellington, NEW ZEALAND. "Reactive Chemical Transport" 244

Process Modeling Applications 250

S. Finsterle, T.O. Sonnenborg and B. Faybishenko, LBNL/Technical University of Denmark. "Inverse Modeling of a Multistep Outflow Experiment for Determining Hysteretic Hydraulic Properties" 250

S.W. Webb and C.K. Ho, Sandia, Albuquerque, NM. "Review of Enhanced Vapor Diffusion in Porous Media" 257

C.M. Oldenburg and G.J. Moridis, LBNL. "Ferrofluid Flow for TOUGH2" 263

S.W. Webb, Sandia, Albuquerque, NM. "Gas-Phase Diffusion in Porous Media: Comparison of Models" 269

W. Schreiber and J. Kuo, University of Alabama, Tuscaloosa, AL. "A Computational Study of some Possible Factors Associated with Melt Eruption Events" 275

S. Finsterle, C. Satik, and M. Guerrero, LBNL/Stanford University. "Analysis of Boiling Experiments Using Inverse Modeling" 281

S.W. Webb and C.K. Ho, Sandia, Albuquerque, NM. "Pore-Scale Modeling Using TOUGH2" 288

Simulation Methods 294

W. Schreiber, University of Alabama, Tuscaloosa, AL. "The Use of an Adaptive Grid with TOUGH2 to Track a Moving Phase Front" 294

G.J. Moridis, LBNL. "TOUGH90: A FORTRAN90 Implementation of TOUGH2" 300

K. Pruess, C. Oldenburg and G. Moridis, LBNL. "Overview of TOUGH2 , Version 2.0" 307

Acknowledgement 315

Appendix A. Author Index 316

Appendix B. Registered Participants 317

Appendix C. Technical Program 324

Appendix D. TOUGH Questions 328

Preface

A workshop on applications and enhancements of the TOUGH/MULKOM family of multiphase fluid and heat flow simulation programs was held at Lawrence Berkeley National Laboratory on May 4 - 6, 1998. The workshop was organized as an open forum for information exchange among developers and users of the TOUGH/MULKOM codes, and was attended by over 80 participants from 12 countries. A unique aspect of the meeting was the strong diversity of subject matter, emphasizing the commonality of interest shared by different engineering disciplines in multiphase flows, and coupled fluid and heat flows. A total of 52 technical papers were presented in oral and poster sessions. Topics covered broad areas that involve complex flows in the subsurface, such as geothermal reservoir simulation, nuclear waste isolation, environmental remediation, vadose zone hydrology, and others.

The present volume includes extended summaries of the papers contributed to the TOUGH Workshop '98. In some cases these were slightly revised by the authors after the workshop, but no editing was performed by Lawrence Berkeley National Laboratory. In the Open Discussion session at the end of the workshop it was suggested to use the Internet as a convenient means for sharing information about code developments and applications. Users are encouraged to submit the URL's of their TOUGH-related web sites to K_Pruess@lbl.gov; these will be posted in a "TOUGH Links" section on the TOUGH2 homepage, at http://ccs.lbl.gov/TOUGH2/.

In planning the workshop and assembling the technical program we had valuable assistance from an international group of advisors which included Alfredo Battistelli, San Lorenzo in Campo, ITALY, Ronald W. Falta, Clemson (South Carolina), René Lefebvre, Québec, CANADA, Marcelo Lippmann, Berkeley (California), Curt Oldenburg, Berkeley (California), Michael O'Sullivan, Auckland, NEW ZEALAND, Rainer Senger, Austin (Texas), Valgardur Stefansson, Reykjavik, ICELAND, César Suarez, Morelia, MEXICO, and Steve Webb, Albuquerque (New Mexico). I am deeply grateful to these individuals for their support and good suggestions, which were crucial in putting together a productive meeting.

Special thanks are due to Sabodh Garg who gave the banquet address. From his unique perspective of more than 25 years of experience in mathematical modeling and reservoir engineering, Dr. Garg highlighted important milestones in the development of geothermal reservoir simulation, and provided a thought-provoking outlook on present and future challenges. He emphasized that numerical models of geothermal reservoirs (as of other subsurface flow systems) tend to be non-unique, requiring careful engineering judgement in their development and use. Model reliability may be improved by aiming for a more comprehensive description of reservoir processes and characteristics, including geophysical and geochemical changes.

I would also like to take this opportunity to thank the various agencies and offices that have over the years supported our efforts in development and application of the TOUGH/MULKOM codes. These include the Geothermal Division and the Office of Basic Energy Sciences of the Department of Energy, the Nuclear Regulatory Commission, the Gas Research Institute, DOE's Yucca Mountain Site Characterization Project, and Sandia's WIPP project.

Last but not least I want to thank the many colleagues, at LBNL and elsewhere, whose continued interest and support has made it possible to develop flow modeling capabilities that are sophisticated, yet robust enough to be practically useful for a wide range of engineering applications.

Berkeley, California, May 1998

Karsten Pruess

Modelling of the Wairakei - Tauhara Geothermal System

M.J. O'Sullivan[1], D.P. Bullivant[1], S.E. Follows[2] and W.I. Mannington[1]

[1] Department of Engineering Science, University of Auckland and [2] DesignPower Genzl, Auckland, New Zealand

Introduction

The Wairakei - Tauhara geothermal system is located in the centre of the North Island of New Zealand in a large geothermally active area called the Taupo Volcanic Zone. Electricity generation at Wairakei commenced in 1953. A plant with a maximum capacity of 192MWe was installed but the supply of steam has never been adequate to reach this figure. The maximum output achieved was approximately 185MWe in 1964. Output subsequently declined and has now stabilised at a steady value of 157MWe. This output is achieved from a total mass take of approximately 130,000 t/d giving a flow of separated steam of 29,000 t/d.

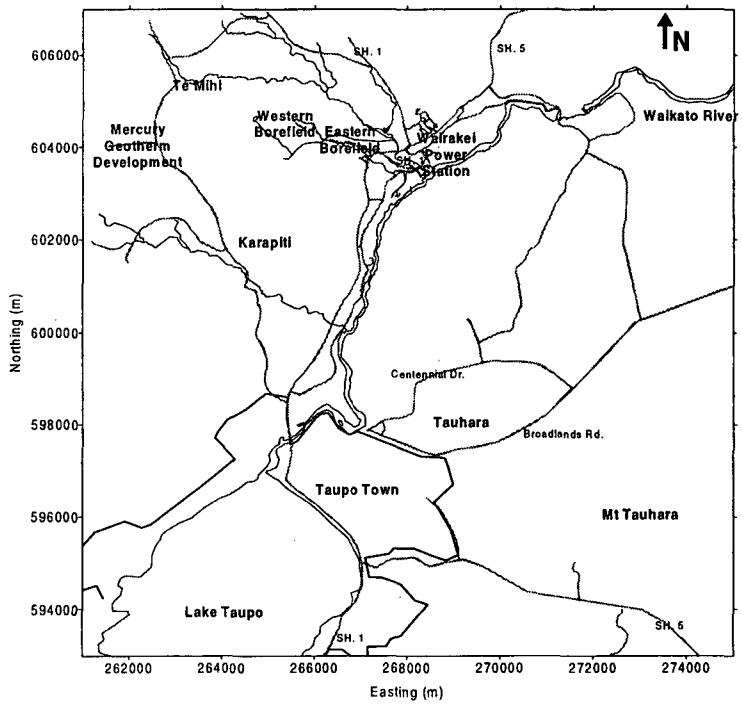

Figure 1 Map of the Wairakei-Tauhara geothermal system

The main hot upflow for Wairakei is in the western part of the field near Te Mihi. In the natural state this hot flow, at 260°C, was diverted horizontally by the low permeability of the Huka Falls formation located between approximately 250 masl and 330 masl (the surface of the Eastern Borefield varies between 380 masl and 420 masl). The capping effect of the Huka Falls formation caused the hot upflow to flow horizontally across the Western Borefield and then to discharge (neutral pH, chloride water) mainly at Geyser Valley in the northwest. There was also some discharge of hot water along the banks of the Waikato River and a small discharge of steam in higher ground at Te Mihi and Karapiti.

Production began in the Eastern Borefield and then spread west into the Western Borefield and Te Mihi. In the natural state almost all of the Wairakei and Tauhara reservoir fluid was hot water but production caused the pressure to drop rapidly (See Fig. 2) and also caused the formation of a steam zone which expanded rapidly vertically and horizontally. This process caused the surface features at Geyser Valley to mostly disappear but in some areas, such as Karapiti, the surface heat flows increased (Allis, 1981).

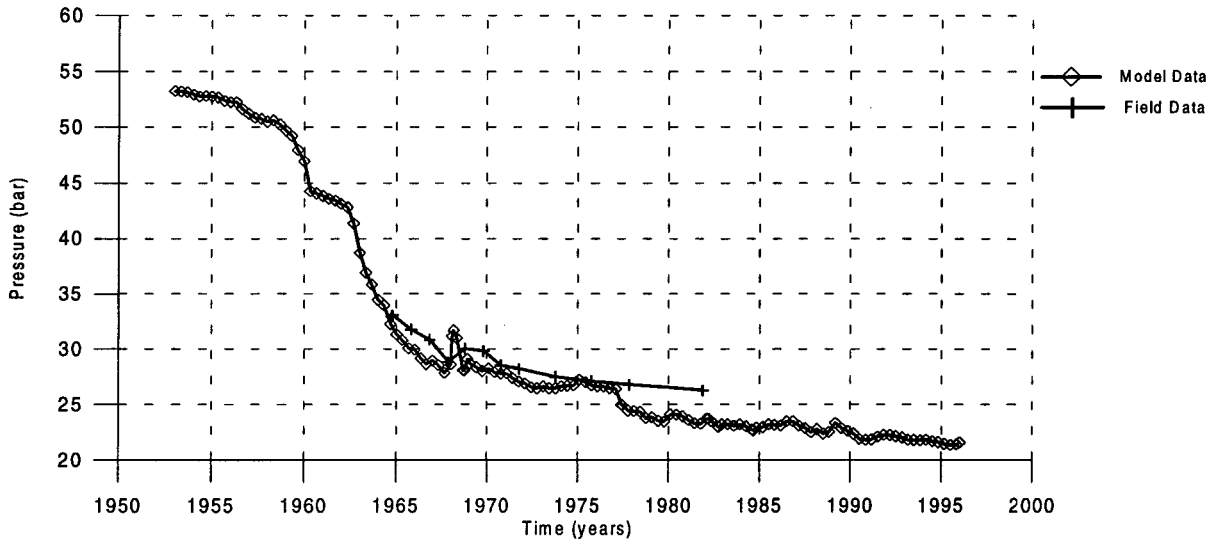

Figure 2. Pressure history for the Western Borefield at Wairakei

Most of the deep wells access liquid water or a wet two-phase zone and in the latter case produce a mixture of steam and water with an enthalpy only a small amount above that for liquid water. The average production enthalpy is shown in Fig. 3. The shallow part of the steam zone has a high steam content and some wells which access it produce dry steam. As Fig. 2 shows the pressure drop slowed down by 1970. This corresponds to the stage when a quasi-equilibrium state had been established at Wairakei - Tauhara with the induced recharge flow matching production.

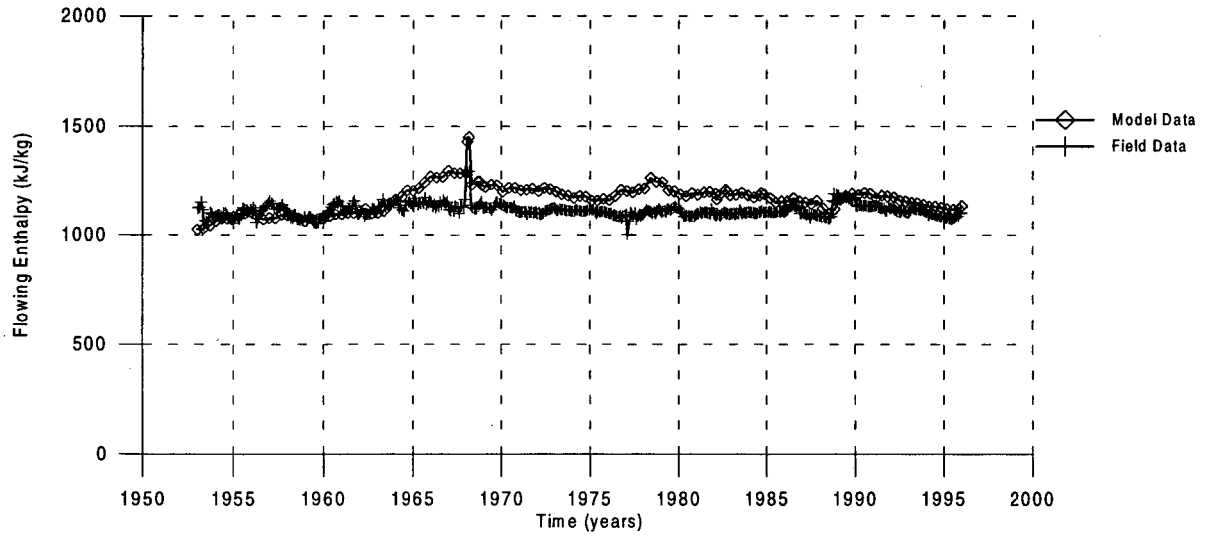

Figure 3. Production enthalpy history for Wairakei

Wairakei - Tauhara is characterised by large permeabilities and the pressure drop extended over a large area with pressures in the Western and Eastern Borefields varying by less than 2 bar. The pressure decline also spread across to the Tauhara part of the system as shown in Fig. 4.

Although mass flows have stabilised temperature declines are continuing as colder recharge fluid moves into the reservoir from the sides and top. Some wells have been "quenched" by this process.

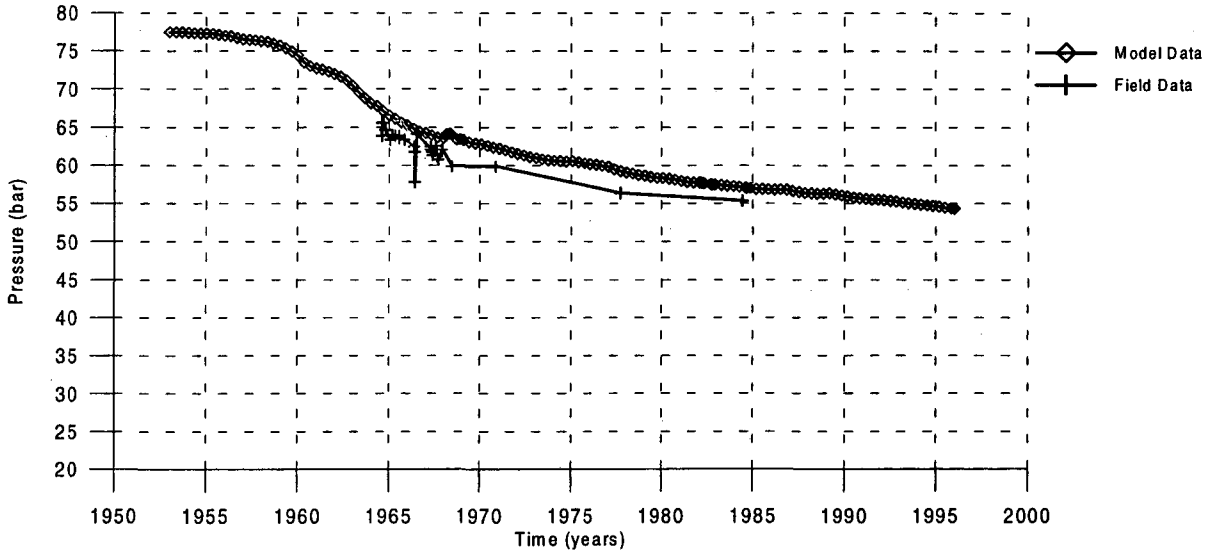

Figure 4. Pressure History for the Tauhara Region

Data

There is a very extensive database for Wairakei. Temperature vs depth profiles are available for many wells although the first available data for some wells is considerably after the start of production in 1953. Maps of pre-exploitation surface features are available although the information is qualitative rather than quantitative. Estimates of the total natural through-flow for Wairakei vary but the generally accepted figures are 400kg/s for mass and 450MW_{th} for energy (Allis, 1981). For Tauhara the heat flow figure is approximately 100MW_{th}. Comparison of these figures with the present take of approximately 1650MW_{th} shows that Wairakei is being "mined" for heat.

Measurements on individual wells have been made regularly and records of mass flow, production enthalpy, pressures and temperatures are available. Records of changes for chemicals such as chloride are available and various geophysical surveys have been carried out. Because of the ready availability of data Wairakei was used as a test case in several early computer modelling studies (Mercer and Faust, 1979; Pritchett et al., 1980) and in discussions of methods for geothermal resource assessment (Donaldson and Grant, 1979). A few lumped parameter models were also investigated (Whiting and Ramey, 1969; Fradkin et al., 1981).

The database for the Tauhara region is not as extensive. Only four deep wells have been drilled and monitored.

Model Design and Calibration

Our computer modelling study of Wairakei - Tauhara has been proceeding for many years (Blakeley and O'Sullivan, 1981, 1982) and our models have grown in complexity, partly as our knowledge of Wairakei - Tauhara has improved, but mainly as software and hardware have improved. Our introduction of conjugate gradient solvers into MULKOM greatly increased the number of blocks we

could use in our model of Wairakei - Tauhara and also increased the computational speed (Bullivant et al., 1991). The development of very fast, cheap, workstations has also greatly increased computational speed. We currently run our models of Wairakei-Tauhara on DEC Alpha and Silicon Graphics workstations.

The grid for one of our most recent models of Wairakei-Tauhara is shown in Fig. 5. There are 118 blocks per layer and 12 layers giving a total of 1417 blocks (including one for the atmosphere).

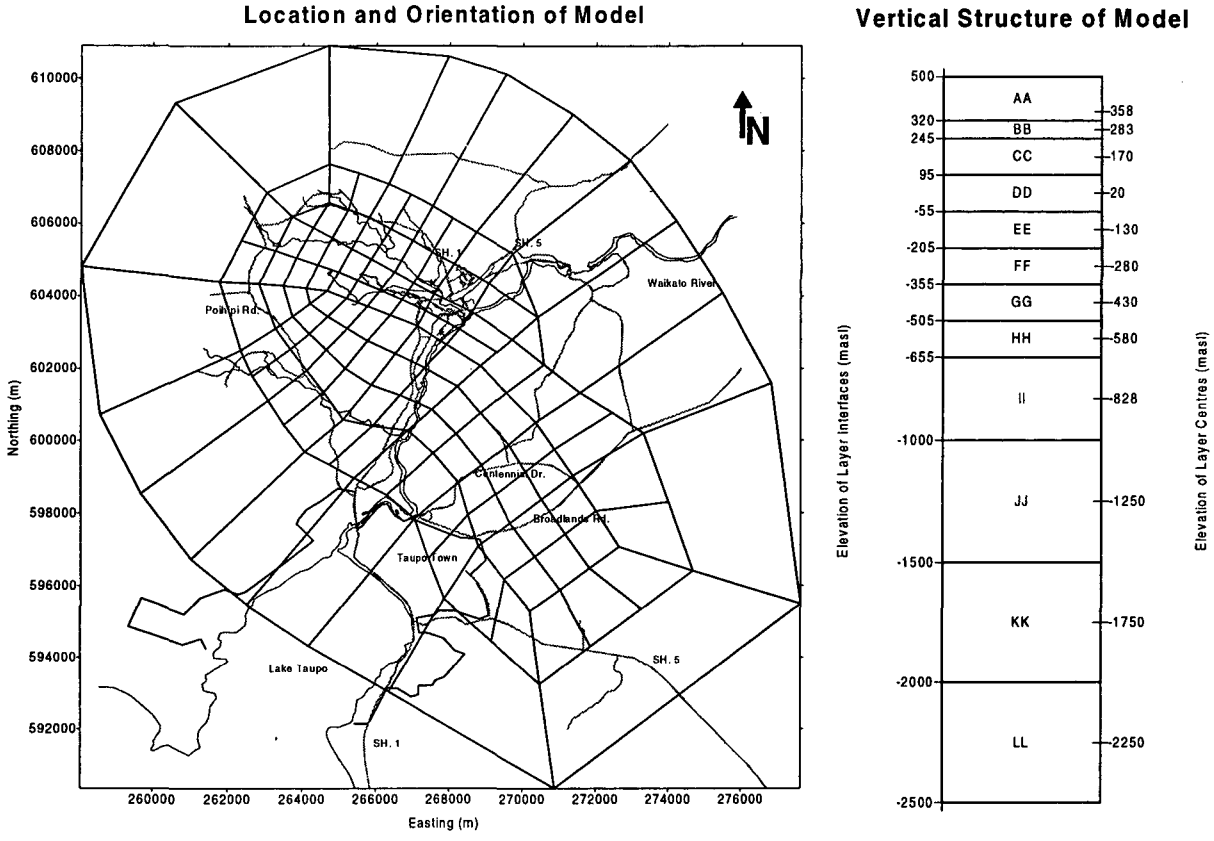

Figure 5. Grid layout for the Wairakei-Tauhara model

The design of this grid was based on several criteria:

(i) The blocks near the Wairakei Borefields are aligned approximately SW-NE along the direction of faults and fractures.
(ii) The adjoining Taupo-Tauhara area is included.
(iii) The boundary of the small blocks in the model corresponds to the resistivity boundary.
(iv) Large "recharge" blocks are included.

It is assumed that the model is sufficiently large so that all recharge at the outer lateral boundaries of the model is negligible and they are treated as closed. At the surface of the model, corresponding to the water table, the temperature and pressure are fixed at atmospheric values. At the base hot water at 260°C is injected over part of the model and a background low heat flow is applied over the rest. During production runs some extra hot inflow at the base is allowed by adding recharge proportional to the pressure drop.

The model is calibrated in two stages, firstly by matching the natural state behaviour and secondly by matching the historical performance (O'Sullivan, 1985). For natural state matching the permeability structure and deep inflows (location and magnitude) are adjusted and the model results are compared

with measured temperature profiles and surface outflows (location and magnitude). Some typical results for the calibrated natural state model are shown in Fig. 6.

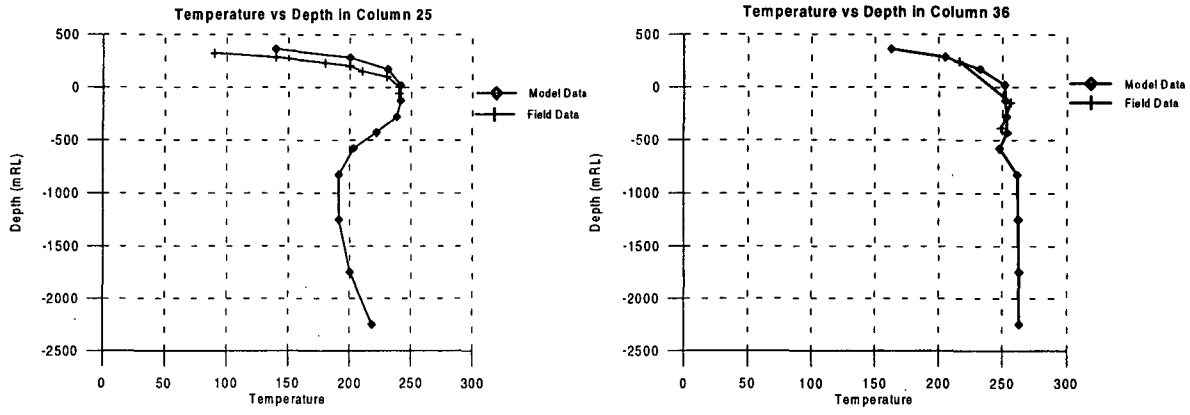

Figure 6. Temperature vs depth in the Western Borefield

For history matching further adjustments are made to the permeability structure and also porosities are adjusted. Model results are then compared with measured pressure declines, enthalpy transients and temperature changes. Typical results are shown in Figs. 2 - 4.

This calibration process required many iterations at each stage (natural state and past history) and between the two stages. Most of the calibration process was carried out by "hand", that is with one of the authors deciding which parameters should be adjusted. Recently we have experimented with computerised calibration (Finsterle et al., 1997) with some success.

The model of Wairakei - Tauhara described here is working well in terms of its match to natural state and historical data. It has reached the state that it produces good results for some data which were not included in the original calibration. For example well-by-well enthalpy data were not included in the calibration process; only the average enthalpies for the Western or Eastern Borefields were used. However the calibrated model gives a good match to the well performance for both its deep (liquid) and shallow (steam) wells in Te Mihi. Our model of Wairakei - Tauhara was used as a test for the chemical transport version of TOUGH2 developed at IRL (White, 1995). A good match between model results and field data was obtained for chloride concentrations at Wairakei (Kissling et al., 1996).

A few aspects of the model need improvement, for example the average field enthalpy in the period 1965 - 1985 is too high in the model. We are currently reviewing the feed-zone data for the Eastern Borefield wells and may adjust our feed-zone depths. However it may be impossible to improve the model greatly without further grid refinement (more thinner layers). Most of the wells concerned are no longer significant producers and therefore this aspect of the model is no longer important.

Some of the model temperature in the zone between Wairakei and Tauhara are too high. This aspect of the model is not particularly important in terms of the model performance but it is being reviewed.

Discussion

Our computer model of Wairakei - Tauhara is working well and is being used by Contact Energy Ltd to assist with field management and planning; for example to study the impact of major reinjection and to investigate the interaction between Wairakei and Tauhara (Contact Energy Ltd was previously part of the Electricity Corporation of New Zealand (ECNZ) which in turn was set up by corporatising the New Zealand Electricity Department (NZED)). Contact's support of our work is gratefully acknowledged.

We have found MULKOM/TOUGH2 to be a very effective tool for geothermal reservoir modelling, both for Wairakei - Tauhara and several other fields. The flexible block structure is very useful and apart from introducing fast solvers (which are now available with the standard version of TOUGH2) we have had to modify MULKOM/TOUGH2 very little. We have introduced extra options for the operation of wells to allow the actual field procedures to be closely modelled.

Perhaps the most important feature we have added to MULKOM/TOUGH2 is the tightly coupled graphical interface MULGRAPH (O'Sullivan and Bullivant, 1995). This enables us to graphically edit the geometry and permeability structure of our model and to very quickly view the results and compare them with field data.

References

Allis, R.G., 1981, "Changes in heat flow associated with exploitation of Wairakei Geothermal Field, New Zealand", *N.Z. Journal of Geology and Geophysics*, 24, 1-19.

Blakeley, M.R. and O'Sullivan, M.J., 1981, "Simple models of the Wairakei reservoir", Proc. 3rd New Zealand Geothermal Workshop, University of Auckland, 131-136.

Blakeley, M.R. and O'Sullivan, M.J., 1982, "Modelling production and recharge at Wairakei", Proc. 4th New Zealand Geothermal Workshop, University of Auckland, 23-31.

Bullivant, D.P., O'Sullivan, M.J. and Zyvoloski, G.A., 1991, "Enhancements of the MULKOM geothermal simulator", Proc. 13th New Zealand Geothermal Workshop, University of Auckland, 175-182.

Donaldson, I.G. and Grant, M.A., 1979, "An estimate of the resource potential of New Zealand geothermal fields for power generation", *Geothermics*, 7, 243-252.

Finsterle, S., Pruess, K., Bullivant, D.P. and O'Sullivan, M.J., 1997, "Application of inverse modeling to geothermal reservoir simulation", Proc. 22nd Workshop on Geothermal Reservoir Engineering, Stanford University, Stanford, California, 8 p.

Fradkin,L.Ju., Sorey, M.J. and McNabb, A., 1981, "On identification and validation of some geothermal models ",*Water Resources Research*, 17, 929-936.

Kissling, W.M., Brown, K.L., O'Sullivan, M.J., White, S.P. and Bullivant, D.P., 1996, "Modelling chloride and CO_2 chemistry in the Wairakei geothermal reservoir", *Geothermics*, 25(3), 285-305.

Mercer, J.W. and Faust, C.R., 1979, "Geothermal reservoir simulation: 3, application of liquid- and vapour-dominated hydrothermal modelling techniques to Wairakei, New Zealand", *Water Resources Research*, 15, 653-671.

O'Sullivan, M.J., 1985, "Geothermal reservoir simulation", *J. Energy Research*, 9, 319-332.

O'Sullivan, M.J. and Bullivant, D.P., 1995, "A graphical interface for the TOUGH family of flow simulators', Proc. TOUGH Workshop '95, Berkeley,California, 90-95.

Pritchett, J.W., Rice, L.F. and Garg, S.K., 1980, "Reservoir simulation studies: Wairakei geothermal field, New Zealand, Final Report", Geothermal Reservoir Engineering Management Program report GREMP-11, Lawrence Berkeley Laboratory.

White, S.P., 1995, "Multi-phase nonisothermal transport of systems of reacting chemicals", *Water Resources Research*, 31, 1761-1772.

Whiting, R.L. and Ramey, H.J. Jr., 1969, "Application of material and energy balances to geothermal steam production", *Journal of Petroleum Technology*, 21, 893-900.

Use of TOUGH2 in studying reinjection strategies

Omar Sigurdsson
Valgardur Stefansson

Orkustofnun, Grensasvegur 9, IS-108 Reykjavik, ICELAND

ABSTRACT

A study was conducted to examine the effects of reinjection into high enthalpy resources. The main objectives of the study were to optimise the high enthalpy fluid extraction from the resource for electrical generation and the longevity of the resource. A hypothetical geothermal system was constructed with initial conditions as water dominated, two-phase and vapor dominated, respectively. The computer code TOUGH2 was used for the numerical calculation. Several well patterns were compared for both shallow and deep reinjection into the resources. Systems with infinite, open and closed boundaries were tested, but a system with closed boundaries was then selected for further study because the effects of the reinjection were more distinct. The main results obtained from the simulations are discussed. They favor peripheral injection sites and reinjection strategy with emphasis on thermal sweep. Further beneficial results of reinjection are observed.

INTRODUCTION

Some debate has been on the benefits of reinjection into high enthalpy geothermal systems in Iceland, as elsewhere, with regard to electrical generation. A project was instigated to investigate in general, whether high enthalpy geothermal systems could benefit from reinjection and then what injection pattern would give the best results. The measure of the benefits would be increases in electrical generation capacity and increased longevity of the system compared to operating the system without reinjection. In order to address this problem in general, a hypothetical geothermal system was constructed. Three types of initial conditions were considered, water dominated, two-phase and vapor dominated. Boundary conditions could be infinite, open or closed. Injection rates could be varied and several different injection patterns needed to be examined. Given all these variable conditions it was clear that a substantial number of model runs had to be made. The computer code TOUGH2 (Pruess, 1986) was selected to carry out the numerical calculation.

The hypothetical geothermal resource studied here consists of four horizontal layers. The top two layers are 300 m thick each and correspond to the ground water system and cap rock of the reservoir. The lower two layers are 400 m thick each and represent the reservoir rock. The areal extension of the layers is 1.6x2.0 km^2 and each layer is divided into 66 elements, most of size 200x200 m^2. A further refinement of the grid was used around the production wells. Figure 1 shows the grid and the three main configurations used for the location of production and injection wells, *intermixed, peripheral* and *dipole.*

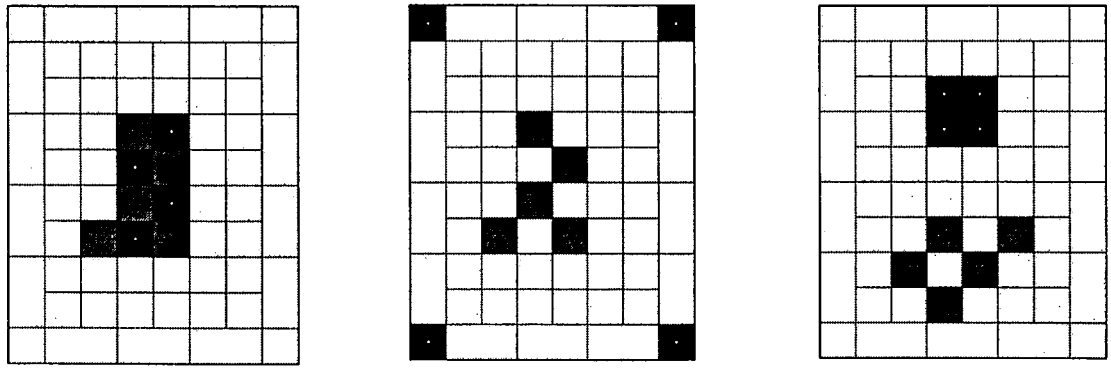

Figure 1. *Numerical grid and location of producers (gray) and injectors (black) for the patterns used. Left is the intermixed pattern, center the peripheral pattern and right the dipole pattern.*

Values for the fixed thermal and mechanical parameters of the model are given in Table 1. They are in general comparable to values used in simulations of real geothermal reservoirs. The model sensitivity to porosity and permeability was tested by running each well pattern for all combinations of low and high values for these parameters. Their lower range is comparable to values obtained in simulations of the Krafla field, Iceland (Bodvarsson et al. 1984a) and of the Olkaria field, Kenya (Bodvarsson et al. 1985). Their higher range is comparable to those used in simulation of the Nesjavellir field, Iceland (Bodvarsson et al. 1990). Furthermore, it was decided to set the separator pressure at 8 bar-a (170.4 °C) and use the conversion factor 2.2 kg/s per MW_e to change steam rate at separator to electrical power. Linear relative permeability curves were used, but they have been found to give reasonable results in modelling real geothermal fields. (Bodvarsson et al. 1984b, 1985, 1990).

Table 1. *Thermal and mechanical parameters used in the numerical model.*

Matrix	
Matrix density, kg/m^3	2650
Specific heat, J/(kg °C)	1000
Thermal conductivity, W/(m °C)	1.7
Porosity, %	5-10
Permeability, m^2	(3.5-17.5) 10^{-15}
Relative Permeability Linear curves	
S_{lr}	0.30
S_{vr}	0.05
S_{pv}	0.70
Well Parameters	
Productivity index, m^3	1.6 10^{-12}
Pressure at upper layer, bar-a	30.
Reinjection enthalpy, kJ/kg	721.0
Separator Conditions	
Pressure, bar-a	8.0
Temperature, °C	170.4

REFINING THE PROBLEM

The simulation study was started with several trial cases for both closed and open boundaries set in a zone, with 43% reduced permeability, extending 1.2 km outside the aforementioned main reservoir area (seen in Figure 1) and with infinite boundaries 6 km outside the same area. It was found that the results for the reference simulations and even reinjection cases did not depend on the boundary chosen during a 30 year production period. Therefore, the permeability, porosity and well productivity indices were adjusted for these cases so that the minimum production from the system corresponded to about 20 MW_e over a period of 30 years. The reinjection rates selected were the 30 years average of the total flow rates and of the separated brine rates as obtained from these reference cases for two-phase conditions. However, it became evident in later runs, especially for the higher permeability cases, that a considerable portion of the reservoir recharge came from the outer zone and was therefore causing the independence of the boundary conditions. To make the effects of the reinjection more pronounced the boundaries around the reservoir were closed in later runs, but reinjection rates were fixed at the earlier determined values and used in later runs for simplifying comparison between different runs.

For the two reinjection rates and the combination of porosity and permeability up to 8 runs were needed for each producer/injector configuration for given initial reservoir conditions. A minimum of 40 model runs, including the reference cases, were required for the three well patterns at given initial conditions. Table 2 summarises the permeability, porosity and reinjection rates used for the different cases. The reinjection rates were mainly divided between four injectors.

Table 2. *Permeability, porosity and reinjection rates for the different cases.*

	Case A	Case B	Case C	Case D
Permeability, md	3.5	17.5	3.5	17.5
Porosity, %	5.0	5.0	10.0	10.0
Lower injection rates, kg/s	40.0	130.0	60.0	140.0
Higher injection rates, kg/s	90.0	220.0	110.0	230.0

To handle the large amount of output that these model runs generated and to get an overview of the outcome for each case, several UNIX shell scripts were written to manage the data. Shell scripts selected data from the outputs for harddisk storage and later analysis as well as for graphical display. The shell scripts included contour mapping of temperature, pressure and steam saturation for each reservoir layer, history of these parameters for selected elements as well as history of production rates, electrical and heat production and cumulatives. Figure 2 shows an example of contour output from one of the shell scripts.

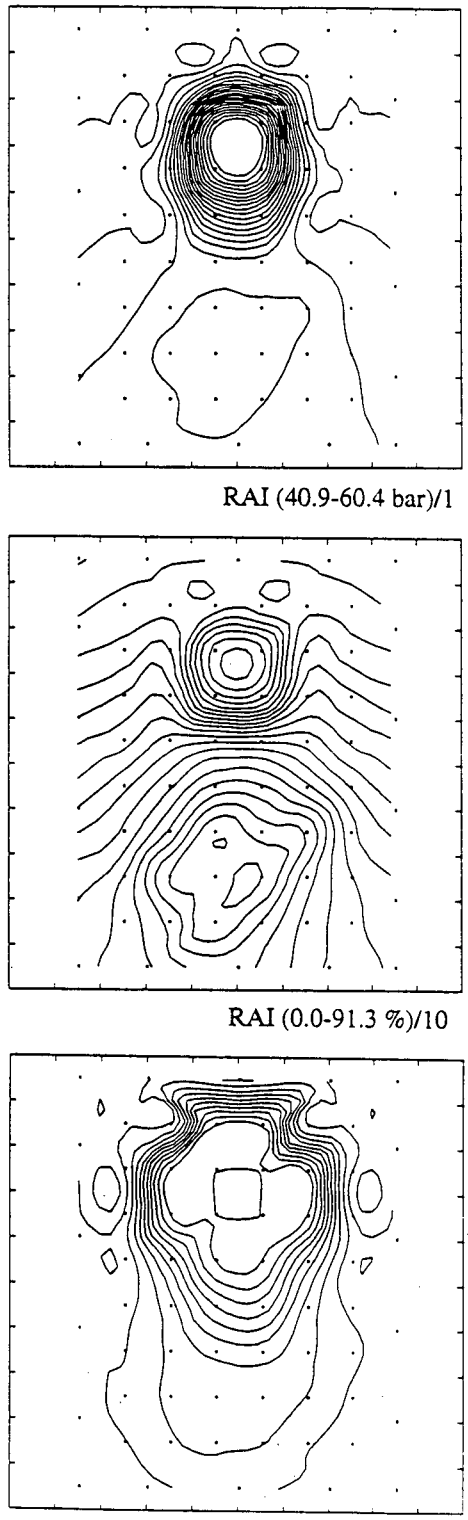

Figure 2. *A shell script collects data from the TOUGH2 output and displays it as contour maps. Here the upper reservoir layer for vapor dominated system and dipole pattern. Top is temperature (°C), center pressure (bar) and bottom steam saturation (%).*

COLLECTED RESULTS

In this study the emphasis was on high enthalpy resources and the effect of reinjection on electrical generation was the desired outcome. The initial conditions used for the various reservoir cases listed in table 3 resemble conditions known in Icelandic geothermal systems. All runs are compared to reference cases which constitute the same reservoir conditions but without reinjection. Some difference is observed between the reference cases for the dipole pattern and the other patterns.

Water dominated systems.

For the water dominated initial conditions the reservoir pressure drops rapidly in the reference cases because the reservoir is closed. The flow rates are low without reinjection and consequently the electrical production is minimal. However, after the initial pressure drop the water dominated resource can be produced over a long period (60 years) with only minor changes in flow rates. Reinjection maintains the pressure in the system resulting in increased flow rates. As the reference level for produced electricity was low for the closed water dominated system, all the reinjection cases showed increased generating capacity. The increased capacity declined after 20-30 years production for the intermixed pattern (Figure 3), but was kept at about constant level for the dipole and peripheral patterns (Figure 4). The increase in electrical generating capacity was about the same for the dipole and peripheral patterns over a 60 year period. However, the dipole configuration was approaching a thermal breakthrough after 60 years of production while a large portion of the reservoir was still hot in the vicinity of the production wells in the peripheral configuration. For the intermixed pattern a slight improvement in electrical production is observed when the injection is to the deeper part of the reservoir.

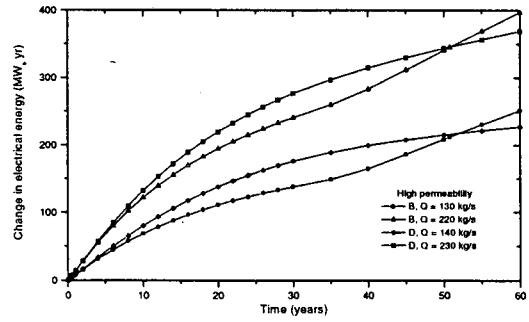

Figure 3. *Change in cumulative electrical energy compared to the reference case for water dominated system and intermixed well pattern.*

Table 3. *Initial conditions for simulation runs.*

	Water dominated		Two phase		Vapor dominated	
	Pressure	Temperature	Pressure	Temperature	Pres./Sat	Temperature
Layer	(bar-a)	(°C)	(bar-a)	(°C)	(bar-a)	(°C)
Ground water	13.9	90.0	13.9	90.0	13.9	90.0
Cap rock	38.8	207.0	38.8	207.0	38.8	207.0
Upper Res.	65.5	240.0	65.5	281.0	0.70	281.0
Deeper Res	93.8	250.0	93.8	306.2	0.70	306.2

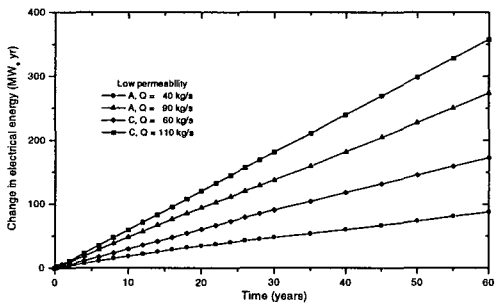

Figure 4. *Change in cumulative electrical energy compared to the reference case for water dominated system and peripheral well pattern.*

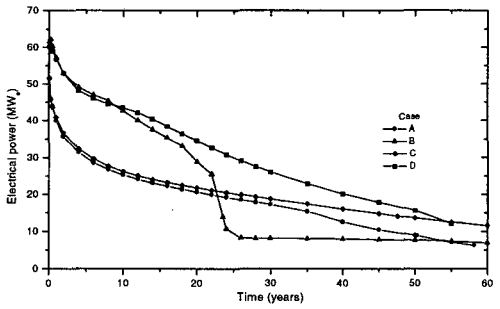

Figure 5. *Generated electrical power in reference cases with centrally located production wells and two phase initial condition.*

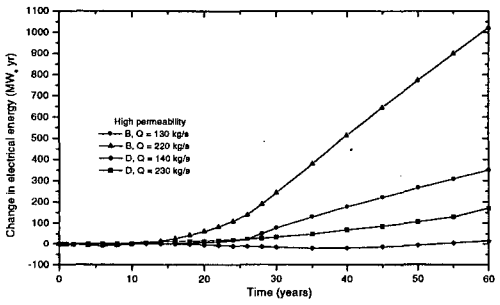

Figure 6. *Change in cumulative electrical energy compared to the reference case for two-phase system and dipole well pattern.*

Two-phase systems.

In the reference runs for the two-phase initial conditions fluid shortage occurs in the vicinity of the production wells in cases of high permeability. For the centrally located production wells this happens after about 22 years for 5% porosity and after about 55 years for 10% porosity. For the dipole pattern this occurs a few years later. When this occurs the pressure drops and so does the production and hence the electrical generation (Figure 5). However, this does not happen if reinjection is implemented which means that the benefits of reinjection often become evident only at late times for the two phase cases.

Benefits of the reinjection are not as obvious for the two-phase system as for the water dominated system. Over the 60 year production period the dipole and peripheral patterns show increased generating capacity and that the increase is achieved mainly after 20-30 years of production (Figure 6). In general the benefits are similar in magnitude for both the dipole and peripheral patterns, over a 60 year period, with the increase occurring slightly later for the peripheral pattern. Considering a longer production period the cumulative capacity of the peripheral pattern will be greater.

No gain in electrical generation is obtained for the intermixed reinjection pattern in the two-phase system. Early on the reason is that even though total flow rates are greatly increased that increase is accompanied by reduction in enthalpy so the usable steam rates at the separator are not increased and hence the electrical production remains unchanged. Later thermal breakthrough occurs and the heat mining diminishes from the vicinity of the production wells causing decreases in steam rates and even lower electrical production than for the reference cases without reinjection. For the intermixed pattern reinjection to the shallower part of the reservoir gave slightly better results, but overall the results were similar for the cases considered here.

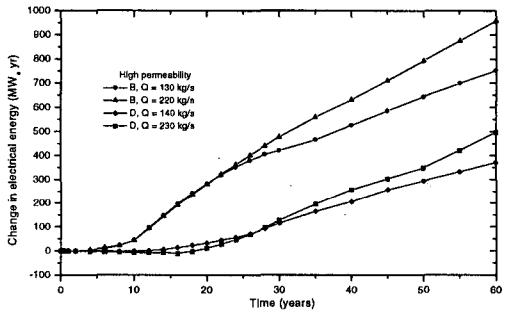

Figure 7. *Change in cumulative electrical energy compared to the reference case for vapor dominated system and peripheral well pattern.*

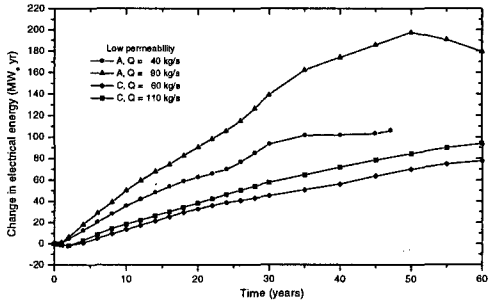

Figure 8. *Change in cumulative electrical energy compared to the reference case for vapor dominated system and with injection to the deeper layer in intermixed well pattern.*

Vapor dominated systems.

The initial conditions for the vapor dominated system was 70% steam saturation, the point at which water becomes immobile according to the relative permeabilities used. When production was initiated the steam saturation rose to nearly dry steam and pressure dropped. This occurred more rapidly for the higher permeability cases (B and D) resulting in fluid shortage around the production wells in 10-25 years and consequently declining production rates.

For the relatively high reinjection rates compared to the production rates in the reference cases the dipole and peripheral patterns gave slightly better results than the runs for the two-phase initial conditions (Figure 7). The increase in electrical generation is nearly identical for both the dipole and peripheral patterns and resembles the behaviour in the two-phase cases (see Fig. 6 and 7). Increased electrical generation is observed for most of the cases for the intermixed well pattern, especially during the earlier part of the production period. After a production history of about 30 years the gain in electrical capacity levels out and even starts to decline. Therefore, the total gain in electrical capacity for the intermixed well pattern becomes smaller than that for the dipole and peripheral patterns. For intermixed pattern reinjection into the deeper part of the reservoir has the advantage (Figure 8).

CONCLUSIONS

In general high enthalpy resources benefit from reinjection, but in situations where reservoirs have strong natural recharge reinjection may not be needed (Sigurdsson et al. 1995). The benefits to the resources are that they will not be limited by fluid reserves and therefore the productive life of the resource is increased in most cases. Better pressure maintenance is generally observed in the deeper part of the reservoir due to effects of gravity and density differences. Considerable time can pass before the reinjection contributes to the electrical generation depending on the conditions in the reservoir when reinjection is initiated

Of the producer/injector well patterns studied here, the dipole and peripheral patterns were advantageous over the intermixed pattern, giving similar results for a production period of 60 years. For those patterns the gain in high pressure steam flow and hence electrical generation was minimal during the first 20-30 years, but was increasing towards the end of the production period. Looking at other parameters as well as a longer time span, the peripheral pattern becomes the most favorable since it results in the best thermal sweep of the resources.

The results of this study cannot be used to decide whether it is better to aim the injection directly to the deeper parts of the reservoir. For the two-phase conditions it is not clear, but for both water dominated and vapor dominated conditions there are only indications that it is better to inject deep into the reservoir.

ACKNOWLEDGMENT

We thank the support of Hitaveita Reykjavikur for this work.

REFERENCES

Bodvarsson, G.S., Benson, S.M., Sigurdsson, O., Stefansson, V. and Eliasson, E.T. (1984a). The Krafla geothermal field, Iceland. 1. Analysis of well test data. *Water Resources Research*, Vol. 20(11), pp. 1515-1530.

Bodvarsson, G.S., Pruess, K., Stefansson, V., and Eliasson, E.T. (1984b). The Krafla geothermal field, Iceland. 2. The natural state of the system. *Water Resources Research*, Vol. 20(11), pp. 1531-1544.

Bodvarsson, G.S., Pruess, K., Stefansson, V., Bjornsson, S. and Ojiambo, S.B. (1985). A summary of modelling studies of the East Olkaria geothermal field, Kenya. *Geothermal Resources Council 1985 International Volume*, pp. 295-301.

Bodvarsson, G.S., Bjornsson, S., Gunnarsson, A., Gunnlaugsson, E., Sigurdsson, O., Stefansson, V. and Steingrimsson, B. (1990). The Nesjavellir geothermal field, Iceland. Part 1. Field characteristics and development of three-dimensional numerical model. *Geothermal Sci. and Tech.*, Vol. 2(3), pp. 189-228.

Pruess, K. (1986). *TOUGH User's Guide*. Lawrence Berkeley Laboratory, Earth Sciences Division, Berkeley, California. 85 p.

Sigurdsson, O., Arason, Þ., and Stefansson, V. (1995). Reinjection strategy for geothermal systems. *Proceedings of the World Geothermal Congress 1995*, Florence, Italy, 18-31 May 1995, Vol. 3, pp. 1967-1971.

HIGHER-ORDER DIFFERENCING FOR FRONT PROPAGATION IN GEOTHERMAL SYSTEMS

Curtis M. Oldenburg and Karsten Pruess

Earth Sciences Division
Berkeley Lab
Berkeley, CA, 94720

ABSTRACT

We have implemented higher-order differencing total variation diminishing (TVD) schemes into the reservoir simulator TOUGH2 to reduce numerical dispersion in concentration and phase front propagation problems. Much of the existing work in the literature on higher-order differencing schemes has focused on one-dimensional tracer transport using explicit formulations for the convection-dispersion equation. We find that higher-order differencing schemes can also increase the accuracy of component transport, phase transport, and thermal energy transport in strongly advective situations in two-dimensional problems using an implicit and multicomponent framework such as TOUGH2. We apply the Leonard TVD scheme to two geothermal reservoir engineering problems involving tracer transport and phase change. The first problem considers the two-dimensional transport of tracer in a reservoir under re-injection. In the second problem, we focus on the non-isothermal phase change occurring in a one-dimensional analog of a reservoir under re-injection. In both cases, the TVD scheme proves robust and useful for reducing numerical dispersion.

INTRODUCTION

The numerical simulation of the advection of phase and concentration fronts by finite difference methods in strongly advective flow systems is affected by numerical dispersion which tends to artificially smooth sharp fronts. This problem is especially relevant to geothermal reservoir engineering problems where strong advective flow of two-phase fluids occurs through fractures during fluid production and re-injection. Numerical dispersion can be diminished by decreasing grid size, but this can greatly increase execution times and computer memory requirements. Another approach for reducing numerical dispersion is to use higher-order differencing schemes instead of single-point upstream weighting.

In higher-order differencing schemes, two upstream gridblocks are used to approximate quantities such as phase saturation (or relative permeability), species concentration, and temperature at interfaces between gridblocks. In strongly advective problems and depending on the weighting scheme used, higher-order differencing can result in oscillatory and non-physical values near sharp fronts. These well-known problems have led to the development of total variation diminishing (TVD) higher-order schemes (e.g., Sweby, 1984). TVD refers to the overall variation of quantities in the system tending to diminish with time rather than increase.

In this paper, we present the theory of TVD schemes and their implementation in TOUGH2 (Pruess, 1987; Pruess, 1991) for two-dimensional regular grids, and we show results from two example applications of geothermal re-injection problems.

MATHEMATICAL DEVELOPMENT

Finite difference methods require an accurate approximation of interface quantities for calculating the fluxes between gridblocks. Below, we briefly review the development of higher-order differencing schemes for the propagation of phase and concentration fronts. We use the symbol S as the advected quantity, but we emphasize that in all of the development below S can stand for concentration, temperature, or relative permeability in addition to saturation. The mathematical development refers to the three gridblocks shown in Fig. 1 where the flow is from left to right as shown by the large arrow. We use fully implicit time-stepping with all quantities taken at the most recent iterative step.

We begin by writing a linear approximation for S at the $i+1/2$ interface as

$$S_{i+1/2} \approx S_i + D1\left(\frac{S_{i+1} - S_i}{D1 + D2}\right) \qquad (1)$$

which can be rearranged to

$$S_{i+1/2} \approx S_i + \frac{D1}{D1 + D2}\left(S_{i+1} - S_i\right) \qquad (2).$$

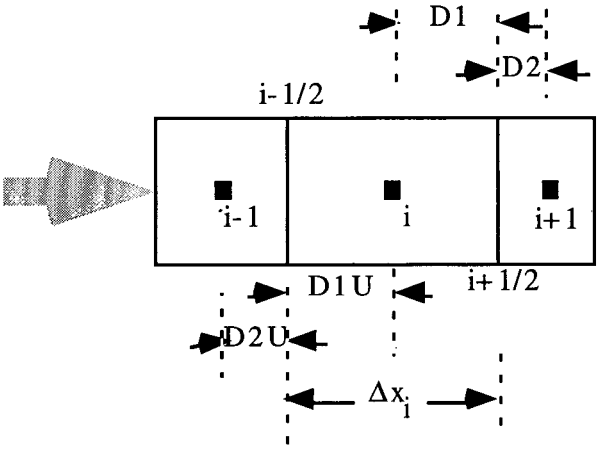

Fig. 1. Three non-uniform grid blocks with flow from left to right. The standard TOUGH2 connection is between i and i+1 and has connection distances $D1$ and $D2$ and an interface at i+1/2. Higher-order schemes use the upstream gridblock i-1 with connection distances $D1U$ and $D2U$ and the interface i-1/2.

Defining r, the ratio of upstream to downstream gradients, as follows,

$$r \equiv \frac{\left(\frac{\partial S}{\partial x}\right)_{i-1/2}}{\left(\frac{\partial S}{\partial x}\right)_{i+1/2}} = \left(\frac{\frac{S_i - S_{i-1}}{D1U + D2U}}{\frac{S_{i+1} - S_i}{D1 + D2}} \right) \qquad (3)$$

and rearranging to

$$r \equiv \frac{D1 + D2}{D1U + D2U} \left(\frac{S_i - S_{i-1}}{S_{i+1} - S_i} \right) \qquad (4),$$

we can propose that

$$S_{i+1/2} \approx S_i + \frac{D1}{D1 + D2} \phi(r)\left(S_{i+1} - S_i\right) \qquad (5).$$

Depending on the function $\Phi(r)$, different approximations for the interface quantity $S_{i+1/2}$ can be made (see Table 1). For example, if $\Phi(r) = 0$, the interface quantity is upstream weighted. If $\Phi(r) = 1$, a weighted average scheme results. For general $\Phi(r)$, limits (flux limiters) are imposed to make the scheme TVD. For the interface weighting scheme to be TVD, $\Phi(r)$ must fall on the heavy lines or within the shaded regions show in Fig. 2 (e.g., Sweby, 1984; Datta-Gupta *et al.*, 1991; Blunt and Rubin, 1992).

Table 1. Higher-order differencing schemes.

$\Phi(r)$	interface approximation
0	full upstream weighting
1	weighted average
r	two-point upstream
$\frac{(r+\lvert r\rvert)}{(1+r)}$	Van Leer scheme
$2/3 + r/3$	Leonard scheme

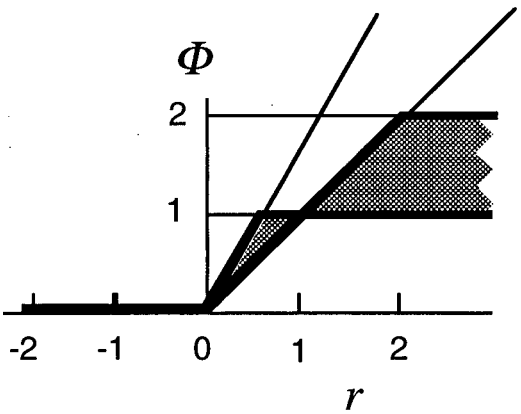

Fig. 2. The heavy lines and shaded regions show the stable values of $\Phi(r)$.

The flux limiter is applied to ensure a decrease in the total variation (TV) of the advected quantity defined as

$$TV(S)^{n+1} \equiv \sum_i \left| S_{i+1}^{n+1} - S_i^{n+1} \right| \qquad (6)$$

where n denotes the time level and the sum runs over all gridblocks i. Thus, as Eq. 6 shows, for a typical front propagation problem, the total variation will increase whenever there are jumps or oscillations in the advected quantity, S. We emphasize again that all of the development above can just as well be written for concentration, temperature, or relative permeability and equivalent weighting schemes derived for many flow situations.

We implemented higher-order differencing schemes in TOUGH2 with the restriction that the grids must be either one or two-dimensional with rectangular gridblocks. Within a TOUGH2 simulation, using higher-order TVD schemes entails finding the two upstream gridblocks, assuming locally one-dimensional flow, calculating $\Phi(r)$, applying the limiters to ensure $\Phi(r)$ is in a stable region of Fig. 2, and approximating interface values of phase saturation, relative permeability, concentration, or temperature accordingly. The Leonard scheme (LTVD) where $\Phi(r) = 2/3 + r/3$ subject to the limiters shown in Fig. 2 has proven robust and accurate (Leonard,

1984; Datta-Gupta *et al.*, 1991; Oldenburg and Pruess, 1997; Oldenburg and Pruess, 1998) and will be applied further in the remainder of this paper.

EXAMPLE APPLICATIONS

Tracer Injection

Here we compare upstream weighting and the LTVD scheme in TOUGH2/EOS7R for a test case involving injection and production from a two-dimensional sub-horizontal fracture zone. Problem specifications are similar to a production/injection problem previously studied by Pruess (1983) and Pruess and Wu (1993). Shown in Fig. 3 are the production and injection wells arranged in a five-spot pattern with 400 m well spacing. Cold water (T ≈ 30 °C) is injected at a rate of 16 kg/s (full-well basis), and production occurs at the same rate. Four kg of tracer is injected over a period of 10 days starting at $t = 0$. We model one quarter of the five-spot pattern, which was discretized into 400 square grid blocks (20 x 20) of length 10 m on a side.

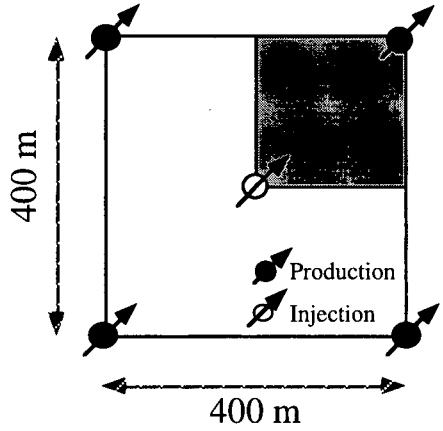

Fig. 3. Five-spot well pattern, with shading showing a 1/4 symmetry element.

The reservoir rock adjacent to the fracture zone is assumed impermeable, and at a uniform initial temperature of 300 °C. Conductive heat transfer to the fracture is modeled with the semi-analytical technique of Vinsome and Westerveld (1980). Boiling occurs near the production well as pressure declines, while cooling occurs near the injection well due to the injection of cold water. We use the module EOS7R (Oldenburg and Pruess, 1995) for components water, brine, tracer1, tracer2, air, and heat. For this preliminary application, the tracer is the brine component which is non-sorbing, non-decaying, and non-volatilizing although EOS7R is capable of handling all of these processes for the tracer1 and tracer2 components. Complete parameters for the problem are presented in Oldenburg and Pruess, 1997.

Results after 6 months computed using upstream weighting for phase saturations, component mass fractions, and thermal energy are shown in Fig. 4. The temperature field shows the effects of cold injection fluid entering the system but being retarded by conductive heating from the reservoir rocks. The tracer mass fraction field is advanced relative to heat since no retarding effects (e.g., adsorption) are present for the tracer. The saturation field shows the development of a two-phase region due to lower pressure at the production well. The final plot gives breakthrough curves of temperature and tracer mass fraction at the production well. Initial tracer breakthrough occurs at about 6 months ($t \approx 1.6 \times 10^7$ s). The retardation of the thermal front is largely masked by cooling due to boiling at the production well. In the absence of induced boiling, thermal breakthrough would be retarded by a factor of

$$R = \frac{\phi\, \rho_w\, c_w}{\phi\, \rho_w\, c_w + (1 - \phi)\, \rho_R\, c_R} \approx .55 \qquad (7)$$

where ρ_w = 800 kg m^{-3} and c_w = 4000 J kg^{-1} °C^{-1}. Note the broad region of tracer in the mass fraction plot and the gentle rise and decline of the tracer mass fraction in the breakthrough curve; these smoothing effects are due mostly to numerical dispersion.

Results after 6 months computed using the LTVD scheme for phase saturations, component mass fractions, and thermal energy are presented in Fig. 5. Comparing Figs. 4 and 5 we see generally similar results; however, note the relatively sharper fronts for temperature and especially tracer mass fraction. The phase saturation front has evolved differently using LTVD and is not as far advanced (see next application for discussion). The breakthrough curves highlight the differences in the schemes. Note the higher maximum and steeper limbs of the tracer breakthrough. Tracer would first be detected at significant concentrations after about 9 months. This sharper tracer breakthrough curve would allow a more accurate prediction of the arrival of the thermal front than the result computed using upstream weighting.

The adaptive time-stepping scheme in TOUGH2 is apparent from the symbol spacing in the breakthrough curves in Figs. 4 and 5 which show that more time steps are needed when using the higher-order scheme. Shorter time steps arise in this problem for two reasons: (1) the sharper front produces larger primary variable changes in grid blocks near the front; and (2) we did not include the dependence of the upstream grid block into the Jacobian matrix for the Newton-Raphson iteration. Because the Jacobian is less accurate, the convergence rate is reduced and the time-step size remains smaller than it would for a more accurate Jacobian matrix.

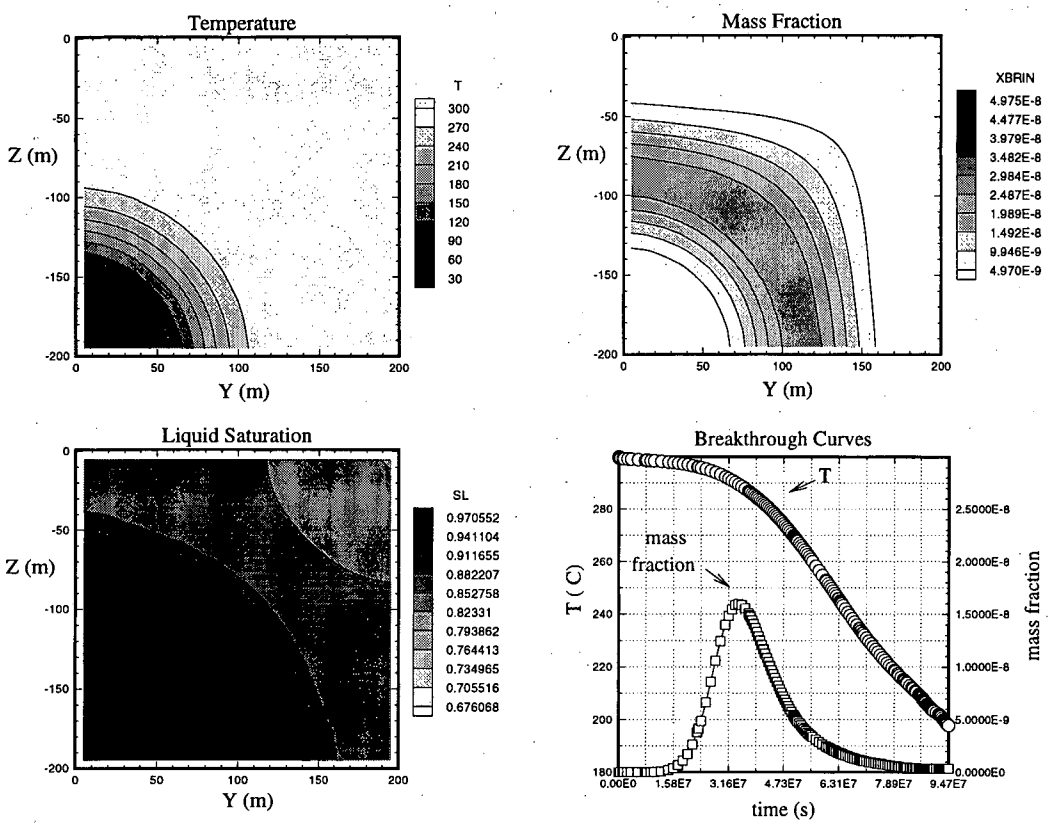

Fig. 4. Results at six months calculated using upstream weighting for two-dimensional geothermal re-injection.

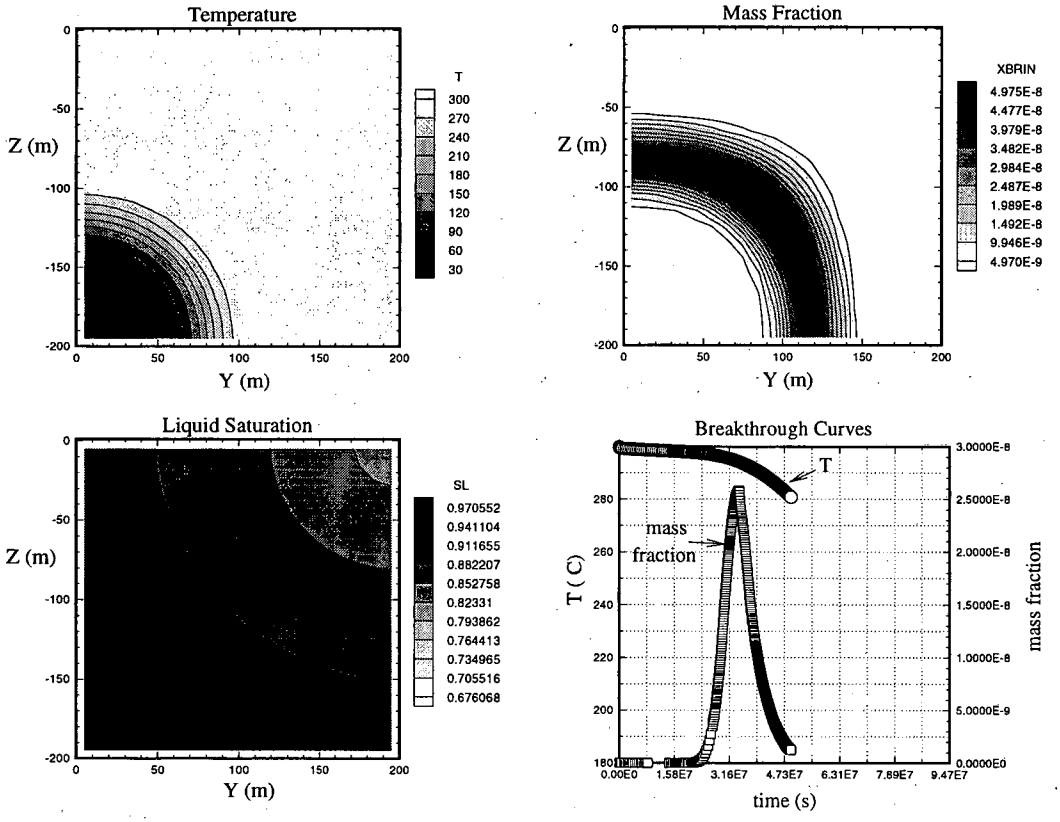

Fig. 5. Results at six months calculated using the LTVD scheme for geothermal re-injection. The run was stopped after the tail of the tracer pulse was detected.

Boiling Front

In this problem, cold ($T = 30°C$) water is injected into a 200 m long one-dimensional domain. The system is initially nearly single-phase liquid at the saturated vapor pressure ($P_0 = 85.93$ bar) at $T_0 = 300$ °C. A schematic of the system and initial and boundary conditions are shown in Fig. 6. Capillarity is neglected, and relative permeability is given by Corey curves. Complete parameters for the problem are presented in Oldenburg and Pruess, 1998.

The evolution begins by injecting cold water at the left-hand side at a rate of 0.4 kg/s and producing mass at the same rate from the right-hand side. The production at the right-hand side lowers the pressure and induces boiling while the cold injection water tends to produce single-phase liquid conditions. The boiling at the right-hand side causes the liquid saturations to decline from the initial conditions. Thus the difference in liquid phase saturation across the moving front increases with time making this problem physically not TVD.

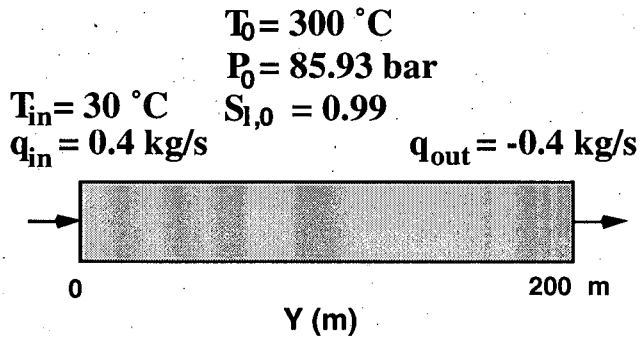

Fig. 6. Boundary and initial conditions for the one-dimensional injection and production problem.

Profiles of liquid saturation and temperature for upstream weighting and LTVD differencing schemes with 100 gridblocks are shown in Figs. 7 and 8, respectively. The temperature profiles are shown by the dashed curves while the saturation is given by the solid curves; the temperature and saturation curves intersect in the figures at the phase front. Note in Figs. 7 and 8 that the upstream-weighted results give a phase front that is farther advanced relative to the LTVD result.

Unlike typical phase displacement problems which show minimal differences whether computed by upstream weighting or by higher-order schemes, the phase front locations in this problem are significantly different in the upstream and LTVD cases. The advancement of the upstream weighted phase front relative to the LTVD phase front occurs because upstream weighting produces greater smearing of the

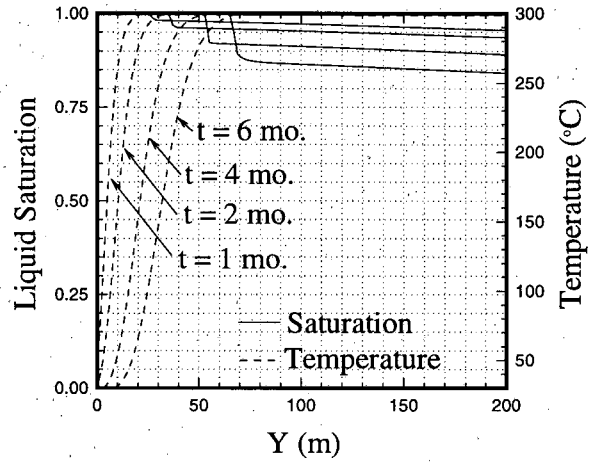

Fig. 7. Liquid saturation and temperature for the geothermal injection and production problem with upstream weighting.

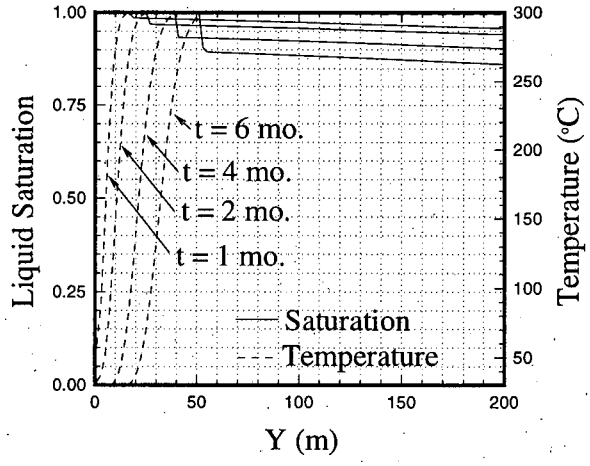

Fig. 8. Liquid saturation and temperature for the geothermal injection and production problem with LTVD scheme.

temperature front, so that saturation temperature at prevailing pressures is reached at somewhat larger distance from the injection point. The phase transition to two-phase conditions then also occurs at larger distance. In addition to the upstream and TVD-weighted simulations shown in Figs. 7 and 8, a third simulation not shown here was performed in which TVD-weighting was applied only to interface temperatures, while phase saturations were upstream-weighted. This produced results very close to those of Fig. 8, confirming that it is the numerical

dispersion of the temperature front, not that of the phase front, which causes the upstream-weighted results in Fig. 7 to deviate from the more accurate LTVD results of Fig. 8. This same phenomenon was seen in the two-dimensional example shown in the previous section.

The differences between the uptream and LTVD schemes diminish with increased resolution. We show in Fig. 9 a summary of the results of phase front location vs. number of gridblocks at a time of 6 months for this one-dimensional injection and production problem. Note in Fig. 9 that the two schemes are converging slowly but that the LTVD scheme was closer to the grid-converged result at much coarser resolution. When upstream weighting is used, numerical dispersion is proportional to ΔY (the grid spacing), and therefore diminshes slowly when grids are refined. Note finally that the fact that the saturation variation increases with time (i.e., was not TVD) posed no problem for the LTVD scheme.

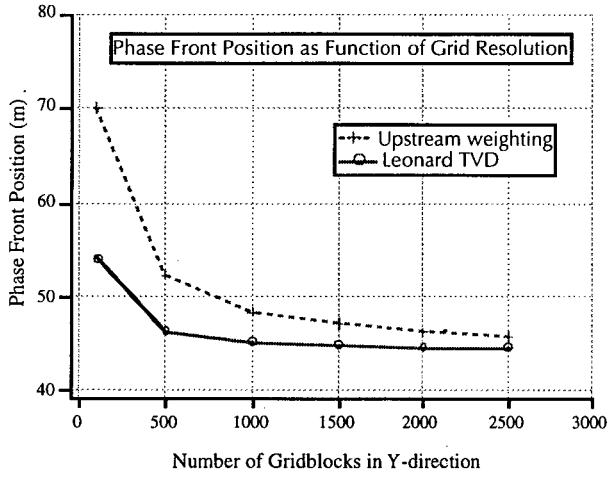

Fig. 9. Phase front location vs. grid resolution for upstream weighting and LTVD schemes at $t = 6$ months.

CONCLUSIONS

The LTVD scheme significantly reduces numerical dispersion of fronts relative to upstream weighting. The LTVD scheme has performed well on a variety of complicated problems relevant to geothermal reservoir engineering. We anticipate making available a choice of higher-order total-variation diminishing schemes in future releases of TOUGH2.

ACKNOWLEDGMENT

We thank Jens Birkhölzer and Tianfu Xu for reviews. This work was supported by the Assistant Secretary for Energy Efficiency and Renewable Energy, Geothermal Division, U.S. Department of Energy, under contract No. DE-AC03-76SF00098.

REFERENCES

Blunt, M., and B. Rubin, Implicit flux limiting schemes for petroleum reservoir simulation, *J. Comput. Physics, 102*, 194–210, 1992.

Datta-Gupta, A., L.W. Lake, G. A. Pope, and K. Sepehnoori, High-resolution monotonic schemes for reservoir fluid flow simulation, *In Situ, 15*(3), 289–317, 1991.

Leonard, B.P., Third-order upwinding as a rational basis for compuational fluid dynamics, in *Computational Techniques and Applications*, Elsevier Science Publishers, North-Holland, 1984.

Oldenburg, C.M. and K. Pruess, EOS7R: radionuclide transport for TOUGH2, Lawrence Berkeley Ntaional Laboratory Report *LBL-34868*, November, 1995.

Oldenburg, C.M. and K. Pruess, Mixing with first-order decay in variable-velocity porous media flow, *Transport in Porous Media, 22*, 161–180, 1996.

Oldenburg, C.M. and K. Pruess, Higher-order differencing for geothermal reservoir simulation, Proc. 22nd Workshop on Geothermal Reservoir Engineering, Stanford University, Stanford CA, January 27–29, 1997. SGP-TR-155

Oldenburg, C.M. and K. Pruess, Higher-order differencing for phase-front propagation in geothermal systems, Proc. 23rd Workshop on Geothermal Reservoir Engineering, Stanford University, Stanford CA, January 26–28, 1998. SGP-TR-158.

Pruess, K., TOUGH User's Guide, *Nuclear Regulatory Commission, Report NUREG/CR-4645*, June 1987 (also *Lawrence Berkeley Laboratory Report, LBL-20700*, June 1987).

Pruess, K., TOUGH2- A general-purpose numerical simulator for multiphase fluid and heat flow, *Lawrence Berkeley National Laboratory Report LBL-29400*, May 1991.

Pruess, K., and Y.-S. Wu, A new semi-analytical method for numerical simulation of fluid and heat flow in fractured reservoirs, *SPE Advanced Technology Series, 1*(2), 63–72, 1993.

Sweby, P.K., High resolution schemes using flux limiters for hyperbolic conservation laws, *SIAM J. Numer. Anal., 21*(5), 995–1011, 1984.

Vinsome, P. K. W. and J. Westerveld. A Simple Method for Predicting Cap and Base Rock Heat Losses in Thermal Reservoir Simulators, *J. Canadian Pet. Tech.*, 19 (3), 87–90, July-September 1980.

FITH2 A SET OF FORTRAN INTERFACES TO PROCESS TOUGH2 INFORMATION, DATA AND RESULTS

Mario-César Suárez Arriaga[1] and Fernando Samaniego Verduzco[2]

[1] UNAM, UMSNH & CFE, e-mail: msuarez@zeus.ccu.umich.mx
[2] UNAM & PEMEX, e-mail: fsv@chall.fi-p.unam.mx

ABSTRACT

Graphic presentation of numerical results, mesh build up and basic data pre-processing are activities routinely carried out in geothermal reservoir simulations. To face this problem in a systematic way, we have developed FITH2 (Fortran Interfaces to process TOUGH2 information), a set of FORTRAN programs having the capabilities to pre-process the data required by TOUGH2 and to post-process its numerical results. FITH2 is external to TOUGH2; not forming part of its original architecture, it performs several useful actions. FITH2 is able to create meshes of simple geometry, including boundaries; it can interpolate thermodynamic and petrophysical variables, assigning values to every element in the mesh. It uses Tchebyschev polynomials for simple spatial interpolation, or universal kriging for estimating non-stationary parameters. This program generates grids and calculates 3D coordinates of every center and nodal point conforming the elements. These are fundamental operations because in this way, many geometric theorems could be applied to the mesh in vectorial form, transforming the original grid as desired. F ITH2 creates ASCII files ready to be included in any graphic commercial software to produce attractive presentations of great visual quality. Another important option is that FITH2 is able to interact with *Mathematica* system for analyzing and plotting TOUGH2 results. In this graphic atmosphere partial or final outcomes can be quickly visualized, in the form of contours and three-dimensional surfaces. It is also possible to create animations or virtual motions of those surfaces in order to see the evolution of the reservoir thermodynamic properties. All this work can be done in a 486 or Pentium PC, 16 Mb RAM and enough free disk space.

INTRODUCTION

TOUGH2 (Pruess, 1991) contains technical and scientific knowledge needful to model and study the behavior of hydrothermal reservoirs. But data processing and presentation of numerical outcomes obtained from simulations are problems not still solved in a general way. In a typical geothermal project, the basic conceptual model data, as well as the results produced by the code, should be seen on a summarized manner by a wide variety of individuals: scientists, technicians, officials, investors and politicians. That is why it is very important to introduce this information in a clear and precise way and at the same time in an elegant, convincing and simple form. The enormous volume of typical numeric columns of simulation outcomes, could be simple, evident and routinely read by the expert, but it does not produce the same effect on the general public.

An expensive and long term solution is the creation of specific software to visualize the information required by TOUGH2 and the corresponding numerical results. But it is difficult to develop a good graphic software and it takes too much time to arrive at the degree of specialization required by TOUGH2, e.g. Sato et al. (1995), Sullivan (1995), GeoCad (1996), Hardeman & Swenson (1998). In the international market there are graphic software able to make great quality graphics in 2 and 3 dimensions, although not related to this code. Such commercial software can be easily coupled to TOUGH2, by developing FORTRAN interfaces to read initial data, final results and to write compatible ASCII files.

On the other hand, TOUGH2 needs continuous spatial distribution of reservoir parameters. Optimum spatial interpolation of geothermal measurements is also necessary for the approximated calculation of non-measured parameters. We introduce a practical, general methodology covering the aforementioned aspects. The origin of the program described herein, was inspired by the first version of a subroutine created by K. Pruess in 1987 to build MESH file automatically which was included in one of the old versions of MULKOM, and corresponds to the present 'XYZ' option in the MESHMAKER module (Pruess, 1991).

BRIEF DESCRIPTION OF FITH2

The program FITH2 is a code written in FORTRAN-77, externally coupled to TOUGH2 through files MESH, INCON and OUTPUT. It is planned as an integrated software system, with a main reading data program and control of options. It is formed by 6 subroutines: MXYZG3, TRANSF2, TCHEBY3, IRFk2, GRAFEL2 and MALLAF3. The first subroutine creates the mesh; the second modifies the grid plane by plane, by means of three optional rigid transformations; the third and fourth subroutines interpolate data and provide estimations of non-measured parameters. Those four subroutines can create the MESH and INCON files required by TOUGH2 (Pruess, 1987). The last two subroutines read the simulation outcomes and generate ASCII files ready to be used by any graphic commercial software.

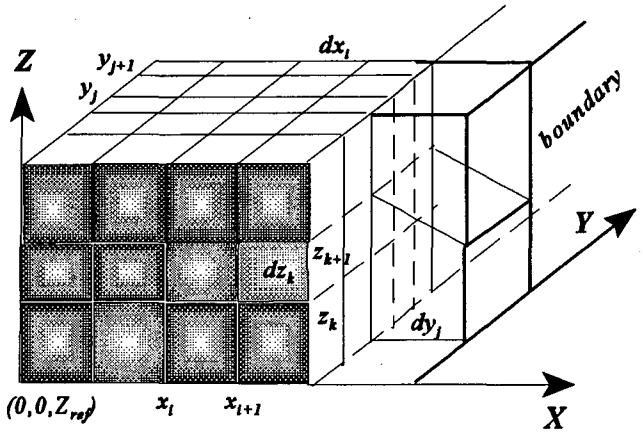

Fig. 1.- A mesh with boundaries created by MXYZG3

At each plane Z, FITH2 creates rectangular elements inside the mesh and rectangles or trapeziums as boundary elements (Fig. 1). These shapes suffice to represent the majority of geothermal reservoir geometries observed in Mexico. Certainly this basic mesh could be modified later on by hand in order to characterize local or regional details of great complexity. FITH2 is neither an expert system nor totally automatic. It requires human judgements and the constant interaction with the user.

FITH2 is open to future innovations and changes. This is an ongoing work in process. The different modules of FITH2 are coupled to TOUGH2 interacting in several ways. General interaction and coupling are illustrated in figure 2.

DESCRIPTION OF THE SUBROUTINES

FITH2.FOR- Is the main program that requests initial information, reading options and calling subroutines in the order wanted by the user. This is still an experimental version and is not documented enough.

MXYZG3- Is the main subroutine, its functions are to build up the mesh starting from few data and to calculate all the coordinates of the elements. It has two initial options: The first one uses a pre-existent file containing basic grid information, the same way as MESHMAKER does. The second option can calculate the whole mesh using only the coordinates of the producing and injection wells, and constructing one element per well. It also requires reservoir's long and width. If the second choice is used the primary distances $dx_i = (x_{i+1} - x_i)$, $dy_j = (y_{j+1} - y_j)$ are calculated at each stratum $dz_k = (z_{k+1} - z_k)$ (Fig. 1).

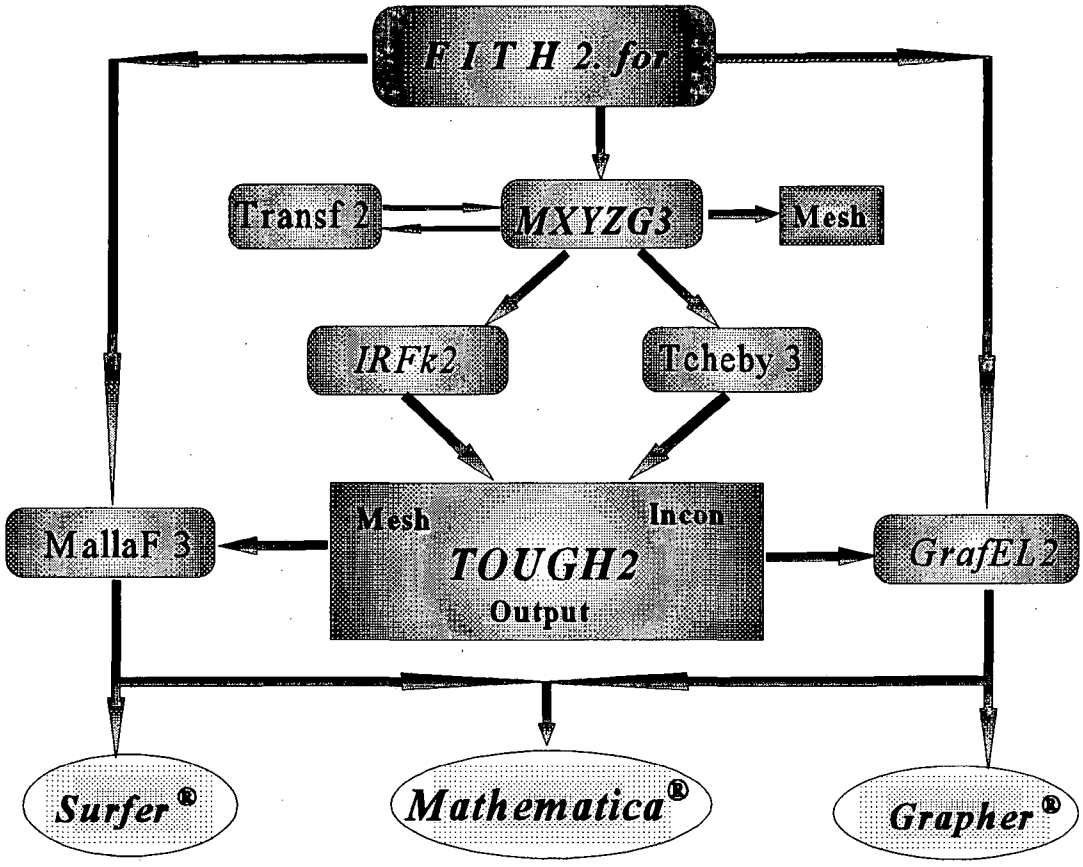

Figure 2.- **Interactions between FITH2 and TOUGH2**

Once defined the basic distances in the three axes (X, Y, Z) the code calculates 3D coordinates of all nodal points conforming the mesh, determines the centers of all the elements and makes user/machine interactive calculations to construct the boundary elements, including the possibility of building blocks of bigger size connected to two or more reservoir elements. Vertical coordinates are referred to a Z_{ref} reference level defined by the user. For example, $Z_{ref} = 0$ means that the deepest reservoir stratum is at sea level. The absolute grid origin corresponds to (0, 0, Z_{ref}), where (0, 0) is the starting point from which the first distance (dx_1, dy_1) is measured. Coordinates calculation for each nodal point in the mesh follows the next algorithm (MARCE-1):

```
k = 0, NZ
      j = k* (NY + 1), (k + 1)* NY + k
            i = j* (NX + 1), (j + 1) *NX + j
            X_i = X_0                      (If i ≤ NX)
            X_i = X(i - NX - 1)            (If i > NX)
            X_0 = X_0 + d X_(i+1)
      Y_i = Y_0                            (If j ≤ NY)
      Y_i = Y(i- (NY+1) *NX - NY-1)        (if j > NY)
      Y_0 = Y_0 + dY_(j+1)
Z_i = Z_0
Z_0 = Z_0 + d Z_(k+1)
```

The geometric center of each element (XC_i, YC_i, ZC_i) is calculated with a slightly different algorithm. (MARCE-2):

```
k = 1, NZ
      j = (k - 1)* NY + 1, k* NY
            i = (j - 1)* NX + 1, j* NX
            XC_i = X_0 + dX_i / 2          (if i ≤ NX)
            XC_i = XC (i -NX)              (if i > NX)
            X_0 = X_0 + dX_i
      YC_i = Y_0 + dY_j / 2                (if j ≤ NY)
      YC_i = YC(i - NY*NX)                 (If j > NY)
      Y_0 = Y_0 + dY_j
ZC_i = Z_0 + dZ_k / 2
Z_0 = Z_0 + dZ_k
```

NX, NY and NZ are the number of distances d_N in each one of the axes respectively. The next actions are to give a name to every element, to calculate areas, distances between connections and volumes. These operations are similar to those performed by MESHMAKER (Pruess, 1987). It is also possible to assign each element to different rock pre-defined types, for example as function of depth, lithology, fault's elements or fractured zones with high permeability.

After introducing the total number of boundary elements connected to the mesh, euclidean distances between centers of boundary blocks and interior elements are calculated:

$$d(\vec{C}_F, \vec{E}_i) = \sqrt{(C_X - X_i)^2 + (C_Y - Y_i)^2 + (C_Z - Z_i)^2} \qquad (1)$$

(C_X, C_Y, C_Z) are the coordinates of the geometric center of the boundary block and (X_i, Y_i, Z_i) are the coordinates of the element interface.

TRANSF2- This subroutine interacts directly with MXYZG3 and is used to transform the mesh. It only carries out two-dimensional rigid transformations. At each plane Z= constant, it can make (Figs. 3 & 4):

a).- Transfers $T(\vec{P}) = \vec{OP} + \vec{v}$; $\forall$ *vector* $\vec{v}$, $\vec{OP} = (x, y)$,
b).- Rotations around axis X: $R(\vec{P}) = x\vec{U} + y\vec{U}^{\perp}$,
c).- Reflections with respect to L: $F(\vec{P}) = x\vec{U} - y\vec{U}^{\perp}$
where vector: $\vec{U} = (u_1, u_2)$, $\vec{U}^{\perp} = (-u_2, u_1)$,

$$\| T, R, F(\vec{P} - \vec{Q}) \| = \| \vec{P} - \vec{Q} \| \qquad (2)$$

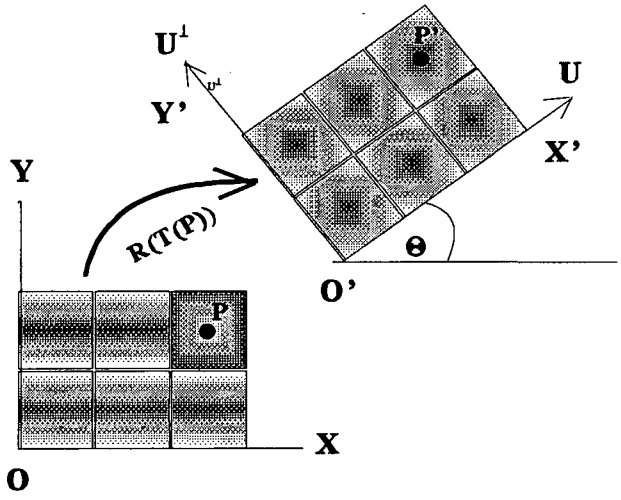

Fig.3.- Transfer & rotation performed by Transf2

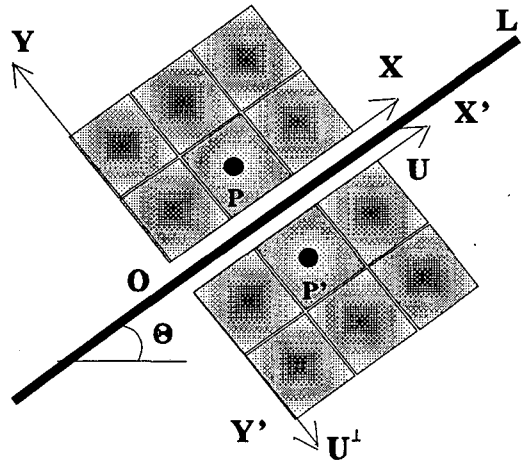

Fig. 4.- Reflection of the mesh around line L

This last transformation is equal to a 180° rotation of the plane containing the OP vector, around line L. This subroutine is useful when the user wants to test several effects produced by different mesh orientations, or to create fictitious wells in order to simulate boundary effects such as natural recharge and/or discharge.

TCHEBY3.- This subroutine interpolates in one, two or three dimensions, considering Tchebyschev polynomials $\{T_m(t)\}$ as the interpolation basis. It is well known that for a high degree of the basis involving powers of order greater than 6, simple polynomials oscillate producing numerical instability. The use of Tchebyschev polynomials avoids this problem. In 1D, these functions are defined by the recurrent relationship (Legras, 1971): $T_{m+1}(t) - 2t\,T_m(t) + T_{m-1}(t) = 0$, with the initial values $T_0(t) = 1$, $T_1(t) = t$. If we know m of its values, any function f (t) is thus interpolated by:

$$f_m(t) \approx \sum_{j=0}^{m} c_j T_j(t) \; ; \quad \forall\, t \; real: \qquad (3)$$
$$-1 \le t \le 1 \; ; \; t = \cos\theta : \; T_m(t) = \cos(m\theta)$$

To contain any real value of t inside the interval [-1, +1] the following change of variable is made:

$$\tau = \frac{a+b}{2} + \frac{b-a}{2}t \;\Rightarrow\; t = \frac{2\tau - a - b}{b-a} \qquad (4)$$
$$Obviously\ in\ all\ cases: \; -1 \le T_m(t) \le +1$$

This last property is responsible for the stable calculations provided by Tchebyschev polynomials. Tcheby3 can also perform least squares approximations in 1, 2 or 3 dimensions:

$$f(\vec{r}) \approx \sum_{j=0}^{N} c_j b_j(\vec{r}) \; ; \quad \forall\, \vec{r} = (x, y, z) \qquad (5)$$
$$b_j(\vec{r}) = T_p(x)\, T_q(y)\, T_r(z) \, , \; \forall\, p, q, r = 0, 1, 2, \ldots, N$$

Where N is the number of basis functions. If n samples are known, the unknown coefficients c_j are solution of the system:

$$\sum_{k=0}^{N} c_k \langle b_k, b_j \rangle = \langle f, b_j \rangle \; ; \quad j = 0, n \qquad (6)$$
$$\langle b_k, b_j \rangle = \sum_{i=0}^{n} b_k(\vec{r}_i)\, b_j(\vec{r}_i) \, , \; \langle f, b_j \rangle = \sum_{i=0}^{n} f(\vec{r}_i)\, b_j(\vec{r}_i)$$

We have used this technique to solve several practical geothermal reservoir engineering problems: interpolation and extrapolation of petrophysical parameters, forecast models for injection/extraction rates, efficient low degree polynomials for the calculation of thermodynamic properties of single phase or two-phase water, integration of very irregular functions, e.g. total fluid rate during several years of production/reinjection history (Suárez, 1985). An integration algorithm based on Tchebyschev polynomials is straightforward and powerful. Any real function can be integrated approximatelly by the following formula (Suárez, 1984):

$$\int_a^b f(x)\, dx \approx \frac{b-a}{n+1} \sum_{j=0}^{Na} \tau_j f_j \qquad (7)$$
$$f_j = f\left(\frac{a+b}{2} + \frac{b-a}{2} y_j \right) \; ; \; y_j = \cos\left(\frac{2j+1}{2n+2} \pi \right)$$
$$\tau_j = 1 + 2 \sum_{k=1}^{n/2} \frac{T_{2k}(y_j)}{1 - 4j^2} \; ; \; T_{k+1}(y_j) = 2 y_j T_k(y_j) - T_{k-1}(y_j)$$

T_k are Tchebyschev polynomials, a and b can be any real numbers, even equal to $-\infty$ or $+\infty$, *Na* is the order of the approximation. Tcheby3 can call internally a real function TI performing the integration defined by (7). Figure 5 shows an application of this method.

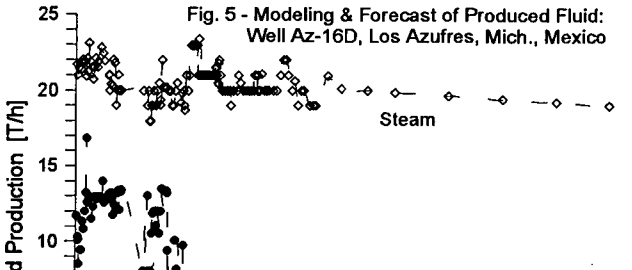

IRFk2- This subroutine uses a technique of non-stationary kriging, based on the theory of intrinsic random functions of order k > 0 (Matheron, 1973), in order to perform optimum interpolation, estimate non-measured parameters and assign values to all the elements in the mesh. It is particularly useful in the spatial modeling of geothermal variables with drift (Suárez & Samaniego, 1998). IRFk2 solves the non-stationary kriging system , also known as universal kriging:

$$P_0 \approx L(P_0) = \sum_{i=1}^{n} \beta_i P_i \, , \; n \le N$$
$$\sum_{i=1}^{n} \beta_i K_{ij} + \sum_{l=1}^{m_k} \mu_l b_l^j = K_{0j} \qquad (8)$$
$$\sum_{i=1}^{n} \beta_i b_j^i = b_j^0 \quad , \quad j = 1, n$$

Where $L(P_0)$ is an optimum linear estimator of any unknown parameter P_0 in the reservoir; β_i are unknown coefficients in the linear estimation of P_0; $b_j^l = b_j(\mathbf{r}_l)$ are polynomial basis functions, $\mathbf{r}_l=(x_l, y_l, z_l, t)$ is a cartesian position vector at time t of sample P_i, μ_l are the classical lagrange multipliers; $K_{ij} = K(\mathbf{r}_j - \mathbf{r}_i)$ is a generalized covariance measuring the spatial correlation between random variables R at $\mathbf{r}_i$, $\mathbf{r}_j$. This portion of the code could pre-process all parameters required by TOUGH2: density, porosity, thermal conductivity, permeability, rock specific heat, pressure, temperature, etc. Also provides an estimate of the uncertainties at every interpolated parameter, through the variance σ^2 of the kriging error:

$$\sigma^2 = \sum_{i=1}^{n} \sum_{j=1}^{n} (\beta_i \beta_j K_{ij} - 2\beta_i K_{i0}) + K_{00} \qquad (9)$$

Table 1 shows estimations of spatial distribution of porosity using this technique. The values were measured at wells of the Los Azufres, México geothermal field. The corresponding generalized covariance for these data is:

$$\vec{h} = \vec{r}_j - \vec{r}_i \Rightarrow K(\vec{h}) = 32.5630\ \delta(\vec{h}) + 0.23474\ 10^{-8}\ |\vec{h}|^3$$

Table 1.- Estimation of Porosity by Point kriging

X	Z	Φ_0	$L(\Phi_0)$	σ^2
3987.30	2900.00	22.7	22.70	-0.3211E-05
2369.50	3004.50	16.7	16.70	0.8326E-06
2389.50	3014.50	?	15.20	0.8631E+01
2422.10	2865.00	11.7	11.70	-0.3871E-05
2432.10	2865.00	?	11.86	0.4041E+01
1793.10	2730.00	7.1	7.10	-0.4480E-05
1803.10	2730.00	?	9.73	0.3951E+01
3100.00	2600.00	?	6.23	0.7847E+02
111.20	2654.00	1.4	1.40	-0.2227E-06
201.20	2744.00	?	42.03	0.5913E+03

GRAFEL2- This subroutine processes the OUTPUT file to plot TOUGH2 results in the form: variable vs. time. Variable could be pressure, temperature, steam saturation, etc. This part of the code separates the outcomes of every selected element in chronological order, generating one ASCII file per each element to be plotted. The format of these files is totally compatible with graphic commercial software. GrafEL2 could even generate its own graphs through the graphic subroutines built in the FORTRAN compiler. The program reads the names of the chosen elements in an auxiliary file. Then opens the OUTPUT file and reads it sequentially looking for several key words. The first one is **MESH**, where it reads the total number of elements and begins to count the simulation time steps. The next key word is **TOTAL TIME**. Here it reads: SUMTIM. Then finds all the **ELEMk** elements to be plotted, reading: ELE, N, PNE, TNE, SNE, etc. The next key word is **ELEMENT SOURCE**, reading the data to plot fluid rates and enthalpies: eleh(k), well, NP, Qf, hf (k). Finallly it writes the properties in columns, as functions of time with the format: write (k, '(6F8.2, 2x, a5)') ST(NT), P(k)/ 1.e5, T(k), S(k)*100., P2(k)/1.e5, hf(k)/1.e3, eleh(k). The iteration ends when the reading operation finds "**END OF TOUGH**" or "**WRITE FILE**". Figure 6 shows an example.

Fig. 6.- Pressure Evolution at Well Az-04, Los Azufres, Mexico

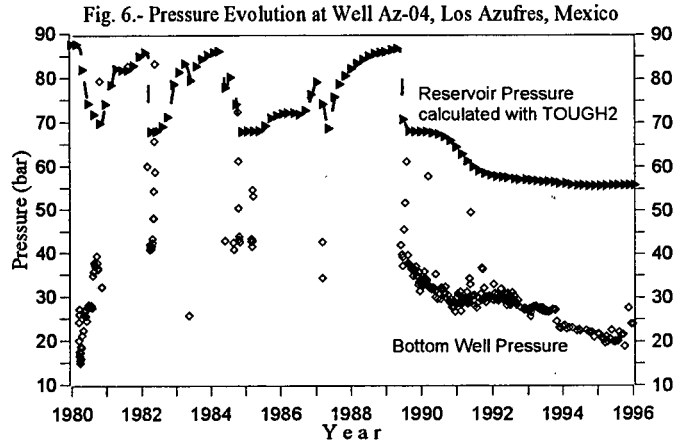

MALLAF3- Reads the final or partial results of TOUGH2 and generates compatible ASCII files to draw 2D contours and 3D surfaces of high visual quality, to include them in final reports or for public presentations. This subroutine reads the mesh data in the file created by MXYZG3: elem(k), ie(k), x(k), y(k), z(k). The code reads sequentially the OUTPUT file looking for different key words. The first one is "**ELEM**", then it reads the same lines as in GrafEL2. A corresponding ASCII file is written following the format: write(1,5050) elem(k), ie(k), x(k), y(k), z(k), PNE/1.e5, TNE, SNE*100. This file is compatible with SURFER® (1995) software. Contours of steam saturation at Los Azufres reservoir were obtained with this part of the code (Fig. 7).

Fig. 7.- Steam Saturation Distribution at 1750 masl Los Azufres, Mexico geothermal reservoir.

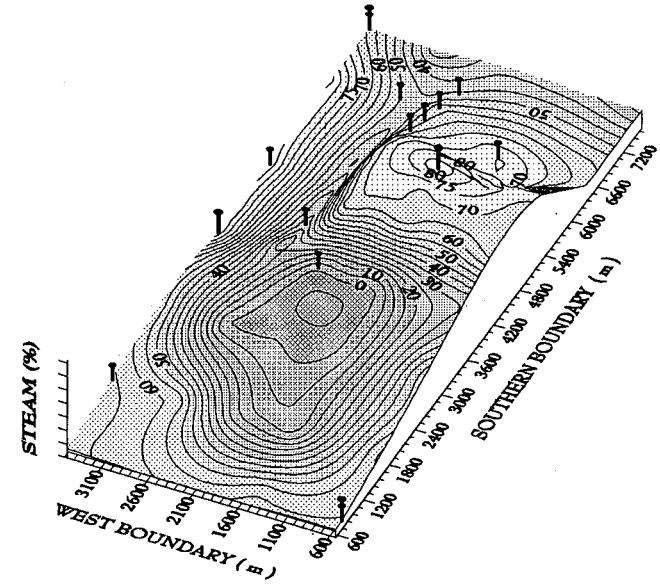

Interfacing with *Mathematica*

Mathematica (Wolfram, 1992), is a commercial software defined as a completely integrated system and general computer language capable to perform symbolic, numerical and graphic mathematical computations at different levels of complexity. MallaF3 also can interact with the *Mathematica* program, through special instructions provided by this software (Wolfram, 1992). In this graphic environment different TOUGH2 outcomes could be visually analyzed, including simple f (t), 2D or 3D graphs. For example the following command:

ReadList["Arch1.dat", Number, RecordLists -> True],

allows *Mathematica* to read numeric data in file "Arch1.dat" created by FITH2, returning a list of those numbers into a *Mathematica* format and making a separate list (vector) of each line in that file. A main advantage is that a whole list of numbers in *Mathematica* can be treated as a single object. If Arch1.dat are composed of two columns, the expression:

ListPlot [$\{x_i, y_i\}$ PlotJoined -> True],

will produce a similar graphic object as in figure 6, if the same data are used. To plot 2D contours or 3D surfaces with *Mathematica* from results processed by MallaF3, the next instructions are used:

ListContourPlot [*vector*] and **ListPlot3D** [*vector*]

Where *vector* means an array of properties (heights) P (x,y), readed by **ReadList**. Other special options could be used with *Mathematica* in order to visualize final or partial simulation results immediately. It is possible to run external programs, such as FITH2, from inside *Mathematica,* which controls the external program and analyzes the generated output.

The cybernetic environment offered by *Mathematica* is useful to analyze data and, particularly, in the dynamic visualization of graphical outcomes. It is also possible to present animations or virtual motions of graphic objects from file OUTPUT simulating the evolution of thermodynamical reservoir properties. First, it is necessary to create a sequence $\{S_i\}$ of graphic objects. Then the instruction:

ShowAnimation [$\{S_1, S_2, S_3, ..., S_N\}$],

will display the animated graphics (Wolfram, 1992).

CONCLUSION

From the results of this work we conclude that FITH2 code has the capabilities to pre-process the data required in typical simulations and to post-process the numerical outcomes produced by TOUGH2. The numeric files created by FITH2 can be used in a wide variety of graphic environments.

REFERENCES

GeoCad for MS-Windows (1996). Software for preparing models of groundwater, geothermal and other muti-phase flows. GERD, Industrial Research Ltd., New Zealand.

Hardeman, B. & Swenson, D. (1998). A Geometric Modeling Framework for the Numerical Analysis of Geothermal Reservoirs. Proceedings, 23rd Workshop on Geothermal Reservoir Engineering, Stanford University.

Legras, J. (1971). Méthodes et Techniques de l'Analyse Numérique. (324 pp.), Ed. Dunod, Paris, France.

Matheron, G., 1973. The Intrinsic Random Functions and their Applications. Adv. In Applied Probability. Vol. 5, No. 2 (pp. 439-468).

Pruess, K. (1991). TOUGH2 - A General-Purpose Numerical Simulator for Multiphase Fluid and Heat Flow. Earth Sciences Division, Lawrence Berkeley National Laboratory, University of California, LBL-29400, UC-251.

Sato, S., Okabe, T., Osato, K. & Takasugi, S. (1995). Graphical User Interface for TOUGH/TOUGH2 - Development of Database, Pre-processor and Post-processor. Proceedings of the TOUGH Workshop'95. Lawrence Berkeley National Laboratory (pp. 271-276), Berkeley, California, March 20-22, 1995.

Suárez, M.C. (1984). Técnicas Avanzadas de Interpolación y Aproximación. Vol. II. Textbook notes written for the Michoacán University (150 pages), Morelia, Mich., Mexico.

Suárez, M.C. (1985). Cálculo Analítico de Propiedades Térmicas del Agua Pura. Geotermia, Vol.1, No.1, (p. 74-77).

Suárez M.C. & Samaniego, F. (1998) Intrinsic Random Functions of high order and their application to the Modeling of non-stationary Geothermal Parameters. Proceedings, 23rd Workshop on Geothermal Reservoir Engineering, Stanford University.

Sullivan, M. & Bullivant, D. (1995). A Graphical Interface to the TOUGH Family of Flow Simulators. Proceedings of the TOUGH Workshop'95. Lawrence Berkeley National Laboratory (pp. 90-95), Berkeley, Ca., March 20-22, 1995.

SURFER® for Windows (1995). User's Guide. Contouring and 3D Surface Mapping. Version 6. Golden Software Inc.

Wolfram, S. (1992). ***Mathematica***. A System for Doing Mathematics by Computer. Wolfram Rersearch, 2nd Edition, Addison-Wesley Publishing Company (961 pp.), New York.

Using ITOUGH2 To Improve Geothermal Reservoir models

Stephen P. White, Roger M. Young, Warwick M Kissling
Industrial Research Ltd., P.O. Box 31310 , Lower Hutt, New Zealand

In this paper we will present two examples of the use of inverse modelling as an aid to the development of a geothermal reservoir model. The first example takes an existing model of the Kawerau geothermal reservoir and attempts to improve it using ITOUGH2. For the second example we intended using inverse modelling as part of our modelling strategy and this influenced the model development. In this example we develop a model of the Tauhara geothermal field. It is a little unusual in that some of the data used for parameter refinement is changes in reservoir conditions in response to production from an adjoining reservoir (Wairakei).

1. Kawerau Reservoir Model

Kawerau geothermal field is the most northeasterly of the major land-based geothermal systems of the Taupo volcanic Zone of New Zealand The field lies between the andesite volcano of Mt Edgecumbe and the rhyolite/dacite domes known as the Onepu hills, and is centred on the flood plains of the Tarawera river (Figure 1).

The TOUGH2 model that formed the basis of the inverse modelling described here was developed over a number of years by several people. This development is summarised in White *et al.* (1997) and will not be repeated in detail here.

1.1 Model Description

The TOUGH2 model developed to represent the Kawerau reservoir covers an area 10 km 10 km encompassing the most recent resistivity boundary and extending as far south as Mt Edgecumbe. Vertically the model extends from deep in the greywacke basement, at a depth of 3.5 km, to the surface.

The model is divided into 15 horizontal layers of varying thickness. Each layer is divided into a number of blocks. The spatial resolution of the model is controlled by the size of blocks in a layer and the thickness of the layer.

The geology of the drilled area of the field is very complex. Basement greywacke is overlain by at least 13 different units, including rhyolites, breccias, andesites, tuffs, sediments and ignimbrites. Currently production is from fractured greywacke or andesite. It is believed the Huka sediments and ignimbrite act as aquacludes over areas of the field. Where possible, geological data from Allis *et al.* (1993) were used to assign a rock type to each element. Where no geological information is available, rock types assigned to an element represent a best guess of the correct type.

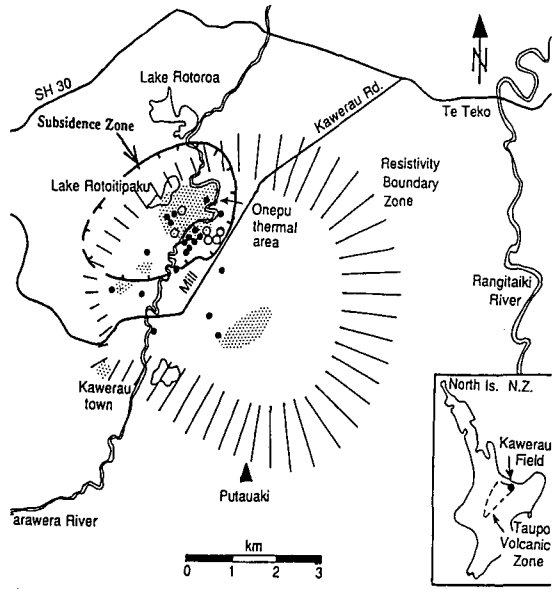

Figure 1: The Kawerau geothermal field.

It is believed that a deep hot source exists in the vicinity of Mt Edgecumbe, with the hot source fluid moving predominantly through faults and permeable zones in the basement greywacke, and mixing with cooler waters flowing horizontally across the field. Secondary permeability is provided by fracturing of brittle rock types and this provides a pathway for interaction between the geothermal fluids and larger volumes of rock than is accessed by the known faults in the system.

Known faults have been included in the model and are represented as areas of enhanced permeability. It is assumed that rocks outside the resistivity boundary have not been subjected to the same thermal stresses as those within the boundary, and consequently permeabilities will not have been enhanced by hydrothermal fracturing.

2. The Natural State

2.1 Manual Method

As a first step in assigning rock properties, a rock type (eg, andesite, greywacke, etc) was assigned to each model element. Values for permeability, porosity and density were assigned to each rock type. These values were obtained from previous estimates of reservoir properties from interference tests and the like. Where no information was available the values chosen were simply guesses.

Grant [Mongillo, Chapter 14] has analysed all the early pressure and temperature measurements from Kawerau

and adjusted the data to one of three reference levels at 750 metres, 1050 metres, and 1400 metres below sea level. This data of Grant, together with data not available to Grant, was used to adjust the permeabilities.

The procedure followed was to run the model until a steady state was reached then a 'goodness of fit' to measurement was calculated. This goodness of fit (SS) is defined by

$$SS = \sum_{i=1} \frac{|X_i - X_{meas}|}{X_{meas}} \qquad (1)$$

where X_i is the calculated value of pressure of temperature and X_{meas} is the measured value. SS is the average relative error in the calculated value. In all 55 data points were included in the match. Permeabilities and inflows were adjusted to approximately minimise SS. The final value achieved for the model represents an average error in calculated values of 3%. However it must be remembered that data are only available over a small part of the modelled volume.

2.2 Match to measured data

After some experimentation the match to measurement shown in Figure 2 was obtained. Apart from one outlier (KA26) with a 12% error in pressure at 750 metres, almost all the other errors are less than 3 % and are distributed more or less evenly about zero. KA26 lies in the south west of the field, well separated from most of the other wells (apart from KA29) and has very poor permeability. There is also an outlier in the calculated temperatures at the nearby KA29.

In this case of temperatures the errors are also reasonably evenly distributed about zero and in most cases are within ± 5%. There is an obvious outlier at 1050 metres with an error of 17%. This is in well KA29 which is located in the south west of the field 80 metres north of KA26 (the location of the largest error in pressure).

3. Inverse Modelling

ITOUGH2 formalises the intuitive approach described in section 2.1 by minimising an objective function calculated from the differences between the model solution and measured data. There are several functional forms of the objective function available, the advantages of the different forms are discussed in Finsterle (1993). For the work described here we have used the default objective function which is a **quadratic** function of the residuals. Note that for the manual method we used a **linear** objective function. The effect of the quadratic objective function is to emphasise the importance of outliers on the objective function. In hind site, it would have been better to choose a linear objective function or one based on a robust estimator as this would have made the comparison with the manual method easier.

We used the same model as in the manual method and allowed ITOUGH2 to vary ten permeabilities in order to reduce the objective function. We used an option that initially calculated the sensitivities of all the parameters and only those with large sensitivities were varied in an attempt to reduce the objective function. All the sensitivities were recalculated each 3 iterations. This reduced the original ten parameters to about five for most of the calculation. After 16 iterations (requiring about 140 TOUGH2 runs) the objective function was reduced to 61% of its original value. While this point was not regarded as a minimum by ITOUGH2 the results presented in this paper are taken from there

From the sensitivities calculated by ITOUGH2 we find the most important parameter is the vertical permeability of the Huka formation (ROCK07) which provides a partial cap to the field at around 500 meters depth. The other important parameters are the vertical permeability of the Opnoke ignimbrite (ROK09) which provides a flow barrier in the southern part of the field and the horizontal permeability in the basement greywacke (ROK03).

Also provided are estimates of the standard deviation for the distributions of the estimated parameters which provide a range within which we expect the parameter to lie. For the three most important parameters the estimated range (3σ) is given in Table 1.

Parameter	Minimum	Mean	Maximum
ROK07z	4.2×10^{-16}	$6.4\times10^{\wedge-16}$	9.8×10^{-16}
ROK09z	3.8×10^{-16}	6.8×10^{-16}	1.3×10^{-15}
ROK03xy	1.1×10^{-14}	1.2×10^{-16}	2.8×10^{-14}

Table 1: Range estimates for important parameters.

Unfortunately the very large amounts of computer time required for a ITOUGH2 run precluded any experimentation with different optimisation functions. We have also added a number of extra data points for the ITOUGH2 run. These were added in an attempt to improve the vertical temperature distribution in the south of the field. Unfortunately this means a direct comparison between Figures 2 and 3 cannot be made.

the manual method easier.

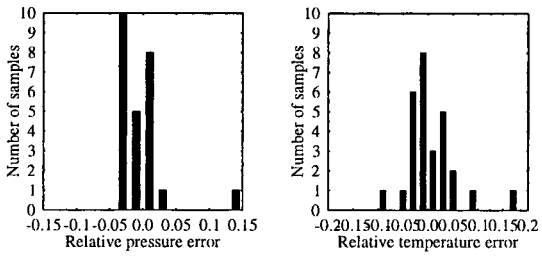

Figure 2: Relative errors in pressure and temperature (manual method)

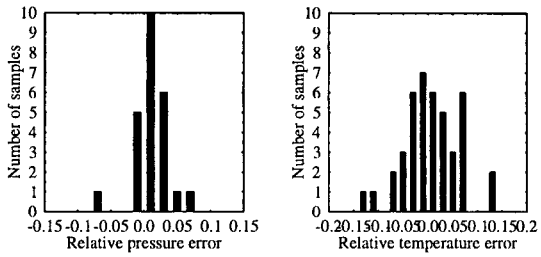

Figure 3: Relative errors in pressure and temperature (ITOUGH method)

4. Tauhara Geothermal Field

The Tauhara field lies close to Lake Taupo in the Taupo Volcanic Zone (Figure 4). We envisage Tauhara field delineated by the resistivity boundary, but open in the west to influence from Wairakei geothermal field. Although the two fields are connected hydrologically, Tauhara is a separate entity because it has its own source of hot upflow. Mount Tauhara and Lake Taupo are significant large scale features in the conceptual model.

The geological cross-sections (Fig) show the existence of surface aquifer(s), a relatively impermeable caprock structure (the Huka layer) and the main geothermal aquifer (the Waiora formation) which extends from 0 mASL downwards. The surface formations follow the line of the land and slope gently downwards to the lake and river where they eventually pinch out.

Somewhere deep down there is a source of hot fluid. The exact location and magnitude of this upflow is not known, but a consistent estimate will be obtained in the course of the model development.

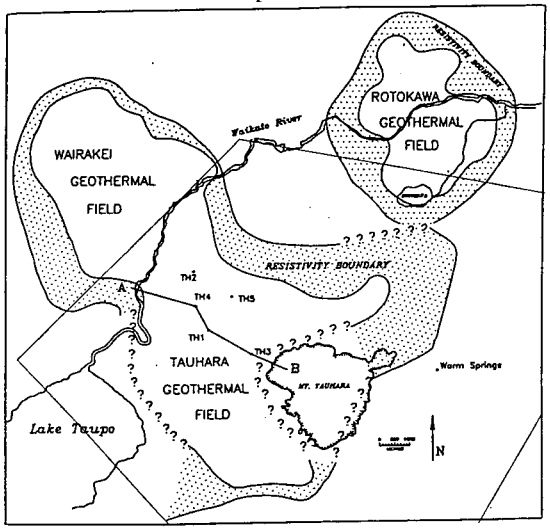

Figure 4: Location of the Tauhara geothermal reservoir and outline of area modeled.

Figure 5 : Geological cross-section of the field

4.1 The Numerical Model

Figure 4 shows the outline of the model superimposed on a map. The model extends beyond the resistivity boundary except in the west where there is a separator across the neck which unites Tauhara with Wairakei. The total area covered by the model is about 195 km^2, and the part within the resistivity boundary about 60 km^2.

The presence of the separator implies that we are modelling Tauhara geothermal field as the principal object, rather than the combined Wairakei-Tauhara system. The influence of Wairakei is still included in the model, but only as a boundary condition.

Vertically the model extends from 1000 mASL down 2.5 km to 1500 mBSL. The topmost level AQ includes the top of Tauhara mountain, Lake Taupo is at level AM, and the Waiora aquifer extends downwards from level AH (0 mASL).

The model has a total of 17 horizontal layers and 1147 elements.

Material properties For each block of the model a rock type is defined following the indications of the conceptual model.

Boundary Conditions The model is open along its boundaries except along the separator (the Wairakei-Tauhara link to be discussed shortly). This allows fluid flow between the area covered by the model and the surrounding countryside, but the low permeability limits the size of these flows. It is believed that the catchment area for the field is larger than the area modelled, and this device keeps the model of a manageable size without detracting from its realism.

The hot upflow is treated as a source of hot fluid at the base of the model. Note that only part of the upflow will reach the surface: the remainder flows out into Lake Taupo or through the other boundaries of the model. The distribution and magnitude of the source will be obtained as part of the modelling process.

The surface boundary condition over the land is air at 1 bar and 15° C, while for Lake Taupo it is water at this pressure and temperature. The air boundary condition means that we can effectively model the vadose zone above the water table and better represent surface heat flows. Rainfall is included in the model by injecting water into the surface elements at an appropriate rate. Hot springs are represented as pressure dependent fluid sinks.

The connection with Wairakei. In the natural state (pre-1957) there is no special connection other than the natural outflow across the separator boundary. During the period 1957-1977 pressures at Tauhara fell by 18 bars. There has never been production from Tauhara itself, so the pressure drawdown must be associated with the exploitation of the Wairakei field (where pressures fell by 26 bars during the same period). The impact of Wairakei production on Tauhara is represented in the model by including a series of sinks along the separator boundary. To ensure that these sinks draw on the hot water inside the model and not on the cold water outside, this boundary is closed between levels AA and AK (-1500m to +300m ASL). Above level AK the separator boundary is open, but it should be emphasised that the "real'" Wairakei-Tauhara connection is *at depth*, represented in the model by the production sinks. The strength of these sinks is adjusted as part of the calibration procedure to give the observed pressure drawdown in the Tauhara aquifer.

4.2 Data and Calibration

Compared with Wairakei there is relatively little data about conditions in the Tauhara field. During the period of investigation there were 3 monitor wells (TH1-3) penetrating the geothermal aquifer. Downhole pressure and temperature profiles from these wells constitute the bulk of the observations. In addition 3 surface heatflow surveys were completed, and later, a repeat gravity survey. Data from several resistivity surveys delineated the field with increasing accuracy.

This information has been incorporated into the numerical model by adjusting material (and other) parameters until model predictions and field measurements were in approximate agreement. The ITOUGH2 program has been largely instrumental in reaching an excellent fit between observation and model predictions.

The steady state. Important adjustable parameters in the model were: (1) the strength of the hot upflow (must exceed the surface heatflow); (2) vertical permeabilities in the various strata; (3) horizontal boundary permeabilities (controls steady state mixing with cold water). The observations were: (1) (inferred) downhole P and T profiles; (2) surface heat flow in the steady state, estimated at 150 MW (Gregg, 1958), later reduced to 107 MW (Fisher, 1965).

Beginning with a ``reasonable" choice of material parameters, ITOUGH2 was run in steady state mode until the average relative error SS (eqn (1)) was minimised. The result was a good fit of model P and T profiles to measured (inferred) values (Figs). In addition the magnitude of the hot upflow of 300^{0} C fluid at the base of the model could be estimated. The thermal energy carried by this fluid was calculated to be 280 MW. Of this, about 100 MW reached the surface in good agreement with observation, the remainder was transported into Lake Taupo or through the other lateral boundaries in the model.

Wairakei production. During the period 1957-1977 Tauhara reacted strongly to fluid extraction from Wairakei. As already noted reservoir pressures fell by 18 bars, and a considerable fraction (unknown) of the hot upflow at Tauhara was diverted to Wairakei. In addition there was a dramatic increase in surface heat flow, from 107 MW (pre-1955) to 220 MW by 1972 (Dickinson 1972, 1975). Even larger heat flows were inferred after 1972 (Mongillo 1989), though these have been disputed. More recently surface heat flows are thought to have declined.

Major adjustable parameters in the model during this phase are: (1) the strength of the sinks along the separator boundary representing Wairakei production; (2) horizontal permeability in the geothermal aquifer (Waiora formation). The observations consist of time-varying downhole P/T profiles and the changing surface heat flows.

Beginning with the natural-state configuration ITOUGH2 was run until the average relative error SS was minimised. This implied a change in the Waiora permeability. The steady-state iteration was run again with this new value. The whole cycle was repeated several times. The final best fit had roughly 50\% of Wairakei production coming from Tauhara, implying an extremely good connection between the two fields. This fluid can be thought of as diverted from the original hot upflow at Tauhara, though there is, in addition, a hot recharge stimulated by the pressure drawdown. Tauhara fluid has a specific chemical signature, but so far no Tauhara component has been identified at Wairakei. This is to be expected since simple calculations suggest that chemical breakthrough is only just now occurring. In another 10 years it should be clearer whether the model predictions concerning the magnitude of the cross-flow are of the right order.

Good agreement was obtained between the time-varying model pressures and temperatures, and field values (Figure 6). In the model a steam zone formed in the geothermal aquifer (in response to Wairakei production) which agrees with the results of the micro-gravity surveys. The observed surface heat pulse was duplicated in the model (Figure 7). The model shows an increase in surface heat flow from just over 100 MW in 1957 to 170 MW in 1967. Heat flow then decreases slightly before increasing slowly to about 200 MW in 1980. The model surface heat flows agree quite well with field estimates in the early stages, but the model does not predict a decline in surface heat flow until after the year 2000.

Summary. Overall the Tauhara model -- incorporating the parameter refinements suggested by ITOUGH2 -- has been very successful. It has been used in water rights applications and to run various production scenarios for the future development of the field. The importance of the air boundary condition should also be emphasised. Without this another model predicted large mass (and energy) *downflows* at Tauhara in response to Wairakei production, rather than the surface heat pulse which was actually observed.

5. Conclusions

We learnt a number of lessons from the Kawerau exercise using ITOUGH2, perhaps the most important were

1. start with a *small* simple model
2. vary only sensitive parameters
3. use the fastest computer you can find
4. it is easier to match time varying data than steady state data.

Also, most importantly, ITOUGH2 cannot work miracles. To obtain good estimates of model parameters you must have data that is sensitive to those parameters. Obviously this is true of any method used to fit parameters but is perhaps ignored when error estimates of fitted parameters are not available.

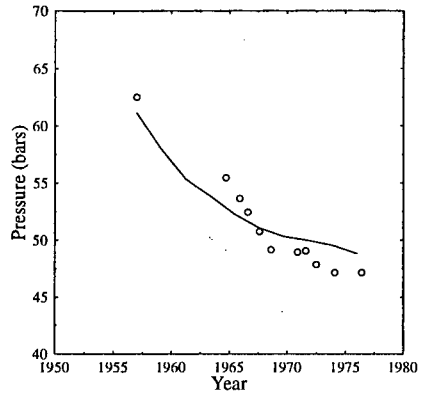

Figure 6: Match to pressure drawdown at well TH1

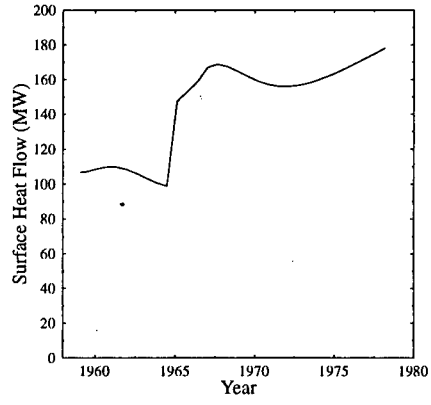

Figure 7: Change in surface heat flows in response to Wairakei production.

For the work on Tauhara we obtained very good results using ITOUGH2. The most positive aspects were the great savings in time and the good match obtained to measured data.

6. References

Allis, R.G., 1983, Hydrologic Changes at Tauhara Geothermal Field, New Zealand, *DSIR Geophysics Division Report 193.*

Dickinson, D.J., 1975, An airborne infrared survey of the Tauhara geothermal field, New Zealand, *Proc. Second United Nations Symposium on the Development and Use of Geothermal Resources*, **2**, 955-961.

Dickinson, D.J., 1976, The 1972 and 1975 Infra-red aerial surveys, Taupo area, *Geophysics Division Report* (unpublished).

DSIR, 1988, Assessment of Development Impacts and Reservoir Response of Tauhara Geothermal Field, *DSIR Report, February 1988.* Confidential report for Waikato Valley Authority.

Fisher, R.G., 1965, Shallow heat survey of Taupo Borough and adjacent country, *N.Z. J. Geol. and Geophys.*, **8**, 752-771.

Gregg, D.R., 1958, Natural heat flow from the thermal areas of Taupo Sheet District (N94), *N.Z. Jour. Geol. Geophys.*, **1**, 65-95.

Mongillo, M.A., 1989, A Re-examination of the 1972 and 1975 Aerial Surveys of the Tauhara Geothermal Field, *DSIR Geophysics Division Research Report 220.*

Mongillo M A (ed) (1986). Kawerau Geothermal Field *DSIR Geothermal Report Number 10.*

White S P, Kissling, W.M., McGuinness M J (1990). Models of the Kawerau Geothermal Reservoir *GRC Tran.* **21** Sept 1997

Transmissivity Distribution at The Ahuachapán-Chipilapa Geothermal Field in El Salvador

Julio E. Quijano, jquijano.reser@salnet.net
Departamento Ingeniería de Reservorios
Comisión Ejecutiva Hidroeléctrica del Rio Lempa (CEL)
Km 11 ½ Carretera al Puerto La Libertad, Santa Tecla, El Salvador

Abstract

Through the analysis of injectivity test in 30 wells in The Ahuachapán-Chipilapa Geothermal Field a transmissivity distribution map has been constructed. The analysis was carried out by simulating injectivity tests with a radial model of 50 elements in a single layer 400 m thick. Previous to the simulation, on base on injectivity test data was calculated the sandface flow (W_{sf}) and reservoir pressure (P_r). W_{sf} was calculated considering a wellbore storage coefficient in a well with free surface and P_r was calculated considering a turbulence regimen in the boundary well-feedzone. The simulations were carried out with the TOUGH2 code changing rock permeability to fit the observed pressure (P_r) with the calculated pressure in the central element. In general, the results show a transmissivity distribution between 1 and 10 Dm in the areas of Ahuachapán and Chipilapa and an anomalous zone with transmissivities between 80 an 140 Dm southern to the Ahuachapán Field.

Introduction

The geothermal development resources in the Ahuachapán-Chipilapa geothermal area have been involved drilling activities in three main areas: Ahuachapán Geothermal Field (AGF), Chipilapa zone located about 3 km from CGF and the Agua Shuca zone (Figure 1). During the explorations stage in the period 1956-1958 were drilled 7 shallow wells in the AGF (Fritz Durr, 1960). After that, in the period 1968-1981, 32 deep wells were drilled in the AGF and a power plant of 95 MW was constructed. Looking for a new geothermal reservoir during the period 1989-1993, 7 deep wells were drilled in the Chipilapa zone. The result, showed that AGF and Chipilapa are parts of the same geothermal system and Chipilapa is a marginal part of its outflow (Aunzo A., 1988). Trying to expand the exploitation zone in the Ahuachapán Field, in order to increase the total mass steam without a fast depletion of the reservoir fluid, 7 deep wells have been drilled in Agua Shuca. Until now some wells are under thermal recovery and the other ones wait for the pipe connection to the plant.

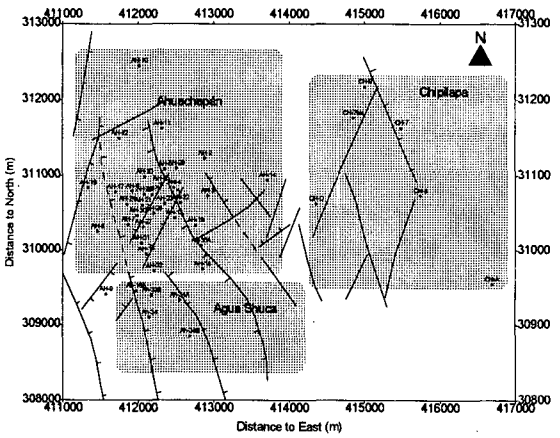

Figure 1. Ahuachapán-Chipilapa Geothermal Field. Geothermal development resources areas in chronological order, Ahuachapán, Chipilapa and Agua Shuca.

One of the most critical parameter in Reservoir Engineering assessment is the transmissivity thickness product kh (Dm). The transmissivity means how easy the fluid flow within the medium.

In order to get the transmissivity kh we can execute pressure transient test by management the wellhead flowrate in drawdown, buildup interference test. If the test is conducted in the short term (usually few hours o days) we can get near wellbore condition such as kh, storage and skin (Horne, 1995). During long term production, pressure is often controlled by production equipment requirements, and production rates and reservoir pressure are monitoring over month and years. In this case the decline analysis give information about reservoir properties, such its volume.

The general theory for well test analysis is based on Theis solution, which consider a radial liquid flow in an isotropic and isothermal porous media. Factors such, non isothermal effect, two phases effects and fractured media make difficult to apply conventional well test analysis (Gudmundur S., 1984). Trying to avoid this, the present study use as a analysis tool a radial model centered in a well using the code TOUGH2 (Tansport of unsaturated groundwater and heat) (Pruess, K., 1993).

Interference Tests in The Ahuachapán-Chipilapa Geothermal Field

In order to have information about the transmissivity and storativity of the Ahuachapán reservoir, several interference test were conducted in the Ahuachapán Field. The first one was carried out in the period from may 6 to August 19, 1982, in which Ah-1, Ah-4, Ah-6, Ah-17, Ah-20, Ah-21, Ah-22, Ah-23, Ah-24, Ah-26, Ah-27 and Ah-28 were used as producers wells, Ah-2, Ah-8 and Ah-29 used as injectors wells, and Ah-25 was used as an observation well. The test was analyzed with the simulator VARFLOW (EG&G and LBL, 1982), which uses the Theis solution and superposition principle. The results show transmissivity and storativity values of 25 Dm y 2.5e10-6 m/Pa respectively (Aunzo Z., 1989).

Another analysis to evaluate the transmissivity and storativity values in the reservoir between Ahuachapán and Chipilapa was carried out by Quijano in 1997. The analysis was based on the production history since 1975 to October 1997. The total extraction by year was concentrated in the well Ah-21, and the observation point in the well Ch-7bis and well Ah-14 located in the boundary between the two areas. The output of the model was fitted with the pressure decline curve observed at 200 m a.s.l. in the observation wells. The results show transmissivity and storativity values of 16 Dm y 2.5e10-6 m/Pa respectively.

Inyectivity Test, Sandface Flow and Wellbore Storativity Effect

From the Reservoir Engineering point of view after the completion well, some well test must be executed: Temperature profiles with fixed injection rates, injectivity tests and temperature profiles during recovery temperature. The step wise injectivity is an experiment with several fixed flow rate injections (10, 40, 60 kg/s etc) for more than one hour. During the test the pressure transient is measured with a gauge tool near the main feedzone.

Previous to the simulation the sandface flow must be calculated, considering the wellbore storage coefficient in a well with a free liquid level. Also we need to calculate the pressure acting on the reservoir considering the turbulent regime in the boundary well-feedzone.

The cause of the wellbore storage effect is that the sandface reservoir boundary flow rate does not necessarily have to equal to the well head flow at all times. If a well is suddenly opened, the wellbore pressure will drop, and cause expansion in boiling wells and water level depletion at first in non-boiling wells. If a well is suddenly shut in, fluid continues to pass through the sandface into the hole. Both effect result in changes of the wellbore storage volume (Kjaran S., 1983). The sand face flowrate can be calculated from the following equation.

$$(1) \qquad W_{sf} = W - \rho C \frac{dp_w}{dt}$$

where W_{sf} is the sand face mass flow, W is the surface mass flow, C is the wellbore store coefficient and P_w is the bottom hole pressure. If the well has free liquid level, the wellbore storage coefficient is given by:

$$(2) \qquad C = \frac{\pi r_w^2}{\rho g}$$

where r_w is the wellbore radius , ρ is the density of the water filling the wellbore and g is the gravity acceleration. If we combine this two equations we can correct the data from a injectivity test as follow:

$$(3) \qquad W_{sf} = \left[W\Delta t - \pi r_w^2 \frac{\Delta p_w}{g} \right] \frac{1}{\Delta t}$$

A injectivity test executed in June 24, 1997 is showed in the Figure 3.

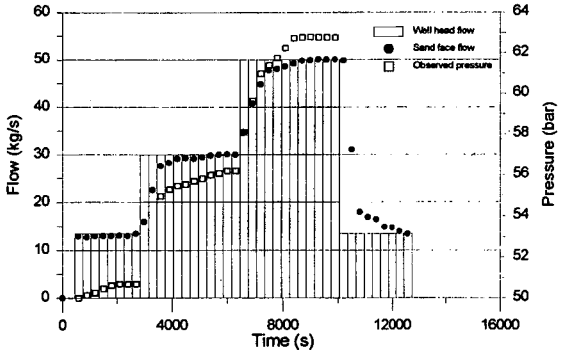

Figure 2. Pressure an flow measured during the injectivity test in the well Ah-34 on Jun-24-97. The filled circles means the estimated sandface flow.

Correction of pressure by turbulence effect

When a stepwise injectivity test is carried out, in the boundary well-feedzone could be formed a turbulent regime. This phenomenon cause a pressure drop and could masked the real pressure acting on the reservoir. To correct this, the calculation of the turbulence coefficient is necessary, considering the sandface coefficient pointed before. Then in a turbulent regime, the pressure at depth is given by the following equation (Todd, 1980):

$$(4) \qquad P = P_o + aW_{sf} + bW_{sf}^2$$

Where W_{sf} is the sand face flow, Po is the static bottomhole pressure and P is the pressure measured by the pressure gauge tool during the injection test. By plotting P versus W_{sf} and fitting it with a second order polynomial equation, we can get the turbulence coefficient b (Figure 3). Then, the measured pressure can be corrected with the following equation.

$$(5) \qquad P_{res} = P - bW_{sf}^2$$

As an example, the corrected pressure observed during the injectivity test in the well Ah-34 Jun-24-97 is the following: From the Figure 3 the turbulence coefficient b = 8.397×10^{-4}, and if it is considered the maximum measured pressure of 50 bar related to a sandface flow of 62.5 kg/s, using the equation 5 we have a corrected pressure of 46.7 bar.

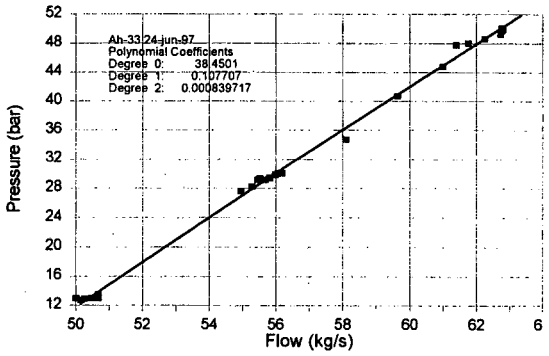

Figure 3. Polynomial fit for a observed pressure versus sandface flow plot for the injectivity test in the well Ah-34 on Jun-24-97.

Numerical Model

To simulate the stepwise injection a numerical model with radial geometry was used. The model consists of 50 elements in a single layer of 400 m thick. The first 10 elements of the model have a constant incremental radius of 1 m and the others ones increase logarithmically until 2000 m.

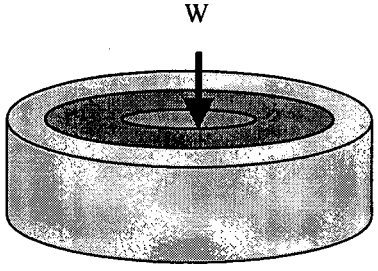

Figure 4. Reservoir model concentrically to the well.

To check the results from the injectivity test two model with 300 and 400 m thick were used, getting similar results. For example, with both models 300 and 400 m, we get transmissivity values of 4.36 and 4.16 Dm respectively.

During the fitting process of calculated and observed pressure the permeability values in the numerical model was changed in a range of 1 to 150 mD. By other side, the simulation result in the Ah-34 also show a cooling effect of 100 °C in the near well formation by the injection of water at 25 °C.

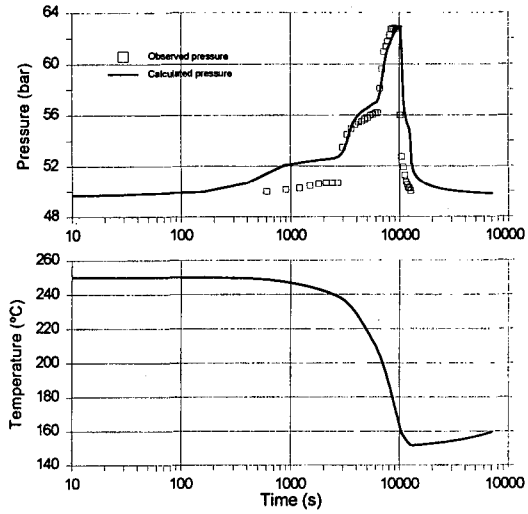

Figure 5. Simulation results of the stepwise injection in the well Ah-34 on Jun-24-97. The top figure show the best fit between observed and calculated pressure and the bottom figure show the cooling effect of 100 °C in the central element.

Analysis of the Results

With respect to the quality an quantity of the injectivity tests collected, going back in time it is more difficult to analyze. The injectivity tests collected from the last wells in Agua Shuca, have a good quality, and sandface flow and corrected pressure was estimated. The results are showed in the table 1.

Table 1. Injectivity index and transmissivity values from the wells in Agua Shuca.

Well	kh (Dm)	Well	kh (Dm)
Ah-4bis	9.5	Ch-7	3.5
Ah-16a	140.0	Ch-7bis	4.2
Ah-32st	6.5	Ch-8	3.2
Ah-33a	1.2	Ch-9	3.6
Ah-33b	85.0	Ch-D	4.1
Ah-34	6.2	Ch-A	--
Ah-34a	5.2	Ch-Abis	--
Ah-34b	5.6	--	--

The analysis of the injectivity tests carried out in the Chipilapa area, also have a good quality, and easy to interpret. But, the analysis of the injectivity test in the first 32 wells drilled in the Ahuachapán Field was difficult to interpreted. This data was analyzed by Campos in 1980, who calculated the injectivity index (kg/s/bar) with the following equation:

$$(4) \qquad I = \frac{\Delta q}{\Delta t} = \frac{q_m}{P_{qm} - P_o}$$

where Po is the initial static pressure at measured depth, q_m is the maximum injection flow and P_{qm} is the pressure associated with maximum flow during the test.

After the completion well in the first 32 wells in Ahuachapán, were performed injection test with steps of 20, 30, 40 y 50 lt/s during 10-15 min each one. The reported pressure by step is a unique value, making difficult to know if that pressure correspond to a stabilized pressure.

This data, also was reinterpreted by LBL in 1989 using conventional well test analysis by computing the transmissivity Kh/μ (m^3/Pa/s). Because of poor information, the present study analyze this injectivity tests without the corrections by storage effect and turbulence regime. The results are presented in the following table:

Table 2. Injectivity index and transmissivity at the Ahuachapán-Chipilapa Geothermal Field

Well	Inj. index kg/s/bar	Kh/μ (10^{-8}) m^3/Pa/s	Kh Dm
Ah-2	3.0	2.2	3.49
Ah-14	2.0	2.2	2.82
Ah-16	8.0	6.2	8.30
Ah-17	8.0	5.5	7.29
Ah-18	2.0	1.1	1.61
Ah-19	6.0	4.4	5.67
Ah-21	12.0	6.6	11.36
Ah-23	8.0	4.0	9.17
Ah-24	6.7	5.1	6.80
Ah-28	7.0	5.1	6.23
Ah-29	4.0	2.2	3.16
Ah-30	4.5	2.6	3.56

The results from the injectivity test give a injectivity index in the range of 1-10 lt/s/bar and transmissivity values in the range of 1e-8 to 7e-8 m3/Pa-s (Aunzo Z., 1988). The results after modelling in the present study, also present transmissivity values in the range of 1-10 Dm. We can observe that good production wells such Ah-21, Ah-27 and Ah-28 have good injectivity index and good transmissivity and non production wells such Ah-14, Ah-18 have low injectivity index and low transmissivity.

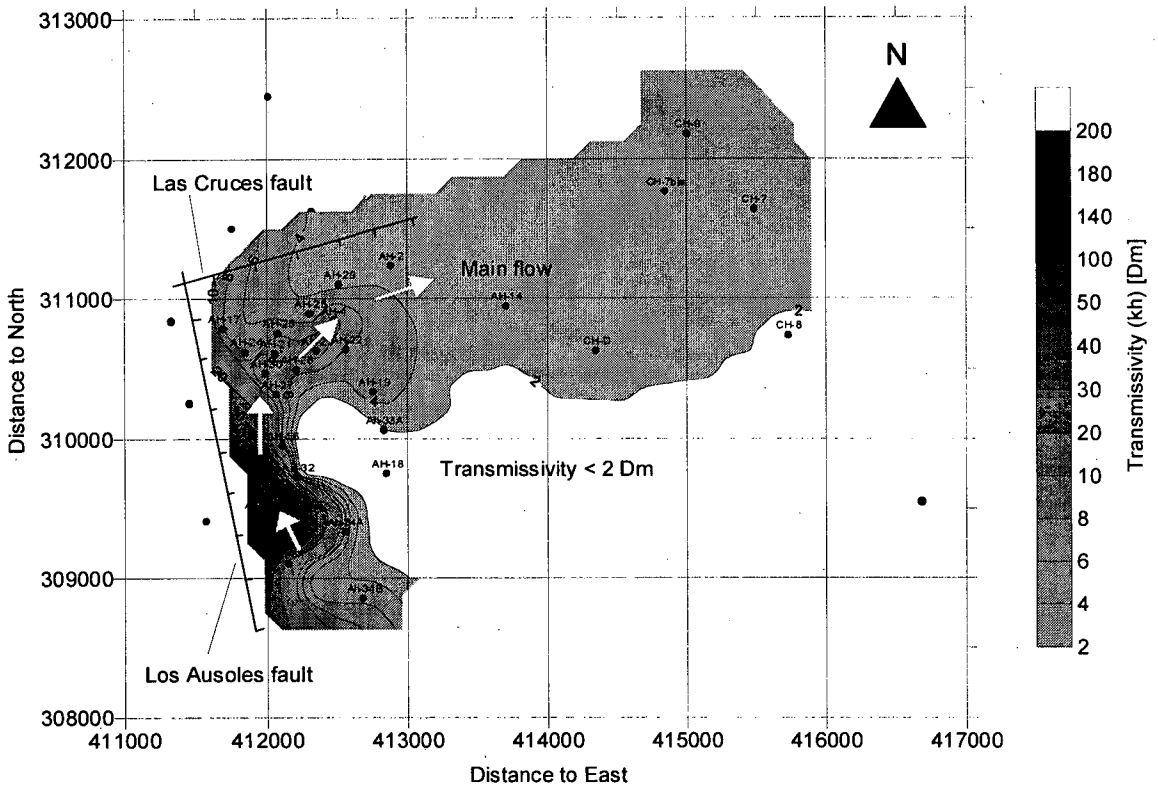

Figure 6. Transmissivity distribution at the Ahuachapán-Chipilapa Geothermal field.

The transmissivity values from simulating with the radial model are mapped in the Figure 6. We can observe that the transmissivity distribution suggest a flow movement in north direction from the upflow zone at the south to The Ahuachapán Field as is indicated by arrows. The main flow movements is governed by Los Ausoles and Las Cruces faults, acting as barriers because the wells outside the mapped zone are completely dry and its lithology does not present the stratum andesitas of Ahuachapán where the reservoir is located.

Conclusions

The transmissivity values obtained from the injetivity test in the Ahuachapán wells are lower than the transmissivity values obtained from the interference test. This is probably due to near well transmissivities determine the pressure response in the well during short duration injection test, whereas interference tests measure global reservoir transmissivities.

Proportionality is observed between the injectivity index and transmissivity values. The calculations show well injectivities in the order of 1-10 l/s-bar and transmissivities in the order of 1 to 10 Dm. The results are generally consistent with the well productiveness, good producers have relatively high transmissivity (~10 Dm), while low transmissivities are found in the poor producers (~ 1 Dm).

The transmissivity distribution in the Ahuachapán-Chipilapa Geothermal Field suggest an entrance of geothermal fluids from the south (near the well Ah-34), into the Ahuachapán reservoir. The fluid primarily feeds the actual exploitation zone in Ahuachapán (kh ~ 6-10 Dm), after that it goes to the east and feeds the Chipilapa Geothermal Field (kh ~ 3-4 Dm). Finally, the flow goes to the north to the discharge zone in the El Salitre Area.

Acknowledgements

I want to express my thanks to Dr. Marcelo Lippmann to induce an update of the trasmissivity distribution in the Ahuachapán-Chipilapa Geothermal Field. Also, thanks to Grimur Bjornsson for his guidance in the data processing and simulation methods to analyze the injectivity tests.

References

EG&G Idaho, Inc., Lawrence Berkeley laboratory, 1982: Low to low moderate temperature hydrothermal reservoir engineering handbook. 40 pp.

Durr Fritz, 1960: Energía Geotérmica. Servicio Geológico Nacional, Ministerio de Obras Públicas.

Snorri Páll Kjaran and Jónas Elíasson, 1983: Geothermal Reservoir Engineering Lecture Notes. Orkustofnun-The United Nation University.

Roland N. Horne, 1995: Modern Well Test Analysis, A Computer-Aided Approach. Second Edition. Petroway Inc.

Gudmundur S. Bodvarsson, Sally M. Benson, Omar Sigurdsson and Valgardur Stefansson, 1984: The Krafla Geothermal Field, Iceland. 1. Analysis of Well Test Data. Water Resources Research. Vol 20. N0. 11 pags. 1514-1530.

Pruess, K., May 1991: A General Purpose Numerical Simulator for Multiphase Fluid and Heat Flow. Lawrence Berkeley Laboratory, University of California.

Pruess, K., May 1987: TOUGH User's Guide. Lawrence Berkeley Laboratory, University of California.

Quijano, Julio, 1996: Evaluación de los Efectos de la Presión en el Reservorio de Ahuachapán por la Reinyección del Agua Residual en Chipilapa, Comisión Ejecutiva Hidroeléctrica del Río Lempa.

Quijano, Julio, 1994: A Revised Conceptual Model and Analysis of Production Data for The Ahuachapán-Chipilapa Geothermal Field in El Salvador. Geothermal Training in Iceland 1994, Report 10. United Nation University, Reikjavik Iceland.

Quijano, Julio, 1997: Simulation of Pressure Changes in The Ahuachapán Geothermal Reservoir due to Reinjection of Residual water into The Chipilapa Geothermal Area. Proceeding, Twenty-Third Workshop on Geothermal Reservoir Engineering, Stanford University.

Todd, D.K., 1980: Groundwater Hydrology. Second Edition. John Wiley & Sons, Inc., New York.

Campos Tomas, 1980: Indices de Inyectividad en el Campo Geotérmico de Ahuachapán. Reporte Técnico LG-2-6. Laboratorio Geotérmico, Recursos Geotérmicos CEL.

Z. Aunzo, G.S.Bodvarsson, C. Laky, M.J.Lippmann, B.Steingrimsson, A.H.Truesdell and P.A.Wotherspoon, 1989: The Ahuachapán Geothermal Field, El Salvador, Reservoir Analysis. Earth and Space Science Division, Los Alamos National Laboratory.

Graphics and TOUGH2

D.P. Bullivant and M.J. O'Sullivan
Department of Engineering Science,
University of Auckland,
New Zealand

The authors have developed a graphical tool to help with the preparation of TOUGH2 input files and the interpretation of TOUGH2 results. It runs on PCs (Windows 95 and NT) and unix workstations.

The tool is mulgraph and it is used to create TOUGH2 input and analyse TOUGH2 results. mulgraph requires a geometry file which describes the locations of the blocks in space. The geometry file is relatively simple and can be created with a text editor.

In order to analyse results, mulgraph needs to be able to read TOUGH2 listing files. In order to make this easier a new version of TOUGH2, autough2 has been created. autough2 has a standardized OUT subroutine and a new FORTRAN module, table.f, which is shared with mulgraph. table.f describes the element, connection and generation tables.

At the poster session, mulgraph and autough2 will be demonstrated. The executables are freely available. Please bring floppy discs if you want copies.

Following are examples of the output produced by mulgraph. The examples come from the 1417 block model of Wairakei described in [1].

References

[1] M.J. O'Sullivan, D.P. Bullivant, S. Follows, and W. Mannington. Modelling of the wairakei geothermal field. TOUGH Workshop '98.

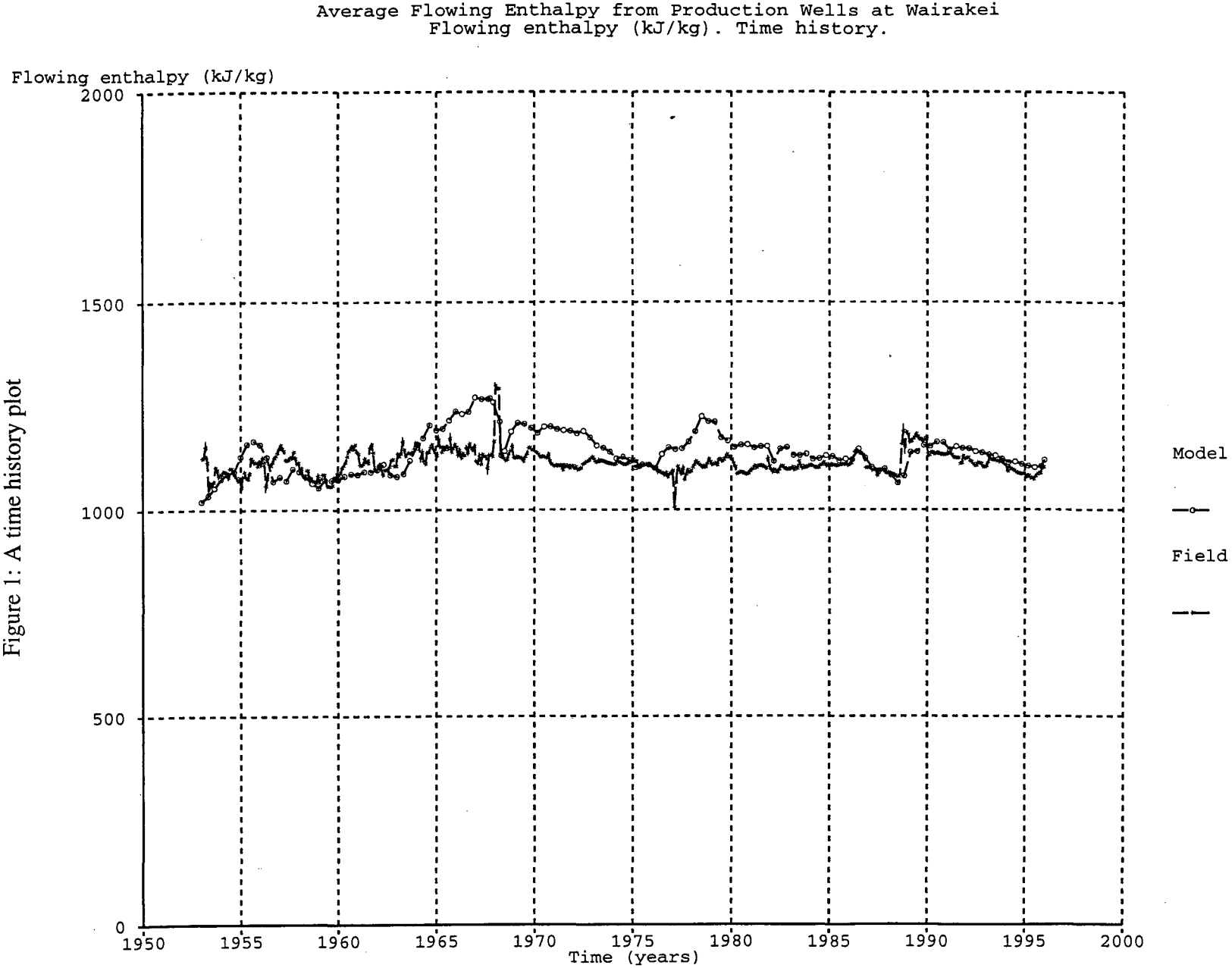

Figure 1: A time history plot

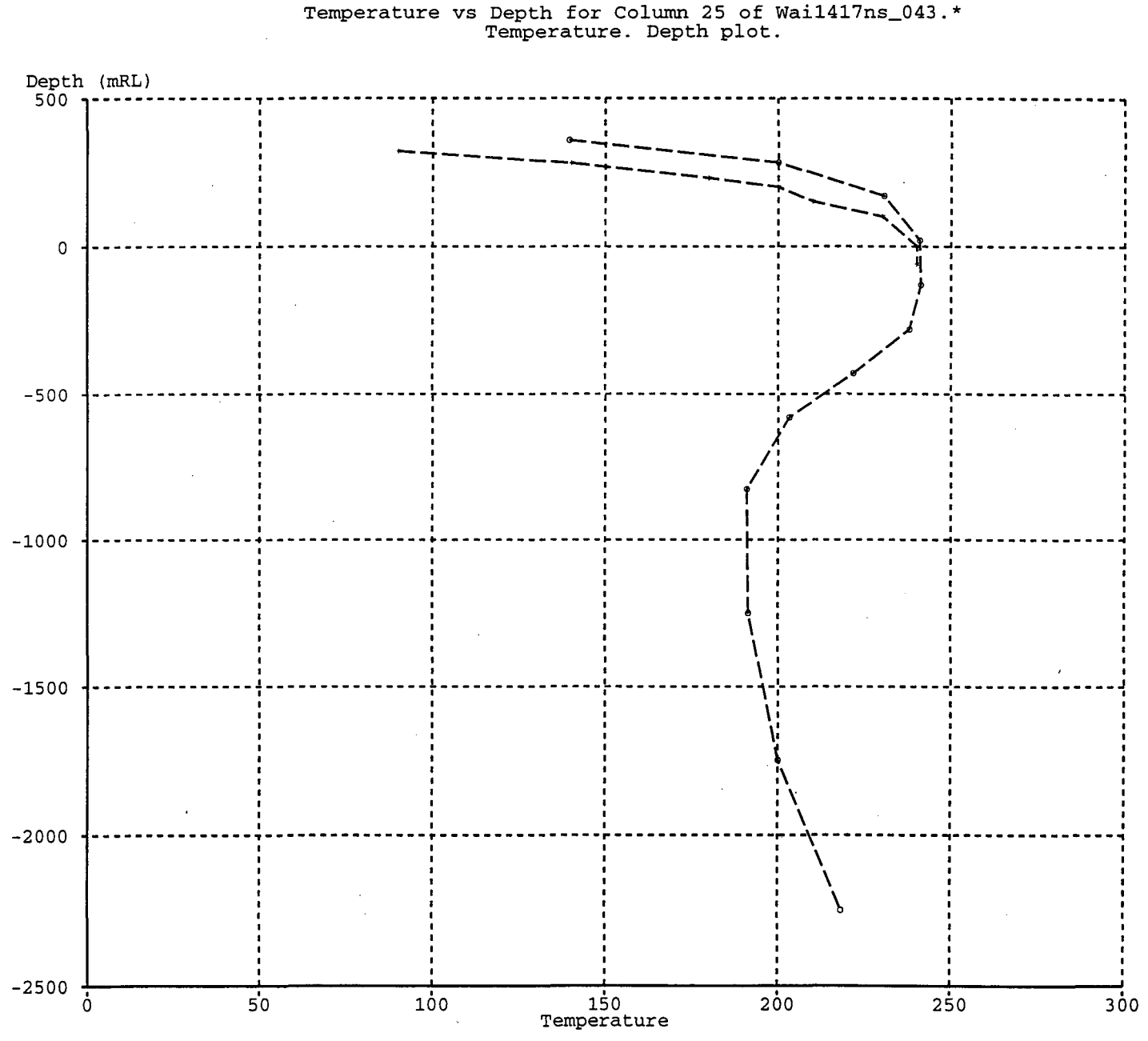

Figure 2: A depth profile

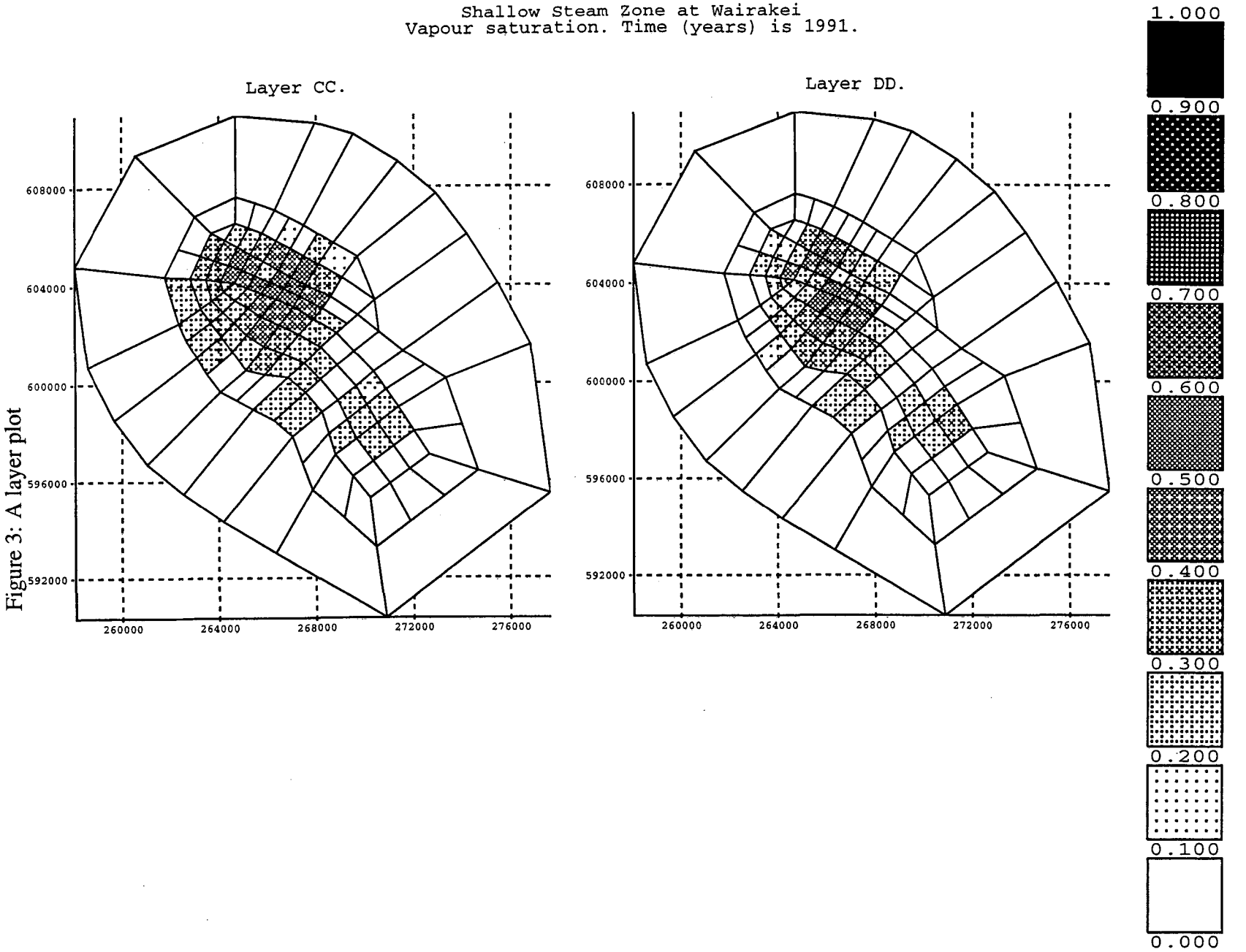

Figure 3: A layer plot

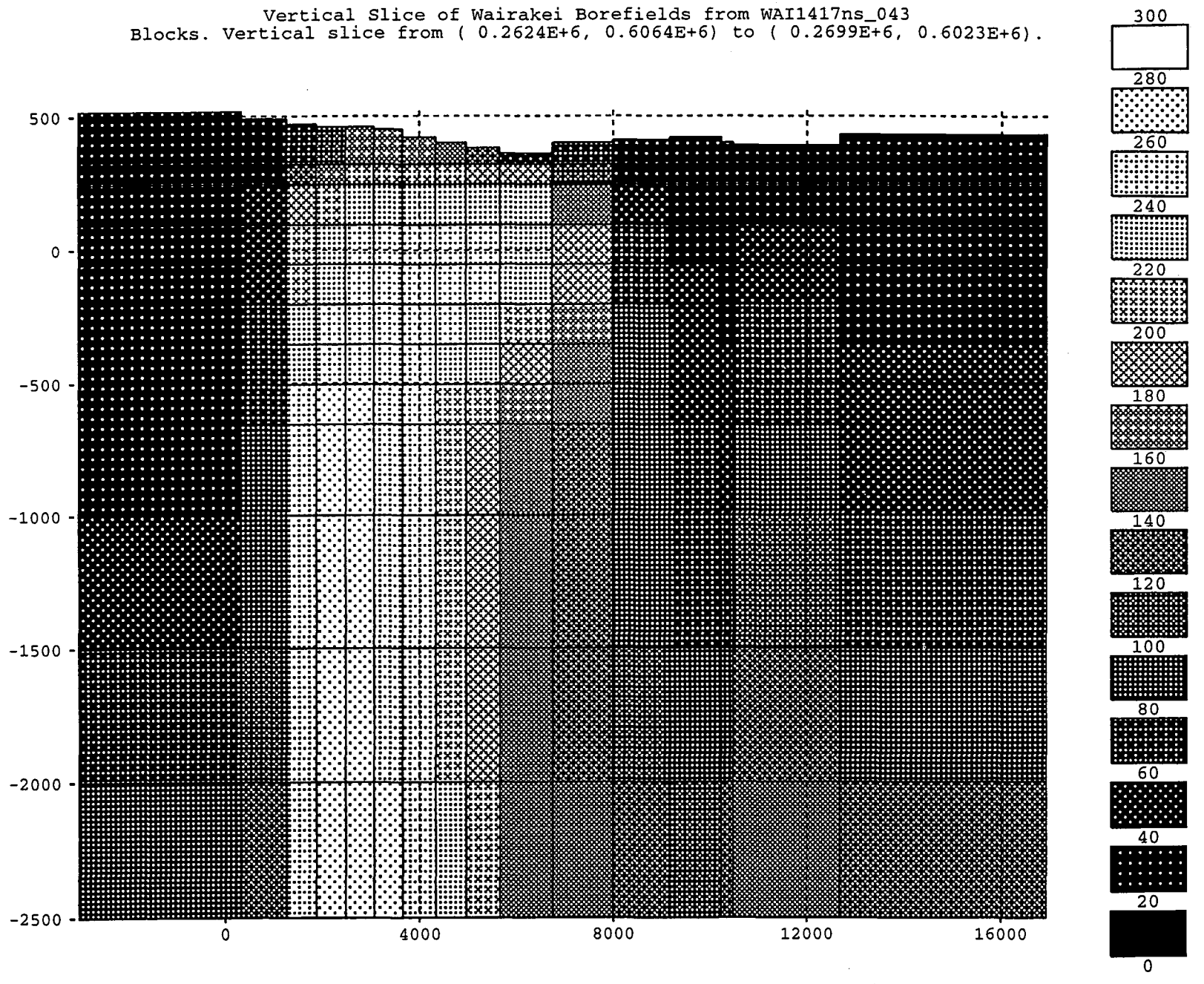

Figure 4: A vertical slice

THE MODELING STUDY USING TOUGH2 AND THE MICRO-GRAVITY CHANGE IN YANAIZU-NISHIYAMA GEOTHERMAL FIELD

Kazumi Osato[*1], Tatsuya Sato[*1], and Seiichi Yokomoto[*2]

[*1]:Geothermal Energy Research and Development Co., Ltd.
11-7 Kabuto-cho, Nihonbashi, Chuo-ku, Tokyo 103, Japan
ohsato@gerd.co.jp/tatuya@gerd.co.jp

[*2]:Okuaizu Geothermal Co., Ltd.
3-2-13, Nihonbashi-honcho, Chuo-ku, Tokyo 103, Japan
oagtky@mxg.meshnet.or.jp

INTRODUCTION

In many existing geothermal power stations, history matching and numerical model review is continuously carried out, even after the start of operations, in order to optimize the numerical model of the geothermal reservoir so that steam can be generated satisfactorily and the accuracy of the production forecast can be improved. In many geothermal power stations flow data from a specific well, or even from a specific flash separator connected multiple wells in extreme cases, are mostly used for production history matching. Many geothermal power stations have some observation wells in which long-term changes in reservoir pressure are to provide data for production history matching. However, in areas where vaporization in the formation occurs, it may be difficult to measure the pressure change behavior due to vaporized areas. When a geothermal reservoir model is constructed from such poor information, it may be difficult to accurately predict the amount of production. In order to overcome such difficulties, it has been tried in actual geothermal areas to estimate the fluid behavior in a reservoir from changes in physical properties measured in surface surveys, e.g., micro-gravity surveys (Allis and Hunt, 1986; Motoyama et al., 1992; Sugihara, 1997).

This report describes the numerical modeling study using TOUGH 2 (Pruess, 1991) and a post-processor "GRAV/TOUGH2" for micro-gravity, to the Yanaizu-Nishiyama geothermal field (65MW) located in Yanaizu-cho in Fukushima Prefecture. Tohoku Electric Power Company is responsible for the power generation section of the station, and Okuaizu Geothermal Co. is responsible for the steam supply section. The station began operation in May 1995. A four-year joint study program was started in fiscal 1994 by both companies. A precision gravity survey was performed each year at 83 measuring points, including 8 benchmark points, in a 12 km^2 area for the purpose of monitoring the gravity change before and after the start of operation of the station and helping understand geothermal fluid behavior in a geothermal reservoir and how it is related to production and injection of fluid.

CONSTRUCTION OF A NUMERICAL MODEL

According to the underground temperature distribution, a range with underground temperature 200℃ or higher, which is considered to be a promising reservoir, spreads from the northeast side of the Oizawa Fault towards the southwest side of the Onogawara Fault. In the high-temperature range, which is assumed to be the center of the up-flow, lost circulation frequently occurs and feed points of production wells are scattered. It was conjectured that there exists an up-flow from an underground high-temperature area along the faults under this high temperature range, and that the convection area extends from the northeast side of the Oizawa Fault and from the southwest side of the Onogawara Fault at a width of approximately 1 km. In the numerical model, the NE-SW length of the area was taken to be 4.6 km so that the fault directions can be taken into consideration and the high temperature range can be covered. The NW-SE length was taken to be 3.2 km so that the Kitanosawa Fault and the Sudarezawa Fault, as well as the faults which are considered to restrict natural convection flow (Chinoikezawa, Sarukurazawa, Oizawa, Takiyagawa, and Onogawara Falt), can be covered. As for the internal grid, the area near the faults relating to production and injection was divided into smaller blocks and the surrounding area was divided into larger blocks. EOS2 (H_2O-CO_2) of TOUGH2 was used as the

state equation to take the CO_2 of geothermal fluid into consideration.

STEADY-STATE MODELING BY MEANS OF NUMERICAL SIMULATION

Since the numerical simulation was done just before the start of operation of the station, the model was optimized according to the steady-state. However, review of the numerical model based on the production history after the start of operation has not been done. The first numerical model was constructed by the optimal model in 1988 for the steady-state simulation taking data from new wells into consideration. Figure 1 shows the underground temperature distribution calculated using the steady-state-optimized numerical simulation, the actual underground temperature distribution (both at 1,500 m below sea level) with the grids of the fourth and Figure 2 shows the NE-SW Cross-sectional view of the underground temperature distribution, lost-circulation points, feed points of production wells, and projected geological columns.

PREDICTION OF THE GRAVITY CHANGE USING THE POST-PROCESSOR

In calculating the gravity change, the Talwani method (Plouff, 1976) for estimating of anomalies in a polygonal prism with abnormal density was used.

To calculate the density change in the rocks, the porosity (ϕ), the mass percent in the vapor phase (S_g), the density in the vapor phase (δ_g), and the density in the liquid phase (δ_w) of each block rock, which are input/output values of TOUGH 2, are used. If the density change in the rocks is ignored, the density change is determined by the density change of geothermal fluid in the pores in the rock. The density of geothermal fluid in the rock density (ρ) is defined below.

$$\rho = \left[s_g \cdot \delta_g + \left(1 - s_g\right)\delta_w \right] \cdot \phi \qquad (1)$$

According to the Talwani method, the gravity change in a polygonal prism under the ground (Figure 3), ΔZ in thickness and ρ in density, is given by the following equation:

$$g = \gamma\rho S_m \sum_{i=1}^{n} \left\{ \begin{array}{l} Sp4\left[Z_2 - Z_1\right] + Z_2\left[\tan^{-1}\dfrac{Z_2 d_1}{PR_{12}} - \tan^{-1}\dfrac{Z_2 d_2}{PR_{22}}\right] \\ -Z_1\left[\tan^{-1}\dfrac{Z_1 d_1}{PR_{11}} - \tan^{-1}\dfrac{Z_1 d_2}{PR_{21}}\right] - P\ln\left[\dfrac{R_{22}+d_2}{R_{12}+d_1}\dfrac{R_{11}+d_1}{R_{21}+d_2}\right] \end{array} \right\} \qquad (2)$$

where g: gravity anomaly in the polygonal prism

γ : universal gravitation constant

ρ : density of block i

S_m=1: the case in which the height of the center of gravity is lower than the observed value

S_m=-1: the case in which the height of the center of gravity is higher than the observed value

S_p=1: the case in which P is a positive value

S_p=-1: the case in which P is a negative value

and A, d_1, d_2, P, R_{11}, R_{12}, R_{21}, and R_{22} are given as follows:

$$A = \cos^{-1}\left(\frac{X_1X_2 + Y_1Y_2}{r_1r_2}\right) = \cos^{-1}\left(\frac{X_1X_2 + Y_1Y_2}{\sqrt{X_1^2+Y_1^2}\sqrt{X_2^2+Y_2^2}}\right)$$

$$d_1 = X_1\frac{X_2 - X_1}{\sqrt{(X_2-X_1)^2+(Y_2-Y_1)^2}} + Y_1\frac{Y_2 - Y_1}{\sqrt{(X_2-X_1)^2+(Y_2-Y_1)^2}}$$

$$d_2 = X_2\frac{X_2 - X_1}{\sqrt{(X_2-X_1)^2+(Y_2-Y_1)^2}} + Y_2\frac{Y_2 - Y_1}{\sqrt{(X_2-X_1)^2+(Y_2-Y_1)^2}}$$

$$P = X_1\frac{Y_2 - Y_1}{\sqrt{(X_2-X_1)^2+(Y_2-Y_1)^2}} - Y_1\frac{X_2 - X_1}{\sqrt{(X_2-X_1)^2+(Y_2-Y_1)^2}}$$

$$R_{11} = \sqrt{X_1^2+Y_1^2+Z_1^2}$$

$$R_{12} = \sqrt{X_1^2+Y_1^2+Z_2^2}$$

$$R_{21} = \sqrt{X_2^2+Y_2^2+Z_1^2}$$

$$R_{22} = \sqrt{X_2^2+Y_2^2+Z_2^2} \qquad (3)$$

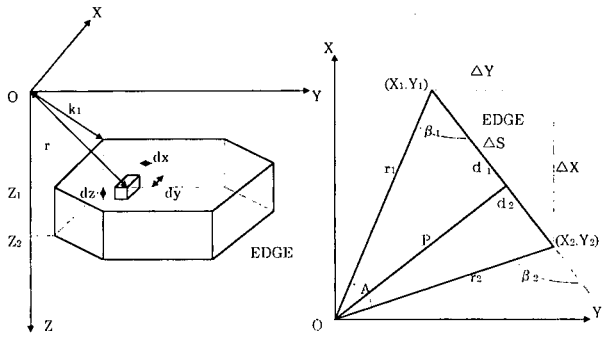

(Left) BASIC ELEMENT-POLYGONAL PRISM

(Right) PLAN VIEW OF ONE EDGE OF PRIZM

Figure 3. Prism Model Used in the Talwani Method

COMPARISON AND EXAMINATION OF REAL DATA

Figure 4 shows the gravity change due to the start of operation estimated from the differences between the data before and after the start of operation (1994 and 1995) obtained from periodic precision gravity measurements after normalizing for the effects of altitude and tide with the results of the gravity change prediction after one year of operation , traces of wells, and the fault distribution. The following facts were clarified from the figure.

(1) In comparison with the predicted values (-10 or less), a much larger negative gravity change (-60 μgal) occurred in the production zone and surrounding area. Such a large gravity change may be due to either a higher rate of vaporization in the reservoir due to less recharge than expected before the start of operation, or a higher rate of steam up-flow through the faults than that used in the numerical simulation, or both.

(2) Although the prediction gives a simple configuration of gravity changes due to the limitation of the division of blocks in the numerical modeling, according to the actual measurement, gravity changes occur according to the fault configuration which restricts the reservoir. This indicates the possibility that a steam phase is formed below the cap lock due to restriction by the faults.

(3) Also in the injection zone, a larger positive gravity change (about +several tens of μgal) was occurred, compared with the predicted value (about +several μgal).

(4) As for differences from the numerical model, since the numerical model is basically a porous model, the rate of steam up-flow was less than in the actual reservoir which is restricted by longitudinal faults. Consequently, the rate of vaporized formation along the faults below the cap lock formation in the actual reservoir was lower than assumed in the numerical model.

(5) Since the gravity value in the injection zone was increased, it may be possible that the underground water level had actually been raised. Since increased gravity values were also observed in areas surrounding the injection zone it may also be possible that the effects of the overall geological changes in the area covering the standard benchmark points are combined with those of the underground water level rise.

In 1996, the second stage of the numerical simulation has been done using the production history from the start of the plant and the production zone was divided more precisely using the location of the newest wells. The layers was also divided more precisely. Figure 5 shows the micro-gravity change after one year production that was calculated by the estimated model. We did not try to match the measurement of the micro-gravity data in this study but the shape and value of the gravity anomaly became more reasonable to the measurement than the last study. The result of calculated micro-gravity change shows the reservoir model was improved by the history matching from the start of the plant. However, the matching of the micro-gravity change is not completely and the more improvement of the numerical model study using both the production history and the micro-gravity change will be required.

CONCLUSIONS

In the above, the following facts were clarified.

(1) Comparison of the results of precision gravity measurement using the post-processor with the results of the previous numerical modeling shows that precision gravity measurement may be used in conjecturing the fine structure inside a reservoir restricted by faults. Therefore, it was proven that precision gravity measurement can be effectively used in the future review of the numerical model.

(2) Since the results of precision gravity measurements cannot explain detailed phenomena quantitatively, it will be necessary in the future to review both the details of the numerical model and to reexamine the measurement method.

ACKNOWLEDGMENT

The authors wish to thank Tohoku Electric Company and Okuaizu Geothermal Co. for their support and permission to publish this paper.

REFERENCES

Allis R. G. and Hunt, T. M. (1986), "Analysis of exploitation -Induced gravity changes at Wairakei geothermal field-", Geophysics, 51, pp.1647-1660

Motoyama, T., Ehara, S., Mogi, T. and Akasaka, C. (1992), "Reservoir monitoring by observations of gravity changes – A case history of Takigami geothermal field-", Abstracts with Programs of 1992 Annual Meeting, GRCJ, A5.

Plouff, D. (1976), "Gravity and magnetic fields of polygonal prisms and application to magnetic terrain corrections", Geophysics, 41, pp.727-741.

Pruess, K. (1991), "TOUGH2 – A General-purpose numerical simulator for multiphase fluid and heat flow.", Report LBL-29400, Lawrence Berkeley Laboratory

Sugihara, M. (1997), "Continuous Gravity Monitoring of Geothermal Activity", Proceeding of the 96th SEGJ Conference, pp.321-323.

Takasugi,S., Sato,T., and Osato,K. (1994), "Parametric Study of Gravity Change Accompanying Geothermal Reservoir Change Calculated by Numerical Simulation", Proceeding of 19th Annual Workshop on Geothermal Reservoir Engineering, Stanford Geothermal Program, pp.277-283.

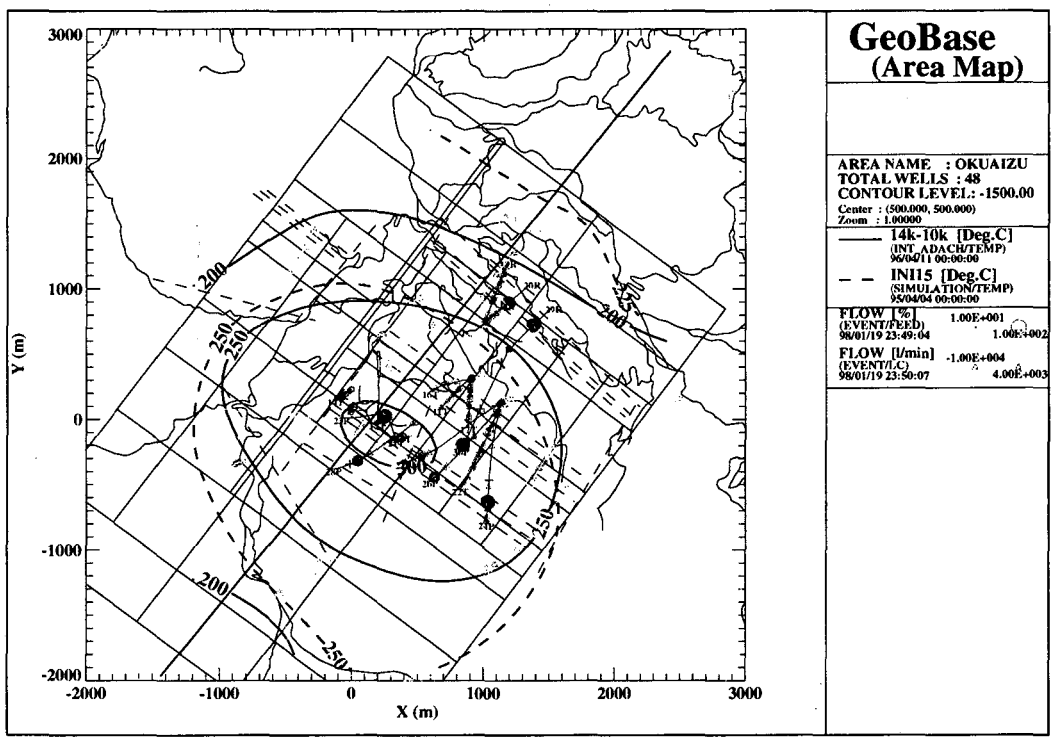

Figure 1. Calculated underground temperature distribution (1,500 m below sea level) optimized by steady-state modeling (dash line), and the actual underground temperature distribution (solid line) with grids of the fourth layer, lost-circulation points (triangle), feed points from PTS logging (circle), faults distribution (solid line) at 1,200m below sea level) and well trajectories (solid line)

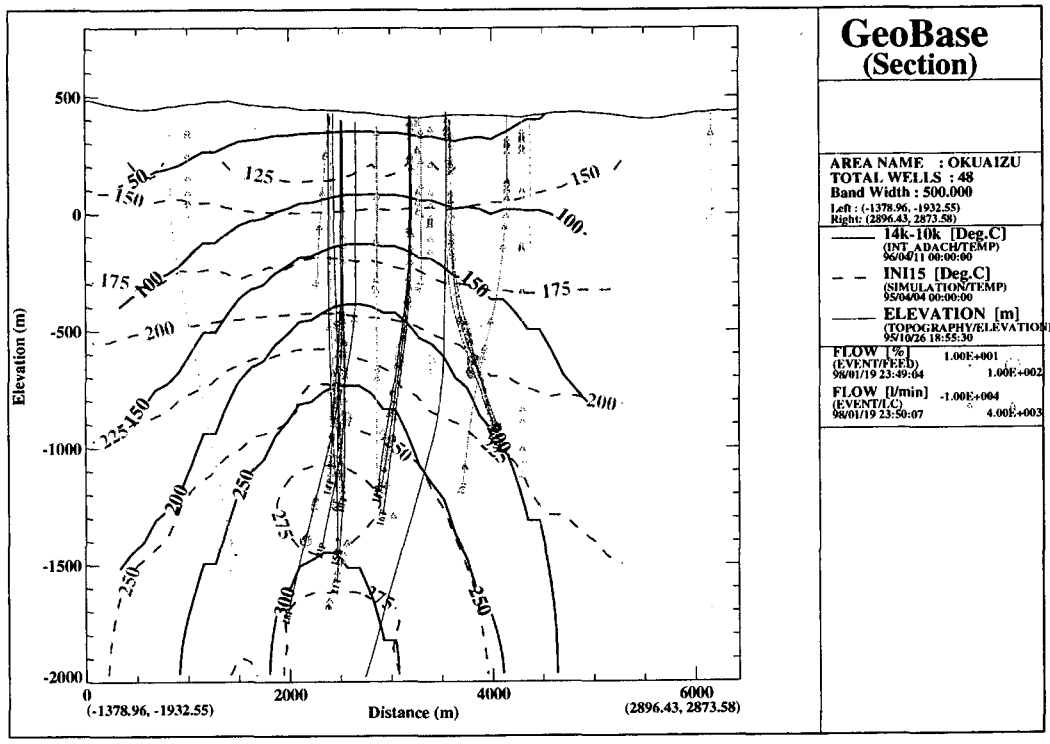

Figure 2. NE-SW cross-sectional view of the underground temperature distribution optimized by steady-state modeling(dash line), and the actual underground temperature distribution (solid line), lost-circulation points (triangle), feed points from PTS logging (circle) and well trajectories (solid line)

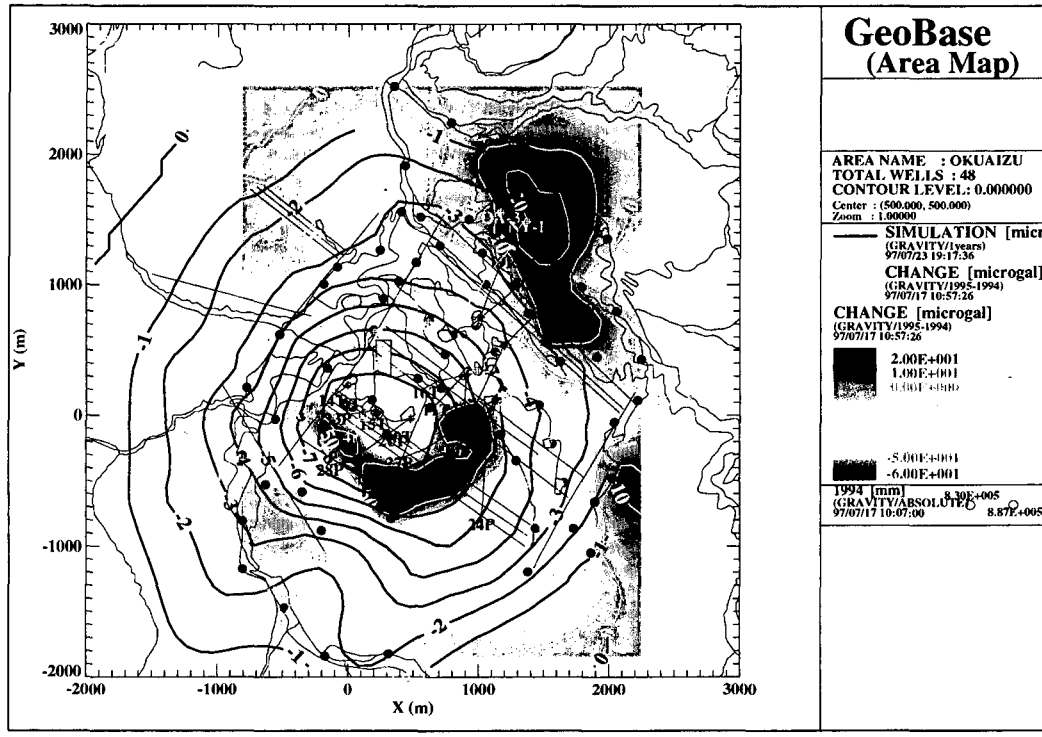

Figure 4 Gravity change predicted one year after the start of production (solid line) and measured values (1995-1994) (filled color & white solid line)

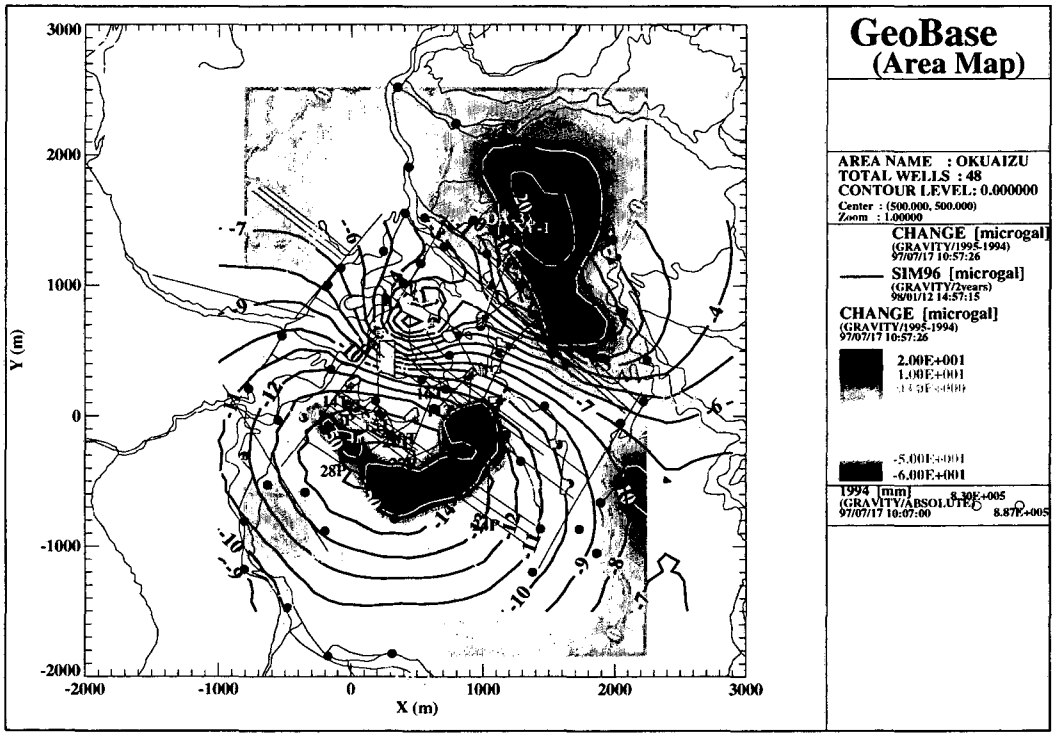

Figure 5 Gravity change predicted one year after the start of production (black solid line) and measured values (1995-1994) (filled color & white solid line) after the production history matching

Development of an Integrated Geothermal Reservoir Modeling System for the Modeling Study using TOUGH2

Tatsuya Sato*1, Kazumi Osato*1, Stephen White*2, John Burnell*2
and Seiichi Yokomoto*3

*1:Geothermal Energy Research and Development Co., Ltd., Japan.
tatuya@gerd.co.jp/ohsato@gerd.co.jp
*2:Industrial Research Limited., NZ. S.White@irl.cri.nz/J.Burnell@irl.cri.nz
*3:Okuaizu Geothermal Co., Ltd., Japan. oagtky@mxg.meshnet.or.jp

ABSTRACT

We developed the integrated geothermal reservoir modeling system on PC (Windows95/NT) or UNIX that can combine database, pre-processor and post-processor for the modeling study using TOUGH2. The system consists of;

(1) Exploration and production database system including the mapping system: GEOBASE2.3.
(2) Pre-Processor : GeoCAD3.0 for constructing a three-dimensional grid model for TOUGH2.
(3) TOUGH2.
(4) Post-Processor for calculation of the micro-gravity change : GRAV/TOUGH2 We here by introduce the performance of the system using Yanaizu-Nishiyama geothermal field data. (Okuaizu Geothermal Co., Fukushima prefecture, Japan).

INTRODUCTION

Geothermal reservoir modeling and the prediction of geothermal production behavior using numerical simulation based on geothermal reservoir modeling are important steps towards the construction of a geothermal power station. In geothermal reservoir modeling it is necessary to combine surface exploration results and well data obtained from various survey stages of rough to detailed examination in order to form an integrated three-dimensional model of a geothermal reservoir. Since exploration data have been collected by many researchers in the fields of geology, geophysics, chemistry, drilling, logging, reservoir engineering, etc., over a long period of time, specialists in geology and reservoir engineering must make a great effort to find information essential for geothermal reservoir modeling out of a tremendous amount of data presented in various formats. Given this situation, construction of a consistent three-dimensional stereoscopic model is a time-consuming job requiring much skill if it is to be done in a human's head. Also, in forming a numerical model grid for ultimate numerical modeling simulation, a considerable amount of time is required to improve the accuracy of modeling because numerical modeling is also time-consuming and requires much skill. Therefore "computer-aided comprehensive analytic techniques" for geothermal reservoir modeling which use the latest in computer technology are becoming popular (Anderson et al., 1995; Stevens et al., 1995; Nakanishi et al.,1997).

In many geothermal power stations flow data from a specific well, or even from a specific flash separator connected multiple wells in extreme cases, are mostly used for production history matching.

This report describes application of the

integrated geothermal reservoir modeling system developed in the present study, which uses an exploration and production database, a pre-processor for designing of a reservoir model, TOUGH 2 (Pruess, 1991), and a post-processor for micro-gravity, to the Yanaizu-Nishiyama geothermal field.

BACKGROUND

The Yanaizu-Nishiyama Geothermal Power Station, located in Yanaizu-cho in Fukushima Prefecture, is a single-unit geothermal power station with the largest steam turbine (of the single-flush type) in Japan, with an approved capacity 65MW. Tohoku Electric Power Company is responsible for the power generation section of the station, and Okuaizu Geothermal Co. is responsible for the steam supply section. The station began operation in May 1995.

Okuaizu Geothermal Co., which is in charge of development of the station and management of the steam production facilities, started computer control of production-injection data immediately after the start of operation. Also, it has been selecting data required for future reservoir control, developing an exploration and production database using GEOBASE (Sato et al., 1995) developed by the authors (K. Osato and T. Sato) and the pre-processor to be used for TOUGH2, and reviewing the production behavior which was predicted using the numerical geothermal reservoir model and TOUGH 2 in 1996.

This paper describes the construction of the database and utilization for numerical simulation of Yanaizu-Nishiyama geothermal field.

OUTLINE OF THE SYSTEM

The system consists of:

(1) Exploration and Production database system GEOBASE2.3 for entering, querying, and displaying all the types of data in a comprehensive manner
(2) Pre-processor GeoCAD3.0 for constructing a three-dimensional numerical model based on the conceptual model obtained by integrated data analysis from the database
(3) Reservoir simulator TOUGH2.

GEOBASE2.3 runs on UNIX (HP9000/700, SUN) or PC (Windows95/NT). GeoCAD3.0 runs on UNIX (HP 9000/700) or PC (Windows95/NT).

The database is based on Oracle (the current version is Oracle 7.2 or Personal Oracle 7.2), a decentralized relational database which is popular all over the world. The database has a simple structure, and it is possible to redefine and enter all types of data which can be fitted in the structure into the database. If Oracle 7.2 is used, it is also possible to form a decentralized system (client-server system) using a LAN or WAN which can easily join PCs and UNIX machines. The retrieval and mapping function of the database allows a two-dimensional or three-dimensional representation of data to be obtained by using single data sets or superimposing various data sets, e.g., geological column diagrams, logging data, surface survey data, production/injection data, results of reservoir simulation. Figure 1 shows the data structure.

CONSTRUCTION OF A NUMERICAL MODEL USING THE DATABASE AND THE PRE-PROCESSOR

Figure 2 shows the underground temperature distribution 1,500 m below sea level constructed using the database, the lost-circulation points, the feed points of production wells obtained by PTS logging, and the fault distribution at 1,200 m below sea level. Figure 3 shows the NE-SW cross-sectional view onto which corresponding geological column diagrams are projected.

High temperature zone exist along the NW-SE fault on south -west side (See Figure 2). Many feed points (Filled circle in Figure.2 and 3) exist along this fault and it is major production zone in this field. Reinjection zone is along NW-SE fault on north-east side. Few feed points exist along it.

In the numerical model, the NE-SW length of the area was taken to be 4.6 km so that the fault directions can be taken into consideration and the high temperature range can be covered. The NW-SE length was taken to be 3.2 km. As for the internal grid, the area near the faults relating to production and injection was divided into smaller blocks and the surrounding area was divided into larger blocks. The first layer of this model was taken to be the range between the surface level, which is about 500 m above sea level. The range from sea level down to -2,000 m below sea level was divided into 300 - 500 m layers. As boundary conditions, the pressure and temperature on the ground surface was assumed to be constant, and closed boundaries were assumed on the side faces of the model. To reconstruct the underground temperature distribution, two recharge blocks were placed on the south side of each of the first to third layers, and one recharge block was placed to the west of the second layer. EOS2 (H2O-CO2) of TOUGH2 was used as the state equation to take the CO2 of geothermal fluid into consideration.

In actual modeling, the pre-processor GeoCAD3.0 that had been developed by the authors (J. Burnell and S. White) was used. Since GeoCAD3.0 can readily form non-uniform (polygonal) grids taking advantage of the IFDM of TOUGH2, input data for TOUGH2 can be prepared by drawing quadrilaterals and polygons using a mouse and indicating the necessary physical properties in the center of each polygon. In this case, general rectangular grid division was made horizontally, and grid division in accordance with the inclination of the faults was made vertically. Figure 4 shows the sample display of GEOCAD3.0.

STEADY-STATE MODELING BY MEANS OF NUMERICAL SIMULATION

Since the numerical simulation was done just before the start of operation of the station, the model was optimized according to the steady-state. However, review of the numerical model based on the production history after the start of operation has not been done. The numerical model was constructed based on the base model used in the 1989 reservoir evaluation taking data from new wells into consideration. Figure 6 shows the underground temperature distribution calculated using the steady-state-optimized

numerical simulation, the actual underground temperature distribution (both at 1,500 m below sea level) with the grids of the fourth layer designed by GEOCAD3.0. Figure 6 shows the NW-SE cross-sectional view of Figure5.

CONCLUSIONS

It was proven that a integrated geothermal reservoir modeling system using a exploration and production database, a pre-processor for reservoir modeling, a reservoir simulator, and a post-processor for micro-gravity can be effectively used in the whole course of modeling, numerical modeling, numerical simulation, and evaluation using production history.

REFERENCES

Anderson, E. B., Clark, G. B. and Ussher, G. N. H. (1995), "A Design and Implementation of the GDManager Geothermal Data Management System", Proc. World Geothermal Congress 1995, Florence Italy, pp.3005-3009.

Pruess, K. (1991), "TOUGH2 - A General-purpose numerical simulator for multiphase fluid and heat flow.", Report LBL-29400, Lawrence Berkeley Laboratory

Sato, T., Okabe, T., Osato, K., and Takasugi, S. (1995), "Graphical User Interface for TOUGH/TOUGH2 - Development of Database, Pre-processor and Post-processor", Proceedings of the TOUGH Workshop'95, LBL, pp.271-276.

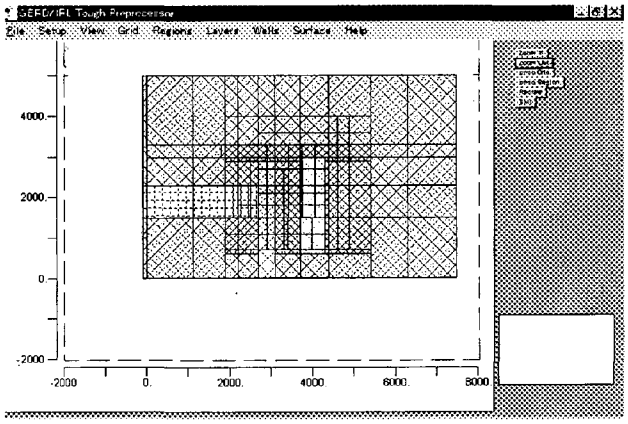

Figure 4. A sample display of GEOCAD3.0 on PC.

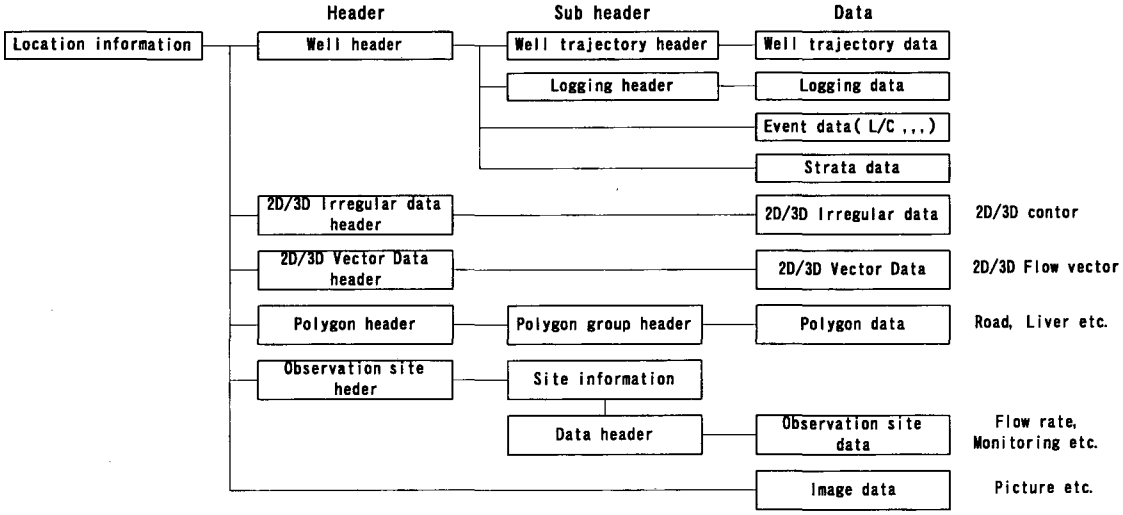

Figure 1. Data Table Structure of GEOBASE

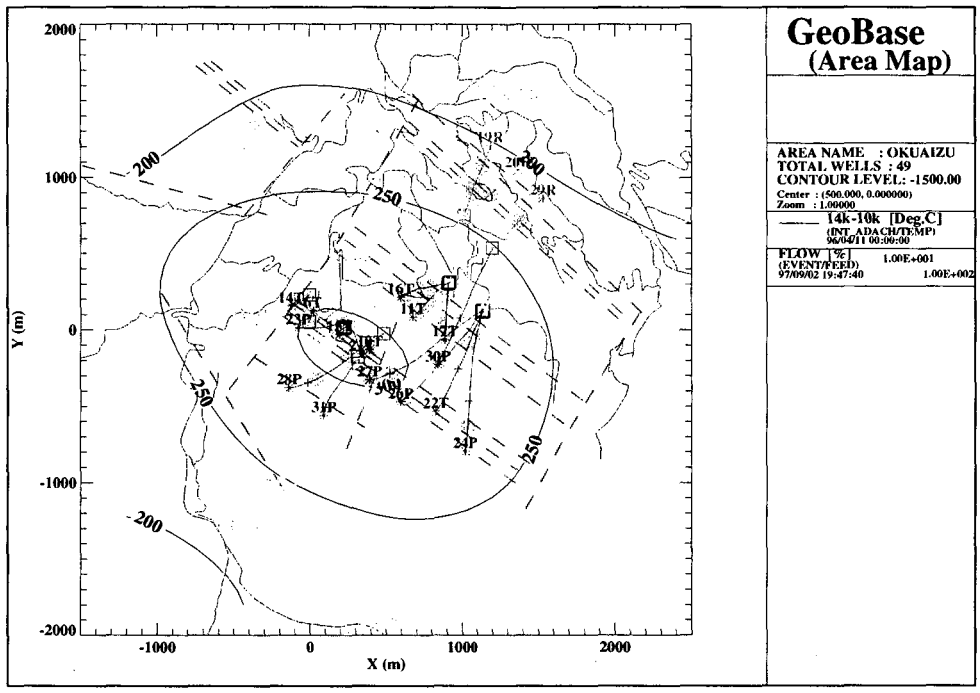

Figure 2. Underground temperature distribution (1,500 m below sea level) constructed from the database, lost-circulation points, feed points of production wells, and fault distribution (1,200 m below sea level)

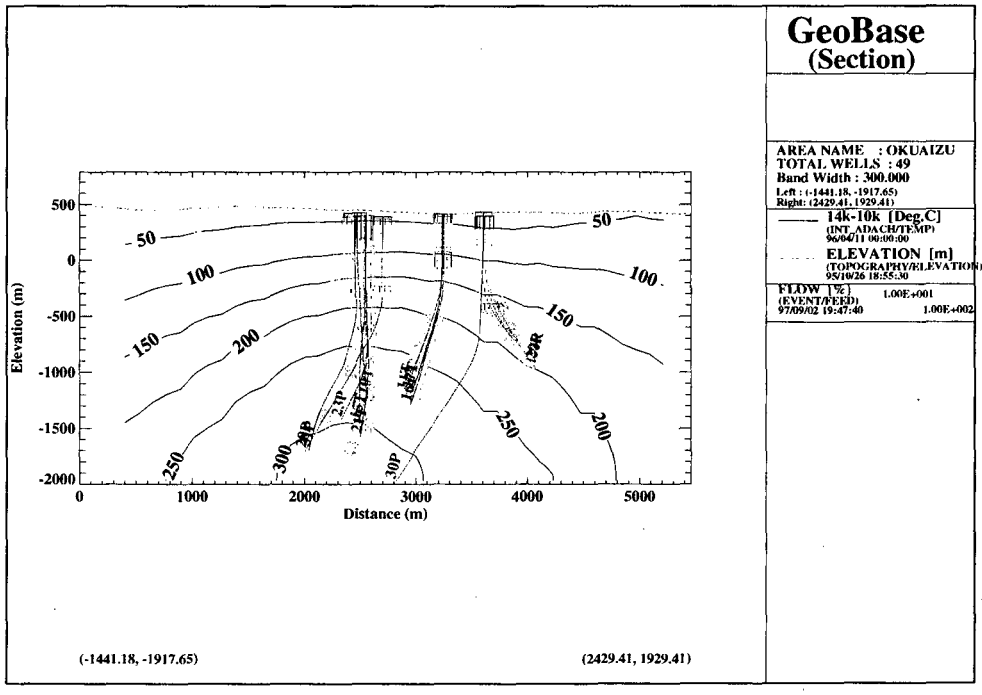

Figure 3. NE-SW Cross-sectional view of the underground temperature distribution, lost-circulation points, feed points of production wells, and projected geological columns

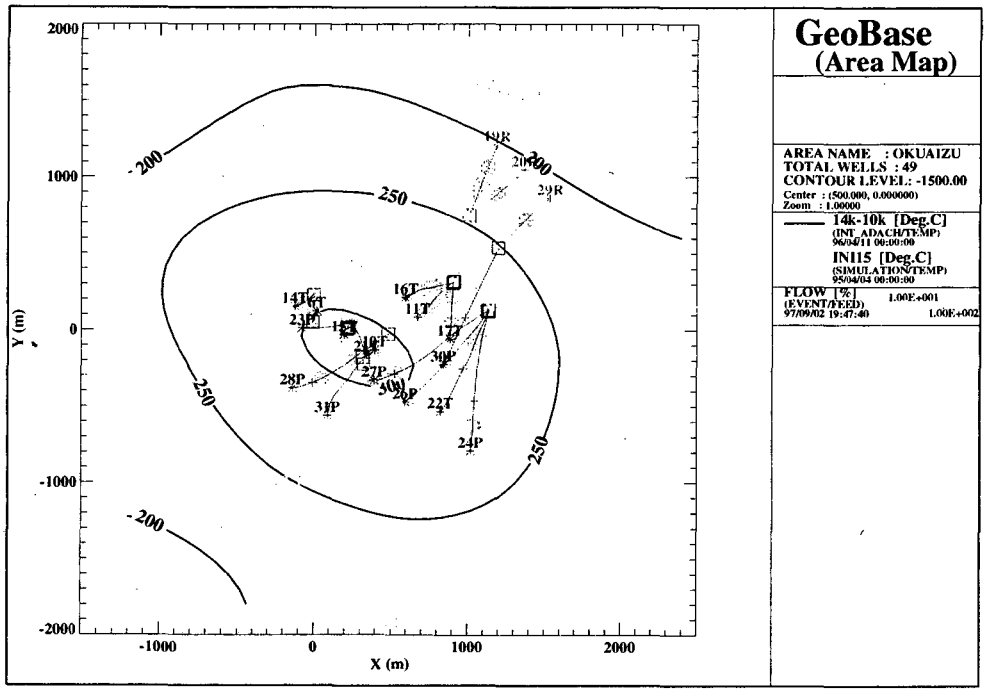

Figure 5. Underground temperature distribution optimized by steady-state modeling (dash line), and the actual underground temperature distribution with grids of the fourth layer designed by GEOCAD3.0

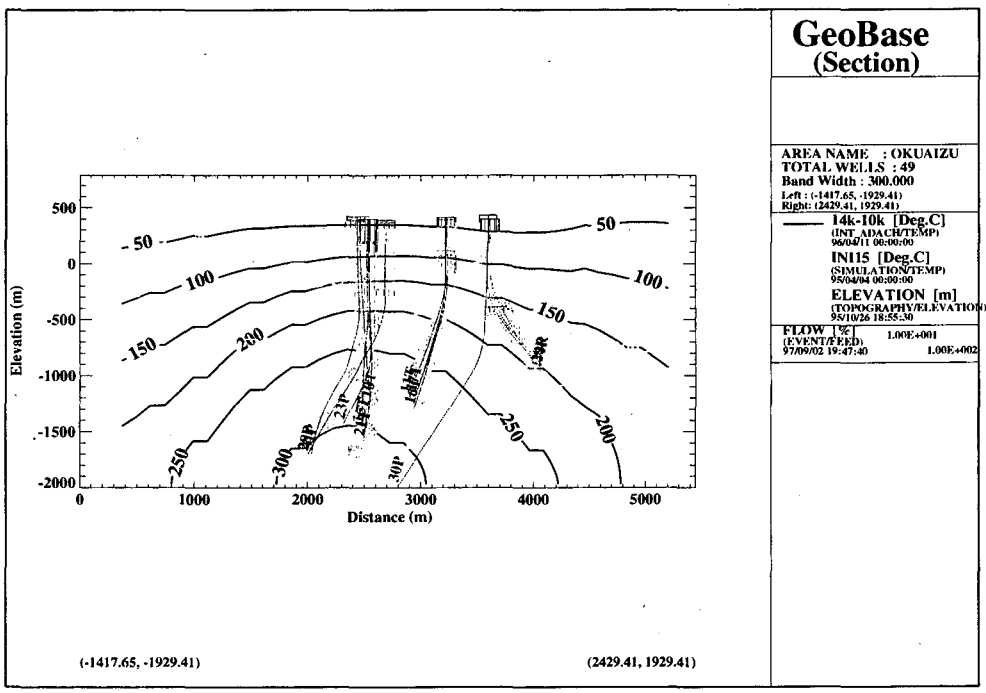

Figure 6 NE-SW cross-sectional view of the underground temperature distribution optimized by steady-state modeling(dash line), and the actual underground temperature distribution at 1,500 m below sea level

Inverse modelling of the Wairakei geothermal field

D.P. Bullivant and M.J. O'Sullivan
Department of Engineering Science,
University of Auckland,
New Zealand

1 Introduction

Wairakei is a liquid dominated geothermal field in the middle of the North Island of New Zealand. It has been in production for 40 years and currently produces 157 MWe. The authors have developed several models of Wairakei for Contact Energy Ltd, the field operators. The model currently being used for field management has 1417 blocks. It is more detailed than previous models, particularly around Tauhara. Tauhara is a second geothermal field to the south-west of Wairakei that is connected to Wairakei (see Figure 1). The development of Tauhara is currently being considered and the affect of this on Wairakei and vice versa is being investigated. Inverse modelling using ITOUGH2 [1] was carried out to help calibrate the enlarged model.

In the following section the 1417 block model will be described. The field data used in the inverse model is detailed in the third section. The last section explains how the inverse model was used to help improve the 1417 block model and what was learned about inverse geothermal modelling.

2 Model description

A brief description of the model is given here. A fuller description is given in the accompanying paper [2].

The model has 118 columns. The layout of the columns and their relationship to the field are shown in Figure 1. The large columns in the outer ring are outside the reservoir and are there to maintain time constant pressures and temperatures at the reservoir boundary. The model extends from the top of the reservoir (varies, approximately 400 m above sea level) to 2500 m below sea level and is divided into 12 layers (thicknesses shown in Figure 2). The thicknesses of the blocks in the top layer vary to represent the top of the reservoir which is assumed to approximately follow the topography of the ground surface. There is a single "wet" atmosphere block.

Heat sources are placed in the bottom block of each column to reproduce the background geothermal gradient. Mass sources are placed in the bottom blocks of some columns to represent the upflow zones. During production the rates for these mass sources vary depending on the pressure in the block to account for production induced recharge. Well tables for the 106 production wells were set up using field data.

3 Inverse model description

A large amount of field data has been collected for Wairakei-Tauhara. The following data were included in the inverse model

Figure 1: A map of Wairakei-Tauhara showing the column layout

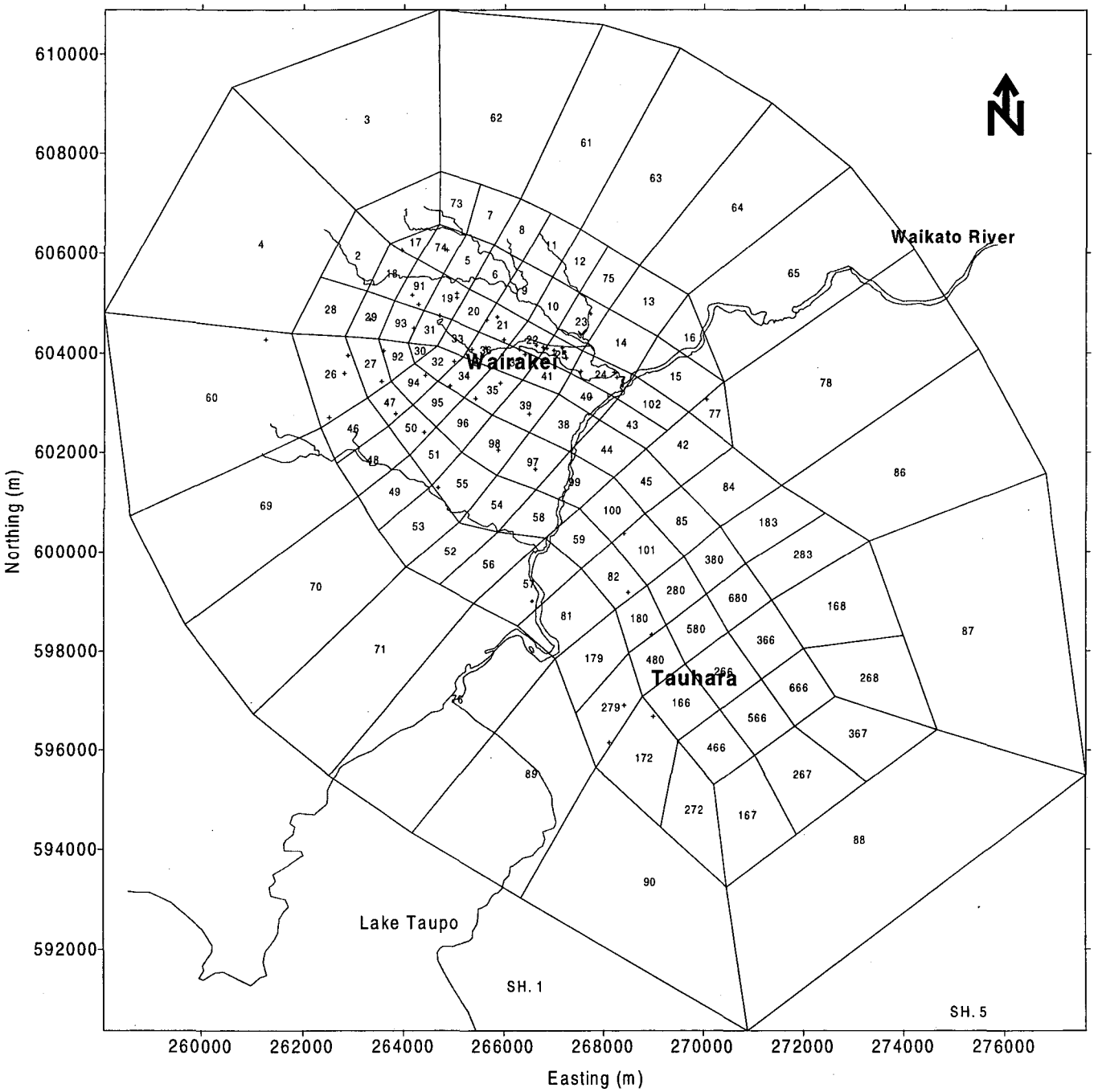

Figure 2: The model layers

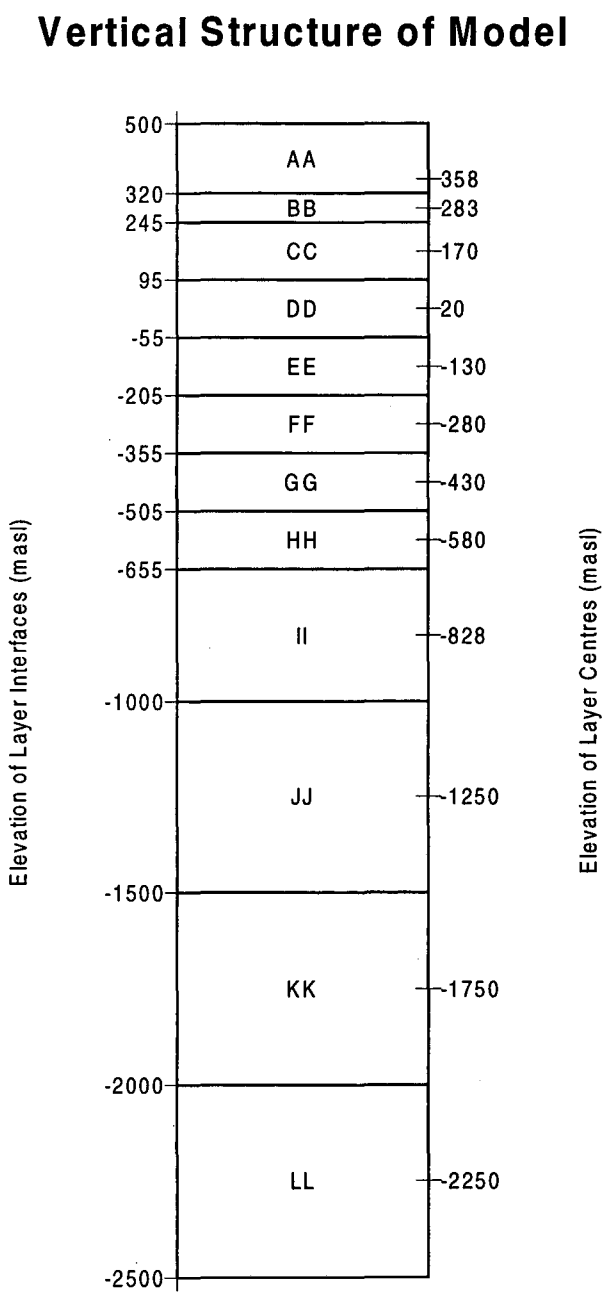

- Well temperature profiles. These were available at different times for different wells. They were assigned to the column containing the well and linearly interpolated to give values at layer centres.

- Well pressure time histories. These were assigned to the block containing the well feed zone and adjusted, assuming a hydrostatic pressure gradient, to the block centre.

- Well flowing enthalpy time histories. These were assigned to the block containing the well feed zone.

The calibration of the Wairakei model by hand has proceeded in two stages - natural state modelling and history matching. In the natural state matching, the permeability structure and the deep hot inflow (location and magnitude) in the model are adjusted and the temperature distribution and surface outflows (location and magnitude) are compared with field data. For history matching, the model permeabilities and porosities are adjusted and pressure declines, temperature changes and production enthalpies are compared with field data.

Both processes are iterative. In fact a cycle of iterations is followed, with several iterations of the natural state followed by iterations of history matching and then a return is made to recheck the natural state.

ITOUGH2 allows both stages (natural state and history matching) to be used in one evaluation of the goodness of fit measure and this feature was used.

Some experimentation was required with the weighting factors used for combining the different types of field data into the overall measure of goodness of fit in order to make ITOUGH2 work well. The L1 error estimator (maximum absolute error) was used instead of the L2 error estimator (sum of squared errors) because it is less biased towards outliers.

ITOUGH2 was run on a Silicon Graphics Power Challenge with 16 R10000 processors and 2 GB of memory. This machine was used because of its large memory and not because of the multiple processors (only one was used). As part of its post-processing, ITOUGH2, calculates the correlation matrices which are very large for this problem. The memory requirements could be reduced by not using some of the post-processing. It is intended to investigate ways of parallelizing ITOUGH2.

4 Results

Most of the work with ITOUGH2 on the model of the Wairakei-Tauhara system was carried out when a coarse grid model (301 blocks) was refined overall and particularly in the Tauhara area, to produce a model with 1417 blocks (described in the accompanying paper [2]). The aims for the recalibration of the 1417 block model were

- To maintain or improve the fit to the Wairakei data. In particular the matches to production enthalpy and pressure drawdown for the Western Borefield (columns 20, 21, 33 and 36).

- To include the Tauhara field data.

- To experiment with conceptual models of the connection between Wairakei and Tauhara.

Some preliminary runs with ITOUGH2 showed up a problem with the location of the feed zones of some wells in the model. The difficulty was highlighted by an apparent failure of ITOUGH2 to improve the match of model results for production enthalpy from some wells to field data. This was because the initial placement (based on estimates of feed elevation) had wells with vastly different boiling characteristics (if and when they boiled) in the same block. The practical solution to this problem was to move the offending wells up or down a layer.

ITOUGH2 was then used to vary the following groups of parameters (each group was included in a separate ITOUGH2 run)

- The rates and enthalpies for the wells that represent the deep upflow at Wairakei.
- The permeabilities in the Wairakei production zone (layers DD, EE and FF).
- The recharge coefficients for the deep upflow (these control how much a change in pressure during production changes the recharge rate).

At Tauhara, there is much less field data available than at Wairakei. The data used for calibration was

- Temperature profiles from 4 deep wells. These were included in the ITOUGH2 input file.
- Locations of surface outflows. This is qualitative data and was not included in the ITOUGH2 input file.

The conceptual model of Tauhara includes high permeability, due to faulting, which runs south-west to north-east. This was included in the model and the permeabilities for the rock types representing this faulting was one of the groups of parameters varied using ITOUGH2. The other group was the flow rates and enthalpies for the wells representing the Tauhara upflow zone.

The conceptual model for the Wairakei-Tauhara connection has the connection leaving Tauhara at a fairly shallow elevation and then taking a step down into Wairakei near Karapiti (columns 55 and 98). There are a few wells between Tauhara and Wairakei and these were used for calibration. The parameters varied were the permeabilities of the connection rock types. To obtain a satisfactory match the connection had to be moved deeper.

The general mode of operation for ITOUGH2 was as follows:

- To include all the field data in the ITOUGH2 input file.
- To vary a small group of parameters (not more than 20 and usually less 10) related to a particular feature of the model.
- To look in general at how much the goodness of fit measure changed and to look in detail at the change in how the model fitted the feature of interest.

The number of parameters varied in an ITOUGH2 run is restricted partly because of the computation time, but mainly because if too many parameters or insignificant parameters are included the minimization procedure "flops" around and does not make progress. Another important component of the inverse modelling is the choice of weights for the field data. If this is incorrect then the match to one part of the data may be improved, but the match to another part may become unacceptable.

In the calibration of the 1417 block model both "hand" calibration and ITOUGH2 were used. This combined process proved to be very effective. Human interaction was necessary to choose groups of parameters and weighting factors for groups of data, while ITOUGH2 quickly sorted out the optimal choices for parameter values. Human intuition and commonsense is still required to sort out strategies for model improvement which require more than parameter adjustment, for example the relocation of feed zones that was discussed above.

In the combined process of manual calibration and computerised calibration, the sensitivity data provided by ITOUGH2 proved to be a useful aid in decision making. The sensitivity data was used to decide which parameters to discard so that others could be included in the limited size parameter set for a new ITOUGH2 run.

The current version of the 1417 block model of the Wairakei-Tauhara system matches the data for both Wairakei and Tauhara well.

References

[1] Stefan Finsterle. ITOUGH2 User's Guide, Version 2.2. Technical Report LBL-34581, Earth Sciences Division, Lawrence Berkeley Laboratory, 1 Cyclotron Road, Berkeley, CA94720, 1993.

[2] M.J. O'Sullivan, D.P. Bullivant, S.E. Follows, and W.I. Mannington. Modelling of the Wairakei-Tauhara geothermal system. TOUGH Workshop '98.

Thermal evolution of hydrothermal systems from a geologic perspective using Tough2, Los Azufres, Mich., Mexico

Gerardo García-Estrada
GPG, Comision Federal de Electricidad of Mexico
Alejandro Volta 655 Col. Electricista, Morelia 58290, Mexico

Abstract

In this paper we comment the use and limitations of Tough2 (Pruess, 1991) to model the thermal evolution of a high enthalpy geothermal zone from a geologic perspective, and the way in which we are working to reach this aim. The project, still in progress, has as one of its objectives to adapt Tough2 to model temperatures measured in exploratory gradient wells, in the same way that modelling is applied in geophysics, as a tool to establish boundaries for the geometry and properties of a hydrothermal system under study.

We use the expression 'from a geologic perspective' to mean the evolution of a hydrothermal system, and the associated volcanic heat source, in geologic time, from its emplacement to its complete cooling. As in gravity studies, in geophysical thermal interpretation we use the concept of regional-residual separation. The regional signal as the effect produced by predictable phenomena, and the residual one, associated with local unpredictable anomalies of heat and mass flow.

Tough2 is used to calculate the regional signal based on geological and geophysical data. If it is modeled as the steady state of the zone based only on the regional heat flow, the residual, calculated as the difference between measured and predicted data, corresponds to the anomalous effect produced by the magmatic heat source, that was not considered in the calculus. On the other hand, if we include parameters of the magmatic body for the calculus of regional, the residual signal corresponds to the effects of anomalies caused by the presence of faults not included explicitly.

Introduction

The Comision Federal de Electricidad of Mexico (CFE) has initiated exploratory drilling in medium to small size geothermal projects under geological environments quite different to that of the well known geothermal zones. Los Azufres Geothermal project, the most important producing field in the Mexican Neovolcanic Belt, is being used as a learning site, in which convective modelling, using PC version of Tough2 (Antunez et al., 1994) with module EOS1, is conducted in order to develop geological and geophysical criteria for the study and interpretation of data in poorly known areas.

A first stage of this project, consisting of geological an geophysical data interpretation, to have an idea of the heat source location, and a research to analyze the utility of thermal data measured in big diameter well during drilling stops, have been concluded. At present, the hydrothermal evolution modelling is currently conducted.

Conventional thermal geophysics modelling

is limited to the use of conductive heat transfer programs. The reservoir is represented by rocks of high thermal conductivities, ten to twenty times a normal value. This procedure permits to fit calculated to measured data, but at the same time conducts to conclusions difficult to accept if convective phenomena are not included as an integral part of the thermal modelling. The need to include convective modelling makes advisable the use of Tough2 program for geophysical studies, profiting of its open architecture that permits the necessary modification to use it in this non conventional way.

The thermal modelling of Los Azufres from an Earth Sciences perspective is a problem that can be divided in four different sub-problems, in the same way that any other geophysical project: data compilation, data reduction, processing and interpretation.

The use of Tough2 as a tool to estimate the 'normal' predictable temperatures can be included as part of data processing. Difficulties associated to compilation, reduction and interpretation are not discussed here, and attention is centered on the activities conducted to adapt Tough2 to temperatures processing.

Procedure

Some times in thermal studies, it is necessary to proceed in a trial and error basis to test the correctness of different analyzed hypothesis, in the same way as in gravity modelling. To make an efficient use of Thoug2, internal subroutines were included to permit graphic display of input and output data: geometry, physical properties, initial and temporal thermodynamic results. They all are used directly as input for commercial graphic and contouring software.

Graphic interface subroutines are completely compatible with Tough2 original structure, input and output data transfer are conducted trough a few additional common blocks. In spite these subroutines are not real time displays they have been very useful, and necessary for the use of Tough2 in this project.

For the study of the heat source in a high enthalpy geothermal system it is convenient to have the capability to model temperatures up to the typical values of magma flows, from 600 to 1200 °C under the assumption that can be representative of magmatic intrusive temperatures.

To reach this goal we included subroutines covering the thermodynamic regions numbered 3 and 4 by the International Formulation Committee, 1997. The implicit formulation are inverted using the Newton-Raphson method.

As preliminary results of this project, Figure 1 shows a profile with geological and geophysical data used to delineate the geometry of Los Azufres, based on recent studies (Garcia, 1995). Figure 2 shows the model's geometry based on Earth Sciences data. The steady state was produced with a fixed 20 °C superficial temperature and a heat flow of 100 mW/m^2 , fixed in the lower boundary (mean value of the heat flow province). Differences between calculated temperatures of Figure 2 and measured data of Figure 1 are the residual effect associated to the magmatic heat source and comprises all the secondary effects not considered explicitly in the calculus (Figure 3).

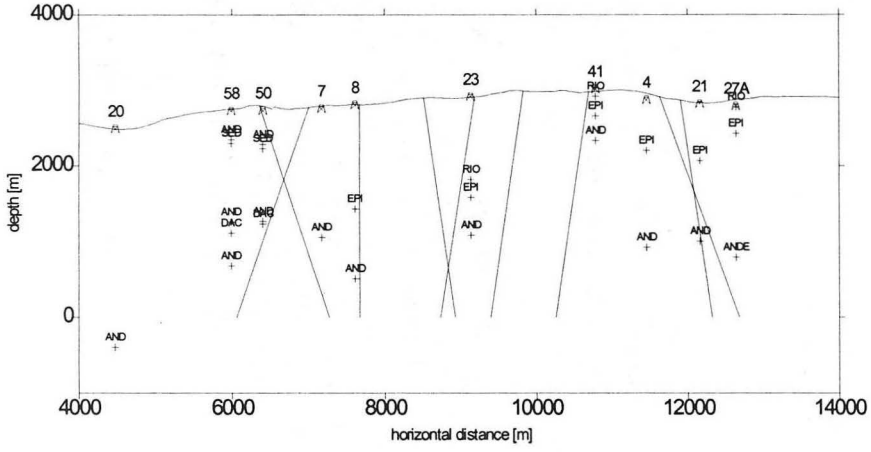

a) RIO = Ryolite, AND= Andesite, EPI= Epidote

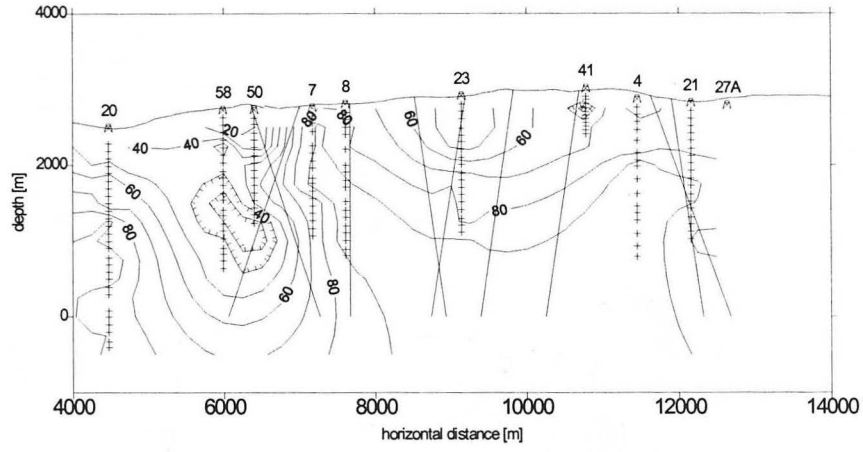

b) Contours in alteration percent.

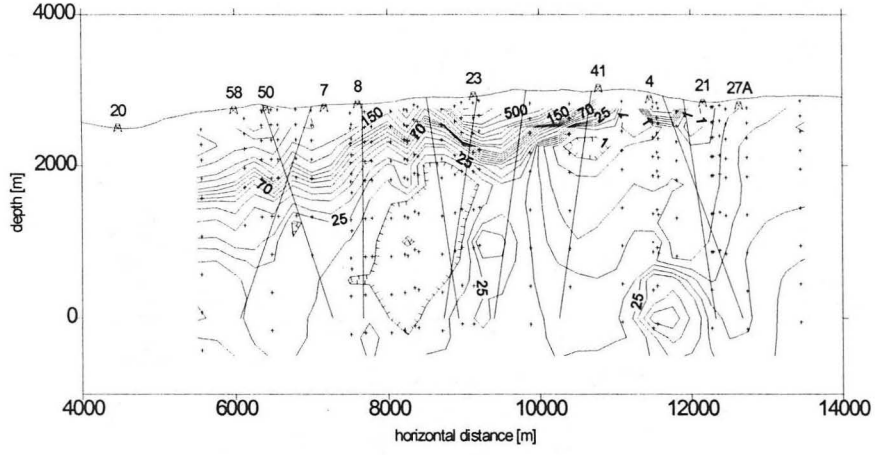

c) Contours in Ohm.m

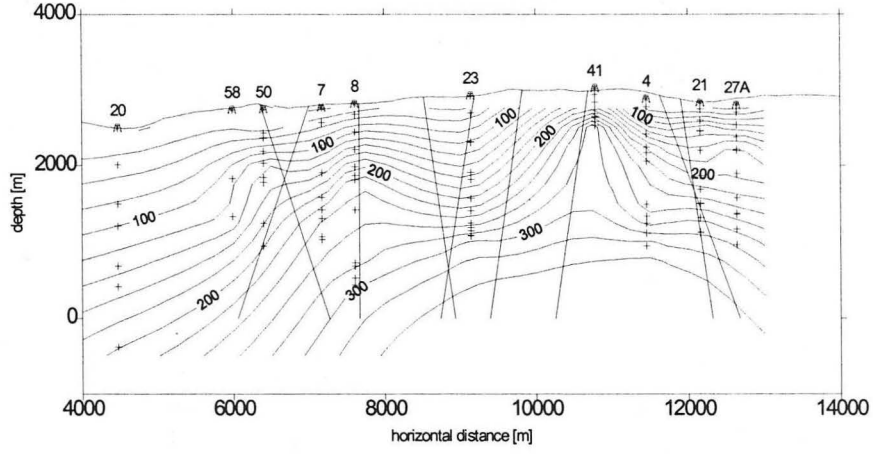

d) Contours in °C

Figure 1.- Los Azufres, Mich. Well numbers are indicated in the upper part.
Straight lines indicate apparent dip of main faults.
a) Litologic contacts.
b) Hydrothermal alteration percent.
c) Apparent resistivity (DC soundings).
d) Drilling temperatures.

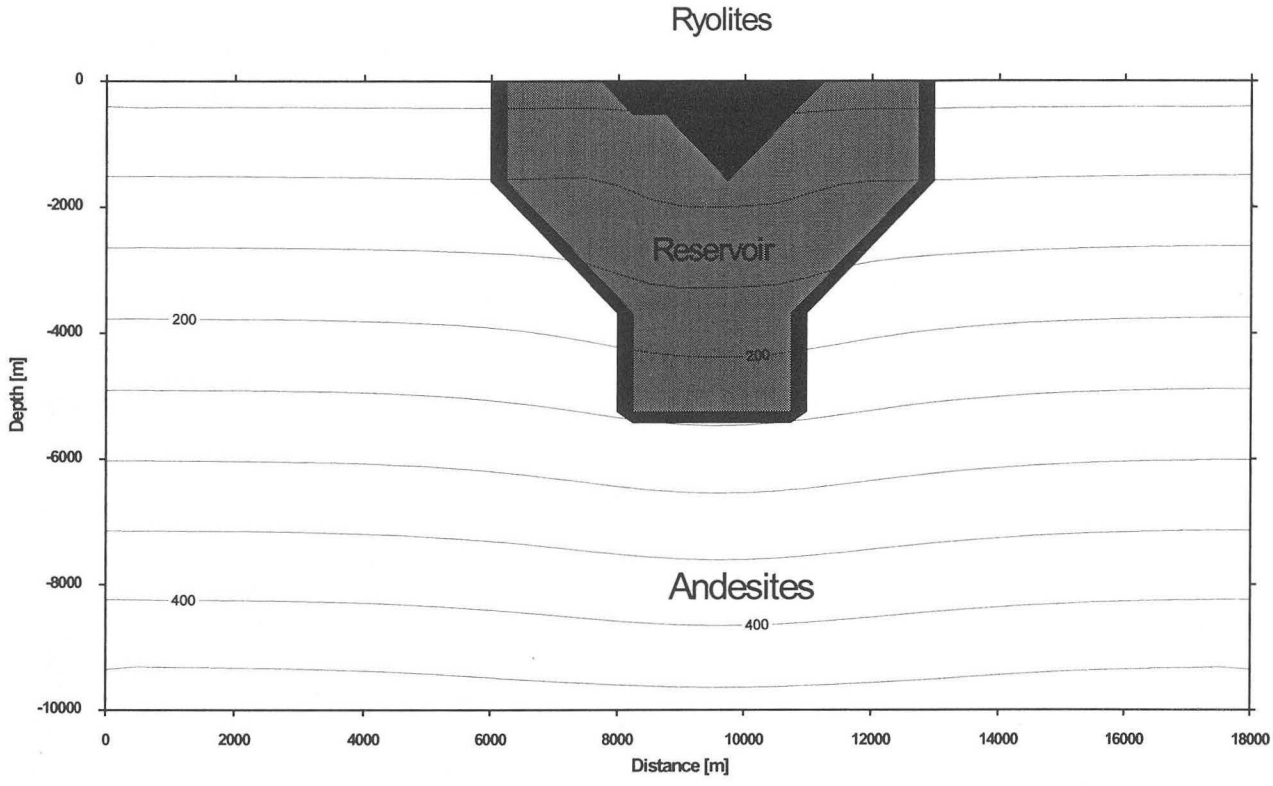

Figure 2.- Model geometry and calculated temperatures with a fixed top temperature of 20 °C and heat flow 100 mW/m2 on the bottom.

Our following objective is the inclusion of a cooling shallow intrusive for the calculus of the theoretical regional temperature, we attempted to simulate its instantaneous placing in the same way that in conductive modelling, but we have found that this procedure produces instabilities in Tough2 solvers. Future developments require to find a way to avoid this instabilities trough the appropriate use of Tough2 options or simulating the progressive ascent of the magmatic source.

Conclusions

The use of Tough2 from an Earth Sciences perspective required the development of efficient graphic interfaces in order to make possible a trial and error procedure to adjust the geologic parameters and geometry to fit calculated and observed data using very simple geometries.

In order to simulate the convective cooling of the intrusive acting as the heat source of the geothermal field and to compare this temperatures with results of the purely conductive models, normally used to interpret temperatures in exploratory wells, we developed subroutines to cover a wider thermodynamic range, up to 1000 bar and 800 °C.

Thermal data of Los Azufres geothermal

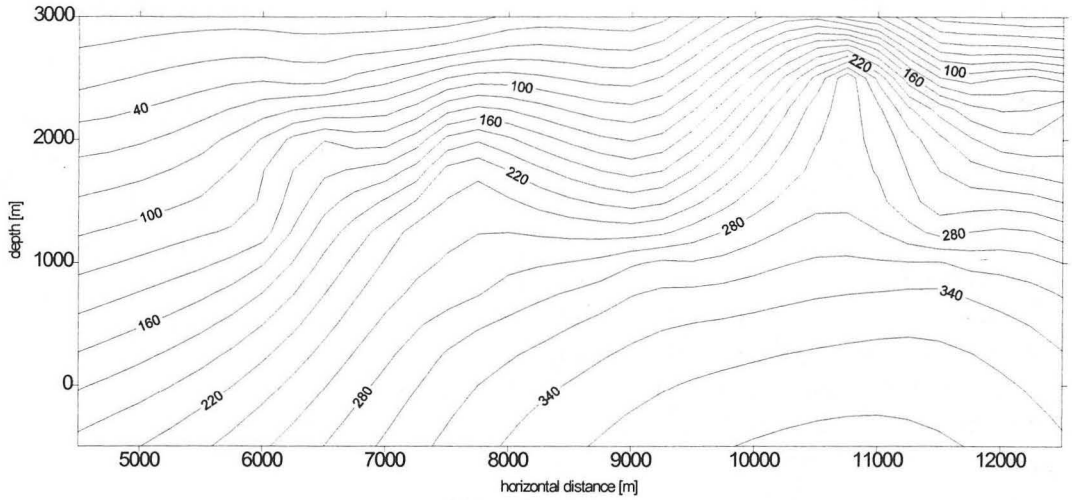

Measured temperatures.

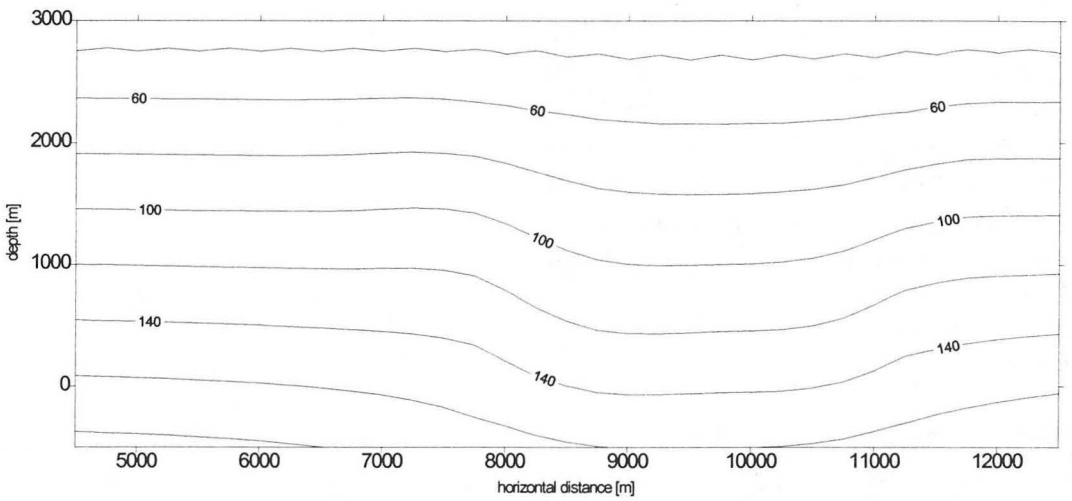

Regional temperatures (calculated with Tough2).

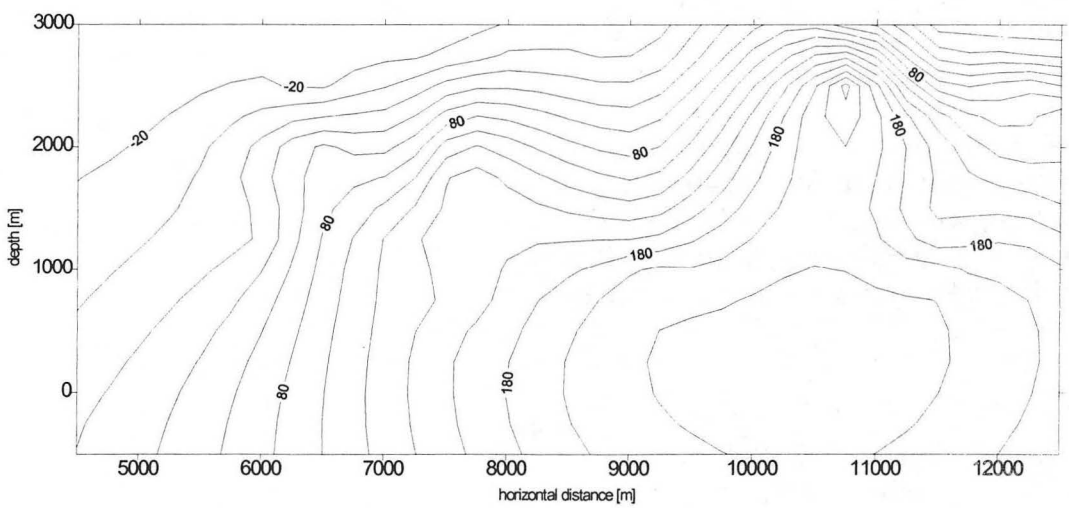

Residual temperatures (measured - calculated).

Figure 3.- Measured, regional and residual temperatures.
Contours in °C.

project are currently used to test these developments and at the same time to develop criteria to interpret temperatures measured in gradient and slim holes in less known exploration zones. The use of these data coming from big diameter wells required a detailed analysis to evaluate the utility of temperature data, measured during drilling stops of production bore holes, as representative of a pre-drilling thermal equilibrium stage.

At present, we work in the development of procedures to simulate the intrusive emplacement, in order to avoid convergence difficulties with the algorithms, caused by the big thermodynamic conditions differences between the intrusion an the host rocks, and problems associated to thermodynamic discontinuities of water properties.

References

Antunez, E., Moridis, G. and Pruess, K., 1994. Large scale three-dimensional geothermal reservoir simulation on PC's.. Proceedings of the Nineteenth Workshop on Geothermal Reservoir Engineering, Sanford University, Stanford, Ca., January 18-20, 1994, pp. 99-106.

García, E. G. H., 1995. Reinterpretación geofísica del campo de Los Azufres, Mich. (Reporte de avance). Informe interno GF-AZ-034/95. Departamento de Exploración, Gerencia de Proyectos Geotermoeléctricos, Morelia, México.

International Formulation Committee, 1967. A formulation of the thermodynamic properties of ordinary water substance, IFC Secretariat, Düsseldorf, Germany.

Pruess, K., 1991. TOUGH2- A General-Purpose Numerical Simulator for Multiphase Fluid and Heat Flow. U.S. Department of Energy, Contract DE-AC03-76SF00098. LBL-29400,UC-251, 102 pp.

TOUGH APPLICATIONS TO ANALYSIS OF THE PRESSURE TRANSIENT DATA OF VERKHNE-MUTNOVSKY SITE, MUTNOVSKY GEOTHERMAL FIELD, KAMCHATKA.

A.V.Kiryukhin , M.D.Lesnykh , A.Y.Polyakov, and E.G.Kalacheva
Institute of Volcanology, Petropavlovsk-Kamchatsky, Russia, 683006.

ABSTRACT

Pressure monitoring data in well #30 (capillary tubing system installed at 950 m depth) cover the time period from Sept. 1995 until Oct. 1997 and revealed two types of pressure responses in the Mutnovsky geothermal reservoir (two phase conditions, 250-270°C):
1.Slow pressure changes synchronized with flow tests of wells 049N, 048 and 055 , and reinjection to well 024N.
2. Fast pressure changes with large amplitude pressure oscillations (pressure variations more than 6 σ (mean square deviation)) synchronized with earthquakes. There were two such pressure anomalies during a one year observation period (Sept. 1996 - Sept.1997) in undisturbed conditions.

A 3D numerical model of the Mutnovsky geothermal reservoir based on the TOUGH2 computer code (Kiryukhin, 1996) was used to explain the first type of pressure response mentioned above. An extended model is under development to explain the second type of pressure response (with fracture properties as controlling parameters).

CHARACTERISTICS AND PRODUCTION ZONE DISTRIBUTION IN GEOTHERMAL RESERVOIR

According to flow test data of production wells we can assume that a north-east (NE) trending production zone controls the upper feed zones of wells 055, 048, 30, 037, and also the Verkhne-Mutnovsky natural steam manifestations. This zone has a NE strike and a 60° SE dip. The upper production intervals of wells 049N, 047, 024N and 30 occur on an east-northeast (ENE) trending production zone with east-southeast (ESE) dip of 60°. Traces of production zones mentioned above at elevation of -250 masl are shown in Fig. 1.

FEATURES OF OBSERVATION WELL #30

Pressure monitoring well #30, where a capillary tubing system was installed at a depth of 950 m, has the following features:

a. Small steam flow rate of 10-30 g/s is used to maintain operating conditions a in wooden shack, where recording equipment for the capillary tubing system is installed.
b. Downhole pressures recorded at a depth of 950 m are rather sensitive to the steam flow rate at the wellhead. For example, pressure build-up was 0.3 bars in 1 hr when the steam flow rate dropped from 25 g/s to zero after the valve was closed (October 10-th , 1997). The well productivity index was estimated as no more than 0.083 kg/s*bar.
c. Gas composition of steam discharged from the wellhead is as follows: CO_2-77.2%, H_2S-17.4%, N_2-2.1%, H_2-1.6%, Ar+O_2-1.2%, CH_4-0.5%. Mass gas concentration was estimated as 7.1 g/kg (Nov. 1996).

TOUGH2 APPLICATIONS TO PRESSURE TRANSIENT DATA ANALYSIS (FLOW TESTS)

3D Model Application to Long -Term Flow-Tests from Well 049N

Analysis of long-term pressure transient data during flow tests of well 049N (Nov.27,1995-May.7,1996) was made using the existing 3D model of the Mutnovsky geothermal field (Kiryukhin, 1996) with some modifications. Rock compressibility C was used as a calibration parameter. $C=3*10^{-8}$ Pa^{-1} gives a satisfactory match for the pressure draw-down period, while the pressure build-up data are shifted upward relative to the model predictions (Fig.2). This 0.1-0.15 bars increase in well #30 is explained by a valve change after the winter time period (as mentioned above, well #30 pressure is very sensitive to the wellhead valve position).

An analysis of long-term pressure transient data during flow tests of well 049N (Nov.27, 1995-May.7,1996) was done using the inversion program DIAGNS of S-Cubed. The estimated parameters of the reservoir are: permeability-thickness 4.8 D*m, storativity - 7.2 10^{-7} m/Pa, and initial undisturbed pressure 46.1 bars (Y.Yano, 1997).

3D+2D Model Application to Short-Term Flow-Tests from Well 048

There was no satisfactory match obtained using the 3-D model (Kiryukhin, 1996) (Fig.3). Therefore a high-permeability feature following the observed trend of the production zone (N-East production zone, Fig.1) was implemented in the 3-D model. This was accomplished by adding a 2-D sub-grid consisting of 91 elements with 236 m * 191 m denoted as FFK J, where K = 1,...,9 corresponding to the X- position (local X axis was chosen along NE direction), J = 1,...,9 corresponding to Y-position (local Y axis chosen along subvertical fracture dip of 60° SE). All

elements of the 2D grid were connected to corresponding elements of the former 3D model grid (main-grid): A276, A287, A298, A2A9, A377, A388, A399, A467, A478, A489, A4910. For example, elements FFK J (K=1,2,3; J =7,8,9) were connected to element A46 7 of 3D model grid , ..., elements FFK J (K=7,8,9; J =1,2,3) were connected to element A2A 9 of 3D model grid. Domain FFF 1 with specified rock properties was assigned to 2D sub-grid elements. As a result a 3D+2D model was developed. The following parameters of the "FFF 1" fracture zone in the 3D+2D model were adjusted to match observed and modeled pressure response: porosity 0.5, compressibility 4 10^{-6} Pa^{-1}, permeability 120 D, thickness 0.6 m (Fig.3).

3D+2D model Application to Long-Term Flow Test from Well 055

The 3D model previously used gives no satisfactory match (Fig.4). So the 3D+2D model described above was used to match observed data. The "FFF 1" fracture parameters obtained are: porosity=0.5, compressibility 10^{-6} Pa^{-1}, permeability 4 D and thickness 1 m (Fig.4).

3D+2D Model Application to Short-Term Flow Tests from Wells 049, 055 and Reinjection in Well 024N

The 3D model previously used gives no satisfactory match (Fig.5). So, implementation of a 2D production zone (east-northeast production zone, Fig.1) in the 3D model was performed.To do this an additional 2D sub-grid consisting of 36 elements 183 m * 191 m denoted as GGK J where K=1,....,6 corresponding to the X-position (local X axis chosen along ENE direction) , J=1, ... 6 (local Y-axis chosen along subvertical fracture dip of 60° SSE). All elements of the 2D grid were connected to corresponding elements of the former 3D model grid (main grid): A387, A398, A497 and A498. For example, elements GGK J (K=1,2,3; J=1,2,3) were connected to element A387 of the 3D model grid, etc. Domain "GGG 1" with specified rock properties was assigned to 2D sub-grid elements.The following parameters of the "GGG1" fracture in 3D+2D model were adjusted to match observed and modeled pressure response: porosity 0.5, compressibility 10^{-7} Pa^{-1}, permeability 1000 D and thickness 0.25 m (Fig.5).

PRESSURE ANOMALIES RELATED TO EARTHQUAKES

At least four pressure anomalies during no-flow periods were detected in well #30 that were clearly related to earthquakes. Two of them have pressure variations of more than 6 σ (mean square deviation):

a. Pressure drawdown of 0.1 bars and, after a seismic event, pressure oscillations of up to 0.85 bars during a time interval of 28 hours (time period = 1.5 hours) - synchronized with an earthquake of magnitude M=4.5, at a distance of D= 82 km,

b. Pressure drawdown of 0.15 bars and, after a seismic event, pressure oscillations of up to 0.95 bars during a time interval of 26 hours (time period = 0.5-1.0 hours) - synchronized with an earthquake of M=4.1, D=112 km. (See Figs.6 and 7).

CONCLUSIONS

1.TOUGH2 application to analysis of observed pressure data at the Verkhne-Mutnovsky site, Mutnovsky geothermal field, during long-term and short-term flow tests has revealed the fractured nature of the geothermal reservoir, and corresponding hydrodynamic properties of the production zones were estimated.

2.Significant pressure perturbations in the reservoir were recorded following seismic activity at distances from 82 - 112 km. An extended TOUGH2 model is being developed to determine the underlying mechanisms.

Acknowledgements

We very much appreciate valuable assistance from Dr. T. Ishido from the Geological Survey of Japan.

References:

1. Kiryukhin A.V. (1996) Modeling Studies: the Dachny Geothermal Reservoir , Kamchatka, Russia // Geothermics, Vol.25, No.1, p.63-90.

2. Kiryukhin A.V.,Yano Y.,Nakao S.,Ishido T., Lesnykh M.D., Polyakov A.Y., Zorin D.G. (1997) Analysis of Pressure Transient Data of Verkhne-Mutnovsky Site, Mutnovsky Geothermal Field , Kamchatka, Russia // Proc. 22-nd Stanford Geoth. Res. Eng. Workshop.

3. Pruess K. (1991) TOUGH2 - A General Purpose Numerical Simulator for Multiphase Fluid and Heat Flow , Lawrence Berkeley Laboratory Report LBL-29400, Berkeley , CA, 102 pp.

Fig.1 Verkhne-Mutnovsky Site Mutnovsky Geothermal Field, Temperature Distribution , Production Zone and Wells Location , Grid Corresponding to 3D Model (Kiryukhin, 1996) -250 masl

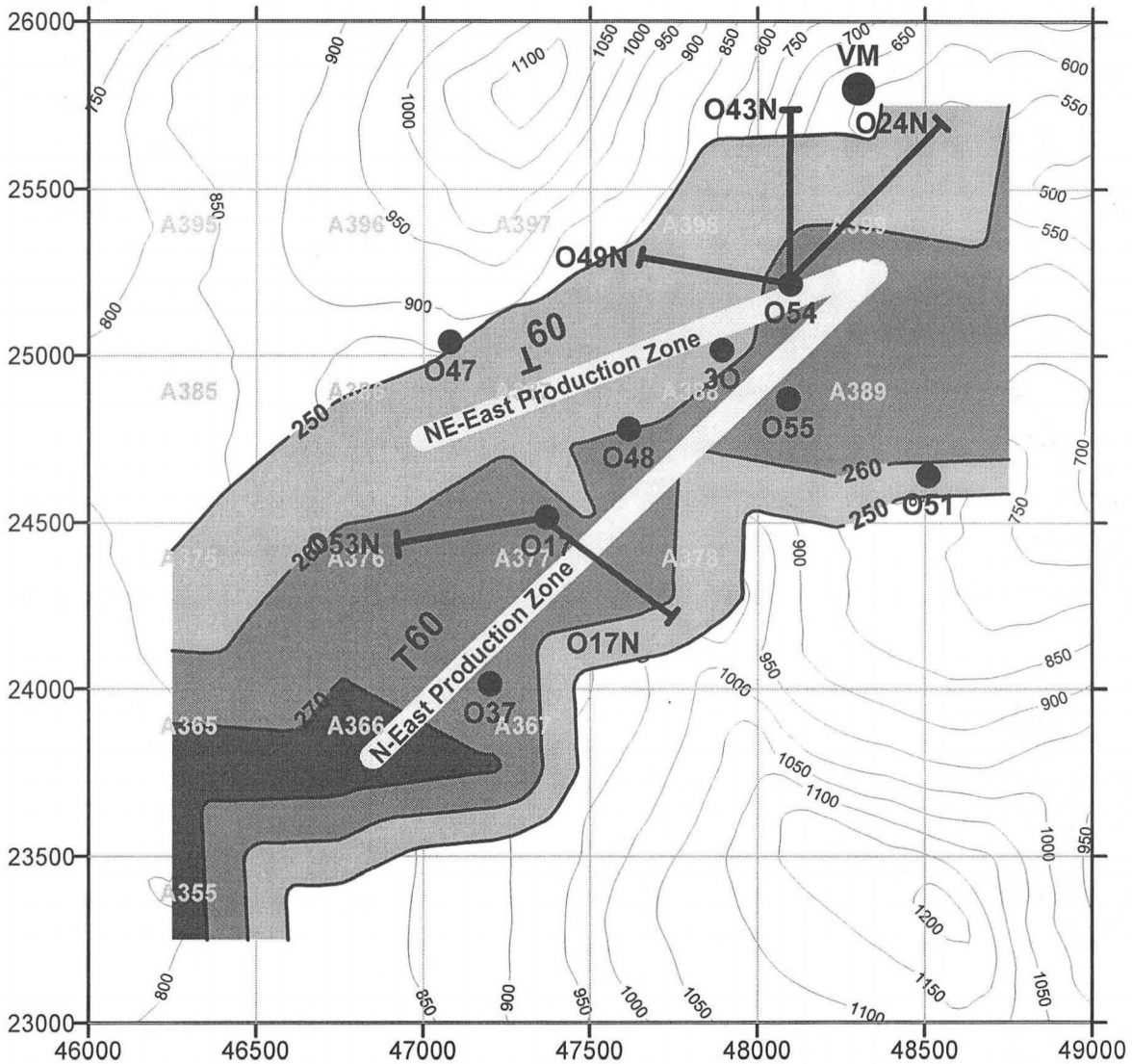

Fig.2 Pressure Match in Well #30 During Long Term Flow Tests from Well 049N (27 Nov. 1995 - 7 May 1996).
Dashed line - Pressure Monitoring Data (running average,21)

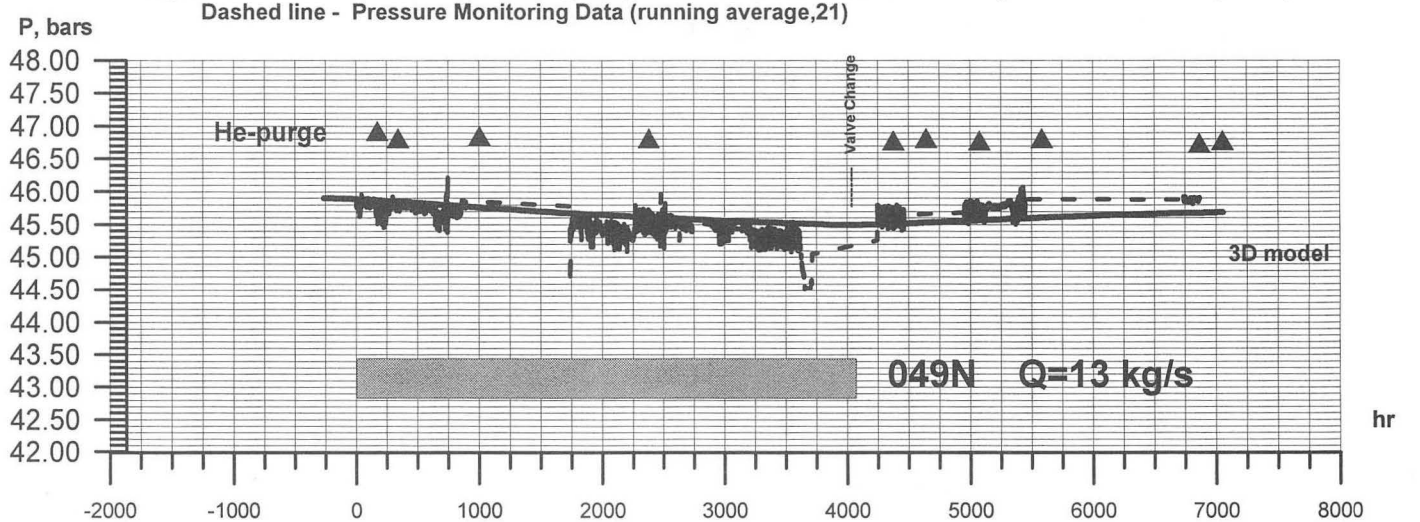

Fig.3 Pressure Match in Well #30 During Short Term Flow Tests from well 048 (Sept.14 - 15 ,1996)
Dashed Line - Pressure Monitoring Data (running average,21)

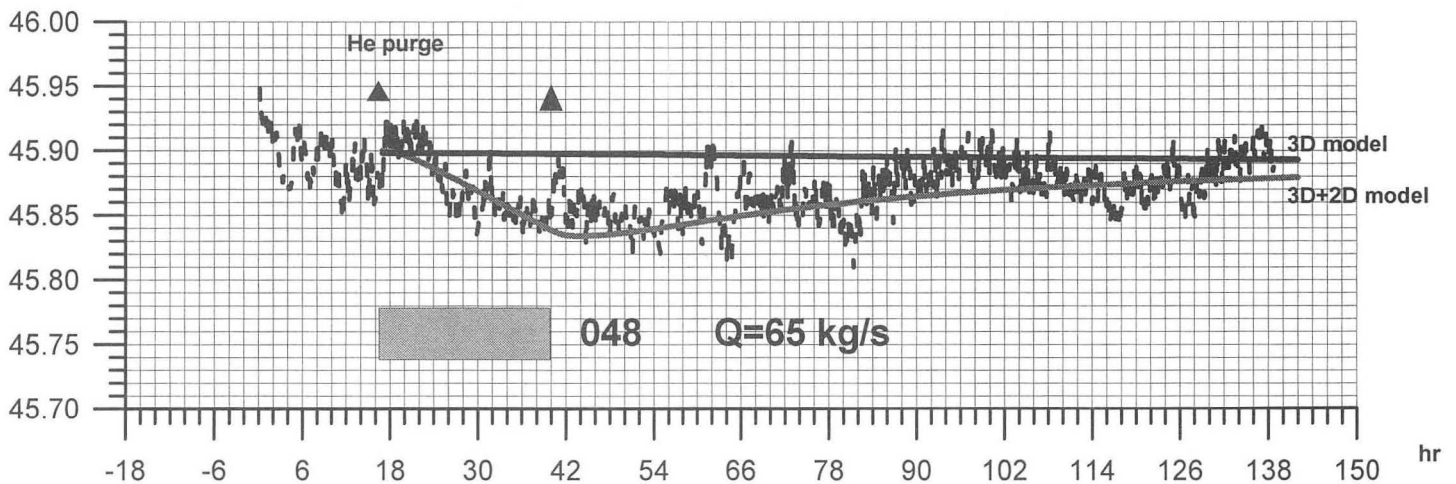

Fig.4 Pressure Match in Well #30 During Long Term Flow Tests from Well 055 (from 9 Dec. 1997) .
Dashed line - Pressure Monitoring Data (running average 21)

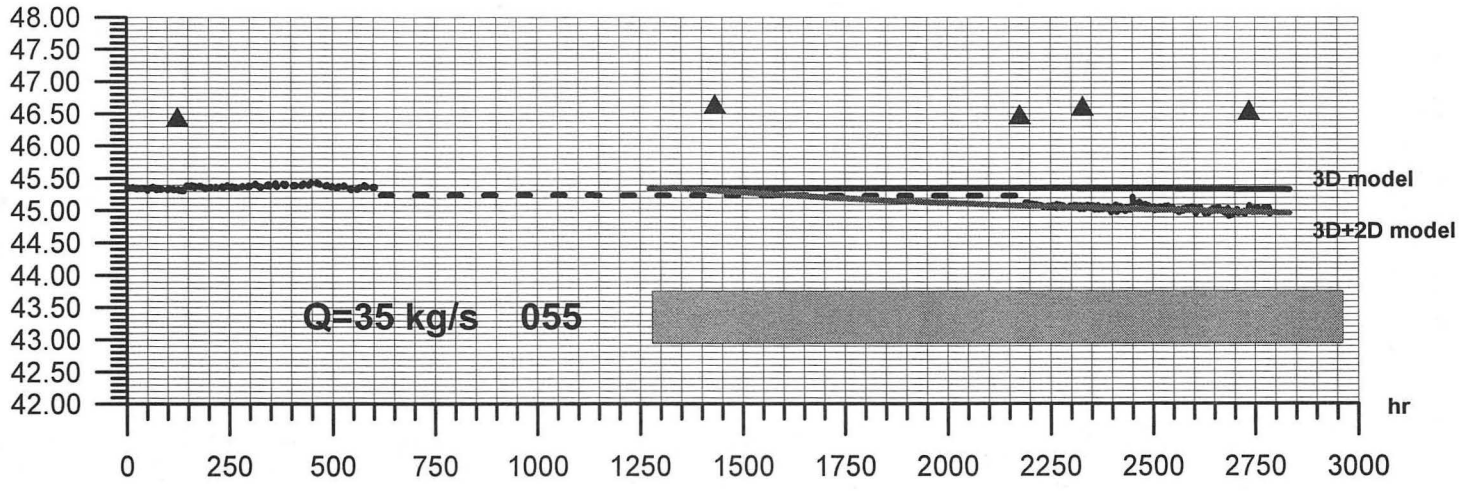

Fig.5 Pressure Match in Well #30 During Flow Tests from wells 049N & 055 , Aug. - Sept. 1997
Dashed Line - Pressure Monitoring Data (running average 21)

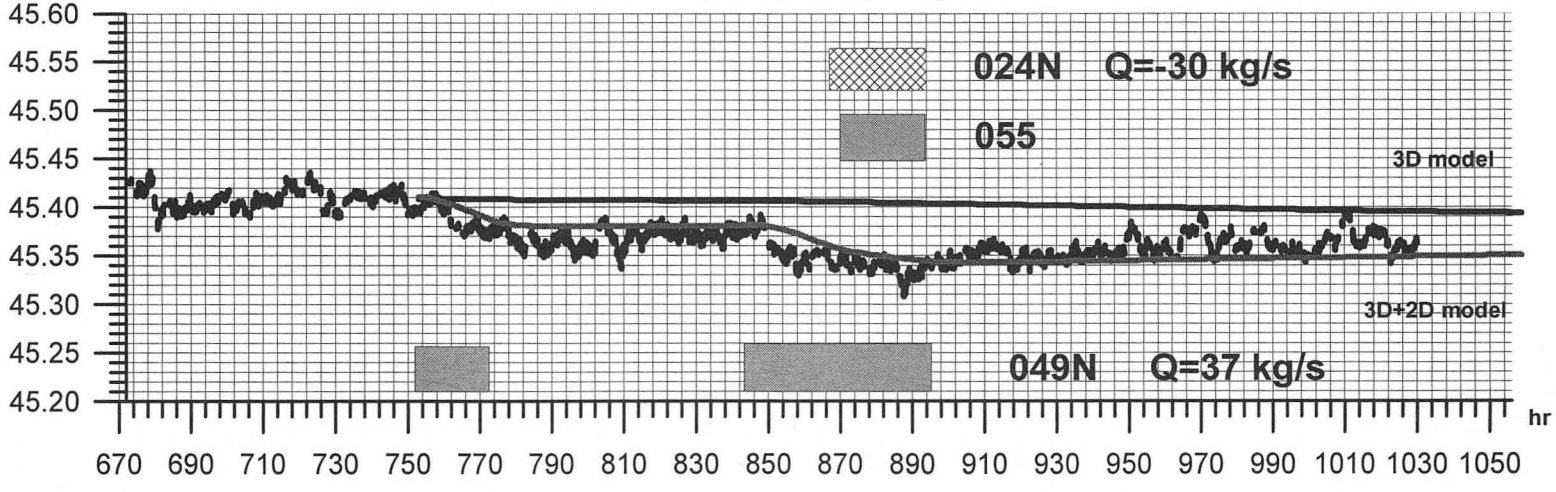

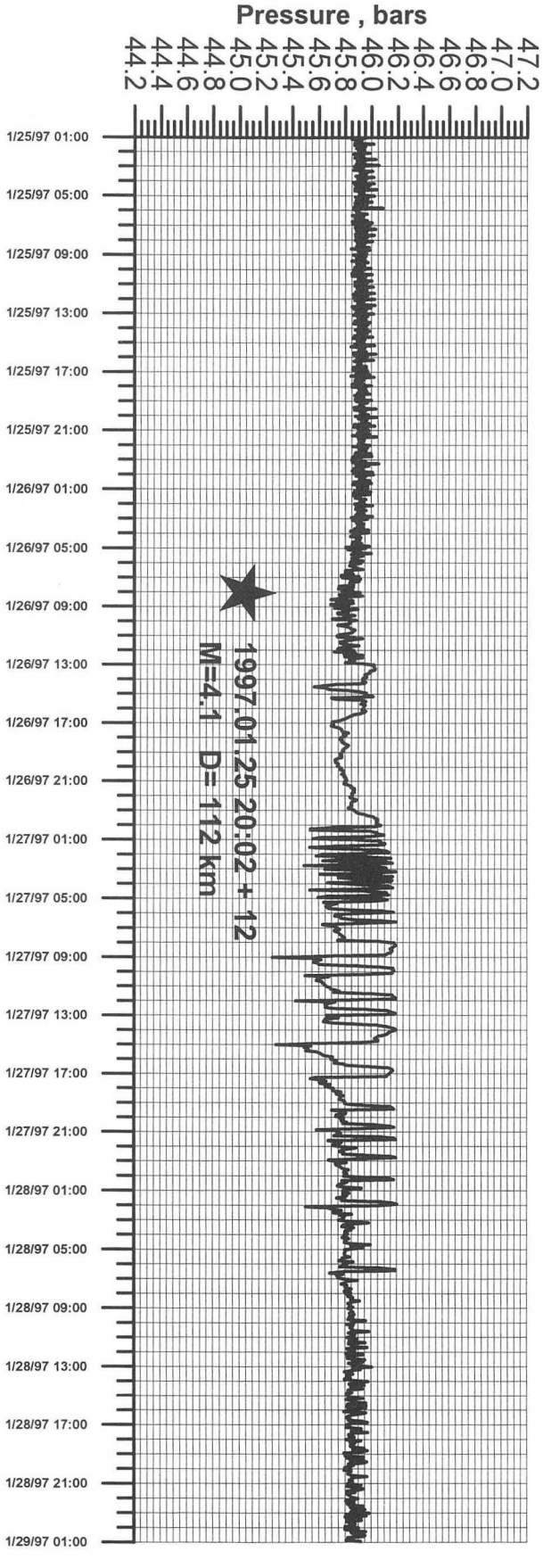

Fig.7 Pressure Variations in Well #30 Related to Earthquake

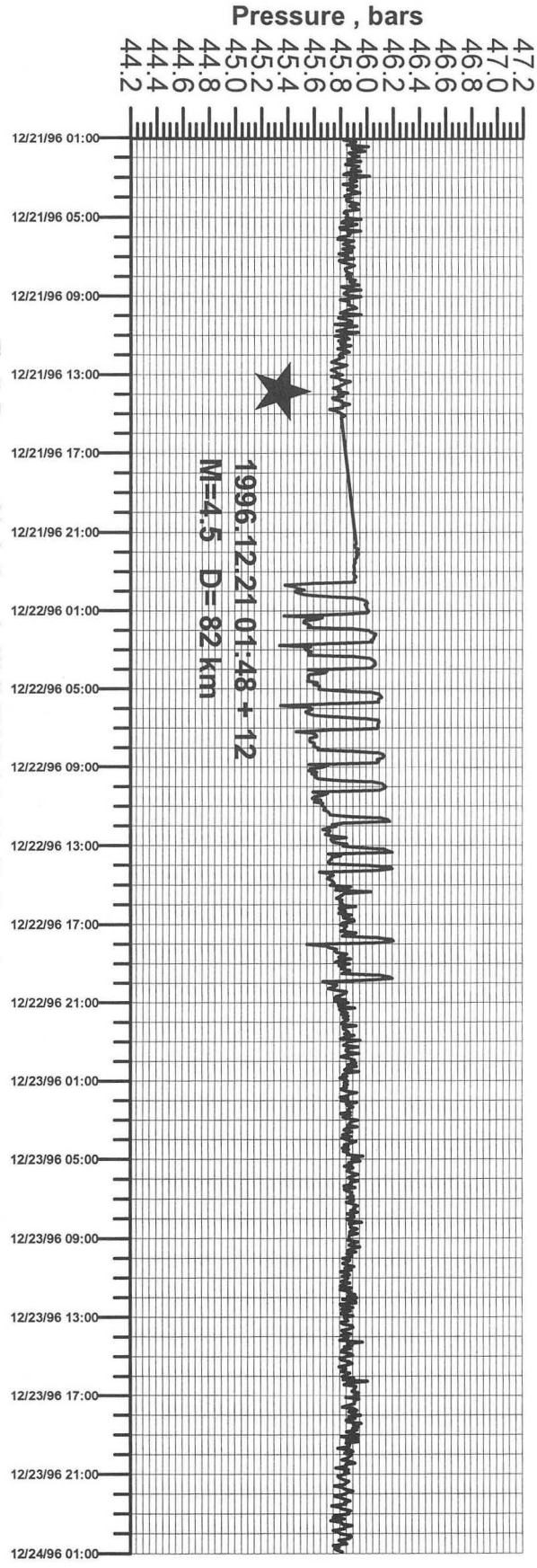

Fig.6 Pressure Variations in Well #30 Related to Earthquake

Assessing Seal Performance and Parameter Sensitivity with a Full-Shaft Model

MARK REEVES, D.G. FRYAR, and W.H. STATHAM
Duke Engineering & Services, 9111 Research Blvd., Austin TX 78758

and

M.K. KNOWLES
Sandia National Laboratories, WIPP Regulatory Compliance
115 N. Main, Carlsbad NM 88220

INTRODUCTION

The Waste Isolation Pilot Plant (WIPP), is a planned geologic repository for permanent disposal of transuranic waste generated by U.S. government defense programs. Located near Carlsbad in southeastern New Mexico, the facility's disposal regions are mined from the bedded salt of the Salado Formation at a depth of approximately 652 m. Four shafts service the operational needs of the facility for air intake, exhaust, waste handling, and salt handling. These shafts range in diameter from 3.5 to 6.1 m and extend from the ground surface to the repository. During repository closure, following an operational life of approximately 50 years, these shafts will be sealed in accordance with an acceptable design. Under contract to the U.S. Department of Energy (DOE), the Repository Isolation Systems Department (RISD) of Sandia National Laboratories has developed a design for the WIPP shaft sealing system. This design has been reviewed by the U.S. Environmental Protection Agency (EPA) as part of the 1996 WIPP Compliance Certification Application (CCA).

An effective shaft sealing system for the WIPP will limit liquid and gas flows, and permanently prevent the migration of radiological or other hazardous constituents through the sealed shafts from repository to accessible environment. Because of these performance objectives, a significant effort has been directed toward evaluation of the seal design. Whereas RISD (1996) provides a comprehensive discussion, this paper focuses on only one aspect of the evaluation effort, namely a full-shaft, fluid-flow model.

DESCRIPTION OF THE PHYSICAL SYSTEM

Two principal elements comprise the WIPP shaft seal system, specifically the seal, which includes individual sealing components, and the surrounding host rock geology, which includes both disturbed and undisturbed rock. As illustrated in Figure 1a, the shafts pass through three different formations as they extend from ground surface to the repository horizon, and the proposed seal design comprises thirteen different seal components. These components fill the entire shaft volume with a variety of low-permeability materials, including compacted bentonite clay, compacted crushed Salado salt, and asphalt. Concrete, used in strategic locations, provides an immediate low-permeability, structural support for sealing and construction needs.

Beginning 15 to 30 m below surface (Figure 1a), the Dewey Lake Redbeds consist of alternating layers of sandstone and siltstone. This formation is not known to have laterally extensive saturated zones. For this reason, Dewey-Lake seal components are meant primarily to eliminate surface access to the shafts and to limit surface-water infiltration. They are not considered by the fluid-flow analyses. Lying immediately below the Dewey Lake Redbeds and composed primarily of anhydrite and dolomite layers, the Rustler Formation contains the only laterally extensive, water-bearing units at the site.

Below the Rustler Formation, the Salado Formation represents a Permian-age evaporite sequence composed of bedded halite, polyhalite, anhydrite, and mudstone lithologic units Several of the thicker layers of Salado anhydrites and polyhalites are designated as "marker beds." Although all Salado units have very low permeabilities, some of the marker beds are more transmissive than the halitic sequences. Furthermore, within the WIPP shafts, several brine-seepage intervals have been noted. These intervals were assigned permeabilities which are an order-of-magnitude higher than values

assigned to marker beds of similar composition. For all the various materials comprising this system, RISD (1996), Appendix C, reports values and sources for the hydraulic parameters, including relative-permeability and capillary-pressure curves.

MODEL CONCEPTUALIZATION

Model Grid. Considering the Air Intake Shaft (AIS) to be representative of the other three shafts, the axisymmetric grid chosen for the analysis extends from the shaft station monolith at a depth of 652 m up to the top of the Rustler Formation at a depth of 162 m. Horizontally, the grid extends radially outward from the center of the shaft to the shaft wall at a radius of 3.09 m and to an outer radius of 30.9 m. Row thicknesses and column widths are chosen judiciously in order to represent both stratigraphy and seal components. These include a concrete liner in the upper portion of the shaft terminated by a "key" at the Rustler-Salado Transition and a disturbed rock zone (DRZ) surrounding both as it extends the full length of the shaft. The grid contains 19 columns and 99 layers.

Boundary Conditions. Invoking a code revision to TOUGH28W, the numerical solution at the outer boundary of the gridded region was coupled to the analytic solution for an infinite aquifer using the approximation of Carter and Tracy (1960). In effect, then, a constant-pressure boundary was applied at infinite radius. Generally, no-flow conditions were applied at the upper and lower boundaries. However, after repository closure, corrosive and/or biochemical reactions in the waste forms may generate hydrogen gas which, over time, could elevate pressures at the bottom of the shaft. After consulting earlier studies (DOE, 1995 and RISD, 1996, Appendix C), we assumed that the boundary pressure increases linearly from zero to 7 MPa in 100 years and remains constant thereafter.

Initial Conditions. Various authors (Mercer, 1983 and Beauheim, 1987) have recognized that *in-situ* pressures within the Rustler and Salado Formations are not in hydrostatic equilibrium. Furthermore, records indicate that, for the latter formation, only two pressure measurements exist, one at the Rustler-Salado Transition and the other at Marker Bed MB139, just below the repository horizon. Considering the likelihood that some portion of the lithostatic load is transferred to Salado fluids, the study developed three initial-pressure distributions, *e.g.,* compare the base-case run with Runs 2 and 8 (Table 1).

DRZ Healing. As a result of stress-induced fracturing, DRZs form around excavations, yielding increased values of permeability and porosity in affected regions. Since the existence of a shaft DRZ raises the possibility of a permeable vertical conduit, it was considered carefully in the design and evaluation efforts. For the Salado subsystem, the seal design (Figure 1a) includes three concrete/asphalt waterstop components which both provide backpressure for DRZ healing and intersect the DRZ with waterstops, low-permeability components containing asphalt.

For the brittle material of the Rustler Formation, no DRZ healing is expected. However, for the Salado Formation, mechanical calculations (RISD, 1996, Appendix D) show that, following closure, the radial extent of the DRZ decreases as a function of time, depth, seal material, and rock type. Using a code revision to TOUGH28W, the present study includes this effect as a monotonically decreasing DRZ permeability. Mechanical calculations (RISD, 1996, Appendix D) also indicate that, for anhydrite and dolomite units of sufficient thickness, stress-induced fracturing does not occur, thus making the DRZ discontinuous. However, after considering construction effects such as blasting damage or the known natural fracturing of dolomites at the WIPP site, the present study assumed a continuous DRZ for the base-case and used a case involving a discontinuous DRZ (Run 7, Table 1) to test for sensitivity.

Fractured/Unfractured DRZ. For the Room Q studies, Munson *et al.* (1996) use the SPECTROM-32 code (Callahan, 1994 and Callahan *et al.* ,1989) to characterize the DRZ. The results divide volumetric strain into elastic and inelastic components giving each as a function of radius and time. If, like Freeze *et al.* (1997), we identify inelastic strain with fracture porosity, then the work of Munson *et al.* (1996) shows that by approximately eight years, the fracture porosity ϕ_f reaches asymptotic values lying within the range $10^{-4} \le \phi_f \le 10^{-3}$, approximately, depending on radial distance from the room face. For the present study, the base case assumes that the DRZ may be satisfactorily approximated as an unfractured medium with altered properties relative to undisturbed rock. To investigate possible effects due to a fracturing, Runs 1, 2, and 3 (Table 1) characterize the DRZ by an effective-continuum permeability model (Pruess *et al.*, 1988) with representative values of fracture porosity.

Salt-Column Consolidation. One of the primary seal components in the Salado Subsystem is composed of crushed salt (see Figure 1a). During emplacement, this material will be dynamically compacted to a density approaching 90 percent of intact salt. Over time, it is assumed that compactional loading due to the creep of intact salt will consolidate the crushed salt and reduce its permeability to a level which is nearly indistinguishable from the host rock.

Two components make up the crushed-salt permeability model, the first of which is density. Since no field analogs exist from which crushed-salt density can be inferred for long times, mechanical analyses were performed to predict density as a function of time, depth, and pore pressure. The second component of the permeability model is a relationship between density and permeability. Here, the effort considered three different experimental studies involving the permeability of consolidated crushed salt (Brodsky, 1994; Hansen and Ahrens, 1996; and Brodsky *et al.,* 1996). Analysis then gave a log-linear relation between permeability and density.

RESULTS

The full-shaft simulations presented here consider two time periods. For the 50-year preclosure period, shaft pressures are fixed at one atmosphere, and host-rock pressures are initialized at *in-situ* levels. For the second, a 200-year postclosure period, shaft-seal pressures are initialized at one atmosphere and allowed to vary, while host-rock pressures are initialized at levels determined by the preclosure simulation. Other simulations consider a 10,000-year postclosure period (RISD, 1966, Appendix C, and Dennis *et al*, 1998).

Verification Results. In an attempt to verify the numerical model, the study reviewed shaft-inflow estimates for the preclosure period (see LaVenue *et al.*, 1990). Prior to lining, estimated inflow rates range from a high of 3,469 m^3/y in 1981 at the Salt Handling Shaft to a minimum of 252 m^3/y in 1987 at the Waste Handling Shaft. After lining, estimated inflow rates range from no observable flow to values as high as those observed prior to lining. Various grouting campaigns have targeted and stopped significant inflows, thus reducing these values. Simulated results give a 50-year annual average of 15.5 m^3/y for the period following lining. Given the level of uncertainty present in the estimated inflow rates and the fact that early-time estimates would be substantially greater than a 50-year annual average, we consider the agreement between estimated and simulated values to be satisfactory.

Base-Case Results. Figure 1b characterizes the liquid resaturation process. The figure shows that, although substantial levels of liquid resaturation have occurred within the seal by 40 years, a major gas pocket remains at Layers 22 - 32 and a minor such pocket remains at Layers 43 - 45. This is significant since both are located in the salt column, and the lowest permeability levels are correlated with gas pockets. For the Salado Formation, one may also note the role of the combined units (marker beds) in resaturating the Salado portion of the seal (Layers 1 - 80).

Sensitivity Results. Table 1 defines 13 runs, the results of which may be compared with those of the base case. These runs probe the seal, DRZ, and host rock seeking significant sensitivities. Consistent with objectives of the study, two performance measures are used to characterize hydrologic performance. Cumulative flows through and/or around the concrete/waterstop components quantify the movement of liquid and gas. Salt-column permeability levels quantify the degree of consolidation of the compacted salt column and its effectiveness in limiting fluid and gas flows.

Generally, one may assume that, after 200 years, backpressures are sufficiently large to prevent further consolidation. Thus, the salt-column permeabilities given in Table 1 represent asymptotic values. Generally, these permeability values are quite low, *i.e.*, approximately one order-of-magnitude greater than that assumed for intact salt (10^{-21} m^2). However, Runs 6, 10, and 11 evidence a strong sensitivity to marker-bed permeability. Here, an order-of-magnitude increase in permeability (Run 11) increases salt-column permeability by four orders of magnitude to 4.35×10^{-16} m^2.

CONCLUSIONS

Except for marker-bed permeability, salt-column permeability evidenced an impressive list of insensitivities. Tests to date indicate that uncertainties in Salado *in situ* pressures, in characterizing the DRZ as fractured or porous, and uncertainties in the fracturing of the thicker anhydrite and dolomite

DRZs do not significantly affect performance. Similarly, altering the seal design by removing the three asphalt waterstops, by removing the middle concrete/waterstop component, or by replacing the asphalt column (10^{-20} m^2) with a more permeable clay column (10^{-15} m^2) do not affect performance. Finally, neither setting all seal-component permeabilities (except that for crushed salt) to their maximum values (RISD, 1996, Appendix C) nor reducing all clay permeabilities from their base-case value of 5×10^{-19} m^2 to 10^{-14} m^2 impact salt-column performance.

For cumulative flows through and/or around concrete/waterstop components, the study calculated 84 different values. Consequently, the results are more difficult to summarize than those obtained for the first performance measure. Suffice it to say that, at the lower concrete/waterstop component, the maximum downwardly directed flow of brine occurred for Run 11. Here, an order-of-magnitude increase in marker-bed permeabilities and a consequent increase in salt-column permeability by four orders of magnitude yielded approximately 2000 kg (1.7 m^3) of brine during the 200-year period following repository closure. This flow exceeds that of the base case by less than a factor of two. Also, at the upper concrete/waterstop component, the maximum upwardly directed flow of gas occurred for Run 5. Here, increasing all seal permeabilities (except that of the salt column) to the maximum permitted by their respective uncertainty ranges yielded approximately 5.6 kg (62 standard m^3) of hydrogen over the 200-year period following repository closure. This flow, though small, exceeds that of the base case by two orders of magnitude.

The results of this study thus reveal a robust seal design which can withstand variations in properties of the seal components and most uncertainties present in both disturbed and undisturbed rock zones. The results also suggest that uncertainties present in marker-bed permeabilities can impact salt-column performance.

REFERENCES

Beauheim, R.L. 1987. *Interpretations of Single-Well Hydraulic Tests Conducted at and Near the Waste Isolation Pilot Plant (WIPP) 1983-1987.* SAND87-0039. Albuquerque, NM: Sandia National Laboratories.

Brodsky, N.S. 1994. *Hydrostatic and Shear Consolidation Tests with Permeability Measurements on Waste Isolation Pilot Plant Crushed Salt.* SAND93-7058. Albuquerque, NM: Sandia National Laboratories.

Brodsky, N.S., F.D. Hansen, and T.W. Pfeifle. 1996. "Properties of Dynamically Compacted Crushed Salt, *Montreal, Quebec, June 17-18, 1996."* SAND96-0838C. Albuquerque, NM: Sandia National Laboratories. (Copy on file at the Technical Library, Sandia National Laboratories.)

Callahan, G. D. 1994. *SPECTROM-32: A Finite Element Thermomechanical Stress Analysis Program Version 4.06,* RSI-0531, prepared by RE/SPEC Inc., Rapid City, SD, for Sandia National Laboratories, Albuquerque, NM.

Callahan, G. D., A. F. Fossum, and D. K. Svalstad. 1989. *Documentation of SPECTROM-32: A Finite Element Thermomechanical Stress Analysis Program*, DOE/CH/10378-2, prepared by RE/SPEC Inc., Rapid City, SD, for the U.S. Department of Energy, Chicago Operations Office, Argonne, IL, Vol. I and II.

Carter, R.D. and C.W. Tracy. 1960. "An Improved Method for Calculating Water Influx", *Transactions of the Society of Petroleum Engineers, American Institute of Mining Engineers*, pp. 219, 415-417.

Dennis, A.W., J.D. Tillerson, J.D. Schreiber, P. Vaughn, and J.F. Bean. 1988. "Waste Isolation Pilot Plant (WIPP) Shaft Seal System Performance Sensitivity and Design Impact." To be presented at the International High-Level Radioactive Waste Management Conference, Las Vegas, NV. May 11-14, 1988.

DOE (U.S. Department of Energy). 1995. *Waste Isolation Pilot Plant Sealing System Design Report.* DOE/WIPP-95-3117. Carlsbad, NM: U.S. Department of Energy, Waste Isolation Pilot Plant.

Freeze, G.A., T.L. Christian-Frear, and S.W. Webb. 1997. *Modeling Brine Inflow to Room Q: A Numerical Investigation of Flow Mechanisms.* SAND96-0561. Albuquerque, NM: Sandia National Laboratories.

Hansen, F.D., and E.H. Ahrens. 1996. "Large-Scale Dynamic Compaction of Natural Salt," *4th International Conference on the Mechanical Behavior of Salt, Montreal, Quebec, June 17-18, 1996"* SAND96-0792C. Albuquerque, NM: Sandia National Laboratories.

LaVenue, A.M, T.L. Cauffman, and J.F. Pickens. 1990. *Ground-Water Flow Modeling of the Culebra Dolomite. Volume I: Model Calibration.* SAND89-7068/1. Albuquerque, NM: Sandia National Laboratories.

Mercer, J.W. 1983. *Geohydrology of the Proposed Waste Isolation Pilot Plant Site, Los Medanos Area, Southeastern New Mexico.* Water-Resources Investigations Report 83-4016. Albuquerque, NM: U.S. Geological Survey.

Munson, D. E., A.L. Jensen, S.W. Webb, and K.L. DeVries. 1996. "Brine Release Based on Structural Calculations of Damage Around an Excavation at the Waste Isolation Pilot Plant (WIPP)", *2nd North American Rock Mechanics Conference , Montreal, Canada, June 17-19, 1996.* SAND95-1704C. Albuquerque, NM: Sandia National Laboratories.

Pruess, K., J.S.Y. Wang, and Y.W. Tsang. 1988. *Effective Continuum Approximation for Modeling Fluid and Heat Flow in Fractured Porous Tuff.* SAND86-7000. Albuquerque, NM: Sandia National Laboratories.

Pruess, K. 1991. *TOUGH2 - A General-Purpose Numerical Simulator for Multiphase Fluid and Heat Flow.* LBL-29400. Berkeley, CA: Earth Sciences Division, Lawrence Berkeley Laboratory.

RISD (Repository Isolation Systems Department). 1996. *Waste Isolation Pilot Plant Shaft Sealing System Compliance Submittal Design Report. Volume 1&2:* SAND96-1326/1&2. Albuquerque, NM: Sandia National Laboratories.

Table 1. Sensitivity Simulations for the Shaft Seal System

Simulation	DRZ		Initial Condition	Parameter Varied	Salt Column Permeability at 200 Years
	Cont.	Fract.			
Base	Yes	No	Fractional lithostatic	---	2.39×10^{-20} m^2
Run 1	Yes	Yes	Fractional lithostatic	Fracture porosity = 10^{-3}	1.43×10^{-20} m^2
Run 2	Yes	Yes	Interpolated	Fracture porosity = 10^{-3}	1.41×10^{-20} m^2
Run 3	Yes	Yes	Fractional lithostatic	Fracture porosity = 10^{-4}	1.77×10^{-20} m^2
Run 4	Yes	No	Fractional lithostatic	Clay k = 10^{-14} m^2	2.40×10^{-20} m^2
Run 5	Yes	No	Fractional lithostatic	All seal k to maximum	2.52×10^{-20} m^2
Run 6	Yes	No	Fractional lithostatic	MB k increased x 2	1.46×10^{-19} m^2
Run 7	No	No	Hydrostatic	Discontinuous DRZ	2.18×10^{-20} m^2
Run 8	Yes	No	Hydrostatic	Hydrostatic initial cond.	2.51×10^{-20} m^2
Run 9	Yes	No	Fractional lithostatic	No water stops	2.50×10^{-20} m^2
Run 10	Yes	No	Fractional lithostatic	MB k increased x 5	1.20×10^{-16} m^2
Run 11	Yes	No	Fractional lithostatic	MB k increased x 10	4.35×10^{-16} m^2
Run 12	Yes	No	Fractional lithostatic	Removed Middle Concrete	2.22×10^{-20} m^2
Run 13	Yes	No	Fractional lithostatic	Asphalt Col Replaced w/ Clay (k = 10^{-15} m^2)	2.39×10^{-20} m^2

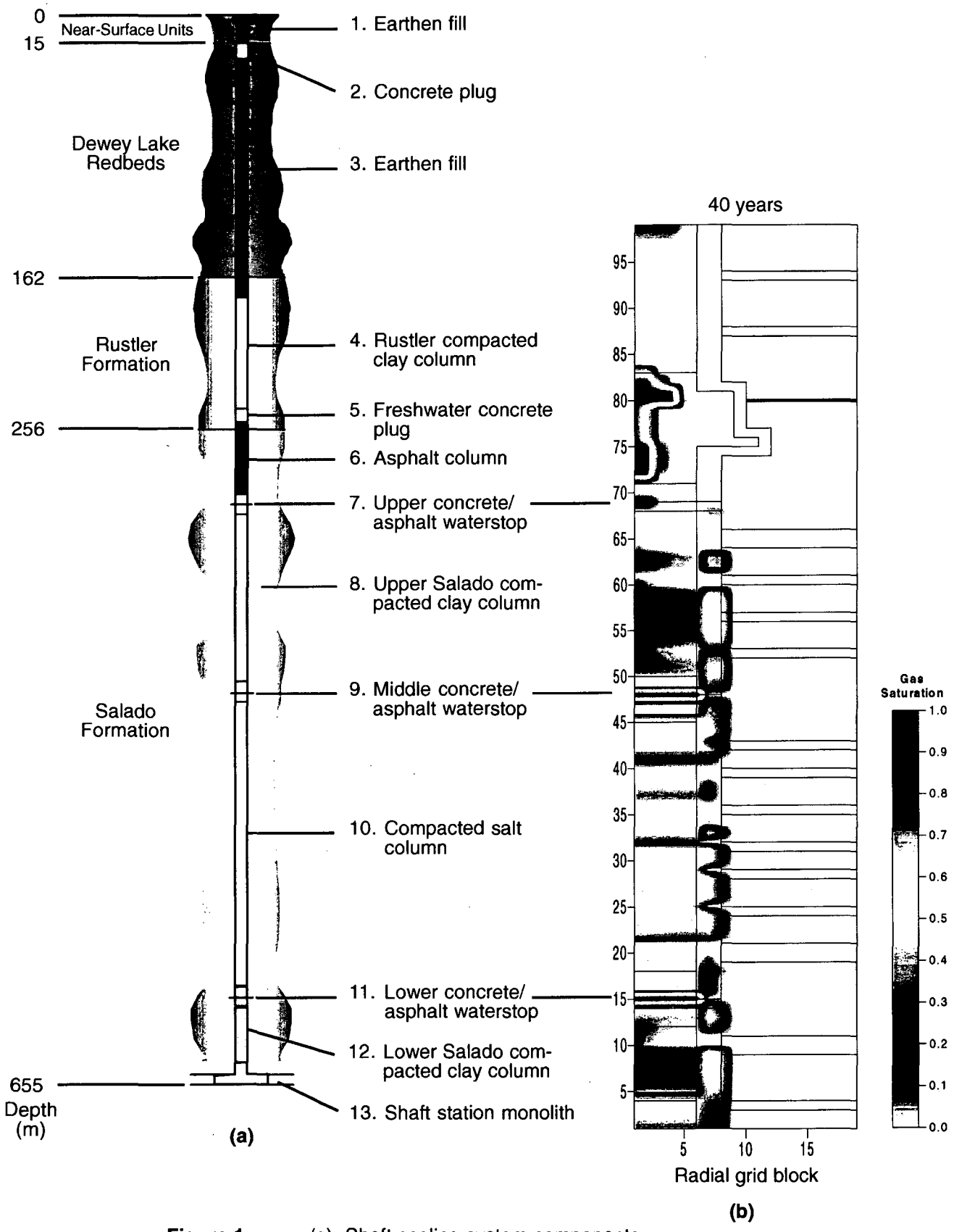

Figure 1: (a) Shaft sealing system components
(b) Base-case gas distribution, 40 years after closure

Combined Gas and Nuclide Transport in a two dimensional Repository considering a variable Rock Convergence

V. Javeri
Gesellschaft für Anlagen- und Reaktorsicherheit (GRS) mbH,
Schwertnergasse 1, 50667 Köln, Germany, e-mail: jav@grs.de

1 Introduction

To assess the long term safety of a repository for the radioactive waste in a deep salt rock formation, generally a brine inflow into the repository is postulated. The brine can react with the radioactive waste or with its containers and can gradually dis-assemble them. The radioactive substances after dissolved in brine can be transported out of the repository by rock convergence. The brine flow and nuclide transport can be enhanced by gas generation, mainly by hydrogen due to corrosion of containers and metallic materials. To analyse the combined impact of gas generation and rock convergence on nuclide transport, TOUGH2 is modified to simulate

- variable rock convergence depending upon porosity and pressure,
- permeability depending upon a variable porosity of a compactible filling material,
- variable fluid flow induced by the rock convergence

in a two dimensional two phase system. Using these modifications in previous reports /JAV 96B, 96C/, combined gas and nuclide transport in a simplified two dimensional configuration consisting of a storage chamber, a drift and a shaft is studied assuming one drift level only. To extend these previous analyses, in the present paper, gas and nuclide transport in a repository with two drift levels is studied considering a hydrogen source influenced by the transient flooding of a repository, two phase flow, different filling materials, excavation disturbed zone, anisotropic diffusion and dispersion.

2 Modification of TOUGH2 Models

TOUGH2 assumes constant permeabilities and does not directly simulate the convergence of a salt rock. Hence, the calculation of a variable porosity n and permeability k of a compactible filling material is introduced considering a variable rock convergence depending upon pressure p and temperature T:

$n = n(p, T, t) = V_{Void}/V_{total}, \quad n \geq n_{min}, \quad n_t = (1/n)(dn/dt) = C_L/n, \quad k = k(n),$

$C_L = C_{ref} f_1(p) f_2(n) f_3(T), \quad C_{ref}$: Reference convergence rate of salt rock = constant,

$f_1 = (1 - p_F / p_{Rock})^m$, $n_1 = 1 - n / n_{Ref}$, $n_2 = (nn_1)^{(1/m)}$, $f_3 = 1$ for T = constant,

$f_2 = 1$ for $n \geq n_{Ref}$, $f_2 = nn_1 (n^2_1 + n_2)^{-m}$ for $n < n_{Ref}$, $C_L = 0$ for $n < n_{min}$.

The porosity change leads to an additional fluid flow Q, which is given by:

$S_F = V_F/V_{Void}$, $S_G = V_G/V_{Void}$, V_{total} = constant, $f_1 = 0$ if $p_F \geq p_{Rock}$,

$Q_{F,1,por} = |nV_{total}\, n_t\, \rho_F\, S_F\, X_1|$, $Q_{F,2,por} = |nV_{total}\, n_t\, \rho_F\, S_F\, X_2|$, $Q_{G,por} = |nV_{total}\, n_t\, \rho_G\, S_G|$.

Since the sophisticated dispersion model of /PRU 93/ assumes a fully two dimensional configuration, it is inexpedient to analyse a system, which consists of drifts and shafts mainly. Hence, a simplified model for dispersive flux G in liquid phase is introduced:

$D_{hor} = nd_{hor}$ (Domain) $S_F + \beta_{hor}$ (Domain) $|u|_{hor}$, $X_1 = m_1/m_F$, $X_2 = m_2/m_F$,

$D_{ver} = nd_{ver}$ (Domain) $S_F + \beta_{ver}$ (Domain) $|u|_{ver}$,

$(G_{1 \text{ or } 2})_{hor} \sim D_{hor}\, [\text{grad}\, (X_{1 \text{ or } 2})]_{hor}$, $(G_{1 \text{ or } 2})_{ver} \sim D_{ver}\, [\text{grad}\, (X_{1 \text{ or } 2})]_{ver}$.

The determination of flux G is similar to flux F in the dispersion model of /PRU 93/. However, this model modification does not assume a full two dimensional system as in /PRU 93/ and can easily be applied to a three dimensional configuration containing drifts and shafts. To implement all the modifications mentioned above, only three subroutines MULTI, QU and CONVER of the original version are extended.

3 Analysis

In the following two dimensional scoping analysis, a network of repository with two drift levels is postulated (Fig. 1). A storage chamber with radioactive materials in the left corner of the bottom drift at a depth of around 500 m is filled with compactible crushed salt and is connected to the shaft via two drifts. Both lower and upper drift are filled with a non compactible sealing material at the chamber side and with a non compactible filling material at the shaft side. Since the sealing material has a low permeability of $1 \cdot 10^{-17}$ m^2, the excavation disturbed zone with the similar permeability along the drifts is also considered. Initialy, the repository is free from brine. The brine flows into the shaft and gradually into the chamber via two drifts. Simultaneously, the crushed salt is compacted by the variable rock convergence depending upon pressure and porosity in chamber. This reduces the void volume of the chamber. The radioactive substances (10^4 kg) in the chamber are simulated with a stable tracer in brine and can be driven out of the chamber by the pressurization due to gas production and by porosity reduction in chamber. The important parameters are /JAV 97B/:

- Variable rock convergence and crushed salt properties: $C_{ref} = -5 \cdot 10^{-5}$ / year, $n_{Ref} = 0.3$, $n_{min} = 0.005$, $m = 4$, $p_{Rock} = 107$ bar, $k = (2 \cdot 10^{-9})\, n^{4,5}$ m^2.
- Liquid phase : $\rho_F = \rho_{Tracer} = \rho_{Brine} = 1.292 \cdot \rho_{Water}\, (p, T)$; $\mu_F = 6.29 \cdot \mu_{Water}\, (p, T)$.

- Gas Phase (Hydrogen): gas constant = 4124 J / (kg·K), $\mu_G = 8.95 \cdot 10^{-6}$ Pa sec.
- Brooks-Corey relations for two phase flow:

$S_{F,eff} = (S_F - S_{Fr}) / (1 - S_{Gr} - S_{Fr})$, $p_{cap} = p_{cap,min} / (S_{F,eff})^{0.5}$, $S_{Gr} = 0.02$; $S_{Fr} = 0.1$;
$k_{F,rel} = (S_{F,eff})^4$, $k_{G,rel} = (1 - S_{F,eff})^2 (1 - S^2_{F,eff})$, $k_F = kk_{F,rel}$, $k_G = kk_{G,rel}$,

$p_{cap,min}$ = 1 bar for domain 8, 9, 12, 14 and 0 for domain 1, 11, 13.

In the first part of analysis, the brine inflow through the shaft without gas generation in chamber is studied with different reference convergence rates and $p_{cap} = 0$:

Case FL1: $-5 \cdot 10^{-5}$ / year, **Case FL2:** $-5 \cdot 10^{-4}$ / year, **Case FL3:** $-5 \cdot 10^{-3}$ / year.

In the second part, a constant hydrogen generation rate in chamber is included from the time point, when $S_F = 0.2$ in chamber is reached, and its total generation depends upon the brine amount already present in the chamber at this time point. The hydrogen generation ends, when this brine amount is supposed to be utilised. To estimate the hydrogen generation depending upon inflow condition, the data of /JAV 97B/ for the same model are used: 133.6 kg/year consuming $5.97 \cdot 10^6$ kg brine in 5000 years. In continuation of above inflow cases, three outflow cases are viewed assuming capillary pressure as defined above:

Case CT1: Initial chamber condition derived from the case FL1: $S_F = 0.2$, n = 0.191, $m_F = 2.04 \cdot 10^6$ kg at t = 9500 years; hydrogen generation 133.6 kg/year between 9500 and 11210 years, Δt_{Gen} = 11210 - 9500 = (2.04/5.97) (5000) years.

Case CT2: Initial chamber condition derived from the case FL2: $S_F = 0.2$, n = 0.0581, $m_F = 6.29 \cdot 10^5$ kg at t = 3900 years; hydrogen generation 133.6 kg/year between 3900 and 4427 years, Δt_{Gen} = 4427 - 3900 = (0.629/5.97) (5000) years.

Case CT3: Initial chamber condition derived from the case FL3: $S_F = 0.2$, n = 0.0113, $m_F = 1.55 \cdot 10^5$ kg at t = 1200 years; hydrogen generation 133.6 kg/year between 1200 and 1330 years, Δt_{Gen} = 1330 - 1200 = (0.155/5.97) (5000) years.

4 Results

These cases were computed with TOUGH2/EOS7 /PRU 91, 91A/ and variable rock convergence assuming three fluid components brine, tracer and hydrogen. The Fig. 2 and 3 show the liquid volume, void volume, liquid saturation and porosity in chamber during brine inflow situation. As expected, void volume and porosity are reduced rapidly with increasing rock convergence. The sealing material with $k = 1 \cdot 10^{-17}$ m^2 at the chamber entrance delays the brine inflow into chamber significantly. With increasing rock convergence, 20 % liquid saturation in chamber is achieved earlier (FL1: 9500, FL2: 3900 and FL3: 1200 years) and the flooding of the chamber ends faster (FL1: 22500, FL2: 7600, FL3: 2900 years). For further details, see the case NW1 in /JAV 97B/ which corresponds to present case FL1.

Fig. 4 to 6 reveal the chamber pressure, the gas and brine flow out of the chamber after the gas generation is initiated. With increasing rock convergence, the maximum chamber pressure is higher, because at the same constant gas generation rate the available void volume in chamber is smaller. But with decreasing rock convergence rate, the pressure peak duration is longer, since the gas generation period is longer. Such a high pressurization exceeding the lithostatic pressure can affect the mechanical stability of the filling or sealing material and repository substantially. The gas and liquid flow out of the chamber increases rapidly, as the chamber pressure due to gas generation rises, and decreases also rapidly as the gas generation ends. After that, the chamber pressure remains nearly constant at the hydrostatic level and the liquid flow is very low corresponding to porosity reduction in chamber due to rock convergence.

For an integral comparison, the nuclide removal from the chamber is depicted in Fig. 7. As expected, with increasing rock convergence the nuclide removal starts earlier. Though the mass flow out of the chamber is low in case CT3, the maximum nuclide removal is seen in case CT3 with the highest rock convergence. This occurs because the nuclide removal is mainly determined by the product $X_2 \cdot u_F$, which is considerably large due to small fluid volume in chamber in case CT3. In cases CT1 to CT3, the nuclide removal from the chamber is around 8 % within 15000 years. In case of no gas generation, there would be nearly no nuclide removal from the chamber within 20000 years, since the flooding of chamber would not be completed or liquid outflow would be negligible. In above cases, there is no nuclide removal at the top of the shaft, because the distance or the flow resistance between the chamber and the top of the shaft is relatively large. Further analyses including nuclide decay and adsorption are reported in /JAV 96C, 97B/. Summarizing, one can conclude from the scoping analyses, that the gas generation can enhance pressure build-up in storage chamber affecting the mechanical stability of the repository and nuclide removal substantially.

Symbols

d : molecular diffusivity [m^2/s]; k : permeability [m^2]; m : mass [kg]; t : time [s];
m : stress parameter; n : porosity; u : Darcy velocity; V : volume [m^3];
D : dispersion coefficient [m^2/s]; S : phase saturation; X : mass fraction;
β : dispersion length [m]; μ : dynamic viscosity [Pa·s]; ρ : density [kg/m^3]

Subscripts

G : gas phase; F : liquid phase
1 : primary liquid component (brine); 2 :secondary liquid component (tracer or nuclide)

References

/JAV 96B/ Javeri, V.: a contribution in GRS-129 (Dec. 1996)
/JAV 96C/ Javeri, V.: GRS-A-2389 (Oct. 1996)
/JAV 97B/ Javeri, V.: GRS-A-2441 (April 1997)
/PRU 91/ Pruess, K.: LBL-29400 (May 1991)
/PRU 91A/ Pruess, K.: LBL-31114 (Aug. 1991)
/PRU 93/ Pruess, K.: LBL-32505 (Sept. 1993)

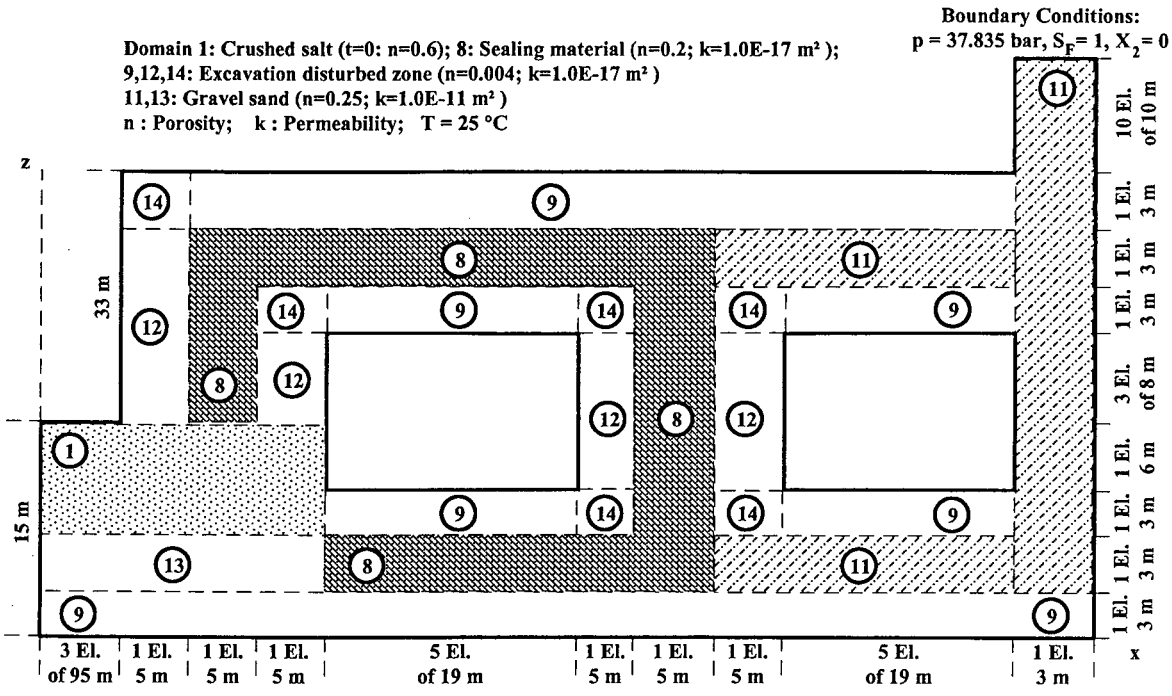

Domain 1: Chamber without gas source, variable porosity, Volume = 40500 m³, nuclide mass = 1.0E+04 kg
Domain 13: Chamber with gas source, constant porosity, Volume = 500 m³
Breadth in y-direction : 4 m ; Initial condition : p = 1 bar, S_F = 0.005

Figure 1 : Two dimensional network of a repository

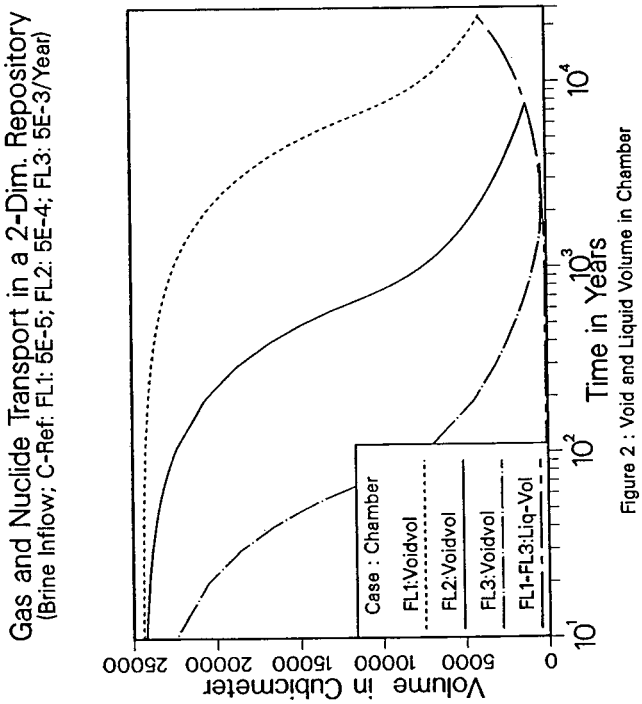

Figure 2 : Void and Liquid Volume in Chamber

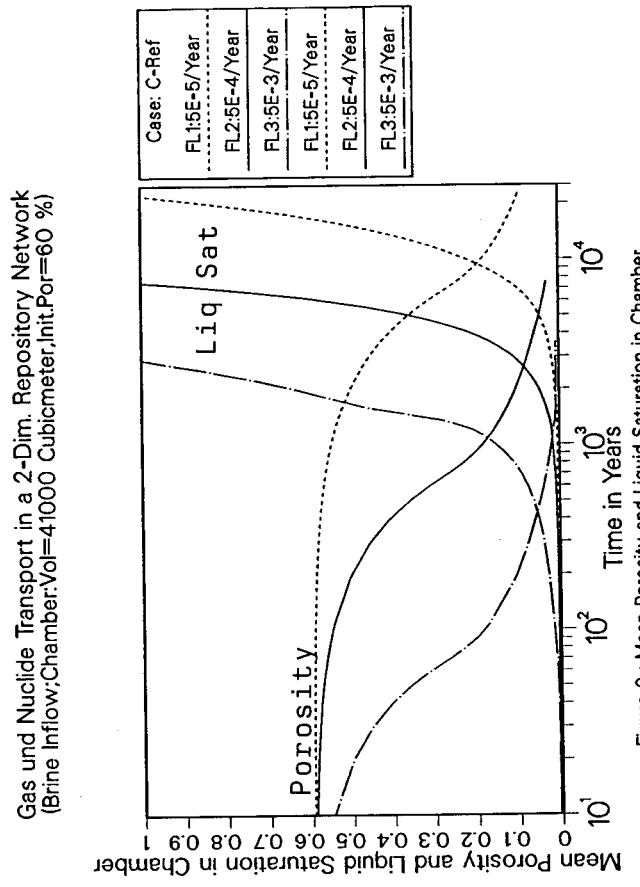

Figure 3 : Mean Porosity and Liquid Saturation in Chamber

Gas and Nuclide Transport in a 2-Dim. Repository Network
(Pressure in Chamber, x = 0 to 300 m, z = upper 9 m)

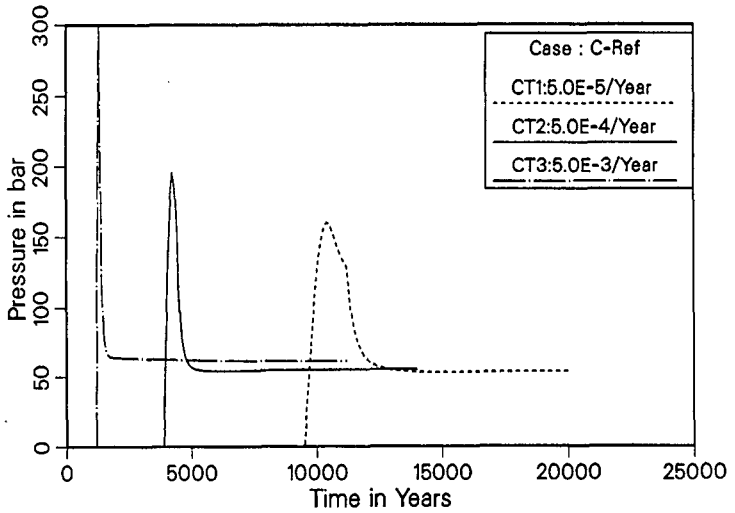

Figure 4 : Chamber Pressure

Gas and Nuclide Transport in a 2-Dim. Repository Network
(Outflow (positive) from the Chamber)

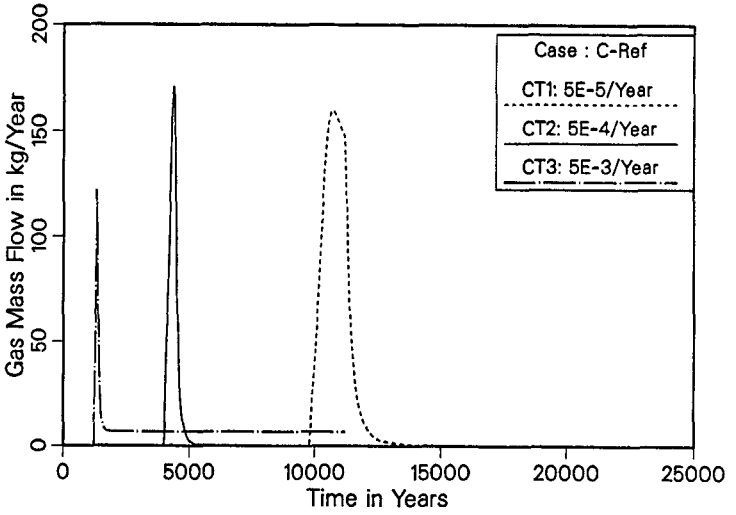

Figure 5 : Gas Flow out of Chamber

Gas and Nuclide Transport in a 2-Dim. Repository Network
(Outflow (positive) from the Chamber)

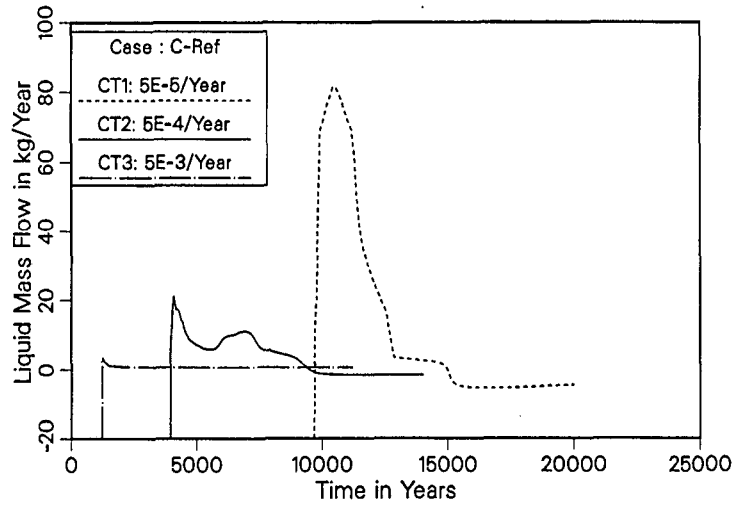

Figure 6 : Liquid Flow out of Chamber

Gas and Nuclide Transport in a 2 -Dim. Repository Network
(Brine Outflow; Initial Nuclide Mass in Chamber:10000 kg)

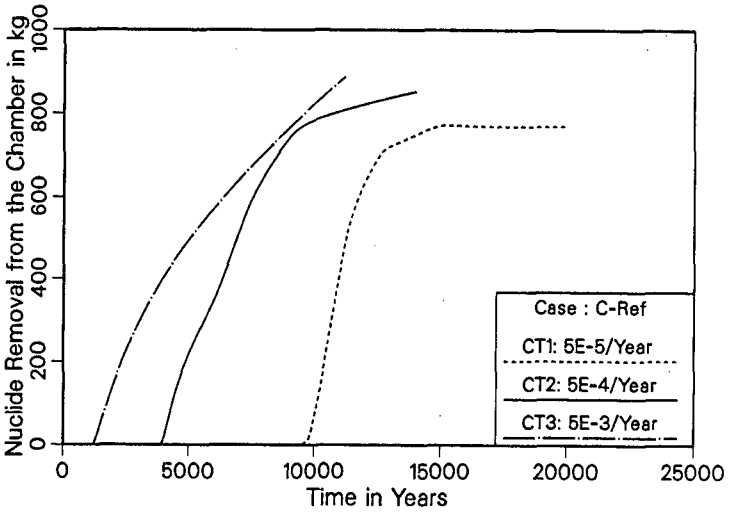

Figure 7 : Nuclide Removal from Chamber

GAS TRACER TRANSPORT IN TWO-PHASE FLOW FIELD: NUMERICAL SIMULATIONS AND FIELD EXPERIMENTS AT THE GRIMSEL TEST SITE (GTS), SWITZERLAND

RAINER SENGER[1], PAUL MARSCHALL[2], and CHRISTOPH BÜHLER[3]
[1] Duke Engineering & Services, 9111 Research Blvd., Austin, Texas, 78758, rksenger@duke-energy.com
[2] Nationale Genossenschaft für die Lagerung radioaktiver Abfälle (NAGRA), Hardstrasse 73, CH-5430 Wettingen, Switzerland, marschall@nagra.ch
[3] Solexperts AG, Ifangstrasse 12, CH-8603 Schwerzenbach, Switzerland, admin@solexperts.ch

INTRODUCTION

During Phase IV of the R&D program at the Grimsel Test Site (GTS), NAGRA (National Cooperative for the Disposal of Radioactive Waste) has been investigating the two-phase flow (TFP) behavior in fracture zones (Marschall et al., 1997). In the proposed repository for low-level/intermediate-level waste (LLW/ILW), gas will be generated by anaerobic corrosion of metals and by chemical and microbial degradation of organic substances. Waste-generated gas from such an underground repository will escape mainly through preferential pathways (e.g., shear zones, fractures) in the host rock, which is initially fully water-saturated. To better understand two-phase flow and transport behavior in shear zones, extensive investigations have been conducted in the FRI zone (Fracture Rock Investigation zone) at GTS (Fig. 1). In addition to hydraulic- and gas-injection tests, the TPF investigations also included the design and implementation of gas tracer tests in the field and in numerical models.

Gas tracer tests were conducted in a two-phase dipole flow field between two boreholes intersecting the initially fully water-saturated fracture zone. Two gas tracers (Helium and Xenon), characterized by different solubility, were injected under approximate steady-state, two-phase flow conditions in the dipole field. The potentially different tracer breakthrough is an indication not only of the mass transfer properties between gas and liquid, but also of the two-phase flow parameters affecting the saturation distribution in the dipole field.

The scope of Phase IV of the TPF Investigation Program at GTS was to develop the experimental procedure for conducting gas tracer tests. Furthermore, the field experiments were used to test the numerical models and the analysis capabilities for gas tracer tests and to develop a conceptual understanding of two-phase flow and transport in fracture zones. This paper briefly describes the field experiments at the FRI zone and the numerical implementation of the tests. Based on the simulations of the field experiments, design simulations were performed in preparation of the next investigation phase of gas tracer testing at GTS.

FIELD EXPERIMET

Figure 1 shows the location of the different test boreholes and intervals within the FRI zone. In addition to the two main boreholes BOTP 95.001 and BOTP 95.002 with injection intervals I2.2 and extraction interval I1.2, respectively, additional monitoring boreholes were completed in the FRI zone. They were used during the hydro- and extended gas threshold pressure tests (EGTPT), which were conducted to determine the hydraulic and two-phase flow properties of the shear zone during an earlier investigation phase (Wyss, 1996, Croise & Senger, 1996). In the current investigation phase, the injection and extraction intervals I2.2 and I1.2 for the tracer test configuration are 0.66 m apart. Also indicated in figure 1 is the location of the new boreholes, which are planned for the next investigation phase and are as much as 4 m away from the main boreholes.

In addition to monitoring the pressure in the injection borehole, the gas tracer test involved measuring the flow rates of gas and water. More importantly, the gas tracers have to be detected in the extraction interval. This required separating the gas-water outflow from the extraction interval in order to continuously analyze the tracer concentration. For this, two separate mass spectrometers were employed to measure the He and Xe concentrations. The details of the experimental procedure is given in Bühler et al. (1997). In this experimental setup, the concentration of gas tracers dissolved in the liquid phase were not measured.

The pressure response in the injection well during the initial gas injection test for establishing the two-phase dipole flow field is shown in Figure 2, based on a constant gas injection rate of 50 ml(STP)/min in the injection well and keeping a constant pressure at the extraction interval of 0.5 bar. The data show a steep pressure increase until gas breakthrough in the extraction interval occurs, after which the injection pressure declines to level off at approximately 3 bar.

For the subsequent gas tracer test, the total gas injection rate remained at 50 ml(STP)/min; the gas, however, consisted of 95% N_2 and 5% He and Xe in equal amounts. The gas tracers were injected for a total of about 111 hours (4.0E+5 sec) followed by continued injection of 100% N_2. Figure 2 shows the breakthrough curves for the He and Xe tracers in the gas phase at the extraction interval. The initial breakthrough of both tracer occurs about 12 minutes after tracer injection started without noticeable differences between the two tracers. Similarly, concentrations of both tracers reach a plateau within a few hours and show similar tailing after the tracer injection stopped.

MODELING APPROACH

The numerical simulations were performed with the EOS7R module, which was developed to provide radionuclide transport capabilities for TOUGH2 (Oldenburg & Pruess, 1995). EOS7R simulates flow of two phases (air and water) with transport of five components: (1) water, (2) brine, (3) parent radionuclide, (4) daughter radionuclide, and (5) air. The radionuclide components can consider first-order decay and may adsorb onto the solid grains. They can be in either the gas or liquid phase, that is, volatile radionuclides can be dissolved in the aqueous phase. Transport of the five components is by advection and molecular diffusion in both phases. EOS7R can be coupled with the dispersion module T2DMR taking into account hydrodynamic dispersion for 2-D rectangular grid geometry. To simulate a gas tracer test with EOS7R, the radionuclide components are represented by the gas tracers having the chemical properties of He or Xe (Table 1). In this case, decay and sorption of the component is set to zero.

The numerical simulations included both the gas injection into the fully water-saturated FRI zone, creating an approximate steady-state two-phase dipole field and the subsequent gas tracer test. For this purpose, a numerical model was constructed for the FRI zone represented by a 2-D cross-sectional model, whereby the thickness of the 2-D mesh corresponds to the inferred thickness of the shear zone. The test configuration was implemented in a rectangular mesh with refined grid spacing near the injection and extraction intervals. The grid orientation was such that the x-direction parallels the line segment through the injection interval and the extraction intervals. In the first model configuration gravitational effects were neglected. With this, the line segment through the injection and extraction intervals corresponds to a symmetry axis which is represented by a no-flow boundary in the numerical model. The borehole intervals are represented by a rectangular grid block with the actual test-interval volumes. Constant pressures are prescribed at the outer model boundaries to allow pressure dissipation across these boundaries during the gas injection test. In the second set of simulations for the design of the planned gas tracer test, where the injection and extraction intervals as much as 4 m apart, a similar mesh configuration was used; this time, the injection and extraction intervals are in the center of the model taking into account potential gravitational effects.

The hydraulic and two-phase flow parameters of the FRI zone used as input for simulation of the dipole gas injection and subsequent gas tracer tests are based on previous analyses of hydro- and extended gas threshold pressure tests in the injection zone I2.2 in borehole BOTP 95.002 (Wyss, 1996, Croise & Senger, 1996). The

relevant input data for the simulations are summarized in Table 1. For the gas injection test establishing the two-phase dipole flow field and for some of the tracer test simulations, different two-phase parameter models were evaluated based on the results of the EGTPT in I2.2 (Croise and Senger, 1996): (a) Parameter set 1 is based on the van Genuchten model (vG/MG), characterized by significant phase interference, and (b) Parameter set 2 is based on a van Genuchten model (vG/M) with enhanced gas relative permeability ($k_{rg} = 1 - k_{rl}$).

Table 1. Relevant Input data for the different simulations

Parameter	**Values**	
Hydraulic data:	**Parameter Set 1**	**Parameter Set 2**
Permeability (k)	2.29E-15 m^2	8.13E-15 m^2
Compressibility (C)	1.51E-9 Pa^{-1}	1.51E-9 Pa^{-1}
Porosity	0.08	0.08
FRI-zone thickness (b)	0.018 m	0.18 m
Test-zone compressibility (C_{tz})	1.95E-8 Pa^{-1}	1.95E-8 Pa^{-1}
Initial pressure (P_i)	1.05E+5 Pa	1.05E+5 Pa
Prescribed pressure in I1.2	0.5 E+5 Pa	0.5 E+5 Pa
Two-phase parameter model:	**vG/MG-model**	**vG/M-model**
vG-parameter: m	0.583	0.583
vG-parameter: $\log_{10}(1/\alpha)$	6.6E+4 Pa	6.6E+4 Pa
Residual water saturation	0.23	0.23
Gas Injection:		
1. Phase (gas injection test)	Q(N2) = 50 ml (STP)/m; Q(air) = 9.902E-7 kg/s	
2. Phase (gas tracer test)	Q(N2) = 49.5 ml(STP)/min; Q(air) = 9.803E-7 kg/s Q(He) = 0.25 ml(STP)/min = 3.422E-10kg/s Q(Xe) = 0.25 ml (STP)/min =1.123E-8kg/s	
Tracer Data:	**He**	**Xe**
Mol. Weight	4.003 g/mol	131.3 g/mol
Density (STP at 20^0C, 1 bar)	0.1642 kg/m^3	5.387 kg/m^3
Molecular Diffusivity liq./gas ()	1.E-5/1.E-9 m^2/s	1.E-5/1.E-9 m^2/s
Solubility[2] (cm^3/cm^3-H_2O)	0.00865	0.168
Inverse Henry Constant (at 1 bar)	1.4708E-11 Pa^{-1}	9.37E-9 Pa^{-1}

SIMULATION RESULTS

The simulation results for establishing the two-phase dipole flow field are shown in Figure 2. The simulated pressures in the injection interval differ for the two parameter set, and show some differences to the measured pressures. The measured injection pressures level off at a much lower pressure compared with the simulation results based on parameter set 1, but is slightly higher than the simulation results based on parameter set 2 (Fig. 2). The distinct pressure change observed after about 100,000 sec could not be reproduced, which may be due to a sudden change in the gas injection rate.

The gas tracer simulations show overall similar tracer breakthrough curves in the extraction interval as those in the field experiment (Fig. 3). The simulation using parameter set 1 (vG/MG model) indicate that the first arrival of the He tracer occurs after about 10 min, which is in good agreement with the field observations, whereas the first arrival of the Xe tracer is somewhat delayed at about 30 min. The simulated tracer breakthrough curves in the gas phase show that during the injection period the relative concentrations of He are higher than of Xe. After tracer injection stopped, Xe concentration tend to be higher than He concentration (Fig. 3). The delayed breakthrough and the higher tailing of Xe is to be expected, because of the much higher solubility of Xe compared with He. Simulations results using parameter set 2 (vG/M model) are similar to those in Figure 3.

The field results did not indicate a distinct difference in the tailing between He and Xe. This is probably due to the small volume in the shear zone and the short flow paths for the tracer between the injection- and extraction interval. The numerical simulations reproduced the overall shape of the gas breakthrough curve, but indicated some differences between He and Xe; the latter showed some more tailing as one would expect from the higher solubility. The difference between the field test and the model is likely due to the assumption of local thermodynamic equilibrium at the grid-block scale. This may suggest that the effective solubility of tracer components is reduced due to diffusion-limited mass transfer at the interface between the gas and liquid phase. Local thermodynamic equilibrium at the grid-block scale cannot account for such microscopic processes; that is, the relatively coarse grid spacing and the close proximity of the test intervals may overestimate the solution of gas tracers.

As a result of the field experiment, a larger gas tracer test is planned at the FRI zone, where the injection and extraction intervals are as much as 4 m apart. In preparation of this next investigation phase, design simulations were performed for a larger dipole field. The design simulations show that for such a two-phase dipole flow field, the first arrival of the tracer occurs within 40 hours for Xe and about 5 hours for He, even with a relatively low gas injection rate of 25 ml(STP)/min. Over that long distance, the breakthrough curve for Xe is significantly different than for He (Fig. 4); Xe indicates significant tailing due to the higher liquid solubility of Xe than He. Also, the different parameter models (vG/MG and vG/M) show different breakthrough curves, even for the gas phase. This could be important for better constraining the two-phase parameter model in the fracture zone.

SUMMARY

The field experiments during Phase IV of the TPF program at the FRI zone at GTS demonstrated the feasibility of conducting and analyzing gas tracer tests in a fracture zone. Two gas tracers (He and Xe), having significant different solubility, were used to evaluate mass transfer between the gas and water phase and to characterized the two-phase flow conditions in fracture zones. Numerical simulations of the gas tracer test were performed with the TOUGH2 module EOS7R, which could reproduce the overall tracer breakthrough behavior observed during the field test. For the greater dipole flow field planned in the next investigation phase, the gas tracers indicate significant different breakthrough curves as a result of the different solubility of He and Xe.

REFERENCES

BÜHLER, C., MARSCHALL, P., and SENGER, R. K., 1987, GTS-TPF: Supplementary Investigations in the TPF Experiment, Nagra Internal Report, Wettingen, Switzerland.

CROISE, J. and SENGER, R. K., 1996, GTS-TPF: Analysis of extended gas threshold pressure tests at the Grimsel Test Site for determination of field-scale two-phase flow parameters in the FRI zone, NAGRA Internal Report, NIB 96-41, Nagra, Wettingen.

MARSCHALL, P., Croise, J, Fischer, U., Senger, R. K., and Wyss, E., 1997, Gas flow through water-saturated shear zones: Field and laboratory experiments and their interpretations, in, Proceedings MRS'97, 21st International Symposium on the Scientific Basis for Nuclear Waste Management, Davos, Switzerland.

OLDENBURG, C. M., and PRUESS, K., 1995, EOS7R: Radionuclide Transport for TOUGH2, Report LBL-34868, Lawrence Berkeley Laboratory, University of California, Berkeley, USA.

PRUESS, K. (1987), TOUGH User's Guide, Report LBL-20700, Lawrence Berkeley Laboratory, University of California, Berkeley, USA.

PRUESS, K. (1991), TOUGH2, A general purpose simulator for multiphase fluid and head flow, Report LBL-29400, Lawrence Berkeley Laboratory, University of California, Berkeley, USA.

WYSS, E., 1996, GTS-TPF: Site preparation, borehole installation, hydraulic characterization and gas threshold pressure tests at the Grimsel Test Site, NAGRA Internal Report, NIB 96-34, Nagra, Wettingen.

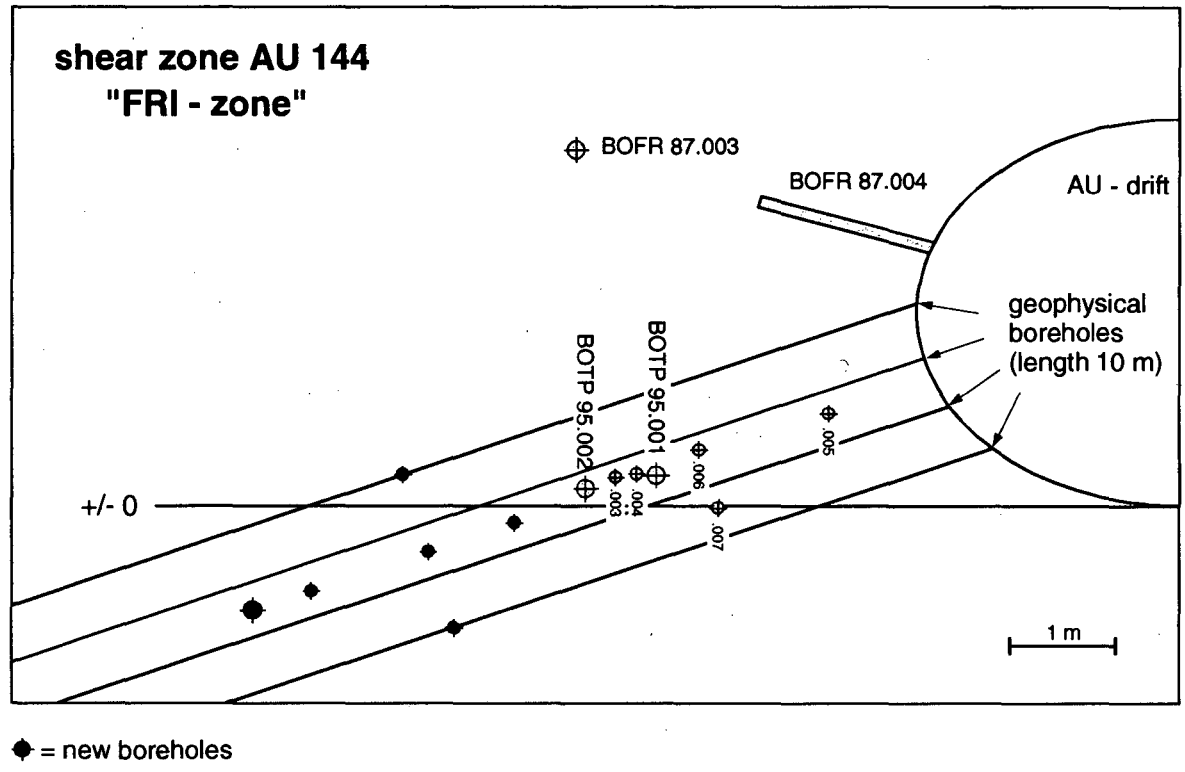

Fig. 1 Location of the boreholes intersecting the FRI zone at the GTS

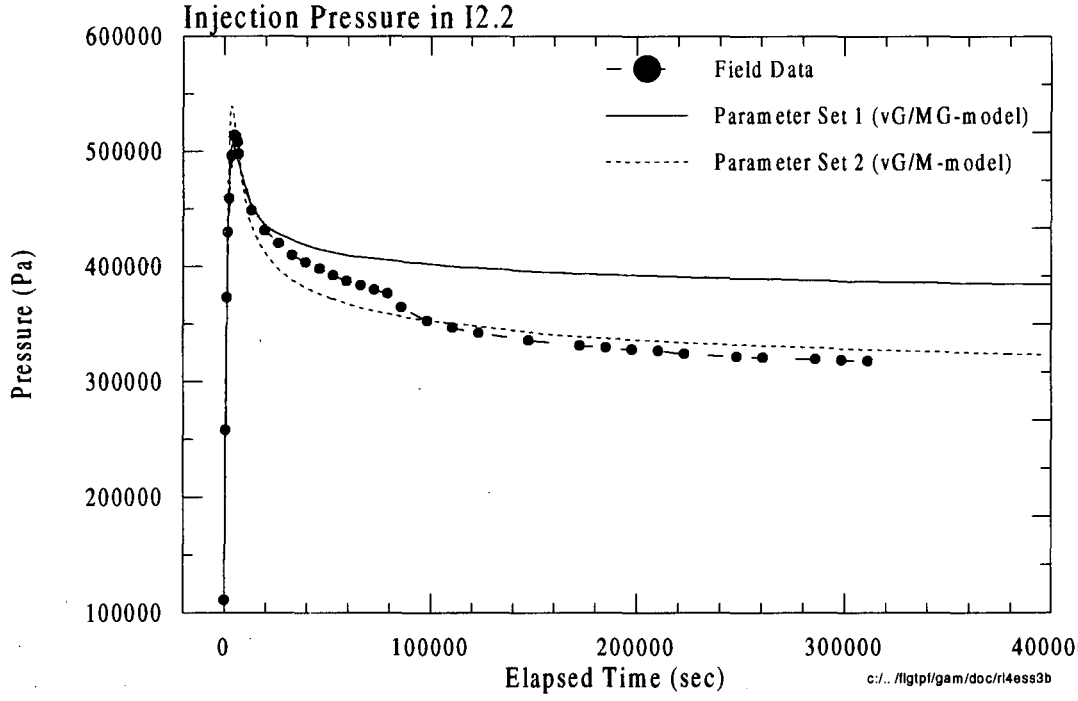

Fig. 2 Injection pressure response for establishing the two-phase dipole flow field

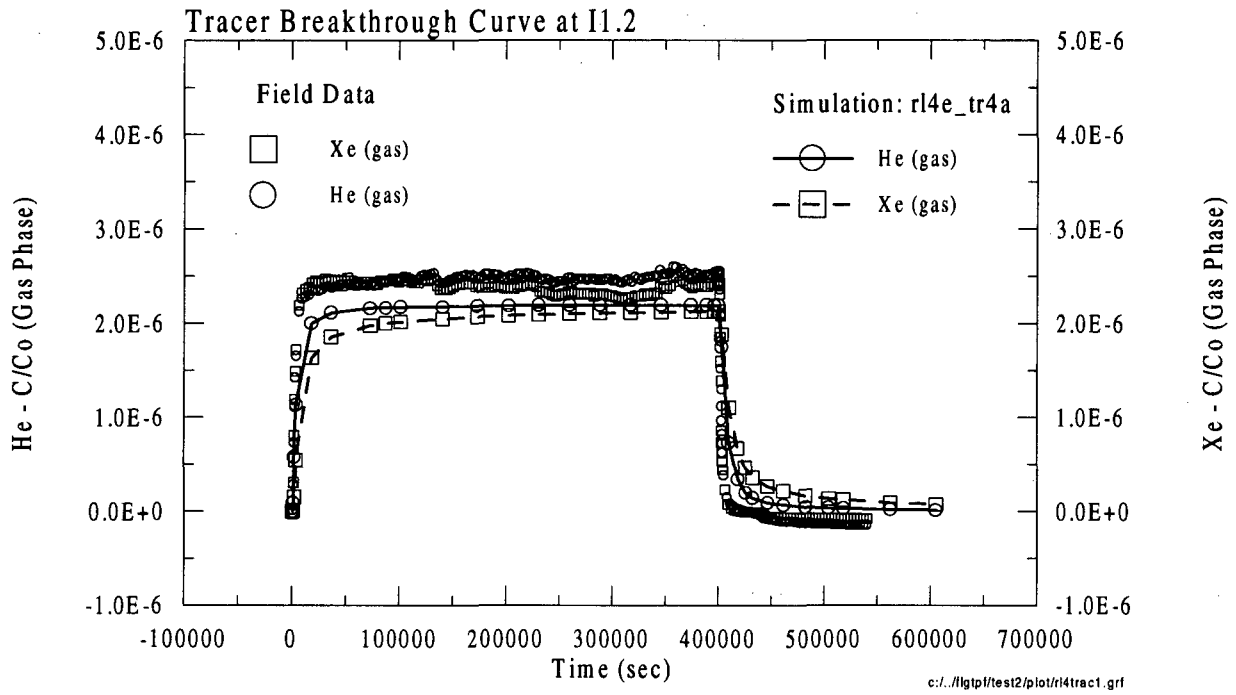

Fig. 3 Gas tracer breakthrough at test interval I1.2 from field experiment and numerical simulations.

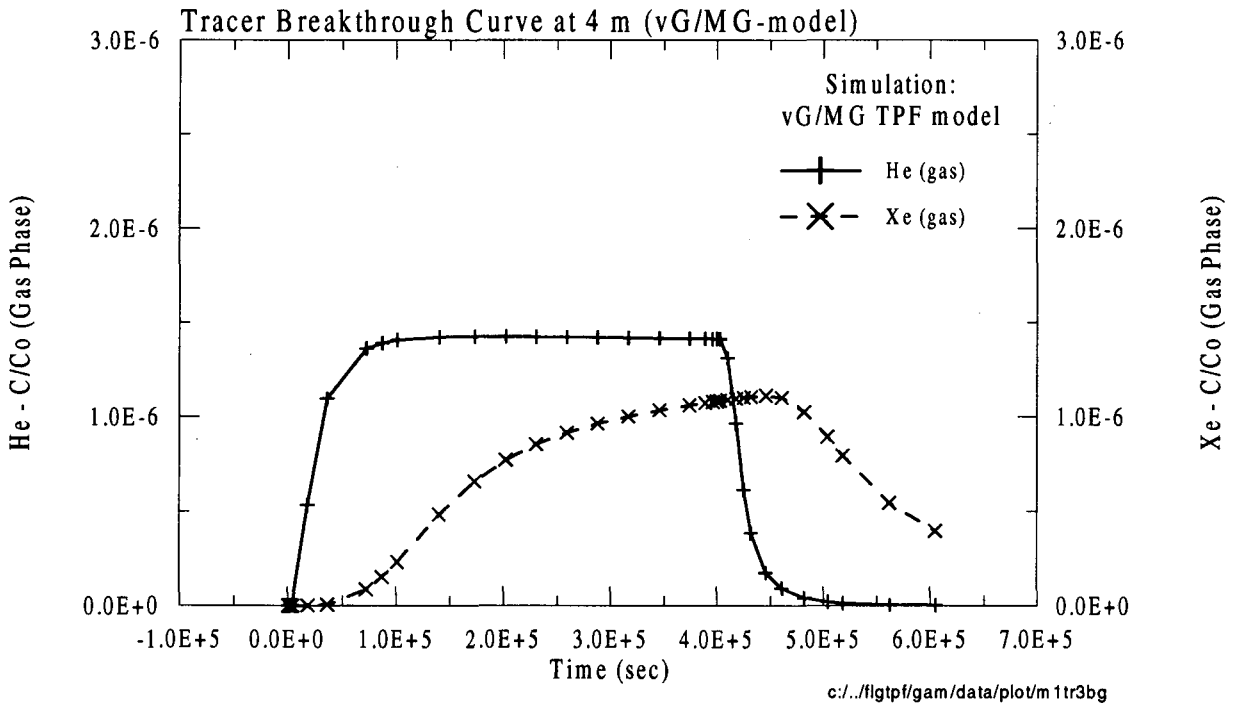

Fig. 4 Simulated tracer breakthrough curves (gas phase) in the planned extraction interval at 4 m.

Several TOUGH2 Modules Developed for Site Characterization Studies of Yucca Mountain

Yu-Shu Wu and Karsten Pruess

Earth Sciences Division, Lawrence Berkeley National Laboratory,
Berkeley, CA 94720, U. S. A.

Abstract

A comprehensive site characterization study has been conducted for the unsaturated zone (UZ) of Yucca Mountain to investigate its suitability as a potential high-level nuclear waste repository. Numerical modeling of moisture, gas, chemicals and heat flow, and their influence on the repository performance has been proven to be essential in understanding unsaturated-zone fluid movement, and the effects of hydrogeologic, geochemical and thermal conditions on various aspects of the overall waste disposal system. In these studies, the TOUGH2 code has been used extensively as a main modeling tool because of its flexibility and robustness in handling multiphase, multi-component fluid and heat flow and chemical transport in porous/fractured rocks.

As part of the UZ modeling efforts at LBNL, several new modules of the TOUGH2 code have been developed to meet different needs of the site characterization studies. In this paper we will summarize some of these new TOUGH2 modules and their specific features in application to the Yucca Mountain project. These new TOUGH2 modules include (1) the effective continuum model (ECM) for treating fracture/matrix flow; (2) single-phase gas flow (EOS1G) in a water-air two phase flow system; and (3) a 3-D radionuclide transport module (T2R3D) for 3-D radionuclide or tracer transport in porous/fractured media under two-phase flow and non-isothermal conditions.

Introduction

Numerical modeling approaches used in the Yucca Mountain project for simulating multiphase fluid flow, heat transfer, and chemical transport processes involve coupled multiphase fluid and heat flow, and chemical component migration formulations based on finite difference, or finite element schemes. Available numerical simulators for variably saturated nonisothermal flow generally employ mathematical and numerical methods similar to those used in the oil industry or geothermal engineering. Since the oil and geothermal industries have different priorities than organizations dealing with nuclear waste repository assessment, the codes must account for a number of additional processes such as the slow and/or rapid movement of fluids in thick, highly heterogeneous, unsaturated systems over very long time periods. The improvement of the modeling capabilities for simulating field-scale problems has been subject to continuous research efforts, and considerable progress in this area has been made over the past two decades.

TOUGH2 (Pruess, 1991) has been used as a main modeling tool in the Yucca Mountain project due to its flexibility and robustness in handling multidimensional, multiphase, and multi-component fluid flow and heat transfer in both porous and fractured rocks. In addition, throughout the development of the TOUGH/TOUGH2 codes, a comprehensive verification and validation study has been conducted (Pruess, 1987 and 1991; Moridis and Pruess, 1992; Pruess et al., 1996). More recently, the TOUGH2 code has been updated and improved in the modeling studies associated with the site characterization of Yucca Mountain, and several new modules have been developed to add to the TOUGH2 family of codes (Wu et al., 1996). The correctness, validity, and capability of the TOUGH2 family of codes have been verified by comparing the simulation results against analytical solutions, and results from other numerical codes, laboratory experiments, and field tests.

In this paper, we will discuss three new TOUGH2 modules, developed during the site-characterization study at Yucca Mountain. These three new TOUGH2 modules are (1) effective continuum model (ECM) for treating fracture/matrix flow; (2) single-phase gas flow (EOS1G) in a water-air flow systems; and (3) a 3-D radionuclide transport module (T2R3D) for 3-D radionuclide or tracer transport in porous/fractured media under two-phase flow and non-isothermal conditions.

Formulations

ECM module was developed to simulate fluid flow, heat transfer and chemical transport in fractured porous media. This module can be used with any of the TOUGH2 EOS modules in simulation studies of flow and transport in fractured rock. The ECM formulation, as implemented in the TOUGH2 code (Wu et al., 1996), is based on the assumption that there is an approximate thermodynamic equilibrium

(locally) between fracture and matrix at all times in the formation. For two-phase flow in a fractured porous medium, the condition of local thermodynamic equilibrium requires that temperatures, phase pressures, densities and viscosities in fracture and matrix systems are the same locally. Addition of the fluxes from Darcy's law for fracture and matrix gives the expressions for total flux through the fracture and matrix system:

$$\mathbf{F}_\beta = -kk_\beta \frac{\rho_\beta}{\mu_\beta}\left(\nabla P_\beta - \rho_\beta \mathbf{g}\right) \qquad (1)$$

where $\mathbf{F}_\beta$ is the total mass flux vector for phase β; β is phase index (β=l for liquid, and β=g for gas); ρ_β is the density of phase β; μ_β is the viscosity of phase β; P_β is the pressure of phase β; and $\mathbf{g}$ is the acceleration of gravity. In Equation (1), k is the effective continuum permeability, defined as

$$k = k_m + k_f \qquad (2)$$

with k_m being intrinsic continuum matrix permeability and k_f intrinsic continuum fracture permeability. The effective continuum relative permeability, k_β, can be defined as

$$k_\beta = \frac{k_m k_{\beta,m} + k_f k_{\beta,f}}{k_m + k_f} \qquad (3)$$

where $k_{\beta,m}$ and $k_{\beta,f}$ are relative permeability to phase β in matrix and fracture, respectively. In these equations we have defined relative permeabilities relative to the total single phase permeability, k, so that $0 \le k_\beta \le 1$. The expression for the total flux of Equation (1) can be interpreted as referring to a single effective continuum with total effective phase permeability of $k_m k_{\beta,m} + k_f k_{\beta,f}$.

The numerical implementation of the ECM scheme for evaluating the effective continuum permeabilities is straightforward once we know fluid saturations in matrix and fracture, respectively. This can be achieved by introducing a fracture/matrix combined (or composite) capillary pressure (P_c) curve (using table lookup, based on the individual fracture and matrix P_c curves from input). Under local equilibrium conditions, the combined P_c curve is

$$P_c\left(S_\beta\right) = P_{c,m}\left(S_{\beta,m}\right) = P_{c,f}\left(S_{\beta,f}\right) \qquad (4)$$

as a function of a combined or average liquid saturation:

$$S_\beta = \frac{S_{\beta,m}\phi + S_{\beta,f}\phi_f}{\phi_m + \phi_f} \qquad (5)$$

where $S_{\beta,f}$ and $S_{\beta,m}$ are saturations of phase β, and ϕ_f and ϕ_m are porosities for fracture and matrix continuum, respectively.

During the Newton iteration in the TOUGH2 run, the liquid saturation obtained from the solution is exactly the combined saturation (5). The saturation value can be used in the combined P_c curve to calculate the value of the combined capillary function. The fracture and matrix saturations can then be determined by inverting the P_c functions of fracture and matrix, respectively. The ECM relative permeabilities are evaluated using Equation (3), where the relative permeabilities $k_{\beta,m}$ and $k_{\beta,f}$ have to be evaluated at saturations $S_{\beta,m}$ and $S_{\beta,f}$, respectively.

EOS1G (Air and Passive Water), the gas-flow-only module, was developed to efficiently simulate gas flow under partially saturated conditions. This module is especially useful in performing large-scale, 3-D pneumatic analyses and modeling studies of Yucca Mountain. The single-phase gas flow module uses the same description of the physical processes of multiphase flow in saturated and unsaturated heterogeneous media as in the standard TOUGH2 EOS3 module. It provides an accurate description of gas flow dynamics, and constitutive physical laws and properties affecting gas flow. It is capable of handling different flow geometries in one, two, and three dimensions, and rapidly changing surface atmospheric conditions.

The difference between the gas flow module and the standard version of the EOS3 module is that the gas flow module solves only one conservation equation for the air component, i.e. the water mass- and energy-balance equations used in the standard TOUGH2 formulation are omitted. Liquid water and heat are assumed to be at steady state, but could be non-uniformly distributed within the system considered. EOS1G differs from the EOS3 module of TOUGH2 in (a) that the only primary thermodynamic variable is the gas pressure, (b) the water phase is treated as a passive phase with stable distribution, and (c) temperature does not change. The system is assumed to be at two-phase or single-phase gas conditions.

T2R3D (Radionuclide or Tracer Transport in 3-D) incorporates a full hydrodynamic dispersion tensor, based on a 3-D velocity field with a 3-D irregular grid, in a heterogeneous geological system. This new module of the TOUGH2 code is designed to simulate processes of tracer/radionuclide transport using an irregular, 3-D integral finite-difference grid in nonisothermal, three-dimensional, multiphase, porous/fractured subsurface systems. The flow of

water and air phases is treated using the TOUGH2 EOS3 formulation.

The major assumptions of the tracer transport module are: (a) a tracer or a radionuclide is present and transported only within the liquid phase, (b) transport mechanisms include molecular diffusion and hydrodynamic dispersion in addition to advection, and (c) first-order decay and linear adsorption onto rock grains are taken into account. The tracer or radionuclide is introduced as an additional mass component into the standard mass-conservation equations of TOUGH2, and the additional component equation is solved fully coupled with the conservation equations for water, air and heat. As a result, T2R3D can be used to study a wide range of transport problems, such as liquid or gas tracer transport, multi-component transport, strongly density-dependent processes, thermal effects, and nonlinear adsorption effects. Some of these applications, e.g. gas tracer and nonlinear absorping effects, may need minor additional modification to the code.

Verification Examples

1. ECM

In this problem we compare the simulation results using the ECM and those from the more rigorous dual-permeability modeling approach. The problem concerns one-dimensional vertical flow in an unsaturated zone of Yucca Mountain. The single vertical column grid is extracted directly from the 3-D site-scale model (Bodvarsson and Bandurraga, eds., 1996). The 1-D grid consists of 24 active grid blocks, 3 for the Tiva Canyon unit (TCw), 5 for the Paintbrush (PTn), 10 for the Topopah Springs (TSw), and 6 for the Calico Hills (CHn). These are the four major hydrogeological units at Yucca Mountain. An overlying and underlying boundary block represent the atmosphere and the water table conditions, respectively. The fracture system in the unsaturated zone of the mountain is also subdivided into the same four units, TCw, PTn, TSw, and CHn. The properties of fractures are as listed in Table 1.

Table 1. The fracture porosity and spacing data

Unit	Porosity	Spacing (m)
TCw	1.38e-3	0.618
PTn	4.12e-3	2.220
TSw	2.75e-3	0.740
CHn	9.98e-4	1.618

Since few fractures exist in the PTn unit, the effects of fractures on moisture flow in the PTn are ignored in this simulation, and the PTn formation is treated as a single porous medium rock. The same set of matrix and fracture properties (Wu et al., 1996) are used for both ECM and dual-permeability simulations.

The same boundary conditions are also specified for both models as Dirichlet-type conditions, i.e., constant pressures, temperatures and saturation. The surface boundary is subject to a constant water infiltration of 3.6 mm/year. The water infiltration on the ground surface is only added into the fracture elements on the top boundary for the dual-permeability model, while it is distributed between fracture and matrix in the ECM model because, realistically, infiltration is expected almost entirely through the fractures. However, the continuum approach of the ECM uses equilibrium partitioning for the infiltration. Also isothermal conditions were assumed.

Both models are run to steady-state, and the simulation results are shown in Figure 1 for the steady-state liquid saturation profiles of matrix, obtained using the ECM and the dual-permeability models.

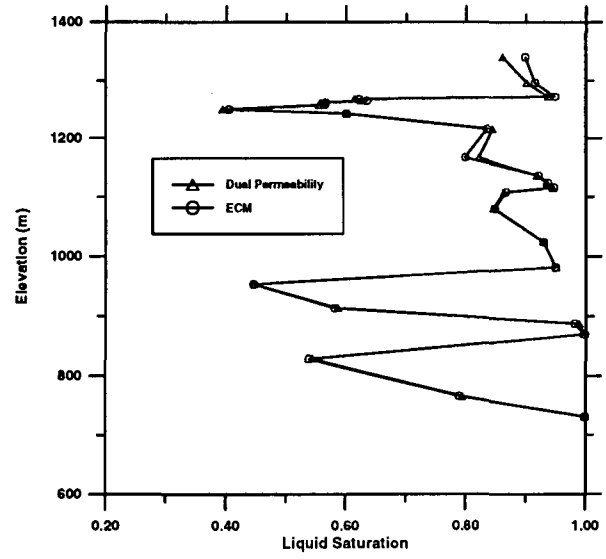

Figure 1. *Steady-state liquid saturation profiles for fractures and matrix, obtained using the ECM and the dual-permeability models.*

Figure 1 shows that almost identical results of matrix saturations are obtained from the two modeling approaches. The only differences between the two solutions may be noticed in the TCw unit (top), or along the interfaces between the PTn and the TSw (at about 1200 m elevation). These minor differences are believed to be due to the conceptual model, rather than the modeling approaches of two considerations.

First, the water infiltration is imposed into fractures only on the top boundary in the dual-permeability simulation, while the ECM model puts the infiltration into both fracture and matrix systems. Second, the PTn unit is treated as a single porous medium, and this creates certain discontinuities in matrix/fracture vertical connections across the interfaces.

2. EOS1G

In this problem we compare the results of a transient gas flow simulation using the single-phase gas module (EOS1G) with those using the EOS3 module. A 1-D grid of 99 gridblocks is arranged vertically with one meter spacing between grid blocks. Steady-state initial conditions are gas static pressures with the bottom pressure of 90 kPa, a uniform temperature gradient from 30 °C at the lower boundary to 10 °C at the upper boundary, and variable liquid saturation from 0.99 at the lower boundary to 0.57 at the upper boundary. Variable liquid saturation distribution is initialized by running the TOUGH2 EOS3 and assuming 1 mm/year water infiltration into the upper boundary, capillary suction characteristic of Yucca Mountain tuffs (van Genuchten model with α = 0.0000167 Pa^{-1} and m = 0.167), and a Brooks-Corey relative permeability function. These parameters are unchanged for the comparison simulations, except that no liquid source term was used with the single-phase gas module. Other relevant parameters are 100 microdarcys absolute permeability and 0.01 porosity. The upper pressure boundary condition is temporally varying and is provided by tabular input to TOUGH2. All other boundaries are no-flow conditions. A constant time step of two hours is used in the simulations.

A comparison of pressure response at 30 m and 90 m below the upper boundary, simulated using the single-phase gas module (EOS1G) and EOS3, is shown in Figure 2. The agreement between the two modules is very good at 30 m and also at 90 m near the bottom boundary of the model. Actually, the results show that the agreement between the two modules is excellent for each gridblock at each time step.

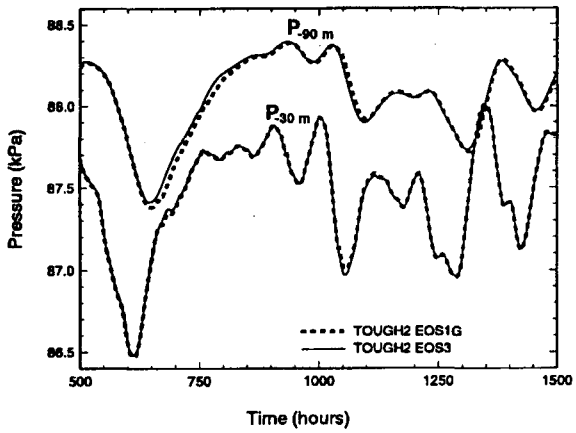

Figure 2. *Time dependent pressures for the TOUGH2 simulations using the EOS3 module and the single-phase gas module (EOS1G).*

3. T2R3D

The simulation presented here is designed to examine the accuracy of the T2R3D code in handling radionuclide transport in a multi-dimensional domain with hydraulic dispersion and molecular diffusion effects. The problem is similar to the one used by Oldenburg and Pruess (1993). It concerns two-dimensional transport of a radionuclide in a homogenous, isotropic, saturated porous medium. An analytical solution for this problem is provided by Javandel et al. (1984) along with a code for calculating the 2-D concentrations. The analytical solution is used here to verify the T2R3D numerical solution. The model domain is rectangular, as shown in Figure 3. There is a steady-state, one-dimensional flow field along the x-direction with pore velocity of 0.1 m/day. A radionuclide is introduced along a line source of length of 0.5 meter at x=0 with a constant concentration. Transport starts at t=0 from the line source by advection, hydraulic dispersion and diffusion.

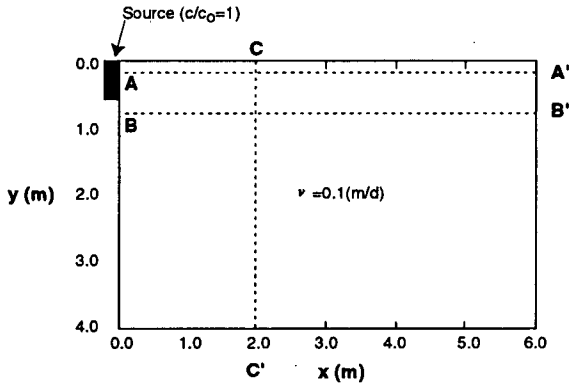

Figure 3. *Schematic of the 2-D model domain for the two-dimensional radionuclide transport problem showing the velocity field and three cross sections for comparisons of the simulation results.*

The T2R3D solution of this problem is accomplished by specifying on both the upstream boundary (x=0) and downstream boundary (x=6 m) a constant pressure, which gives rise to a steady-state flow field of 0.1 m/day flow velocity. Also, in the T2R3D simulation, a uniform grid spacing was used for both x and y directions with $\Delta x = \Delta y = 0.1$ m. The grid was generated using the TOUGH2 MESHMAKER. The system is kept at single liquid-phase and isothermal conditions. Air mass fraction is set to zero and a constant temperature of 25 °C is specified. Decay or adsorption effects are not included in the simulation. The properties used in the comparison study are: porosity $\phi = 1$, tortuosity $\tau = 1$, molecular diffusion coefficient $D_m = 1.0 \times 10^{-10}$ m^2/s, longitudinal dispersivity α_L is 0.1 m, and transverse dispersivity α_T is 0.025 m. The liquid properties are internally generated by the code. The initial and boundary conditions for the radionuclide are: initially there is no radionuclide in the system; $X^{radionuclide} = 1.0 \times 10^{-5}$ along the 0.5 m line source; and $X^{radionuclide} = 0$ at the downstream boundary (x=6 m) at all times.

Comparison between the normalized radionuclide concentrations along the three cross-sections of the rock column from the T2R3D and the analytical solution is shown in Figures 4, 5, and 6 for time = 20 days, respectively. The figures indicate that the T2R3D simulated concentration profiles in the two-dimensional domain are in good agreement with the analytical solution. Figure 4 shows the radionuclide profile at y=0.15 m (cross section A-A' in Figure 3), indicating an excellent agreement between the two solutions along this cross section. Figure 5 shows the concentration profile at y = 0.75 m (cross section B-B'), just below the line source which extends from y = 0 to y = 0.5 m, and this figure displays both longitudinal and transverse dispersion effects.

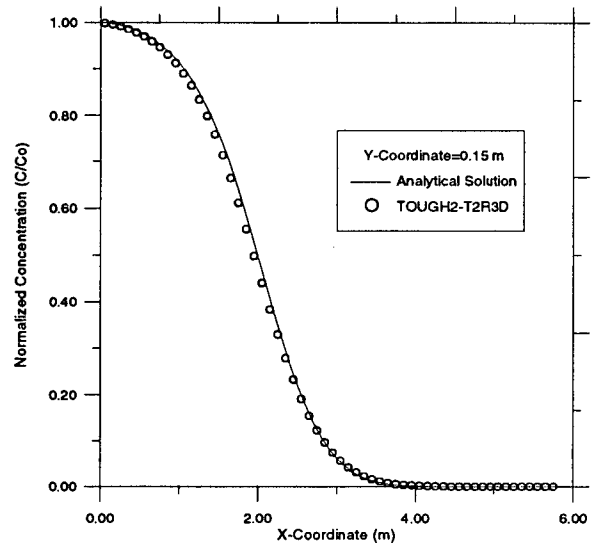

Figure 4. *Comparison of radionuclide concentration profiles along cross section (A-A') for analytical and numerical solutions at t=20 days.*

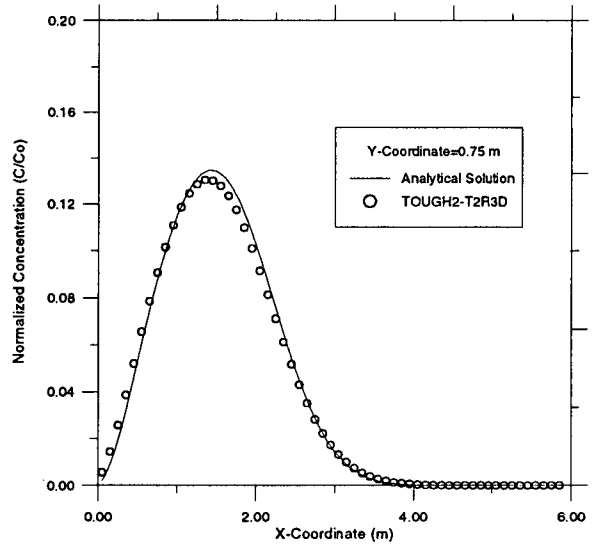

Figure 5. *Comparison of radionuclide concentration profiles along cross section (B-B') for analytical and numerical solutions at t=20 days.*

As shown in Figure 5, the comparison is good even though small numerical errors are introduced in the numerical solution. Figure 6 gives the comparison of concentration profiles along the transverse direction (C-C') at x = 2 m, indicating an excellent agreement between the analytical and numerical solutions at this location.

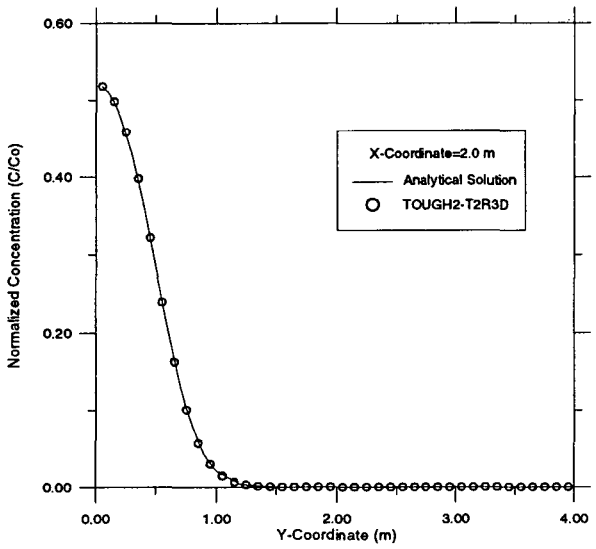

Figure 6. *Comparison of radionuclide concentration profiles along cross section (C-C') for analytical and numerical solutions at t=20 days.*

Summary

This paper summarizes three new TOUGH2 modules, ECM, EOS1G and T2R3D developed during the site-characterization studies of Yucca Mountain. The model formulations are discussed briefly, and several verification examples are given. All the three modules are currently being used in the Yucca Mountain project.

Acknowledgments

The authors are grateful to H.H. Liu, A. Mishra, and D. Mangold for review of this paper and to M. Villavert for formatting this paper. This work was in part supported by the Director, Office of Civilian Radioactive Waste Management, U.S. Department of Energy, through Memorandum Purchase Order EA9013MC5X between TRW Environmental Safety Systems Inc. and the Ernest Orlando Lawrence Berkeley National Laboratory. The support is provided to Lawrence Berkeley National Laboratory through the U.S. Department of Energy Contract No. DE-AC03-76SF00098.

References

Bodvarsson, G.S., and Bandurraga, T.M. Eds., 1996. Development and Calibration of the Three-Dimensional Site-Scale Unsaturated Zone Model of Yucca Mountain, Nevada. Lawrence Berkeley Laboratory Report, Berkeley, CA: Lawrence Berkeley National Laboratory.

Javandel, I.; Doughty, C.; and Tsang, C.F. 1984. Groundwater Transport: Handbook of Mathematic Models, American Geophysical Union, Water Resources Monograph 10, Washington, D.C.

Moridis, G.J. and Pruess, K. 1992. TOUGH Simulations of Updegraff's Set of Fluid and Heat Flow Problems, Report LBL-32611, Berkeley, CA: Lawrence Berkeley National Laboratory,.

Oldenburg, C.M., and Pruess, K. 1993. A Two-Dimensional Dispersion Module for the TOUGH2 Simulator, Report LBL-32505, Berkeley, California: Lawrence Berkeley National Laboratory.

Pruess, K., 1987. *TOUGH User's Guide,* Report NUREG/CR-4645 (Nuclear Regulatory Commission, Washington, D.C.), *and* Report LBL-20700, Berkeley, California: Lawrence Berkeley National Laboratory.

Pruess, K., 1991. TOUGH2 - A General-Purpose Numerical Simulator for Multiphase Fluid and Heat Flow, Report LBL-29400, Berkeley, California: Lawrence Berkeley National Laboratory.

Pruess, K., Simmons, A.; Wu, Y.S.; and Moridis, G.; 1996. TOUGH2 Software Qualification, Report LBL-38383, Berkeley, CA: Lawrence Berkeley National Laboratory.

Wu, Y.S., Ahlers, C.F.; Fraser, P.; Simmons, A.; and Pruess, K.; 1996. Software qualification of selected TOUGH2 modules, Report LBNL-39490, Berkeley, CA: Lawrence Berkeley National Laboratory.

Effects of Faulted Stratigraphy on Saturated Zone Flow Beneath Yucca Mountain, Nevada

Andrew J. B. Cohen and Curtis M. Oldenburg
Earth Sciences Division
E. O. Lawrence Berkeley National Laboratory

1 Introduction

The S^4Z Model[1] ("sub-site-scale saturated zone") is a 3-D TOUGH2[2,3,4] model that was developed to study the saturated zone (SZ) at Yucca Mountain, Nevada, and to aid in the design and analysis of hydrologic tests. Yucca Mountain is the proposed site for a nuclear waste repository for the United States.

The model covers an area of approximately 100 km^2 around Yucca Mountain, as shown in Figure 1. The proposed repository is located in the unsaturated zone, immediately above the area of equidimensional gridblocks east of Solitario Canyon fault, which defines the crest of Yucca Mountain. The finely discretized region near the center of the domain corresponds to the area near a cluster of boreholes used for hydraulic and tracer testing[5]. This discretization facilitates simulation of tests conducted there. The hydrogeologic structure beneath the mountain is comprised of dipping geologic units of variable thickness which are offset by faults. One of the primary objectives of the S^4Z modeling effort is to study the potential effects of the faulted structure on flow. Therefore, replication of the geologic structure in the model mesh is necessary. This paper summarizes (i) the mesh discretization used to capture the faulted geologic structure, and (ii) a model simulation that illustrates the significance of the geologic structure on SZ flow and the resulting macrodispersion.

2 Mesh Construction

A horizontal 2-D mesh of unit thickness was constructed first to define a gridblock distribution and geometry that is common to all model layers with depth. The locations of nodes are based on the location of boreholes, faults, and discretization considerations. Gridblock geometries and connection interfaces are then calculated using a numerical grid generator. Nodes in and around faults are defined such that the gridblock contact areas along strike remain constant. The lateral continuity of faults is preserved. The locations of fault gridblocks correspond to the location of their surface traces, as shown in Figure 1. Faults are represented as vertical features.

The thickness, orientation, dip, and lateral continuity of strata, and the offset along faults are defined in the ISM2.0 3-D geologic model of Yucca Mountain[6]. This model was used directly to define the vertical discretization in S^4Z. Figure 2 shows the vertical layering in S^4Z, and the corresponding cross-section through ISM2.0. Note the preservation of geologic unit displacement and variation in layer thickness, elevation, and intersection of different units at the water table. Every gridblock column consists of 23 model layers. The model has approximately 50,000 gridblocks for the single continuum version.

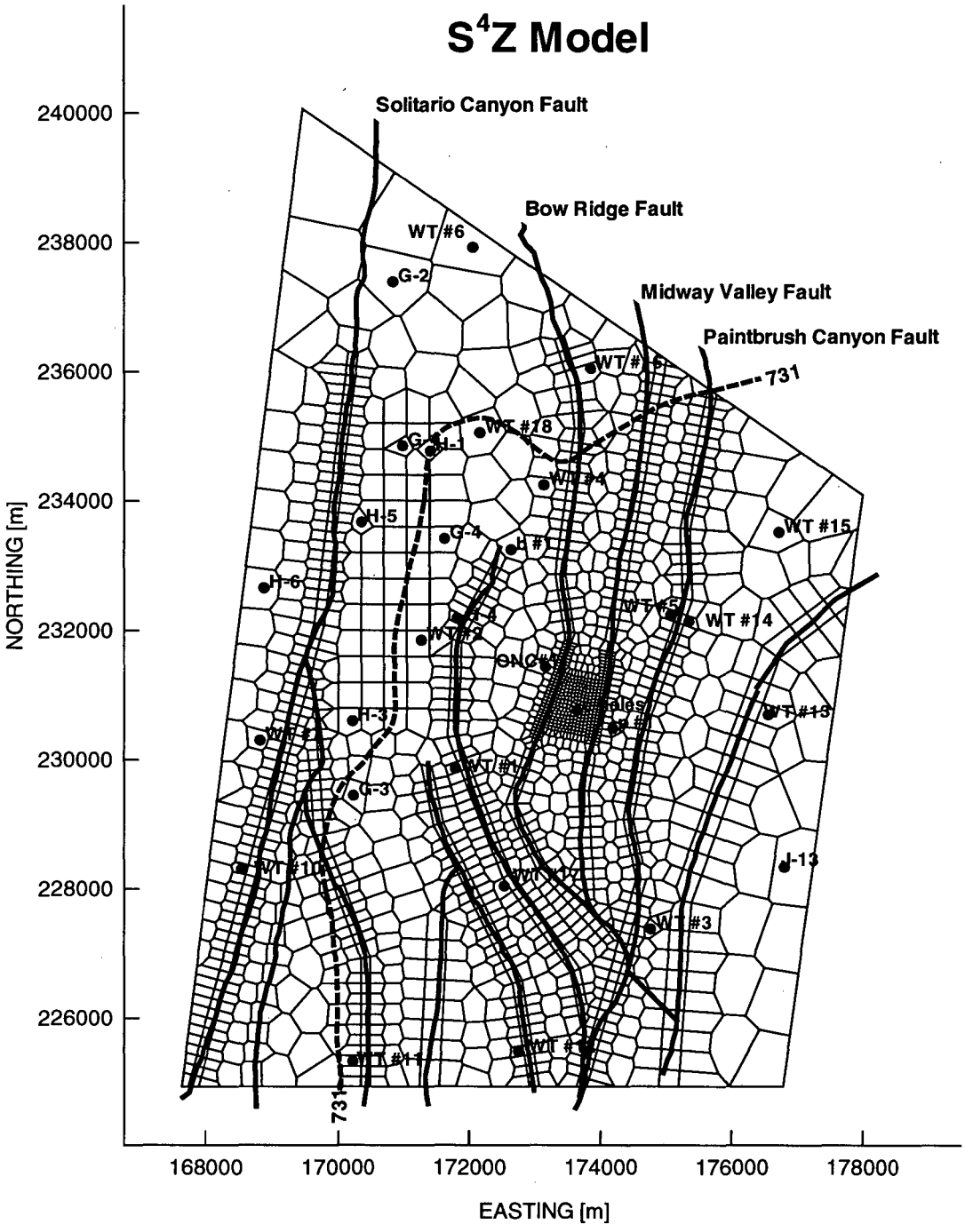

Figure 1. Numerical grid of the S^{4}Z Model. Dots mark location of saturated zone boreholes. Heavy lines represent fault traces. Dashed line is 731 meter water table elevation contour. Coordinates are Nevada state plane coordinates.

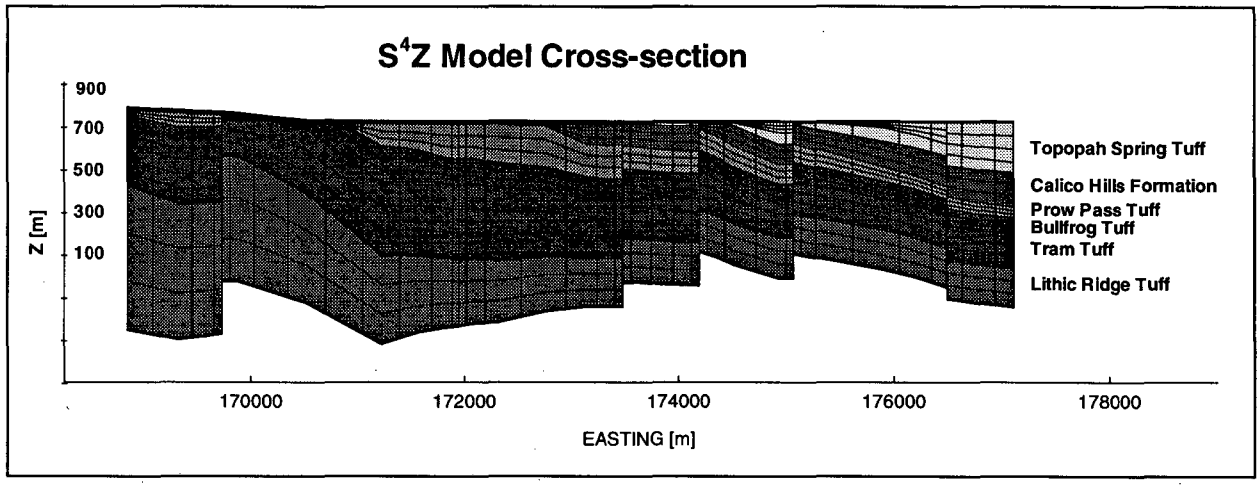

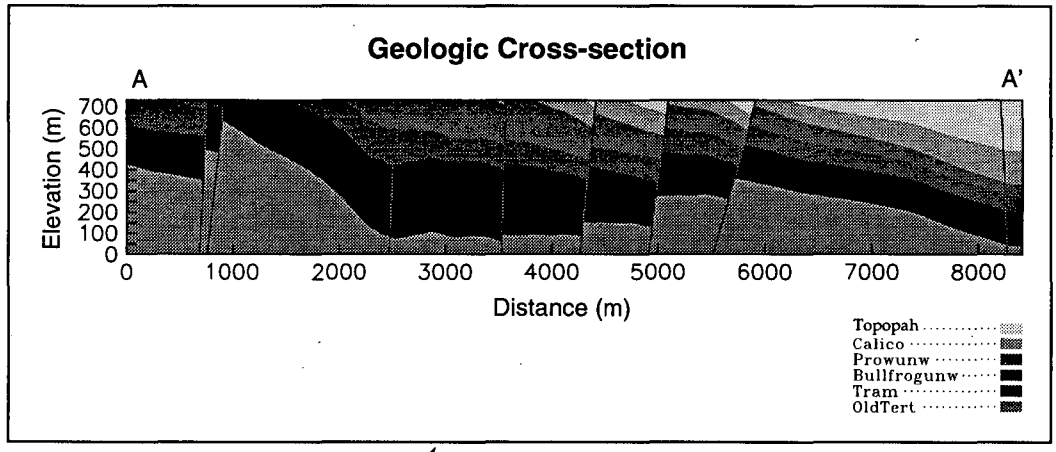

Figure 2. Cross-sections through S⁴Z Model and ISM2.0 3-D Geologic Model, showing detailed geologic structure preserved by S⁴Z discretization scheme.

The water table defines the top of the model, and the bottom represents the base of the Lithic Ridge Tuff, a thick confining unit[7]. Each S⁴Z geologic unit is divided into three hydrogeologic layers to account for the layered permeability variation due to rock welding and associated fracture characteristics[7,8]. In order to account for the unit "pinch-outs" at the water table, the uppermost model layers in gridblock columns are assigned thicknesses between 1 and 3 m, and these gridblocks are assigned the rock property of the unit present at the water table. The distribution of units at the water table defined in the 3-D geologic model[6] is replicated.

A hydrogeologic unit or subunit is displaced at a fault and can abut against a different unit, or parts of multiple units on the adjacent fault side. This structure is accounted for by assigning lateral connections from a particular unit on one fault side to multiple units it abuts on the adjacent fault side. The proper gridblock interface areas and dips between adjacent fault layers is preserved. S⁴Z fault displacement varies with strike, as observed in the field. In addition, a combined fault displacement and fault zone permeability structure can be considered by assigning a particular permeability to the fault zone blocks. High-permeability fault zones, low permeability fault zones, or faults with displacement only can be modeled, for example. The mesh generation method is similar to that used to construct an unsaturated zone model of Yucca Mountain[9], which is also based on TOUGH2. This reference describes the gridblock discretization technique in greater detail.

3 Simulation Results

The following simulation examines the effects of displacement-only faults on flow and resulting macrodispersion. These faults displace units and have no internal fault zone. The results illustrate potential fault effects in similar geologic environments, not only at Yucca Mountain. The simulation models the SZ pathway of waters that infiltrate into the Bullfrog Tuff, a high-permeability unit located at the water table directly down-gradient from the proposed repository. The infiltrating water may contain radionuclides from the repository. Only flow in the region east of the 731 m water table contour is considered, where the hydraulic gradient is approximately 0.0002[6]. A steady-state flow field is first established using constant head boundary conditions along the 731 contour, and along the eastern model side, where the head is 728.5 m. The northern and southern sides of the model east of the 731 contour are approximately perpendicular to the water table gradient. We use EOS7[10] to inject a passive tracer into the steady-state flow field. This tracer is used to observe the pathway of the infiltrating water.

Figure 3a shows the tracer distribution within the eastward-dipping Bullfrog Tuff five years after initiation of tracer injection. The black dots mark the locations of tracer injection. A high pore velocity results from the small fracture porosities used (~$2x10^{-4}$). Because steady-state fluid travel time is inversely proportional to porosity, the figure also represents the tracer plume at 50 yrs for a porosity of $2x10^{-3}$, or 500 years for a porosity of $2x10^{-2}$. This discussion focuses on the mechanical macrodispersion that results from the complex flow geometry, which is independent of porosity.

Figure 3a shows that both plumes are diverted southward along strike of the Bow Ridge and Midway Valley faults. These faults partially offset the Bullfrog Tuff against neighboring units that are assigned permeabilities 10^3 to 10^4 times less than the Bullfrog Tuff. This hydrogeologic structure effectively creates a lower permeability obstruction in these areas.

Figure 3b shows the plume distribution at the water table. Rather than a dispersed plume emanating from the constant source upstream, isolated areas of high concentration, up-gradient-source fluid are present. This behavior is not predicting by analytic dispersion models, and was not anticipated. The process that leads to this distribution is illustrated with simulation results of flow in a 2-D cross-section in the same area. Figure 3c shows how the plume descends within the high permeability and dipping Bullfrog Tuff. The complete abutment of the Bullfrog Tuff against lower permeability units at the Paintbrush Canyon fault causes flow bifurcation and hence vertical upwelling. Mixing and vertical hydraulic gradients result, even without a fluid source under the lower confining unit. Numerical dispersion contributes to the observed tracer distribution, but the general flow geometry is still observable. The large permeability contrast and the particular boundary conditions on the model sides contribute to the resulting macrodispersion. Sensitivity studies are being carried out to examine the range of effects under different fault and layer property distributions, and boundary conditions. Calibration to hydrologic, thermal, and geochemical data is used to constrain SZ properties and the resulting SZ flow behavior. Particle tracking is also being used to examine flow geometry in more detail.

4 Conclusions

A 3-D integral finite difference flow model called S^4Z was developed to study SZ flow beneath Yucca Mountain, Nevada. The model discretization captures the stratified and faulted structure present at Yucca Mountain, and fault offset is handled explicitly. Numerical simulations of the flow downstream from the region directly below the potential repository show that the high permeability Bullfrog Tuff may act as the primary conduit for repository source water, and because all geologic units are offset by faults, flow is diverted and bifurcated laterally and vertically downstream. This gives rise to unforeseen and complicated flow geometries that greatly contribute to mechanical macrodispersion.

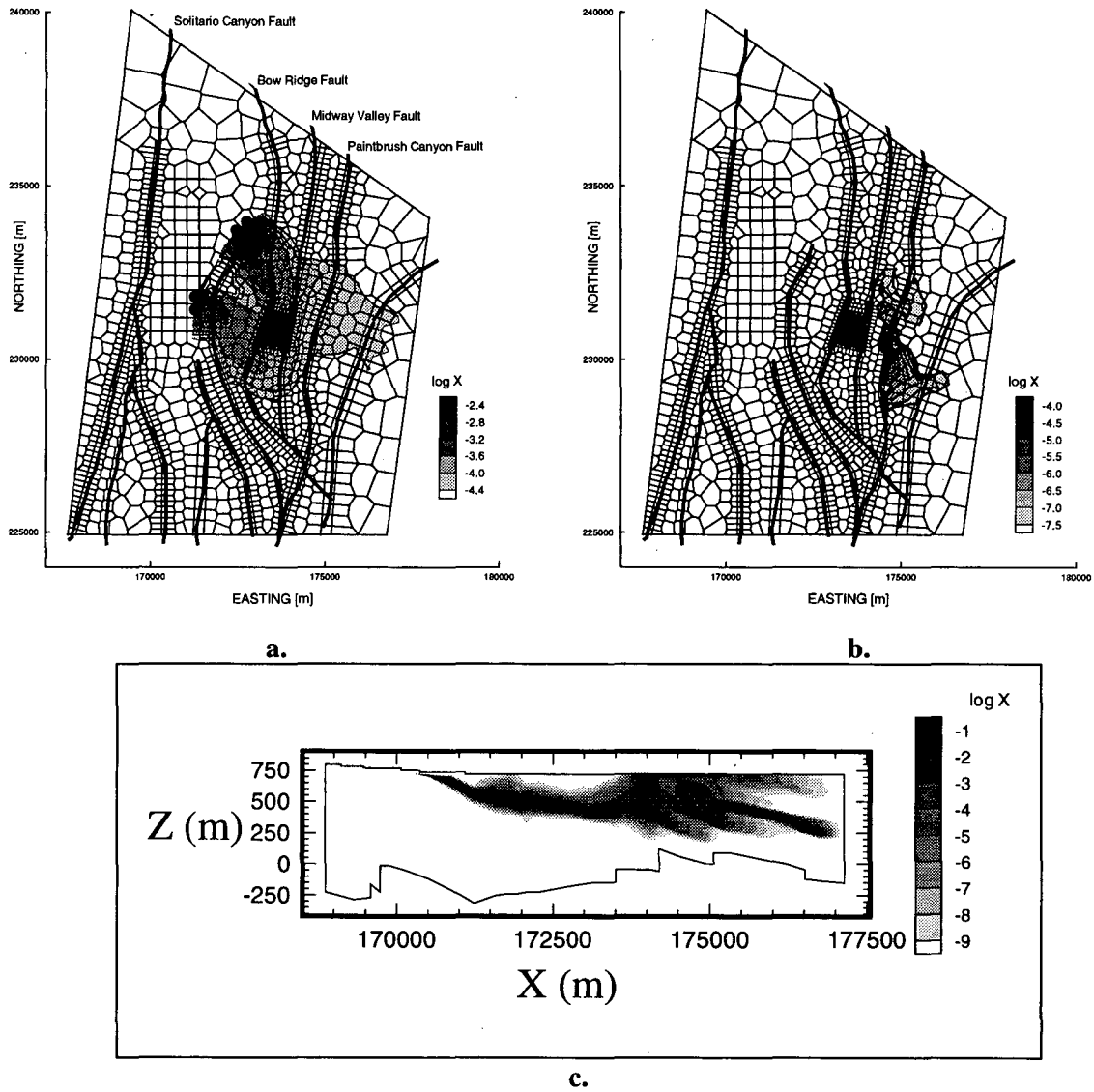

Figure 3. Log tracer mass fraction (log X) at 5 yrs ($\phi = 2x10^{-4}$), or 500 yrs ($\phi = 2x10^{-2}$): a) in the middle Bullfrog Tuff; b) at the water table; c) along west-east cross-section at latitude 232000 m. The sources of tracer are shown in Figure 3a by the black circles.

5 Acknowledgments

This work was supported by the Director, Office of Civilian Radioactive Waste Management, U. S. Department of Energy, through Memorandum Purchase Order EA9013MC5X between TRW Environmental Safety Systems Incorporated and Ernest Orlando Lawrence Berkeley National Laboratory, under Contract No. DE-AC03-76SF00098. Summary reviews by Stefan Finsterle and April James are appreciated.

6 References

1. Cohen, A. J. B., C. M. Oldenburg, A. M. Simmons, A. K. Mishra and J. Hinds, 1997. S^4Z: Sub-Site-Scale Saturated Zone Model for Yucca Mountain, Yucca Mountain Site Characterization Project Milestone SP25UM4, Lawrence Berkeley National Laboratory, Berkeley, CA.
2. Pruess, K., 1987. TOUGH user's guide, Nuclear Regulatory Commission, report NUREG/CR-4645. (also Lawrence Berkeley Laboratory Report, LBL-20700, Lawrence Berkeley National Laboratory, Berkeley, California, June 1987).
3. Pruess, K., 1991. TOUGH2 - a general-purpose numerical simulator for multiphase fluid and heat flow, Report LBL-29400, Lawrence Berkeley National Laboratory, Berkeley, CA.
4. Pruess, K., A. Simmons, Y. S. Wu, and G. Moridis, 1996. TOUGH2 software qualification, Report LBL-38383, Lawrence Berkeley National Laboratory, Berkeley, CA.
5. Geldon, A. L., A. M. A. Umari, J. D. Earle, M. F. Fahy, J. M. Gemmell and J. Darnell. 1997. Analysis of a multiple-well interference test in Miocene tuffaceous rocks at the C-hole complex, May-June 1995, Yucca Mountain, Nye County, Nevada, U. S. Geological Survey Water-Resources Investigation Report 97-4166, U.S. Geological Survey, Denver, CO.
6. Clayton, R. W., W. P. Zelinski, and C.A. Rautman (CRWMS), 1997. ISM2.0: A 3-D geologic framework and integrated site model of Yucca Mountain, ID B00000000-01717-5700-00004 Rev 0, MOL.19970122.0053, Civilian Radioactive Waste Management System Management and Operating Contractor.
7. Luckey, R. R., P. Tucci, C. C. Faunt, E. M. Ervin, W. C. Steinkampf, F. A. D'Agnese, and G. L. Patterson, 1996. Status of understanding of the saturated zone ground water flow system at Yucca Mountain, Nevada as of 1995, U.S. Geological Survey Water Resources Investigations Report 96-4077, U.S. Geological Survey, Denver, CO.
8. Cohen, A. J. B. and A. M. Simmons, 1997. Development of the sub-site-scale three-dimensional numerical zone saturated zone flow model: evaluation of flow processes, Yucca Mountain Site Characterization Project Milestone SP33SM4, Lawrence Berkeley National Laboratory, Berkeley, CA.
9. Haukwa, C., and Y. S. Wu, 1997. Grid generation and analysis, Chapter 4 of "The site-scale unsaturated zone model of Yucca Mountain, Nevada, for the viability assessment," G. S. Bodvarsson, T. M. Bandurraga, and Y. S. Wu, (eds.), Report LBNL-40376, Lawrence Berkeley National Laboratory, Berkeley, CA.
10. Pruess, K., 1991. EOS7, An equation of state module for the TOUGH2 simulator for two-phase flow of saline water and air, Lawrence Berkeley Laboratory Report, LBL-31114, Berkeley, CA.

MODELING THE EFFECT OF EXCAVATION-DISTURBED-ZONE POROSITY INCREASE ON GROUNDWATER INFLOW TO AN UNDERGROUND REPOSITORY

Geoff Freeze, Duke Engineering & Services Inc., Albuquerque, NM, USA
Greg Ruskauff, Duke Engineering & Services Inc., Albuquerque, NM, USA
Tracy Christian-Frear, Sandia National Laboratories, Albuquerque, NM, USA
Stephen Webb, Sandia National Laboratories, Albuquerque, NM, USA

Introduction

The excavation of underground radioactive waste repositories produces conditions where the repository is underpressured relative to the surrounding host rock, resulting in groundwater inflow to the repository. Groundwater, ranging from relatively fresh water in sedimentary and crystalline rocks to highly saline brine in salt formations, has been shown to enhance gas generation from emplaced waste forms, which in turn expedites repository pressurization (NEA, 1992). Repository pressurization from waste-generated gas results in an increased driving force for dissolved radionuclide movement away from the repository. Repository excavation also produces a zone surrounding the repository having disturbed hydrologic and geomechanical properties. Within this disturbed rock zone (DRZ), intrinsic permeability and porosity change over time due to the formation of microfractures and grain boundary dilation. Additionally, elastic and inelastic changes in pore volume, driven by excavation-related stress redistribution, may cause variations in the near-field fluid pressure and fluid saturation distributions that influence groundwater flow toward the repository excavation. Increased permeability, decreased pore-fluid pressure, and partially saturated conditions within the DRZ also contribute to enhancing potential release pathways away from the repository.

Freeze et al. (1995a; 1995b) describe an enhanced version of TOUGH2 (called TOUGH28W) and its application to model the coupled processes of gas generation, multiphase flow and geomechanical deformation at the Waste Isolation Pilot Plant (WIPP) repository. This paper describes a new application of TOUGH28W that couples time-dependent DRZ property changes with multiphase groundwater flow around an underground excavation at WIPP. The results are relevant not only to other salt repositories, but also to repositories in other geologic formations where groundwater inflow and DRZ effects are a concern.

Brine Inflow to WIPP Room Q

The WIPP is a U.S. Department of Energy (DOE) facility designed for the safe underground disposal of transuranic (TRU) waste from U.S. defense-related activities. The WIPP is located in southeastern New Mexico in the bedded salts of the Permian-age Salado Formation at a depth of approximately 655 m below land surface. Room Q is an experimental room designed to gain insight into the flow processes around the WIPP repository. It is a 109 m long cylindrical room with a 2.9 m

diameter that was drilled horizontally in the WIPP underground. Following excavation, Room Q was sealed to try to prevent evaporative losses. Data were collected from inside the sealed room over a six-year period to characterize and quantify brine inflow to the room. Measured Room Q data, which includes brine accumulation volume, relative humidity, room closure/DRZ deformation, resistivity, barometric pressure, and temperature, are summarized in Jensen et al. (1993a; 1993b). Hydraulic tests were performed to determine permeability and near- and far-field pore pressures.

Darcy flow from the far-field was expected to produce brine inflow to Room Q immediately following excavation (Figure 1). However, brine accumulation was not observed in Room Q for the first two years following excavation. The lack of measured brine accumulation in the room for the first two years following excavation is attributed to (1) far-field brine flowing into newly created DRZ porosity, and (2) evaporation of brine from the walls of the room due to ineffective seals. Measured brine accumulation in the room from 2-5 years following excavation is consistent with Darcy flow from the far-field. The lack of measured brine accumulation after 5.5 years is due to brine leakage under a test zone seal and does not reflect a change in brine flow behavior. Scoping calculations concluded that evaporation was not likely responsible for all of the early-time brine loss. Therefore, a modeling study was performed with TOUGH28W to examine the influence of a time-dependent DRZ porosity on brine inflow to Room Q.

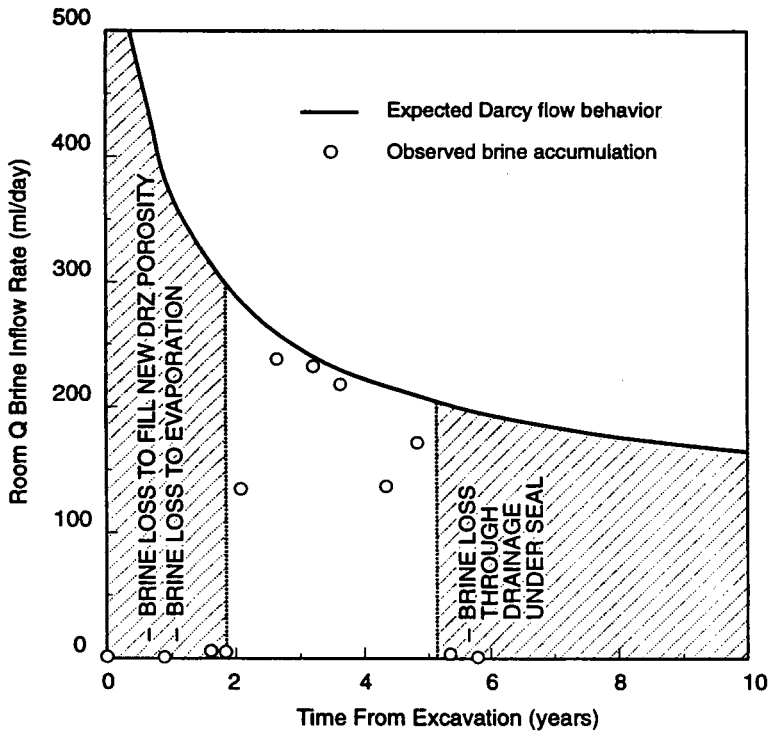

Figure 1. Comparison of expected Darcy flow behavior with observed brine accumulation in Room Q.

Modeling Brine Inflow Coupled With a Time-Dependent DRZ Porosity

Structural and hydrologic data and observations were examined to develop a conceptual model for brine inflow to Room Q that assumes far-field Darcy flow combined with an increasing DRZ pore volume. Numerical simulations were performed with TOUGH28W to examine the influence of a time-dependent DRZ porosity on flow into Room Q. The time-dependent DRZ porosity changes were based on observed room closure and deformation and on simulation results from the geomechanical code SPECTROM-32. A constitutive model for salt deformation, implemented in the SPECTROM-32 code, was used to predict room closure and DRZ formation around Room Q. The SPECTROM-32 simulations calculated damage stress, total volumetric strain, and inelastic strain. Inelastic strain is representative of increased interconnected porosity of the salt. The calculated inelastic strain was used to construct look-up table relationships in TOUGH28W between DRZ porosity, time, and distance from the excavation (Figure 2). At the end of each TOUGH28W iteration, the DRZ porosity was adjusted to match the temporal and spatial SPECTROM-32 prediction of DRZ porosity. TOUGH28W pressures and saturations then equilibrated with the porosity in subsequent iterations.

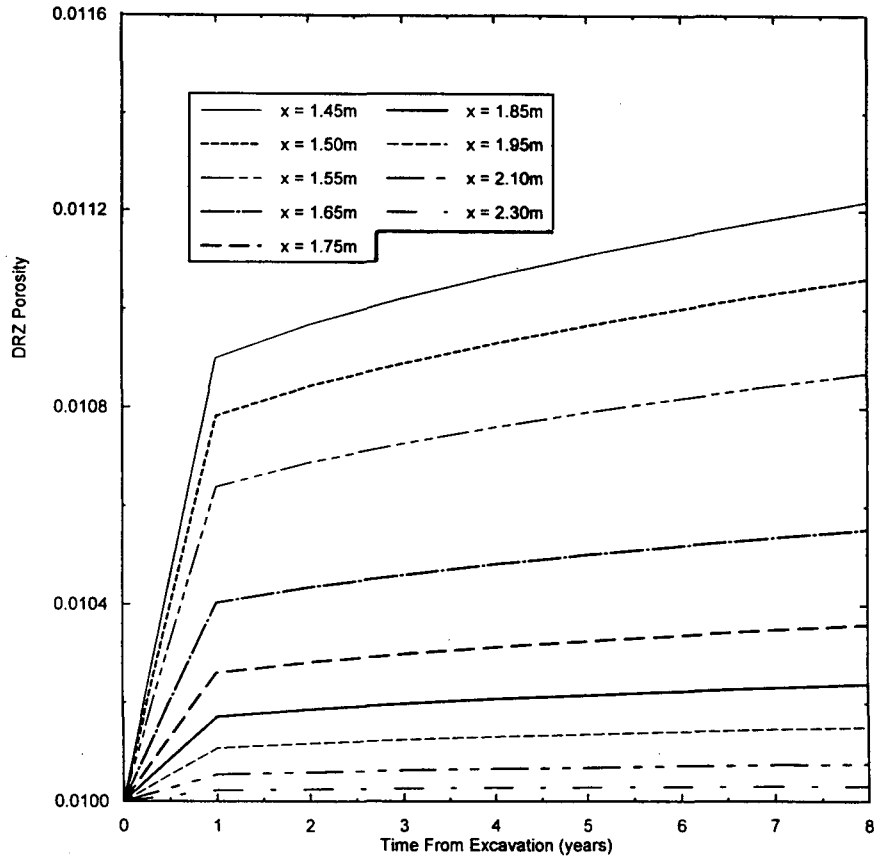

Figure 2. Room Q DRZ porosity as a function of time predicted with SPECTROM-32.

TOUGH28W simulation results of brine inflow to Room Q were compared with measured brine accumulation in the room. Simulation results (Figure 3) show that early-time brine inflow to the room can be reduced to zero if an increasing DRZ porosity with time is simulated. Reasonable assumptions about the DRZ pore volume can produce enough new DRZ porosity in the first 2 years such that brine inflow to the room is zero. This behavior is consistent with the lack of observed early-time brine accumulation in Room Q. Simulation results also show good agreement with observed brine inflow from 2-5 years following excavation. Sensitivity simulations indicated that early-time brine inflow to the room was very sensitive to the DRZ pore volume. It is therefore important to obtain good estimates of inelastic strain before applying this methodology.

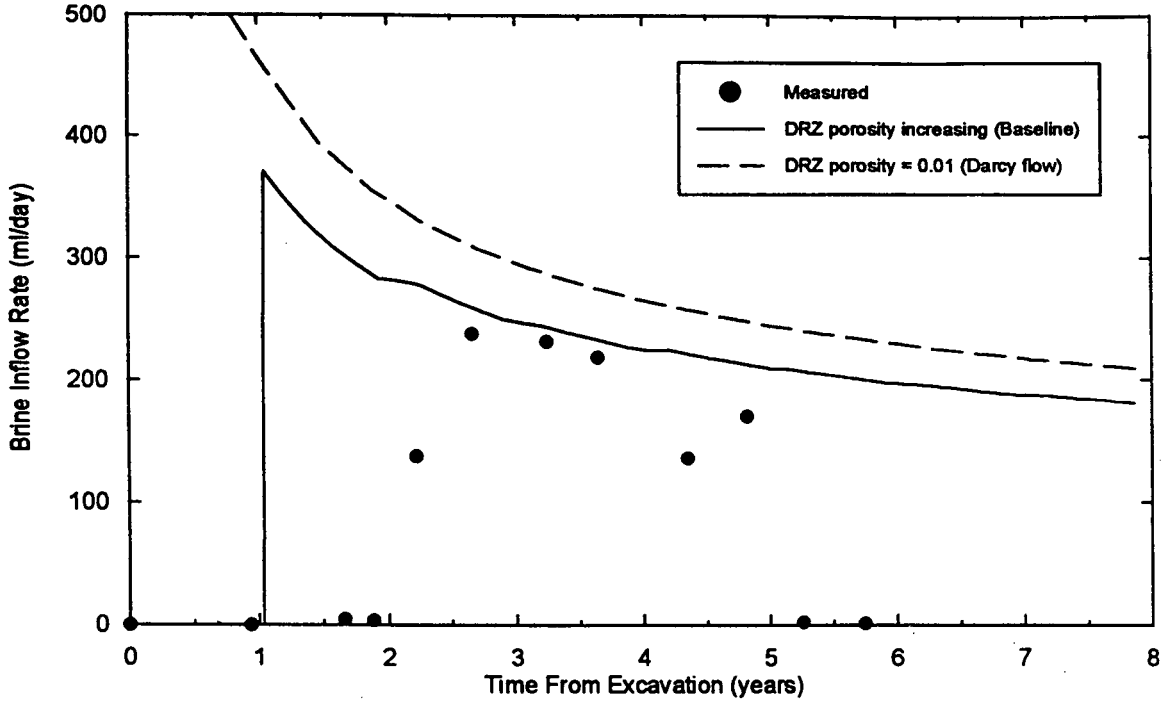

Figure 3. TOUGH2 simulated brine inflow to Room Q combining far-field Darcy flow with time-dependent DRZ porosity increases.

Summary and Conclusions

The proposed model, which uses far-field Darcy flow and a time-varying DRZ porosity, reproduces the measured Room Q brine accumulation data. Early-time brine inflow to Room Q can be reduced to zero if the DRZ porosity increases with time in a manner consistent with room closure/rock mechanics calculations. This type of flow behavior, demonstrated using an example from the WIPP repository in bedded salts, should be expected in any geologic formation where a significant DRZ forms around a repository excavation. This flow behavior is important, because a delay or reduction in groundwater inflow can limit gas generation and reduce the pressure buildup in a repository.

References

Freeze, G.A., K.W. Larson, and P.B. Davies. 1995a. *Coupled Multiphase Flow and Closure Analysis of Repository Response to Waste-Generated Gas at the Waste Isolation Pilot Plant (WIPP).* SAND93-1986. Albuquerque, NM: Sandia National Laboratories.

Freeze, G.A., K.W. Larson, and P.B. Davis. 1995b. *A Summary of Methods for Approximating Salt Creep and Disposal Room Closure in Numerical Models of Multiphase Flow.* SAND94-0251. Albuquerque, NM: Sandia National Laboratories.

Jensen, A.L., C.L. Howard, R.L. Jones, and T.P. Peterson. 1993a. *Room Q Data Report: Test Borehole Data From April 1989 Through November 1991.* SAND92-1172. Albuquerque, NM: Sandia National Laboratories.

Jensen, A.L., R.L. Jones, E.N. Lorusso, and C.L. Howard. 1993b. *Large-Scale Brine Inflow Data Report for Room Q Prior to November 25, 1991.* SAND92-1173. Albuquerque, NM: Sandia National Laboratories.

Nuclear Energy Agency (NEA). 1992. *Gas Generation and Release from Radioactive Waste Repositories: Proceedings of a Workshop Organised by NEA in co-operation with ANDRA, Aix-en Provence, France, September 23-26, 1991.* Paris, France: Organisation for Economic Co-Operation and Development/Nuclear Energy Agency (OECD/NEA).

Modification and application of the TOUGH2 code for modeling of water flow through swelling unsaturated sealing constructions

M. Jobmann
Deutsche Gesellschaft zum Bau und Betrieb
von Endlagern für Abfallstoffe mbH (DBE)
Woltorfer Strasse 74, 31224 Peine, Germany

Abstract

Making use of the TOUGH2 capabilities to model two-phase flow driven by capillary forces fluid movement through a sealing construction can be analyzed. The original version of the TOUGH2 code does not simulate the arise of a swelling pressure which is partly time-dependent and the corresponding reduction of the permeability. Based on publications and laboratory results during the project, in this paper a validated modification of the code is proposed to study the influence of an increasing swelling pressure as a function of saturation on the fluid movement through a sealing construction.

1. Introduction

Sealing of underground cavities are main topics during and after the operational period of a final disposal of radioactive and/or toxic waste. The penetration of water into unsaturated clay plugs, which seems to be the favorite material, is characterized by a swelling of the clay which is a function of the kind of the clay, i.e. the chemical composition and the dry density of the material. Many investigations can be found in the literature mainly focused on the hydraulic behavior of saturated clays. The installation of a clay plug for sealing of underground cavities is feasible by using clay which is dry and highly compacted. After an open or backfilled cavity is filled up with groundwater, the fluid penetrates into the plug and the material begins to swell. Due to this behavior a swelling pressure will arise which, among other things, results in a reduction of the permeability of the material and the sealing requirements can be met.

To convert this knowledge into practical application the Federal Ministry for Education, Science, Research and Technology in Germany launched a R&D project to demonstrate feasibility and to investigate engineered barriers for safe shaft closure for hazardous waste repositories. One of the DBE tasks is to perform model calculations to analyze the fluid movement through the sealing yielding in predictive calculations of the tightness of the plug.

2. Modification of TOUGH2

The original version of TOUGH2 (Pruess, 1991+1987) assumes a constant permeability and does not allow to use a time dependent decrease of

permeability. Due to this reason, a permeability function is introduced based on constitutive laws obtained from laboratory measurements.

2.1 Constitutive Laws

Laboratory measurements on Calcium- and Sodium-bentonite performed by Börgesson et al. (1995) yield relationships between swelling pressure and void fraction as well as hydraulic conductivity and void fraction. In figure 1 a,b the values are plotted in a double logarithmic scale together with the corresponding fitting curves.

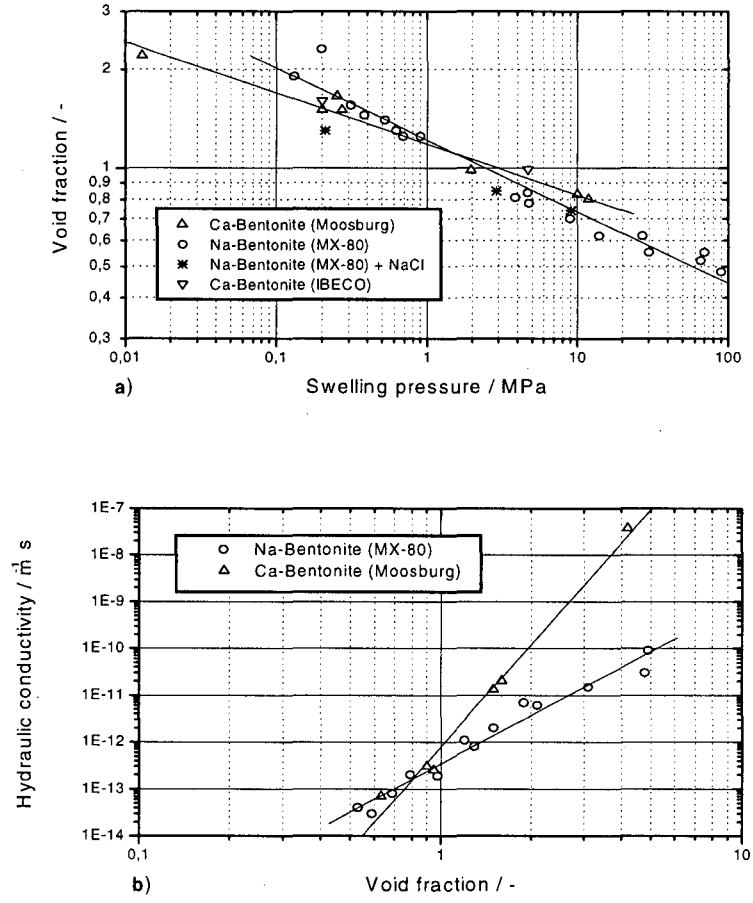

Fig. 1: a) Void fraction versus swelling pressure and b) Hydraulic conductivity versus void fraction for Ca- and Na-bentonite after Börgesson et al. (1995).

In the double logarithmic scale the relationship in figure 1 are characterized by a linear functions according to equation (1) and (2)

$$e = e_o \cdot \left(\frac{P}{P_o} \right)^{\beta} \qquad (1)$$

$$K_f = K_{fo}\left(\frac{e}{e_o}\right)^{\eta} \tag{2}$$

where e is the void fraction, P the swelling pressure, k_f the hydraulic conductivity, $\beta = \Delta(\ln e)/\Delta(\ln P)$ and $\eta = \Delta(\ln k_f)/\Delta(\ln e)$. The index 0 indicate reference parameters.

With regard to the above mentioned problem of modelling the effect of swelling on the hydraulic behavior of the clay the void fraction can be eliminated by insertion of equation (1) in (2). Using the relation between permeability and hydraulic conductivity, the permeability of the bentonite can be expressed as a function of the swelling pressure (3).

$$k(P) = k_{fo} \cdot \left(\frac{P}{P_o}\right)^{\beta\cdot\eta} \cdot \frac{\mu}{\rho \cdot g} \tag{3}$$

where k(P) is the permeability, μ and ρ are the dynamic viscosity and the density of the fluid and g is the gravitational acceleration. A graph of this function is plotted in figure 2 for Calcium and Sodium bentonite.

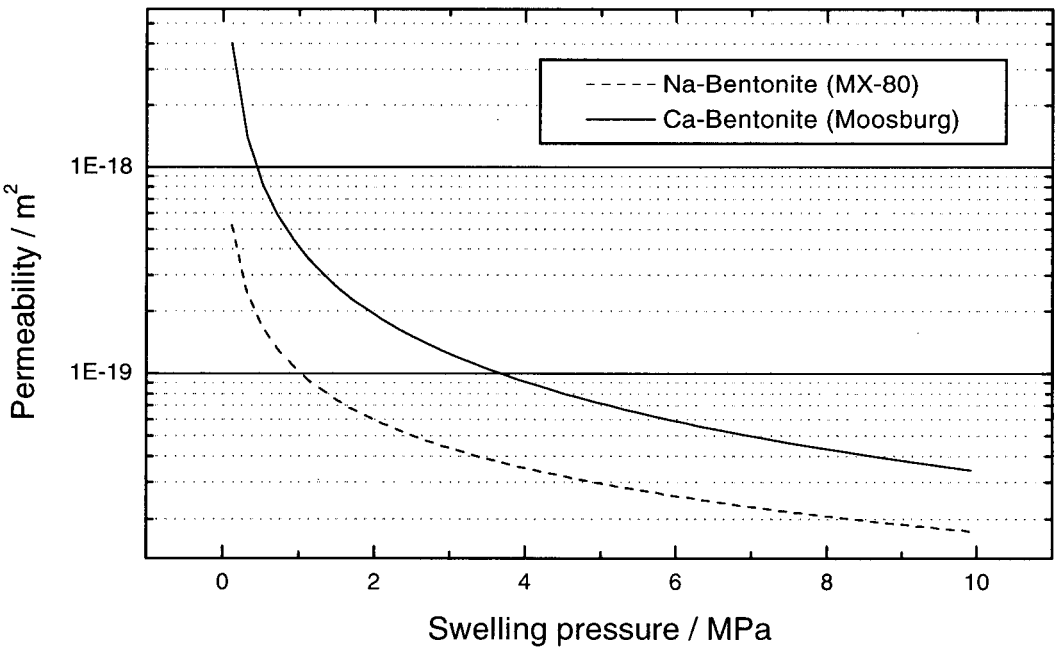

Fig. 2: Permeability as a function of swelling pressure according to equation (3).

To implement this dependency of the permeability in the TOUGH2 code, another relationship is necessary to combine the swelling pressure with one of the parameters modeled in TOUGH2. This relation can be found by Studer et al. (1984) and Börgesson (1984).

Figure 3 shows the result of tests on samples with dry densities of 1760 kg m^{-3} and 1570 kg m^{-3}. The swelling pressure seems to be direct proportional to the degree of saturation according to equation (4).

$$P = S_l * P_s \tag{4}$$

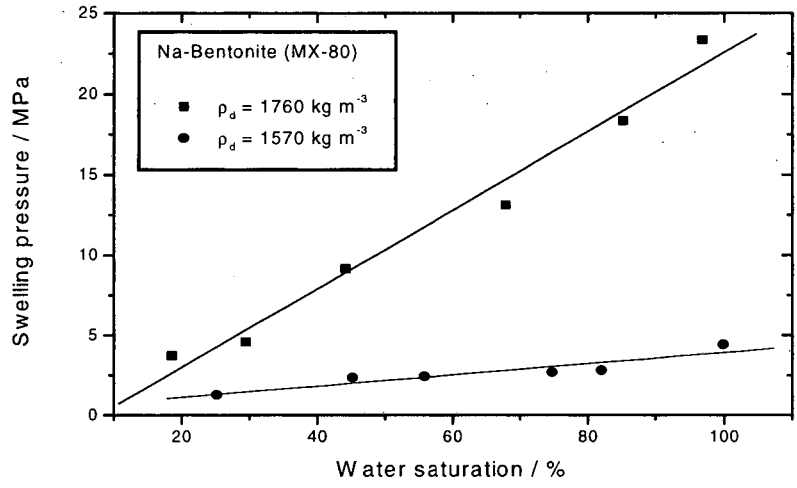

Fig. 3: Swelling pressure as a function of the degree of water saturation for Na-Bentonite with different dry densities after Studer et al. (1984) and Börgesson (1984).

P_s is the swelling pressure at saturation and S_l is the degree of liquid saturation. The maximum swelling pressure which could be reached depends on the initial dry density. Based on oedometer tests Villar & Rivas (1994), for example, proposed the following expression for montmorillonitic clay:

$$\ln (P) = 5.9 * \rho_d - 7.9 \tag{5}$$

with ρ_d being the dry density of the clay. As a result, the determination of the initial clay dry density allows the calculation of the swelling pressure development during the water infiltration into the bentonite. The time (saturation) dependent increase of the swelling pressure simultaneously decreases the permeability according to equation (3).

2.2 Implementation in TOUGH2

To implement the modification concerning the time dependence of the permeability as mentioned above, a slightly extension of the two subroutines CONVER and MULTI was necessary. The extended calculation of the permeability according to equation (3) yields an effective permeability expressed by equation (6)

$$k = k_{rel} * k(P) \tag{6}$$

where k_{rel} ist the relative permeability.

3. Validation

To check, whether the explained modification yields reliable calculations, a validation to measured values was performed. Börgesson (1984) performed several tests on samples consisting of pure bentonite and bentonite-sand mixtures. During these oedometer tests the water uptake of the samples was measured at different distances to the water inlet and at two different times. Hence, the calculated results could be compared to the real spatial distribution of the water content and simultaneously to the time dependence at several distances. In figure 4 the laboratory values are plotted together with the calculated results obtained by using equation (3). For the „relative permeability - saturation" relationship the linear function was used. The degree of saturation was converted into the water content w using the equation (Studer et al. (1984):

$$w = S_l \cdot \rho_w \cdot \left(\frac{1}{\rho_d} - \frac{1}{\rho_s} \right) \tag{7}$$

where ρ_w is the density of the water and ρ_s the density of the clay particles.

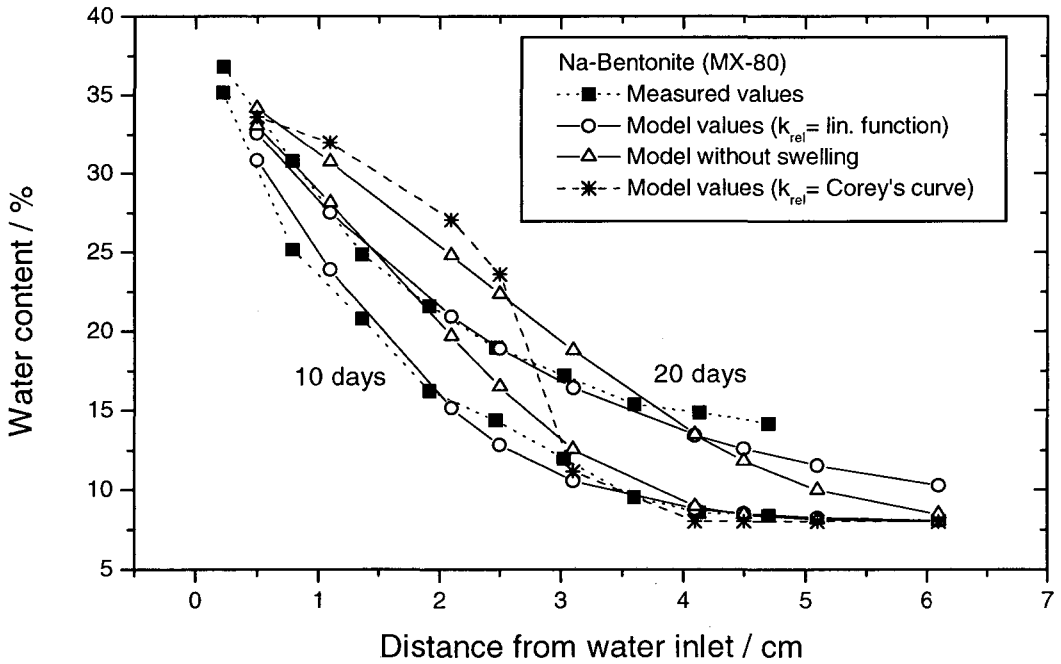

Fig. 4: Measured and calculated values of the water content distribution for two different times.

Additionally, results obtained by using a constant permeability and another „relative permeability - saturation" relationship (Corey's curve) are plotted. A good correspondence of the measured and the calculated values, especially regarding the curvature of the functions, could be reached with the new permeability function.

4. Application

As mentioned above, within a running research project DBE's tasks is to perform measurements and model calculations to analyze the fluid movement through a prepared sealing in a shaft. The modified TOUGH2 code will be applied to this sealing construction accompanying the in situ investigations. Recurrent comparison with in situ measurement of water flow into the plug will be used for validation of the model, respectively the used constitutive laws. The last step will be the performance of predictive calculations for evaluation of the tightness of the complete sealing.

References

Börgesson, L. 1984: Water flow and swelling pressure in non-saturated bentonite-based clay barriers. Clay barriers for isolation of toxic chemical waste. International Symposium, May 28-30, Stockholm, Sweden.

Börgesson, L., Johannesson, L-E., Sandén, T., Hernelind, J. 1995: Modelling of the physical behaviour of water saturated clay barriers. Laboratory tests, material models and finite element application. SKB Technical Report 95-20, Stockholm, Sweden.

Pruess, K., 1987: TOUGH User's Guide, Nuclear Regulatory Commission Report NUREG/CR-4645; also Lawrence Berkeley Laboratory Report LBL-20700.

Pruess, K. 1991: TOUGH2 - A general purpose numerical simulator for multiphase fluid and heat flow, Lawrence Berkeley Laboratory Report LBL-29400, Lawrence Berkeley Laboratory, Berkeley, CA.

Studer, J., Ammann, W., Meier, P., Müller, Ch., Glauser, E. 1984: Verfüllen und Versiegeln von Stollen, Schächten und Bohrlöchern, Band 2 Anhänge, Nagra Technischer Bericht 84-33, Baden, Schweiz.

Villar, M.V. & Rivas, P. 1994: Hydraulic properties of montmorillonite-quartz and saponite-quartz mixtures, Applied Clay Science 9, pp. 1-9.

Preliminary investigation of radionuclide release under two-phase conditions from a proposed L/ILW repository in Switzerland

Peter Gribi and Matthias Niemeyer,
Colenco Power Engineering Ltd., Baden, Switzerland (gri@colenco.ch and nim@colenco.ch)

Rainer Senger
Duke Engineering and Services, Austin, Texas (rksenger@duke-energy.com)

Piet Zuidema
National Cooperative for the Disposal of Radioactive Waste (NAGRA), Wettingen, Switzerland (zuidema@nagra.ch)

Introduction

The Swiss National Cooperative for the Disposal of Radioactive Waste (NAGRA) is investigating the feasibility of siting a low- and intermediate-level radioactive waste (L/ILW) repository in subsurface geological environments. The design of the L/ILW repository consists of a horizontally accessed cavern system located in a low-permeable host rock. One of the issues in the safety analysis is the effect of gas generation (primarily hydrogen) from anaerobic corrosion and degradation of waste material. The development of a free gas phase can result in the displacement of contaminated pore waters out of the repository.

In a previous study (Senger et al. 1994) the effect of gas generation on pressure buildup in backfilled caverns was investigated. It was concluded that, inititally, gas dissolves until gas saturation in the pore water is reached. Thereafter, a free gas phase is established coinciding with a pressure increase and a concomitant porewater displacement out of the caverns into the geosphere. These processes are mainly controlled by the following parameters: gas generation rate, intrinsic permeability of the host rock, relative permeability, and initial gas saturation.

For the investigation of the effects of gas-related phenomena on radionuclide transport preliminary near field calculations were carried out using TOUGH2/EOS7R (Oldenburg & Pruess 1996a,b) with the objectives of i) comparing the calculated radionuclide release rates under fully saturated conditions (no gas generation) with results from NAGRA's standard L/ILW near field code SEFTRAN (NAGRA 1994), and ii) investigating the release of non-volatile radionuclides under two-phase conditions, taking gas generation into account.

Modeling approach

The model domain is represented by a 2-D vertical cross section through a single L/ILW repository cavern and the adjacent host rock (Figure 1). The 2-D model is oriented perpendicular to the cavern axis, incorporating the engineered barriers of the repository (waste packages, container backfill, container walls and lid, cavern backfill, liner) and the host rock (disturbed zone around the cavern, undisturbed host rock). The model domain has an extension of 140 m horizontally and 160 m vertically.

The finite element mesh used in the simulations of radionuclide release under saturated conditions with NAGRA's standard near field transport code SEFTRAN is shown in Figure 2. The rectangular mesh consists of 4'320 elements grouped into 8 hydraulic units. As can be seen in Figure 2, some of the engineered barriers are very thin (e.g. thickness of container walls is 0.2 m) and are represented by only one row of elements. To test potential grid effects,

a finer finite element grid with 14'672 elements was used. In the case of radionuclide transport simulations with TOUGH2/EOS7R only the centres of the elements of the original coarse grid are taken into consideration for the finite difference grid.

When neglecting the gas generation in the caverns, the release of radionuclides from the near field into the geosphere is driven by the external hydraulic gradient associated with the regional groundwater flow system at the proposed site for the L/ILW repository. When gas generation is taken into account, a free gas phase is established. In this case the radionuclide release out of the caverns is driven by two processes: i) the pressure build-up due to gas generation, which leads to the displacement of contaminated pore water out of the cavern, and ii) the external hydraulic gradient.

A selected set of parameters used for the simulation of radionuclide release is summarised in Table 1. Both the engineered and natural barriers are characterised by material dependent properties such as absolute permeability, relative permeability, porosity, pore diffusion constants, mass of sorbing material, and distribution coefficients. The absolute permeabilities within the engineered barriers range from 10^{-15} m^2 for the backfill material (coarse monokorn mortar) to 10^{-17} m^2 for the container walls (concrete). Sorption is assumed to take place only on cementitious materials. Because the cavern liner is assumed to be fractured, a permeability of 10^{-16} m^2 is used and sorption within the liner is neglected. For the pore diffusion constant in the waste matrix and in the backfill a high value of 10^{-9} m^2/s has been chosen, whereas for the tighter materials (container walls and liner) a value of 10^{-10} m^2/s has been adopted.

For the host rock, a mean absolute permeability of 10^{-18} m^2 and a porosity of 1% is chosen. The permeability of the excavation damaged zone is assumed to be two orders of magnitude higher than the value for the intact host rock.

Table 1: Selected parameters for radionuclide transport calculations

Hydraulic Unit	**Porosity** [-]	**Absolute Permeability** [m^2]	**Pore Diffusion Constant** [m^2/s]
Waste Matrix	0.25	5e-16	1e-09
Container Backfill	0.35	1e-15	1e-09
Container Wall	0.05	1e-17	1e-10
Container Lid	0.35	1e-15	1e-09
Cavern Backfill	0.35	1e-15	1e-09
Cavern Liner	0.02	1e-16	1e-10
Excavation damaged Zone	0.05	1e-16	2e-10
Host Rock (Marl)	0.01	1e-18	2e-10
Hydraulic Gradient (regional scale): 0.4 m/m			

Hydrodynamic dispersion cannot be modelled with TOUGH2/EOS7R[1]. For compatibility, longitudinal and transversal dispersion lengths for the SEFTRAN model calculations have been set to the minimum value allowed by this code (i.e. 0.01 m).

For the modeling of the release of non-volatile radionuclides under two-phase conditions, a gas generation rate[2] of 0.5 m^3 H_2 (STP) / (y $\cdot m^3$ waste) and a very small value for the Henry constant were used. The cavern was conservatively assumed to be fully water saturated at the onset of gas generation. A Brooks-Corey type of constitutive relationship for the relative permeability was used in all hydraulic units. The residual saturations of water and gas were chosen to be 25% and 5%, respectively. Capillary pressure and compressibility of the solid phase are neglected.

In the model a hydraulic gradient of 0.4 m/m from left to right is assumed by imposing constant heads on the vertical model boundaries (Figure 2). For the transport simulations, zero concentration was prescribed on the vertical boundaries. Both for flow and transport calculations, no-flow boundary conditions were specified on the top and bottom of the model domain.

As a quantitative measure of contaminant release from the caverns to the surrounding host rock, the release rate of non-decaying species normalised to their initital mass is calculated for different distribution coefficients (K_d). This quantity is calculated at the interface between cavern liner and excavation damaged zone and is termed „fractional release rate".

Results

The comparison of the results calculated by SEFTRAN and TOUGH2/EOS7R for saturated conditions is carried out by inspection of

- stationary flow fields
- fractional release rates of sorbing, non-decaying species

The stationary flow fields are nearly identical, as expected. In Figure 3 the fractional release rates for saturated conditions are plotted as a function of time for different distribution coefficients (K_d = 0, 10^{-3}, 10^{-2}, 10^{-1}, 1 m^3/kg). For most of the relevant time period the fractional release curves corresponding to specific K_d-value are nearly identical. At early times, a minor discrepancy is observed.

In the case of the code SEFTRAN, potential grid effects are tested by using a finer mesh with 14'672 instead of 4'320 elements. This grid refinement shows no effect on the fractional release curve for K_d = 0 m^3/kg. For K_d = 10^{-2}, 10^{-1}, and 1 m^3/kg, the curves match very well for most of the time period considered. At early times, the fractional release rates calculated by the coarse mesh are slightly higher compared to the values calculated with a finer mesh.

Alternative weighting schemes for mobilities and permeabilities were investigated with TOUGH2/EOS7R by setting the parameter MOP(11) to 0 (base case), 1, and 2. It turned out that the agreement between SEFTRAN and TOUGH2/EOS7R results is best, when an

---

[1] Hydrodynamic dispersion can be treated with the code T2DMR which is a descendant of the TOUGH2/MULKOM family of codes (Oldenburg & Pruess 1996a)

[2] This gas generation rate was multiplied by the molecular weight ratio of air and hydrogen, in order to produce the correct molar amount of gas in the cavern.

upstream-weighting of both mobilities and permeabilities is chosen (base case). In the other cases, a significant discrepancy between SEFTRAN and TOUGH2/EOS7R results is observed at later times.

In the case with consideration of gas generation in the repository caverns, preliminary calculations for non-volatile, non-decaying species have been performed with TOUGH2/EOS7R. The calculated fractional release rates are shown in Figure 4 as a function of time and for distribution coefficients of 0 and 10^{-3} m^3/kg. The CPU-times needed for these simulations on a DEC/ALPHA 4100 (400 Mhz) are in the order 10 h, which is substantially more than the CPU-times for the calculational cases assuming saturated conditions. A comparison of Figures 3 and 4 indicates that the release of non-volatile radionuclides under two-phase conditions takes place somewhat earlier and with considerably higher rates compared to the case of fully saturated conditions. The fractional release rates are compared to the time dependent mass release of water and gas (Figure 4). This comparison shows that the release of non-volatile, non-sorbing species appears slightly retarded when compared with the release of pure water out of the caverns. This retardation is due to the travel time of dissolved species through the container walls/lid and the cavern backfill and liner. The onset of gas release takes place when a free gas path has been established from the waste through the backfill and the liner into the host rock. As can be seen in Figure 4, gas release occurs 10 years after the start of gas generation.

In this simulation, it was conservatively assumed that the caverns are fully saturated when the gas generation starts. For partially saturated conditions in the cavern at the onset of gas generation, the release of dissolved species is expected to take place at later times and with lower release rates.

Conclusions

The preliminary results of the investigation can be summarized as follows: i) The comparison of radionuclide release rates under fully saturated conditions calculated by TOUGH2/EOS7R and the standard NAGRA near field code SEFTRAN shows good agreement, and ii) the release of non-volatile radionuclides under two-phase conditions takes place somewhat earlier and with considerably higher rates compared to the case of fully saturated conditions.

References

NAGRA, 1994. Bericht zur Langzeitsicherheit des Endlagers SMA am Standort Wellenberg. NAGRA Technischer Bericht NTB 94-06. NAGRA, Wettingen, Switzerland

Oldenburg, C. & Pruess, K., 1996a. EOS7R: Radionuclide Transport for TOUGH2. LBNL-34868, Lawrence Berkeley National Laboratory, Berkeley, CA

Oldenburg, C. & Pruess, K., 1996b. Application of TOUGH2/EOS7R to Modeling of of Radionuclide Release from a L/ILW Repository under Two-Phase Conditions. LBNL-38837, Lawrence Berkeley National Laboratory, Berkeley, CA

Senger, R.K., Zuidema, P., Hugi, M., Mishra, S. & Jaquet O., 1994. Investigating the effects of near-field characteristics on gas and water transport from a L/ILW repository. Proceedings of Post-Conference Seminar No. 10 of 12th International Conference on Structural Mechanics in Reactor Technology (SMiRT-12), Stuttgart, Germany

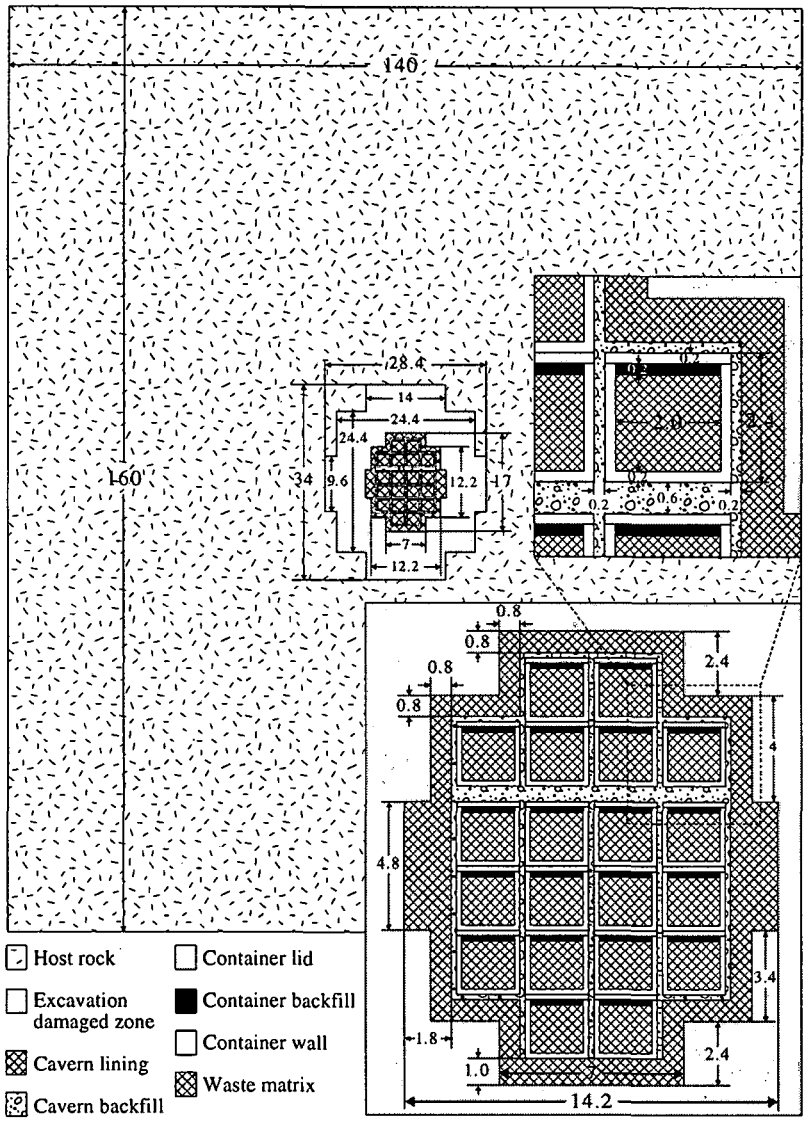

Figure 1: Model domain and definition of hydraulic units of the L/ILW repository cavern

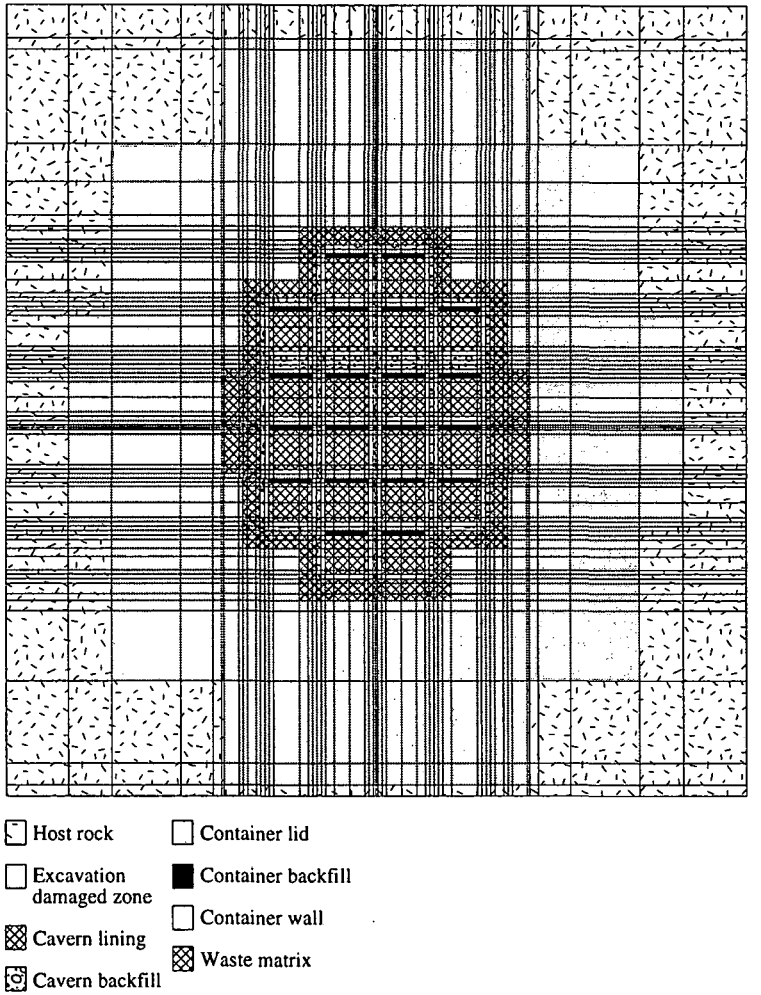

Figure 2: Finite element mesh for model simulations with SEFTRAN

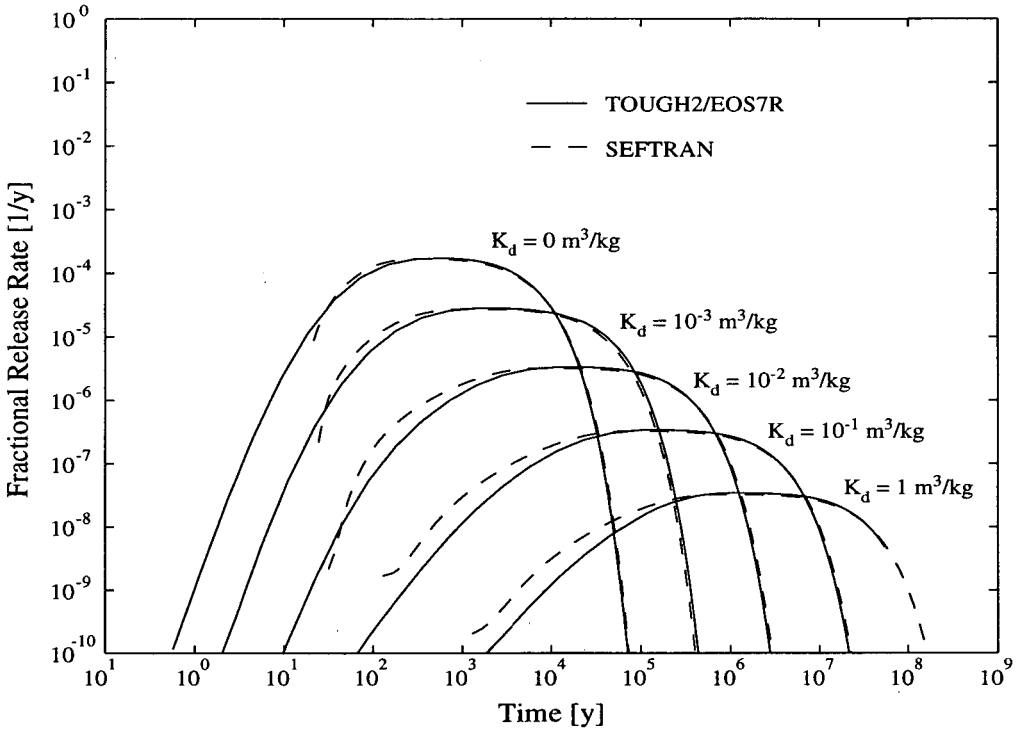

Figure 3: Fractional release rates for non-decaying species under saturated conditions as a function of time for different distribution coefficients

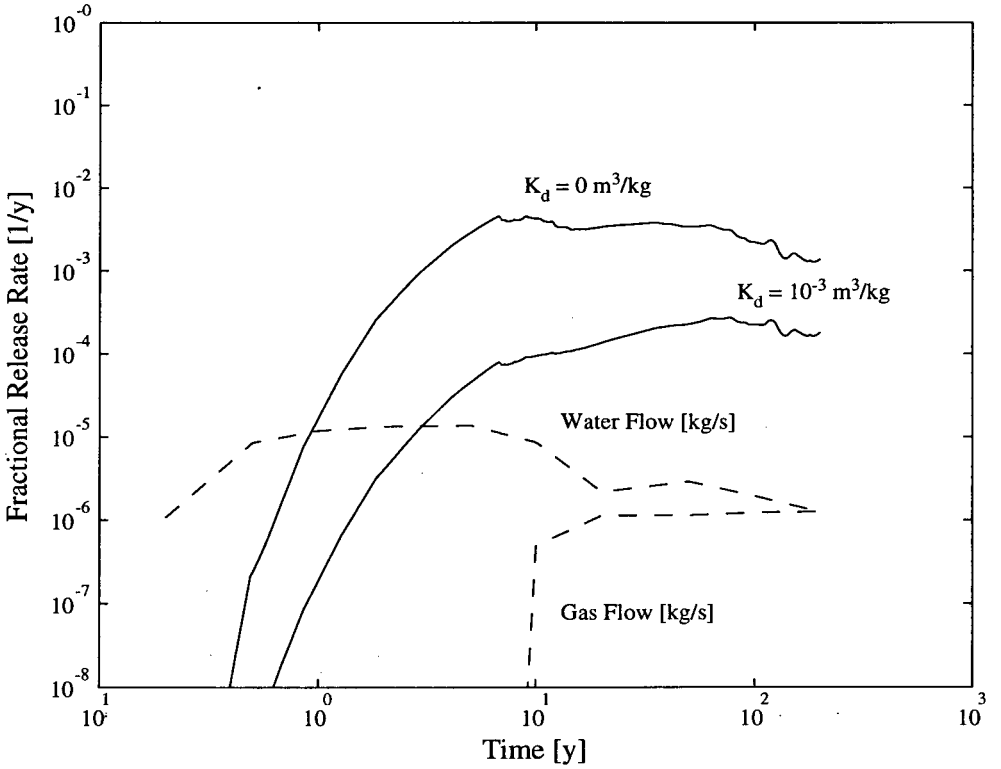

Figure 4: Fractional release rates for non-volatile, non-decaying species as a function of time for different distribution coefficients, with a gas generation rate of 0.5 m^3 H_2 (STP) / ($y \cdot m^3$ waste); also shown are water and gas release rates from the liner into the excavated disturbed zone (in kg/s)

Numerical Analysis of Thermal-Hydrological Conditions in the Single Heater Test at Yucca Mountain

Jens T. Birkholzer and Yvonne W. Tsang
Earth Sciences Division, Lawrence Berkeley National Laboratory
Berkeley, CA, 94720

Introduction

The Single Heater Test (SHT) is one of two *in-situ* thermal tests included in the site characterization program for the potential underground nuclear waste repository at Yucca Mountain. The heating phase of the SHT started in August 1996, and was completed in May 1997 after 9 months of heating. The coupled processes in the unsaturated fractured rock mass around the heater were monitored by numerous sensors for thermal, hydrological, mechanical and chemical data. In addition to passive monitoring, active testing of the rock mass moisture content was performed using geophysical methods and air injection testing. The extensive data set available from this test gives a unique opportunity to improve our understanding of the thermal-hydrological situation in the natural setting of the repository rocks. The present paper focuses on the three-dimensional (3-D) numerical simulation of the thermal-hydrological processes in the SHT using TOUGH2. In our comparative analysis, we are particularly interested in the accuracy of different fracture-matrix-interaction concepts such as the Effective Continuum Method (ECM), the Dual Continuum Method (DKM), and the Multiple Interacting Continua (MINC) method.

Test Configuration

The SHT consists of a 5-m long, nominal 4 kW heating element, horizontally placed among 30 instrumented boreholes, which span a block of approximately 13 m x 10 m x 13 m in a side alcove of the underground Exploratory Studies facility (ESF) at Yucca Mountain. The test block resides in the potential repository formation of the Topopah Spring welded tuff approximately 200 m above the groundwater table. Though the welded tuff has very low matrix permeability, it is intensely fractured with the fracture permeability several orders of magnitude higher than the matrix permeability. At ambient conditions, the fractures are essentially drained and not very conductive to water. However, strong capillary forces hold a significant amount of water in the matrix pores. This water can be mobilized due to the heating of the rock mass, raising the liquid saturation in the fractures, so that the water flux in the fractures can be enhanced by several orders of magnitude from its ambient values.

3-D Numerical Model of the SHT

Modeling of the thermal-hydrological processes in the SHT is carried out using the EOS4 module of the TOUGH2 simulator (Pruess, 1991). The fractured tuff in the test block is conceptualized using ECM, DKM, and MINC formulations, respectively. All these conceptual models appropriately describe the characteristics of unsaturated flow in fractures and matrix; however, they differ in the way fracture-matrix interaction is treated. The ECM is the most simplified method; it assumes that a local thermodynamic equilibrium is maintained between the fractures and the matrix at all times, thus implying infinitely fast mass and energy exchange between fractures and matrix. The DKM conceptualizes the fractured rock as two interacting continua, one representing the matrix, one representing the fractures, with the fracture-matrix exchange explicitly calculated from the local pressure and temperature difference. Thus the DKM can account for the different transient behavior of fractures and matrix. However, it sometimes tends to underestimate fracture-matrix interaction particularly for fast and rapid perturbations at early times, when steep gradients can occur at the fracture-matrix interfaces. Such steep gradients can not be appropriately modeled with the DKM because a linear pressure/temperature distribution is assumed within the matrix blocks. The MINC method solves this problem by subdividing the matrix continuum into a number of nested continua defined at different distances from the surface. This concept allows for representing a non-linear distribution of pressure or temperature in the matrix; therefore the MINC method should be best suited for simulating a localized intense perturbation such as that encountered in the SHT.

The hydrological and thermal input parameters used in the numerical simulations for the SHT are mainly determined from site-specific measurements, such as the matrix properties from core samples and fracture permeability values from air injection tests. Fracture parameters for the capillary pressure and relative permeability relationships have not been directly measured and are extracted from mountain-scale calibrations performed for the ambient present-day flow field. Possible chemical or mechanical alterations in response to the heating are not included in our model. The initial conditions for the model domain were chosen as 87.0 kPa for gas pressure, 25 °C for temperature, and 0.92 for matrix saturation, as given by pre-heating characterization of the SHT. Details concerning the model input parameters and initial conditions are given in Birkholzer & Tsang (1996).

The computational domain for the thermal-hydrological simulations includes the entire 3-D SHT block plus significant rock volumes added in all directions to guarantee a proper definition of boundary conditions. Small grid blocks are used around the heater hole to be compatible with sharp gradients of temperature, saturation and pressure. The 3-D grid for the ECM runs comprises about 30,000 grid blocks and more than 100,000 connections between them. Compared to that, the number of grid blocks used for the DKM and MINC runs increases by a factor of 2 and a factor of 5, respectively, indicating that the latter methods are extremely computationally intensive.

Simulation Results

Introducing a heat source in the unsaturated fractured tuff at Yucca Mountain gives rise to strong two-phase flow effects, typically characterized as follows:

(1) drying of the rock and vaporization of pore water close to the heater,

(2) vapor transport away from the heated area due to gas pressure build-up,

(3) condensation of the vapor in cooler regions outside of the drying zone,

(4) reflux of condensate to the vicinity of the heating due to capillary suction, and

(5) drainage of water away from the heated area due to gravity.

These processes are reflected in the spatial variation and temporal evolution of the liquid saturation in the rock mass. They also contribute to heat transfer in the near-field environment, as heat-induced gas and liquid fluxes may give rise to significant convective heat transport. For example, strong vapor-liquid counterflow may be reflected in a distinct "heat pipe" temperature signal, i.e., the temperature values remain at the nominal boiling point for some time before they continue to increase. Thus, close analysis of the numerous temperature measurements in the SHT can help to identify and constrain moisture redistribution, while the comparison of measured and modeled temperatures may serve to determine the suitability of different modeling approaches used to describe heat-induced flow and transport processes.

As a typical example for the temperatures observed in the SHT, we present the time evolution of measured temperature at one particular sensor located approximately 0.7 m away from the heater borehole in Figure 1. The down spikes register incidences of power outages. Temperature increases to nominal boiling within about 50 days, and continues to increase without evidence of a significant heat pipe signal. Since the other sensor observations show similar trends, the temperature data indicate that the SHT hydrogeological and thermal properties allow for only limited liquid reflux from the condensation zone back to the heater; i.e., heat conduction appears to account for most of the temperature rise. Figure 1 also gives the simulated results, obtained using the ECM, DKM, and MINC method, respectively. Note that the ECM results display only one temperature curve due to the local equilibrium assumption, while DKM and MINC have separate curves for fracture and matrix temperatures. In the latter case, the measured temperature values should be compared with the simulated matrix results, as the sensor is placed in a grouted borehole. Generally, the agreement between the measured and simulated data is very good for the three models, indicating that the thermal-hydrological response of the SHT is well represented. However, the ECM results display a subtle heat pipe signal, which retards the temperature increase at nominal boiling for some time and gives rise to a slight underestimation of temperature for the remaining heating period. The temperature curves obtained with the DKM and MINC method are almost identical: Both simulated matrix curves match the measured data curve exactly without showing a heat pipe signature. The fracture temperatures, on the other hand, display a distinct plateau at nominal boiling, indicative of substantial vapor-liquid counterflow.

Analysis of the simulated moisture redistribution processes demonstrates more substantial differences between the three model concepts. Figure 2 shows matrix saturation contours in a vertical plane at 3 months of heating. (The heater borehole is located in the center perpendicular to the cross-section displayed.) In all three cases, drying occurs up to a radial distance of about 1 to 1.5 meters from the heater; beyond that is the condensation zone where liquid saturation is higher than at ambient conditions. While strong gravity drainage in the fractures is obtained using DKM, indicated by the saturation build-up below the heater, no gravity drainage is observed using the ECM. The ECM concept involves the crucial assumption that pressure equilibrium between the fractures and matrix is maintained at all times. As a result, gravity driven liquid flow in the fractures tends to be underestimated, since vapor condensing on the fracture walls is readily imbibed into the matrix pores and driven back towards the heater. The MINC approach yields moisture redistribution processes bounded by the two "extreme" model concepts DKM and the ECM. Geophysical data seem to indicate that the moisture content below the heater is larger than above, suggesting that gravity drainage is present during the heating phase. However, the data at this point do not clearly show which one of the two models, DKM or MINC, is better suited in representing the thermal-hydrological processes.

Summary

In the present paper, we have simulated the thermal-hydrological processes in the SHT using a 3-D numerical model of the fractured tuff in the heater vicinity. Three different fracture-matrix conceptualizations were employed, the ECM, the DKM, and the MINC method. Generally we obtained a reasonably good agreement between data and simulation results for all three models. A closer analysis shows that the ECM method is least capable of capturing the transient nature of the processes in the SHT. In order to clearly discriminate between the DKM and MINC conceptual models, more data and more analysis is needed.

References

Birkholzer, J.T. and Y. W. Tsang, 1996. Forecast of thermal-hydrological conditions and air injection test results of the Single Heater Test at Yucca Mountain, LBNL-39789, E.O. Lawrence Berkeley National Laboratory, Berkeley, California.

Pruess, K., 1991. TOUGH2 — A general purpose numerical simulator for multiphase fluid and heat flow, LBL-29400, UC-251, Lawrence Berkeley National Laboratory, Berkeley, CA.

Acknowledgment

We thank C. Oldenburg and R. Trautz for their review of the manuscript and comments for improvement. This work was supported by the Director, Office of Civilian Radioactive Waste Management, U.S. Department of Energy, through Memorandum Purchase Order EA9013MC5X between TRW Environmental Safety Systems. Inc. and the Ernest Orlando Lawrence Berkeley National Laboratory, under Contract No. DE-AC03-76SF00098.

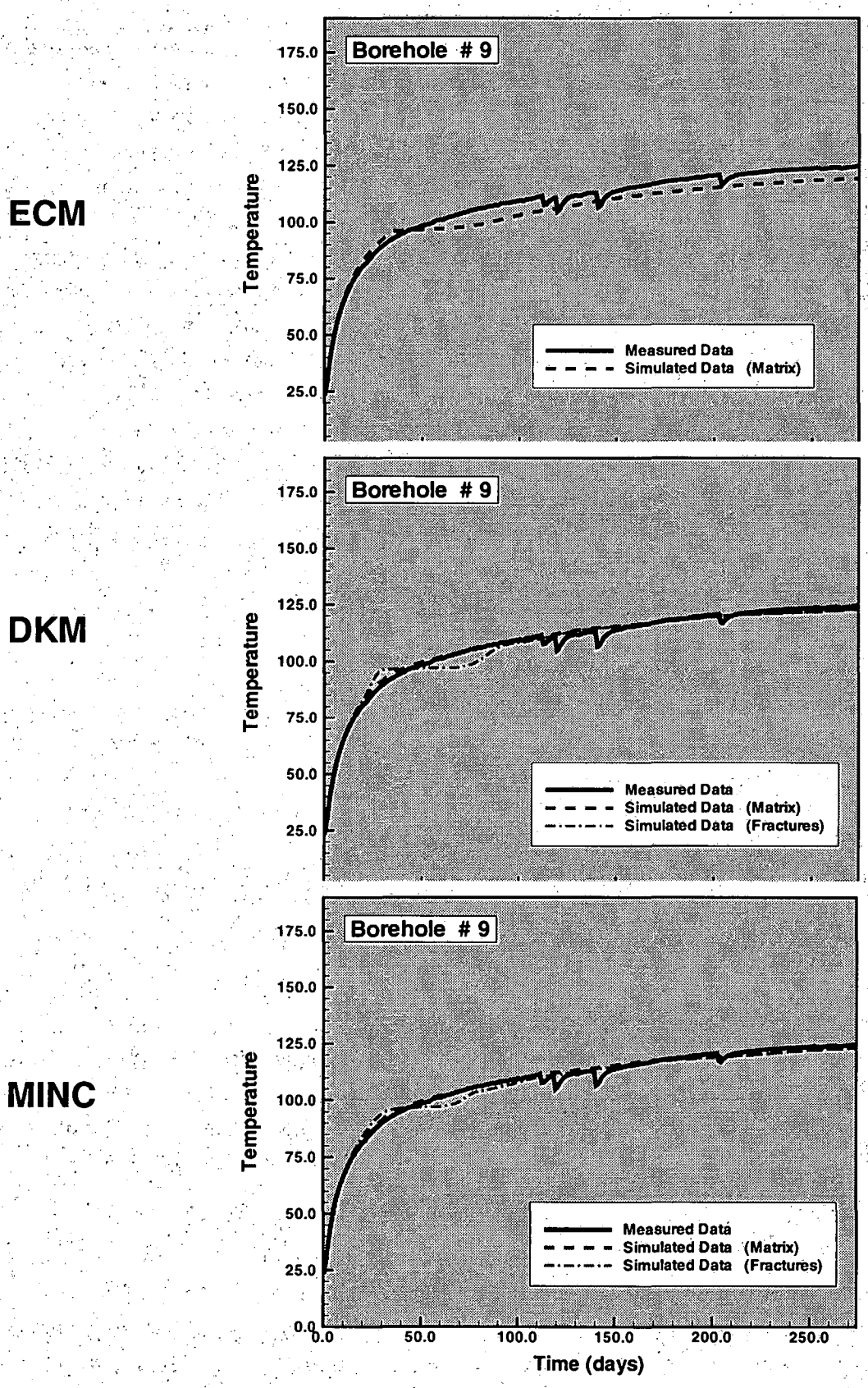

Figure 1: Measured versus simulated temperature evolution for ECM, DKM, and MINC

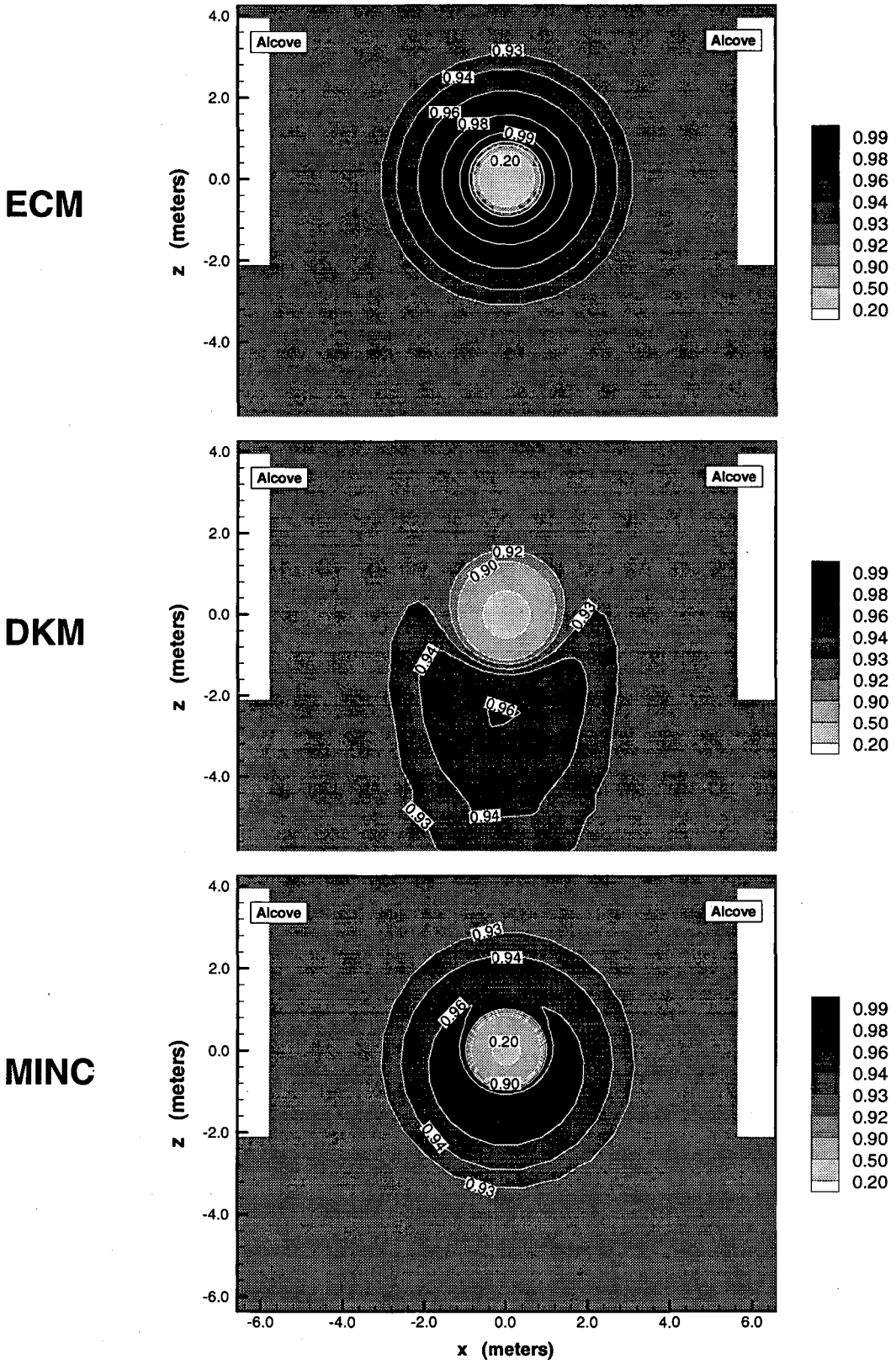

Figure 2: Simulated matrix saturation at 3 months of heating for ECM, DKM, and MINC

Prediction of the TNT Signature from Buried UXO/Landmines

Stephen W. Webb[1], Stefan A. Finsterle[2], Karsten Pruess[2], and James M. Phelan[1]
[1]Sandia National Laboratories, Albuquerque, NM 87185
[2]Lawrence Berkeley National Laboratory, Berkeley, CA 94720

ABSTRACT

The detection and removal of buried unexploded ordnance (UXO) and landmines is one of the most important problems facing the world today. Numerous detection strategies are being developed, including infrared, electrical conductivity, ground-penetrating radar, and chemical sensors. Chemical sensors rely on the detection of TNT molecules, which are transported from buried UXO/landmines by advection and diffusion in the soil. As part of this effort, numerical models are being developed to predict TNT transport in soils including the effect of precipitation and evaporation. Modifications will be made to TOUGH2 for application to the TNT chemical sensing problem. Understanding the fate and transport of TNT in the soil will affect the design, performance and operation of chemical sensors by indicating preferred sensing strategies.

INTRODUCTION

The goal of locating buried UXO and landmines is a significant challenge to science and technology. The chemical signature is affected by multiple environmental phenomena that can enhance or reduce its presence and transport behavior, and can affect the distribution of the chemical signature in the environment. For example, the chemical can be present in the vapor, aqueous, and solid phases. The distribution of the chemical among these phases, including the spatial distribution, is key in designing appropriate detectors, e.g., gas, aqueous or solid phase sampling instruments. A fundamental understanding of the environmental conditions that affect the chemical signature is needed to describe the favorable and unfavorable conditions of a chemical detector based survey to minimize the consequences of a false negative.

The fate and transport of the chemical signature emanating from the buried UXO/landmine is poorly understood. As an initial step in the evaluation of the chemical signature, a screening model based on pesticide and Volatile Organic Compound (VOC) movement in soils has been adapted to evaluate UXO/landmine chemical behavior. Future efforts to develop more mechanistic and sophisticated chemical transport models are needed to bridge the gap to more realistic fate and transport conditions.

Figure 1 shows a conceptual model of the environmental fate and transport processes that impact the movement of UXO/landmine chemical constituents, such as TNT and DNT, to the land surface for chemical detection. Chemical vapors emanate from a buried UXO/landmine by permeation through plastic case materials or "leakage" through seals and seams, and from surface contamination of the case.

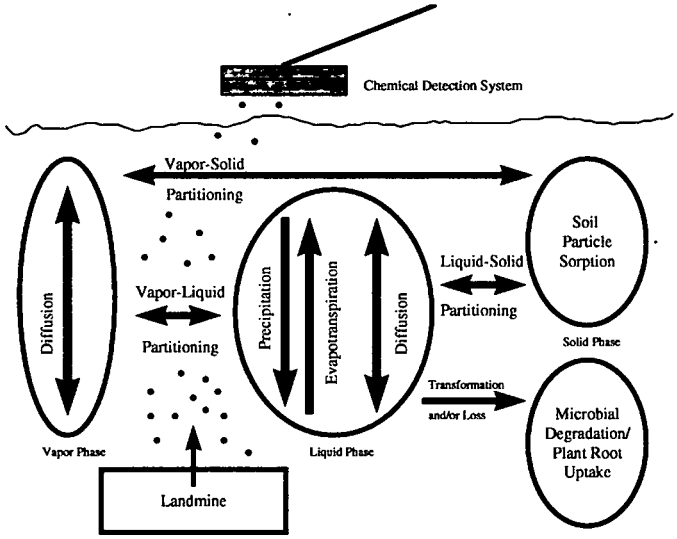

Figure 1. Environmental Fate and Transport Model for Chemical Detection of Buried UXO/Landmines.

Table 1. TNT and DNT Properties at 20°C

	TNT	DNT
Vapor Density ($\mu g/m^3$)	43.5	122
Water Solubility (mg/l)	130	270
Henry's Law Constant	3.35E-7	4.51E-7
Sorption Coefficient (cm^3/g)	3.8	4.4

CHEMICAL PROPERTIES

The chemical properties of TNT and DNT are important in determining the transport rate of these vapors through the soil. These chemical vapors exist in the gas, liquid, and solid phases of the soil. Typical properties for TNT and DNT are shown in Table 1. Because of the low value of Henry's constant and the value of the soil water partition coefficient, about 90% of the explosive mass fraction is sorbed to the soil solid phase, about 10% is in the water; and less than 10^{-6}% is in the gas phase as shown in Figure 2.

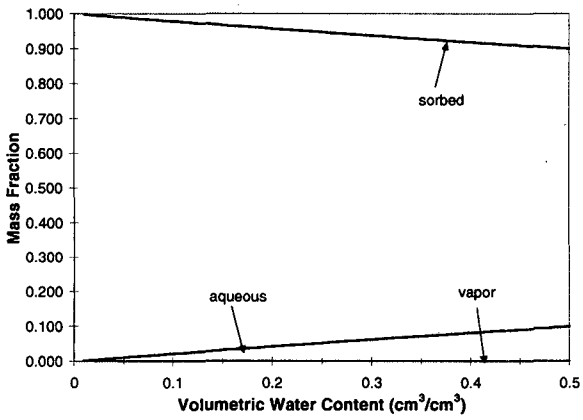

Figure 2. Phase Mass Fraction of TNT

The transport rate of TNT in soil can be estimated by evaluating pure diffusion conditions. An effective diffusivity can be defined for the total chemical concentration by considering the distribution among the phases (Jury et al., 1983). By applying the Millington and Quirk (1961) tortuosity relationship to the liquid phase, the effective diffusivity for the total chemical concentration can be expressed as

$$D_E = \frac{a^{10/3} K_H D_g^a + \theta^{10/3} D_l^w}{\phi^2 (\rho_b K_d + \theta + a K_H)} \qquad (1)$$

Figure 3 shows the variation in this effective diffusivity with water content. Note that the diffusivity value is low due to the value of Henry's constant and sorption onto the solid phase that acts as a sink for the explosive chemical. The effective diffusivity is generally much higher at higher moisture contents.

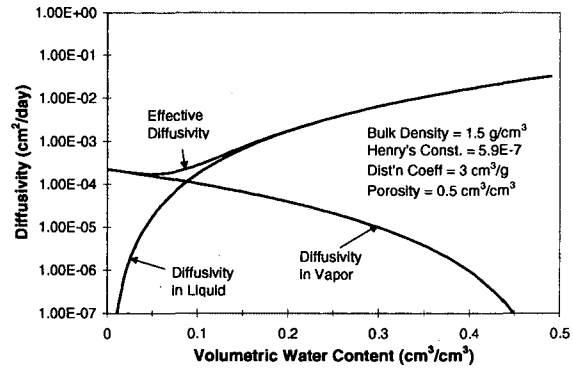

Figure 3. TNT Effective Diffusivity

INITIAL TRANSPORT STUDIES

Jury and his colleagues (Jury et al., 1983, 19841,b,c) developed a one-dimensional screening model to study the behavior of various pesticides under different environmental conditions. Mechanisms modeled include gas and liquid diffusion, sorption onto the soil, degradation, and infiltration/precipitation. Subsequently, this model was extended to buried chemicals, such as VOCs, by Jury et al. (1990). TNT properties (Henry's constant and sorption coefficient) are very similar to some pesticides, especially Prometron. Therefore, Jury's model has been used for some initial studies of the TNT transport in soils from buried UXO/landmines.

In addition, Prometron exhibits some interesting behavior that may be particularly important for the sensing of TNT for UXO/landmine detection. Under evaporation conditions, a surface "crust", or a soil layer greater in concentration than the subsurface soil, has been observed in laboratory tests; this surface "crust" is also predicted by Jury's screening model (Spencer et al., 1988). Some evidence of this type of behavior for TNT has been noted in field surveys and lab experiments, although the data are not definitive. The occurrence of a surface "crust" would greatly enhance the concentration available to chemical sensors and the efficiency of the technique.

Initial studies of the transport rate of TNT in soils from UXO/landmines have been conducted by Phelan and Webb (1997, 1998a,b) using Jury's model. The results of Phelan and Webb for UXO/landmine detection indicated a significant influence of the soil type and environmental conditions, including precipitation and evaporation, on the TNT flux at the soil surface which is available to chemical detectors.

Table 2. Phase Specific Concentration of TNT at the Ground Surface After One Year				
		Volumetric Water Content/Saturation		
Concentration	Units	0.20/0.46	0.25/0.58	0.30/0.69
Solid Phase	µg TNT/g soil	1.8E-8	3.1E-6	2.8E-5
Liquid Phase	µg TNT/ml soil water	4.8E-9	8.4E-7	7.6E-6
Gas Phase	µg TNT/cm^3 soil air	2.8E-15	5.0E-13	4.5E-12

Results from this screening model are shown below for a UXO/landmine buried 5 to 15 cm beneath the surface; details are given by Phelan and Webb (1997, 1998a,b). Note that the screening model was developed to assess the behavior of different chemicals under specific environmental conditions; it is not intended as a purely predictive model due to a number of simplifying assumptions, such as constant soil moisture content. Therefore, these results are only an indication of expected conditions, and more detailed numerical models, such as TOUGH2, are necessary for a fully predictive simulation.

Figure 4 shows the TNT surface flux at the land surface for a Gulf coastal lowlands soil type as a function of soil saturation. The oscillations in the surface flux are a result of precipitation/evaporation cycles, which were constant over the simulation. As the soil saturation increases, the surface flux increases dramatically.

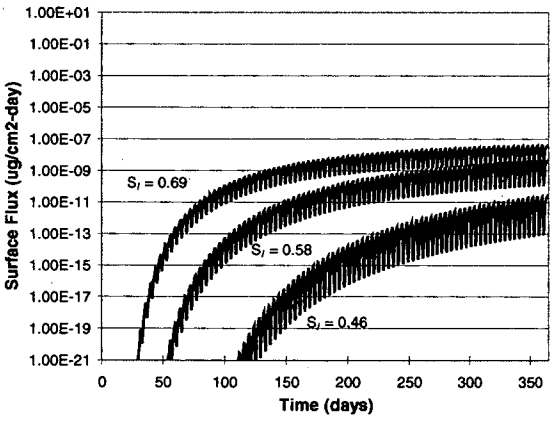

Figure 4. Surface Flux of TNT

Figure 5 shows the surface distribution of TNT after 1 year for the three soil saturations. The UXO/landmine was buried from 5 to 15 cm below the ground with an initial concentration based on contamination on the casing. In addition, UXO/landmines "leak" TNT through the casing, which was represented by a source at 10 cm. The movement of the TNT away from its initial location is slow and is a function of the liquid saturation.

Note the low total concentrations in Figure 5. The total concentration can be further broken down into solid, liquid, and gas phase values as summarized in Table 2, which indicate extremely small concentrations in the gas phase. This information will be valuable in the design and operation of chemical sensors for UXO/landmine detection.

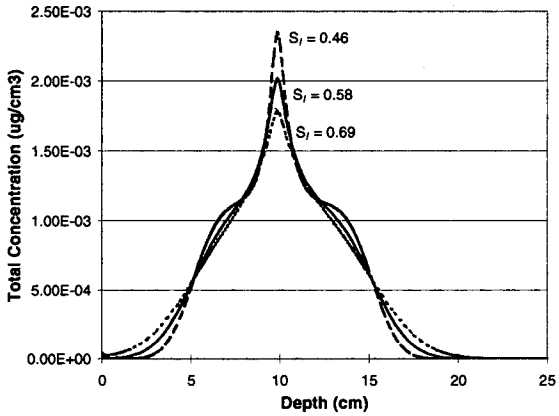

Figure 5. Subsurface Distribution of TNT After One Year

The effect of burial depth is a critical parameter. Figure 6 shows how the lag time for the surface vapor flux becomes dramatically shorter by moving the top of the initial source zone up from 10 cm to 5 cm to 1 cm and 0 cm.

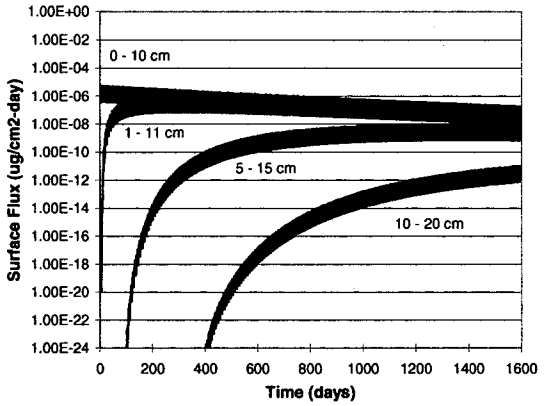

Figure 6. Effect of Burial Depth on Surface Flux

The effect of precipitation (positive water flux, J_w) and evaporation (negative water flux, J_w) is one of the most important environmental factors in the transport of explosive chemicals in soils. Figure 7 shows that with only precipitation occurring, the surface flux is about 3 orders of magnitude less than the case of zero precipitation or evaporation. The case of constant evaporation is about 2 orders of magnitude greater than the zero water flux case. If one examines the model formulation, the mass transport upwards is controlled by the effective diffusion (D_E) and the effective chemical velocity (V_E). In the constant precipitation case, upward mass transport is a function of D_E minus V_E. For the case of zero precipitation/evaporation, upward mass transport is a function of only D_E. In the constant evaporation case, upward mass transport is a function of D_E plus V_E.

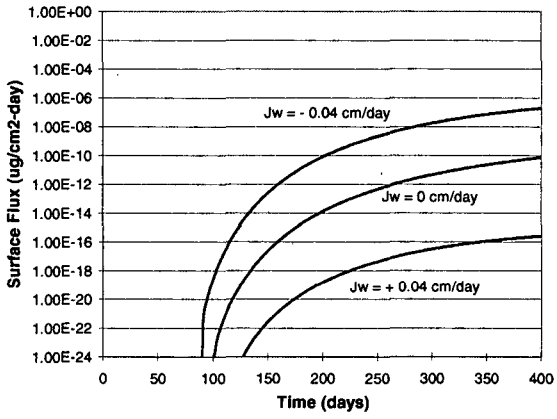

Figure 7. Effect of Water Flux (Precipitation/Evaporation) on Surface Flux

The occurrence of a surface soil layer that is greater in concentration than the subsurface soil layers, or a surface "crust", was discussed earlier. Simulations were performed to evaluate what influences the creation of the enhanced concentrations in the surface soil layers. Initial simulation runs (Phelan and Webb, 1997, 1998a) used cyclic precipitation/evaporation that was equal in magnitude; this condition did not create an enhanced surface layer. In order to create an enhanced surface layer, enough of the mass must be transported from deeper regions to the ground surface. This condition only occurs during evaporation conditions. In Figure 8 the buried chemical layer is shown to move upward until it intersects with the ground surface. Figure 9 shows the depth and magnitude of the enhanced layer. It is believed that the air boundary layer and the low Henry's Law Constant (K_H) contribute to the formation of the enhanced surface layer (Spencer et al., 1988). It appears that the upward transport through the soil exceeds the loss through the air boundary layer. Transport though the air boundary layer is controlled by diffusion and limited by the transfer of chemical from the aqueous phase to the gas phase by the very low K_H.

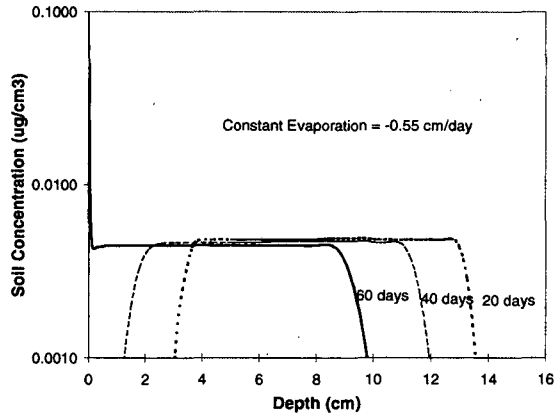

Figure 8. Upward Transport and Development of a Surface Layer

Figure 10 shows the effect of developing the enhanced surface layer with 60 days of evaporation (-0.5 cm/day), followed by precipitation for 5 days (0.5 cm/day). The enhanced surface layer found in the top 0.1 cm of soil is transported down leaving just a small enhancement at a depth of about 0.5 cm. Another simulation was run that included the same evaporation and precipitation, but was followed by another 5 day evaporation period (-0.5 cm/day) and the surface enhancement returned at about the same concentration.

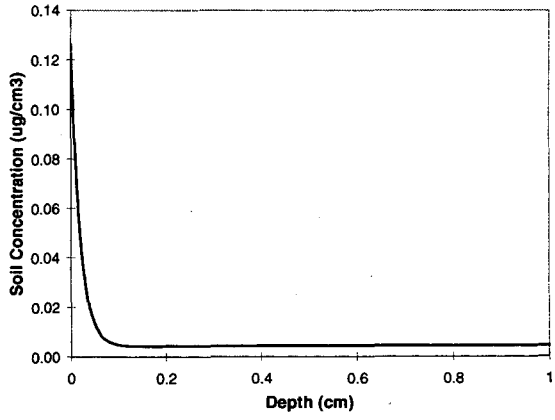

Figure 9. Detail of the Surface Layer Formed by Evaporation

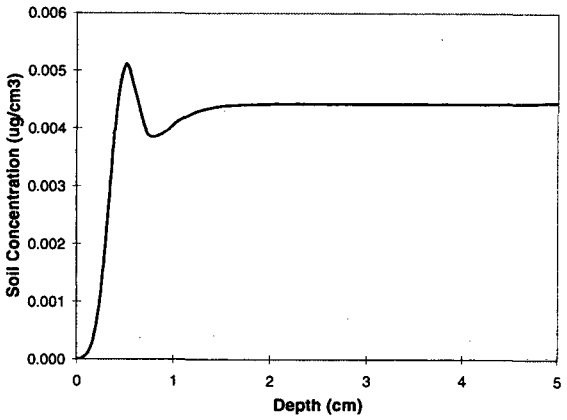

Figure 10. Effect of Precipitation on the Enhanced Surface Layer

DISCUSSION

As a result of these initial results, a more detailed mechanistic numerical model is being developed. This model is being based on TOUGH2 (Pruess, 1991) with modifications pertinent to the UXO/landmine application and will be called T2TNT. Modifications being made or planned to be made include:

1. Addition of TNT and DNT vapor components. – UXO/landmines typically emit TNT and DNT vapors. The vapor pressure of DNT is higher than TNT and, if present, will probably reach any chemical sensor before TNT.
2. Dusty Gas Model for gas diffusion. – Gas diffusion is a dominant transport mode for TNT and DNT vapors in the subsurface. Therefore, the Dusty Gas Model (Webb, 1998) will be implemented.
3. Liquid diffusion of dissolved TNT and DNT. – Liquid diffusion is not present in the standard version, although some special EOS modules include it. Liquid diffusion analogous to gas diffusion will be included because of the significant chemical concentration in the liquid phase.
4. Partition coefficient as a function of saturation. – The solid partition coefficient may be a strong function of saturation, especially at low moisture content where the partition coefficient may increase dramatically (Petersen, et al. 1995).
5. Boundary layer specifications for transport at soil surface. – For transport from the soil to the atmosphere, a boundary layer for heat and mass transfer will be implemented. The exact modifications are still being developed.
6. Precipitation and evaporation boundary conditions. – Precipitation boundary conditions will be added. The evaporation boundary condition may simply involve specification of a boundary layer and a boundary relative humidity, which will be time dependent.
7. Diurnal and seasonal variations in atmospheric conditions – In order to simulate daily and seasonal fluctuations, time-dependent boundary conditions for the pressure, temperature, and relative humidity will be implemented.

The resulting code will be used to develop an effective operational strategy for the design and deployment of UXO/landmine chemical sensors. The code will also be used within the ITOUGH framework to assist in the design of column experiments to be conducted at New Mexico Tech during the next few years. T2TNT will play an important part in the effective use of chemical sensors for UXO/landmine detection and removal.

CONCLUSIONS

The environmental fate and transport of chemical signatures from UXO/landmines is important for the design and operation of chemical sensors. The explosive vapors are predominantly found sorbed to soil particles or in the liquid phase; only a small fraction is present in the gas phase. As a result, diffusion and advection of the liquid water dominates the transport of the chemicals from the buried UXO/landmine to the land surface. Precipitation and evaporation also strongly influence the movement of the chemical signature. The results of initial screening studies have confirmed the influence of environmental conditions and soil parameters. The burial depth of the UXO/landmine is a significant factor. For shallow UXO/landmines, the chemical appears much sooner and at a much higher concentration than for deeper UXO/landmines. Precipitation and evaporation have a significant effect on the transport of TNT in the subsurface. The chemical concentration at the surface varies by many orders of magnitudes depending upon whether precipitation or evaporation is occurring. Under evaporation conditions, a surface "crust" can form where the surface concentration is higher than in the subsurface. These conditions would greatly enhance the detection capability of chemical sensors. As a result, a mechanistic numerical model based on TOUGH2 (Pruess, 1991), called T2TNT, is currently being developed. T2TNT will include a number of modifications and enhancements that should be of general interest to many TOUGH2 users. The use of T2TNT in understanding the environmental fate and transport of TNT in the soil will contribute to the improved design, performance and operation of chemical sensors in the detection of buried UXO/landmines.

NOMENCLATURE

a air volume fraction = $\phi - \theta$
D diffusion coefficient
K_d distribution coefficient for sorption
K_H Henry's Law constant
θ volumetric moisture content
ϕ porosity
ρ density

Subscripts
E effective
g gas
l liquid

Superscripts
a air
w water

ACKNOWLEDGMENTS

This work was performed with internal laboratory-directed research and development funds at Sandia National Laboratories to explore applications for miniaturized chemical sensors. Follow-on work to develop a numerical model is just beginning with funds from the Strategic Environmental Research and Development Program (SERDP) for application to unexploded ordnance (UXO) chemical sensing and from the Defense Advanced Research Projects Agency (DARPA) for application to buried landmines. Sandia is a multiprogram laboratory operated by Sandia Corporation, a Lockheed Martin Company, for the United States Department of Energy under Contract DE-AC04-94AL85000.

REFERENCES

Jury, W.A., Spencer, W.F., and Farmer, W.J., 1983, "Behavior Assessment Model for Trace Organics in Soil: I. Model Description," *J. Environ. Qual.*, 12:558-564.

Jury, W.A., Farmer, W.J., and Spencer, W.F., 1984a, "Behavior Assessment Model for Trace Organics in Soil: II. Chemical Classification and Parameter Sensitivity," *J. Environ. Qual.*, 13:567-572.

Jury, W.A., Spencer, W.F., and Farmer, W.J., 1984b, "Behavior Assessment Model for Trace Organics in Soil: III. Application of Screening Model," *J. Environ. Qual.*, 13:573-579.

Jury, W.A., Spencer, W.F., and Farmer, W.J., 1984c, "Behavior Assessment Model for Trace Organics in Soil: IV. Review of Experimental Evidence," *J. Environ. Qual.*, 13:580-586.

Jury, W.A., Russo, D., Streile, G., and Abd, H., 1990, "Evaluation of Volatilization by Organic Chemicals Residing Below the Surface," *Water Resour. Res.*, 26:13-20.

Millington, R.J., and Quirk, J.M., 1961, "Permeability of porous solids," *Trans. Faraday Soc.*, 57:1200-1207.

Petersen, L.W., Rolston, D.E., Moldrop, P., and Yamaguchi, T., 1994, "Volatile Organic Vapor Diffusion and Adsorption in Soils," *J. Environ. Qual.* 23:799-805.

Phelan, J.M. and Webb, S.W., 1997, *Environmental Fate and Transport of Chemical Signatures from Buried Landmines - Screening Model Formulation and Initial Simulations*, Sandia National Laboratories, SAND97-1426.

Phelan, J.M. and Webb, S.W., 1998a, "Chemical Detection of Buried Landmines," Proceedings of the 3rd International Symposium on Technology and the Mine Problem, April 6-9, 1998. Mine Warfare Association.

Phelan, J.M. and Webb, S.W., 1998b, "Simulation of the Environmental Fate and Transport of Chemical Signatures from Buried Landmines," International Symposium on Aerospace/Defense Sensing, Simulation, and Controls, Orlando, FL, April 13-17, 1998, SPIE.

Pruess, K., 1991, *TOUGH2 - A General-Purpose Numerical Simulator for Multiphase Fluid and Heat Flow*, LBL-29400, Lawrence Berkeley Laboratory.

Spencer, W.F., Cliath, M.M., Jury, W.A., and Zhang, L.-Z., 1988, "Volatilization of Organic Chemicals from Soil as Related to Their Henry's Law Constants," *J. Environ. Qual.* 17:504-509.

Webb, S.W., 1998, *"Gas Diffusion in Porous Media: Comparison of Models,"* TOUGH '98 Workshop, Lawrence Berkeley National Laboratory, May 4-6, 1998.

Distinguishing the Contributions of Multiple Sources from a Gasoline Release

Mark J. Lupo

KW Brown Environmental Science & Engineering
13101 Northwest Freeway Suite 314, Houston, TX 77040

Kirk W. Brown

Soil and Crop Sciences Department
Texas A&M University, College Station, TX 77843

Introduction

The T2VOC model (Falta, et al., 1995) with the T2CG1 conjugate gradient package (Moridis and Pruess, 1995) was used to simulate the motion of gasoline released from a petroleum storage terminal. An aboveground storage tank lost 15.5 m^3 of gasoline over a 56-hour period. Plant workers recovered 1.25 m^3 of gasoline by removing over 6 m^3 of the saturated surface soil. Sixteen years later, the local government remediated the site with the petroleum company bearing the cost. At that time, the local government remediated a neighboring downgradient site. The second site also had decades-old gasoline releases. In both cases, the remediation method was the excavation and replacement of the contaminated soil. A dispute arose as to who should pay for the cleanup of the second site. Resolving the dispute using field data alone was not possible, since much of the contaminated soil was removed during the remediation process. There was also a dispute concerning the groundwater flow direction at the time of the releases due to a subsequent engineering project of a major scope.

To protect itself from potential liability, the first petroleum company used T2VOC to determine the potential distance and extent of contamination resulting from their release. This project utilized the unique capabilities of T2VOC because the simulation was to include the full history of the gasoline spill in three dimensions. This history included the release itself, the removal of some surface soil, the movement of gasoline through the unsaturated zone, the depression of the water table and the forward motion of the free-phase plume until it was overcome by capillary forces, and the degradation of the plume. Clearly this problem required a simulator that could handle vadose zone hydrology as well as groundwater flow. It had to be able to handle several phases simultaneously.

Procedure

Soil borings taken before the excavation revealed the stratigraphy. A permeable sand was divided by a thin silt layer. The lower sand was underlain by dense glacial clay. The core from one boring had been preserved. A petrophysical laboratory used samples from this boring to determine the unsaturated flow parameters for use in the Parker functions (Parker, et al., 1987). These parameters are the irreducible water saturation S_m, an exponential parameter n, and the parameter α. Porosity and permeability of the strata were measured as well. These values are presented in Table 1. A 5,415-block grid was devised for a 95 x 75 m^2 area that was 9.5 m deep. The grid blocks were 5 x 5 m squares of varying thickness. The grid was oriented in the

direction of groundwater flow in the vicinity of the release. A cross section of the grid is presented as Figure 1.

Local meteorological data made it possible to determine the air pressure, the deep percolation rate, and the moisture content of the soil. Groundwater monitoring data allowed the determination of boundary conditions. Groundwater flowed in a southeasterly direction, and curved more eastward in response to the subterranean topography as one moved away from the point of the release. Dynamic steady state was determined in one dimension for the corners of the domain. These columns were used to obtain dynamic steady state in two dimensions for the four sides. Achieving dynamic steady state in three dimensions with T2VOC was challenging because the silt layer was near the water table.

Next, the gasoline release was simulated. Eye witness accounts of the release and records of product loss helped in the construction of the loss scenario. The release was a spray of gasoline that continued undetected for up to 56 hours. Using an evaporation model, it was conservatively estimated that 20% of the gasoline was lost to evaporation (Seginer, 1967; Sutton, 1953; Mackay and Matsugu, 1973). The mass of the remaining gasoline was introduced to the model by placing a "COM3" source in the GENER block for a surface grid block at the location of the release.

Benzene and xylene were used as surrogates for the complex mixture of hydrocarbons that constitute gasoline. Chemical properties were mostly taken from Reid, et al. (1987). The model predictions were not very sensitive to the differences between these two constituents. The biodegradation rates were taken from land treatment data (API, 1984). The lower end member was taken from the error bar on the degradation rate of benzene. This value was divided by 10 to account for the reduced oxygen content at depth.

Runs were conducted with several choices for the length of the release event, and the final results were not sensitive to the length of the time of the release. However, the model ran more smoothly with a longer release time. Therefore, 56 hours was chosen. A model run for a 56-hour release using benzene as the surrogate resulted in a column of grid blocks extending to the water table whose pores were over 50% saturated with "gasoline." The water table was depressed, as expected from the literature (van Dam, 1967).

The SAVE file from the release scenario was used to depict the initial conditions of the long simulation covering the 20 years that followed. One modification to this INCON file was that the VOC concentration was zeroed out in all phases in the surface block where the release took place. This was done to simulate the replacement of some of the contaminated sand by the plant workers. There was a string of warm-start runs to cover the ensuing period of 20 years.

Results

In the simulation, soil gas transport ceased to be important after the initial months. Over the next five years, the free-phase plume moved 40 m from the source. Most of the longitudinal motion of the free-phase plume occurred in the first three years (Figure 2). The final two years of free-phase migration was transverse (Figure 3). During this time, the size of the free phase increased in boxes with a y coordinate of L, while the free phase decreased on the upgradient side. The free-phase plume contaminated no new grid blocks after the fifth year. Beginning with the sixth year, the plume began to shrink, beginning from the upgradient side. The free-phase plume disappeared entirely after the twelfth year. The dissolved-phase plume continued to

decrease until the end of the twentieth year, when the maximum concentration of surrogate was less then 5 μg/L everywhere in the domain.

Discussion

The forward motion of the free-phase plume was halted when the size of the gasoline phase in the pores became too small at the leading edge of overcome capillary forces. Thus the prediction by the T2VOC model was governed by the values chosen for the unsaturated flow parameters. Biodegradation played a lesser role in stopping the plume. Biological action limited the increase in concentration in the dissolved phase ahead of the free phase. This action is only important when the plume is moving slowly and marginal increases in hydrocarbons would cause a phase change. Biodegradation became more important in later stages of the simulation, when the free-phase plume was halted.

Note that the geometry of the grid played a role of the evolution of the free-phase plume in the latter stages of its motion (years 3 to 5). The drop in the silt layer at row M created a permeability trap for the gasoline at a point in the plume's history in which the size of the free phase was becoming small (Figure 4). This effect is artificial, because the silt layer at the site slopes gently, without a "stair step." The grid contained such a step to account for the slope within the limits of the discretization. Without such a trap, the plume would not have widened at row L. It may have traveled somewhat farther along its longitudinal axis, until the size of the free phase at the leading edge was too small to continue to overcome the surface tension of the grains. That the free phase traveled as far as it did is a tribute to the low value (0.09) of the irreducible water saturation, S_m. The sand at this site was very well sorted. This was particularly true of the upper sand.

Although the subject of surrogate chemicals is a wide topic worthy of a study in itself, it is important to consider. Benzene was chosen as our surrogate, even though it constitutes only a few percent of most gasoline. The monoaromatic hydrocarbons are an important component of gasoline, but xylene is more abundant than benzene, and the isomers of trimethylbenzene are more abundant than xylene. Branched alkanes are most abundant, led by isopentane. To exactly simulate a release such as this one would require a program that allowed multiple volatile constituents. The more mobile constituents of gasoline are the most prone to biodegradation and evaporation. In a release that began as a spray on a warm week in the summer, the gasoline that actually entered the subsurface environment would have had its composition skewed to the heavier end, and would have moved more slowly. It would lose its more mobile constituents first. The less mobile, less degradable constituents would have governed the latter history of the plume. Thus it is likely that the free-phase plume would not have traveled as far as the pure benzene, but it would have survived longer than 12 years.

There are simple methods of estimating the extent of a free-phase plume by hand calculations. Van Dam (1967) presented one such method. His method produces the diameter of a circular plume with a capillary tongue in which the principles of multiphase flow dictate stabilization of the plume. Using this simple method, the plume was computed to have a diameter of 50 m. The plume simulated by T2VOC had a longitudinal extent of 45 m when the small (5 m) upgradient segment is included (Figure 2). Given the simplicity of the van Dam model, this agreement should be considered good.

There was also a good match between the location of the free-phase plume predicted by T2VOC and field data. The local government excavated soil for which benzene, toluene, ethylbenzene, or xylene were detectable above stringent state standards. During the excavation, measurements were made on the boundaries to determine if further removal was required. That the boundaries of the excavation and the predicted maximum extent of the free-phase plume matched is a further confirmation of the T2VOC modeling effort.

The T2VOC model allows a user much more than an estimate of the free-phase plume extent. It gives an investigator a window into the history of the evolution of the plume as a whole, with all of its phases and components. It also helps one delineate the contribution of the various transport mechanisms, such as soil vapor transport by diffusion and density-driven flow and account for losses to the atmosphere, as well as the motion of free-phase and dissolved-phase plumes. T2VOC allows a user to bring in as much topographic detail as the study warrants (and the CPU-size allows).

Conclusions

The T2VOC model simulated the motion of a gasoline plume in a specific stratigraphic setting. The maximum extent of the free-phase plume predicted by T2VOC matched the location of the excavation and the size predicted by hand calculations using a formula derived from the generalized three-phase flow equations (van Dam, 1967). This match helped establish the model results and its detailed account showing the motion of hydrocarbons in every phase. The T2VOC model demonstrated the limited extent of the motion of the release. This helped vindicate the petroleum company that employed it of responsibility for contamination beyond its property line.

References

American Petroleum Institute (API), 1984, The Land Treatability of Appendix VIII Constituents Present in Petroleum Industry Wastes, API Publication 4379, Washington, DC.

Falta, R. W., K. Pruess, S. Finsterle, and A. Battistelli, 1995, T2VOC User's Guide, Lawrence Berkeley Laboratory, Berkeley, CA, LBL-36400.

Mackay, D. and R. S. Matsugu, 1973, Evaporation Rates of Liquid Hydrocarbon Spills on Land and Water, *Canadian J. Chem. Eng., 51,* 434-439.

Moridis, G. J. and K. Pruess, 1995, T2CG1: A Package of Preconditioned Conjugate Gradient Solvers for the TOUGH2 Family of Codes, LBL Report Number 36235, Lawrence Berkeley Laboratory, Berkeley, CA.

Parker, J. C., R. J. Lenhard, and T. Kuppusamy, 1987, A Parametric Model for Constitutive Properties Governing Multiphase Flow in Porous Media, *Water Res. Res., 23,* (4), 618-624.

Reid, R. C., J. M. Prausnitz, and B. E. Poling, 1987, *The Properties of Gases and Liquids,* McGraw-Hill, New York.

Seginer, I, 1967, Net Losses in Sprinkler Irregation, *Agric. Meteor.*, 4, 281-291.

Sutton, O. G, 1953, *Micrometeorology*, McGraw-Hill Book Company, New York.

van Dam, J, 1967, The Migration of Hydrocarbons in a Water-Bearing Stratum, in *The Joint Problems of the Oil and Water Industries*, ed. Peter Hepple, Institute of Petroleum, London, 55-96.

Table 1. Petrophysical Properties of the Site Soils

Soil Type	Grain Density kg/m^3	Porosity -	Permeability (h) m^2	Permeability (v) m^2	Unsaturated Flow Parameters S_m -	n -	α l/m
Upper Sand	2635	0.399	5.961E-12	6.336E-12	0.013	1.521	101.94
Silt	2660	0.429	1.086E-15	1.678E-13	0.09	1.424	4.1
Lower Sand	2650	0.401	1.697E-12	1.697E-12	0.06	1.84	5.2
Clay	2740	0.395	5.645E-16	5.645E-16	0.36	1.86	3.2

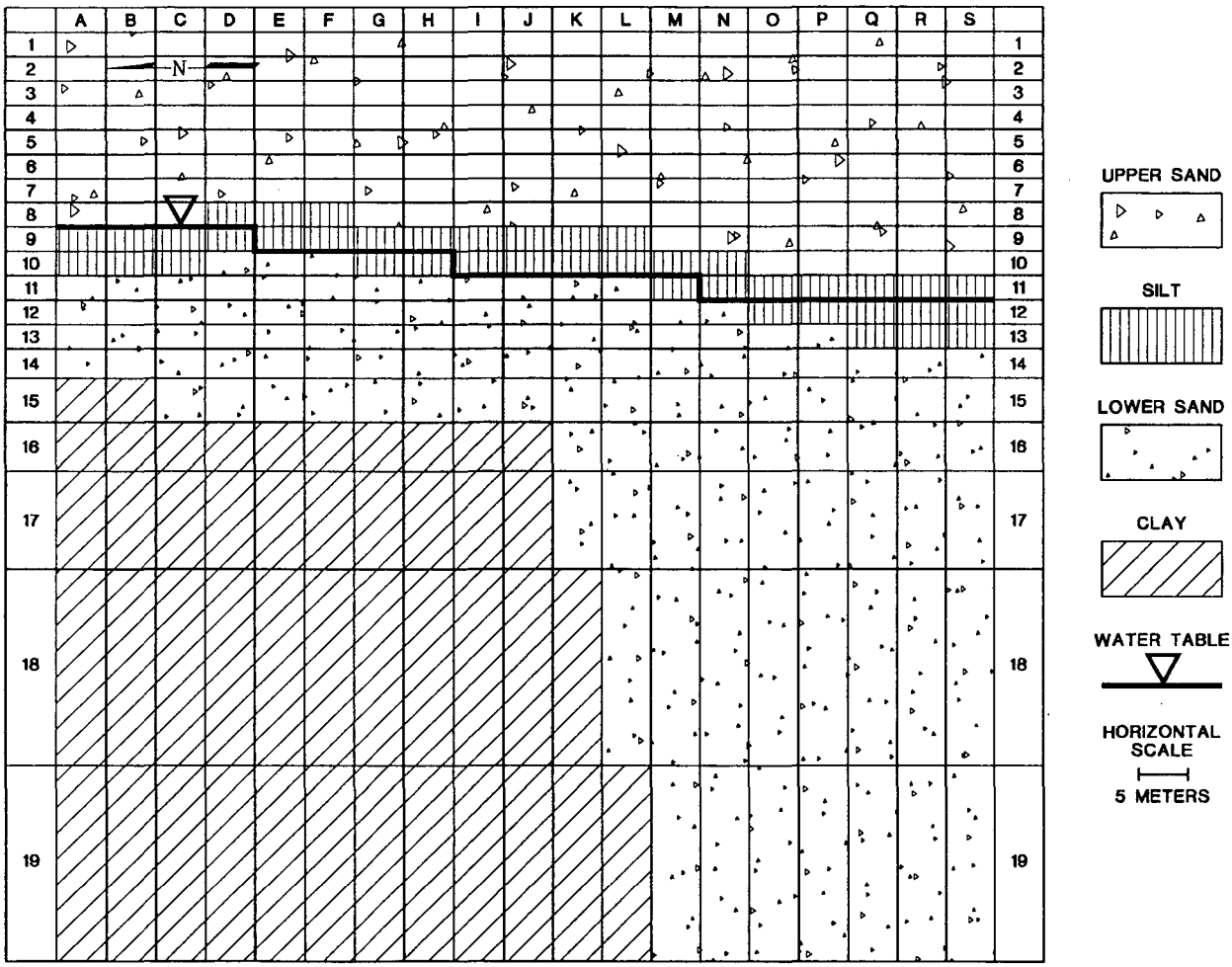

Figure 1. Cross Section of the Three-Dimensional Grid.

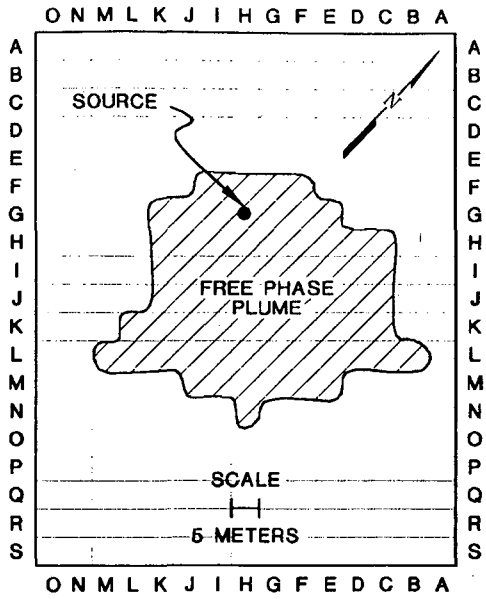

Figure 2. Extent of the Free-Phase Plume at 3 Years.

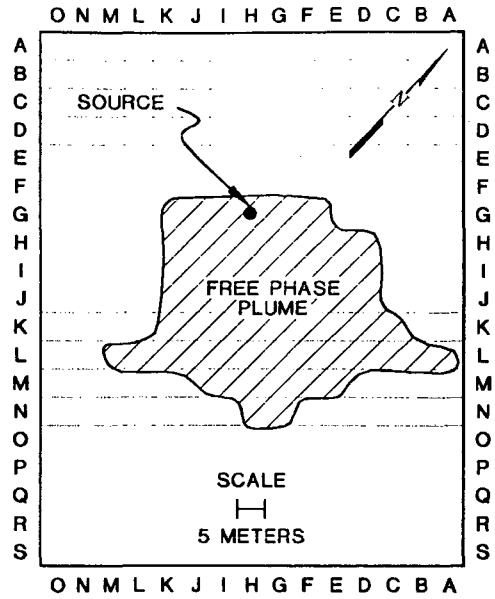

Figure 3. Maximum Extent of the Free-Phase Plume at 5 Years.

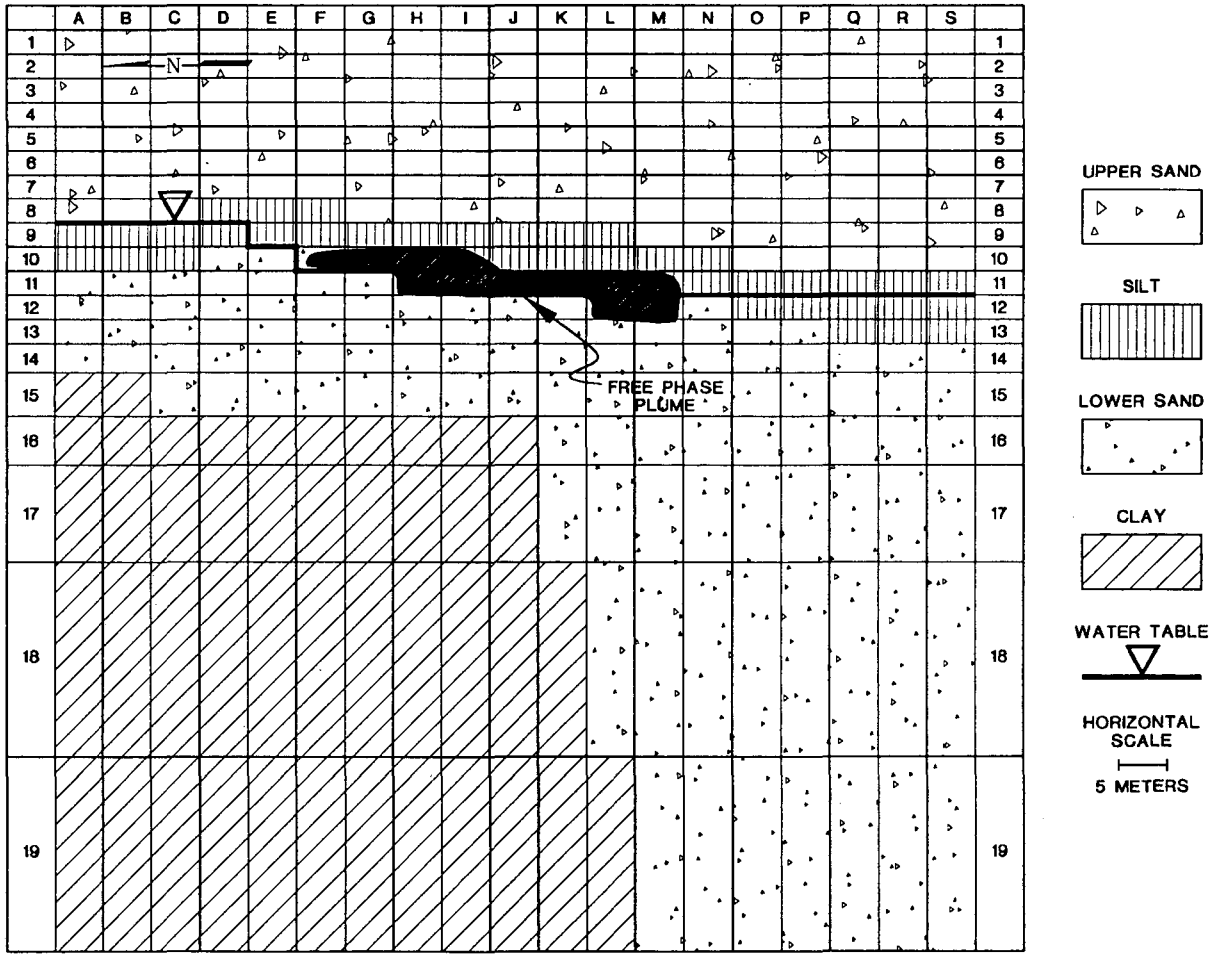

Figure 4. Extent of the Free-Phase Plume at 5 Years, Vertical Cross Section at H.

THREE-DIMENSIONAL SIMULATION OF DNAPL TRANSPORT AT THE SAVANNAH RIVER SITE

HODGES, Rex A.[1], FALTA, Ron W.[1],and FINSTERLE, S.[2]

ABSTRACT

The M Area of the Savannah River Site was used for processing materials for nuclear production reactors. From 1958 through 1985, process effluent was sent to the M Area Settling Basin through a process sewer line. Because of disposal to the unlined settling basin, approximately 2.0 million pounds of chlorinated solvents were released to the subsurface in M Area. Results from ongoing groundwater and soil clean up programs indicate that relatively large amounts of DNAPL are present in the subsurface. Detailed studies have shown that a substantial fraction of the DNAPL at M Area is trapped above the water table in clays and silts and that DNAPL is present below the water table in isolated pockets and ganglia. As a DNAPL invades the saturated zone, it accumulates in coarser sediments overlying finer grained sediments such as clays. As DNAPL accumulates on top of clay layers below the water table, it can continue to flow down-dip, towards local topographic lows in the clay surface.

The geologic and hydrogeologic data were used in conjunction with generated geostatistical parameters for three lithologic units at M Area to develop a conditional model of hydrogeologic parameter distribution. This information, along with historical contaminant release profiles, was used as model input for the numerical flow simulator. The results from the initial simulations indicate that the modeling under-predicts the extent of free-phase DNAPL in comparison to what has been found in the subsurface. This is believed to be the result of element size with respect to the amount of DNAPL released. The smallest element area for the initial simulations was 100 by 100 feet. Simulations are ongoing with elements as small as 20 by 20 feet and this should improve the resolution.

1.0 INTRODUCTION

M Area was used in the past for processing uranium, lithium and other materials into fuel elements and targets for nuclear production reactors. These processes involved metallurgical and mechanical operations, and as a part of these operations, solvent cleaning and acid/caustic etching were used to prepare materials. During a period beginning in 1958, and ending in 1985, process effluent was sent to the M Area Settling Basin through a process sewer line. Because the effluent contained large amounts of chlorinated solvents, contamination of soils and groundwater occurred in this area as a result of breaks in the old process sewer line, and disposal to an unlined settling basin. It is estimated that approximately 2.0 million pounds of chlorinated solvents, mainly tetrachloroethylene (PCE) and trichloroethylene (TCE) were released.

The settling basin covers a small area of about 75,000 ft^2 (300' by 250') allowing the DNAPL emplacement to be modeled as a point source. Leaks in the process sewer line that was used to transport DNAPL to the settling basin will in actuality spread the source. The DNAPL will migrate downward through permeable zones until it accumulates on an impermeable layer, where it will then move down-dip along the surface. However, the dissolved plume is affected by ground-water movement and is carried down the hydraulic gradient with the water flow. Current maps of dissolved contaminant plumes, the subsurface structure of the "green clay" confining unit (Looney

[1] Geological Sciences Department, Brackett Hall, Box 341908, Clemson University, Clemson, SC 29634-1908. [2] Earth Sciences Division, Lawrence Berkeley Laboratories, Berkeley, CA, 94720.

et al., 1992), and the water table were considered when deciding on the model boundaries (Figure 1). The dissolved plume maps indicate a west/southwesterly (SRS coordinates) migration direction, consistent with the ground-water gradient in the area. The subsurface structure of the "green clay" confining unit generally dips to the west in the model area. Based on this information, the model is positioned to center the settling basin in the eastern half of the model grid, placing the settling basin in an up-gradient and up-dip location. The model extends to the west to fully encompass the down-gradient 1 ppm contour of the dissolved TCE plume (Figure 1).

1.1 Site Geology and Hydrogeology

SRS is situated over Coastal Plain sediments comprised of interbedded sands and clays. The sediments are almost flat-lying with a gentle regional dip of about 25'/mile to the southeast, though locally dip directions are variable. The first relatively continuous confining zone at M Area is the "green clay" whose thickness ranges from 2 to 20 feet, thinning to the northeast. It underlies the water table aquifer ("M Area" Aquifer Zone) and overlies the "Lost Lake" Aquifer Zone. The vadose zone is relatively thick, ranging from 75' to 135' across the model area (about 120' at the settling basin). The thick vadose zone limits the downward migration of contaminants and captures some of the DNAPL in the clays above the water table. Only in areas where large quantities of DNAPL were disposed, such as the settling basin, has DNAPL been found as a separate phase below the water table.

2.0 MODELING METHOD

2.1 Mesh Development and Generation of Geostatistical Permeability Field

Formerly, the 3D Cartesian grid generated by T2VOC was restricted to orthogonal x, y, and z dimensions. This is limiting in an area where the primary surface (the "green clay") on which DNAPL accumulates and migrates is deformed. To perform simulations that adequately model contaminant migration in the heterogeneous subsurface, a fine mesh is required for the green clay and for several feet above the clay. To address this shortcoming, a vertically conformable mesh generator (STRAT) was developed by Stefan Finsterle while at Clemson in the spring of 1996. Using an input file with lines consisting of surface x and y coordinates along with elevations of lithologic units, STRAT generates a mesh that conforms to the topography of each lithologic unit. Each unit can be further subdivided into equal parts allowing for a fine vertical grid.

Prior to generating the vertical component of the model grid, lithologic units must be identified and assigned a ROCK type. At M Area, three distinct vertical units were identified. The shallow-most extends from the land surface to the top of the "green clay" and is referred to as the M Area aquifer zone (MAZ). It includes both the vadose and unconfined saturated zones. The middle unit is the low permeability "green clay" confining zone (GCCZ). The lower most unit incorporated in the model is the Lost Lake aquifer zone (LLAZ).

A "fine" grid (surface elements of 100 ft by 100 ft) was designed in the vicinity of the settling basin. The x and y element dimensions were gradually increased to 500 ft by 500 ft at the model boundaries. The total number of surface elements is 780 (30 in the x direction by 26 in the y direction). The upper portion of the MAZ was divided into twelve layers with an average thickness of 12 feet. The lower 10 feet of the MAZ, where DNAPL is expected to accumulate, was divided into 5 layers, each 2 feet thick. The GCCZ was divided into 5 layers that averaged 1 feet thick. The LLAZ was divided into 5 layers that averaged nearly 14 feet in thickness. The final number of elements in the model mesh is 21,840 (28 divisions in the z-direction).

Figure 1. Cross section across the model area. The vertical extent of the model is from the surface to the "Upper Clay" Confining Zone.

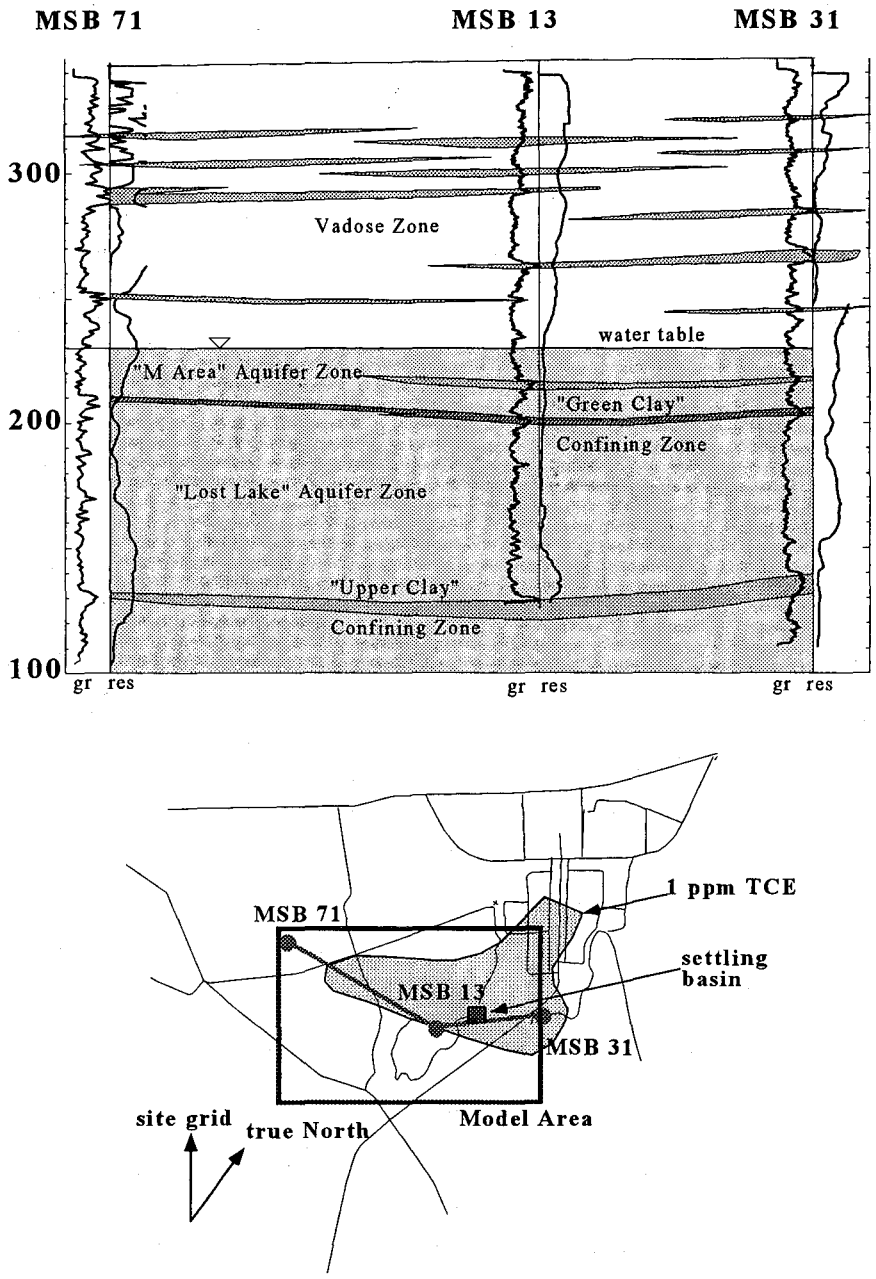

A heterogeneous permeability field is geostatistically generated for each lithologic unit. The program used was SIMAN3D, developed by Stefan Finsterle, and is based on the simulated annealing method. Within a given set of parameters, SIMAN3D will generate a spatially correlated random field based on a specified variogram. Key parameters include correlation length (x, y, and z directions), standard deviation, and a three-dimensional array of locations equivalent to the portion of the overall model mesh intended for the lithologic unit. The output file from SIMAN3D contains a permeability modifier that is added to each element in the ELEME block of

the input file. The average permeability for the lithologic unit (x, y, and z directions) is specified in the ROCKS block of the T2VOC input file and can be changed without regenerating the geostatistical field. If measured permeability data at locations in the model area are available, the data can be used to condition the location of lower and higher permeability zones within the generated field.

The permeability distribution for the initial simulations at M Area was generated "randomly" using the average statistics of each rock unit to control the spatial correlation within the unit. This resulted in a permeability distribution similar to M Area, high and low permeability bodies approximately the same size, but randomly situated within each rock type. Average horizontal and vertical permeabilities used were 1 and 0.1 darcys for the MAZ, 0.0005 and 0.00001 darcys for the GCCZ, and 10 and 1 darcys for the LLAZ.

Figure 2. Heterogeneous permeability field used for modeling.

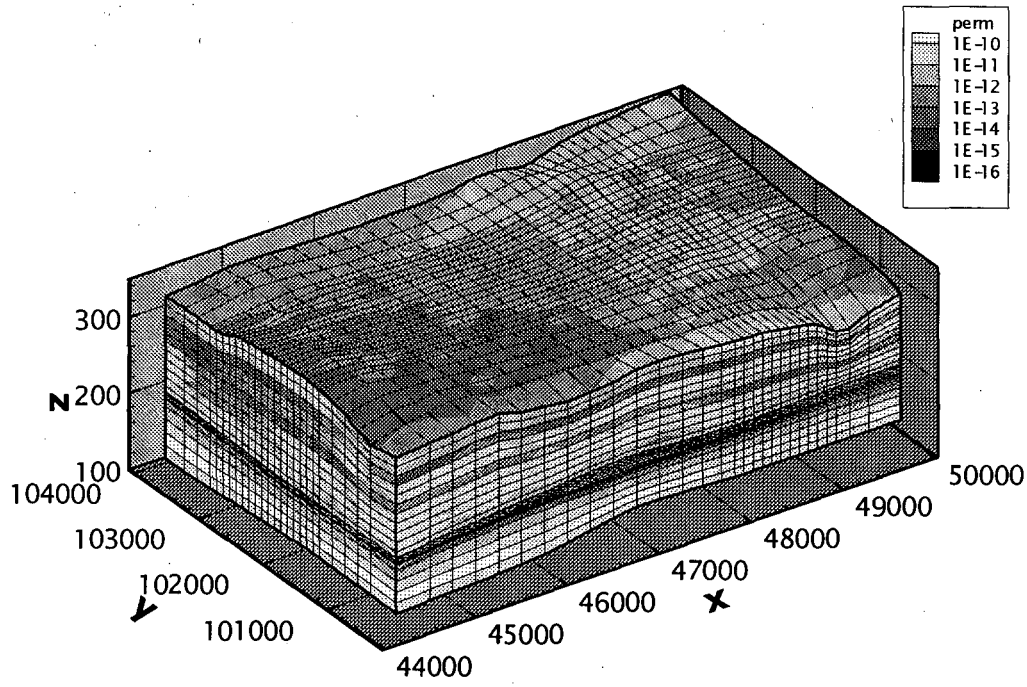

2.2 Multiphase Flow Simulations

Once a T2VOC mesh file has been designed and assigned permeability modifiers, a set of initial conditions for each element is generated under gravity-capillary equilibrium conditions. All elements are filled with water (assigned a gas saturation (Sg) of 0.0) and allowed to drain in a two-phase simulation until equilibrium is achieved. An infiltration rate of 6"/year (Aadland, 1995) was included in the simulations at M Area.

Waste effluent was sent to the settling basin over a period of about 27 years, from 1958 to 1985. From 1958 to 1971 trichloroethene (TCE) was the primary cleaning solvent. In 1971 tetrachloroethene (PCE) was substituted for TCE and there was a marked increase of waste solvent

sent to the settling basin. The quantity of effluent sent to the settling basin sharply declined in 1977. Based on the actual yearly estimated release history, the simulated spill began with a rate of 25,000 pounds per year and continued for 12 years. The rate was increased to 100,000 pounds per year for 5 years. The last spill rate was 300,000 pounds per year for 4 years, after which no more DNAPL was released. After 21 years of simulated DNAPL release (2.0 million pounds), from 1958 to 1979, and an additional 15 years for redistribution, the NAPL phase was limited in extent, and did not reach the water table.

As DNAPL migrates through a thick vadose zone, significant amounts will remain as residual NAPL saturation (Snr). A normal average Snr is about 10%, depending on the relative permeability and capillary pressure of the sediments. However, since DNAPL forms preferential pathways, a 10% Snr for elements the size of the model mesh (the smallest are 100 by 100 by 12 feet) is unrealistic. Therefore, the Snr was set at 1% (possibly still too high without a much finer mesh) in the ROCKS block of the T2VOC input file. Also, the release point for DNAPL was only one 100' by 100' grid block while the settling basin is roughly 300 by 250 feet. The aquifers (MAZ and LLAZ) were given a porosity of 30% and the GCCZ was given a porosity of 40% for all simulations. A finer mesh will be needed to simulate detailed NAPL migration and special numerical techniques may be required as well. Reducing the Snr in consideration of the mesh element size is considered to be a temporary "fix" and reflects the fact that handling sub-grid block scale physics need to be addressed in future research. No conditioning points were used to preferentially locate high and low permeability zones. Therefore, the model results are only a generality, though lithologic unit elevations, spill rates, average unit permeabilities, and the static ground-water flow field were matched as closely as possible.

Modifications were made to the T2VOC code to improve the modeling of heterogeneous media. Previously, T2VOC used a single three phase capillary pressure (Pcap) function for each ROCK type with no adjustments for a heterogeneous permeability field. The Pcap for each element in a rock unit is now varied from the average Pcap function of that rock unit by the square root of the ratio of the average unit permeability to the cell permeability (avg k / cell k)$^{1/2}$ providing more realistic simulations for heterogeneous media. T2VOC was also modified to write key parameters (such as pressure, NAPL saturation, concentration of NAPL in the aqueous phase) for each element to files formatted for graphical display (using the commercially available program, TECPLOT) at user specified times during a simulation and at the end of the simulation.

3.0 MODELING RESULTS

We believe that the initial model greatly under-predicts both the lateral and vertical extents of the DNAPL distribution in the M-Area. An interesting aspect of the simulation is the size of the dissolved DNAPL plume above and below the water table. The simulation suggests that high concentrations in the dissolved plume can travel relatively far from the NAPL phase by these mechanisms. Figure 3 shows the plume in 1994 (these plots have a cutoff of 1 ppm). A top view of the PCE plume for 1994 is qualitatively similar to the mapped TCE plume shown in Figure 3.

Figure 3. Simulated dissolved contaminant plume in 1994, 1 ppm cut off, cut away view [log g/l].

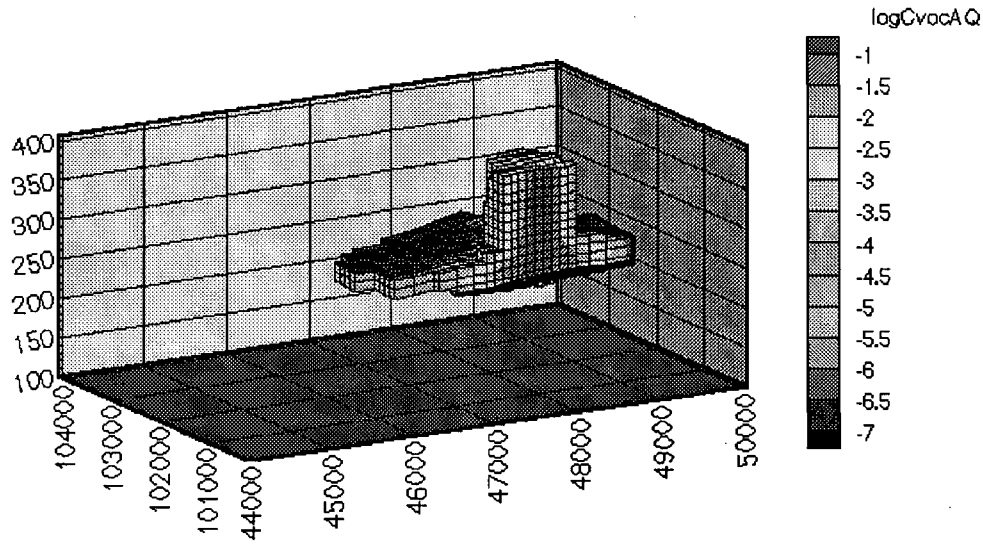

3.1 Ongoing Models

To begin addressing the problem of residual NAPL saturation in relatively large elements, the model volume has been re-gridded to create a finer mesh. The number of elements was increased from 780 (30 x 26) to 980 (35 x 28) per layer. The number of vertical layers was also increased, from 28 to 32. This increased the number of total elements from 21,840 to 31,360. The elements beneath the settling basin are 20 by 20 by 8, significantly smaller than the original 100 by 100 by 14 elements.

In order to more closely match the geology, the M Area Aquifer Zone is being subdivided into four lithologic units (MAZ1 through MAZ4). Additionally, 721 conditioning points are being used to condition the permeability distribution to be more representative of the true distribution at M Area. Estimated mud fractions from foot by foot core descriptions were converted to conductivities based on a function from Hydrogeologic Inc (1996). Of the 721 conditioning points, 130 are in the MAZ1, 123 in the MAZ2, 103 in the MAZ3, 184 in the MAZ4, 88 in the GCCZ, and 93 in the LLAZ.

5.0 REFERENCES

Aadland, R.K., Gellici, J.A.,and Thayer, P.A. (1995). *Hydrogeologic Framework of West-Central South Carolina* (Vol. 5): State of South Carolina Department of Water Resources.

Looney, B.B. and Moore-Shedrow, D.B. (1992). *Assessing DNAPL Contamination in A/M Area , SRS: Phase 1 Results* (Westinghouse Savannah River Company-RP-92-1302). Savannah River Technology Center - Environmental Sciences Section.

Hydrogeologic Inc., (1996). *Development of a Fully Three Dimensional Flow Model for the A/M Area Using data Fusion*, Westinghouse Savannah River Company Report # WSRC-OS-97-00002.

EOS9nT: A TOUGH2 Module for the Simulation of Flow and Solute/Colloid Transport

G.J. Moridis, Y.S. Wu and K. Pruess

Earth Sciences Division, Lawrence Berkeley National Laboratory
University of California, Berkeley, CA 94720

Abstract

EOS9nT is a new TOUGH2 module for the simulation of flow and transport of an arbitrary number *n* of tracers (solutes and/or colloids) in the subsurface. The module first solves the flow-related equations, which are comprised of (a) the Richards equation and, depending on conditions, may also include (b) the flow equation of a dense brine or aqueous suspension and/or (c) the heat equation. A second set of transport equations, corresponding to the *n* tracers, are then solved sequentially. The low concentrations of the *n* tracers are considered to have no effect on the liquid phase, thus making possible the decoupling of their equations. The first set of equations in EOS9nT provides the flow regime and account for fluid density variations due to thermal and/or solute concentration effects. The *n* tracer transport equations account for sorption, radioactive decay, advection, hydrodynamic dispersion, molecular diffusion, as well as filtration (for colloids only). EOS9nT can handle gridblocks of irregular geometry in three-dimensional domains. Preliminary results from four 1-D verification problems show an excellent agreement between the numerical predictions and the known analytical solutions.

1. Introduction

EOS9nT is a module for the TOUGH2 general-purpose fluid and heat flow simulator [*Pruess*, 1991]. It is designed to simulate the flow of fluids and the transport of an arbitrary number *n* of independent tracers (solutes and/or colloids, SCs) in complex subsurface systems involving porous and/or fractured media. EOS9nT can simulate the following scenarios:

(F1) Isothermal flow of the aqueous phase, and SC transport at concentrations too low to have any measurable effect on the water density and the flow regime.
(F2) Isothermal flow of the aqueous phase, and SC transport at concentrations sufficiently high to affect the water density and the flow regime.
(F3) Non-isothermal flow of water, and SC transport at tracer levels (i.e., at low concentrations).
(F4) Fully-coupled non-isothermal flow of water under variable density conditions, and SC transport.

2. Design, Approach and Capabilities

2.1. Modeled Processes

EOS9nT allows the modeling of the following processes:

(1) Flow of the liquid phase under saturated and/or unsaturated conditions and with variable fluid density (due to concentration, thermal and pressure effects)
(2) Transport of *n* SCs, which accounts for advection, molecular diffusion, hydrodynamic dispersion, sorption (linear, Langmuir and Freundlich), radioactive decay, and filtration (for colloids only).
(3) Heat transport, which includes advective and diffusive effects.

2.2. Assumptions and Governing Equations

Under the F1 flow regime, EOS9nT solves a single equation, the *Richards* [1931] equation, which describes the flow of water in the subsurface under saturated or unsaturated conditions. The flow of the gaseous phase is not considered. The assumptions for the F1 regime include:

(A1) The water flow is isothermal.
(A2) The concentration of the SCs is at a tracer level, i.e., too low to have any measurable effect on the flow regime.
(A3) The pressure of the gaseous phase does not deviate significantly from the reference pressure of the system.
(A4) There is no phase change.
(A5) No chemical reactions occur between the rock and the tracers, or among the tracers.

(A6) In colloid transport, the porosity and permeability of the medium are unaffected by the colloid filtration.

These assumptions allow decoupling of the flow and transport equations. The Richards equation is first solved, followed by the sequential solution of the n independent tracer transport equations.

The F2 regime differs from F1 in that assumption (A2) no longer holds true. This necessitates the solution of a SC transport equation in addition to the Richards equation, for a total of 2 coupled equations. The SC equation corresponds to the dominant species (e.g., the heavy brines, but not the accompanying radioactive tracers, in the wastes leaking from the Hanford tanks) which controls the water density dependence, and accounts for all the aforementioned phenomena. In the F3 regime, assumptions (A2) through (A6) apply, and the heat transport equation must be solved coupled with the Richards equation.

The F4 regime represents the most general scenario tractable by EOS9nT, in which the valid assumptions are (A3) through (A6). F3 necessitates the solution of 3 coupled equations, i.e., (a) the Richards equation, (b) the transport equation of the dominant species, and (c) the heat transport equation. Following the solution of the coupled equations in F2, F3 or F4, the n independent tracer transport equations are solved sequentially.

EOS9nT cannot be used for the simulation of systems in which the gas pressure is substantial, phase changes (i.e., evaporation and condensation) occur, and/or the tracer is gaseous or volatile. Such problems are tractable by the companion module EOS3nT (currently in development) which can handle gas and liquid flows in addition to all the EOS9nT capabilities.

2.3. The Time-Stepping Process

Under transient flow conditions, the time-stepping process in EOS9nT is shown in **Figure 1**, in which Δt_f is the time step in the flow equation (or the coupled equations) and $\Delta t_{t,i}$ is the time step in the transport equation of tracer i. A total of $n+1$ separate simulation times are independently tracked.

After the flow solution at $t+\Delta t_f$ is obtained, the water saturations, flow velocities and flow rates across the element interfaces are recorded. The time is then reset to t_0 in the transport equation of tracer i, and the maximum allowable $\Delta t_{t,i}$ is determined from limitations on (a) the grid Courant number, (b) the grid Peclet number, and (c) the tracer half life. The tracer transport in the Δt_f interval is simulated using a total of $m_i=\Delta t_f/\Delta t_{t,i}$ (i.e., the next largest integer of the ratio) equal time steps. The process is repeated for all n independently-tracked tracers. The time step sizes of the various tracers are not generally equal.

As the flow field becomes invariant, the size of the Δt_f in TOUGH2 increases, and convergence is achieved after a single Newtonian iteration. Contrary to the standard TOUGH2, which prints the invariant solution and stops the simulation after 10 such time steps of convergence on the first iteration, involves, EOS9nT prints the flow solution and continues solving the tracer equations. The time step in the solute transport equations becomes uniform and equal to the shortest of the $\Delta t_{t,i}$ after the flow has reached a steady state.

EOS9nT also allows solute transport simulations when the initial flow field is time-invariant. In this case, EOS9nT solves the flow field only once in order to obtain the constant water saturations, flow velocities and flow rates across the element interfaces. After printing the flow data, only the tracer transport equations are solved.

Time-step control in the flow equation (or the coupled equations) is provided internally by the Newtonian convergence criteria employed in TOUGH2 [*Pruess*, 1991]. The time-step size in the n transport equations is specific to each tracer, and is controlled by inputs which place limitations on the grid: (a) Peclet number, (b) Courant number and (c) the maximum allowable fraction of the SC half-life $T_{1/2}$ (if radioactive) for limiting the $\Delta t_{t,i}$.

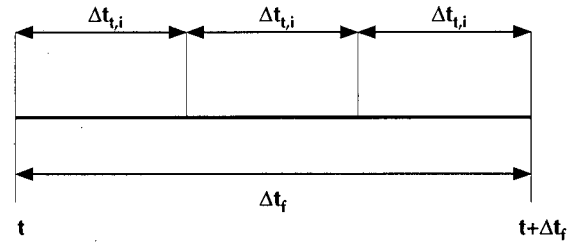

Figure 1. The time steps for flow and transport in EOS9nT.

2.4. Treatment of the Dispersion Tensor

In the treatment of the general 3-D dispersion tensor, EOS9nT follows closely the approach of the radionuclide transport module T2R3D [*Wu et al.,* 1996] for TOUGH2. Velocities are averaged by using the *'projected area weighting method'*, in which a velocity component $v_{n,i}$ $(i=x,y,z)$ of the vector v_n is determined by vectorial summation of the components of all local connection vectors in the same direction, weighted by the projected area in that direction. Mass fraction gradients of the n SCs are evaluated using *the 'interface area weighting scheme'* [*Wu et al.,* 1996].

This approach allows the solution of the transport problem in irregular grids. EOS9nT provides an option for the removal of numerical dispersion by using the corrections proposed by *Lantz* [1971. These involve an adjustment of the dispersion coefficient, which for 1-D problems is

$$D_C = D - \frac{1}{2}U\Delta x - \frac{1}{2}\frac{U^2\Delta t}{\phi},$$

where D_C and D are the corrected and the original dispersion coefficients, respectively, U is the Darcy velocity, ϕ is the medium porosity, and Δx is the grid size.

2.5. Treatment of Colloidal Filtration

Colloidal particles moving through porous media are subject to filtration, the mechanisms of which have been the subject of several investigations, e.g., *Herzig et al.*, 1970; *Wnek et al.*, 1975; *Tien et al.*, 1979; *Corapcioglu et al.*, 1987. EOS9nT assumes conditions of *'deep filtration'*, i.e., no interaction between the colloidal particles and no effects on porosity and permeability. Under these conditions, the variation in the concentration of the retained colloids is described by the equation [*Herzig et al.*, 1970; *Dieulin*, 1982]

$$\frac{\partial\sigma}{\partial t} = \lambda UX,$$

where σ is the concentration of the retained colloid, λ is the filter coefficient, and X is the colloid mass fraction in the liquid. The linearity of the colloid equation allows its combination with the colloid transport equations. If no experimental values are available, EOS9nT computes an estimate of the parameter λ as a function of the particle and grain sizes, using the relationships of *Tien et al.* [1979].

2.6. Other Capabilities of EOS9nT

EOS9nT can simulate the transport of any combination of solutes and colloids. As with all other members of the TOUGH2 family of codes [*Pruess*, 1995], EOS9nT can handle multi-dimensional flow domains and cartesian, cylindrical or irregular grids. Initialization is possible using (a) pressure, (b) water saturation or (c) capillary pressure, and EOS9nT has the capability of determining the initial pressure and/or water saturation distribution (gravity-capillary equilibrium) in relation to an initial, areally variable, watertable elevation map.

Heterogeneity is described through the use of domain permeability modifiers, which can be externally supplied or internally generated using linear or logarithmic modifications based on random numbers. Scaling of the capillary pressures is then obtained by using the *Leverett* [1941] function.

Parameters for linear, Langmuir and Freundlich sorption isotherms are provided for all the combinations of rock/soil types and SCs.

3. Verification of EOS9nT

Four sets of simulations were conducted to verify EOS9nT against known analytical solutions of flow and solute transport. The first three test problems involved saturated regimes and invariant flow fields. The fourth test problem involved unsaturated flow and transport. The maximum allowable Peclet and Courant numbers were 2 and 1 respectively, and, when radioactive SCs were involved, the $\Delta t_{t,i}$ was not allowed to exceed $0.05T_{1/2}$. In all the verification problems, numerical dispersion was removed by using the *Lantz* [1971] corrections. It must be pointed out that the four test problems do not cover the whole range of the EOS9nT capabilities, and only reflect to-date results of a continuing effort.

3.1. Test Problem 1

This test problem involves the distribution of five independent solutes being transported at a constant pore velocity V = 0.1 m/day in a semi-infinite horizontal column of a medium with a dispersion coefficient D = 0.1 m^2/day. The solutes do not decay (λ = 0). The retardation factors R

$$R = 1 + \frac{1-\phi}{\phi S_w}\rho_R K_d$$

of the five tracers in the porous medium were 1, 2, 3, 4 and 5. In this equation ϕ = 0.3, S_w is the water saturation (=1), ρ_R is the rock

density, and K_d is the distribution coefficient. A uniform grid size of Δx = 1 m was used.

Figure 2 shows a comparison between the numerical predictions (symbols) and the analytical solutions [*Bear*, 1979] at t = 400 days. An excellent agreement between the two sets of solutions is observed.

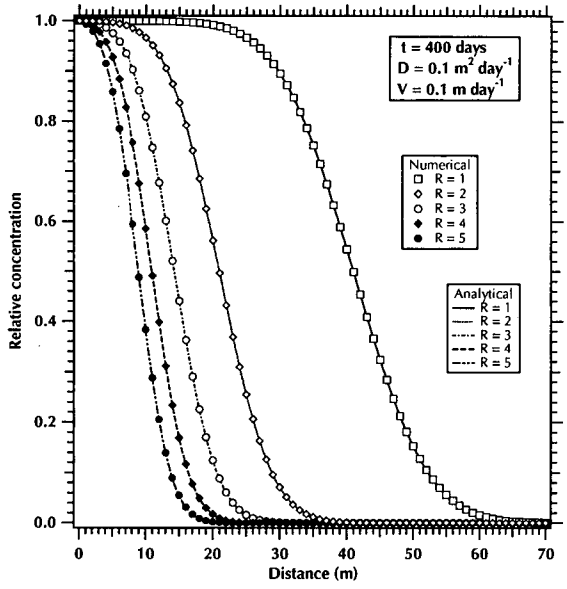

Figure 2. Analytical and numerical solutions of the concentration distribution of 5 non-radioactive tracers of variable R in a semi-infinite column (Test problem 1).

3.2. Test Problem 2

The second test problem involved the transport of three radionuclides in a saturated semi-infinite horizontal column. Water flowed at a constant V = 0.2 m/day, and the dispersion coefficient D = 0.05 m^2/day. The first radionuclide had a R = 1 and a $T_{1/2}$ = 69.32 days. The second radionuclide differed from the first in that R = 2. The third radionuclide had a R = 1.5 and a $T_{1/2}$ = 693.2 days. The porosity and discretization were the same as in Test Problem 1.

Figure 3 shows a comparison between the numerical predictions (symbols) and the analytical solutions of [*Bear*, 1979] at t = 200 days. The two sets of solutions are practically identical.

3.3. Test Problem 3

The third test problem involved the transport of three non-sorbing, non-radioactive colloids in a saturated semi-infinite horizontal column. Water flowed at a constant Darcy velocity of U = 2 m/day, D = 1 m^2/day, and ϕ = 0.3. The filter coefficient λ of the three colloids were 30 m^{-1}, 100 m^{-1}, and 3000 m^{-1}. A uniform grid size of Δx = 0.01 m was used. At t = 7600 s, the analytical and numerical solutions in **Figure 4** practically coincide.

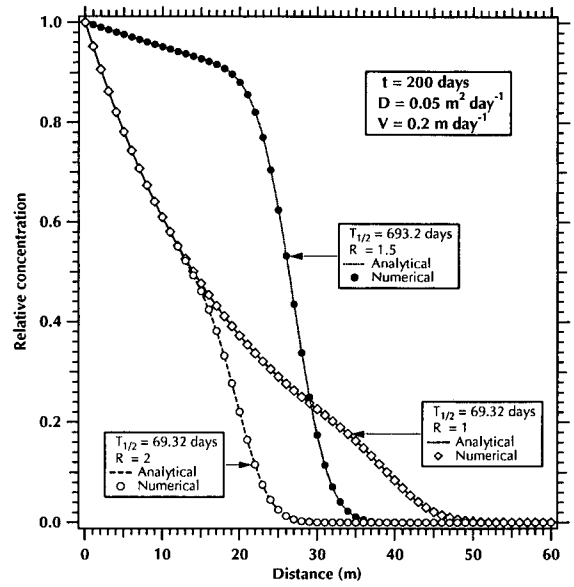

Figure 3. Analytical and numerical solutions to the problem of transport of three radioactive tracers flowing in a semi-infinite column (Test problem 2).

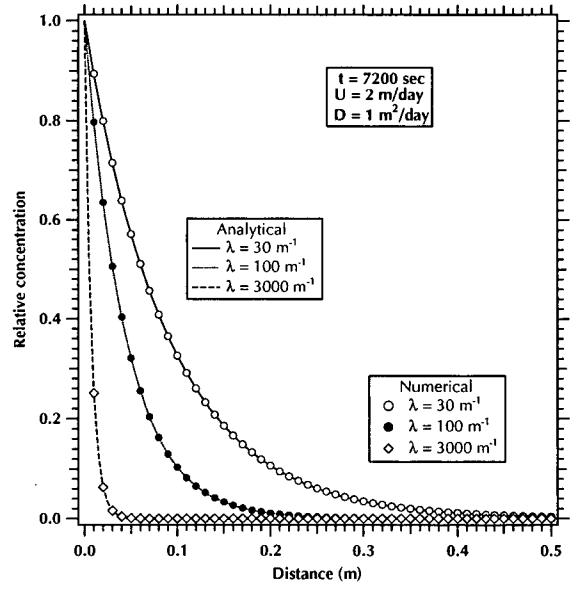

Figure 4. Analytical and numerical predictions of the concentrations of three non-sorbing, non-radioactive colloids (Test problem 3).

3.4. Test Problem 4

Test problem 4 was the horizontal infiltration problem originally solved by *Philip* [1955]. The problem was described by *Ross et al.* [1982], and was featured as Sample Problem No. 2 in the TOUGH User's Guide [*Pruess,* 1987]. A semi-infinite horizontal tube filled with a homogeneous soil is partially saturated with water. The soil porosity is $\phi = 0.45$, and the initial moisture content is $\theta = 0.2$, corresponding to a liquid saturation of $S_w = \theta/\phi = 0.44$. The liquid saturation at the $x=0$ boundary is held constant at $S_w = 1$ for $t>0$. Due to a capillary pressure differential, water infiltrates into the horizontal system. Air is considered a passive phase, and its effects are neglected.

The problem was augmented by adding two tracers to the water at the $x=0$ boundary. The mass fraction of the first and second tracers were 10^{-3} and 10^{-4}, respectively. The first tracer was non-decaying, and had a $R = 2$. The second tracer was non-sorbing ($R = 1$) and had a $T_{1/2} = 1$ day.

TOUGH2 predictions using the EOS9nT module were obtained for $t = 0.01$ day, $t = 0.06$ days, and $t = 0.11$ days, at which *Ross et al.* [1982] specify exact solutions. A uniform grid size of $\Delta x = 0.002$ m was used.

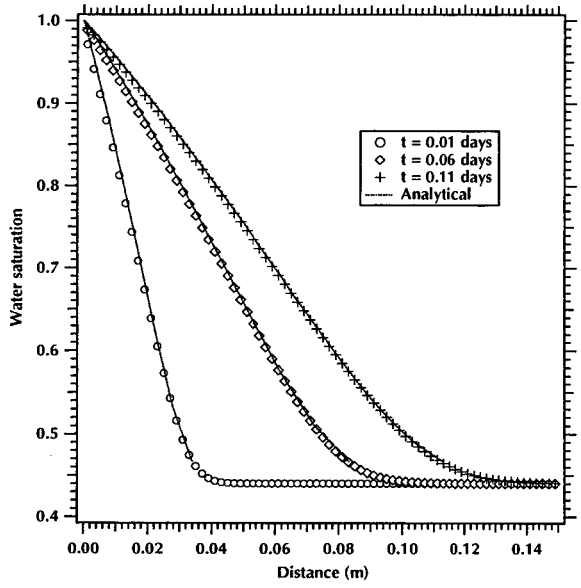

Figure 5. Analytical and numerical solutions of the water saturation distribution in Test problem 4.

In **Figure 5** we compare the numerical and analytical solutions [*Philip,* 1955] of saturation at the three observation times. The two sets of solutions are in excellent agreement. **Figures 6** and **7** show the EOS9nT solution of the concentration distributions of the two tracers at the same times. These solutions are practically identical with the ones obtained using TOUGH2 with the EOS7R module [*Oldenburg and Pruess,* 1995].

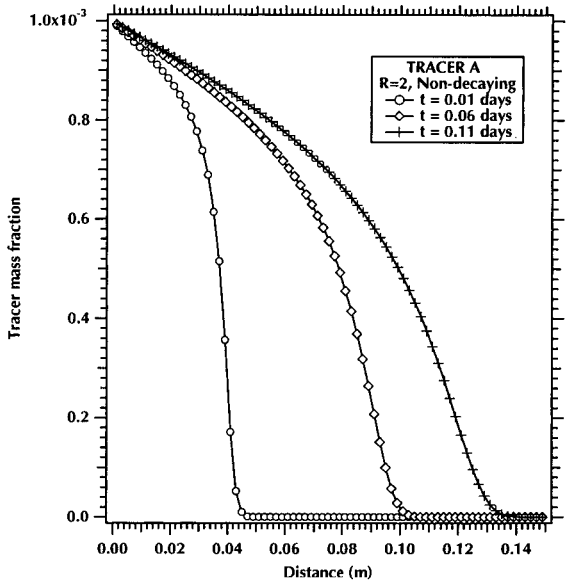

Figure 6. Numerically predicted concentration of a sorbing non-decaying tracer in Test problem 4.

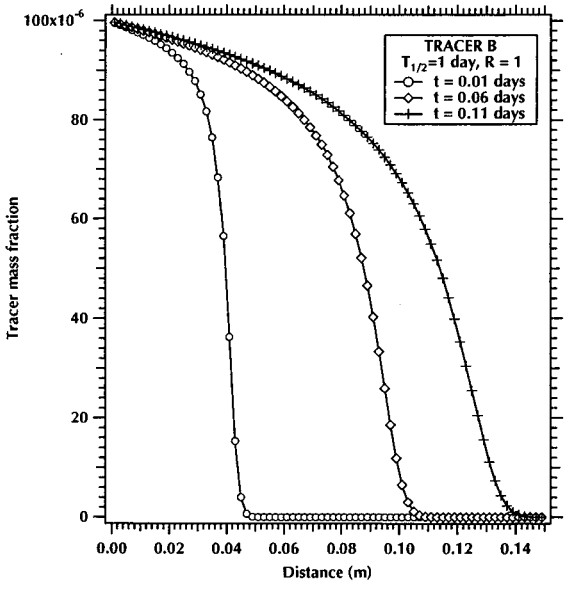

Figure 7. Numerically predicted concentration of a non-sorbing radioactive tracer in Test problem 4.

4. Conclusions

We evaluated the performance of the EOS9nT module for the TOUGH2 general-purpose fluid and heat flow simulator [*Pruess*, 1991] using a set of four 1-D test problems of flow and transport of solutes and colloids. The first three test problems, which involved SC transport in fully saturated media under steady-state flow conditions, have known analytical solutions. The fourth test problem, which involved flow and SC transport in an unsaturated medium, has a known analytical solution of saturation distribution, but no analytical solution of the SC concentration.

Comparison between the analytical solutions and the EOS9nT/TOUGH2 numerical predictions of the SC concentration distribution in the first three test problems showed that the two practically coincided. An excellent agreement was observed between the analytical and numerical solutions of saturation in the fourth test problem. In the same problem, the numerical results coincided with the numerical results obtained when using TOUGH2 with the EOS7R module [*Oldenburg and Pruess*, 1995], another module of flow and transport.

It must be clearly indicated that the evaluation results in this paper represent the (F1) flow regime only, are limited to comparisons with known solutions in 1-D systems, and do not correspond to the full range of capabilities of EOS9nT, as its evaluation is still in progress. A more thorough evaluation, including flow and transport problems in complex 2- and 3-D heterogeneous domains with variable liquid density (i.e., the (F2) and (F3) flow regimes), will be presented in a forthcoming report.

5. Acknowledgements

This work was supported by the Director, Office of Civilian Radioactive Waste Management, U.S. Department of Energy, through Memorandum Purchase Order EA9013MC5X between TRW Environmental Safety Systems, Inc., and the Ernest Orlando Lawrence Berkeley National Laboratory, under Contract No. DE-AC03-76SF00098. Drs. C. Oldenburg and S. Finsterle are thanked for their insightful review comments.

6. References

Bear, J., Hydraulics of Groundwater, McGraw-Hill, New York, 1979.

Corapcioglu, M.Y., N.M. Abboud and A. Haridas, Governing equations for particle transport in porous media, In: J. Bear and M.Y. Corapcioglu (eds.), *Advances in Transport Phenomena in Porous Media*, Series E: Applied Sciences Series No. 128, Martinus Nijhoff, Dordrecht, The Netherlands, 1987.

Dieulin, J., Filtration de colloides d' actinides par une colonne de sable argileux, *Report LHM/RD/82/83*, Paris School of Mines, Fontainebleau, 1982.

Herzig, J.P., D.M. Leclerc, and P. Le Goff, Flow of suspension through porous media, *Ind. Eng. Chem.* **62**(5), 129-157, 1970.

Lantz, R.B, Quantitative evaluation of numerical diffusion (truncation error), *Soc. Pet. Eng. J.*, **11**, 315-320, 1971.

Leverett, M.C., Capillary behavior in porous media, *Trans. AIME*, **141**, 341-358, 1941.

Oldenburg, C.M. and K. Pruess, EOS7R: Radionuclide transport for TOUGH2, *Rep. LBNL-34868*, Lawrence Berkeley Laboratory, Berkeley, CA, 1995.

Pruess, K, TOUGH User's Guide, *Rep. LBL-20700*, Lawrence Berkeley Laboratory, Berkeley, CA, 1987.

Pruess, K, TOUGH2 - A general-purpose numerical simulator for multiphase fluid and heat flow, *Rep. LBL-29400*, Lawrence Berkeley Laboratory, Berkeley, CA, 1991.

Pruess, K (ed), Proceedings of the TOUGH2 Workshop '95, *Rep. LBL-37200*, Lawrence Berkeley Laboratory, Berkeley, CA, 1995.

Philip, J.R., Numerical solution of equations of the diffusive type with diffusivity concentration dependent, *Transactions. Faraday Society*, **51**, 885-892, 1955.

Richards, L.A., Capillary conduction of liquids through porous mediums, *Physics*, **1**, 318-333, 1931.

Ross, B., J.W. Mercer, S.D. Thomas, and B.H. Lester, Benchmark problems for repository siting models, *NUREG/CR-3097*, Geotrans, Inc., Reston, VA, December 1982.

Tien, C., R.M. Turian and H. Pendse, Simulation of the dynamic behaviour of deep bed filters, *AICE J.*, **25**(3), 385-395, 1979.

Wnek, W.J., D. Gidaspow and D.T. Wasan, The role of colloid chemistry in modelling deep bed liquid filtration, *AICE J.*, **25**(3), 385-395, 1975.

Wu, Y.S. , C.F. Ahlers, P. Fraser, A. Simmons and K. Pruess, Software qualification of selected TOUGH2 modules, *Rep. LBNL-39490*, Lawrence Berkeley Laboratory, Berkeley, CA, 1996.

The behavior of volatile organic contaminants in the vadose zone with respect to barometric pumping and the estimate of residual mass and mass removal using T2VOC.

Joe Rossabi , Savannah River Technology Center, Aiken, SC 29808, joseph.rossabi@srs.gov

Ron W. Falta, Clemson University, Clemson, SC, faltar@clemson.edu

Estimates of residual contaminant mass and removal rates in the zone of influence of a barometric pumping well can be determined by T2VOC analysis of time-series measurements of contaminant concentrations at the well head and flow rate produced by atmospheric pressure changes, under two flow conditions. T2VOC has been augmented by the inclusion of liquid diffusion in addition to gaseous diffusion to more accurately match the conceptual model of mass transfer in the vadose zone.

At the Savannah River Site (SRS), significant fluxes of contaminants out of vadose zone wells have been observed in response to atmospheric pressure drops. The airflow in and out of barometric-pumped wells is a result of the difference in pressure between the formation at the screened zone of the well and the atmosphere at the surface. Earlier work confirmed that atmospheric pressure is transmitted through the subsurface but that this energy is damped and delayed when it encounters zones of lower permeability. The delay and attenuation of the pressure signal in the subsurface with respect to the surface pressure produces a pressure differential between the two zones when they are directly connected as by an open well. Airflow through the well is sustained during the period that the surface pressure is different than the pressure in the subsurface zone accessed by the well. If volatile contaminants are present near the well, gas phase contaminants will be removed during periods of flow out of the well and surface air will be injected during periods of flow into the well.

When concentration and flow are measured under two different conditions: a) simple venting (inflow and outflow) resulting from surface atmospheric pressure fluctuations, and b) controlled venting in which only barometric- produced airflow out of a well is allowed, a significantly different contaminant concentration profile is observed at the well head during outflow periods. This behavior results from both the clean air dilution of soil gas during inflow and mass transfer of the contaminant from liquid or aqueous phases to the gas phase. Using contaminant concentration data collected during these two flow regimes, geology information such as cone penetrometer logs, and T2VOC to model potential contamination scenarios, the amount of contaminant mass in the zone of influence and mass transfer rates can be determined. This simple and inexpensive test strategy may help characterize contaminated sites and determine expected cleanup time.

EXPERIMENTAL

A 2.5 cm diameter well with short screen (approximately 1.5 m) was used in this experiment. The screen zone ranged from a depth of 32.3 m to 33.8 m. A core description from a nearby, conventionally cored well, indicates that all but the top 0.35 m of screen was in a clayey material. The top part of the screen was in a medium sand. The well was monitored for pressure response to atmospheric pressure changes to establish that the formation had sealed adequately and no short-circuiting was occurring through the annulus. A logging station was deployed that monitored surface and well pressure and through the well at ten minute intervals. The system was powered with gel cell batteries charged by solar panels.

Concentration data were monitored and logged separately from the pressure and flow data using a Bruel and Kjaer Model 1302 multigas monitor. The monitor is an infrared photoacoustic system using optical filters selected for specific target analytes. The instrument is capable of effectively discriminating between TCE, PCE, and carbon dioxide in a multigas mixture and has a lower detection limit of around 200 ppbv for both TCE and PCE. The model 1302 was programmed to monitor at ten minute intervals for these experiments.

A one way valve (Baroball®) was used to prevent surface air flow into the formation for part of these experiments. The Baroball is a simple, yet effective check valve that will open in the allowed direction of flow under very low differential pressure (approximately 100 Pa) yet will prevent flow in the opposite direction.

MODEL

The models were developed to simplify the extremely heterogeneous vadose zone system to three major zones with two different materials. This simplification maintains the general integrity of the actual site located in the M area of SRS. The system includes a partially-penetrating well screened in a medium sand which is confined by two relatively wet clayey materials. The models assumed radial symmetry with an infinite lateral extent (for the scope of the simulations that were run). For the more idealized simulation, tetrachloroethylene non aqueous phase liquid (NAPL) was distributed uniformly within the interior of the uppermost clay at a saturation of 0.001. This value was selected based on characterization results obtained from NAPL investigations at several areas of the SRS A/M Area. Although this saturation value appears low when compared with NAPL saturation values assumed in much of the literature, it is quite close to the highest values found in many investigations performed here.

Simulations were also performed with a more accurate depiction of the actual subsurface conditions. In this scenario, a 2.5 cm-diameter well with 0.35 m of effective screen length (the rest of the screen is in the clay) is located in the sandy section just above the lowermost clay. A residual NAPL saturation of 0.05 was used here. Figure 1 depicts the grids for the two scenarios.

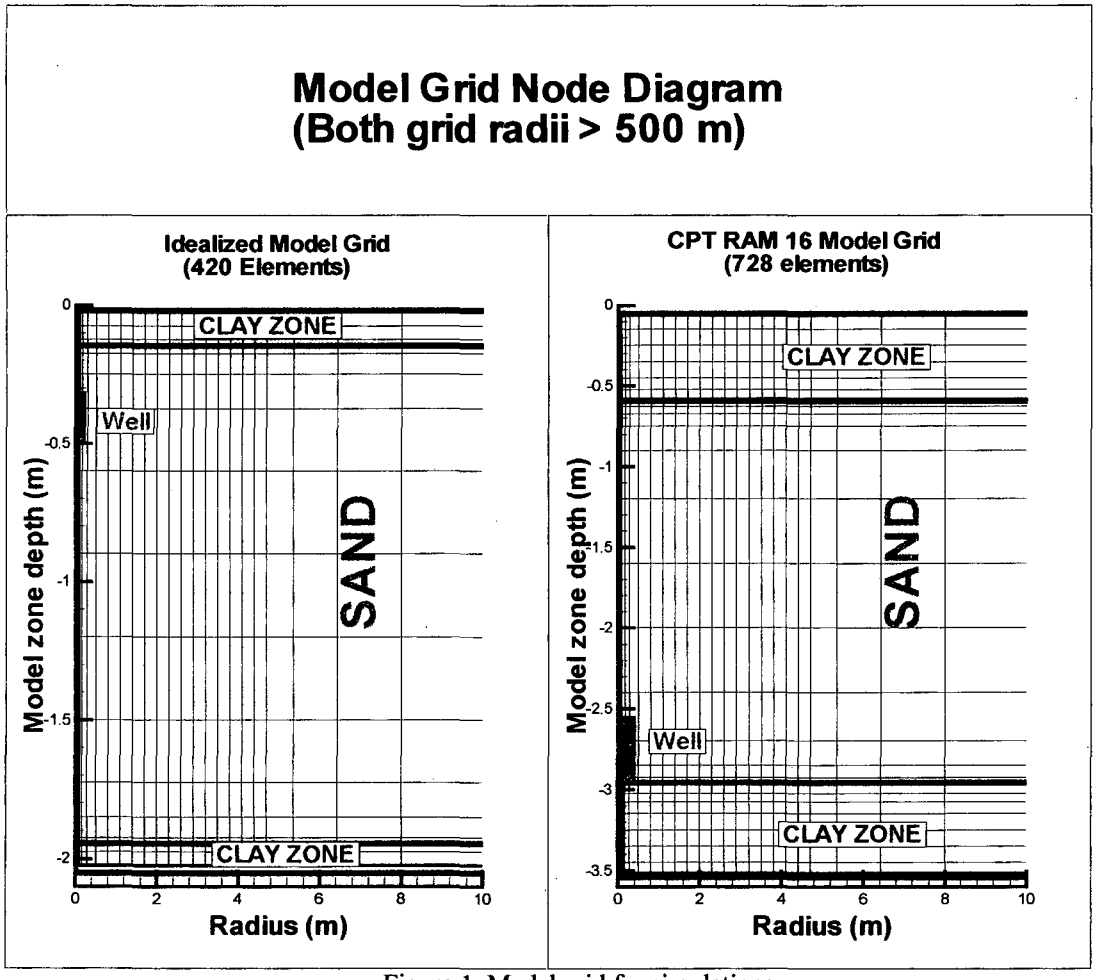

Figure 1. Model grid for simulations.

The subsurface volume was assumed to be at a steady state residual saturation based on porosity, and capillary and relative permeability parameters of the two materials, and the height above the water table with no contaminant present. Once the gas water relations were defined, contaminant in the form of a non-aqueous phase fluid was manually introduced into the system. The NAPL was assumed to be residing in the fine grain materials, held by capillary pressure. NAPL in the form of a residual saturation of approximately 0.001 was deposited in a horizontal grid row of clay residing between two layers of "clean" clay. The closed system was then allowed to come to equilibration (through diffusion for a period of five years). Relatively steady states were achieved within 30 days. The system's water, gas, and NAPL distribution at a time of one year was used as the initial condition for the modeling of barometrically produced flows in and out of a well in the otherwise closed system. The well was placed at the center of the radial system. The injection parameters were defined by dividing the total mass flow (as measured by the mass flow meter) between water and air assuming a constant temperature equivalent to the relatively constant temperature of the SRS subsurface at this depth (19 degrees C) and a relative humidity of 50%. This prevented rapid drying of the system during flow. The mass flow data were converted from slpm to kg/sec and input at the same intervals as the data were obtained, i.e., every 10 minutes.. The program was forced to solve the system matrices at least as often as the flow rate data were read (every 600 seconds). As a result, gas phase concentrations of contaminant at the well grid blocks were available for each 10 minute interval. The simulations were run on a Pentium II computer with microprocessor clock speed of 300 MHz. The average time for each simulation was approximately 6 hours. Table 1 contains the relevant grid data input to the model.

	CPT RAM 16 as built.		Model	
			Idealized	CPT RAM 16
	Elevation MSL (m)	Depth (m)	Depth (m)	Depth (m)
Ground surface.	109.0	0.0	---	---
Top of upper clay.	79.4	-29.6	0.0	0.0
Bottom of upper clay.	78.8	-30.2	-0.15	-0.6
Top of well screen.	76.6	-32.4	-0.3	-2.65
Bottom of well screen.	75.1	-33.9	-0.45	-3.0
Top of lower clay.	76.4	-32.6	-1.95	-3.0
Bottom of lower clay.	75.8	-33.2	-2.05	-3.6
Water table.	69.4	-39.6	-7.45	-10.1

Table 1. Input parameters for model.

The model concentration time plots were compared with experimental concentration time plots in an inverse modeling approach. Fitting parameters were the properties of the two different types of sediment material and the spatial distribution and amount of NAPL. Some trends in behavior became apparent after running multiple simulations, i.e., the smaller the lateral extent of the NAPL distribution, the more rapidly the decline in concentration. Similarly, the slower the diffusion through a material, the more rapid the decline in concentration given a scenario in which the well is allowed to inspire and expire. In addition, the lower the intrinsic permeability of the material, the more sensitive it was to flow variations.

RESULTS AND DISCUSSION

Model results and field data for the idealized model are compared in figure 2. From the figure, it is clear that this conceptual model accurately matches the subsurface contaminant behavior. Although this scenario depicts a sand layer with a well screen sandwiched between two clays, it is a bit different than the more realistic scenario depicted in the second simulation. In this first scenario, the well is assumed to be nearer to the upper clay and was given an effective screen length of 0.1 meters. The table of flow rates was reduced by a factor of 0.1 to compensate. DNAPL was assumed to be in the upper clay zone.

In this idealized simulation, a better match to the actual initial concentration was not attempted. The initial concentration could be increased in the model by changing the location of the DNAPL and/or the residual

water saturation of the clay, (i.e., the type of clay). The model concentration and field concentration data are plotted on two different scales simply to compare the relative concentration behavior through time.

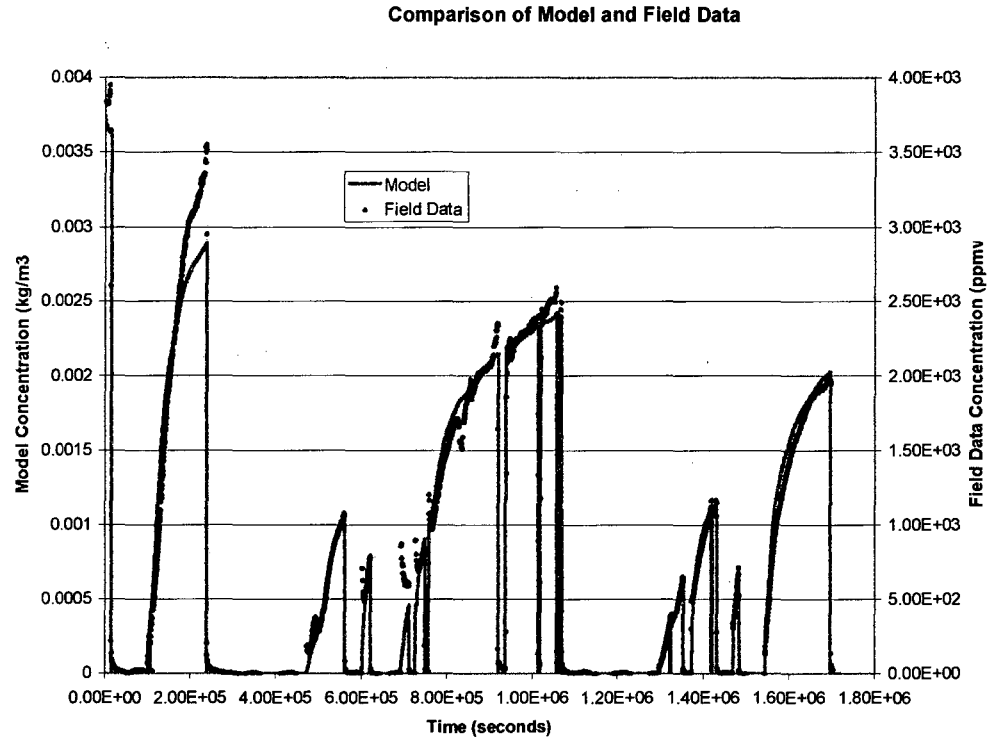

Figure 2. Idealized model comparison with field data.

The second simulation, although still somewhat idealized, more closely matched the actual subsurface conditions as measured. The clay-sand-clay interval between depths of 29.6 m and 33.2 m were matched to the well log to more accurately create the grid. The 0.35 meter long well was placed just above the clay to mimic the as-built placement of the well with approximately 1.2 meters of screen set in the clay and 0.35 meters just above in the sand. Flow rates used for this model matched the flow rates measured but were divided proportionally based on the grid block size of the well element. The DNAPL was postulated to be in the lower clay and several different combinations of materials were tested for the sand and clay zones. All of the materials were modeled after actual data of sediment samples collected at the site and analyzed in the laboratory. All of the sediment samples are from an interbedded sand and clay unit of approximately the same age.

From the close match of the model to the experimental data (Figure 3), we can conclude that the generalized conceptual model for the system is accurate. Shorter outflow events are not precisely matched but the longer intervals are well fit. The higher concentrations of the shorter intervals may be caused by small heterogeneities in the DNAPL distribution not accounted for in this simulation. The ability of the model to track the concentration profile through several in- and outflow events signifies an accurate description of the effective diffusion rate through the system and the response of the system to advective flow. Using the parameters derived from this simulation, projections of removal under various conditions can be used to determine optimum remediation strategies.

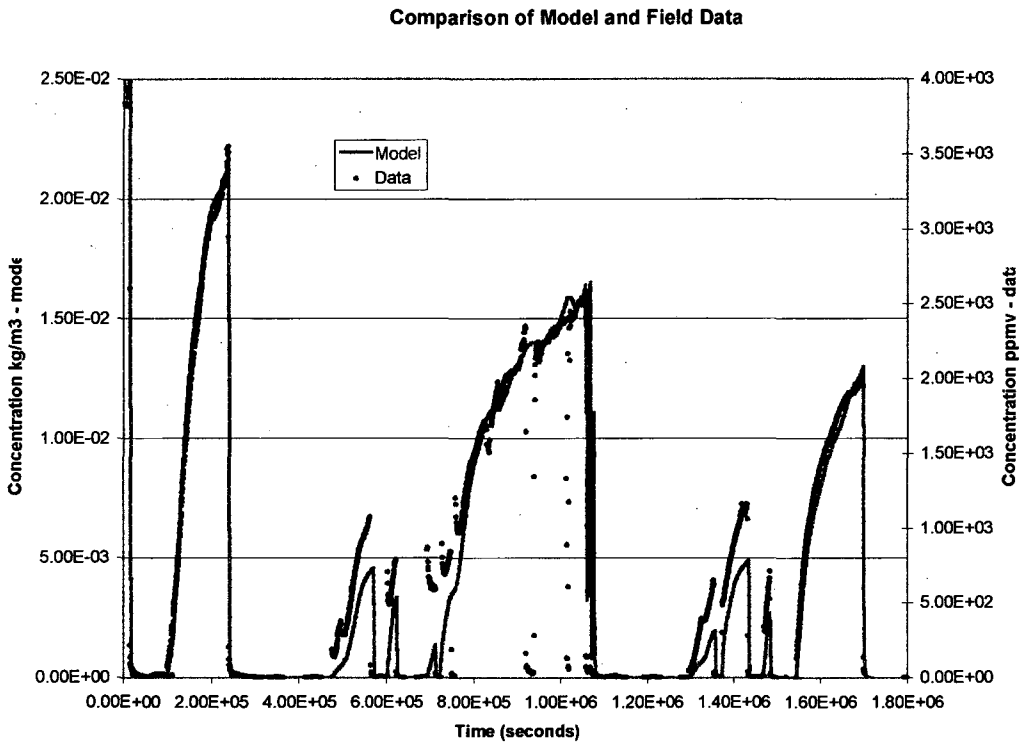

Figure 3. CPT RAM 16 model comparison with field data.

The match of the model to the data during the period when the Baroball was used to constrain flow from the subsurface to the surface and not vice versa can be used to refine the estimate of the extent of the source and relative proximity to the barometric pumping well. For example, if concentrations remain relatively constant during several cycles of outflow, we can conclude that the gaseous plume has diffused over a large volume in the more permeable zone or that diffusion through the less permeable source zone to steady state is occurring at a rate comparable to the frequency and magnitude of the volume depleted by barometric flow, or some combination of the above. Figure 4 shows the comparison between model and field data for the period when the Baroball prevented inflow. Overall, the model matches the data fairly well. The first outflow period seems to follow the behavior of the field data very closely. During the second brief outflow period (4.75E5 seconds), the model and field data do not match well. This deviation is most likely caused by the monitoring configuration. During the third outflow period, the model and field data begin to diverge. This period seems to indicate that the source may be a small distance away from the well or that there are heterogeneities of DNAPL disposition that are not accounted for in the model.

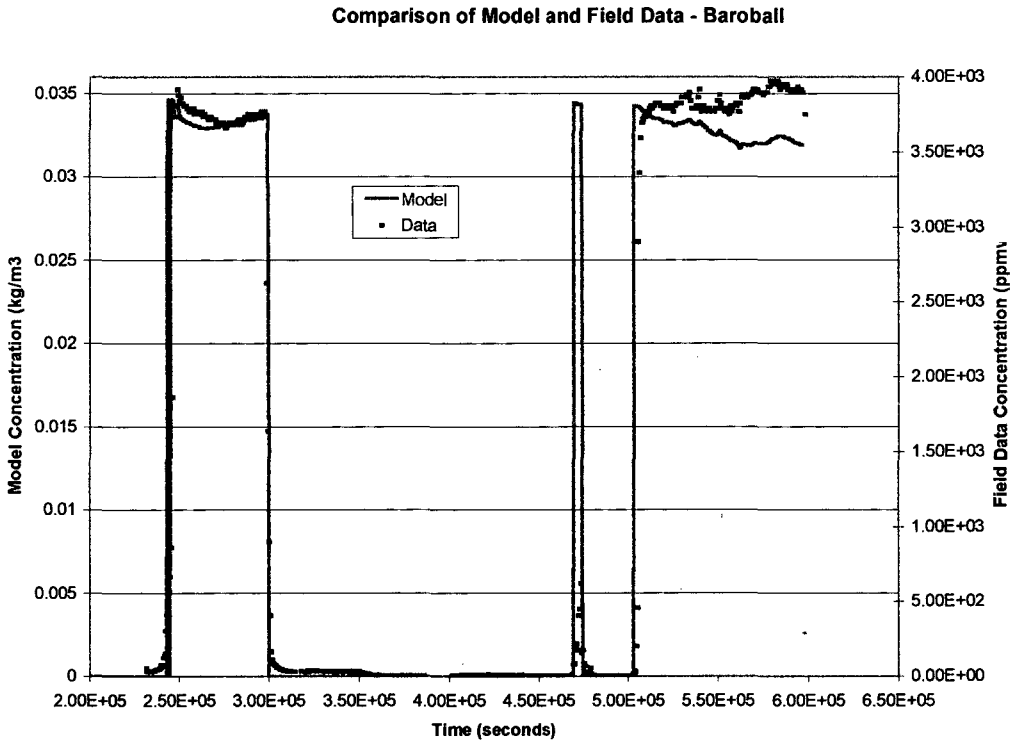

Figure 4. CPT RAM 16 model comparison with field data for Baroball operation.

NUMERICAL MODELING OF LANDFILL GAS PRODUCTION AND MIGRATION WITH A N_2-CO_2-CH_4-H_2O SYSTEM AND A PRODUCTION FUNCTION

Miroslav Nastev[1], René Lefebvre[2], René Therrien[3], and Pierre J. Gélinas[3]
Groupe de recherche *IN SITU*
1: Soprin-ADS, 2: INRS-Géoressources, 3: Université Laval

ABSTRACT

Biodegradation of the organic part of refuse disposed at landfills generates large quantities of methane and carbon dioxide, referred to as landfill gas. Most of the produced gas is emitted directly to the atmosphere while smaller quantities migrate beyond landfill boundaries through the adjacent soils. The numerical model TOUGH2-LGM was developed to simulate landfill gas production and migration processes within and beyond landfill boundaries. The model is derived from the original version of TOUGH2. TOUGH2-LGM has a new equation of state module and considers the migration of five components in partially saturated media: four fluid components (water, nitrogen, methane and carbon dioxide) and one energy component (heat). The four fluid components are present in both gas and liquid phases. The model incorporates gas-liquid partitioning of all of fluid components by means of dissolution and volatilization. Multiphase flow and heat transfer is described as in TOUGH2 whereas multi-component diffusion is an added capability. Landfill gas production is modeled as a simple exponentially decreasing function of time. The overall kinetic coefficient of landfill gas production was adjusted according to observed recovery rates in different age material. The numerical simulator was successfully used for modeling gas migration at two landfill sites: the Complexe environnemental de Saint-Michel (CESM) landfill at the City of Montreal and the St-Étienne-des-Grès landfill. The combination of field data and numerical simulations provides a good description of landfill gas production and migration mechanisms.

INTRODUCTION

Landfill gas can be viewed as a threat to safety and the environment that must be controlled but also as an energy resource. In either case, the production and migration mechanisms of landfill gas have to be well understood.

Landfills are complex systems in which many coupled processes take place: biodegradation of organic compounds, gas production and migration, leachate infiltration, heat production and transfer, ...

Numerical models can be used to provide a better fundamental understanding of landfill systems, and also as design tools for landfill gas recovery systems. The design and operation of these systems actually represent a very interesting engineering optimization problem. Landfill gas must no be allowed to migrate to the atmosphere or beyond landfill boundaries. On the other hand, gas recovery wells must not be pulled too hard to avoid the introduction of atmospheric oxygen within the refuse. Oxygen is lethal to anaerobic bacteria responsible for landfill gas production and stabilization of the organic matter.

We describe in this paper a numerical model representing the processes involved in landfill gas production and migration. The numerical model was developed from TOUGH2 (Pruess, 1987 and 1991).

LANDFILL GAS PROCESSES

Fresh organic materials, disposed along with other refuse components, supply the microbial inocula and form the necessary substrate for bacterial metabolism. As soon as refuse is placed in a landfill, two main biological transformation processes are initiated: *aerobic* and *anaerobic decomposition*. Both are controlled by microorganisms that transform and stabilize organic compounds towards simpler, mainly inorganic, substances (Farquhar and Rovers, 1973; McInerney and Bryant, 1981; Senior and Balba, 1987; Christensen and Kjeldsen,1989).

Initially, atmospheric air is trapped within the refuse, and bacterial decomposition occurs under aerobic conditions. This phase is characterized by a microbial activity in which labile molecules, such as simple sugars, are rapidly metabolized, while biodegradation of natural polymers (lignin, tannin)

proceeds at a comparatively slower rate. A whole range of chemical intermediates along with a gas mixture of mostly CO_2 and NH_3 and significant amounts of water are generated in this phase. Heat is produced immediately after refuse placement and the temperature of the refuse is raised above the ambient temperature. However, the oxygen fraction of the trapped air is soon exhausted, and the long term decomposition is continued under anaerobic conditions.

If the moisture content is sufficiently high and a sufficient amount of microbial inocula is present, anaerobic digestion will start as soon as the oxygen gas fraction is depleted. Decomposition of the organic compounds is carried out by anaerobe microorganisms resulting in the production of methane and carbon dioxide as the two most reduced forms of carbon. For convenience, anaerobic microbial activity can be considered as a chain of continuous processes which proceed in several successive stages: *hydrolysis, acidogenesis, acetogenesis* and *methanogenesis.*

Many important physical processes accompany landfill gas production in landfills. Refuse is a partially saturated porous media in which multiphase flow of leachate and gas occurs. Gas migrates by advection under pressure gradients but also by diffusion of components under concentration gradients. Heat production and transfer is an important part of landfill gas production since most fluid properties vary with temperature.

We are mainly interested here by gas migration processes. As mentioned above, pressure and concentration gradients are the main factors causing gas movement. Gas generation increases the pressure and concentrations to which gases are submitted within the landfill. Gas migration, which is not necessarily proportional to the gas generation rate, will also be influenced by refuse properties. Since refuse is very heterogeneous, there will be a wide diversity of gas concentrations and pressures within different parts of the landfill. Once concentration and pressure gradients are established, landfill gas migrates vertically and laterally towards the low concentration and low pressure areas.

Landfill gas migration beyond landfill boundaries occurs in three basic directions: vertical emissions to the atmosphere, lateral migration to the adjacent soils, and dissolution and migration in the saturated zone.

LANDFILL GAS PRODUCTION MODEL

Following Monod's expression for a first-order reaction, the gas production rate Ω (m^3/tonne·year) can be approximated by an exponentially decreasing function of the initial gas production potential Π_o (m^3/tonne) and the overall kinetic rate constant k (s^{-1}) as follows:

$$\Omega = k \Pi_o e^{-kt}$$

This equation can be applied either globally to all the refuse or to refuse categories classified according to their respective biodegradability.

In order to completely define the gas production model, we have to determine the landfill gas production potential and the biodegradation rate. This can be accomplished by calibrating the coefficients of the gas production model according to the computed recovery rates at a given site. This is illustrated for the *Complexe environnemental de Saint-Michel (CESM)* landfill site in Montreal, Quebec.

Figure 1 shows the specific production rate in four different zones of the *CESM* in 1996. These zones have received refuse for various operation periods. The proportion of the total landfill gas production obtained from each zone was used to evaluate the recovery rate against the corresponding age. Besides zone 4, the manual fit of an exponential model through the data reproduces the change in production rate. Zone 4 is the active landilling area. In other zones, landfill gas recovery is estimated at least at 90% of the total production. It is believed that much more gas escapes however from zone 4. Landfilling operations require interruptions of the gas recovery system in this zone from time to time so gas recovery is reduced.

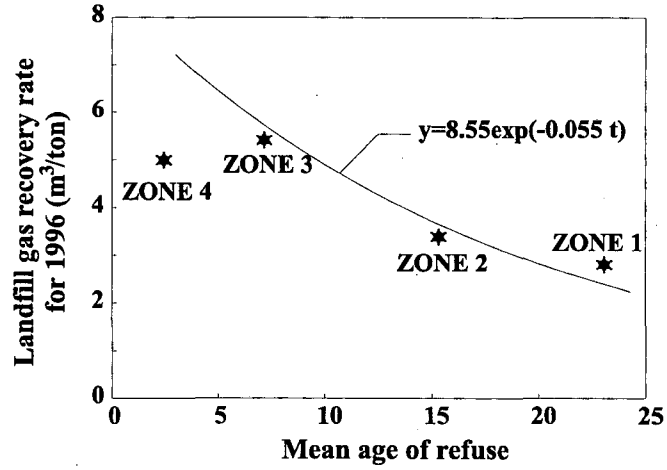

Figure 1. Landfill gas recovery rate for 1996 as a function of average refuse age in the four *CESM* landfill zones

Taking into account the assumed 90% gas recovery efficiency, the exponential fit in figure 1 implies an overall biodegradation coefficient k of 0.055 year^{-1} (or a half life $t_{1/2}$ of 12.6 years), an initial landfill gas potential Π_o of 172 m^3/tonne of refuse and an initial recovery rate Ω_o of 9.5 m^3/tonne·year. The average methane and carbon dioxide contributions are 55% and 45% of the recovered volume respectively. Methane production potential is thus 94.6 m^3/tonne of refuse.

This estimate of landfill gas production kinetics is based on a single point in time in 1996. In order to validate this estimate, the landfill gas production history is calculated based on the assumed kinetic constant and potential as well as the known refuse mass accumulation history and gas recovery at the site. Figure 2 shows predicted landfill gas production rate through time compared to the values obtained by previous studies and field data. Our prediction agrees quite well with the landfill gas production history available for the past few years.

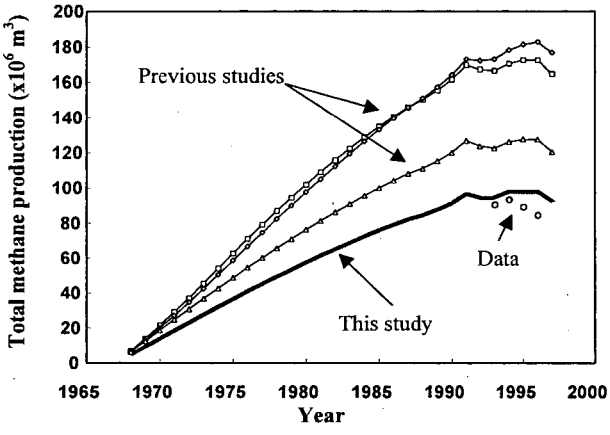

Figure 2. Total methane production through time as predicted by the production model compared to observed data and previous predictions

NUMERICAL MODEL DESCRIPTION

Numerical models have been developed to represent either landfill production or migration (Findikakis and Leckie, 1979; Mohsen et al., 1980; Metcalfe and Farquhar, 1987; El Fadel et al., 1989; Lang and Tchobanoglous, 1989). Some of these use rather complex landfill gas production models but most have shortcomings with respect to the representation of physical processes. Since physical processes control in large part the migration processes within and outside landfills, we have put more emphasis on developing an accurate representation of the physical processes. TOUGH2 was the ideal starting point to develop such a model. We used a practical approach with a simplified landfill gas production model that can be calibrated with field data.

Our numerical model, TOUGH2-LGM, has the following specifications:

1) Time dependent landfill gas production model;
2) Equation of state for a gas mixture of nitrogen, methane, carbon dioxide and water;
3) Advective and diffusive gas migration processes;
4) Multiphase flow of gas and liquid phases;
5) Exchanges of components between fluid phases;
6) Temperature effects on fluid properties and heat transfer processes.

The numerical model has evolved from a modified version of TOUGH2 (Lefebvre, 1995) used to model chemically reactive multiphase flow processes related to acid mine drainage production. Details on the numerical model are provided by Nastev (1998).

The central modification required to TOUGH2 is the development of a new equation of state module for a system with one energy component (heat) and four fluid components: N_2, CO_2, CH_4, and H_2O. Fluid components partition between the liquid and gas phase is controlled by temperature dependent Henry's law constants. The enthalpy of CO_2 and CH_4 dissolution in water is taken into account. This module also computes the viscosity of a gas mixture of these components as well as temperature dependent multi-component molecular diffusion coefficients. Effective diffusion coefficients in partially saturated porous media can be calculated with three different formula.

The other important addition required to the program is a subroutine representing the landfill gas production model to calculate the production rates of CH_4 and CO_2 as well as the accompanying heat generation. The overall anaerobic biodegradation reaction is exothermic and is assumed to produce 2528 kJ of heat per kg of CH_4 generated.

Five primary thermodynamic variables are needed to specify the state of the system. As in TOUGH2, the first variable is pressure and the last one is temperature. Again, similarly to TOUGH2, the second variable is either the "air" mass fraction for single phase conditions or water saturation (+10) for two phase conditions. The two additional primary variables are the mass fractions of CH_4 and CO_2 in "air" which is a mixture of N_2, CH_4 and CO_2. As in TOUGH2, the secondary parameters describing the properties of the fluid phases required for flux

calculations are saturation, relative permeability, viscosity, density, specific enthalpy and capillary pressure. The same form of mass conservation as TOUGH2 is used to establish a set of simultaneous equations to be solved. The Newton-Raphson direct solver is used for that purpose.

The gas transport processes represented by the model were verified against one-dimensional, two-dimensional and radial analytical solutions.

THE *CESM* MODELS

The *Complexe environnemental de Saint-Michel* (*CESM*) landfill is operated by the city of Montreal. It is the third largest landfill in North America and has been in operation for almost 30 years. The landfill occupies a former limestone rock quarry. The refuse covers a 74 ha area and reaches a volume of 47 million m^3 with an average thickness of 64 m.

The leachate is pumped by a central well and monitored by a system of peripheral wells in the surrounding limestone. The landfill gas recovery system relies on more than 300 vertical collecting wells. An important network of peripheral monitoring wells is used to regulate the suction in the recovery system based on indications of lateral gas migration. This is very important since the landfill is located at the heart of a dense urban area. A large part of the landfill gas is sold to an onsite electric plant.

The *CESM* provides a unique opportunity to validate and apply the landfill gas numerical model. Important monitoring infrastructures and landfill cover test plots provide information on the physical conditions within the refuse and on gas production. The first application of these data was the calibration of the landfill gas production model discussed earlier. The first application of the numerical model uses a one dimensional grid to study the evolution of physical conditions through time within the refuse and the effect of variations in atmospheric pressure. The portion of refuse modeled is the unsaturated zone with a representative thickness of 40 m.

The model is run without gas recovery systems and shows the natural evolution of processes in the landfill. Figure 3 shows the pressure distribution through time within the refuse. Since gas production is at its peak in the earlier part of the landfill life, pressure builds up early to more than 3 kPa above atmospheric pressure (100 kPa used in the model). Pressure remains high in the first 20 years and decreases steadily thereafter. Temperature follows a similar pattern after reaching values beyond 35 °C.

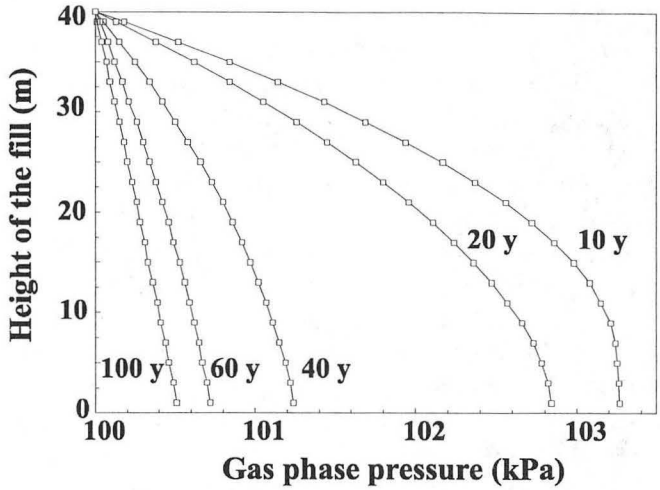

Figure 3. Pressure distribution through time as a function of depth for the one-dimensional model

Landfill gas production occurs for long periods. Even after gas production slows down, landfill gas has to be replaced by atmospheric gas. This is illustrated by figure 4. It shows the evolution in methane concentration through time at different depths within the landfill. In the early life of the landfill, a relatively even methane concentration is established. After production slows down (about 40 years), landfill gas pressure is reduced and landfill gas surface emissions are reduced. Under these conditions, diffusion of atmospheric air from the surface is no longer balanced by the outward gas flux, and methane concentration within the landfill is reduced steadily.

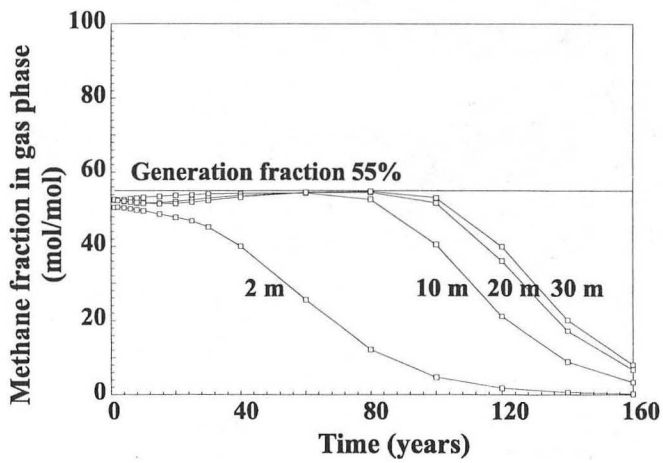

Figure 4. Evolution of methane concentration through time at different depths in the one-dimensional model

The concentration of methane in landfill gas is known to be highly variable through time. This goes against the fact that methane production ratios in landfill gas is supposed to be quite steady. Figure 5 provides part of the explanation for these fluctuating concentrations. This figure shows the changes in landfill gas concentration near the landfill surface when atmospheric pressure variations occur. It can be seen that the proportion of nitrogen (labeled "air") varies because of the barometric pumping effect. However, this effect is not alone responsible for the variations in methane concentration. The two main landfill gasses, methane and carbon dioxide, have quite different physical properties and behaviors. These properties affect their response to atmospheric pressure changes as shown in figure 5.

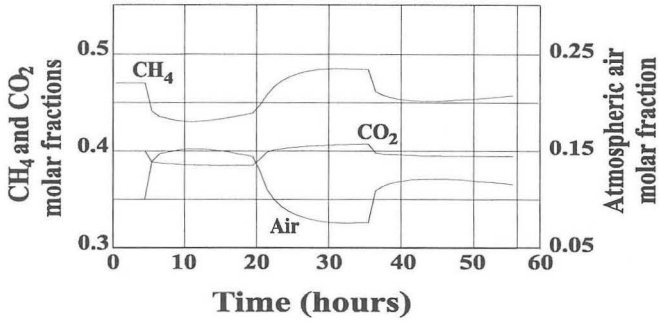

Figure 5. Changes in gas composition through time caused by variations in atmospheric pressure

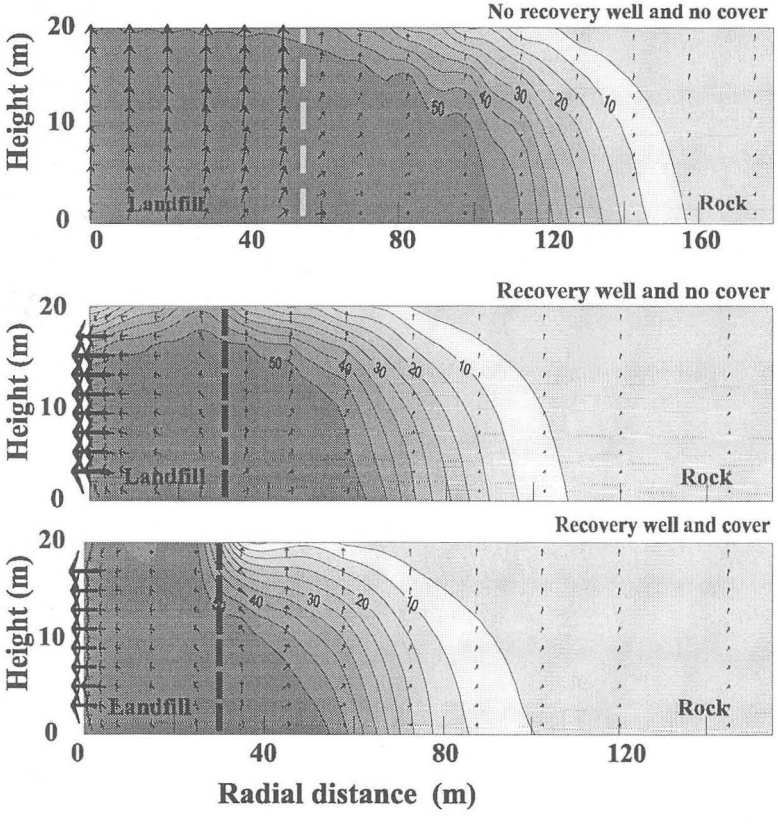

Figure 6. Predicted methane concentration and total flux at the limit of the landfill in contact with limestone bedrock for three model conditions: (Top) no cover layer and no gas recovery well; (Middle) no cover layer but with a gas recovery well; (Base) both with a cover layer and a gas recovery well.

Two-dimensional vertical sections were used to study landfill gas migration processes at the interface between refuse and the surrounding limestone rock. Figure 6 shows the concentrations and fluxes in methane for three cases in present day conditions. The case without recovery well shows that methane can migrate at great distances out of the refuse even in this low permeability material. The presence of a gas recovery well improves the situation. However, if such a well is at an important distance from the refuse limit or if the imposed suction is low, it cannot be operated efficiently to both limit landfill gas migration and prevent the entry of air in the refuse. The last case shows that the capping of refuse with a low permeability material prevents both the migration outside the refuse and the introduction of atmospheric air. The presence of a cover thus facilitates landfill gas recovery and the control of its migration.

THE SAINT-ÉTIENNE-DES-GRÈS MODEL

The second landfill site studied is at St-Étienne-des-Grès, Quebec. This landfill covers 39 ha with an average 12 m of refuse resting on the unsaturated zone of a sand.

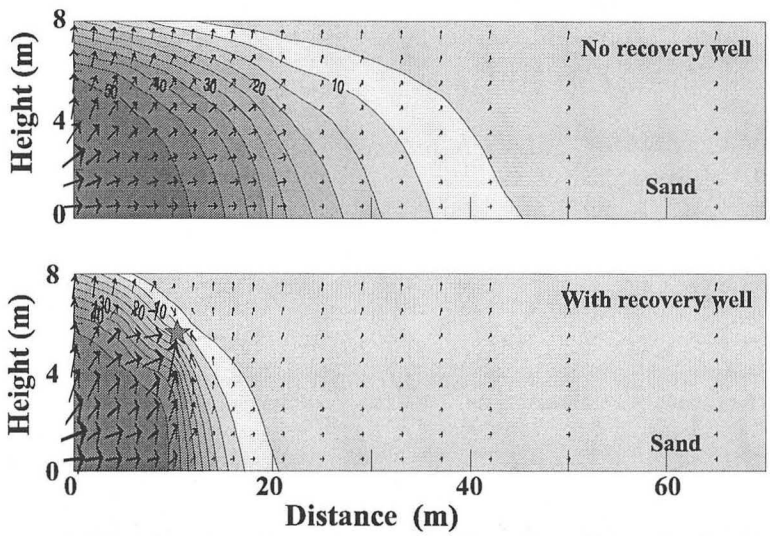

Figure 7. Predicted methane concentration away from the limit of the landfill in an unsaturated sand unit: (Top) without gas recovery system; (Base) with a horizontal gas recovery well.

At the site, landfill gas migration control is achieved by a peripheral horizontal well connected to a single pumping station. The modeling work was prompted by reports of gas concentrations observed in monitoring wells 10 m away from the landfill boundary close to the horizontal well. It appeared that the pumping system was insufficient to provide a vacuum in the entire length of the well.

Figure 7 (top) shows the conditions prevailing without a recovery well in the sand at the contact with the refuse as predicted by the model. As can be seen, methane migration at a concentration of 5% (the *lower explosive limit*) reaches as far as 40 m from the landfill boundary. The application of a small 0,5 kPa suction on the horizontal well is sufficient to prevent any migration of methane away from the landfill .

CONCLUSION

The numerical model developed is an efficient tool both to understand the fundamental mechanisms of landfill gas production and migration processes as well as to support the engineering design of gas recovery systems. TOUGH2 was a sound starting point to represent multiphase non isothermal landfill systems.

REFERENCES

Christensen, Kjeldsen, 1989: Basic biochemical processes in landfills. Sanitary Landfilling: Process, Technology and Environmental Impact. Academic Press, 29-50.

El-Fadel, Findikakis, Leckie, 1989: A numerical model for methane production in managed sanitary landfills. Waste Manag. & Res., 7, 31-42.

Farquhar, Rovers, 1973: Gas production during refuse decomposition. Water, Air and Soil Pollution, 2, 483-495.

Findikakis, Leckie, 1979: Numerical simulation of gas flow in sanitary landfills. Journal of Env. Eng., 115, 927-945.

Lang, Tchobanoglous, 1989: Modeling emissions of trace gases from landfills. 82 An. Meet.& Ex. Anaheim, 1-14.

Lefebvre, 1995: Modeling Acid Mine Drainage in Waste Rock Dumps. TOUGH Workshop '95, LBL-37200.

McInerney, Bryant, 1981: Review of methane fermentation fundamentals. Fuel Gas Production from Biomass, Vol.I, Wise, D.L., ed., CRC Press, 19-47.

Metcalfe, Farquhar, 1987: Modeling gas migration through soils from waste disposal sites. Water, Air and Soil Pollution, 32, 247-259.

Mohsen, Farquhar, Kouwen, N., 1980: Gas migration and vent design at landfill sites. Water, Air and Soil Pollution, 13, 79-97.

Nastev, 1998: Modeling Landfill Gas Generation and Migration in Sanitary Landfills and Geological Formations. Ph.D. thesis, Laval University, 373 p.

Pirt, 1978: Aerobic and anaerobic microbial digestion in waste reclamation. Appl. Chem. Biotech., 28, 232-236.

Pruess, 1987: TOUGH user's guide. LBNL.

Pruess, 1991: TOUGH2 - A general purpose numerical simulator for multiphase fluid and heat flow. LBNL.

Senior, Balba, 1987: Landfill Biotechnology. Bioenvironmental Systems, Vol.II, Wise, ed., CRC Press, 17-65.

AKNOWLEDGEMENTS

The collaboration of the *CESM* engineering staff, especially Mr. Martin Héroux, was essential for model development. Support and encouragement by Karsten Pruess of LBNL is gratefully acknowledged.

TOUGH Workshop '98, Lawrence Berkeley National Laboratory,
Berkeley, CA 94720, May 4-6, 1998.

SIMULATION OF THE TRANSPORT OF AROMATIC AMINES IN THE UNSATURATED ZONE FOR THE EVALUATION OF AN ENVIRONMENTAL REMEDIATION PROJECT

Alfredo Battistelli(*),Corrado Ferragina(*), Alessandro Chersicla(*),Giovanni Matarrese(#) and Mario Pieroni(*)

(*) Aquater SpA, Via Miralbello 53, 61047 S. Lorenzo in Campo (PS), Italy;
e-mail: ambid@aquater-sl.aquater.it
(#) EniChem SpA, Piazza della Repubblica 16, 20120 Milano, Italy.

ABSTRACT

The T2VOC code was used to evaluate the efficiency of environmental remediation activities planned on a portion of the ex-ACNA area, an industrial site where the Chemical Company ACNA carried out its industrial activity from the end of 1920 up to 1983. First industrial activity started at the end of 19th century. The area is close to Cesano Maderno town, located some 15 km NNW of Milan in Northern Italy.

Since the mid-seventies, part of the study area was used as a landfill for inert materials as well as for surface disposal of contaminated wastes which were then covered with local soil. The chemicals present in the wastes are heavy metals and organic chemicals, with a predominance of aromatic amines. Soil and groundwater analyses showed that the chemicals diffusion through the thick unsaturated zone was already affecting the underlying unconfined aquifer.

Main planned remediation activities included the removal of most contaminated wastes and landfill capping to avoid the infiltration of meteoric water, responsible for the downward transport of chemicals. The T2VOC code was employed for 3-D simulations of the unsaturated zone to evaluate the efficiency of the planned remediation activities in preserving groundwater quality. First the steady state flow field, then a reasonable reconstruction of aromatic amines diffusion over the previous 20 years were simulated. Finally, the forecast of aromatic amines transport evolution was simulated, both in the absence of any remediation, as well as after the execution of planned remediation activities.

INTRODUCTION

The study area represents the southern portion of the Cesano Maderno chemical complex run by ACNA SpA company and closed down in 1983. During the past activity many different productive activities took place in the area and several companies are still using the area for their chemical productions. The study area shown in Fig.1 was never employed for production activities but, starting from the early seventies, was used for the surface disposal of inert and contaminated wastes. These landfills were located mainly in ground surface depressions previously created by the exploitation of a clay layer which initially covered most of the area. The shaded areas in Fig. 1 represent the main discharge locations: zone 2, located East, and zones 3 and 4, located West of Garbogera stream; zone 6 located on the West side of the area.

Fig. 1 also shows 7 basins which were used for approximately ten years since the mid-seventies for the thickening of industrial muds derived from chemical processes which included the production of pigments and colorings.

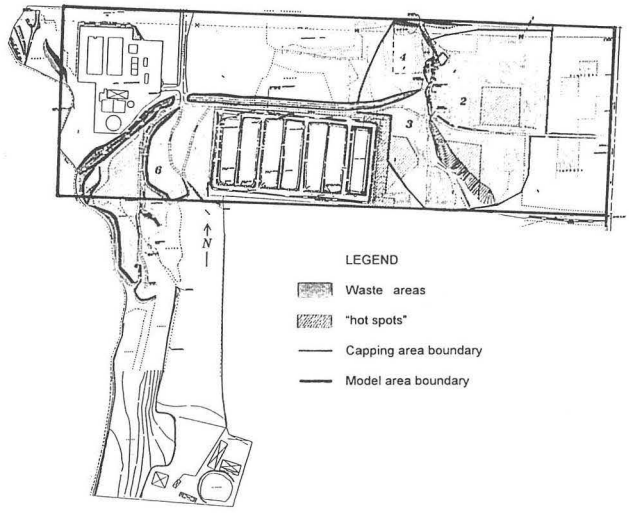

Fig. 1 The Cesano Maderno ex-ACNA site. The waste areas and the model grid location are shown.

The chemicals present in the wastes are heavy metals and organic chemicals, with a clear predominance of aromatic amines. Whereas heavy metals predominate in zone 6, aromatic amines have been identified as the most important compounds in zones 2, 3 and 4 as far as possible groundwater contamination is concerned. As an important unconfined aquifer is present in the area, starting in the early nineties a series of investigations were performed on different locations of the chemical complex area in order to define the local geology and hydrogeology, identify the contaminant species present in the soil and in groundwaters, and reconstruct their distribution. The surveys led to the identification of priority zones for which immediate remediation projects were requested by control Authorities. EniChem SpA was asked to provide for the general setting of the area shown in Fig. 1. This included the remediation of zone 6, of the basins area, of zones 2,3 and 4, and the construction and operation of an hydraulic barrier downstream of the chemical complex. EniChem entrusted Aquater with the design of remediation activities and the execution of contaminant transport simulations to confirm the effectiveness of the planned activities in preventing pollution in the unconfined aquifer (Aquater, 1997). This paper describes the modeling studies performed to verify the effects of the remediation project designed for zones 2, 3 and 4 located in the eastern portion of the area.

GEOLOGICAL AND HYDROGEOLOGICAL BACKGROUND

The study area is located in the Upper Lombardian plain that lies within the Po River Valley. The local stratigraphy was reconstructed by means of over 200 wells and boreholes drilled both for industrial water supply and during the above mentioned surveys. Starting from the ground surface the following stratigraphy was encountered:

a. weathered clay layer, made up by a reddish silts and clays layer up to 5 m thick, known as "Ferretto";

b. fluvioglacial deposits, consisting of sands and gravels with silty-clay lenticular interbeddings, down to 25 to 30 m from ground level, within a silty-sandy matrix;

c. sands and gravels with low cemented conglomerates and sandstone interbeddings down to about 40 m from ground surface, where the top of an almost continuous silty-clay layer is encountered, with thickness ranging from 1 m to 3 m.

d. alternating sand and gravel layers with lenticular cemented levels interbedded down to about 70 m below ground surface;

e. clay layer extending over the entire area with thickness ranging from a few meters to some tens of meters. It represents the top of a confined regional aquifer having an average thickness of some 30 meters.

The confined aquifer is not locally affected by contamination. Above it, an unconfined aquifer, located in the d. unit mentioned above, is present with average water level some 60 m below ground level. Groundwater flows in a SE direction. The area is thus characterized by a thick heterogeneous unsaturated zone. Above the silty-clay layer at 40 m depth, a saturated zone was detected. Its thickness, ranging from a few tens of centimeters up to a couple of meters, varies throughout the year depending on meteoric recharge and the recharge operated by the two surface streams: the Lombra river which borders the west side of the study area, and the Garbogera stream which divides zones 3 and 4 from zone 2. The piezometric surface of this perched saturated level was observed over the central portion of the study area with a general NS flow direction.

Depending on the presence of low permeability lenses, scattered saturated levels were also encountered in the first 30 m.

PLANNED REMEDIATION MEASURES

The surveys performed on zones 2, 3 and 4 pointed out the presence of a consistent amount of wastes having quite variable concentrations of contaminants and the presence of chemicals at depths which make the removal of contaminated soil unfeasible. Thus, the remediation project was based on a series of integrated activities including:

- complete removal of the most contaminated hot spots from the 3 zones (dashed areas in Fig.1);
- capping of the surface occupied by wastes (the shaded area in Fig.1) and the construction of a lateral impervious trench from the ground surface down to the top of the surface clay layer (Ferretto);
- impermeabilization of the whole Garbogera stream bed to avoid further infiltration of stream water into the unsaturated zone.
- impermeabilization of the ponds area shown in Fig.1;
- removal of small amounts of wastes located outside the capping area and their transport inside the capping area.

NUMERICAL MODEL SET UP

In order to assess the planned remediation activities, the control Authorities requested the evaluation of the expected reduction of contaminant flux through the unsaturated zone. They asked to verify that the concentration of specific contaminants be maintained below given limits, defined accounting also for a safety factor. They requested to compute the concentration in the unconfined aquifer through a simple mass balance using the evaluated aquifer natural flow and the computed contaminant flux through the unsaturated zone and assuming instantaneous mixing. According to their

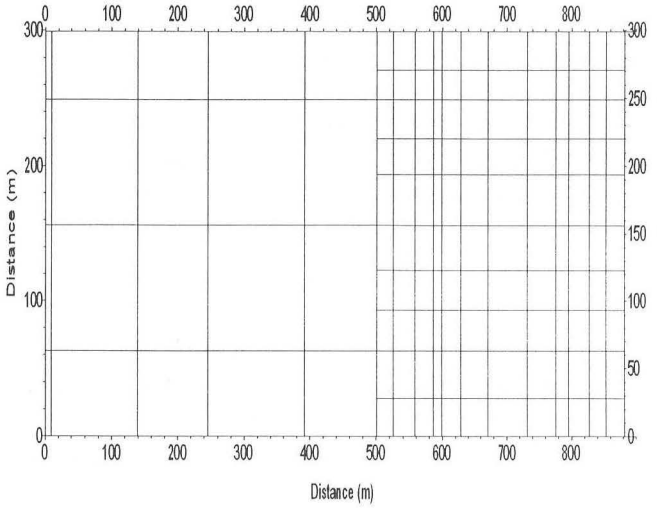

Fig. 2 Model grid layout showing the grid refinement on the east side.

specifications, the model grid included only the unsaturated zone, whereas the unconfined aquifer was simulated as a constant pressure boundary. The extension of model grid is shown in Fig.1: it covers all 3 zones of interest: zones 2, 3 and 4, and is extended westwards up to the Lombra river to account for its possible recharge of the perched saturated level.

Fig. 2 shows grid discretisation on the horizontal plane: the grid extends for 882 m EW and for 299 m NS. It is made up of a main grid, called grid A, of 4 x 9 elements and 20 layers. On the east side and limited to the first 10 m, a grid refinement was included to properly account for the more detailed knowledge of zones 2, 3 and 4, acquired through the drilling of shallow boreholes on a regular mesh of about 30 m side. The main grid has 560 elements and the refinement has 1200 elements for a total of 1760 elements.

Considering that a sub-vertical flow direction prevails in the unsaturated zone, impervious lateral grid boundaries were assumed. Bottom boundary is held at constant pressure to represent the unconfined aquifer water level, whereas the upper boundary is held at atmospheric pressure using inactive elements. The ground surface and the Ferretto clay layer morphology were followed to accurately reproduce the spatial distribution of wastes disposed of in zones 2, 3 and 4. The vertical grid discretisation and an example of different rock domain distribution is shown in Fig. 3, where a WE vertical section through the third slice of grid A and the sixth slice of grid B is represented. This representative section, referred to as section A3-B6, crosses the central part of zone 2 where the largest layer of wastes and the highest concentration of chemicals were found.

The rock domain properties were partially defined using site measurements such as permeability tests in the unsaturated zone, pumping tests in the unconfined aquifer, and laboratory tests on undisturbed samples collected in clay and silty-clay levels. Grain size analysis and water content determinations were extensively performed on coarse sediment samples collected in the unsaturated zone in the attempt to use published correlations and suggested properties ranges. In particular the range of aqueous phase saturation was estimated from the water content, assuming reasonable values of rock porosity according to the observed lithology. The Van Genuchten (1980) model was used for the capillary pressure whereas the Stone first model (1972) implemented on the T2VOC code was used for the relative permeability correlations.

SIMULATION OF NATURAL STATE

The modeling study was performed using the T2VOC computer code developed at LBNL (Falta et al., 1995), assuming constant temperature for every simulation.
The first step was the reproduction of a reasonable natural state which included the evaluated meteoric recharge, the evaluated recharge from surface streams, the observed water level of perched aquifer at 40 m depth, and the presence of a perched saturated level in zone 2, located above the Ferretto clay layer at the bottom of the wastes.
In order to reproduce the above data and the evaluated water saturation distribution with depth, several runs were made using mainly the permeability and relative permeability of rock domains as matching parameters.

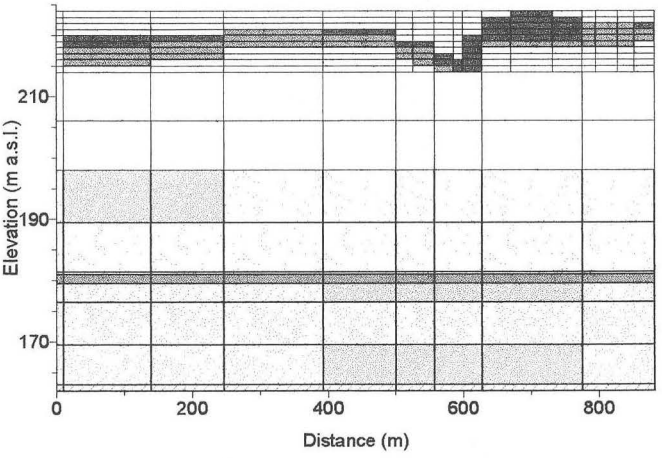

Fig. 3 A2-B6 vertical section showing the discretisation grid and the rock domain distribution.

Main result of the natural state simulation was the indication of the effect of the Garbogera stream in determining a concentrated vertical flow both because of its direct recharge and because of the drainage operated by the stream bed which cuts the Ferretto clay layer and thus determines horizontal flow components from zones 2, 3 and 4.

AROMATIC AMINES DISTRIBUTION

Most of material disposed of in the area during the seventies is contaminated at different degrees by organic compounds and heavy metals. Organic compounds are the most important chemicals in zones 2, 3 and 4 as far as the contamination of ground water is concerned. Among them the aromatic amines, which were used for the production of pigments, were by far the most abundant. About 30 different amines were identified in the wastes. According to National Italian regulations, the aromatic amines are assigned to different classes depending on their known, or assumed toxicologic effects. In order to simulate the effects of the planned remediation activities in the presence of multiple contaminants, we made reference to the aromatic amines of class 1, defined as very toxic with cumulative effects. Public Italian regulations do not specify the concentration limits for the aromatic amines. For the modeling study, we assumed for the aromatic amines of class 1 the maximum acceptable concentration in ground water specified for pesticides: 0.1 ppb. For the present project a safety factor of 4 was requested (Provincia di Milano, 1995), thus the concentration in ground water of class 1 aromatic amines had not to exceed 0.025 ppb. We used at any sampling point, the sum of concentrations of aromatic amines of class 1, whereas the transport properties of N,N-diethylaniline (CAS number 91-66-7) were used to simulate all the class 1 aromatic amines. The measured average concentration of class 1 aromatic amines was determined and assigned to each rock domain. When greater than the average value plus the mean deviation, the measured concentration was assigned to single elements to reproduce the presence of the so called 'hot spots'. The variation of measured concentrations with depth was also accounted for.

The N,N-diethylaniline is a toxic aromatic amine characterized by low water solubility, relatively low saturation pressure, and limited adsorption on organic carbon. In particular, both the water solubility and the octanol/water partition coefficient (K_{ow}) were experimentally determined at the laboratory. The organic carbon/water partition coefficient K_{oc} was then computed from the K_{ow} using an empirical correlation for dinitroanilines and pesticides given by Olsen and Davis (1990). To check the reliability of computed K_{oc}, laboratory batch tests were also performed on soil samples collected at different depths to experimentally determine the solid-aqueous distribution coefficient K_D. As we found experimental K_D values systematically higher than the value computed according to the estimated K_{oc} value and measured fraction of organic carbon f_{oc}, we decided to use the computed K_{oc} evaluated from the K_{ow}. This choice was also justified by the difficulties encountered in reproducing the conditions present at the field during laboratory testing. In order to account for the long-term effects of molecular diffusion in the aqueous phase when the advective flow becomes negligible, the molecular diffusion in liquid phases was included in a fashion similar to that used for the EOS7R module of TOUGH2 (Oldenburg and Pruess, 1995).
Considering the low concentration of chemicals, for all the simulations the value of the convergence criterion for relative error was decreased from the default value of 1E-5 to 1E-8.

The measured distribution of contaminants in the waste materials was quite variable and fairly dependent upon natural transport processes, as it depends on the initial concentration of contaminated wastes and the procedure followed during disposal at the site. Thus, it was necessary to input the observed concentration of contaminants for each element in the obtained natural state run. They were available on a mass fraction basis referred to the total mass of soil including the moisture content, whereas T2VOC requires the molar fraction of chemicals in the aqueous or gaseous phases according to the combination of phases present. The code was slightly modified to read initial chemical concentrations given in ppm over total mass and to convert them internally into the appropriate primary variable according to local porosity, water phase saturation and the mass fraction of organic carbon. The f_{oc} distribution was also determined by means of laboratory analysis both on soil and waste samples and accordingly used in the model.

SIMULATION OF PREVIOUS CONTAMINANT TRANSPORT

The reconstruction of site history pointed out that the disposal of wastes in zones 2, 3 and 4 began during the mid-seventies. Organic chemicals characteristic of the study area had already been detected in the ground water, proving that the transport of organic chemicals through the thick unsaturated zone had already affected the unconfined aquifer. On the other hand, the concentration distribution of organic chemicals was reasonably reconstructed only down to about 20 m depth, both because of the high costs involved and the decrease in chemicals concentration with depth, often below the detection limit of analytical methods used. The simulation of chemicals transport in the previous 20

years was then performed following the steps described below:

1. Simulation of chemical transport for 20 years through the unsaturated zone driven by infiltrating meteoric water and recharge from surface stream using the chemical distribution measured in the upper 20 m. Determination of the amount of chemicals flowing into the unconfined aquifer.
2. Considering that all the chemicals were initially contained only in the wastes, the estimated initial amount of chemicals was distributed among the elements representing the wastes, proportionally to the concentration measured in 1996.
3. The transport of chemical was then simulated from 1976, considered as the approximate beginning year, to 1996 using the reconstructed reasonable initial distribution of chemicals. The fraction of organic carbon was the only matching parameter used to reproduce the average chemical concentration measured in groundwater in 1996 downstream from the study area. It was slightly increased compared to the measured average values for deep rock domains for which limited experimental data were available. With respect to the measured distribution, the computed chemical distribution in 1996 pointed out the role of Garbogera stream in producing preferential downward flow of chemicals transported by the infiltrating water. This is clearly shown in Fig. 4 which presents the simulated concentration of chemicals in 1996 on the vertical section A3-B6 (concentrations are in ppm over total mass).

The simulated chemical distribution in 1996 represented the initial conditions for the forecast of chemical flux into the unconfined aquifer for additional 80 years in the absence of any remediation activity and following implementation of the planned remediation project.

FORECAST OF AROMATIC AMINES TRANSPORT

The forecast of chemical flux through the unsaturated zone was then performed both in the absence of interventions (no-actions option) and accounting for the described remediation measures. The simulation was extended for a period of 80 years from 1996 to 2076. The computed average concentration in the unconfined aquifer, assuming instantaneous mixing, is shown in Fig. 5 for the two different simulations as a function of time. With no remediation activities, the average chemical concentration in groundwater is expected to increase with time, reaching 1 ppb after about 30 years from the beginning of transport and 3 ppb after 100 years. As the target concentration is only 0.025 ppb, the simulation clearly pointed out the need to undertake remediation measures.

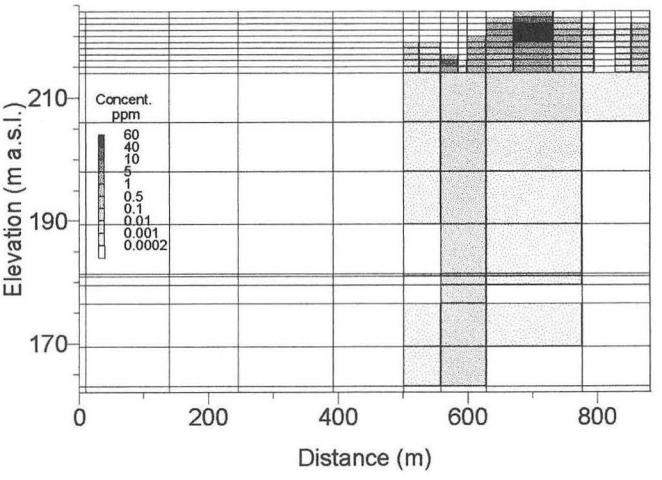

Fig. 4 Simulated N,N diethylaniline concentration in soil on the vertical section A3-B6 (year 1996).

When the effects of the planned remediation project were accounted for, the concentration of chemicals in ground water declined consistently during the first ten years owing to the reduction of water flow through the unsaturated zone due to surface capping. The concentration trend then flattens around a value of 0.02 ppb showing an increase at late time after about 50 years. The residual chemical flux is due to the reduction of water phase saturation below the capped area towards a gravity-capillarity equilibrium in the absence of recharge, and to the effects of lateral flows above the clay layer at 40 m depth which can convey the chemicals reaching this depth further downwards.

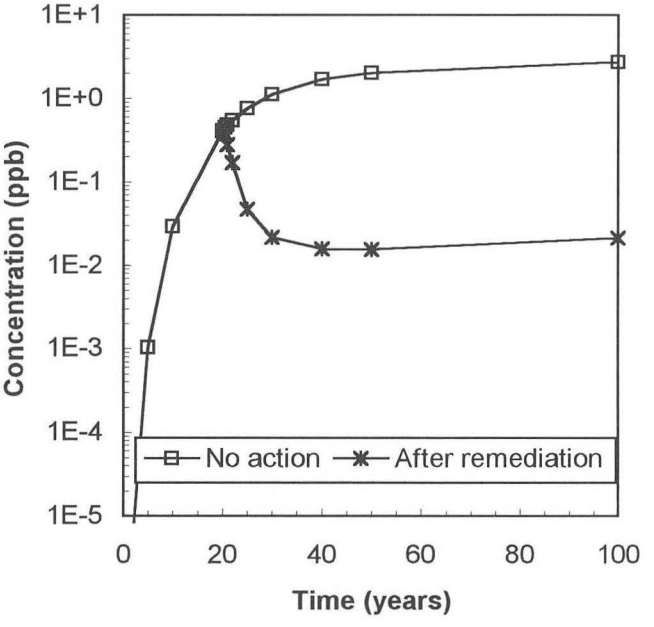

Fig. 5 Forecast of chemical concentration in ground water with and without the planned remediation

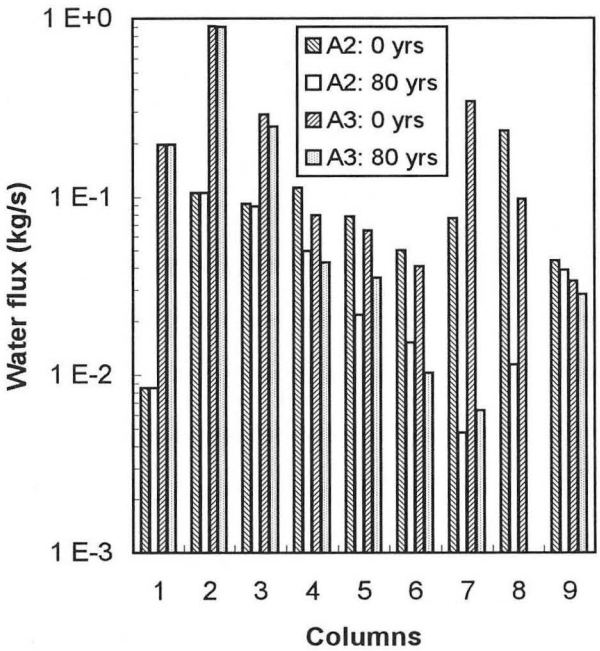

Fig. 6 Reduction of water flux across the water table after 80 years since the surface capping on vertical sections A2 and A3.

The presence of residual fluxes 80 years after the capping is clearly shown in Fig. 6 where the residual aqueous phase flux entering the aquifer surface is compared with the undisturbed flux on two vertical sections: the A2 and A3 sections. Fig. 6 shows that the capping mainly affects the grid columns from 4 to 8, with marginal influence on the other columns. The greatest effects are felt on columns 7 and 8, where most of wastes are located.

As regards the suggested increase of groundwater concentration at late time, it must be pointed out that the possible biodegradation of chemicals was neglected. This choice was based on the lack of reliable data regarding the biodegradation features of aromatic amines, and considering that conservative results were obtained in this way. Additional simulations considering a half life in the order of 100 years with the biodegradation described by the first order model presently implemented in the T2VOC code, suggested that no increase of chemical concentration at late time should be expected.

CONCLUSIONS

The simulation of chemical transport through the unsaturated zone after the execution of planned remediation activities confirmed the effectiveness of the designed measures in limiting future contamination of the unconfined aquifer.

Despite the complexity of hydrogeology in the thick unsaturated zone present in the subsurface of the study area, and the difficulties encountered in achieving proper characterization of this heterogeneous system, the numerical simulations provided a reasonable quantitative assessment of the effects of planned remediation activities.

As far as the performances of the T2VOC code are concerned, the study pointed out the need for a meshmaker capable of generating grids that follow the shape of sloping layers of varying thickness, in order to properly account for the sub-horizontal flow components that can occur in the unsaturated zone when low permeability sub-horizontal layers are present.

ACKNOWLEDGMENTS

The authors wishes to acknowledge EniChem SpA and Aquater SpA for their permission to publish the data included in this paper. Thanks are also due to several colleagues involved in the project activities who made possible the modeling study: F. Mattalia and L. Patata (project management), C. Luzi (chemistry) and G. Rossi (remediation project design).

REFERENCES

Aquater (1997). Cesano Maderno Ex-ACNA area: risk analysis on zones 2, 3, 4, 6. Numerical modeling of contaminant diffusion in the unsaturated zone and forecast of the effects of planned remediation measures. Aquater report 6002, Job 253400 (in Italian).

Falta R. W., Pruess K., Finsterle S. and Battistelli A. (1995). T2VOC User's guide. LBL-30758, Earth Science Division, Lawrence Berkeley National Laboratory, Berkeley, CA, March 1995.

Oldenburg C. M. and Pruess K. (1995). EOS7R: Radionuclide transport for TOUGH2. LBL-34868, Earth Science Division, Lawrence Berkeley National Laboratory, Berkeley, CA, November 1995.

Olsen R. L. and Davis A. (1990). Predicting the fate and transport of organic compounds in groundwater. HMCo May/June 1990, pp. 43-64.

Provincia di Milano (1995). Soil quality standards for the safeguard of ground waters. U.O. Tecnica Progetti Speciali (in Italian).

Stone H. L. (1972). Probability model for estimating three-phase relative permeability. Trans. SPE of AIME, Vol. 249, pp. 214-218.

Van Genuchten M. Th. (1980). A closed-form equation for predicting the hydraulic conductivity of unsaturated soils. Soil Sci. Soc. Am. J., Vol. 44, pp. 892-898.

NUMERICAL MODELING OF JP-8 REMEDIATION BY STEAM INJECTION INTO ARTIFICIAL FRACTURES IN A CLAY MATRIX.

Peter Kroopnick

Fluor Daniel GTI, Suite 700, 555 S. Renton Village Place, Renton, WA 98055
Phone 425-228-9645, Fax 425-228-9793, email pkroopnick@gtionline.com

Abstract

The in situ extraction of semivolatile hydrocarbons from low permeability soils requires extraordinary techniques such as extremely high vacuums, solvent flooding, or the injection of warm air. Fluid migration and associated mass transfer rates are very low in these cases and result in unacceptably close well spacings or long durations to achieve desired remediation goals. An alternative technique is the injection of steam to both increase the volatilization rate and flush the hydrocarbon from the pore spaces of the soil matrix.

We report here the results of from an Advanced Applied Technology Demonstration Facility (AATDF) project which investigated the effect of hydraulic fracturing and steam injection in order to develop a design and implementation guide to the remediation of semi-volatile contaminants in fine grained soils. This paper addresses numerical simulation experiments conducted to assist in selecting appropriate spacings for the fractures and the vapor extraction wells relative to the steam injection wells. In addition, the simulations will be used to gain a better understanding of the processes involved so that these pilot scale studies can be expanded to remediate larger areas.

Numerical experiments were carried in two dimensions represented by depth and distance (z,x). This domain, representing a depth of 6.2 meters and a distance of 7.5 meters was descritzed into a 27 by 21 matrix. Spacing between elements varied, with smaller horizontal spacings (0.25) adjacent to the sand layers and smaller vertical spacing (0.25) adjacent to the wells. The fractures themselves were 0.025 m. The matrix was assumed to be a homogeneous clay with extremely low permeability (K_h.=0.1 darcy, K_v =0.05 darcy) and an effective porosity of 10%. Steam injection was simulated by adding water with an enthalpy of 2.66×10^6 J/Kg directly to the appropriate elements. Under most conditions, this resulted in a temperature of approximately 107^EC at the injection point. Vacuum extraction wells were simulated using the On Deliverability well type, with a production index of 2×10^{-12}.

The numerical simulation of the injection of steam into a narrow sand fracture surrounded by a clay matrix, was found to be extremely sensitive to the initial water saturation conditions. In addition, the rapid changes in water saturation and temperature that ensue as the steam front propagates through the media resulted in many non-convergent simulations. Results from the numerical simulation experiments for varying fracture spacing and differing scenarios for the vacuum and injection rates will be presented. The simulations will be compared with actual field data to demonstrate that the steam can be focussed to increase the area (volume) raised to above 75 ^{E}C. For sites where the production of steam is expensive, configurations which minimizes amount of steam while maximizing the heating are proposed.

The experimental results clearly demonstrate that steam injection through artificially created fractures is an effective process for the remediation of volatile and semi-volatile hydrocarbons in low permeable environments. Vapor extraction without the accompaniment of steam was not possible due to the low permeability of the soil. Thus, using the combined process of hydro-fracturing and steam heating, the TPH as JP8 concentrations, within the treated areas to a depth of 20 feet, were reduced from between 2,000 and 7,000 mg/kg to less than 300 mg/kg in about 3 months.

NUMERICAL MODELING OF JP-8 REMEDIATION BY STEAM INJECTION INTO ARTIFICIAL FRACTURES IN A CLAY MATRIX

Dr. Peter Kroopnick, Principal Hydrogeologist
Peter Pope, Senior Hydrogeologist
Jay Dablow, Project Manager
May, 1998

Fluor Daniel GTI, Renton, WA
pkroopnick@gtionline.com

AATDF FRACTURE/STEAM DEMONSTRATION PROJECT
Fort Hood, TX

FLUOR DANIEL GTI

Model for Subsurface Heating by Steam Injection

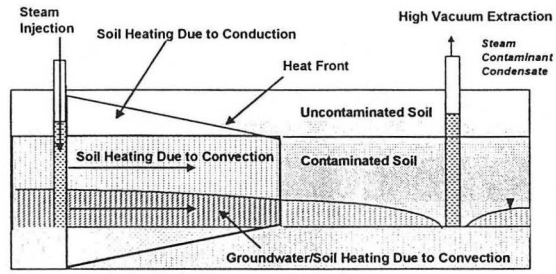

FLUOR DANIEL GTI

Steam Injection Technology Description

- Steam is injected into vadose and saturated zone to heat the soils by forced convection
  - ✔Increases semi-volatile vapor pressure
  - ✔Decreases viscosity
  - ✔Decreases interfacial tension and residual saturation
- Steam generated by on site source
- Target Temperature = 212° F

FLUOR DANIEL GTI

Technology Description
Essential Elements

- **Heat Transfer to Soil**
  - Forced Convection
  - Conduction (Heat Loss)
- **Vapor Pressure Increase**
  - Faster VOC Removal
  - Semivolatile Removal
- **Viscosity Reduction**
  - Increase Heavy Oil Mobility
  - Easier Free Product Pumping
- **Thermal Desorption**
  - Steam Distillation
  - Reduced Interfacial Tension
  - Reduced Residual Saturation
- **Thermal Enhancement Methods**
  - Hot Air Injection
  - Steam Injection
  - RF Heating

FLUOR DANIEL GTI

Kinematic Viscosity Vs Temperature
ASTM D-445 Results

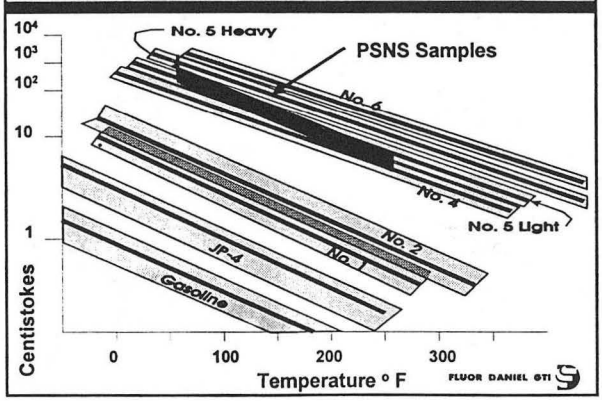

FLUOR DANIEL GTI

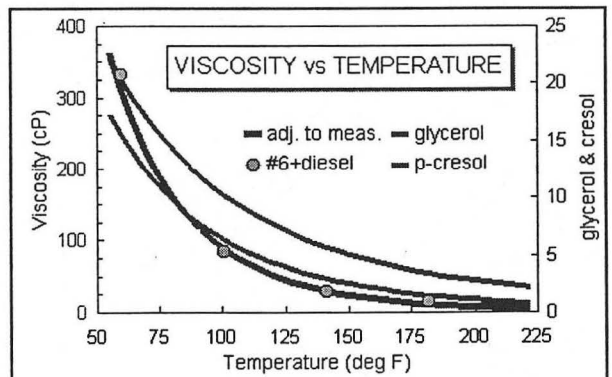

The effect of temperature on the viscosity of several hydrocarbons.
Note that water has a value of 1.0 and that glycerol and cresol are plotted on the right axis, while that for the #6 fuel refers to the left axis.

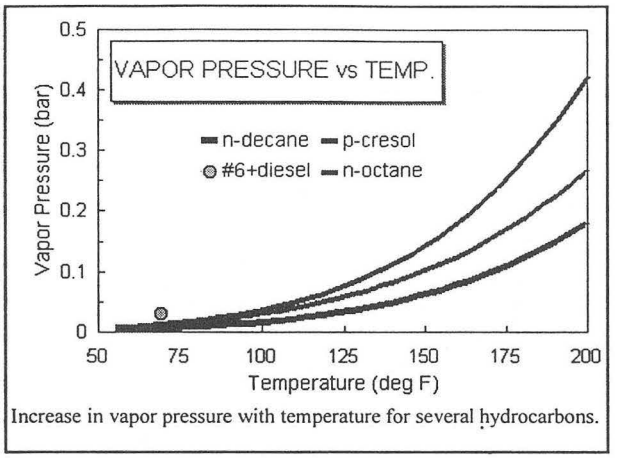

Increase in vapor pressure with temperature for several hydrocarbons.

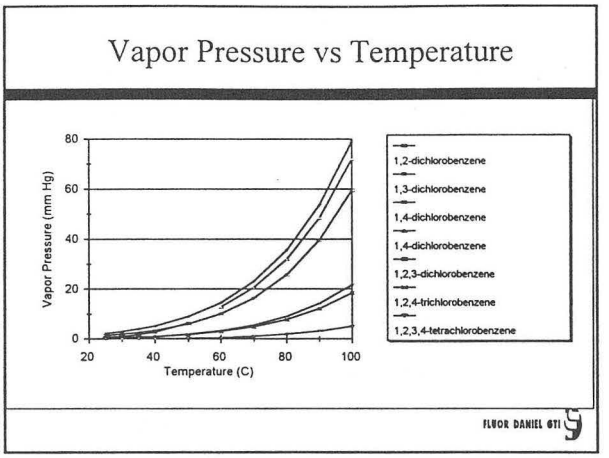

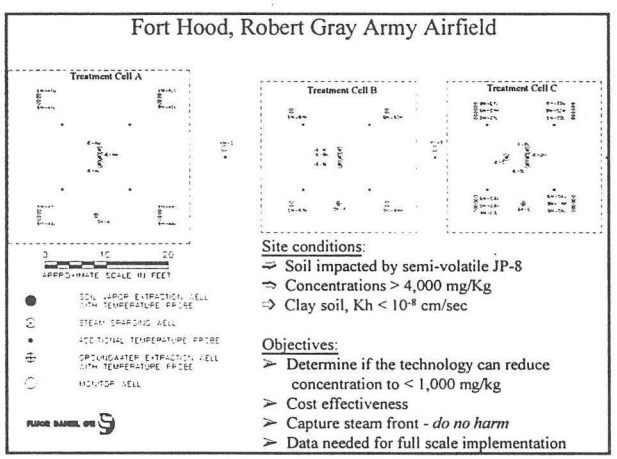

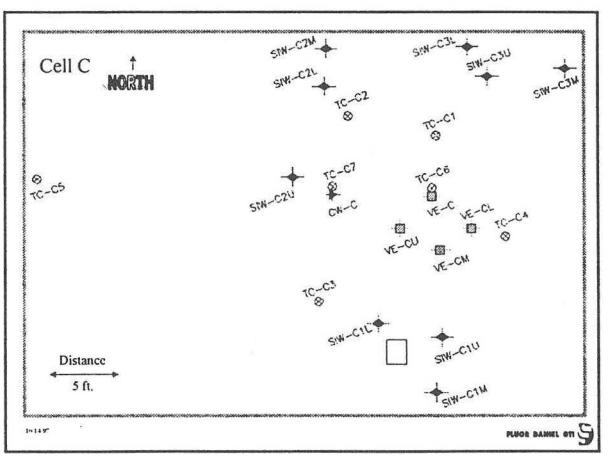

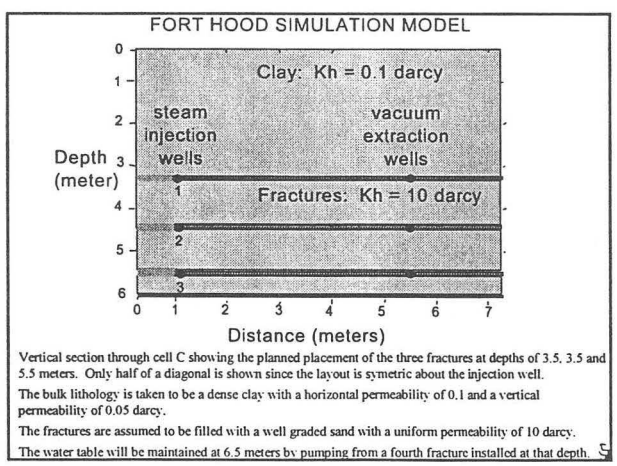

Vertical section through cell C showing the planned placement of the three fractures at depths of 3.5, 3.5 and 5.5 meters. Only half of a diagonal is shown since the layout is symetric about the injection well.

The bulk lithology is taken to be a dense clay with a horizontal permeability of 0.1 and a vertical permeability of 0.05 darcy.

The fractures are assumed to be filled with a well graded sand with a uniform permeability of 10 darcy.

The water table will be maintained at 6.5 meters by pumping from a fourth fracture installed at that depth.

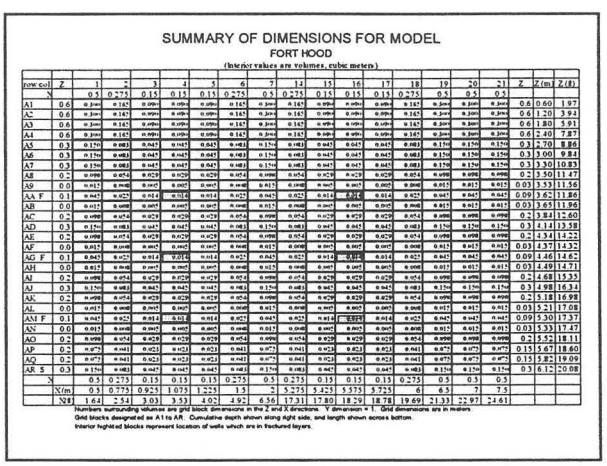

SUMMARY OF DIMENSIONS FOR MODEL

FORT HOOD

(Interior values are volumes, cubic meters)

row col	Z	1	2	3	4	5	6	7	15	16	17	18	19	20	21	Z	Z (m)	Z (ft)
	X	0.5	0.275	0.15	0.15	0.15	0.275	0.5	0.275	0.15	0.15	0.15	0.275	0.5	0.5	0.5			
A1	0.6	0.300	0.165	0.090	0.090	0.090	0.165	0.300	0.165	0.090	0.090	0.090	0.165	0.300	0.300	0.300	0.6	0.60	1.97
A2	0.6	0.300	0.165	0.090	0.090	0.090	0.165	0.300	0.165	0.090	0.090	0.090	0.165	0.300	0.300	0.300	0.6	1.20	3.94
A3	0.6	0.300	0.165	0.090	0.090	0.090	0.165	0.300	0.165	0.090	0.090	0.090	0.165	0.300	0.300	0.300	0.6	1.80	5.91
A4	0.6	0.300	0.165	0.090	0.090	0.090	0.165	0.300	0.165	0.090	0.090	0.090	0.165	0.300	0.300	0.300	0.6	2.40	7.87
A5	0.3	0.150	0.083	0.045	0.045	0.045	0.083	0.150	0.083	0.045	0.045	0.045	0.083	0.150	0.150	0.150	0.3	2.70	8.86
A6	0.3	0.150	0.083	0.045	0.045	0.045	0.083	0.150	0.083	0.045	0.045	0.045	0.083	0.150	0.150	0.150	0.3	3.00	9.84
A7	0.3	0.150	0.083	0.045	0.045	0.045	0.083	0.150	0.083	0.045	0.045	0.045	0.083	0.150	0.150	0.150	0.3	3.30	10.83
A8	0.2	0.098	0.054	0.029	0.029	0.029	0.054	0.098	0.054	0.029	0.029	0.029	0.054	0.098	0.098	0.098	0.2	3.50	11.47
A9	0.0	0.015	0.008	0.005	0.005	0.005	0.008	0.015	0.008	0.005	0.005	0.005	0.008	0.015	0.015	0.015	0.03	3.53	11.56
AA F	0.1	0.045	0.025	0.014	0.014	0.014	0.025	0.045	0.025	0.014	0.014	0.014	0.025	0.045	0.045	0.045	0.09	3.62	11.86
AB	0.0	0.015	0.008	0.005	0.005	0.005	0.008	0.015	0.008	0.005	0.005	0.005	0.008	0.015	0.015	0.015	0.03	3.65	11.96
AC	0.2	0.098	0.054	0.029	0.029	0.029	0.054	0.098	0.054	0.029	0.029	0.029	0.054	0.098	0.098	0.098	0.2	3.84	12.60
AD	0.3	0.150	0.083	0.045	0.045	0.045	0.083	0.150	0.083	0.045	0.045	0.045	0.083	0.150	0.150	0.150	0.3	4.14	13.58
AE	0.2	0.098	0.054	0.029	0.029	0.029	0.054	0.098	0.054	0.029	0.029	0.029	0.054	0.098	0.098	0.098	0.2	4.34	14.22
AF	0.0	0.015	0.008	0.005	0.005	0.005	0.008	0.015	0.008	0.005	0.005	0.005	0.008	0.015	0.015	0.015	0.03	4.37	14.32
AG F	0.1	0.045	0.025	0.014	0.014	0.014	0.025	0.045	0.025	0.014	0.014	0.014	0.025	0.045	0.045	0.045	0.09	4.46	14.62
AH	0.0	0.015	0.008	0.005	0.005	0.005	0.008	0.015	0.008	0.005	0.005	0.005	0.008	0.015	0.015	0.015	0.03	4.49	14.71
AI	0.2	0.098	0.054	0.029	0.029	0.029	0.054	0.098	0.054	0.029	0.029	0.029	0.054	0.098	0.098	0.098	0.2	4.68	15.35
AJ	0.3	0.150	0.083	0.045	0.045	0.045	0.083	0.150	0.083	0.045	0.045	0.045	0.083	0.150	0.150	0.150	0.3	4.98	16.34
AK	0.2	0.098	0.054	0.029	0.029	0.029	0.054	0.098	0.054	0.029	0.029	0.029	0.054	0.098	0.098	0.098	0.2	5.18	16.98
AL	0.0	0.015	0.008	0.005	0.005	0.005	0.008	0.015	0.008	0.005	0.005	0.005	0.008	0.015	0.015	0.015	0.03	5.21	17.08
AM F	0.1	0.045	0.025	0.014	0.014	0.014	0.025	0.045	0.025	0.014	0.014	0.014	0.025	0.045	0.045	0.045	0.09	5.30	17.37
AN	0.0	0.015	0.008	0.005	0.005	0.005	0.008	0.015	0.008	0.005	0.005	0.005	0.008	0.015	0.015	0.015	0.03	5.33	17.47
AO	0.2	0.098	0.054	0.029	0.029	0.029	0.054	0.098	0.054	0.029	0.029	0.029	0.054	0.098	0.098	0.098	0.2	5.52	18.11
AP	0.2	0.072	0.041	0.023	0.023	0.023	0.041	0.072	0.041	0.023	0.023	0.023	0.041	0.072	0.072	0.072	0.15	5.67	18.60
AQ	0.2	0.072	0.041	0.023	0.023	0.023	0.041	0.072	0.041	0.023	0.023	0.023	0.041	0.072	0.072	0.072	0.15	5.82	19.09
AR S	0.3	0.150	0.083	0.045	0.045	0.045	0.083	0.150	0.083	0.045	0.045	0.045	0.083	0.150	0.150	0.150	0.3	6.12	20.08
	X	0.5	0.275	0.15	0.15	0.15	0.275	0.5	0.275	0.15	0.15	0.15	0.275	0.5	0.5	0.5			
	X(m)	0.3	0.775	0.925	1.075	1.225	1.5	2	5.275	5.425	5.575	5.725	6	6.3	7	7.3			
	X(ft)	1.64	2.54	3.03	3.53	4.02	4.92	6.56	17.31	17.80	18.29	18.78	19.69	21.33	22.97	24.61			

Numbers surrounding volumes are grid block dimensions in the Z and X directions. Y dimension = 1. Grid dimensions are in meters.
Grid blocks designated as A1 to AR. Cumulative depth shown along right side, and length shown across bottom.
Interior highlited blocks represent location of wells which are in fractured layers.

MODEL PARAMETERS

PARAMETER	CLAY	SAND	FLUID
Permeability, horizontal (m2)	1E-13	1E-11	
Permeability, vertical (m2)	5E-14	1E-11	
Porosity (%)	10	30	
Rock density (Kg/m3)	2650	2650	1000
Heat conductivity, sat (W/m-C)	0.7	3.1	0.6
Heat conductivity, unsat (W/m-C)	0.1	0.04	
Sp. heat capacity (J/Kg-C)	1120	1000	4200
Steam enthalpy (J/Kg)			2.77E+06
Compressability (m2/N)	0	0	
Expansivity (1/C)	0	0	
Tortuosity factor	0	0	
Production Index (m3)			2E-12
Relative permeability	**Modified Stone 3 phase**	**Completely mobile**	
S(wr)	0.2		
S(nr)	0.05		
S(gr)	0.01		
n	3		
Capillary pressure	**Parker, 3 phase**	**Parker, 3 phase**	
S(m)	0.2	0	
n	1.86	1.84	
a(gn)	10.8	9.9	
a(nw)	6	11	

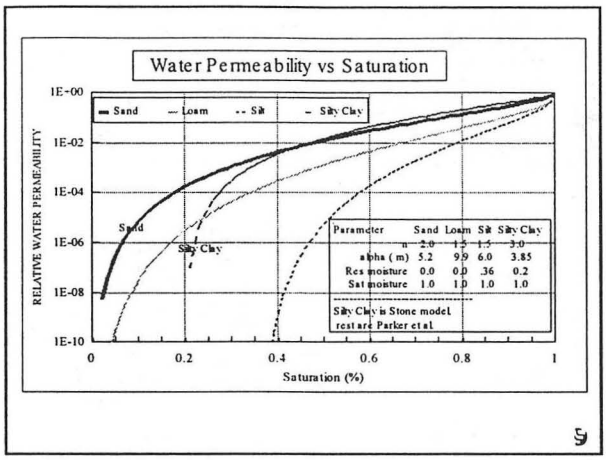

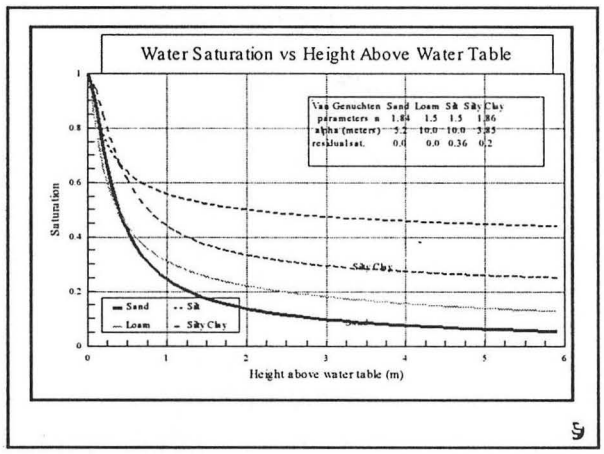

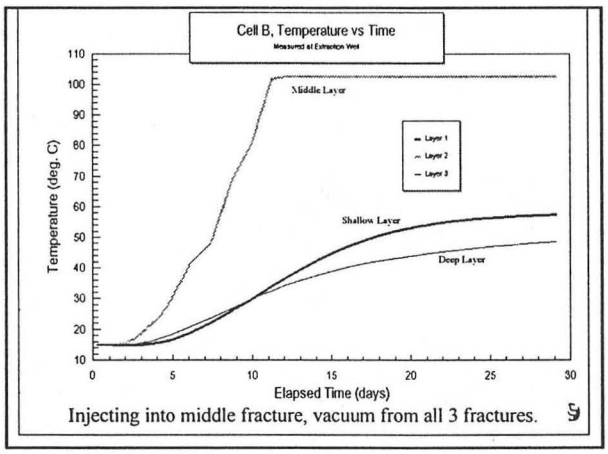

Injecting into middle fracture, vacuum from all 3 fractures.

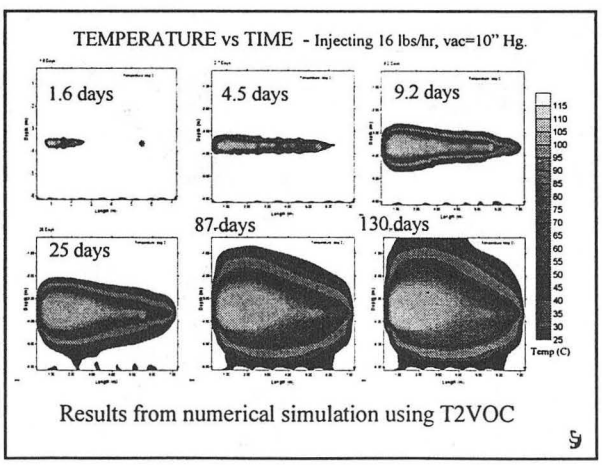

Results from numerical simulation using T2VOC

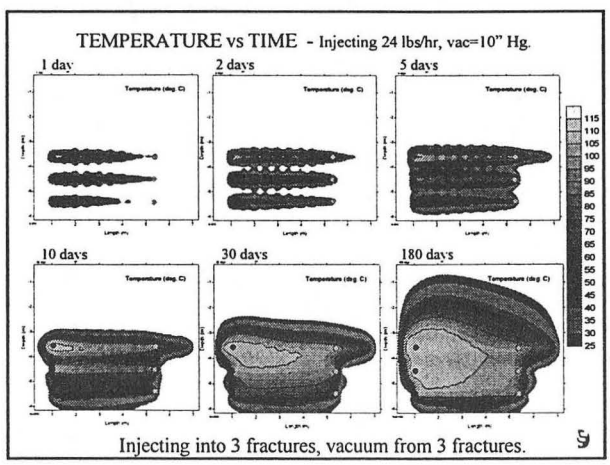

Injecting into 3 fractures, vacuum from 3 fractures.

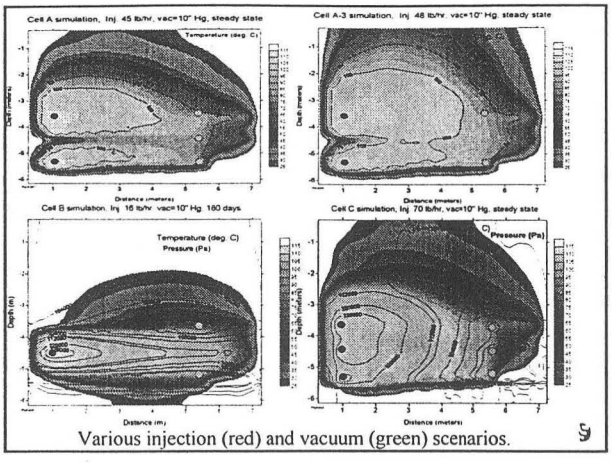

Various injection (red) and vacuum (green) scenarios.

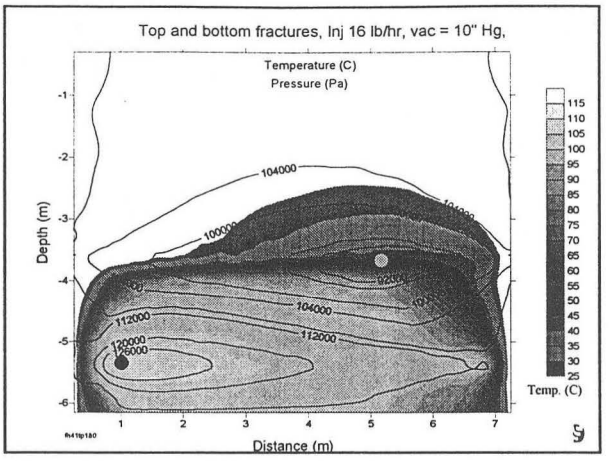

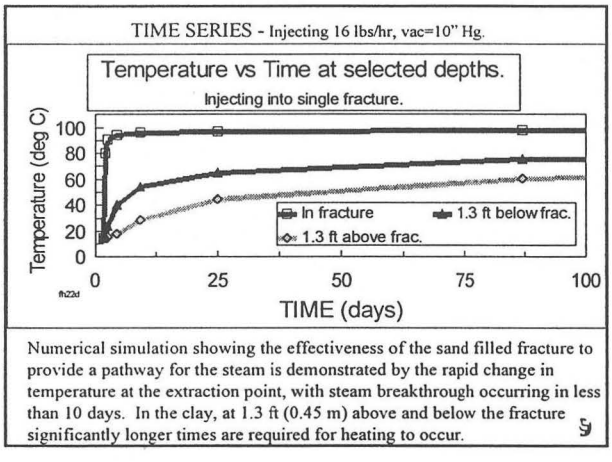

Numerical simulation showing the effectiveness of the sand filled fracture to provide a pathway for the steam is demonstrated by the rapid change in temperature at the extraction point, with steam breakthrough occurring in less than 10 days. In the clay, at 1.3 ft (0.45 m) above and below the fracture significantly longer times are required for heating to occur.

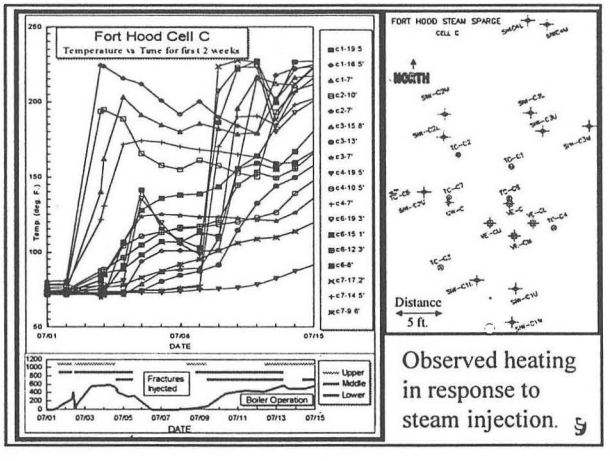

Observed heating in response to steam injection.

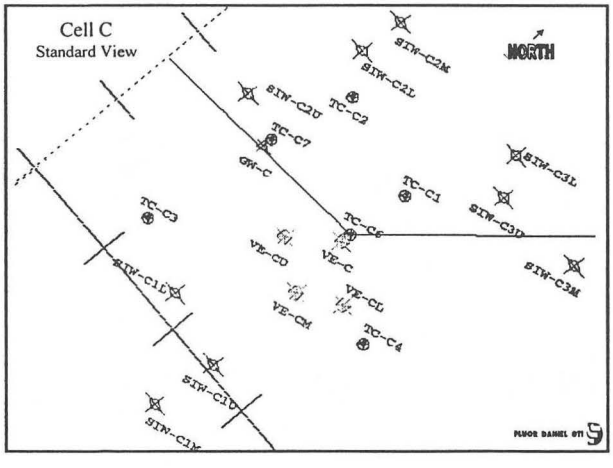

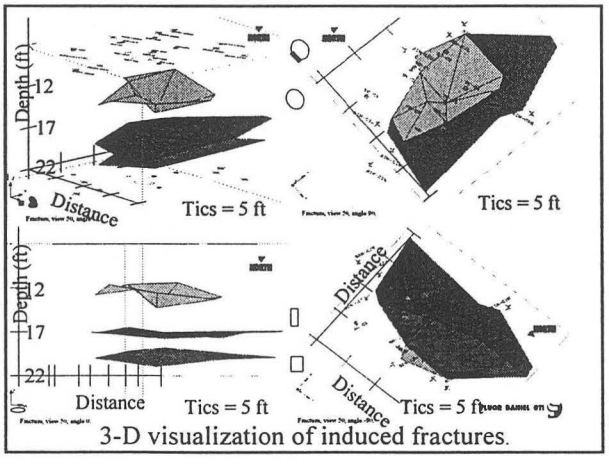

3-D visualization of induced fractures.

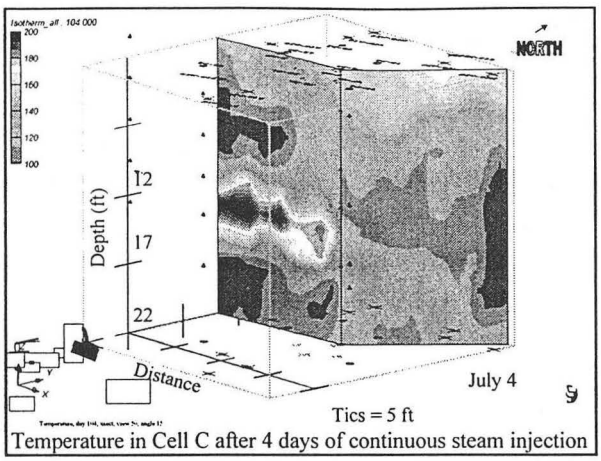

Temperature in Cell C after 4 days of continuous steam injection

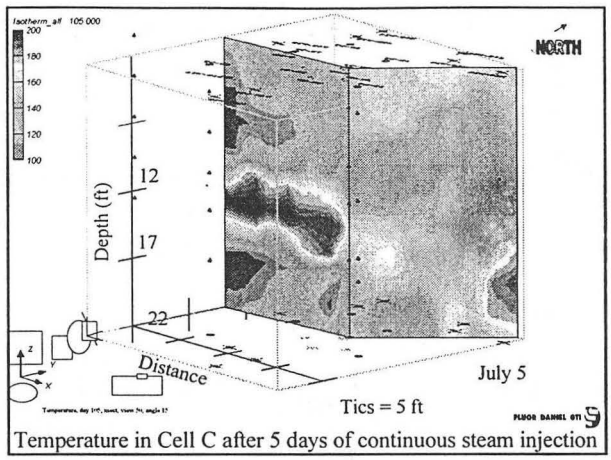

Temperature in Cell C after 5 days of continuous steam injection

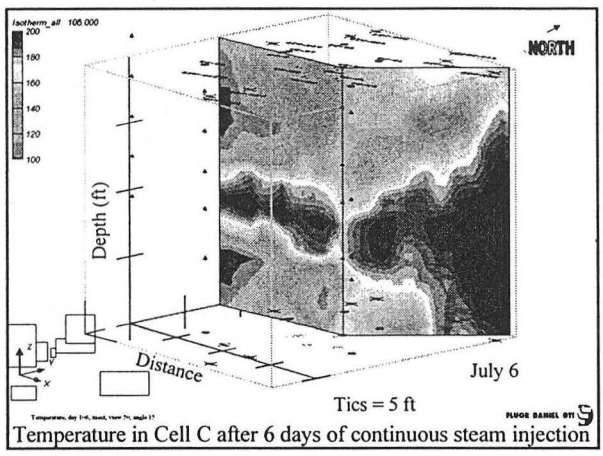

Temperature in Cell C after 6 days of continuous steam injection

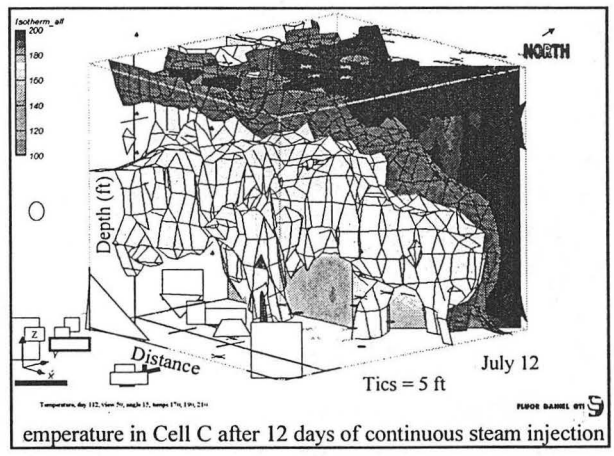

emperature in Cell C after 12 days of continuous steam injection

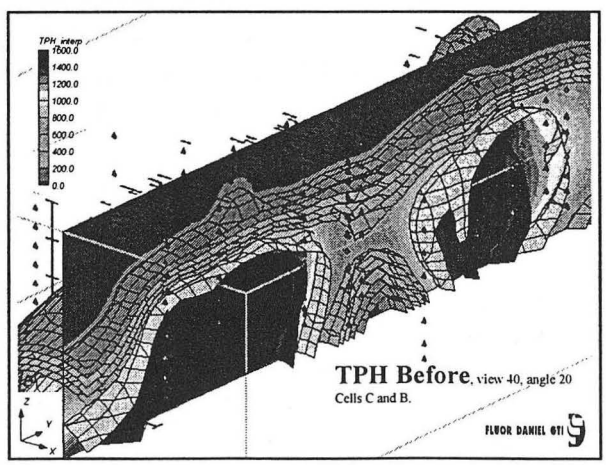

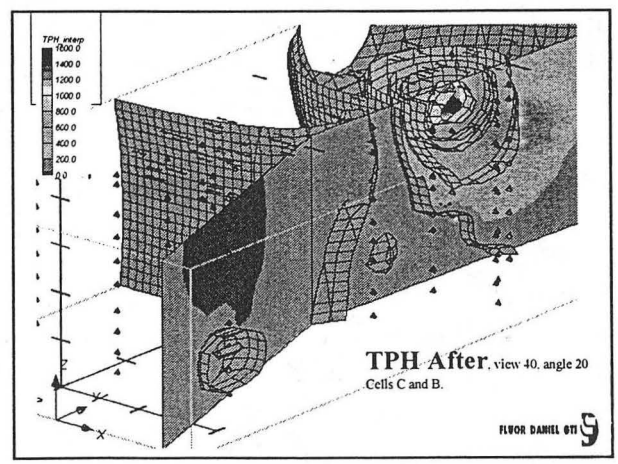

Predicting the Fate of Trichloroethylene and Its Daughters in a Heterogeneous Environment

Mark J. Lupo

KW Brown Environmental Science & Engineering
13101 Northwest Freeway Suite 314, Houston, TX 77040

George J. Moridis

Earth Sciences Division, Lawrence Berkeley National Laboratory
University of California, Berkeley, CA 94720

Kirk W. Brown

Soil and Crop Sciences Department
Texas A&M University, College Station, TX 77843

Introduction

The T2VOC model (Falta, et al., 1995) was used to simulate the motion of chlorinated hydrocarbons released to the groundwater over a period of years from an industrial plant. This included thousands of kilograms of trichloroethylene (TCE) as well as other solvents and several kinds of alcohol. Anaerobic dehalogenation of chlorinated alkenes is favored in the presence of alcohol. All three isomers of dichloroethylene (DCE) and vinyl chloride were detected in the analytical field data. Using T2VOC in its standard form would allow one to estimate the motion of TCE and its daughters as a single species. However, to account for TCE and the daughter constituents in an individual way required two code modifications.

Code Modifications

First, the biodegradation rate of TCE differed from one part of the domain to another. Dehalogenation was fastest in the presence of high concentrations of dissolved-phase alcohol that occurred in a zone from 10 m upgradient to more than 200 m downgradient from the point of discharge. In the rest of the saturated zone, as well as in the entire vadose zone, the rate of dehalogenation was about one-tenth as great. In the underlying bedrock, the biodegradation rate was virtually zero. In the presence of nonaqueous phase liquids (NAPL) or at very high dissolved-phase concentrations of solvents, the biodegradation rates were likewise zero due to the toxicity of these constituents to the microorganisms that perform the biotransformation work. Thus, it was desirable to be able to assign more than one biodegradation rate to the constituent and to let it vary by grid block. Such a modification was accomplished in this study. In the CHEMP block, the parameter ALAM was replaced by six decay constants, ALAM-1 through ALAM-6. In ELEME, a new input was added for every grid block. This integer variable assigned the appropriate ALAM value to the specific grid block to be the local degradation rate. With this modification, the fate and transport of the parent constituent could be better modeled.

To allow for the modeling of the daughters, a second modification was needed. This modification counted the number of parent molecules destroyed in each grid block and recorded

them in a file named DAUGTR. In the code modification, the molecular weight of the daughter constituent was a new input in the CHEMP module. Thus, the mass reported in DAUGTR was the created mass of the daughter. For example, if TCE was converted to DCE, the ratio of the two molecular weights was used to account for the mass loss from the chlorine atom that was lost from each transformed TCE molecule. The DAUGTR file also contained the length of time of the T2VOC run. After the model run, a new program was used to calculate generation rates for the daughter in each grid block. These values were printed in GENER format and added to the data in a separate file that represented deep percolation of water into the domain, thus creating a GENER file for the next T2VOC run. In that run, there was a source of the daughter constituent in every grid block in which biotransformation had occurred in the last run. The rate of generation was determined such that the creation rate would match the decay from the previous run by mole.

Procedure

To solve a practical problem of an industrial release of TCE, a three-dimensional grid was devised. The grid represented a tilted system of rectangular blocks. Because the entry of soil gas into residences was a potential issue, every column of grid blocks had an atmospheric block at its top. The stratigraphy was relatively simple, with a sandy soil underlain by fractured bedrock. The petrophysical parameters for each layer were determined by a field study. Dynamic steady state was obtained for this grid. The source and its history were determined from records kept by the management of the industrial plant. The subsurface emission occurred at several locations and the amount of the loss differed from year to year. Therefore, separate T2VOC runs were needed for each year with different values for the sources in GENER for the given year of the release. Following this, runs were conducted for the subsequent years to study the evolution of the plume.

A preliminary run was conducted for the release of TCE without accounting for biodegradation. This run helped to determine which grid blocks would have NAPL. Blocks containing the NAPL were recorded on a list. A second preliminary run was conducted in which alcohol was released for two years at its maximum rate. The purpose of this run was to determine which grid blocks were likely to contain sufficient levels of alcohol to more rapidly degrade TCE. Any block with an alcohol concentration of 100 mg/L at the end of two years was recorded on a list (Figure 1). It was experimentally determined that the biodegradation of TCE at this site was enhanced by a factor of ten when alcohol was present at about 100 mg/L. Now the TCE release could be simulated. Three biodegradation rates were assigned. Any block within the bedrock was assigned a biodegradation rate of zero. Any grid block in which a NAPL was recorded to be present was also assigned a zero biodegradation rate. Grid blocks below the water table with more than 100 mg/L alcohol in the special alcohol run discussed above were given a high degradation rate, unless NAPL was present. All other blocks were assigned a biodegradation rate one order of magnitude lower than the experimental value. Field data revealed the presence of DCE even though there were no records of DCE ever being used at the plant in large quantities. This suggested that the DCE being detected in monitor wells was a daughter of TCE degradation. The predominant isomer detected was cis-1,2-dichloroethylene. Thus, to simplify the modeling procedure, all TCE destroyed by biodegradation was assumed to have been transformed into cis-1,2-dichloroethylene, which will be referred to as DCE in the remainder of this paper.

The modified code produced a new file that gave the mass of the DCE produced in each grid block. The new file was converted into GENER format. Thus a GENER file was produced for each year of the TCE simulation. Thus a set of DCE runs could be undertaken with the DCE created from the biodegradation of TCE being the unique source of DCE. From these runs, an experimentally determined value was used for the biodegradation of DCE into vinyl chloride. The same set of years was modeled to give a history of the motion of DCE and a set of GENER files that would allow the modeling of vinyl chloride. Lastly, a set of runs was conducted to give a history of the transport of vinyl chloride.

Results

The first simulations with this code modification did not succeed. There were problems in grid blocks with very high concentrations of the parent constituent, leading to unrealistically high generation rates of the daughter compound. To correct this problem, the biodegradation/biogeneration rates were reduced in these specific grid blocks. The model behaved much better with a low value for degradation in such grid blocks. Eventually, it was considered simpler to set the decay constant to zero for these blocks.

A second concern was the build-up of vinyl chloride. The biodegradation rate had initially been set to a very low rate. Any degradation rate for vinyl chloride that was lower than that for DCE seemed to lead to an increase in concentration that was hard to believe. Vinyl chloride did not seem to be volatilizing and migrating out of the domain as quickly as expected. Thus, the degradation rate of vinyl chloride was increased to that of DCE.

With these adjustments, the simulation was run to completion (Figures 2 – 4). After just nine years, the T2VOC model predicted groundwater concentrations of TCE at the ppm level 700 m from the source. The model predicted groundwater concentrations of TCE and DCE at the level of parts per million (ppm) more than one kilometer from the source several years later. It also predicted unacceptably high fluxes of soil gas into the dwellings of residents nearly one mile from the release. Predictions of TCE and DCE at later times when data were available were consistent with soil gas and groundwater monitoring data. However, the predicted vinyl chloride concentrations were too high. Some of the problem could be due to the age of the data and the possibility that there were inaccuracies in measuring this highly volatile species.

Discussion

Attempts to calibrate a model like T2VOC to groundwater analytical data are always difficult due to variability in soil conditions on a scale that is often too fine to simulate in a model. The problem is even more difficult in a multiconstituent simulation with the generation of daughters. In a one-species simulation, the biodegradation rate and the source term may be among the most important calibration parameters. If a model over-predicts field-measured concentrations, one can obtain the same result by lowering the estimate of the source term or by increasing the biodegradation rate. In a multichemical simulation with daughter generation, the method of calibration makes a large difference. Reducing the estimate of a source term to calibrate for TCE may reduce the strength of the DCE below field measurements. Increasing biodegradation will reduce TCE concentrations while increasing DCE and vinyl chloride.

The biodegradation rates were such that the constituents had half-lives in the presence of alcohol of 70 to 100 days. The time step in a model run one-year long can approach one month

in length or longer depending on how the maximum time step is limited. Thus it would be possible to have a time step that was more than half of the biological half-life of a constituent. To prevent too much error from entering into the computation, it is recommended that the maximum time step (DELTMX) be limited to one-fourth of the shortest constituent half-life of the six implied by the decay constants presented in the ALAM array.

Another potential source of error in this methodology is introduced by the linearity of the daughter generation function. The first-order degradation of an organic chemical is modeled by T2VOC as an exponential function of time. Although the total moles of parent destroyed in a runtime unit (one year) was set equal to that which was created, it should be noted that the total number of moles in the domain during a simulation will be less than the expected total in the middle of a run. For example, if you have two functions,

$$y_1 = e^{-t}$$

and

$$y_2 = at$$

where t is time and a is the reciprocal of e, the sum of y_1 and y_2 is always less than one over the range of zero to one except at the endpoints. It reaches a minimum at $t = 0.459$ of 0.922. This error may be acceptable given the uncertainties in the inputs. However, it may be possible under some set of circumstances for this small amount of error to lead to underestimates of the transport of the daughter.

Conclusion

Simulations were run with this modified code for TCE, DCE, and vinyl chloride in sequence. Each of the simulations was composed of a set of model runs, each one-year long. Given the limitations in the field data, there was a good match for the TCE and the DCE data with the T2VOC output. Vinyl chloride generated in the model exceeded the values measured in the field, but this could be due in large part to the difficulties in accurately measuring this extremely volatile species.

Successfully predicting the concentration of a degradable constituent and a string of daughter compounds places a high demand on the quality of the biodegradation data. However, without the ability to vary the degradation rate in a large domain, or the ability to allow the generation at continuous points in time, it could be impossible to simulate the fate and transport of a daughter constituent with accuracy of T2VOC in its simultaneous handling of several phases, components, and transport mechanisms. These two code modifications bring this goal within the reach of a mathematical modeler.

References

Falta, R. W., K. Pruess, S. Finsterle, and A. Battistelli, 1995, T2VOC User's Guide, Lawrence Berkeley Laboratory, Berkeley, CA, LBL-36400.

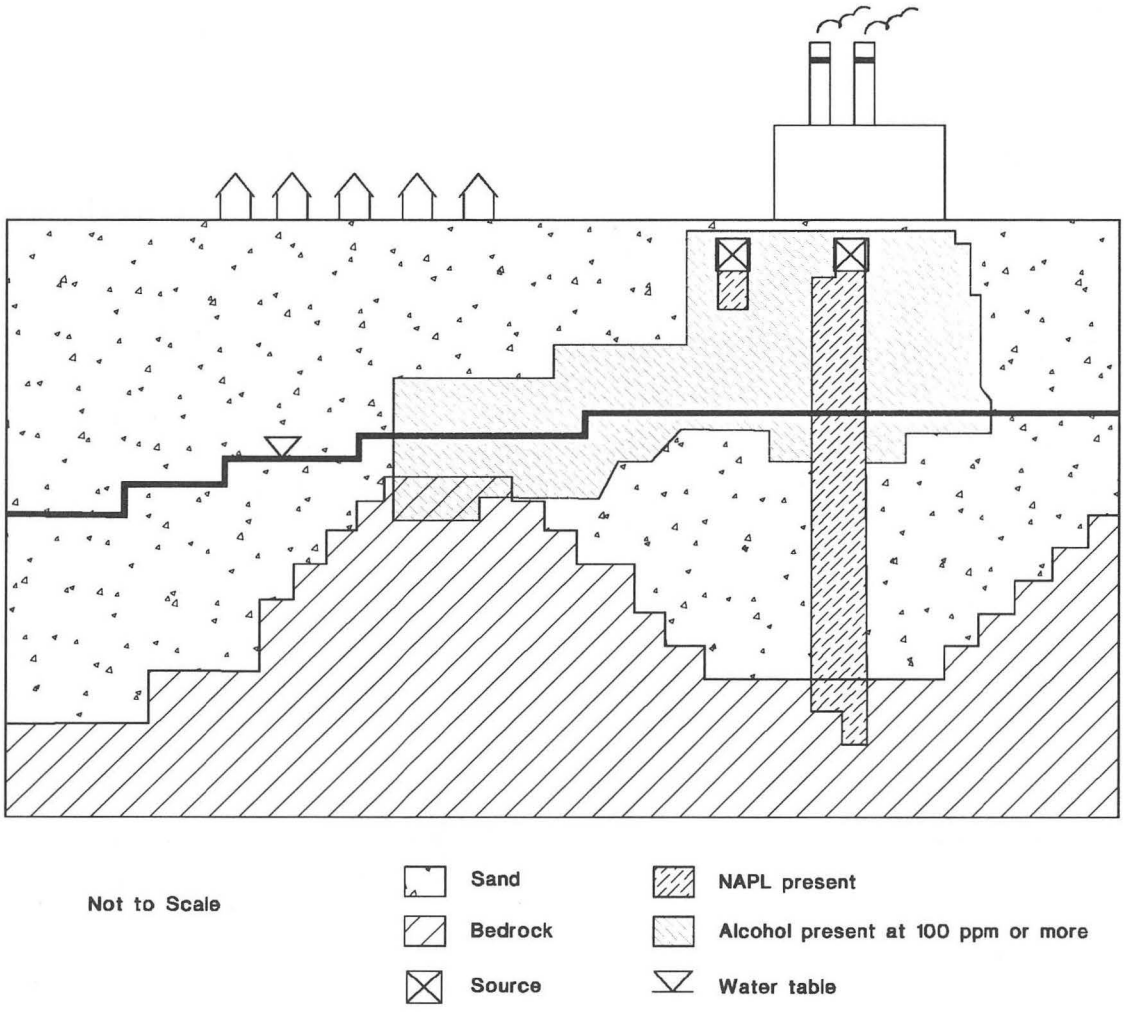

Figure 1. Schematic of the Site Grid.

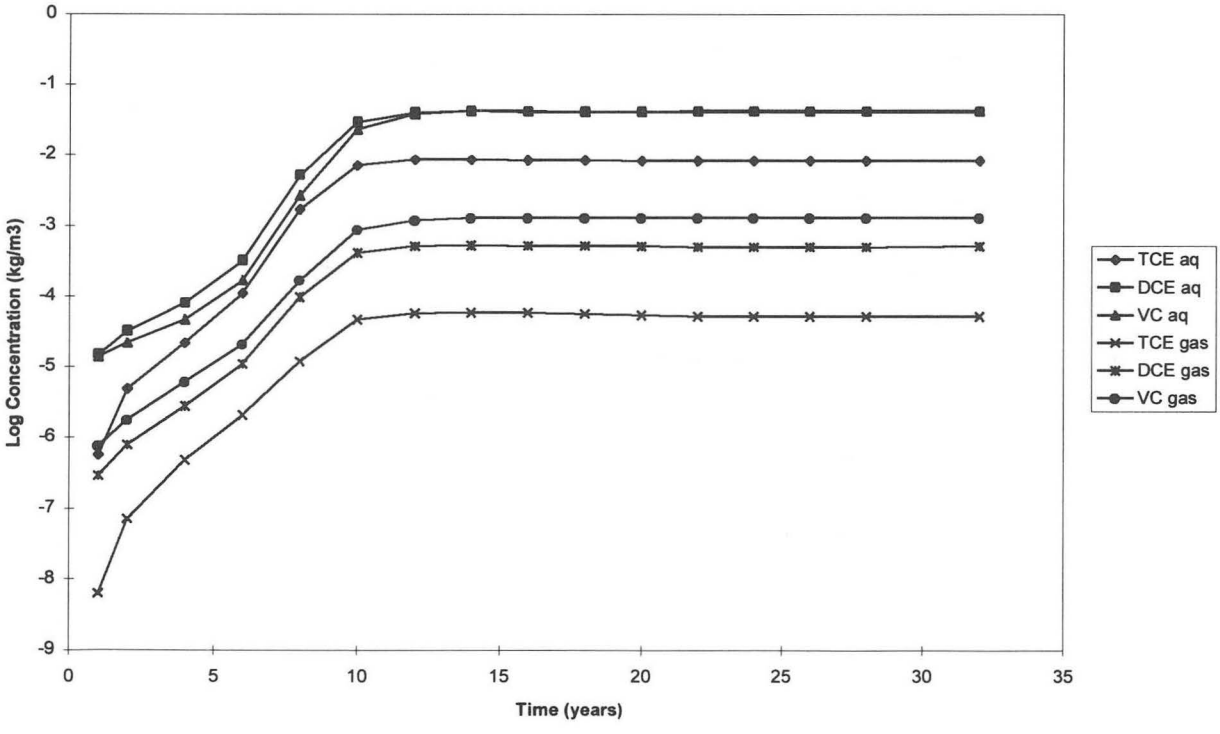

Figure 2. Groundwater Concentration History of a Water Table Grid Block 200 m from the Source with Soil Gas Concentration at the Surface.

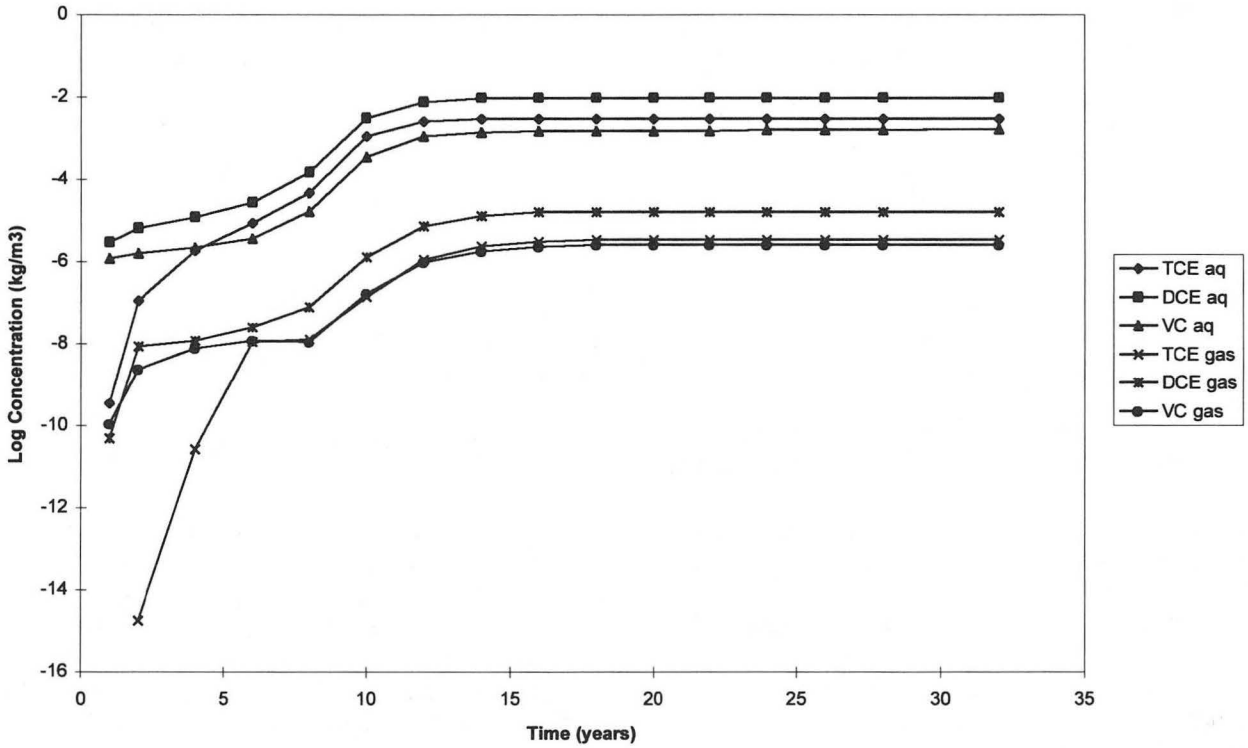

Figure 3. Groundwater Concentration History of a Water Table Grid Block 500 m from the Source with Soil Gas Concentration at the Surface.

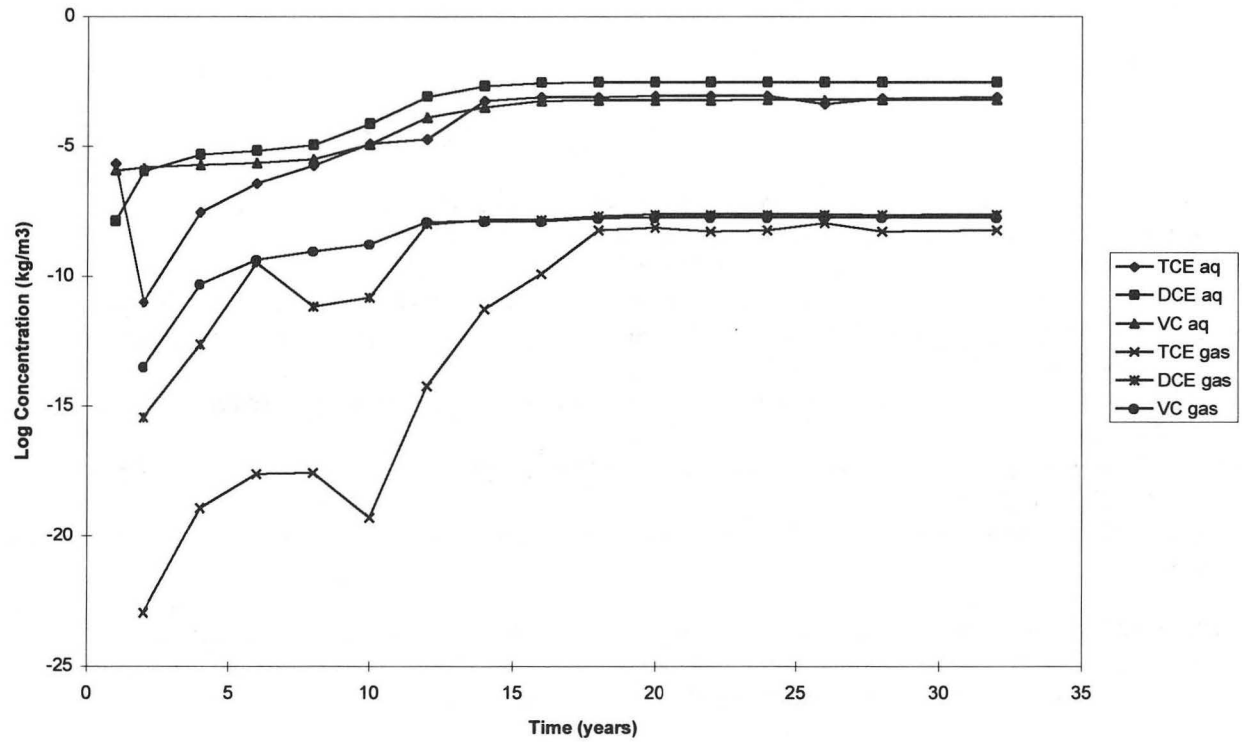

Figure 4. Groundwater Concentration History of a Water Table Grid Block 700 m from the Source with Soil Gas Concentration at the Surface.

T2VOC Simulation and Optimization of SVE System Pulse Pumping of Vadose Zone Carbon Tetrachloride Contamination at the Idaho National Engineering and Environmental Laboratory

Patrick J. Schwind[1] and Eric C. Miller[2]

INTRODUCTION

Vadose zone vapor and aqueous phase carbon tetrachloride contamination beneath an Idaho National Engineering and Environmental Laboratory (INEEL) subsurface disposal area, due to evaporation, diffusion and density-driven flow of vapor, and aqueous phase advection from breached barrels of nonaqueous phase waste, is being remediated with a SVE system. The unsaturated zone in the area of interest consists of fractured basalt intercalated with thin, relatively impermeable sedimentary interbeds. This study focused on a contaminated zone, approximately 88 acres in area, at and above the first sedimentary interbed, 110 feet below ground surface.

While it was recognized that 100% SVE system operation maximizes mass recovery, it was assumed that the diffusion-limited nature of mass transport results in diminishing rates of mass recovery with continued pumping. Pulse pumping may be a more cost-effective means of remediation in such circumstances. T2VOC was used to assess the relative performance of various continuous and pulse pumping schemes starting from common initial conditions and operating for the same length of time. In particular, single-well T2VOC simulations were used to answer two questions: 1) What is the optimum duration, in terms of relative mass recovery, of a single pulse pumping on/off cycle? 2) Given existing SVE pump/treatment system operation, what percentages of the maximum possible treated mass can be achieved with continuous or pulse pumped wells feeding a reduced number of offgas treatment units?

With information on system operation cost per unit time, an answer to the first of these questions makes it possible to estimate reduction in cost per unit mass recovered and treated due to pulse pumping. Resolution of the second question allows a similar evaluation of operating cost reduction, and also an assessment of the capital savings (by foregoing additional or replacement treatment units) while still achieving a given percentage of the maximum possible treated mass.

MODELING ASSUMPTIONS AND APPROACH

Inevitable uncertainties in subsurface structure and properties, initial and boundary conditions, source distribution and loading rates, etc., led to the use of simplifying assumptions. Among these were:

- The modeled subsurface consists of constant thickness, laterally homogeneous basalt and sedimentary layers.
- Contaminant transport results from evaporation at the source and consists of downward redistribution due to combined diffusion and density-driven flow.
- Due to the arid climate, the vadose zone is very dry except in the immediate vicinity of the sedimentary interbed at 110 feet BGS.
- The basalt has little organic content and sorption may be neglected; significant sorption will occur in the interbed.
- Local chemical equilibrium holds.
- A single simulated well may be constructed that represents the average behavior of the three operational wells in the SVE system.

To reduce the impact of these assumptions, results were obtained in relative terms, so that any inaccuracies "canceled out". This consisted of determining maximum achievable mass removals at 100% SVE operation and calculating removal effectiveness of any particular pumping scheme as a percentage of the maximum.

[1] Patrick J. Schwind, B.S. Geophysics (Bowling Green State University), Senior Engineer, Parsons Engineering Science, Inc., 175 Tri-County Parkway, Cincinnati, OH 45246, (513) 648-6811; FAX: (513) 648-6892; E-mail: pat_schwind@fernald.gov
[2] Eric C. Miller, B.A. Chemistry (Idaho State University), Senior Scientist, Lockheed Martin Idaho Technologies Company, P.O. Box 1625, Idaho Falls, ID 83415, (208) 526-9410; FAX: (208) 526-9473; E-mail: ecm@inel.gov

Modeling consisted of single-well simulations in radial coordinates for a vertical sequence extending 40 feet above and 5 feet below the 5-foot thick interbed. The shallow, breached barrels, buried between 1966 and 1970, remain in place and a great deal of uncertainty exists as to the initial and remaining carbon tetrachloride inventories. Therefore, the contaminant source was accounted for by specifying a constant vapor phase loading rate over a portion of the model top surface. The rate and radial extent of loading was iteratively adjusted to produce a radially symmetric initial plume that roughly matched measured vapor concentrations above and below the interbed. The loading distribution was also adjusted by comparing simulated and measured SVE mass recovery rates starting from similar initial plumes.

All simulations used the same model domain and grid, initial and boundary conditions, and material properties. Cycle duration optimization runs used a constant 235 scfm pumping rate with varied on/off schedules for a total simulation time of 180 days. Runs to assess relative mass treated as a function of the number of treatment units varied both pump rates and schedules, and simulated a 10-week period with 10% down time (effectively a 9-week simulation).

MODEL DOMAIN AND GRID

Figure 1 is a schematic cross-section of the conceptual model domain and numerical grid. The waste drums are buried in surface alluvium and contain a carbon tetrachloride oil absorbed in a calcium silicate binder. The NAPL source is assumed to remain bound within the barrels, which have degraded structurally allowing carbon tetrachloride vapor to migrate downward by diffusion and density-driven flow. The sedimentary interbed at 110 feet BGS, by virtue of matrix sorption and partitioning to its relatively abundant aqueous phase, acts as a barrier, slowing the passage of the contaminant. The extraction well is screened over the 10-foot interval immediately above the interbed.

The model grid begins at 70 feet BGS and extends downward to 120 feet BGS, 5 feet below the bottom of the sedimentary interbed. Vertically, the grid is composed of 12 layers. The bulk of the model domain is composed of the middle 10 layers, each 5 feet thick. The top and bottom layers are very thin for accurate placement of boundary conditions.

Radially, the grid begins at the extraction well centerline and extends outward 1000 feet. There are 37 grid blocks in the radial dimension. The first 13 radial increments have spacings that increase by a constant factor from 6.3 inches at the wellbore to 25.85 feet. The next 23 grid blocks have a constant 39.37 ft radial spacing, and the outer grid block is very thin.

Figure 1. Conceptual Model Domain and Numerical Grid

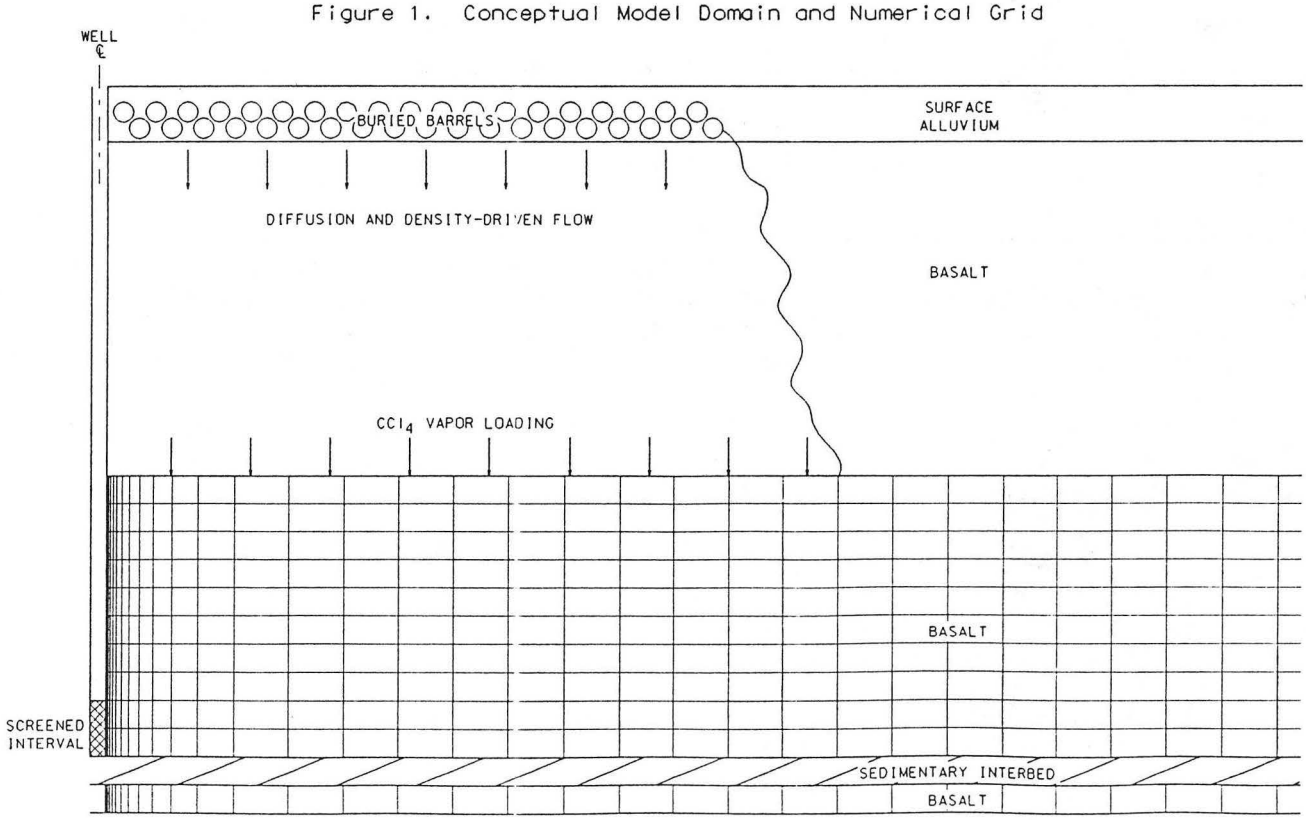

MATERIAL PROPERTIES

Table 1 summarizes the material properties used for all of the T2VOC simulations. Porous medium parameters were taken from previous INEEL vadose zone studies of the same basalt and interbed bodies[1,2,3]. Relative permeabilities were calculated, for basalt, using a modified version of Stone's three phase method, and for the sedimentary interbed, using Parker's three phase functions[4]. Sedimentary interbed capillary pressures were calculated using Parker's three phase functions. For basalt, it was necessary to code a new capillary pressure routine to match that used in the previous INEEL studies. All parameters used to calculate the thermophysical properties of carbon tetrachloride were taken from the T2VOC VOC data set in the file "voc.dat".

The basalt properties are such that the significance of density-driven flow relative to diffusion is difficult to estimate. Previous studies have shown that density-driven flow may dominate vapor phase transport of carbon tetrachloride if sorption and moisture content are low, and if gas phase permeability is high[5]. It appears that the criteria for significant density-driven flow are met for the present study, except that basalt permeabilities are anisotropic, with a horizontal component above the approximate limit found in Falta, et al[5] (1×10^{11} m^2) and a vertical component well below.

Parameter	Value
Basalt Porosity	.05
Sedimentary Interbed Porosity	.48
Basalt/Sediment Grain Density	2650 kg/m^3
Basalt Horizontal Absolute Permeability	8.88×10^{-11} m^2
Basalt Vertical Absolute Permeability	2.96×10^{-13} m^2
Sedimentary Interbed Absolute Permeability	3.95×10^{-15} m^2
Basalt Organic Carbon Fraction	0.000
Sediment Organic Carbon Fraction	0.002
Temperature	13.8 C
CCl_4 Molecular Weight	153.8 g/mole
CCl_4 Saturated Vapor Pressure	9068 Pa
CCl_4 K_{OC}	.439 m^3/kg
CCl_4 Water Solubility	9.21×10^{-5} mole/mole
CCl_4 - Air Binary Diffusivity	7×10^{-6} m^2/s

Table 1. Material Properties Used for All T2VOC Simulations.

INITIAL AND BOUNDARY CONDITIONS

The first step in T2VOC simulations was to establish a gravity-capillary equilibrium at a net background infiltration rate of 1 cm/yr[6]. This infiltration rate was maintained at the top of the model grid for all subsequent runs. Next, to provide realistic initial and boundary conditions, a period of carbon tetrachloride source vapor loading was simulated, followed by a period of combined loading and SVE operation. Rates and radial extent of loading were iteratively adjusted until field-measured concentrations and past mass recovery rates were reasonably approximated. It was found that a constant loading of 4.54 kg/d over a circular area with a radius of 525 ft produced the best fit to measured concentrations and mass recovery rates. This loading was maintained at the top of the model grid for all subsequent runs. Figure 2 depicts an r-z cross-section of the initial plume obtained from this procedure. All T2VOC optimization simulations commenced from these common starting conditions.

At the bottom of the model grid, thermodynamic variables were held constant at their initial values. These Dirichlet conditions were implemented by specifying the bottom row of grid blocks as inactive. The outer radial boundary was placed far enough away from the well (1000 feet) to make the model domain effectively infinite. Both inner and outer radial boundaries were left in their default zero-normal flux conditions.

To avoid the necessity of allocating an arbitrary division of flux to the well among the two screened grid blocks, the wellbore was assigned atmospheric material properties. This allowed assignment of pumping rates to a single block at the

Figure 2. SVE Simulation Initial CCl_4 Vapor Plume (ppmv)

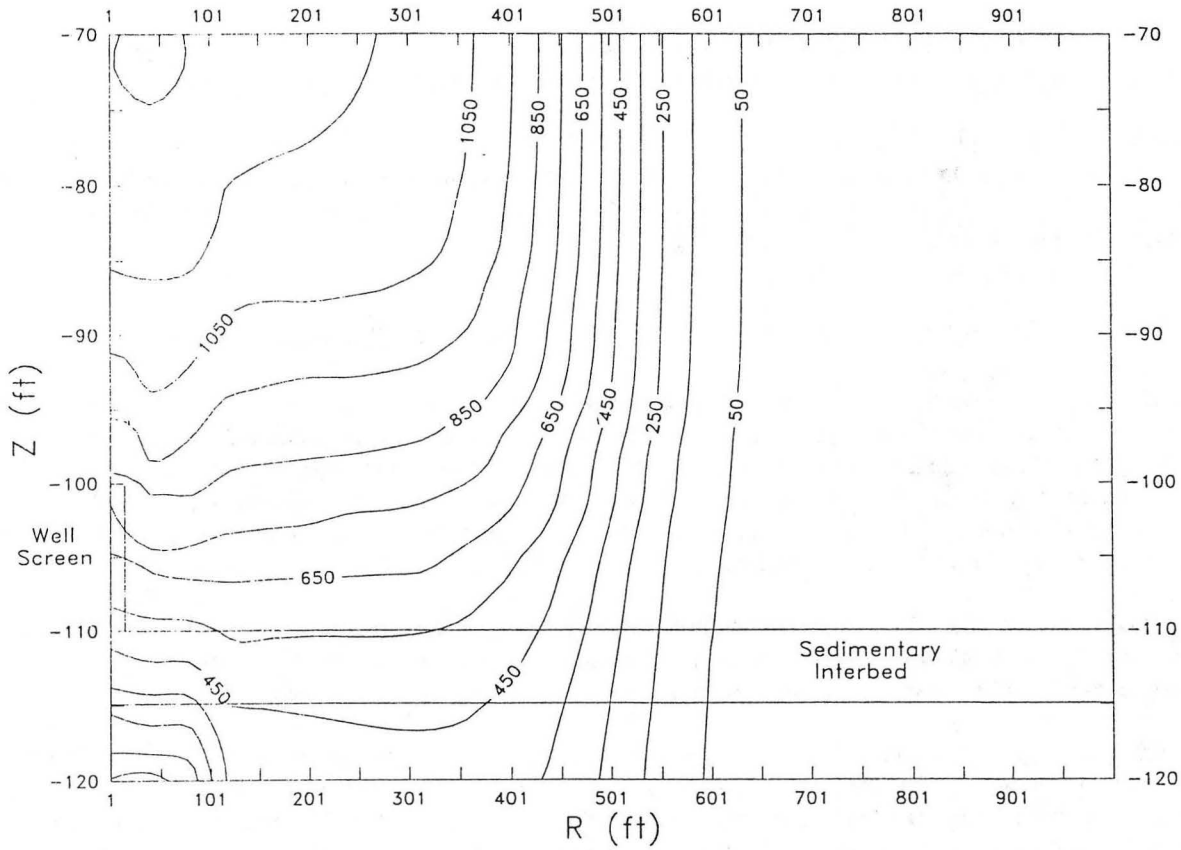

Figure 3. Steady Gas Phase Velocities, 235 scfm Pumping Rate

Maximum = 2.1 m/s, Minimum = 3e−6 m/s

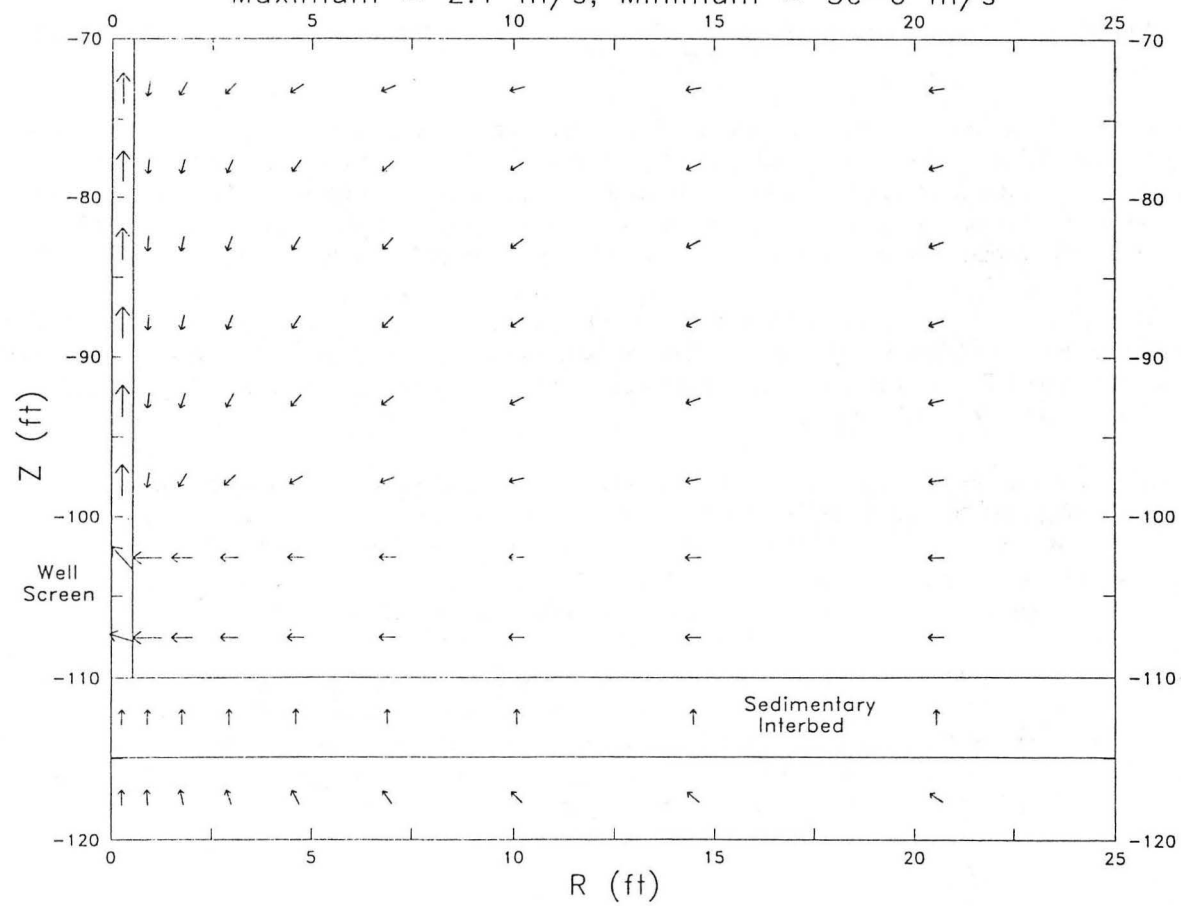

top of the wellbore and resulted in a natural division of flux through the screened grid blocks. Horizontal permeabilities were set to zero within the wellbore to eliminate advective and diffusive fluxes across the well casing.

Figure 3 is a vector plot depicting gas phase velocities within a 25-foot radius of the well for a constant pumping rate of 235 scfm. As the transient flow field develops very quickly compared to pump operating periods, this is the steady flow pattern that controls vapor movement to the well during active SVE pumping. For different pumping rates, the velocity field is essentially a scaled version of the pattern in Figure 3.

SIMULATIONS FOR OPTIMUM PULSE PUMPING CYCLE DURATION

The basic distinction between the various simulated pumping schedules was cycle duration. On/off cycles were repeated until the total simulation time of 180 days was reached. For each cycle duration, different schedules were obtained by varying the percent of the cycle that pumping was active. For example, at 10% pump-on, a 60-day cycle would be composed of 6 days of pumping and 54 idle days; at 20% pump-on, it would be 12 days of pumping followed by 48 idle days; etc. The rate for all periods of active pumping was held constant at 235 scfm. For each schedule, relative results were assessed as the percent of maximum possible mass removal (at 100% operation) for the 180-day simulation time.

It was necessary to modify the T2VOC source code to output, at every time step, the transient carbon tetrachloride vapor mass flux rate at the grid sink block. T2VOC's variable time-stepping facility produced dense time series, which were numerically integrated with a trapezoidal rule to obtain total mass removed by the SVE well.

Cycle durations of 60, 30, 15, 7, and 3 days were simulated at 10% pump-on to 90% pump-on in 10% steps, for a total of 45 runs. Figure 4 summarizes the results of these runs. As would be expected, differences between the various cycle durations narrow as the percent pump-on time approaches 100%. In general, shorter cycle periods are better, with 3-day cycles more favorable up to 30 % pump-on and 7-day cycles producing slightly higher recoveries at pump-on percentages above 40%. Because the greatest interest was in obtaining relative recoveries in the 90% range, 7-day cycles were considered optimal. It should be noted, however, that only small differences exist between 3-, 7-, and 15-day cycles in the desired range.

SIMULATIONS FOR RELATIVE RECOVERY AND TREATMENT WITH A REDUCED NUMBER OF OFFGAS TREATMENT UNITS

The most recent SVE system configuration has consisted of three extraction wells, each feeding a dedicated Recuperative Flameless Thermal Oxidation (RFTO) treatment unit. The number of RFTO units required to remove and treat a specified amount of carbon tetrachloride may be reduced by placing a manifold between the wells and the treatment units. T2VOC simulations were performed to assess, given system throughput limits, the percent of maximum possible recovery that can be achieved by routing effluent from three wells to only one or two RFTO units.

For a given operating period, the maximum mass of carbon tetrachloride that can be removed and treated by the SVE system is limited by process throughput parameters. The extraction wells can each deliver a maximum of 350 scfm of vapor effluent and each RFTO unit is capable of treating a maximum of 400 scfm. Operational history of the SVE system has included approximately 10% down time.

Given these limits, the maximum possible mass removal and treatment would be achieved by operating each well at 350 scfm for 90% of the given operating period, with a dedicated treatment unit for each well (3 wells, 3 units). A 10-week base period was chosen, resulting in a 9-week total simulation time. All pulse pumping scenarios used 7-day cycle durations as per the results presented in the previous section. The simulated well is assumed to represent the average behavior of the three wells in the SVE system, and interaction effects between wells are neglected.

The system may operate with fewer RFTO units than wells either by pulse pumping with staggered start times or pumping all wells continuously at a reduced rate. If n represents the number of units to which the combined effluent from m wells is routed, then the maximum allowed pumping rate for m simultaneously operating wells is (400n/m) scfm or 350 scfm, whichever is lower. Pulse pumping schedules must have on-time percentages equal to (100m/3), with start times staggered by one-third of the cycle length, so that treatment capacity is not exceeded.

Figure 4. Percent of Maximum Possible Mass Removed vs. Percent of Cycle Pump is On for Different Cycle Durations.

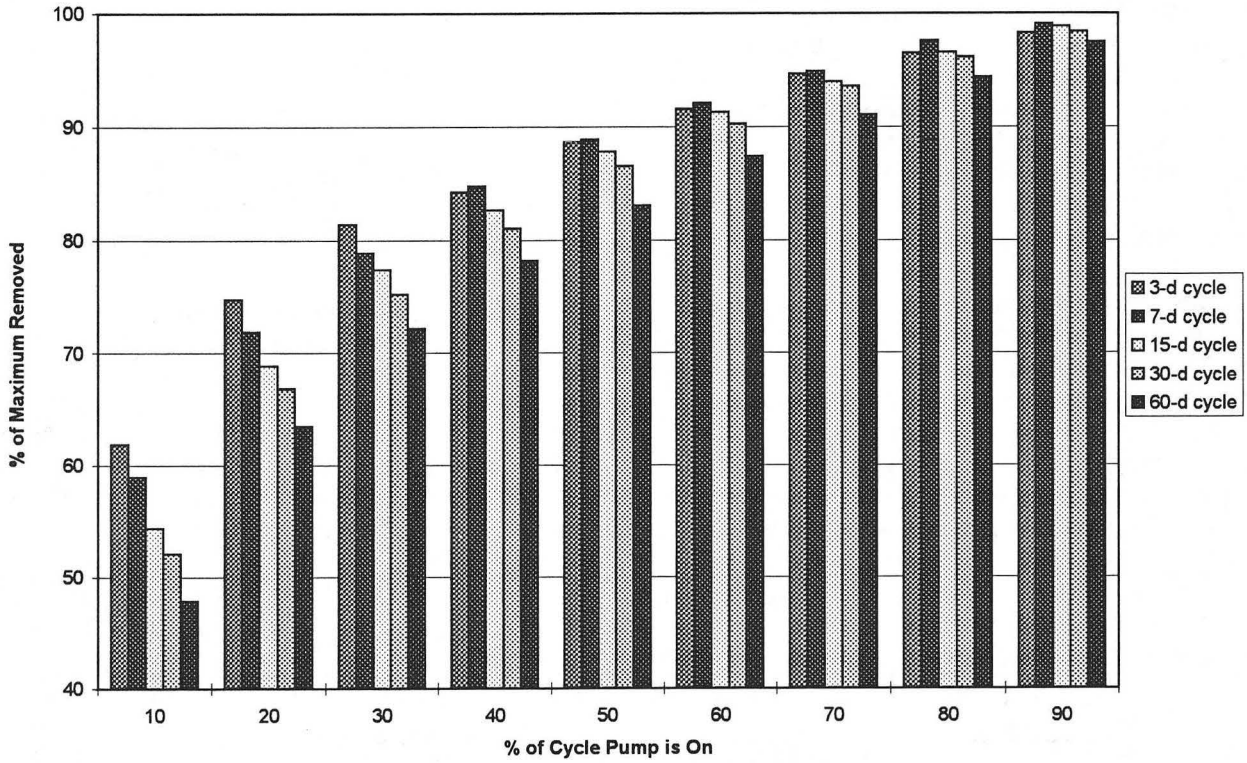

Figure 5. Achievable Percent of Maximum Possible Mass Removal and Treatment for Different Numbers of RFTO Units.

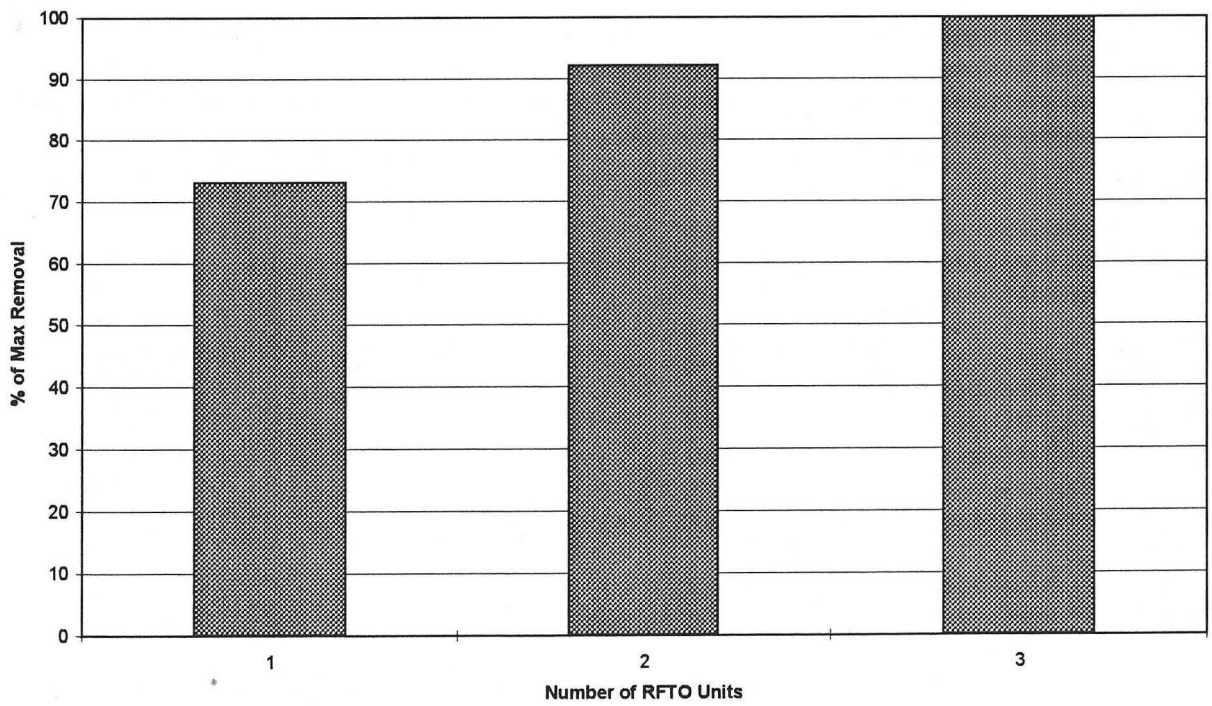

For a number of wells (m) equal to or greater than the number of treatment units (n), the possible unique permutations that adhere to the system throughput limitations are described in Table 2. It is important to remember that staggered start times for pulse pumping schemes allow all three wells to operate for the entire 9-week period while fewer than three are pumped simultaneously. Table 2 also lists simulation results for the various 1- and 2-unit schemes. The total system mass recovered is the combined figure for all three wells.

A total of six runs were required to determine the percentage of the potential maximum removal that can be achieved with a particular configuration over the 63-day operating period. The first run was a continuous pumping run at 350 scfm for 63 days to determine the maximum possible mass removal and treatment. As noted above, this case corresponds to the use of three RFTO units. The remaining runs consisted of continuous and pulse pumping scenarios for each of the two possible treatment unit configurations.

While results were similar for continuous and pulse pumping, continuous pumping recovered slightly more mass. The difference was most noticeable in the 2-unit scenarios, as the only pulse pumping scenario was limited by the maximum well rate, leaving unused treatment capacity. The difference narrows for 1-unit scenarios because the most efficient pulse pumping scheme can make full use of the available treatment capacity.

Figure 5 is a histogram of the achievable percentage of maximum possible removal for the different unit configurations. For one unit, 73.1% of maximum removal can be achieved by pumping all three wells continuously at 133 scfm. For two units, 92.1% of maximum removal can be obtained by continuously pumping all 3 wells at 267 scfm each.

Configuration # Units, # Wells Operating Simultaneously	Run Description	Total System Mass Recovered (kg)	Percentage of Max Possible Removal
3 Units, 3 Wells	350 scfm on 100% for 63 days	2965.2	100
2 Units, 3 Wells	267 scfm on 100% for 63 days	2730.3	92.1
2 Units, 2 Wells	7-d cycle, 67% on @ 350 scfm for 63 days	2574.9	86.8
1 Unit, 3 Wells	133 scfm on 100% for 63 days	2166.9	73.1
1 Unit, 2 Wells	7-d cycle, 67% on @ 200 scfm for 63 days	2153.4	72.6
1 Unit, 1 Well	7-d cycle, 33% on @ 350 scfm for 63 days	2057.4	69.4

Table 2. Percentage of Maximum Mass Recovery and Treatment for All Applicable Unit/Well Configurations.

CONCLUSIONS

T2VOC simulations have shown that both capital equipment and SVE system operation cost savings can be realized by reduced rate continuous pumping with fewer treatment units and/or pulse pumping. For recoveries greater than 80% of maximum, 7-day cycles have been found to be near-optimal for pulse pumping. If lower recoveries are acceptable, use of 3-day cycles would be more efficient.

While reduced rate continuous pumping was shown to be slightly more efficient than pulse pumping in terms of mass recovery for treatment with only one or two RFTO units, pulse pumping may be preferable if it reduces operating costs sufficiently. Reliable cost estimates may be combined with T2VOC simulation results to determine a SVE system configuration that maximizes carbon tetrachloride mass recovered and treated per dollar spent.

REFERENCES

[1] Magnuson, S.O., 1995, *Inverse Modeling for Field-Scale Hydrologic and Transport Parameters of Fractured Basalt*, INEL-95/0637, Lockheed Martin Idaho Technologies, Idaho Falls, ID.

[2] Magnuson, S.O., and D.L. McElroy, 1993, *Estimation of Infiltration from In Situ Moisture Contents and Representative Moisture Characteristic Curves for the 30', 110', and 240' Interbeds*, EG&G Engineering Design File #RWM-93-001.1, EG&G Idaho, Inc., Idaho Falls, ID.

[3] Magnuson, S.O., and A.J. Sondrup, 1996, *WAG 7 Subsurface Pathway Flow Model Development and Calibration*, INEL-96/0297, Lockheed Martin Idaho Technologies, Idaho Falls, ID.

[4] Falta, R.W., K. Pruess, S. Finsterle, A. Battistelli, 1995, *T2VOC User's Guide*, LBL-36400, Lawrence Berkeley Laboratory, UC Berkeley, CA.

[5] Falta, R.W., I. Javandel, K. Pruess, P.A. Witherspoon, October 1989, "Density-Driven Flow of Gas in the Unsaturated Zone Due to the Evaporation of Volatile Organic Compounds", Water Resources Research, Vol. 25, No. 10, pp 2159-2169.

[6] Cecil, L.D., J.R. Pittman, T.M. Beasley, R.L. Michel, P.W. Kubik, P. Sharma, U. Fehn, and H. Gove, 1992, "Water Infiltration Rates in the Unsaturated Zone at the Idaho National Engineering Laboratory Estimated from Chlorine-36 and Tritium Profiles, and Neutron Logging," Proceedings of the 7th International Symposium on Water-Rock Interaction - WRI-7, Y.K. Kharaka and A.S. Meest editors, Park City, UT.

Using T2VOC to Model Kinetic Interphase Mass Transfer During Air Sparging

Ronald W. Falta[1], John S. Gierke[2], and Gretchen L. Hein[2]

[1]Departments of Geological Sciences and Environmental Engineering and Science, Clemson University, Clemson, SC
[2]Departments of Geological Engineering and Sciences and Civil and Environmental Engineering, Michigan Technological University, Houghton, MI

ABSTRACT

The unstable nature of air sparging gas flow below the water table causes injected gas to flow locally through small channels, which are separated by a distance of one or several millimeters. Although it is possible to model the average air sparging darcy flux using a conventional multiphase flow approach, this type of model does not resolve local mass transfer effects which arise due to the millimeter scale gas channels. For this reason, compositional multiphase flow simulators such as T2VOC which assume local chemical equilibrium between the phases overestimate the rate of contaminant mass transfer to the gas phase during air sparging.

An alternative method is proposed for modeling the local mass transfer during air sparging. The method is based on the existing dual media formulation which is commonly used for modeling flow and transport processes in fractured media [see Pruess and Narasimhan, 1985]. Instead of considering fractures and matrix blocks, the method is applied to porous media to simulate the local gas channels which form during air sparging. This allows resolution of the local diffusive mass transfer between the flowing gas phase, and nearby stagnant water filled zones. Because each media is modeled with a single node separated by some local average distance, the diffusive mass transfer is mathematically analogous to a first order interphase mass transfer reaction.

INTRODUCTION

Recent studies have demonstrated that VOC removal during air sparging is limited by mass transfer into the flowing gas phase. Mass transfer limitations occur at several scales due to the heterogeneous nature of gas distributions during air sparging. At a large scale, the air sparging zone is very strongly influenced by heterogeneities which form capillary and permeability barriers to the gas flow. If the geometry and locations of these heterogeneities are well known, or if the media is homogeneous, it is possible to accurately model the sparge gas flow field using a conventional multiphase flow numerical approach [Hein et al., 1997; McCray and Falta, 1997]. This type of simulator, however, cannot resolve local (subgridblock) mass transfer effects which arise due to the millimeter scale gas channels which form during sparging. For this reason, compositional multiphase flow simulators which assume local chemical equilibrium between the phases overestimate the rate of interphase mass transfer during air sparging.

Figure 1 shows the effluent concentration measured during a recent air sparging experiment conducted at Michigan Tech. In this experiment, a clean, initially water-filled vertical column was sparged with gas containing 1000 ppmv trichloroethylene vapor. The water saturation in the column during sparging was about 75 percent, so significant TCE

retardation would be expected due to partitioning into the stagnant water phase (TCE has a dimensionless Henry's constant of 0.35). However, the experimental column effluent concentration, (solid line), exhibits a rapid breakthrough, followed by a very gradual increase up to the injected composition. An attempt to model this experiment with a conventional local equilibrium approach (solid triangles) results in a poor match of the data. The local equilibrium model predicts a strongly retarded breakthrough, followed by little tailing of the concentration profile. This poor match is largely a result of over predicting the rate of local interphase mass transfer.

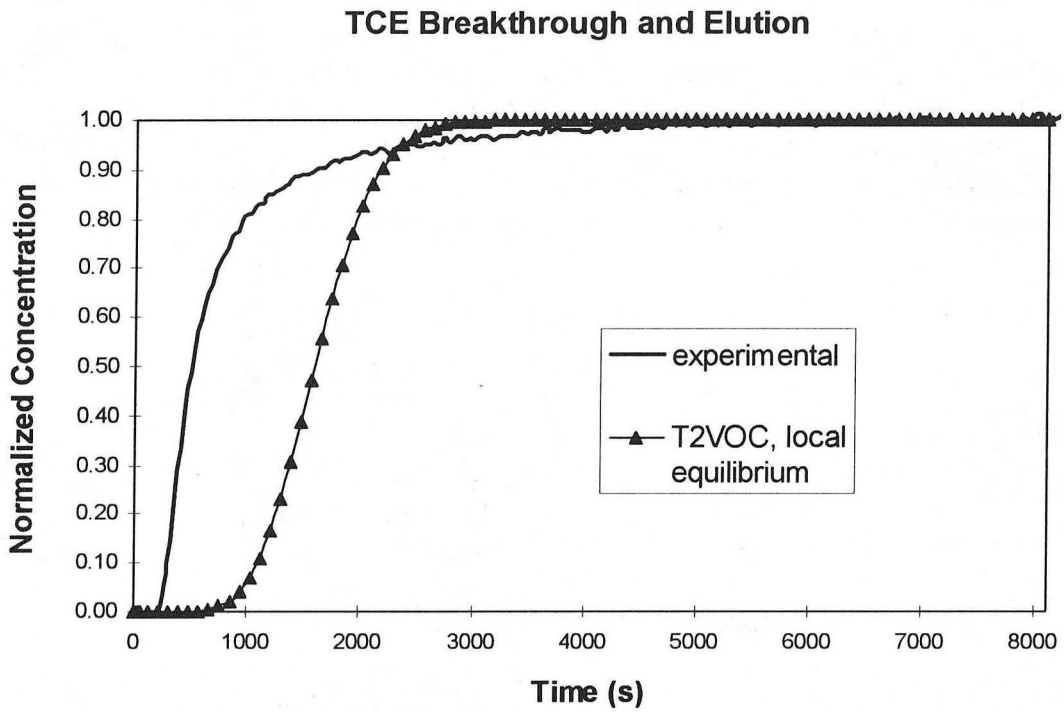

Figure 1. Comparison of experimental and simulated column effluent concentrations during a sparging experiment.

While most of the current 3-D compositional multiphase flow simulators assume local equilibrium between phases, there have been some efforts to model kinetic interphase mass transfer in multiphase contaminant transport [Sleep and Sykes, 1989]. The most widely used formulation assumes that the kinetic interphase mass transfer can be modeled as a heterogeneous first order reaction in each gridblock:

$$Q^c_{imt} = k_{imt} a (C^c_w / H - C^c_g)$$

where Q^c_{imt} is the rate of chemical mass transfer from the water to the gas phase per unit volume of porous media, C^c_w is the aqueous phase chemical concentration, C^c_g is the gas phase chemical concentration, and $k_{imt}a$ is the mass transfer coefficient-interfacial area

product. Implementing this type of mass transfer formulation in a compositional multiphase flow code is not trivial because the aqueous phase and gas phase forms of the chemical must be treated as separate components, with separate mass balance equations.

MODELING INTERPHASE MASS TRANSFER WITH A DUAL MEDIA APPROACH

We propose an alternative method for modeling the local mass transfer during air sparging. This technique is fairly straightforward, and can be easily implemented in existing compositional multiphase flow simulators which assume local phase equilibrium. The method is based on a dual media formulation which is commonly used for modeling flow and transport processes in fractured media [see Pruess and Narasimhan, 1985]. Instead of considering fractures and matrix blocks, the method is applied to porous media to simulate the effect of local gas channels which form during air sparging. This allows resolution of the local mass transfer kinetics between the flowing gas phase, and nearby stagnant water filled zones. Compared to the usual local equilibrium approach, the dual media approach doubles the number of equations to be solved at each time-step.

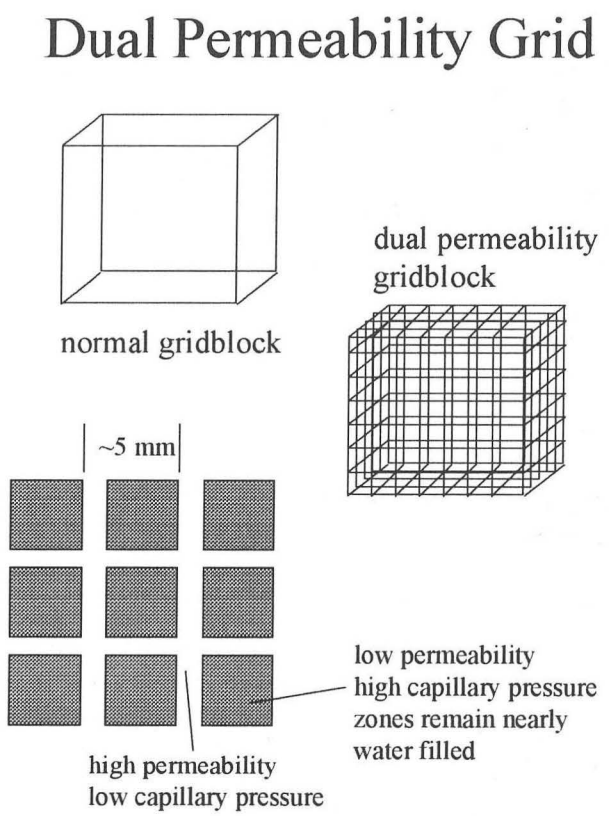

Figure 2. Schematic representation of a dual media gridblock.

Figure 2 shows a schematic diagram of the dual media formulation. Each "normal" gridblock is subdivided into two media. In the classical application of this method, these media would be fractures and matrix, and the fracture spacing would

typically be on the order of one to several meters. The two media are connected inside the gridblock by a single one-dimensional connection, with a single average interfacial area between the two media in the gridblock. The average distance between the two media, and the average interfacial area are computed based on the distributions of the two media within the gridblock (the three-dimensional fracture spacing in the fractured rock case). Each dual media gridblock is connected to other gridblocks in the normal way, but with connections for both media [Pruess and Narasimhan, 1985]. The method can be applied to complex heterogeneous 3-D grids if desired.

In the present application, we consider two types of porous media: a high permeability, low capillary pressure media, and a lower permeability, higher capillary pressure media. Compared to fractured rock applications, we assume a much smaller spacing between the two media, with a correspondingly larger interfacial area. For the case shown in Figure 2, the high permeability zones are separated by only 5 mm, so the average distance from the high permeability to the low permeability zones is only a millimeter or so, depending on the geometric model. The average interfacial area is very high in this case, approximately 768 m^2 of interface per m^3 of porous media. Other conceptual models of the two phase distributions (eg. the gas flowing through parallel cylindrical channels) are easily implemented by adjusting the interfacial area and distance terms in the dual media grid generation step (subroutine MINC in the MESHMAKER module). The properties of the two media, and their distributions are chosen so that the sparging gas will form the characteristic local channels through the high permeability media. Currently, we do not have a technique for determining these parameters based on traditional porous media measurements, and rely instead on fitting. This is a significant limitation to the method, and it is an area where further research could provide important practical developments.

During an air sparging simulation, almost all of the gas flows through the high permeability/low capillary pressure zone. If the gas composition is not in equilibrium with the pore water, this gives rise to a concentration gradient between the nearly water filled low permeability/high capillary pressure zone and the gas filled high permeability zone. Because each media is modeled with a single node separated by some average distance, this diffusive mass transfer between the media is mathematically analogous to the first order interphase mass transfer formulation described earlier, (except that local equilibrium occurs between the gas and water in the low capillary pressure media). For the dual media approach, the mass transfer-interfacial area product, $k_{iml}a$ can be calculated from

$$k_{iml}a = \frac{(\phi S_w \tau_w D_w / H)A}{d}$$

where $\phi S_w \tau_w D_w$ is the effective porous media diffusion coefficient in the water-filled matrix, A is the average interfacial area between the two media per unit volume of porous media, and d is the average distance from the liquid filled matrix to the gas interface.

A series of numerical simulations were performed to illustrate the method. These were conducted using T2VOC [Falta et al., 1995], modified to account for aqueous phase diffusion. The dual permeability mesh generator (subroutine MINC in the MESHMAKER module) was modified slightly to allow for direct input of interfacial area and distance.

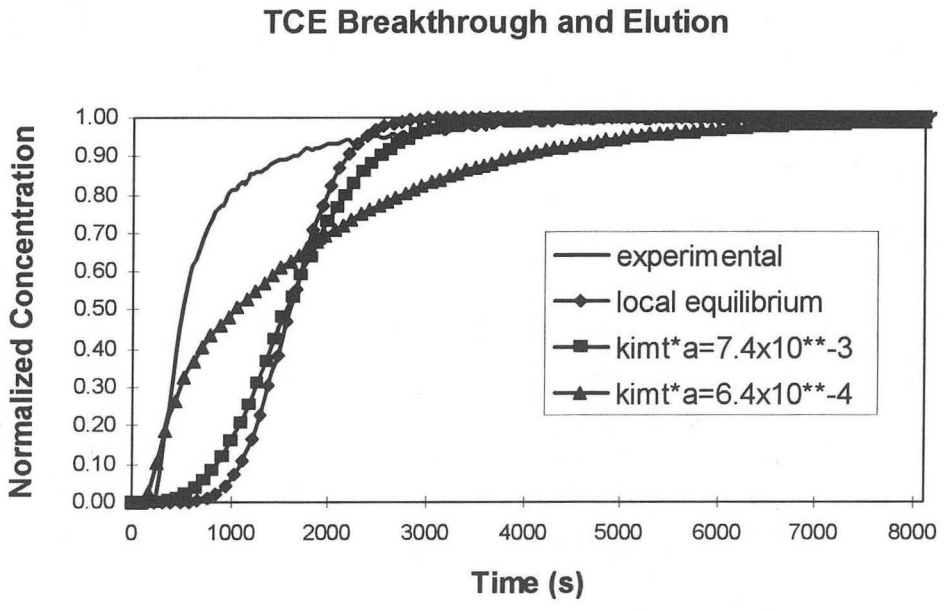

Figure 3. Numerical simulations of air sparging with local kinetic interphase mass transfer at high rates.

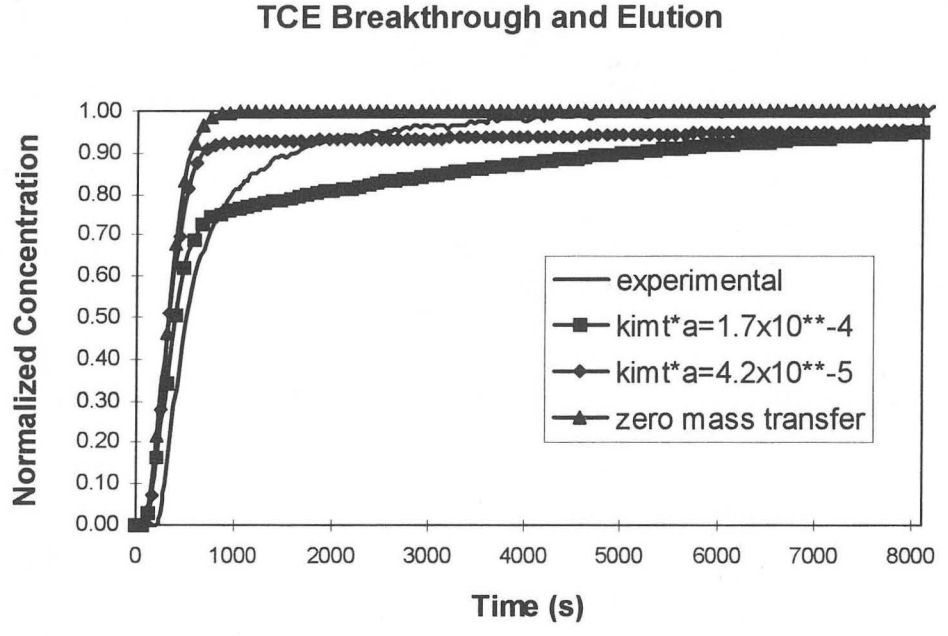

Figure 4. Numerical simulations of air sparging with local kinetic interphase mass transfer at low rates.

Figures 3 and 4 show the results of simulations assuming that all of the gas flows through 30% of the total media, with various rates of interphase mass transfer. At very high rates of interphase mass transfer (Figure 3), the dual media model essentially

duplicates the single media local equilibrium curve, as expected. As the interphase mass transfer rate constant is decreased, the curve shifts dramatically, showing an earlier initial breakthrough, followed by a long period of tailing. The case with a mass transfer coefficient of 6.4×10^{-4} s^{-1} corresponds to a conceptual model consisting of the gas flowing through parallel cylindrical tubes with diameters of about 1mm. This diameter is similar to the average grain size diameter of the sand in the experiment (about 0.6 to 0.8 mm). In the low mass transfer cases (Figure 4), the simulated breakthrough occurs quickly, followed by extensive tailing. The zero mass transfer case results in simple advection and diffusion through the gas filled 30% of the media, with no interphase mass transfer to the water filled media. The curve in this case is still affected by retardation in the pore water located in the gas zone (S_w=.25).

Unfortunately, none of the simulations shown here were able to provide a close match with the experimental data over the entire range. It is possible that the match can be improved by adjusting the relative volumes of the two-phase and liquid zones. However, it is also possible that a higher order mass transfer model is required to match this experiment. Such a higher order model could be implemented using the idea of multiple interacting continua (MINC) as described by Pruess and Narasimhan [1985]. With this approach (which already is included in the MESHMAKER module), the local liquid diffusion would be modeled using several nested blocks, improving the resolution of the local concentration gradients in the stagnant water phase. This and similar approaches will be a focus of our future research in this area.

ACKNOWLEDGEMENTS

This work is supported by the U.S. Department of Energy's Morgantown Energy Technology Center, under Contract Number DE-RO21-95MC33082 with Michigan Technological University, with a subcontract to Clemson University.

REFERENCES

Falta, R.W., K. Pruess, S. Finsterle, and A. Battistelli, T2VOC User's Guide, *Lawrence Berkeley Laboratory Report LBL-36400,* March, 1995

Hein, G.L., N.J. Hutzler, J.S. Gierke, and R.W. Falta, Three-Dimensional Experimental Testing of a Two-Phase Flow-Modeling Approach to Air Sparging, *Ground Water Monitoring and Remediation*, Vol. 17, No. 3, 1997.

McCray, J.E. and R.W. Falta, Numerical Simulations of Air Sparging for Subsurface NAPL Remediation, *Ground Water Vol. 35, No. 1,* 1997.

Pruess, K. and T. N. Narasimhan, A practical method for modeling fluid flow and heat flow in fractured porous media. *Society of Petroleum Engineers Journal*, 25(1), 14-26, February, 1985.

Sleep, B.E., and J.F. Sykes, Modeling the transport of volatile organics in variably saturated media, *Water Resources Research, Vol. 25, No. 1*, 81-92 1989.

Using TOUGH2 to Model Capillary Barriers

Stephen W. Webb
Sandia National Laboratories
Albuquerque, New Mexico 87185

ABSTRACT

Ross (1990) developed an analytical relationship to calculate the diversion length of a tilted fine-over-coarse capillary barrier. Oldenburg and Pruess (1993) compared TOUGH2 simulation results to the diversion length predicted by Ross' formula using upstream and harmonic weighting. The results were mixed. The qualitative agreement is reasonable but the quantitative comparison is poor, especially for upstream weighting. The proximity of the water table to the fine-coarse interface at breakthrough has been proposed as a possible reason for the poor agreement. In the present study, the Oldenburg and Pruess problem is extended to address the water table issue. When the water table is sufficiently far away from the interface at breakthrough, good qualitative *and* quantitative agreement is obtained using upstream weighting.

INTRODUCTION

Capillary barriers, consisting of tilted fine-over-coarse layers under unsaturated conditions, have been suggested as a means to divert water infiltration away from sensitive underground regions. The capillary diversion formula of Ross (1990) (Steenhuis et al., 1991, and Stormont, 1995, present additional variations) is of particular interest because it can be easily used in capillary barrier design and evaluation. Oldenburg and Pruess (1993) compared TOUGH2 (Pruess, 1991) simulation results using upstream and harmonic weighting with Ross' formula; the results were mixed. While the comparison is reasonable qualitatively, the quantitative agreement is generally poor, especially for upstream weighting. A reason that has been proposed for this poor agreement is the proximity of the water table (Pruess, private communication, 1994). In Ross' derivation, the fine-coarse interface is assumed to be infinitely far away from the water table. In Oldenburg and Pruess (1993), the water table is only a few meters below the interface when breakthrough occurs. In order to address the water table proximity question, the Oldenburg and Pruess (1993) model is extended in the present study to allow for different initial water table locations. The applicability of upstream weighting to transient unsaturated flow conditions including capillary barrier behavior is also discussed.

While comparison of Ross' diversion equation with numerical modeling results is of interest, it must be kept in mind that capillary barrier leakage and breakthrough involve complicated unsaturated flow phenomena including fingering (Hill and Parlange, 1972; Glass et al., 1989a,b,c) as discussed by Oldenburg and Pruess (1993). Fingering phenomena are not treated in the analytical solution of Ross or in the TOUGH2 numerical code at present. In addition, heterogeneities and their spatial distribution may have a significant impact on the diversion length of tilted capillary barriers (Ho and Webb, 1998), which are not included in Ross' expression. Therefore, while comparison of Ross' expression with numerical results is of interest, comparison of modeling results to actual data is also needed.

ROSS' DIVERSION FORMULA

Ross (1990) developed an analytical relationship to calculate the diversion length of a tilted fine-over-coarse capillary barrier with constant infiltration, assuming that the upper boundary (infiltration surface) and the lower boundary (water table) are far away from the fine-coarse interface. The only flow in the system is due to infiltration. The analysis assumes steady-state conditions and defines breakthrough from the fine to the coarse layer as the occurrence of downward flow through the coarse layer equal to the infiltration rate. This assumption, along with the infiltration surface boundary condition, allows one to calculate the vertical relative permeability in the fine soil at breakthrough and, therefore, the horizontal flow in the fine layer. This horizontal flow is equal to the total amount of water diverted up until breakthrough

$$Q_{\max} = K_s \tan\phi \int k_r d\psi \qquad (1)$$

where ϕ is the angle of the fine-coarse interface with respect to horizontal. If the relative permeability is given by the quasi-linear function

$$k_r = e^{\alpha\psi} \qquad (2)$$

where α is the sorptive number and ψ is the moisture potential ($\psi = P_c / \rho g$), then the equation reduces to

$$Q_{max} = K_s \frac{\tan\phi}{\alpha}\left[\left(\frac{q}{K_s^*}\right)^{\alpha/\alpha^*} - \frac{q}{K_s}\right] \qquad (3)$$

where the starred value refers to the coarse layer parameter. For constant infiltration, the capillary diversion length is simply the total water diverted by the capillary barrier divided by the infiltration rate

$$L = K_s \frac{\tan\phi}{q\alpha}\left[\left(\frac{q}{K_s^*}\right)^{\alpha/\alpha^*} - \frac{q}{K_s}\right] \qquad (4)$$

where L is the horizontal distance. Equation (1) above is general and can be used with any relative permeability function. Equations (3) and (4) are derived from equation (1) using the quasi-linear relative permeability function. The diversion length can be evaluated numerically for other relative permeability expressions such as van Genuchten (1980) as discussed by Webb (1997).

TOUGH2 NUMERICAL SIMULATIONS

Oldenburg and Pruess (1993) analyzed a two-dimensional tilted fine-over-coarse capillary barrier with a water table and vertical infiltration using TOUGH2 (Pruess, 1991) modified to include the quasi-linear wetting-phase relative permeability function discussed above. A sketch of the capillary barrier problem is given in Figure 1; properties and problem parameters are summarized in Table 1. A fine layer 50 m thick overlies a coarse layer 10 m thick. The layers are tilted at a 5° angle with respect to horizontal. Infiltration occurs at the top of the fine layer at a constant rate of 0.60 m/year, and a water table is specified at 59 m along the left boundary.

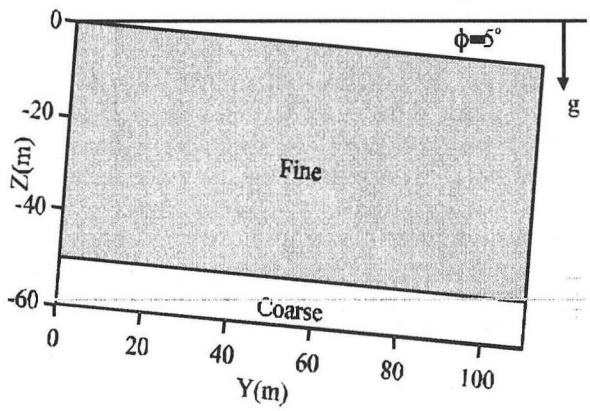

Figure 1
Comparison Problem Schematic
(after Oldenburg and Pruess, 1993)

Table 1
Original Problem Parameters

	Upper Layer (Fine)	Lower Layer (Coarse)
Thickness	50 m	10 m
Length	750 m	750 m
Permeability	10^{-13} m^2	2 x 10^{-13} m^2
Porosity	0.30	0.40
Relative Permeability		
(Fine)	$k_r = e^{\alpha Pc}$; $\alpha = 0.1$ m^{-1}	
(Coarse)	$k_r = e^{\alpha^* Pc}$; $\alpha^* = 4.$ m^{-1}	
Capillary Pressure		
(Fine)	$P_c = -10^6 (1.-S_l)$	
(Coarse)	$P_c = -10^6 (1.-S_l)$	

Boundary Conditions

Left Side	No flow.
Right Side	No flow.
Top	Constant Infiltration rate (0.60 m/yr).
Bottom	Horizontal water table with a depth of 59 m at left boundary.

For the conditions summarized in Table 1 (α = 0.1 m^{-1}; α^* = 4.0 m^{-1}), the predicted capillary diversion length from Ross (1990) is 39.3 m.

The discretization employed by Oldenburg and Pruess (1993) consisted of thirty rows each 2 m high with varying column widths. The column width was 4 m for the first 80 m downdip, which increased thereafter. A higher resolution grid was examined between 32 and 80 m downdip using 2 m wide columns. The results from the original grid and the higher resolution grid are essentially the same.

The results from the simulations are presented as a ratio of the leakage past the fine-coarse boundary divided by the infiltration rate. A value of zero shows complete diversion of the infiltrating water, while a value of 1.0 means no diversion. The ratio should increase with distance downdip until breakthrough occurs, which is defined as a ratio of 1.0. Values higher than 1.0 are expected further downstream when the diverted water flows into the coarse layer.

Oldenburg and Pruess (1993) investigated two numerical weighting schemes for the permeability-mobility product ($k\, k_r/\mu$). The differences in the two schemes illustrate some of the complexities associated with unsaturated flow modeling. Harmonic weighting, which considers upstream and downstream parameters, is appropriate for steady-state one-dimensional flow without phase change or phase propagation based on flux conservation.

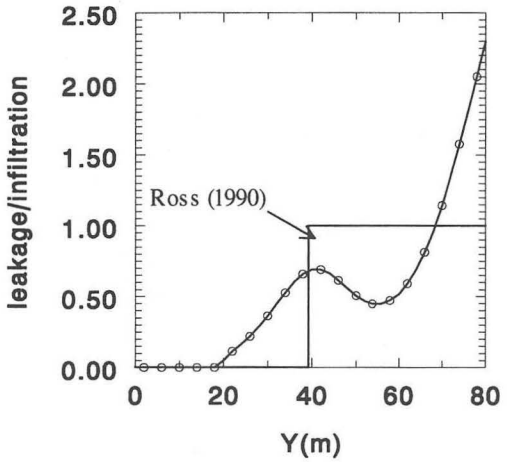

Figure 2a
TOUGH2 Leakage/Infiltration Ratio Results for Harmonic Weighting

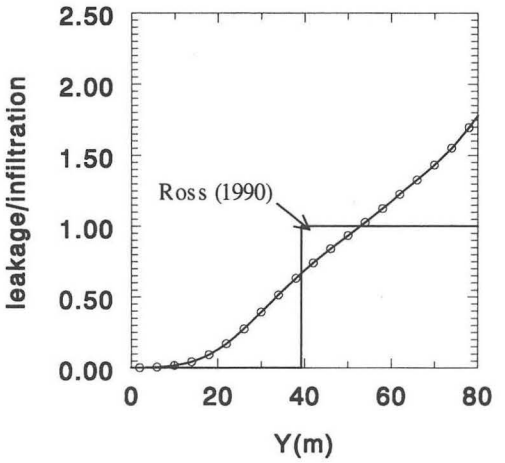

Figure 2b
TOUGH2 Leakage/Infiltration Ratio Results for Upstream Weighting

However, for transient conditions involving phase propagation, flux conservation is not applicable, and upstream weighting is more appropriate. Upstream weighting, which only uses the upstream parameters, is numerically much more efficient and robust than harmonic weighting.

The use of harmonic weighting for transient unsaturated flow can lead to large errors and upstream weighting is preferable (Aziz and Settari, 1979; Tsang and Pruess, 1990). In fact, harmonic weighting can lead to unphysical results in transient analyses of tilted capillary barriers such as the complete saturation of the upper fine layer without any leakage or flow into the lower coarse layer. Upstream weighting results are predominantly shown in this paper.

The leakage/infiltration ratio as a function of distance downdip is given in Figures 2a and 2b for the Oldenburg and Pruess (1993) problem with coarse and fine layer sorptive numbers of 4.0 m^{-1} and 0.1 m^{-1}, respectively. This ratio is shown for harmonic and upstream weighting as calculated by the present author; the results are essentially the same as Oldenburg and Pruess (1993). The behavior of the leakage/infiltration ratio using harmonic weighting shows an initial breakthrough at about 40 m. This ratio decreases slightly after this location because some of the water has flowed into the coarse layer. The ratio then increases again. In contrast, for upstream weighting, the ratio increases monotonically with distance. The agreement between the numerical results and Ross' formula is mixed. The comparison is reasonable qualitatively because the breakthrough location is in general agreement. However, the quantitative agreement is poor, especially for upstream weighting, because the leakage/infiltration ratio behavior is considerably different than the Ross (1990) model for both numerical weighting schemes.

As discussed earlier, one reason that has been proposed for the poor agreement between the numerical simulations and Ross formula is the proximity of the water table. In Ross' derivation, the fine-coarse interface is assumed to be infinitely far away from the water table, while the water table is only a few meters below the interface when breakthrough occurs in the Oldenburg and Pruess (1993) problem. If the water table is near the fine-coarse interface, the moisture content and relative permeability of the coarse material will increase due to the added moisture from the capillary fringe, and the capillary pressure will be reduced. The net effect is to decrease the contrast between the fine and the coarse layers, which will reduce the capillary barrier effectiveness. In order to address the water table proximity question, the initial water table location is varied in the present investigation.

In order to perform the modeling with different water table locations, the model domain was expanded. The depth of the coarse layer was increased from 10 meters to 50 meters for a total model depth of 100 meters. The vertical discretization was kept constant at 2 meters similar to Oldenburg and Pruess (1993), resulting in 50 elements in the z-direction. In addition, because the location of breakthrough is expected to change with water table depth, the y (downdip) discretization was kept at a constant value of 4 meters for a total distance of 800 meters (Oldenburg and Pruess had a total distance of 750 meters) with a total of 200 elements in the y-direction. Therefore, the total grid consisted of 10,000 elements.

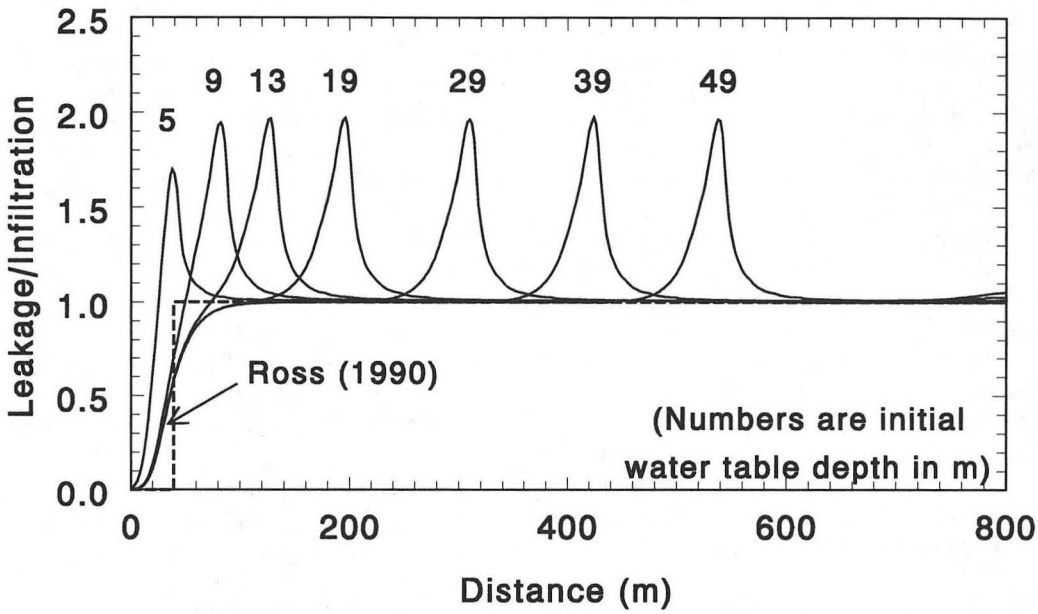

Figure 3
TOUGH2 Leakage/Infiltration Ratio As a Function of Initial Water Table Depth

The standard version of TOUGH2 (Pruess, 1991) employs a full two-phase treatment of unsaturated flow with conservation equations for both the air and water phases. A Richards' equation treatment, which only considers water movement, is also available (Pruess and Antunez, 1995). As shown by Webb (1996), the full two-phase treatment and the Richards' equation results are essentially the same for the Oldenburg and Pruess capillary barrier problem, and the Richards' equation solution time is only 1/10 of the full two-phase treatment. Therefore, the Richards' equation version has been used in the present study including Figure 2 above.

The water table in Oldenburg and Pruess is at z=-59 meters along the left edge of the domain, or 9 meters (m) below the fine-coarse interface. In the present study, water table locations of 5, 9, 13, 19, 29, 39, and 49 m below the fine-over-coarse interface have been considered with upstream weighting. The problems were run in two parts. Initial conditions were established by running a false transient to steady-state with the water table but without infiltration. The infiltration transient was then performed by using the calculated initial conditions and applying the infiltration uniformly along the top surface. The bottom boundary pressures remained constant during the transient, which provided a sink for the infiltrating water that breaks through. The simulation was run until steady-state conditions were achieved. Leakage across the fine-coarse boundary was then compared to the infiltration rate to determine the leakage/infiltration ratio.

Figure 3 compares the results from TOUGH2 and Ross' (1990) formula for the various initial water table depths. For an initial water table elevation 5 m below the fine-coarse interface, the leakage/infiltration ratio increases monotonically, reaching a maximum value of about 1.7 at 38 m. For an initial water table elevation 9 m below the interface, the leakage/infiltration ratio increases monotonically, and the ratio reaches a maximum value approaching 2.0 at 82 m. These results are similar but not exactly the same as given by Oldenburg and Pruess (1993). Small differences between the two results are expected due to the expanded computational domain employed in the present simulations and the different treatment of unsaturated flow. For an initial water table 13 m below the interface, the leakage/infiltration ratio again increases monotonically, although the ratio shows a tendency to "flatten out" slightly at intermediate distances. The peak ratio is about 2.0 at 126 m downdip.

Results for initial water table depths of 19 m, 29 m, 39 m, and 49 m are also shown in Figure 3. As the initial water table depth increases, three regions are evident. They are 1) initial increase in leakage/infiltration ratio, 2) leakage/infiltration plateau at a value of 1.0, and 3) increase in the ratio above 1.0 as the water table is approached. (The downdip distance corresponding to the intersection of the water table with the fine-coarse interface is simply the initial water table depth divided by tan 5°, or 0.0875.) For example, the leakage/infiltration ratio from 0 to 100 m is essentially the same for

water table locations 19 m or more below the fine-coarse interface. The breakthrough location is similar to that predicted by Ross (1990) although considerably more diffuse due to the numerical behavior of upstream weighting (see, for example, Oran and Boris, 1987). The ratio then remains at a value of 1.0 until the water table is approached. The leakage/infiltration ratio then increases to a value of about 2.0 as water flows down to the water table in the capillary fringe region.

In summary, for initial water table depths of 13 m or less, the location of the water table significantly influences the initial behavior of the leakage/infiltration ratio; this range includes the original Oldenburg and Pruess (1993) problem specification of 9 m. For larger initial water table depths of 19 m or more, the initial leakage/infiltration ratio is not affected by the location of the water table.

DISCUSSION AND CONCLUSIONS

Results from numerical simulations using upstream weighting have been compared to Ross' tilted capillary barrier diversion formula for the Oldenburg and Pruess (1993) capillary barrier problem with variable water table locations. For a sufficiently deep water table, which is consistent with the assumption used by Ross (1990), the simulations are in good qualitative *and* quantitative agreement with Ross' capillary barrier diversion formula. For shallower water tables, including the Oldenburg and Pruess (1993) location, the results are significantly influenced by the water table. These results indicate that upstream weighting can accurately model capillary barrier behavior as evidenced by good agreement between the simulations and Ross' formula for the deeper water table locations.

These conclusions are significantly different than Oldenburg and Pruess (1993). Oldenburg and Pruess concluded that while upstream weighting may describe the general behavior of capillary barriers, it is not able to model the details of capillary barrier flow; harmonic weighting is required to resolve the details of breakthrough. Their results are based on the difference between their upstream weighting results and Ross' (1990) formula as shown in Figure 2. Their conclusion has significant implications in unsaturated flow modeling for capillary barriers. As mentioned earlier, upstream weighting is often required for transient unsaturated flow modeling. Therefore, according to Oldenburg and Pruess (1993), modeling of transient unsaturated flow in capillary barriers involves numerical compromises; while upstream weighting is often required for numerical efficiency and stability, it is not as accurate as harmonic weighting. As mentioned by Oldenburg and Pruess (1993), this compromise not only applies to engineered capillary barriers such as discussed in this paper, but it also has important implications for simulation of natural capillary barrier effects such as encountered in potential nuclear waste repositories.

In contrast, the present study has shown that the disagreement observed by Oldenburg and Pruess (1993) was significantly influenced by the proximity of the water table. If the water table is deep enough, which is consistent with the assumption made by Ross (1990), simulations using upstream weighting agree well with Ross' capillary barrier diversion formula. Based on the present results, upstream weighting *can* be used to accurately model transient unsaturated flow including capillary barrier behavior.

Nomenclature

K_s	saturated hydraulic conductivity for fine layer
K_s^*	saturated hydraulic conductivity for coarse layer
k_r	relative permeability
L	horizontal diversion length
P_c	capillary pressure
q	infiltration rate
Q	total horizontal flux
S_l	liquid saturation
α	sorptive number for fine layer
α^*	sorptive number for coarse layer
ρ	fluid density
ϕ	angle of the fine-coarse interface with respect to horizontal
ψ	moisture potential

Acknowledgments

This work was supported by the United States Department of Energy under Contract DE-AC04-94AL85000. Sandia is a multiprogram laboratory operated by Sandia Corporation, a Lockheed Martin Company, for the United States Department of Energy.

References

Aziz, K., and Settari, T., 1979, Petroleum Reservoir Simulation, Applied Science Publishers, London.

Glass, R.J., Parlange, J.-Y., and Steenhuis, T.S., 1989a, "Wetting front instability, 1, Theoretical discussion and dimensional analysis," *Water Resour. Res.*, 25:1187-1194.

Glass, R.J., Steenhuis, T.S., and Parlange, J.-Y., 1989b, "Wetting front instability, 2, Experimental determination of relationships between system parameters and two-dimensional unstable flow field behavior in initially dry porous media," *Water Resour. Res.*, 25:1195-1207.

Glass, R.J., Steenhuis, T.S., and Parlange, J.-Y., 1989c, "Mechanisms for finger persistence in homogeneous unsaturated porous media: Theory and verification," *Soil Sci.*, 148:60-70.

Hill, D.E., and Parlange, J.-Y., 1972. "Wetting front instability in layered soils," *Soil Sci. Soc. Am. Proc.*, 36:697-702.

Ho, C.K., and Webb, S.W., 1998, "The Effects of Heterogeneities and Wavy Interfaces on Capillary Barrier Performance," TOUGH '98 Workshop.

Oldenburg, C.M., and Pruess, K., 1993, "On Numerical Modeling of Capillary Barriers," *Water Resour. Res.*, 29:1045-1056.

Oran, E.S., and Boris, J.P., 1987, Numerical Simulation of Reactive Flow, Elsevier, New York.

Pruess, K., 1991, *TOUGH2 - A General-Purpose Numerical Simulator for Multiphase Fluid and Heat Flow*, LBL-29400, Lawrence Berkeley Laboratory, May 1991.

Pruess, K., and Antunez, E., 1995, "*Applications of TOUGH2 to Infiltration of Liquids in Media with Strong Heterogeneity*," in Proceedings of the TOUGH Workshop '95, K. Pruess, ed., pp. 69-76, LBL-37200, Lawrence Berkeley Laboratory.

Ross, B., 1990, "The Diversion Capacity of Capillary Barriers," *Water Resour. Res.*, 26:2625-2629.

Ross, B., 1991, "Reply", *Water Resour. Res.*, 27:2157 (see Steenhuis et al., 1991).

Steenhuis, T.S., Parlange, J.-Y., and Kung, K.-J.S., 1991, "Comment on 'The Diversion Capacity of Capillary Barriers,' by Benjamin Ross," *Water Resour. Res.*, 27:2155-2156 (see Ross, 1991).

Stormont, J.C., 1995, "The Effect of Constant Anisotropy on Capillary Barrier Performance," *Water Resour. Res.*, 31:783-785.

Tsang, Y., and Pruess, K., 1990, *Further Modeling Studies of Gas Movement and Moisture Migration at Yucca Mountain*, Nevada, LBL-29127, Lawrence Berkeley Laboratory.

van Genuchten, M.Th., 1980, "A Closed-form Equation for Predicting the Hydraulic Conductivity of Unsaturated Soils," *Soil Sci. Soc. Am. J.*, 44:892-898.

Webb, S.W., 1996, *Selection of a Numerical Unsaturated Flow Code for Tilted Capillary Barrier Performance Evaluation*, SAND96-2271, Sandia National Laboratories.

Webb, S.W., 1997, "Generalization of Ross' Tilted Capillary Barrier Diversion Formula For Different Two-Phase Characteristic Curves," *Water Resour. Res.*, 33:1855-1859.

Numerical Simulation Experiments on Water Seepage in Unsaturated, Heterogeneous Fractures

Tai-Sheng Liou [1,2], *Karsten Pruess* [1], *and Yoram Rubin* [2]

[1] Earth Science Division, Lawrence Berkeley Laboratory, University of California, Berkeley, California 94720
[2] Department of Civil and Environmental Engineering, University of California, Berkeley, California 94720

Abstract

In this paper, we discuss the study of unsaturated flow in fractures with a detailed resolution of heterogeneity. Fractures were simulated as two-dimensional porous media characterized by a heterogeneous and spatially correlated permeability field that was numerically generated by simulated annealing (SA). By introducing the concept of neighborhood into the Metropolis algorithm (Metropolis, 1953), we were able to capture the correlation structure near asperity contacts. Flow in such heterogeneous fractures was simulated by using the module EOS9 in TOUGH2. Simulation results showed that flow depends strongly on scales of heterogeneity and boundary conditions. Preferential flow paths, bypassing and ponding were observed in all realizations reported here. Increasing the percentage of asperity contacts resulted in more tortuous flow channels, but also significantly changed the breakthrough behavior and the seepage pattern.

Introduction

Fluid flow and solute transport in unsaturated, fractured rocks have generated increasing interest in recent years. The Department of Energy has been investigating the feasibility of building a repository for high-level nuclear waste at Yucca Mountain, an arid region near the Nevada-California border with the geological formation composed primarily of welded and non-welded tuffs having fractures with different scales of heterogeneity. The potential repository site at Yucca Mountain is approximately 375 m beneath the land surface and the water table is at a depth of approximately 600 m. Since fast preferential flow has been observed in a similar semi-arid environment at Rainier Mesa (Lawrence Berkeley National Laboratory, 1991), there is a concern that radionuclides released from canisters in the potential site at Yucca Mountain might be transported downward through fractures to the saturated zone. The focus of the present study is flow in heterogeneous fractures in order to understand water seepage and its implications in unsaturated fractured media such as are encountered at Yucca Mountain.

Naturally fractured rocks generally form a complex, three-dimensional network composed of interconnected and heterogeneous fractures. Predicting flow behavior in such media is generally difficult. One approach to understanding flow behavior in fracture networks is to simulate flow in a single fracture and extrapolate the results to the overall network (Nordqvist *et al.*, 1992). Thus, simulating flow in a single fracture is necessary for understanding flow and transport in naturally fractured rocks. The ultimate goals of this study are to interpret the unsaturated flow regime observed in the field and to provide guidelines for field experiments.

In this paper, we discuss the investigation of unsaturated flow in a single, vertical fracture plane. The heterogeneous and correlated permeability field in this fracture plane was generated with simulated annealing (SA) using a modified perturbation mechanism. The fracture plane was discretized into 10,000 square grid blocks with a grid block size of 0.2 m. This allows the applicability of the relative permeability and capillary pressure relationships based on the macroscale continuum concepts (Persoff and Pruess, 1995). Typical value of the matrix permeability for unfractured welded tuffs at Yucca Mountain is of order 10^{-18} m^2 or lower.

Therefore, impact of the matrix permeability on seepage pattern was neglected because of its much smaller magnitude than the reference permeability for fractures in welded tuffs (10^{-9} m^2), and the short timescale of interest (days). The isothermal flow of water was simulated by the general purpose simulator TOUGH2 (Pruess, 1991) with EOS9 module. EOS9 solves the Richards' equation, considering only single component aqueous phase flow and treating gas phase as a passive bystander. We focus on transient and steady state flows of water in unsaturated fractures under different boundary conditions. Also, we study the influence of the percentage of asperity contacts on the breakthrough behavior and seepage pattern. All flow simulations were performed on a personal computer with a Pentium-150 processor.

Heterogeneous Fractures

Simulated annealing (SA) was used to generate the heterogeneous permeability field in fractures. The algorithm of SA is based on an analogy between the physical process of annealing and the optimal ordering of a system with various components. Beginning with an initial state, SA perturbs the system by choosing one random pair at each perturbation and deciding whether exchanging the members of this pair is favored or not according to a particular perturbation mechanism, for example, Metropolis algorithm (Metropolis *et al.*, 1953). Annealing proceeds until the system reaches the state with the minimum global energy, or until the system energy cannot be further reduced. Here, the energy is a measure of the difference between the desired distribution and the realization of some spatial features. In this paper, we used the isotropic exponential semi-variogram model with nugget=0.0, sill=190.0 and integral scale=0.2 m to describe the spatial correlation structure. Details of SA can be found elsewhere, e.g., Deutsch and Journel (1992) and Deutsch and Cockerham (1994).

A vertical fracture plane 20 m wide by 20 m deep, and with a nominal thickness of 1cm, is discretized into 100×100 grid blocks, i.e., $\Delta x=\Delta z=0.2$ m. Permeability modifiers, ζ, are used to describe the permeability field according to $k = k_{ref} \times \zeta$, where k is the intrinsic permeability and k_{ref} is the reference permeability of $10^{-9}m^2$. The initial field for SA was synthesized by first generating the initial asperity contacts ($\zeta=0$), then filling-in non-conditioning grid blocks with univariate random numbers generated from a log-normal distribution with mean and standard deviation of the log-transformed ζ as 1.0 and 1.5, respectively. The initial asperity contacts were generated prior to SA and were used as the conditioning data. In order to have a gradual change of apertures near asperity contacts, the log-normal distribution was further shifted by a constant, Δ, i.e., $\zeta'=\max(\zeta-\Delta,0)$, such that additional unconditioning asperity contacts were produced. Because of the heterogeneity introduced by the permeability field, the capillary pressure is scaled by the factor $1/\sqrt{\zeta'}$ (Leverett, 1941).

Pruess and Antunez (1995) suggested that, for "small" fractures in hard rock, a realistic representation of heterogeneity should have the following characteristics: (1) the presence of asperity contacts; (2) a gradual change towards larger apertures away from the asperities; (3) a small-scale roughness of the fracture wall, and (4) a finite spatial correlation length among apertures. We found that the Metropolis algorithm was not adequate to capture the correlation structure near asperity contacts. Therefore, we modified the algorithm by introducing the concept of neighborhood such that the vicinity of conditioning asperity contacts can be emphasized. The neighborhood of a conditioning asperity contact is defined as the non-conditioning grid blocks that are at most 3 grid blocks away from the asperity contact. After investigating several possible combinations, we determined that the following algorithm is successful in annealing towards simply-connected asperities, i.e., if both of the data in a random pair are inside or outside of any neighborhoods, the Metropolis algorithm is still used; if only one of the data is in a neighborhood, this pair is unconditionally

accepted if the data outside the neighborhood has a smaller ζ than the one inside the neighborhood. We call this new algorithm the 'modified Metropolis algorithm'.

Figure 1 shows a typical realization annealed with the modified Metropolis algorithm for isotropic conditioning asperity contacts. The total percentage of asperity contacts was increased from 10% to 25%, i.e., Δ=0.64. This percentage was chosen heuristically based on fracture wall coating data from Yucca Mountain (Wang and Narasimham, 1985). Figure 2 shows the corresponding conditioning asperity contacts used in Figure 1. The spatial correlation structure and the clustering effects can be clearly seen in Figure 1. However, we found that visually distinctive permeability fields may give the same "perfect" match to the prescribed semi-variogram shown in Figure 3. This perfect match raised the issue of whether such a crude characterization of heterogeneity as is embodied in a semi-variogram is adequate for describing heterogeneous fractures. Despite its limitations, we used the semi-variogram as the correlation model in our simulations because of its simplicity and the lack of better correlation models in the literature.

Flow simulations

Variably saturated isothermal flow in heterogeneous fractures is described by the Richard' equation (Oldenburg and Pruess, 1993). This equation was solved using TOUGH2 with the module EOS9. EOS9 considers only single-component aqueous phase flow and treats gas phase as a bystander at constant pressure. The relative permeability and capillary pressure used in Richards' equation were expressed by van Genuchten's (1980) equations

$$k_{rl} = \sqrt{S^*}\left\{1-\left(1-\left[S^*\right]^{1/\lambda}\right)^{\lambda}\right\}^2, \quad P_{cap} = -P_0\left(\left[S^*\right]^{1/\lambda}-1\right)^{1-\lambda} \qquad (1),$$

$$S^* = (S_l - S_{lr})/(1-S_{lr})$$

where S^* is the effective saturation, S_l is the liquid (water) saturation, S_{lr} is the residual saturation, λ is a fitting parameter related to the pore-size distribution, and P_{cap} is the capillary pressure. Parameters used in Eq(1) were derived from a coarse sand material, i.e., λ=0.457, S_{lr}=0.15 for k_{rl} and S_{lr}=0.0 for P_{cap}, and P_0=195.9 Pa. The porosity of the medium was assumed to be 0.35 in all simulations, and the reference permeability was 10^{-9} m^2.

In the simulations reported here, water was initially at the residual saturation (S_{lr}), i.e., S_l=0.15. No-flow boundary conditions were assumed for lateral boundaries. Water was injected either locally at the center of the top boundary over a 1 m interval or uniformly over the entire top boundary. The injection rate was a constant 10^{-3} kg/s. For localized injection cases, no-flow boundary condition was assumed at the top boundary outside the injection region. To simulate the steady state flow in fractures far above the water table, a unit head gradient boundary condition was imposed at the bottom boundary. For simulating transient flow to the time of first breakthrough at the bottom boundary, no flow condition was assumed at the bottom boundary.

Figures 4 and 5 show transient flows in the fracture of Figure 1 for localized and uniform injection, respectively, at the time of breakthrough at the depth of -19.5 m. Flow evolves by gravity, capillarity and pressure force. Preferential flow paths are evident in both simulations, some of which pond upon some asperity contacts, merge with other flow paths, and keep evolving as they proceed downward. Flow ponding and bypassing caused by asperity contacts can be identified in both cases. For the localized injection case, the

breakthrough point may or may not be at the center of the bottom boundary. All the above phenomena are induced by the heterogeneity of the medium. Figures 4 and 5 show significantly different evolution of flows, indicating that flow behavior changes dramatically with different boundary conditions.

Figures 6 and 7 show unsaturated flows at steady state for localized and uniform injection, respectively. Here, an approximate "steady state" flow field is recognized when the ratio of the fluxes at the bottom to the top reaches 0.999. We noted that the saturation field continues to evolve even if the flux ratio exceeds 0.999 but at much slower time scales than in Figures 6 and 7. Figure 7 shows that some areas of the fracture will never be visited by water because of the heterogeneity of the medium.

Natural fractures may have more or less asperity contacts than was assumed in the above simulations. Experimental data (Raven and Gale, 1985) have demonstrated that increasing the contact areas in fractures results in more tortuous flow channels. This motivated us to study the effect of percentage of asperity contacts on the flow behavior. Figures 8, 9 and 10 show the steady state flow in the fracture plane of Figure 1 but with 15%, 35% and 40% asperity contacts, respectively. The effect of the percentage of asperity contacts on flow is evident. For better illustration of the effects of asperity contacts on flow behavior, the 35% and 40% asperity contacts are also superimposed on their corresponding flow fields in Figures 9 and 10, respectively. Figure 10 shows that only one finger reaches the bottom. In contrast, in Figures 7 and 8 water contacts almost the entire bottom boundary. Also, flow ponding increases with increasing percentage of asperity contacts.

Breakthrough curves are shown in Figure 11 for asperity contacts ranging between 15% and 40%. The curve becomes steeper as the percentage of asperity contacts increases. The breakthrough curve at 40% asperity contacts shows repeated cycles of fast and retarded breakthrough, suggesting that the breakthrough behavior is non-uniform and depends on the contact areas in fractures. The curves also show a general trend of faster breakthrough with increasing percentage of asperity contacts. Note that average vertical permeability decreases with increasing asperity contacts. Thus, we have the interesting result that seepage may proceed faster in fractures of lower average permeability. These results indicate that the breakthrough behavior as well as the seepage pattern are greatly influenced by the percentage of asperity contacts.

Conclusions

High resolution of the spatial discretization has enabled us to simulate the correlated heterogeneities in fractures on the scale of decimeters. Heterogeneous fractures generated by SA using a modified Metropolis algorithm were able to capture realistic correlation structure, especially near asperity contacts. Different scenarios of flow simulation showed complex flow phenomena like preferential flow paths, ponding, and bypassing, which are due to different scales of heterogeneity and boundary conditions. Results also implied that seepage pattern and breakthrough behavior depend strongly on the percentage of asperity contacts. Our numerical simulation experiments are consistent with field observations of preferential flow, and provide some insights into the flow and transport mechanisms within the fracture plane.

Acknowledgement

This work was funded by the Director, Office of Energy Research, Office of Health and Environmental Sciences, Biological and Environmental Research Program, of the U.S. Department of Energy under Contract No. DE-AC03-76SF00098. Thanks are due to Jil Geller and George J. Moridis for reviewing the manuscript and suggesting improvements.

References

Deutsch, C.V., and A. G. Journel, GSLIB, Geostatistical Software and User Guide, Oxford University Press, New York, 340p., 1992.

Deutsch, C. V., and P. W. Cockerham, Practical Considerations in the Application of Simulated annealing to Stochastic Simulation, *Mathematical Geology*, Vol. 26, No. 1, pp. 67-82, 1994.

Lawrence Berkeley National Laboratory, Geologic Repository Project, A Review of Rainier Mesa Tunnel and Borehole Data and Their Possible Implications to Yucca Mountain Site Study Plans, Lawrence Berkeley National Laboratory Report LBNL-32068, 99p., December 1991.

Leverett, M. C., Capillary Behavior in Porous Solids, *Trans. Soc. Pet. Eng. AIME*, Vol. 142, pp.152-169, 1941.

Metropolis, N., A. Rosenbluth, M. Rosenbluth, A. Teller, and M. Teller, Equations of State Calculations by Fast Computing Machines, *Journal of Chemical Physics*, Vol. 21, pp.1087-1092, 1953.

Nordqvist, A. W., Y. W. Tsang, C. F. Tsang, B. Dverstrop, and J. Anderson, A variable aperture fracture network model for flow and transport in fractured rocks, *Water Resou. Res.*, Vol. 28, No. 6, pp. 1703-1713, 1992.

Oldenburg, C. M., and K. Pruess, On Numerical Modeling of Capillary Barriers, *Water Resou. Res.,* Vol. 29, No. 4, pp. 1045-1056, 1993.

Persoff, P., and K. Pruess, On Numerical Modeling of Capillary Barriers, *Water Resou. Res.,* Vol. 31, No. 5, pp. 1175-1186, 1995.

Pruess, K., TOUGH2 - A General Purpose Numerical Simulator for Multiphase Fluid and Heat Flow, Report No. LBL-29400, Lawrence Berkeley Laboratory, Berkeley, CA, May 1991.

Pruess, K., and E. Antunez, Application of TOUGH2 to Infiltration of Liquids in Media with Strong Heterogeneity, Proceedings of the TOUGH Workshop '95, Lawrence Berkeley Laboratory Report LBL-37200, pp. 69-76, Berkeley, CA, March 1995.

Raven, K. G., and J. E. Gale, Water Flow in a Natural Rock Fracture as a Function of Stress and Sample size, *Int. J. Rock Mech. Sci. & Geomech. Abstr.*, Vol. 22, No. 4, pp. 251-261, pp. 1985.

van Genuchten, M. Th., A Closed-Form Equation for Predicting the Hydraulic Conductivity of Unsaturated Soils, *Soil Sci. Soc. Am. J.*, Vol. 44, p. 892-898, 1980.

Wang, J.S.Y., and T. N. Narasimhan, Hydrologic Mechanisms Governing Fluid Flow in A Partially Saturated, Fractured, Porous Medium, *Water Resou. Res.,*, Vol. 21(12), pp. 1861-1874, 1985.

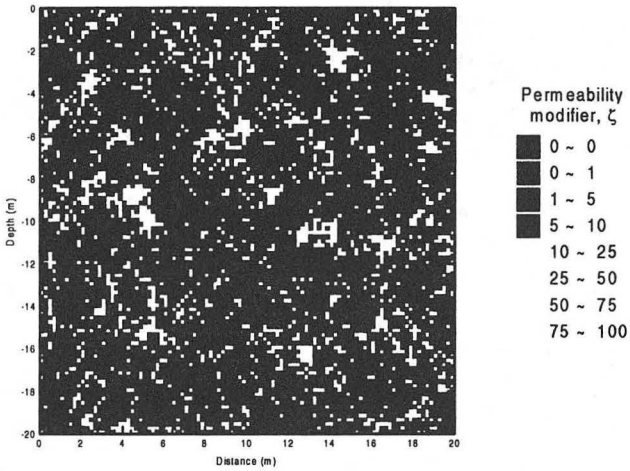

Figure 1. Permeability field generated with SA using the modified Metropolis algorithm and isotropic conditioning data. The percentage of asperity contacts is 25%.

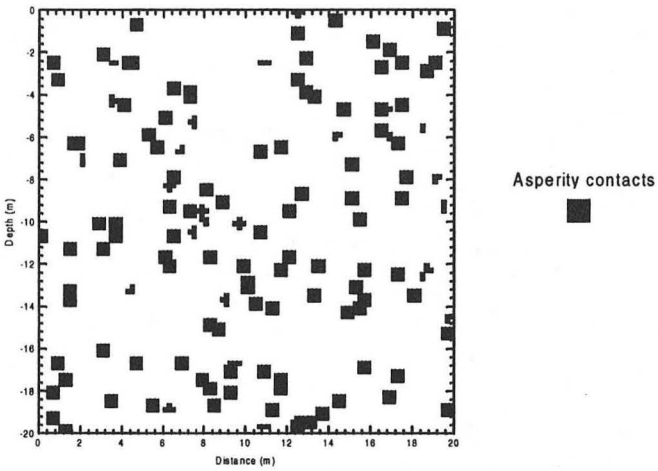

Figure 2. Asperity contacts used as the initial conditioning points for the permeability field in Figure 1. The percentage of conditioning asperity contacts is 10%.

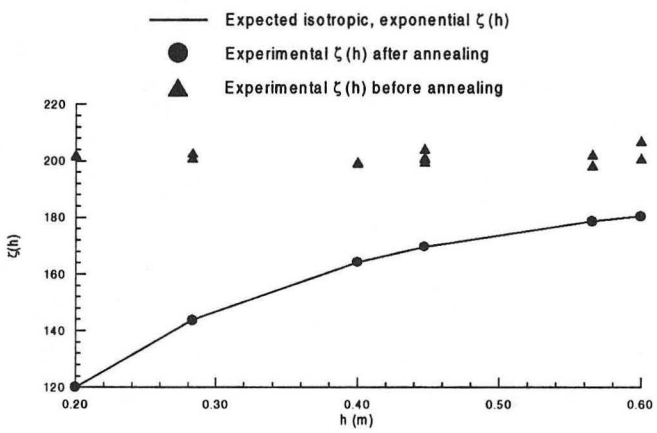

Figure 3. Expected and simulated spatial correlation relationships for the permeability field shown in Figure 1.

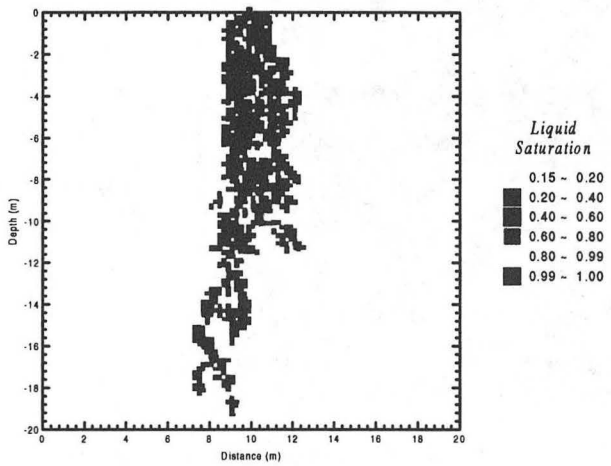

Figure 4. Liquid saturation for localized injection in fracture of Figure 1 at the time of first breakthrough at the depth of -19.5 m (Time=14.36 hrs).

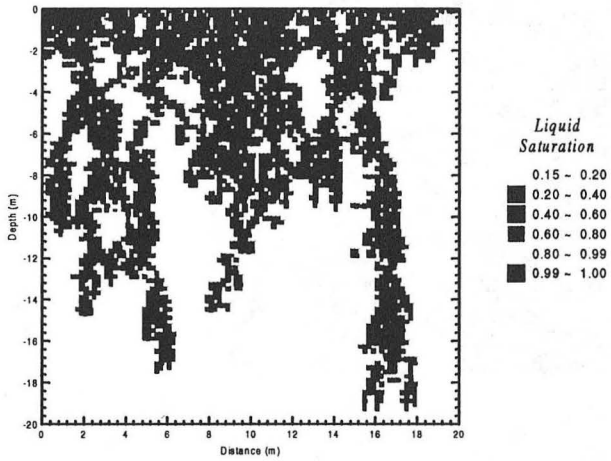

Figure 5. Liquid saturation for uniform injection in fracture of Figure 1 at the time of first breakthrough at the depth of -19.5 m (Time=40.85 hrs).

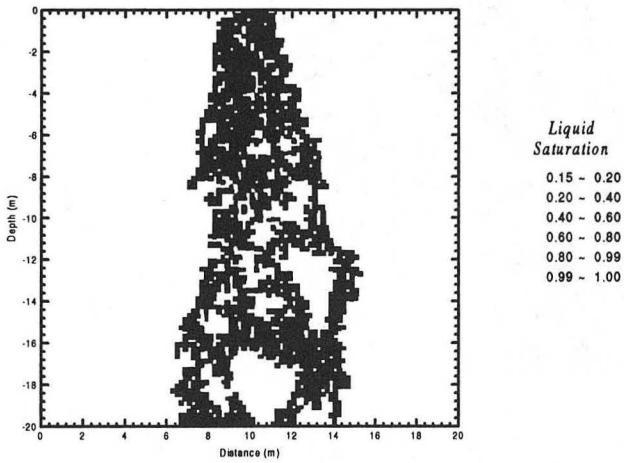

Figure 6. Steady state liquid saturation for localized injection in fracture of Figure 1. Simulation time=9.73 days.

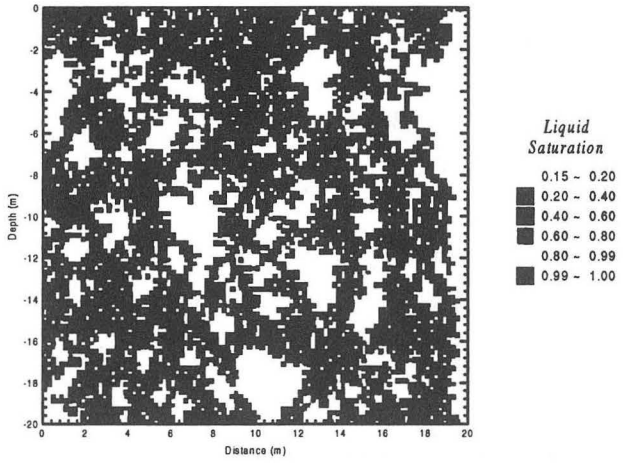

Figure 7. Steady state liquid saturation for uniform injection in fracture of Figure 1 with 25% asperity contacts. Simulation time = 55.56 days.

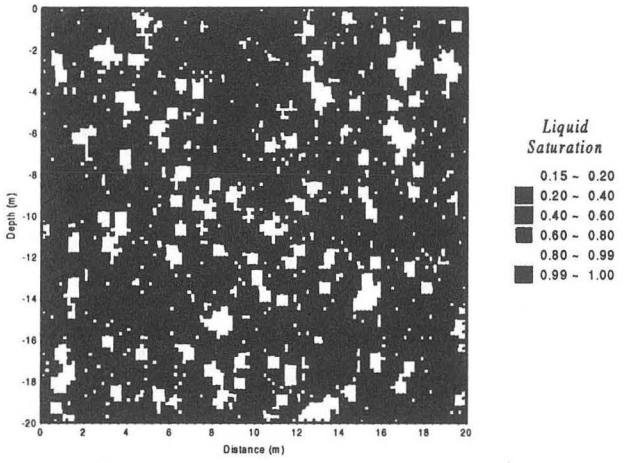

Figure 8 Steady state liquid saturation for uniform injection in fracture of Figure 1 but with 15% asperity contacts. Simulation time = 15.31 days.

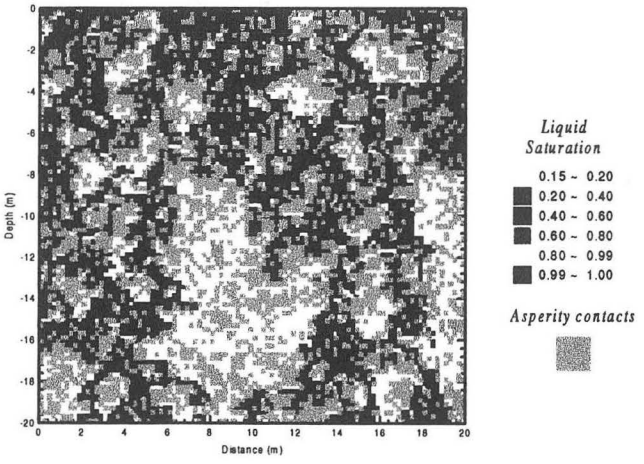

Figure 9. Steady state liquid saturation for uniform injection in fracture of Figure 1 but with 35% asperity contacts. Simulation time = 49.00 days.

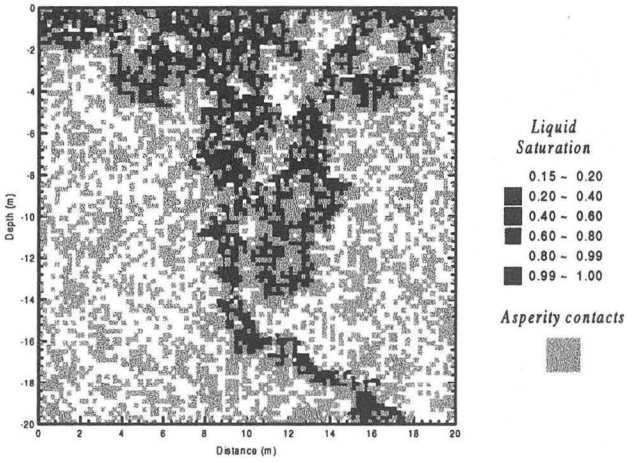

Figure 10. Steady state liquid saturation for uniform injection in fracture of Figure 1 but with 40% asperity contacts. Simulation time = 9,96 days.

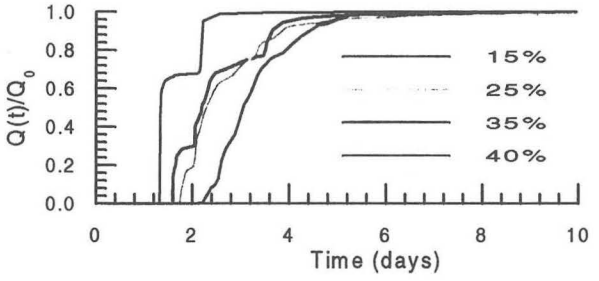

Figure 11. Breakthrough curves of the steady flow fields for the uniform injection cases with different total percentage of asperity contacts.

Analysis of Uncertainty for 2-D Fracture Flow and Seepage Into an Excavated Drift

A. L. James, C. M. Oldenburg and S. Finsterle
Earth Sciences Division
Lawrence Berkeley National Laboratory

Introduction

In this study we perform simulations of fracture flow by releasing a finite water pulse above an excavated niche in a 2-D vertical cross section. The amount of water that infiltrates the niche is observed through time and we analyze its sensitivity with respect to permeability, k and van Genuchten's fitting parameter analogous to the inverse of air entry pressure, $1/\alpha$. Evaluation of uncertainty in the total percent infiltrate as a result of parameter uncertainty is performed using linear First-Order-Second-Moment and Monte Carlo methods. In addition, the effects of heterogeneity within the fracture continuum on flow and infiltration are observed by replacing the homogeneous fracture continuum with two randomly generated permeability and air entry pressure heterogeneous continua.

Conceptual Model

Fluid flow through a 2-D vertical cross section fracture continuum is simulated using TOUGH2, an integral finite difference simulator developed at LBNL (Pruess, 1991). In this study TOUGH2 is used to calculate an isothermal, 2-D solution to Richards Equation for unsaturated flow above and around a short excavated drift, or niche.

Simulations of fluid flow presented here are loosely based on field experiments currently being performed at Yucca Mountain, Nevada, in which a water pulse of a known volume is released above an excavated niche. In the field, movement of the water pulse is observed by collecting infiltrate through the niche ceiling. Similarly, in this numerical study, we quantify the amount of water infiltrating the niche by means of the percent infiltrate, defined as the percentage of the total liquid release volume that enters the niche. In the simulations, a water pulse of 1.4 l is released instantaneously at time zero, roughly 1 m above the niche ceiling. Within the niche, a boundary condition of 100% relative humidity is assumed such that the excavated niche acts as a capillary barrier. Table 1 describes the homogeneous fracture continuum parameter distributions for the two uncertain parameters. Mean values of permeability and air entry pressure are based on a 30 μm fracture aperture and cubic law. Figure 1 illustrates saturation contours within the 2-D fracture continuum surrounding the excavated niche 12 hrs after the water pulse release.

Sensitivity Analysis

Figures 2 and 3 illustrate the sensitivity of total percent infiltrate to permeability and air entry pressure. For the simulation conditions of water ponded in the release wellbore, permeability (Figure 2) affects the time frame over which infiltration occurs, but not the amount of infiltration entering the niche. Figure 3 shows percent infiltrate sensitivity to air entry pressure; as air entry pressure increases, percent infiltrate drops and as $1/\alpha$ decreases, more water infiltrates the niche. Air entry pressure significantly affects the percent infiltrate but only mildly alters the time frame over which infiltration occurs.

Uncertainty Analysis

Uncertainty analysis is performed using ITOUGH2 (Finsterle, 1997), an inverse modeling code written to interface with the TOUGH2 family of codes. In this study, ITOUGH2 provides estimates of uncertainty in the amount of water that enters the niche as a result of parameter uncertainty by linear First-Order-Second-Moment (FOSM) and Monte Carlo methods. Linear FOSM analysis assumes that uncertainty in any observable system response (e.g. percent infiltrate) can be approximated as a linear function of all uncertain

system parameters (e.g. k and $1/\alpha$). Generally, this method will not provide acceptable estimates of uncertainty for non-linear system behavior. A Monte Carlo analysis of uncertainty in the total percent infiltrate is performed for comparison purposes and is regarded as a more accurate but computationally costly estimation method. One hundred Monte Carlo simulations are executed, drawing randomly generated values of permeability and air entry pressure from lognormal distributions described in Table 1.

Figure 4 illustrates the results of both FOSM and Monte Carlo uncertainty analyses for parameter set 1. Horizontal lines bound the area that describes physically plausible values of percent infiltrate, from 0% to 100%. The 100 Monte Carlo simulations are presented as dashed lines. Results of the FOSM analysis are indicated on either side of the mean total infiltrate of 78%. Monte Carlo results produce percent infiltrate values ranging over 38%. The FOSM analysis fails to estimate transient uncertainties, often exceeding the boundaries of what is physically plausible. Figure 5 shows the analysis repeated for a domain of higher permeability and lower capillarity described in Table 2. This system allows a greater mean percent infiltrate (88%) while reducing uncertainty to 24%. The reduction of uncertainty in the percent infiltrate with a higher mean percent infiltrate shows the sensitivity of the uncertainty analysis to the mean.

We repeated the uncertainty analysis, this time introducing two randomly generated permeability fields. Each field was created with a vertically dominant structure (vertical correlation length of 3.0 m; horizontal correlation length of 0.2 m). Correspondingly heterogeneous air entry pressure fields were created using the J-Leverett function (Bear, 1972) to relate k and $1/\alpha$. Uncertainty analyses resulted in mean percent infiltrates (and Monte Carlo ranges) of 88% (23%) and 92% (14%) for the two fields, respectively. Due to the sensitivity of the uncertainty in percent infiltrate to the mean, it is difficult to separate the effects of heterogeneity on uncertainty.

Conclusions

The amount of water to infiltrate the niche is very sensitive to van Genuchten's air entry pressure. Under these simulated conditions, (i.e., ponding conditions in the borehole) permeability affects only the time frame over which infiltration occurs and does not affect the total percent infiltrate. Linear FOSM analysis does not produce an acceptable estimate of the uncertainty in the amount of water to infiltrate the niche. The effect of heterogeneity on the uncertainty in percent infiltrate is not resolved due to the sensitivity of uncertainty to the mean percent infiltrate.

Acknowledgments

This work was supported by the Director, Office of Civilian Radioactive Waste Management, through a Memorandum Phase Order EA9013MC5X between TRW Environmental Safety Systems, Inc. and E.O. Lawrence Berkeley National Laboratory through U.S. Department of Energy Contract No. DE-AC03-76SF00098.

References

Bear, J., Dynamics of Fluids in Porous Media, Dover Publications, Inc., New York, 1972, p. 446.

Finsterle, S., ITOUGH2 command reference, 3.1, Rep. LBL-40041, UC-400, Lawrence Berkeley National Laboratory, Univ. of Calif., Berkeley, 1997.

Pruess, K., TOUGH2- A general purpose simulator for multiphase fluid and heat flow, Rep. LBL-29400, Lawrence Berkeley National Laboratory, Univ. of Calif., Berkeley, 1991.

Table 1. Parameter Set 1 (Based on a 30 μm fracture aperture and cubic law).

Parameter	mean μ	standard deviation σ
log k (m^2)	-14.58 (2.6 millidarcies)	0.5
log 1/α (Pa)	3.66 (4550 Pa)	0.166

Table 2. Parameter Set 2 (Higher permeability, lower capillarity).

Parameter	mean μ	standard deviation σ
log k (m^2)	-13.96 (11 millidarcies)	0.5
log 1/α (Pa)	3.45 (2818 Pa)	0.166

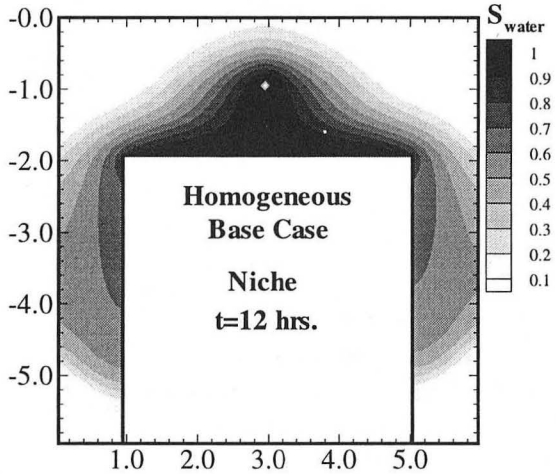

Figure 1. Contours of liquid saturation within the 2-D fracture continuum surrounding the excavated niche 12 hrs after the water pulse release.

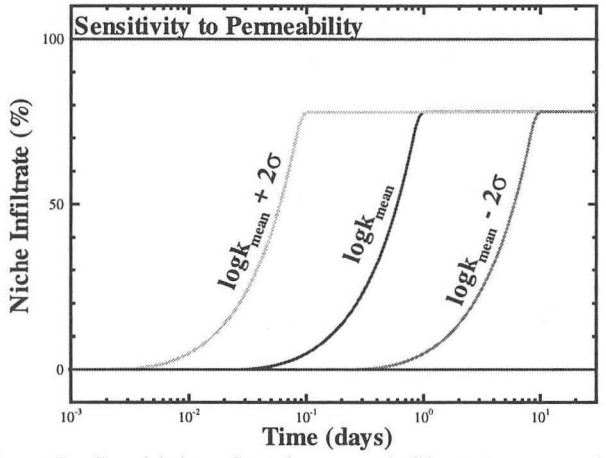

Figure 2. Sensitivity of total percent infiltrate to permeability.

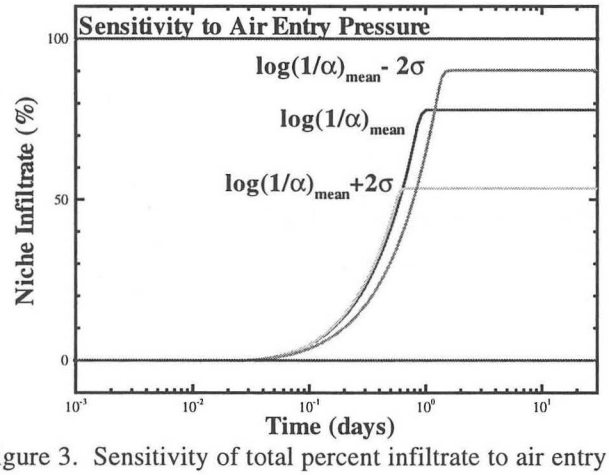

Figure 3. Sensitivity of total percent infiltrate to air entry pressure.

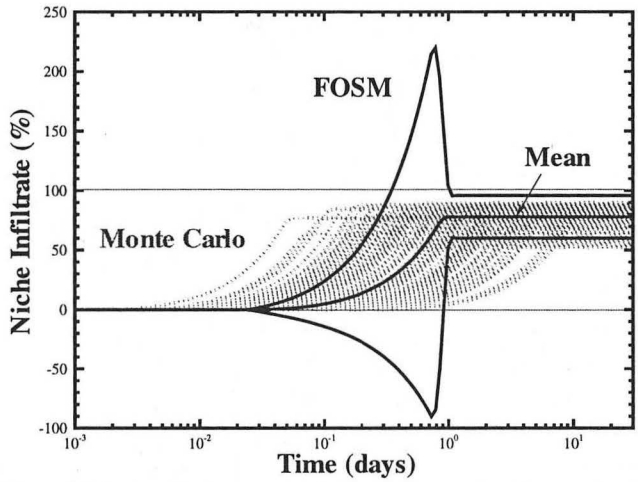

Figure 4. FOSM and Monte Carlo uncertainty analyses for Parameter Set 1. The mean percent infiltrate is 78%. Uncertainty in steady-state percent infiltrate is 38%.

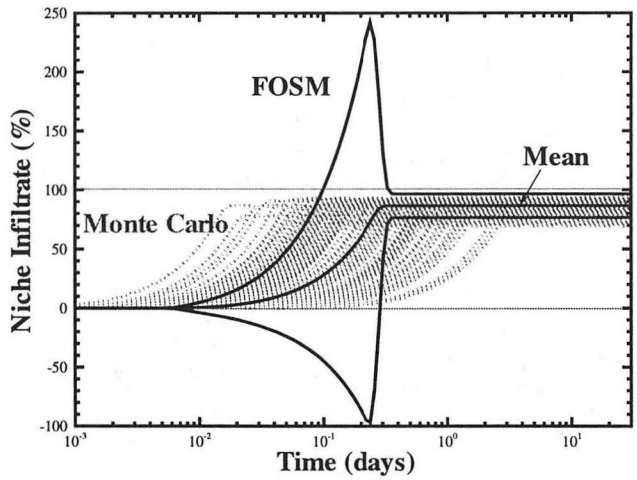

Figure 5. FOSM and Monte Carlo uncertainty analyses for Parameter Set 2 (higher permeability, lower capillarity). The mean percent infiltrate is 88%. Uncertainty in steady-state percent infiltrate is reduced and ranges over 24%.

Numerical Modeling of Field Tests in Unsaturated Fractured Basalt at the Box Canyon Site

Christine Doughty
Earth Sciences Division
E.O. Lawrence Berkeley National Laboratory

Abstract

A TOUGH2 model of a ponded infiltration test has been developed and used to predict the results of a field experiment conducted in the vadose zone of the fractured Snake River Plain basalts, at the Box Canyon site in southeastern Idaho. The key question addressed is how fracture-pattern characteristics and connectivity affect the pattern of liquid infiltration. The numerical model, a two-dimensional vertical cross-section, uses half-meter discretization for the shallow field site, which extends about 20 m from the ground surface to an underlying perched water body. The model includes explicit but highly simplified representations of major fractures and other important hydrological features. It adequately reproduces the majority of the field observations, confirming the notion that infiltration is largely fracture-controlled.

1. Introduction

E.O. Lawrence Berkeley National Laboratory (Berkeley Lab), in collaboration with Idaho National Engineering and Environmental Laboratory (INEEL) and Stanford University, is involved in an ongoing project to study flow and transport in fractured basalt vadose zones, for the purpose of improving performance of environmental remediation activities in such environments, and to develop improved monitoring techniques for both fundamental studies and remediation actions. Field work is conducted at Box Canyon, located near INEEL in the Eastern Snake River Plain, Idaho. At the Box Canyon site, a clean site designed to serve as an analog for contaminated sites located within INEEL, a 20 by 20 m well field consisting of 35 vertical and slanted boreholes has been developed, and a 7 by 8 m infiltration pond has been constructed. A nearby cliff-face exposure of the fractured basalts and minimal soil cover provide excellent views of the basalt flow structure, enabling extensive geologic mapping.

Field tests conducted at the Box Canyon site include hot air injection tests (Long et al., 1995), cross-hole air interference tests, and ponded infiltration tests (Faybishenko et al., 1998). The present paper describes mathematical modeling conducted prior to the first ponded infiltration test using TOUGH2 (Pruess, 1987, 1991). Simulations were conducted prior to the field test to aid in experimental design, to study the importance of different factors affecting the test, and to predict the results of the test in order to assess our understanding of the salient features of flow and transport in a fractured vadose zone. Simulations were also conducted after the field test to help explain the observed results, to assess the adequacy of the conceptual and numerical models, to infer the importance of various physical processes and the values of material properties, and to help design future tests.

One of the key questions to be addressed by modeling studies is how fracture-pattern characteristics and connectivity affect the pattern of water infiltration. For example, will flow occur predominantly through fractures or will matrix flow be significant? Is vertical connectivity great enough to allow purely vertical infiltration with little lateral spreading, or will extensive spreading occur? The deterministic modeling approach was chosen over the more traditional stochastic approach to represent heterogeneity because there is a great deal known about the formation process and resulting geometric structure of the fracture patterns for the Snake River Plain basalts (e.g., Aydin and Lore, 1997; Grossenbacher and Faybishenko, 1998). Available random field generators, even those which allow multiple anisotropic correlation scales, are not likely to capture the features of fracture connectivity that we believe are essential for modeling liquid infiltration and transport realistically. Flow and transport through heterogeneous media may be studied at a variety of scales, ranging from laboratory to regional, and the choice of modeling approach will certainly depend on the scale of interest. At the intermediate field scale of the Box Canyon site (tens of meters), we feel that we know enough about the hydrogeologic setting to be comfortable treating it deterministically.

2. Model Development

Figure 1 shows a schematic geologic cross-section through the Box Canyon site, which identifies the principal hydrogeologic components. The model for the ponded infiltration test is a two-dimensional vertical cross-section that extends from the ground surface to a depth of 20 m, the approximate depth of a local perched water body. It is comprised of an upper basalt flow, shown in Figure 1, an underlying rubble zone, and the upper portion of a lower basalt flow. The model underlies the NE-SW diagonal (10 m

length) of the infiltration pond, and extends beyond the pond 5 m on both sides. The model includes explicit representations of features observed in boreholes such as soil infilling in shallow fractures, lens-shaped vesicular zones between depths of 0 and 6 m, a central horizontal fracture zone at a depth of about 7 m, a sparsely-fractured massive basalt between depths of 7 and 10 m, and a vesicular zone overlying a rubble zone at a depth of about 10 m. Some of these features are shown in Figure 1. Low- and high-permeability layers inferred from the results of the hot air injection test are also included in the model. Additionally, the model incorporates the general pattern of column-bounding and column-normal fractures whose spacing increases with distance from the top and bottom edges of the basalt flow, by copying the pattern mapped at the cliff-face exposure of the upper basalt flow in Box Canyon (Figure 2). A hierarchical structure has been developed to categorize the fractures (B. Faybishenko, personal communication), and fracture permeability values are assigned based on this structure, as given in Table 1. The material property distribution of the model is shown in Figure 3. The grid spacing is 0.5 by 0.5 m.

There are three significant limitations of the present representation of fractures within the vertical cross-section model. Firstly, although we believe that the general structure of the fracture pattern mapped at the Box Canyon cliff face represents the fracture pattern underlying the infiltration pond correctly, specific locations for individual fractures are very likely to be wrong. This is because the distance from the cliff face to the infiltration pond is about 25 m, whereas the maximum extent of fractures perpendicular to the cliff face is probably less than 5 m (the maximum observed fracture spacing along the cliff face is about 5 m and the fracture pattern is expected to be isotropic in plan view). Therefore, the model cannot make detailed predictions for individual point observations. It can, however, be used to predict behavior at 'generic' locations, for example the time-dependence of wetting for a location adjacent to a primary vertical fracture. The model can also be used to study the effect of different parameters and processes on the spatial variability of the infiltration process.

Secondly, although the model is finely enough discretized to label individual grid blocks as either representing a fracture or matrix (grid block dimension 0.5 m, with fracture spacing ranging from 0.5 to 5 m), it cannot locate fractures more precisely than within the 0.5 m grid block width. The model does not allow a rigorous treatment of flow within a fracture, in which apertures probably range from microns to millimeters, or fracture/matrix interactions, which require fine discretization of the matrix adjacent to the fractures. Instead, an effective continuum approach is used, in which grid blocks that represent fractures actually encompass the 0.5 m wide zone of basalt in which the fracture lies. The grid block is assigned a large permeability to account for flow through the fracture and a small porosity to account for the small aperture of the fracture.

Thirdly, there are problems associated with representing a three-dimensional fracture network with a two-dimensional model. In general, water becomes trapped more easily in a two-dimensional model because the connectivity of the model is too low.

3. Model Application

Processes Modeled

Two alternative approaches were taken to model the ponded infiltration test. The first uses the traditional soil physics approach, in which air is a passive spectator, and liquid saturation is the only variable to be calculated. The EOS9 module of TOUGH2 implements this approach (Wu et al., 1996). The second, more rigorous, approach is to consider the fully coupled two-phase flow of water and air, which can be done using the EOS3 module of TOUGH2, and requires calculating both gas pressure and liquid saturation. The primary motivation for using EOS9 is numerical efficiency. The addition of air to infiltration problems can cause severe numerical difficulties, especially for highly heterogeneous media, because the physical processes occur on very different time scales. The primary motivation for using EOS3 is that it allows the development of entrapped air, which is believed to be an important effect for infiltration into heterogeneous media (Faybishenko, 1993, 1995).

Corey (1954) curves are used to describe relative permeability as a function of liquid saturation. Capillary pressure is set to zero in most of the pre-test calculations. This is done because there is no real data to specify what kind of capillary pressure-liquid saturation relations are appropriate for the fractured basalts at Box Canyon, although fracture capillary pressure strength is commonly assumed to be small. Generally, flow paths and moisture distributions develop in response to a combination of capillary and gravity forces, with gravity acting to localize flow to high-permeability pathways and capillary forces

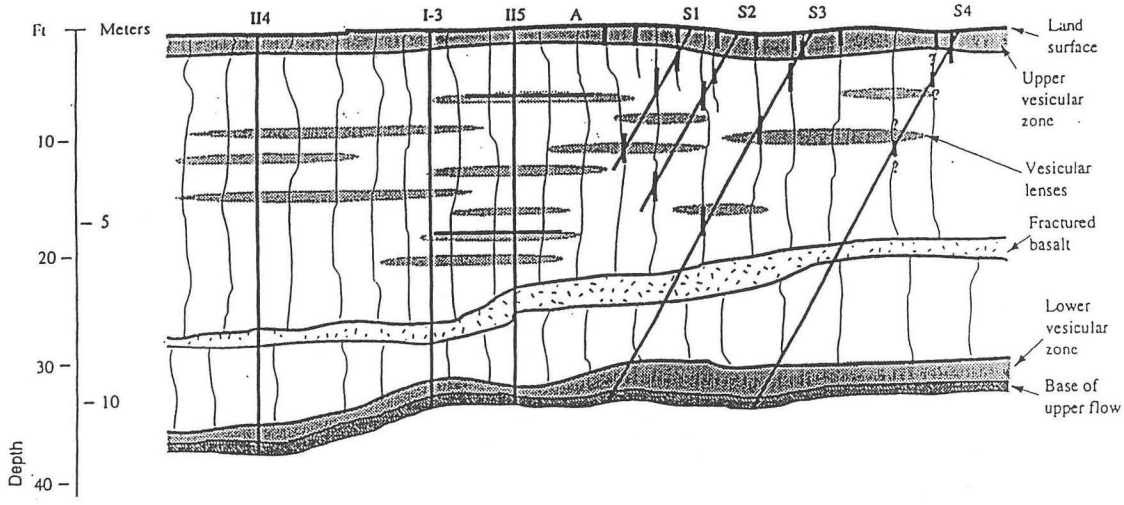

Figure 1. A schematic geologic cross-section through the Box Canyon field site, showing the upper of the two basalt flows modeled. The base of the flow is the upper boundary of the rubble zone (after Long et al., 1995).

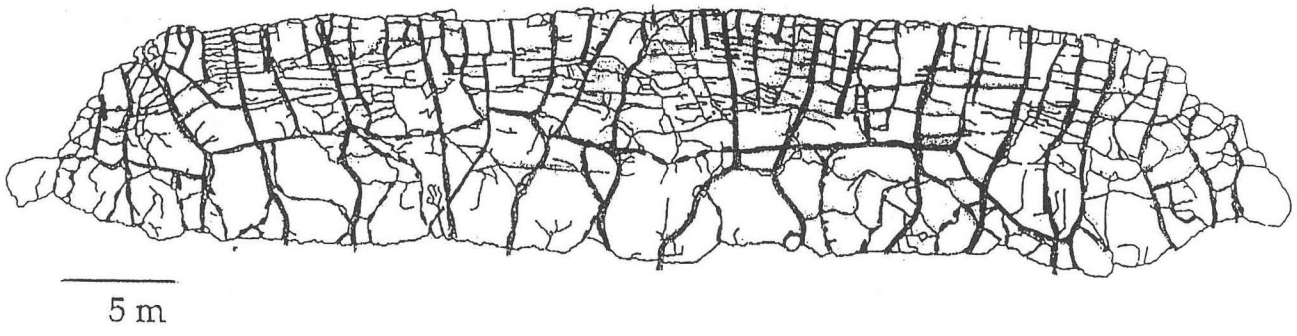

Figure 2. Fracture pattern in the upper basalt flow mapped at the Box Canyon cliff face exposure near the ponded infiltration test site (after Aydin and Lore, 1997). Primary (through-going) vertical fractures are shown bold.

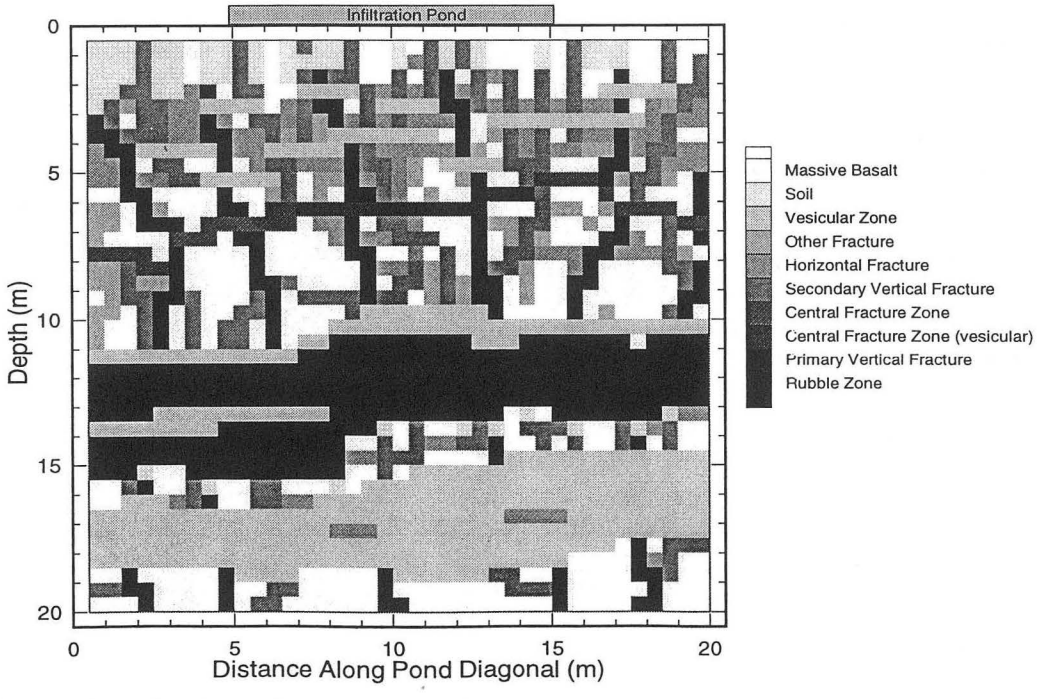

Figure 3. Two-dimensional vertical cross-section model used for the ponded infiltration test.

spreading moisture to low-permeability regions diffusively. By ignoring capillary forces, we produce a sharper picture of preferential flow paths than is likely to exist in the field. Ultimately, we hope to use the results of laboratory and field infiltration tests, in conjunction with inverse modeling, to infer appropriate characteristic curves for the Box Canyon site.

Initial and Boundary Conditions

For the EOS9 calculations, the initial condition is a uniformly partially-saturated medium with $S_l = 0.1$, in which water is immobile ($S_{lr} = 0.12$). For the EOS3 calculations, a gas-static pressure profile is also specified.

The pond boundary is represented by a liquid-saturated, constant-pressure boundary at 0.3 m of head. For the EOS3 calculations, a constant-pressure boundary representing the atmosphere overlies the non-pond portion of the model upper boundary, whereas for the EOS9 calculations this is a closed boundary. Lateral and lower boundary conditions are constant saturation (and constant pressure for EOS3). Lateral boundaries are open to liquid flow (and gas flow for EOS3) and the lower boundary, which represents a local perched water body, is open to liquid flow. Ponding lasts for four weeks.

Simulation Results

Two simulations were done, one with EOS9 and one with EOS3. The predicted saturation distributions and liquid flow fields at a series of times are shown in Figures 4 and 5 for the EOS9 and EOS3 cases, respectively. In both cases, the infiltration does not proceed uniformly, but follows highly irregular paths, bypassing the massive basalt sections, and focusing in the high-permeability fractures. A moderate amount of lateral spreading occurs, with the plume width increasing from the pond width of 10 m to about 15-18 m near the bottom of the model. The primary avenues for lateral flow are vesicular lenses and the central fracture zone. Flow through most of the rubble zone (11-14 m depths) is purely vertical, with lateral spreading occurring only in limited zones along the bottom margin.

Figure 6 compares the observed pond outflow rate with the simulated values for the two cases. For the model, pond outflow is entirely due to infiltration, whereas for the observed data it includes both infiltration and evaporation, which is estimated to be about 1-2 cm/day). The general time variation of pond outflow rate is reproduced in both cases, but the simulations show a smaller overall decrease in outflow rate. The early-time under-prediction of outflow rate may arise because of leaks that existed in the pond during the first few days of the test, resulting in a larger area available for infiltration than in the models. The late-time over-prediction of outflow rate may be the result of decreases in permeability caused by clogging of flow paths by fine materials, which is not included in the model.

The EOS3 simulation yields significantly different results than does the EOS9 simulation, suggesting that entrapped air plays an important role, and needs to be included in the model. Although the infiltrating water generally finds the same preferential pathways for the EOS9 and EOS3 simulations (compare Figures 4 and 5), more regions are bypassed and the saturation distribution is much less uniform when entrapped air develops. Subsurface flow rates are also smaller, due to the countering of gravity forces by pressure gradients caused by the development of entrapped air. The pond outflow rate is consequently smaller as well.

4. Conclusions

The modeling studies suggest that infiltration will not occur uniformly, but will follow irregular flow paths through the highest-permeability features. Some lateral spreading is expected through vesicular zones and the central fracture zone, but flow through the rubble zone is expected to be nearly vertical. Entrapped air is expected to have an important effect. Although the present model does not include capillary forces, a sensitivity study suggests that while capillary forces tend to smooth the distribution of water in the subsurface, they are not the primary factor controlling pathways through the subsurface or outflow rate from the pond. Overall, the model results have been consistent with field observations, and modeling has been an effective tool to assess and improve our understanding and aid in experimental design.

Acknowledgements

The careful review of this work by S. Finsterle and B. Faybishenko is greatly appreciated. This work was supported by the Assistant Secretary for Environmental Restoration and Waste Management, EM-50, Office of Technology Development, Characterization, Monitoring and Sensor Technology Program, of the U.S. Department of Energy under Contract No. DE-AC03-76SF00098.

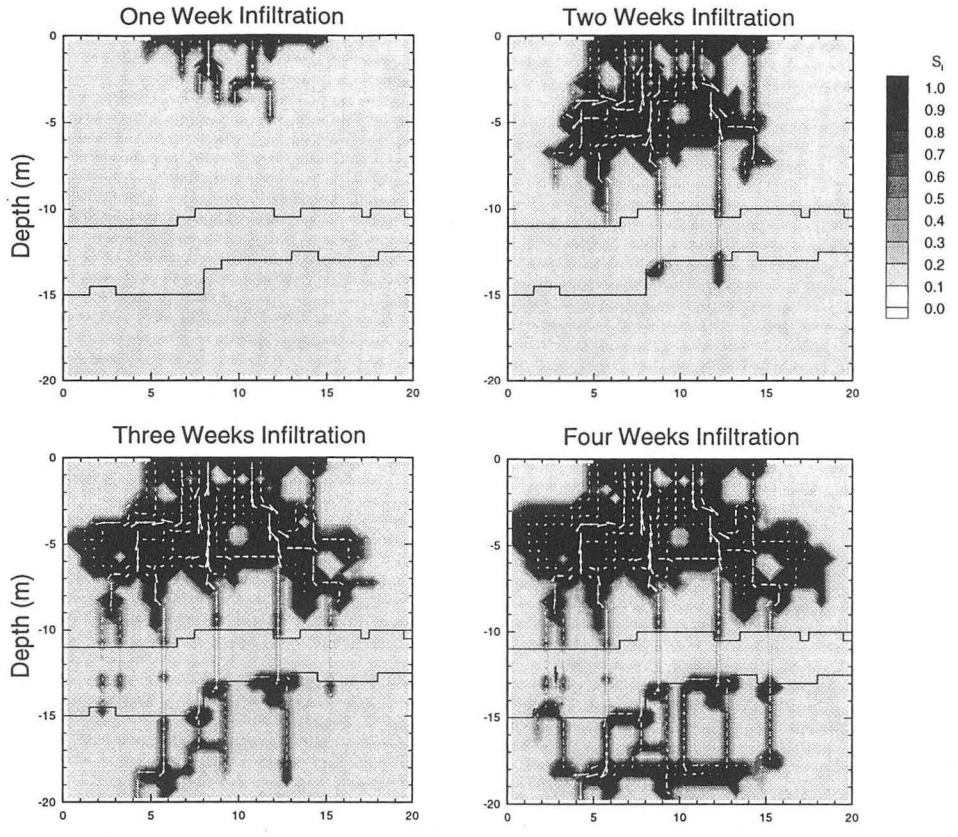

Figure 4. Simulated liquid saturation distribution and liquid flow field during the infiltration test, for the EOS9 case. The injection pond and rubble zone boundaries are also shown.

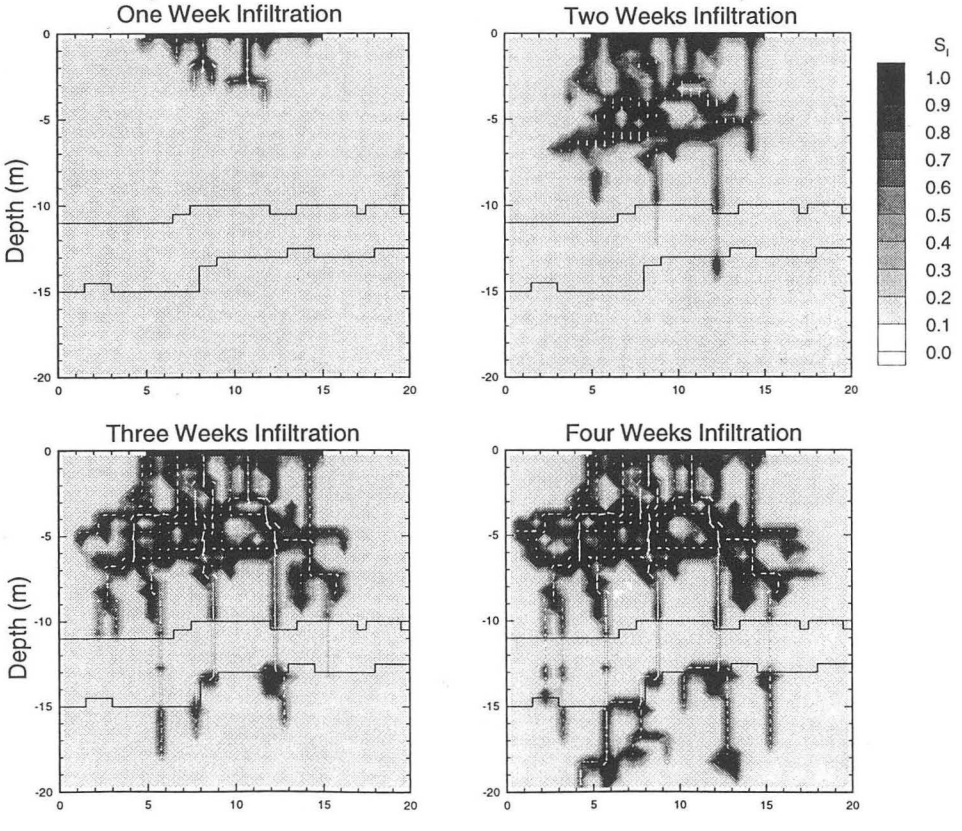

Figure 5. Simulated liquid saturation distribution and liquid flow field during the infiltration test, for the EOS3 case.

References

Aydin, A. and J. Lore, Characterization of the fracture patterns in basalt flows at Box Canyon, Idaho, internal report, Lawrence Berkeley National Laboratory, Berkeley, CA, 1997.

Baca, R.G., S.O. Magnuson, H.D. Nguyen, and P. Martian, A modeling study of water flow in the vadose zone beneath the Radioactive Waste Management Complex, Rep. EGG-GEO-10068, Idaho National Engineering Laboratory, Idaho Falls, Idaho, 1992

Bishop, C.W., Hydraulic properties of vesicular basalt, M.Sc. Thesis, Dept. of Hydrology and Water Resources, University of Arizona, Tucson, AZ, 117 pp., 1991.

Corey, A.T., The interrelation between gas and oil relative permeabilities, Producers Monthly, 19, 38-41, 1954.

Faybishenko, B., Two field experiments for ponded infiltration in foundation pits, presented at AGU 13th Annual Hydrology Days, Colorado State University, Fort Collins, Colorado, March 30-April 2, 1993.

Faybishenko, B.A., Hydraulic behavior of quasi-saturated soils in the presence of entrapped air: laboratory experiments, Water Resources Res., 31(10), 2421-2435, 1995.

Faybishenko, B. et al., Ponded infiltration test at the Box Canyon site: data report and preliminary analysis, Rep. LBNL-40183, Lawrence Berkeley National Laboratory, Berkeley, CA, 1998.

Grossenbacher, K.A. and B. Faybishenko, Spacing of thermally induced columnar joints in basalt: variation with depth, Lawrence Berkeley Laboratory Report, 1998.

Knutson, C.F., K.A. McCormick, J.C. Crocker, M.A. Glenn, and M.L. Fishel, 3D RWMC vadose zone modeling, Rep. EGG-RD-10246, Idaho National Engineering Laboratory, Idaho Falls, Idaho, 1992.

Long, J.C.S., C. Doughty, B. Faybishenko, et al., Analog site for fractured rock characterization, Annual Report FY 1995, Lawrence Berkeley National Laboratory Report LBL-38095, October, 1995.

Pruess, K., TOUGH user's guide, Rep. LBL-20700, Lawrence Berkeley Laboratory, Berkeley, CA, 1987.

Pruess, K., TOUGH2 - A general-purpose numerical simulator for multiphase fluid and heat flow, Rep. LBL-29400, Lawrence Berkeley Laboratory, Berkeley, CA, 1991.

Wu, Y.S., C.F. Ahlers, P. Fraser, A. Simmons and K. Pruess, Software qualification of selected TOUGH2 modules, Rep. LBNL-39490, Lawrence Berkeley National Laboratory, Berkeley, CA, 1996.

Table 1. Material properties used for the TOUGH2 simulations of the ponded infiltration test.

Material	Porosity	Horizontal Permeability (10^{-15} m^2)	Vertical permeability (10^{-15} m^2)
Rubble zone	0.50	10^6	10^6
Primary vertical fractures	0.08	50	5000
Central fracture zone (vesicular)	0.15	5000	50
Central fracture zone (non-vesicular)	0.10	5000	50
Secondary vertical fracture (Knutson et al., 1992)	0.07	0.05	500
Horizontal fracture	0.05	5000	0.05
Other fracture	0.05	50	50
Vesicular basalt (Bishop, 1991)	0.20	1000	1000
Soil (Baca et al., 1992)	0.50	78	78
Massive basalt	0.05	0.05	0.05

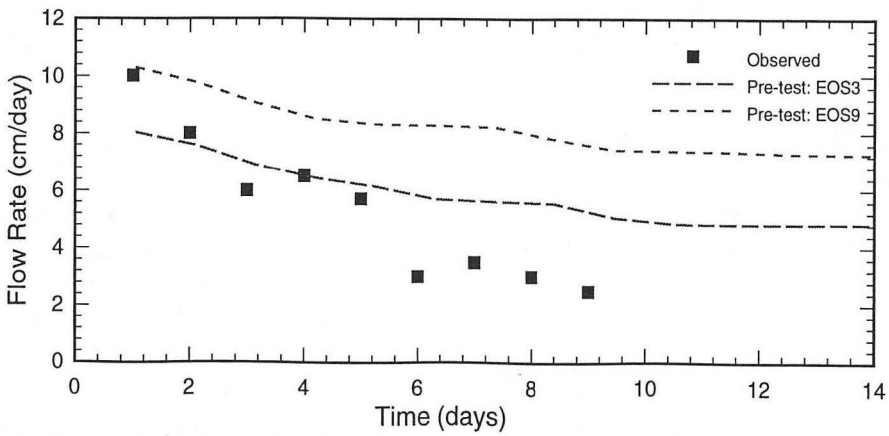

Figure 6. Simulated and observed pond outflow rate during the ponded infiltration test.

The Effects of Heterogeneities and Wavy Interfaces on Capillary Barrier Performance

Clifford K. Ho and Stephen W. Webb
Sandia National Laboratories
Albuquerque, New Mexico 87185
ckho@sandia.gov, swwebb@sandia.gov

Abstract

The performance of capillary barriers with heterogeneities and wavy interfaces has been investigated by numerically simulating three systems comprised of a fine soil layer overlying a coarse gravel layer with 1) homogeneous, 2) layered heterogeneous, and 3) random heterogeneous property fields. The amount of lateral diversion above the coarse layer under steady-state infiltration conditions was compared among the simulations. Results indicated that the performance of capillary barriers can be significantly influenced by the spatial variability of hydraulic properties. Simulations of capillary barriers have also been performed using non-uniform interfaces between the fine and coarse layers. "Wavy" interfaces have been generated using periodic functions of varying amplitude and frequency. Preliminary results of these simulations indicated that breakthrough into the coarse layer was contained primarily in the troughs of wavy interfaces, which may prove useful in waste isolation by providing drainage points between waste packages.

1. Introduction

Engineered and natural capillary barriers in the subsurface have been suggested as an effective means of diverting water away from buried waste. These capillary barriers generally consist of two or more interspersed sloping layers of fine and coarse porous materials (such as sand or soil). Under unsaturated conditions, the capillary pressures in the fine layer are large relative to the capillary pressures in the coarse layer. Therefore, water can be held in fine layers overlying coarse layers. If the layers are tilted, water can be diverted down-dip along the interface of the two layers. This phenomenon has applications and significant impacts in fields including nuclear waste management [*Prindle and Hopkins*, 1990; *Ross*, 1990; *Wilson*, 1996], landfill cover design [*Morris and Stormont*, 1997; *Webb et al.*, 1997], and soil remediation [*Ho and Udell*, 1992].

To date, nearly all of the predictive models that have been used to assess the performance of capillary barriers have assumed that the regions comprising the fine and coarse layers are homogeneous [*Ross*, 1990; *Prindle and Hopkins*, 1990; *Oldenburg and Pruess*, 1993; *Wilson*, 1996; *Webb*, 1996; *Webb*, 1997; *Selker*, 1997; *Warrick et al.*, 1997]. The assumption of homogeneous materials allows uniform, smooth interfaces between the fine and coarse layers, which may over-predict the diversion capacity of actual heterogeneous systems. Homogeneous models also neglect small scale behavior caused by heterogeneities within each layer that may positively or negatively impact the performance of capillary barriers. Therefore, the purpose of this study is to investigate the impact of various intra-unit heterogeneities and inter-unit interface conditions on the performance of capillary barriers. Three cases are presented that include homogeneous, layered heterogeneous, and random heterogeneous realizations of a system comprised of a fine soil layer overlying a coarse gravel layer. A homogeneous simulation with a wavy interface is also presented.

2. Numerical Approach

The computational domain is two-dimensional and consists of a fine layer of soil (1 m high x 6 m wide) overlying a coarse layer of gravel (0.3 m high x 6 m wide). The domain is discretized into 9750 equally spaced elements that are each 0.02 m high x 0.04 m wide. Boundary conditions include infiltration within each element along the top row at a steady rate of 4.62×10^{-7} kg/sec (1 mm/day), no-flow lateral boundaries, and a saturated boundary that is connected to the ten right-most elements in the bottom row to allow outflow of water. The entire domain is tilted 5 degrees clockwise by rotating the gravity vector in the simulations. Only steady-state conditions are considered.

The numerical code TOUGH2 [*Pruess*, 1991] is used to simulate water movement in the unsaturated domains. In the current studies, the gas phase is passive with a constant temperature and pressure (20°C, 1 bar). Only the transport of liquid water is investigated using the TOUGH2 equation of state module *EOS* 9. Full upstream weighting of the unsaturated conductivity is used in this study.

The properties of the domain are taken from two sources: an internal Sandia National Laboratories (SNL)

Table 1. Parameters used in the simulation of homogeneous and heterogeneous property fields. E is the expected value in real space and μ and σ are the mean and standard deviation in natural log space.

	(Fine Layer)			(Coarse Layer)		
	$E^{\dagger}$	μ	σ	$E^{\dagger}$	μ	σ
porosity	0.4	—	—	0.42	—	—
K_{sat} (cm/sec)	$1.43\text{x}10^{-4}$	-9.10	0.700	10	2.30	$6.99\text{x}10^{-2}$
α (1/cm)	0.021	-4.24	0.864	4.9	1.59	$4.52\text{x}10^{-3}$
β	1.87	0.609	0.184	2.19	0.772	0.157
S_r	0.21	-1.63	0.198	0.012	-5.67	1.58

$^{\dagger}E = \exp(\mu + \sigma^2/2)$

report of typical soils and gravel in Albuquerque, NM [*McTigue, D.F., Moisture Retention Properties of Soils from the Chemical Waste Landfill, Sandia National Laboratories, Albuquerque, NM, internal Sandia Letter Report dated* 12/9/94], and a paper describing capillary barrier experiments performed at SNL [*Stormont*, 1995]. The means, μ, and standard deviations, σ, of four properties (in natural log space) are listed in Table 1 along with the expected mean value, E, in real space. The four properties that are allowed to vary spatially in the simulations include the saturated conductivity, K_{sat} (cm/sec), the van Genuchten curve-fitting parameters for capillary pressure and relative permeability, α and β, and the residual liquid saturation, S_r.

For the homogeneous simulation, the expected values, E, are used for the fine and coarse layers. For the heterogeneous simulations, unconditioned sequential Gaussian simulations are performed using GSLIB [*Deutsch and Journel*, 1992] with subsequent standardization to obtain a standard normal distribution of values for all the elements in the domain. Exponential semivariogram models are used with different ranges and anisotropy factors to produce two distinct fields: 1) a layered heterogeneous field and 2) a random heterogeneous field. Ten realizations of each of the two heterogeneous systems are simulated. The layered heterogeneous fields display horizontal features with an effective range of 3 m and an anisotropy ratio of 100:1 in the x-direction, while the random heterogeneous field contains a "salt and pepper" distribution with an effective range of 0.09 m and an anisotropy ratio of 1:1.

Once the standardized variables have been generated, the means and standard deviations in Table 1 are then used to map the standardized variables, Z, to corresponding properties, X, for the fine and coarse layers of the computational domain using the following transformation:

$$X = \sigma Z + \mu \tag{1}$$

If a standardized variable lies between y = 0 m and y = 0.3 m, the means and standard deviations of the coarse layer are used in Equation 1. If a standardized variable lies between y = 0.3 m and y = 1.3 m, the means and standard deviations of the fine layer are used in Equation 1. Because the mean, μ, and standard deviation, σ, are in natural log space, the real space property values are found by taking the exponent of the property values, X, given in equation (1).

A wavy interface between the fine and coarse layers can be generated with a periodic function, $y_{int}(x)$, that defines the interface y-coordinate as a function of any x-coordinate:

$$y_{\text{int}}(x) = A\cos\left(\frac{2n\pi x}{L}\right) + y_1 \tag{2}$$

where A is the amplitude of the "wave", n is the frequency, L is the total width of the domain (6 m), and y_1 is the y-coordinate of the origin of the interface (0.3 m). If the y-coordinate of an element is less than $y_{int}(x)$, then properties of the coarse layer are assigned. If the y-coordinate of an element is greater than $y_{int}(x)$, then properties of the fine layer are assigned. An example of the wavy interface model is applied to the homogeneous model and is presented at the end of the next section.

3. Numerical Results and Discussion

Steady-state liquid saturations and mass flows are simulated for all realizations of the heterogeneous and homogeneous property fields. Saturations and mass flow vectors are plotted for one realization of each of the layered heterogeneous and random heterogeneous fields in Figure 1 along with homogeneous results to illustrate general features. Recall that the infiltration along the top row of elements is constant and that the domain is tilted 5 degrees clockwise. Also, it is worth noting that the criterion for steady-state conditions is that the mass

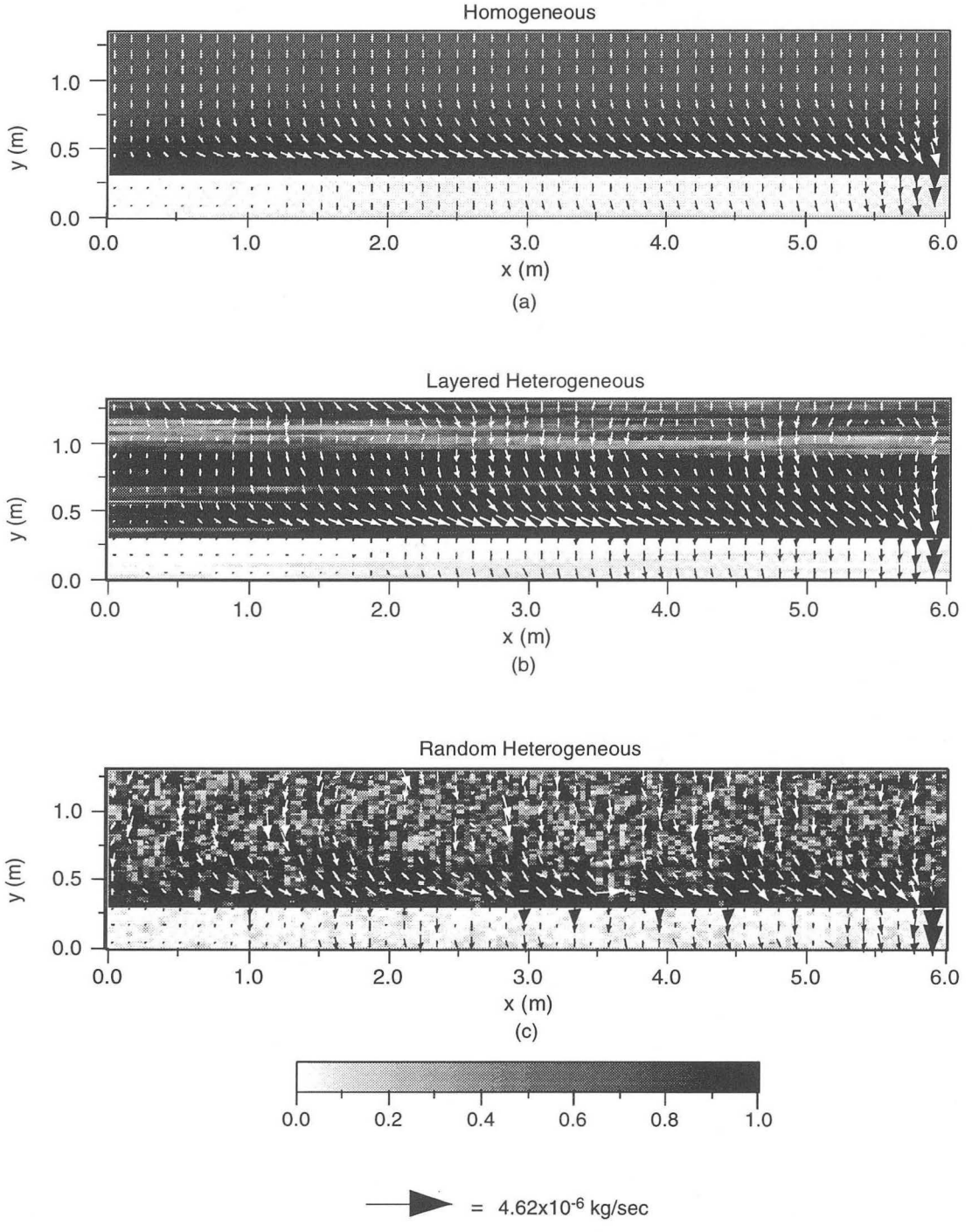

Figure 1. Simulated steady-state liquid saturations and mass flow vectors: a) homogeneous field, b) layered heterogeneous field (realization 7), and c) random heterogeneous field (realization 7). The domains are tilted 5 degrees clockwise.

flow exiting the bottom right corner, which is connected to a saturated boundary, must equal the total mass flow entering the system from infiltration.

The resulting saturation profiles and mass flow vectors for the different fields are very distinct. The homogeneous field (Figure 1(a)) displays a fairly uniform saturation distribution in the fine layer, with saturation increasing near the interface of the fine and coarse layers. Water flow is primarily vertically downward except at the interface, where lateral

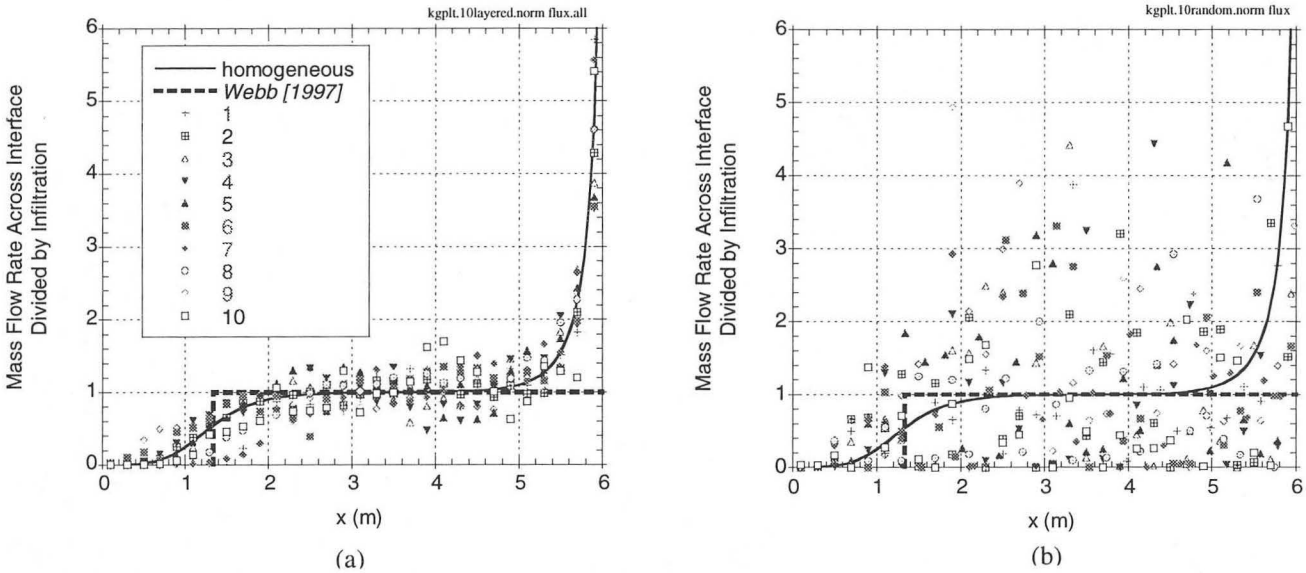

Figure 2. Mass flow rate across the interface of the fine and coarse layers divided by the infiltration rate (1 mm/day): a) ten layered heterogeneous realizations b) ten random heterogeneous realizations. The homogeneous solution and modified solution of *Ross* [1990] (detailed in *Webb* [1997]) are also shown.

diversion exists. In addition to diversion at the interface, the layered heterogeneous field shown in Figure 1 (b) also exhibits regions of lateral diversion *within* the fine layer of soil. Thin lenses of high permeability (and low liquid saturation) within the fine layer at $y \sim 1$ m act as localized capillary barriers that contribute to additional lateral diversion. The random heterogeneous field shown in Figure 1(c) yields localized channeling of downward flow through high permeability zones. Also, the "salt and pepper" saturation distribution is indicative of the highly variable permeability field that causes the localized flow in the random heterogeneous field. The channeled flow results in numerous locations of breakthrough along the interface of the fine and coarse layers.

The diversion capacities of the different fields is quantified in Figure 2, which displays the mass flow rate of water entering the coarse layer divided by the infiltration rate as a function of distance along the interface. Figure 2(a) shows that the results of the layered heterogeneous fields bound those of the homogeneous field. The distance that water is diverted before flowing into the coarse layer is twice that of the homogeneous field in realization 7, but the diversion distance is approximately half that of the homogeneous field in realization 9. The homogeneous results appear to give a reasonable approximation to the mean behavior of the ten layered heterogeneous realizations. In contrast, the random heterogeneous field (Figure 2(b)) displays a chaotic breakthrough pattern and a diversion distance that is shorter than the homogeneous model in nearly all the realizations. The results of a semi-analytical solution using a modified formulation of *Ross* [1990] as described in *Webb* [1997] is also shown, where appropriate van Genuchten functions have been used. Note that the no-flow right boundary causes significantly higher mass flow rates along the right side of the domain, but for regions greater than one meter from the right boundary, the influence of the right boundary is minimal.

Another useful means of quantifying the performance of capillary barriers is to define a cumulative breakthrough ratio, χ, by integrating the mass flow of water entering the coarse layer with respect to distance along the interface and dividing this quantity by the integrated infiltration with respect to distance along the surface:

$$\chi = \frac{\int_0^x \dot{m}(x)\,dx}{\int_0^x q\,(x)\,dx} = \frac{1}{q\,x}\int_0^x \dot{m}(x)\,dx \qquad (3)$$

where $m(x)$ is the mass flow rate of water entering the coarse layer at a location x and q is the infiltration rate (assumed constant in this study). Figure 3 shows the mean cumulative breakthrough ratio for all realizations of the random and layered heterogeneous systems. The homogeneous results are also shown for comparison. The homogeneous results are quite similar to the mean cumulative breakthrough ratio curve of all the layered heterogeneous realizations, indicating that the homogeneous model may be used to predict the average behavior of layered heterogeneous systems. The mean cumulative breakthrough curve for the random

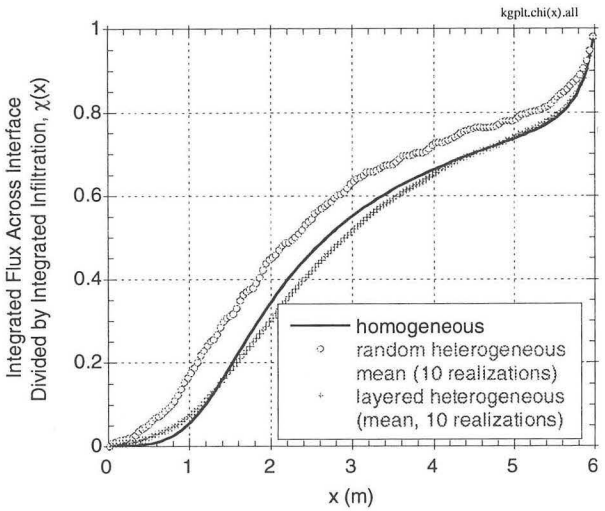

Figure 3. Mean of the cumulative breakthrough ratio curves (Equation (3)) for all simulations.

heterogeneous realizations lies above the homogeneous curve for all locations, indicating that the homogeneous model over-predicts the diversion capacity of random heterogeneous fields. The random heterogeneous systems perform poorly because of the numerous preferential pathways that channel liquid downward, causing an immediate breakthrough in nearly all of the realizations.

Figure 4 shows the liquid saturation profile and mass flow vectors for a homogeneous simulation with a wavy interface. The amplitude of the wave, A, is 0.1 m and the frequency, n, is 5. The breakthrough into the coarse layer is restricted primarily to the troughs of the wavy interface. This feature can be exploited by designing capillary barriers that have troughs, or drainage points, between areas that need to be isolated, such as waste packages.

One final comment should be made regarding the computational performance of each of the simulations. The homogeneous and layered heterogeneous simulations took on the order of several hours to reach steady-state from residually saturated initial conditions. However, the random heterogeneous field had difficulty reaching steady-state from residually saturated initial conditions. A uniform initial saturation greater than residual was imposed to allow the random heterogeneous simulation to reach steady-state. Different initial saturations were imposed, and while the results were identical, the duration and number of time steps required to reach steady-state were highly dependent on the value of the initial saturation.

4. Conclusions

Simulations have been performed to investigate the effects of heterogeneities on the performance of capillary barriers. Homogeneous, layered heterogeneous, and random heterogeneous representations of a system comprised of a fine soil layer overlying a coarse gravel layer were simulated to determine the amount of lateral diversion above the coarse layer under steady-state infiltration conditions.

Multiple realizations of the layered heterogeneous system resulted in breakthrough curves that bounded the homogeneous results. Realizations that consisted of highly stratified regions in the fine layer yielded the least amount of breakthrough in upstream regions due to additional local capillary barrier effects in the fine layer. Realizations that consisted of a fine layer that was graded from coarse at the top to fine at the bottom experienced earlier breakthrough relative to the homogeneous simulation due to increased saturations and decreased capillarity above the interface of the fine and coarse layers. All realizations of the random heterogeneous system resulted in earlier breakthrough compared to the homogeneous and layered heterogeneous runs. Preferential vertical pathways channeled flow that produced numerous localized regions of breakthrough into the coarse layer.

These results indicate that engineered capillary barriers may be improved through emplacement and packing methods that induce highly stratified features within the fine layer of a capillary barrier system. In addition, homogeneous models can be used to estimate the average behavior of layered heterogeneous systems with reasonable accuracy. The modified analytical solution of *Ross* [1990], which predicts diversion capacity for homogeneous systems [*Webb*, 1997], accurately predicted the mean diversion capacity of the layered heterogeneous systems. However, results also indicate that simple homogeneous simulations will over-predict the diversion capacity of capillary barriers if the fine layer consists of randomly distributed properties that act to channel the downward flow through preferential pathways.

Simulations of capillary barriers have also been performed using non-uniform interfaces between the fine and coarse layers. "Wavy" interfaces have been generated using periodic functions of varying amplitude and frequency. The resulting interfaces can range from smooth parabolic to highly irregular and "jagged" interfaces. Preliminary results of these simulations indicate that breakthrough into the coarse layer is contained primarily in the troughs of wavy interfaces.

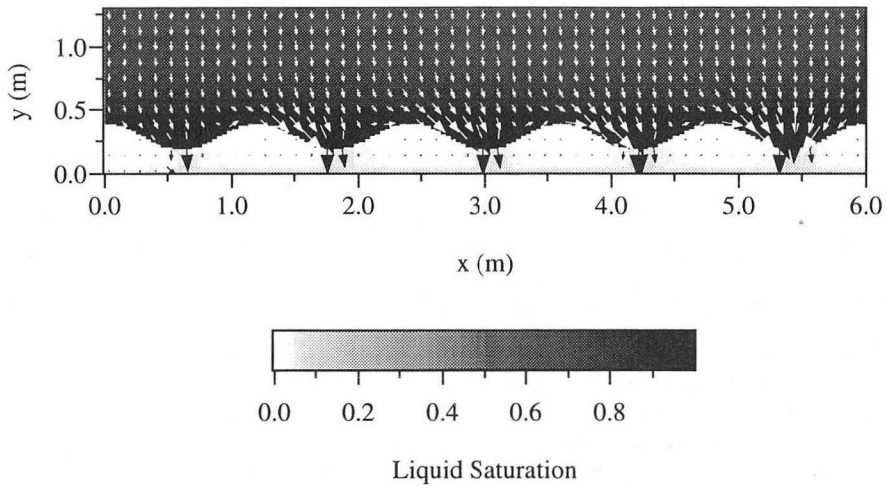

Figure 4. Liquid saturation and mass flow vectors for wavy interface simulation (A=0.1, n=5; Equation (2)).

This design may be useful in waste isolation by providing drainage points between waste packages.

Acknowledgments

The authors would like to thank Sean McKenna, Ray Finley, Eric Ryder, Mike Wilson, and Peter Davies for their discussions and review of this work. Sandia is a multiprogram laboratory operated by Sandia Corporation, a Lockheed Martin Company, for the United States Department of Energy under Contract DE-AC04-94AL85000.

References

Deutsch, C.V. and A.G. Journel, *GSLIB: Geostatistical Software Library and User's Guide*, Oxford University Press, New York, 1992.

Ho, C.K. and K.S. Udell, An Experimental Investigation of Air Venting of Volatile Liquid Hydrocarbon Mixtures from Homogeneous and Heterogeneous Porous Media, *J. Contam. Hydrol.*, 11, 291-316, 1992.

Morris, C.E. and J.C. Stormont, Capillary Barriers and Subtitle-D Covers: Estimating Equivalency, *J. Env. Eng.-ASCE*, 123(1), 3-10, 1997.

Oldenburg, C.M. and K. Pruess, On Numerical Modeling of Capillary Barriers, *Water Resour. Res.*, 29, 1045-1056, 1993.

Prindle, R.W. and P.L. Hopkins, On Conditions and Parameters Important to Model Sensitivity for Unsaturated Flow Through Layered, Fractured, Tuff: Results of Analyses for HYDROCOIN Level 3 Case 2, *SAND89-0652*, Sandia National Laboratories, Albuquerque, NM, 1990.

Pruess, K., TOUGH User's Guide, *LBL-20700*, Lawrence Berkeley Laboratory, Berkeley, CA, 1987.

Pruess, K., TOUGH2—A General-Purpose Numerical Simulator for Multiphase Fluid and Heat Flow, *LBL-29400*, Lawrence Berkeley Laboratory, Berkeley, CA, 1991.

Ross, B., The Diversion Capacity of Capillary Barriers, *Water Resour. Res.*, 26, 2625-2629, 1990.

Selker, J., Design of Interface Shape for Protective Capillary Barriers, *Water Resour. Res.*, 33, pp. 259-260, 1997.

Stormont, J.C., The Performance of Two Capillary Barriers During Constant Infiltration, in Landfill Closures, *ASCE Geotechnical Special Publication No. 53*, Edited by Bunn and Singh, pp. 77-92, 1995.

Warrick, A.W., P.J. Wierenga, and L. Pan, Downward Water Flow Through Sloping Layers in the Vadose Zone: Analytical Solutions for Diversions, *J. Hydrology*, 192, 321-337, 1997.

Webb S.W., Selection of a Numerical Unsaturated Flow Code for Tilted Capillary Barrier Performance Evaluation, *SAND96-2271*, Sandia National Laboratories, Albuquerque, NM, 1996.

Webb, S.W., Generalization of Ross' Titlted Capillary Barrier Diversion Formula for Different Two-Phase Characteristic Curves, *Water Resour. Res.*, 33(8), 1855-1859, 1997.

Webb, S.W., J.T. McCord, and S.F. Dwyer, The Applicability of the HELP Model in Predicting Tilted Capillary Barrier Performance, in Proceedings of the *1997 International Containment Technology Conference and Exhibition*, St. Petersburg, FL, 1997.

Wilson, M.L., Lateral Diversion in the PTn Unit: Capillary-Barrier Analysis, in Proceedings of the *1996 International High Level Radioactive Waste Management Conference*, Las Vegas, NV, 111-113, 1996.

Characterization and Prediction of Subsurface Pneumatic Pressure Variations at Yucca Mountain, Nevada

C. Fredrik Ahlers, Stefan Finsterle, Gudmundur S. Bodvarsson

Earth Sciences Division, Lawrence Berkeley National Laboratory, University of California, Berkeley, California 94720

Yucca Mountain, Nevada is being investigated as the proposed site for geologic disposal of high level nuclear waste. A massive data collection effort for characterization of the unsaturated zone is being carried out at the site. The USGS is monitoring the subsurface pressure variations due to barometric pumping in several boreholes. Numerical models are used to simulate the observed subsurface pressure variations. Data inversion is used to characterize the unsaturated system and estimate the pneumatic diffusivity of important geologic features. Blind predictions of subsurface response and subsequent comparison to recorded data have built confidence in the models of Yucca Mountain.

Introduction

Barometric pumping of the subsurface was first described by Buckingham (1904), and he provided an analytical solution for gas pressure as a function of depth for the idealized conditions of a single homogeneous layer bounded above by a sinusoidally varying pressure boundary condition and bounded below by an impermeable boundary. Actual field measurements of subsurface response to barometric pumping have been used to estimate hydrologic properties by several researchers. Stallman (1967) and Stallman and Weeks (1969) describe estimation of permeability assuming a single layer bounded below by an impermeable boundary. Rozsa et al. (1975) describe estimation of diffusivity assuming a semi-infinite model. Weeks (1978) describes a numerical technique for estimation of permeability of a multilayered system and results from several field tests. Shan (1995) describes an analytical solution to the multilayered problem and its application to field data from one site.

This paper will present the results of subsurface pneumatic pressure data inversion using ITOUGH2 (Finsterle, 1997a), an automated inversion program based on the TOUGH2 (Pruess, 1991) multiphase numerical simulator. *In situ* measurements of surface and subsurface pneumatic pressure, gathered by the USGS, are used together with geologic based numerical models of Yucca Mountain to estimate the pneumatic diffusivity of several layers.

Site Description

Yucca Mountain, Nevada, located approximately 120 km northwest of Las Vegas, is the proposed location for a geologic repository designed to permanently store high level radioactive waste. Many surface based boreholes have been drilled in the Yucca Mountain area and several of these have been instrumented to monitor *in situ* air pressure. A 9 km long tunnel, the Exploratory Studies Facility, ESF, has been excavated to nearly 300 m below the surface in the unsaturated zone.

The unsaturated zone at Yucca Mountain is up to 700 m thick. The volcanic rocks that make up the unsaturated zone are alternating layers of welded and nonwelded ash flow and air fall tuffs. Figure 1 shows a cross section with the hydrogeologic units of Montazer and Wilson (1984) labeled. These units are based mainly on degree of welding. From the surface down, these units are the Tiva Canyon welded (TCw), the Paintbrush nonwelded (PTn), and the Topopah Spring welded (TSw). The TCw and TSw are highly fractured and very permeable to air. The PTn is less fractured and much more porous than the overlying or underlying units making it an impediment to gas flow and thus an important layer to characterize. Sublayering of the PTn using the nomenclature of Buesch et al. (1995) is also shown on Figure 1. The Yucca Mountain and the Pah Canyon Tuffs, Tpy and Tpp, respectively, are partially welded while the other PTn sublayers are nonwelded, bedded tuffs. Very little pneumatic pressure data is available to characterize rocks below the TSw.

Data

Subsurface gas (pneumatic) pressure data have been collected at twelve boreholes on the Yucca Mountain site by several principal investigators and organizations. For this paper, data from two boreholes, NRG-6 and NRG-7a, are analyzed. Data from NRG-7a, shown in Figure 2, are characteristic of a typical data set. The pressure at the land surface shows the largest variation (and the lowest pressure because it is at the highest elevation). With increasing depth below the surface, the pressure signal shows increasing amplitude

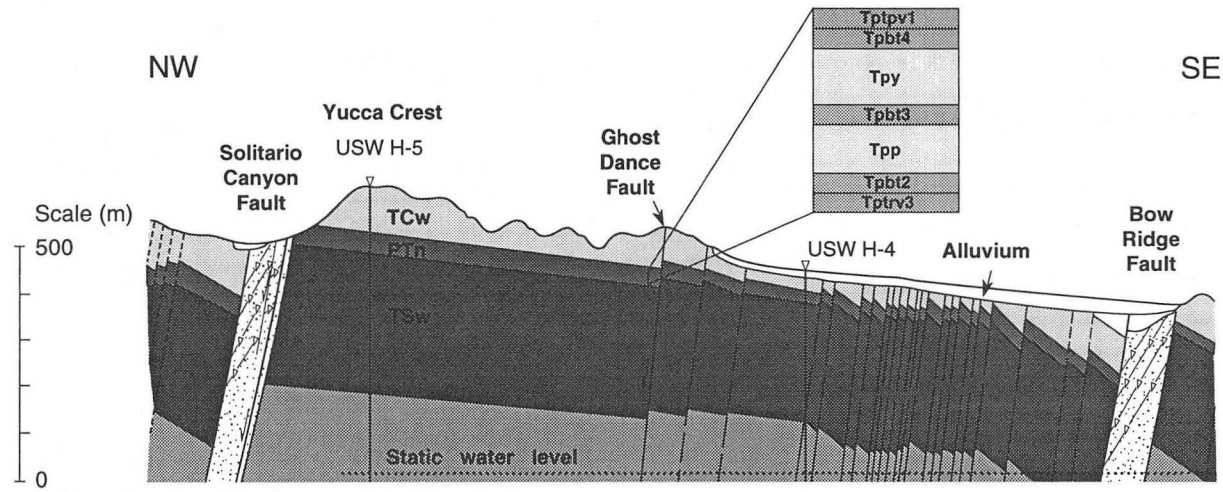

Figure 1. Cross-section of Yucca Mountain, Nevada, showing stratigraphic location of major hydrogeologic units (modified from Scott and Bonk, 1984). PTn is expanded to show sublayering. Vertical exaggeration is approximately 2:1.

attenuation and time lag with respect to the surface signal.

Both boreholes have one instrument station at the surface and one in the TCw. In NRG-6, there is one instrument station in PTn sublayer Tpp and five in the TSw. In NRG-7a, there is one instrument station in PTn sublayer Tpy and three in the TSw.

Physical Processes

Barometric pressure variation at the land surface is due to a variety of causes, each having a different characteristic period. Short period variations, which occur daily (diurnal) and every half day (semi-diurnal), are due to heating and cooling of the atmosphere and tidal effects. Longer period variations, on the order of days to weeks, are due to weather and frontal systems as they move across the earth's surface. The longest period variation occurs yearly and is due to seasonal heating and cooling of the atmosphere. This variation is more pronounced away from the equator where there are larger annual temperature variations.

The pneumatic diffusivity of the system is the property that describes how much attenuation and lag the barometric signal will undergo as it propagates into the subsurface. Pneumatic diffusivity is defined here as

$$D_g = \frac{k\overline{P}}{n_g \mu}$$

where D_g is pneumatic diffusivity, k is the intrinsic (saturated) permeability times the relative gas permeability at the prevailing saturation, n_g is the drained porosity (total porosity times gas saturation), μ is the dynamic viscosity of the gas, and $\overline{P}$ is the average gas pressure. Similar expressions are given by Weeks (1978) and Shan (1995).

The conceptual model of gas flow at Yucca Mountain is that gas flow occurs on a mountain scale mainly in the fractures. The gas filled matrix porosity in the welded units is not thought to contribute significant storage for transient gas flow because the high prevailing liquid saturation significantly reduces the already low matrix permeability for gas flow. In the nonwelded PTn, higher intrinsic matrix permeability coupled with lower matrix liquid saturation mean that matrix storage does affect transient gas flow in this unit.

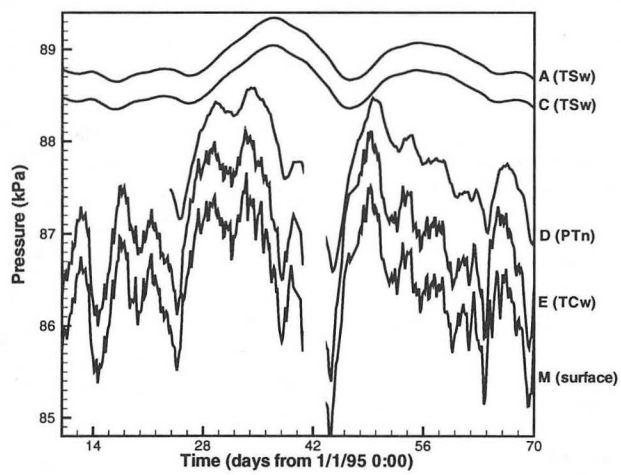

Figure 2. *In situ* pneumatic pressure data from borehole NRG-7a representing data sets typical of Yucca Mountain. Instrument stations are located in the middle TSw, upper TSw, PTn, and TCw geologic layers, and the surface. Sixty (60) days of data are shown from January 11th until March 12th, 1995.

Code Modifications

In order to apply a transient pressure boundary condition, it was necessary to slightly modify ITOUGH2 (Finsterle, 1997a). Moridis and Pruess (1992) recommend using large boundary elements and applying a similarly large source or sink to the boundary element in order to apply a transient pressure boundary condition to a model. For this problem, that technique did not work well, mainly because of the large number of barometric pressure data points necessary to adequately describe the surface pressure signal (no less than 8 per day for simulations that are 60 days long). We found that in order to use this technique it was necessary to use ITOUGH2 on the generation table to optimize the source and sink values to better match the observed surface pressure data. Even then, the match was not always satisfactory.

In order to directly use the surface pressure data, we have implemented a tabular input to ITOUGH2 that describes the transient pressures at the surface boundary element (Finsterle, 1997b). The input table includes a table of times at which the surface pressure is defined and tables of pressures at those times for each boundary element. Defining pressures for each element allows mean pressure differences due to elevation difference to be included. At each time step, the pressure for each element named in the table is calculated by linear interpolation, and that pressure is passed to the EOS module for calculation of other primary and secondary variables.

Pneumatic Data Inversion

One-dimensional, vertical models of the stratigraphy at boreholes NRG-6 and NRG-7a are used to simulate the effect of barometric pumping on the subsurface, which is assumed to be a one-dimensional, vertical process. Water is assumed to be immobile over the time scale of the simulations (60 days to several years). This assumption is based on the low estimates of infiltration to the unsaturated zone at Yucca Mountain, an average of approximately 5 mm/yr over the site, and the low matrix permeability of the rocks that make up Yucca Mountain, on the order of milli-darcys to micro-darcys. With the assumption of immobile water, a single continuum model is assumed to be adequate for simulation of the pneumatic system. These models extend from the mountain surface to the water table.

No flow boundary conditions are specified on the lateral boundaries and at the lower boundary, which is coincident with the water table. A time varying pressure boundary condition is applied to the upper boundary that simulates the observed barometric pressure signal, as explained above.

Initial conditions are gas static equilibrium (i.e., gravity equilibrium in the gas phase) with the initial boundary pressure. Because the barometric pressure is constantly changing, gas static conditions are never actually expected to exist. Therefore, the simulation is allowed to run for 30 days so that the subsurface pressures are in a dynamic state reflecting the constantly changing conditions in the mountain. Only after 30 days of simulation time are the observed pressures compared to the calculated pressures for estimation of pneumatic diffusivity.

Practically, because diffusivity is proportional to the ratio of permeability to porosity, ITOUGH2 estimates either permeability or porosity; a value for the other parameter is assumed. In this case, we assume a value for the porosity of each layer and estimate the permeability.

Time step size is limited to six hours so that the diurnal component of the barometric signal is appropriately simulated.

Because the welded layers are intensely fractured, they have a very high diffusivity. This can be seen in Figure 2. There is very little difference between the surface signal and the signal recorded in the TCw (i.e., there is little difference between the amplitude and phase of the two signals; mean pressure difference is caused by a difference in elevation between the instrument stations). There is no difference between the two signals recorded in the TSw. The largest change in the signal that is observed occurs across the PTn, from instrument station E to instrument station C. For the inverse problem, we have chosen to estimate five values of diffusivity corresponding to five sublayers in the PTn. These five sublayers are 1) Tpcpv1 and Tpbt4, 2) Tpy, 3) Tpbt3, 4) Tpp, and 5) Tpbt2 and Tptrv3 as shown in Figure 1.

Data from both NRG-6 and NRG-7a are jointly inverted. This means that models of both boreholes are run simultaneously. Data from both NRG-6 and NRG-7a are matched to the computed pressures. A single value of diffusivity is estimated for each geologic layer and applied to that layer in the models of both boreholes. This assumes that each geologic layer at Yucca Mountain is homogeneous. By making this assumption, we have better constrained the problem by increasing the amount of data that is inverted for the estimation of any one parameter.

The optimized match between the data and the simulation for borehole NRG-7a is shown in Figure 3 (a). Note that the amplitude attenuation at instrument station D appears to be slightly over-predicted by the simulation, and the lag at instrument station C is under-predicted.

As a comparison, the data from each borehole are individually inverted (i.e., the layers are not assumed to be homogeneous between the two borehole, thus separate estimates of diffusivity are made for the layers in each of the boreholes). Figure 3 (b) shows the comparison between the observed data and the calculated pressures for borehole NRG-7a. Note that the amplitude at instrument station D and the lag at instrument station C predicted by the simulation appear to match the observed data better than in the joint inversion.

ITOUGH2 also provides a quantitative assessment of the match between the data and the simulation. The mean and the standard deviation of the residuals (difference between observation and simulation at each data point) give a measure of the goodness of fit. Table 1 shows the mean and standard deviation of the residuals for each borehole for both the joint and individual inversions. With the exception of the mean for NRG-6, the numbers indicate an improved match for the individual inversions. The increase of the mean from the joint to the individual inversions for borehole NRG-6 reflects a small systematic error between the observed and predicted pressures.

Although the individual inversions provide a better match to the data, the uncertainty of the diffusivity estimates is expected to increase. This is because less data is being used for each estimate of diffusivity. In the joint inversion, there were estimates of diffusivity for five layers; in the individual inversion, the same amount of data was used for two estimates of diffusivity for each layer or nine estimates of diffusivity (the Tpy layer is not present in NRG-6). ITOUGH2 also provides a measure of the uncertainty of each parameter estimate. Figure 4 shows the diffusivity estimates and the uncertainty of the estimate for each layer from each of the three inversions. Note that the values of uncertainty are not meant to reflect all the uncertainty in the system, but are measures of relative uncertainty between the different inversions. For three of the sublayers, the uncertainty of the individual inversion estimates is increased with respect to the joint inversion estimate, as expected. The small uncertainty of the joint inversion estimate of Tpbt3 diffusivity (as compared to the individual inversion estimates) is because data from the overlying layer (from NRG-7a) and underlying layer (from NRG-6) are used in the inversion effectively bounding layer Tpbt3. Interestingly, the uncertainty of both individual inversion estimates for layer Tpbt2/Tptrv3 and one for layer Tpp are less than the uncertainty of the joint inversion estimate for those layers. Both boreholes have several instrument stations in the TSw, and all this data was used in the inversions. The improvement of the overall match between the simulation and the

Borehole	Joint		Individual	
	Mean [Pa]	Std. Dev. [Pa]	Mean [Pa]	Std. Dev. [Pa]
NRG-6	13.8	80.1	15.4	78.9
NRG-7a	26.2	70.0	24.4	62.2

Table 1. Comparison of mean and standard deviation of residuals for joint vs. individual inversion of *in situ* pneumatic pressure data.

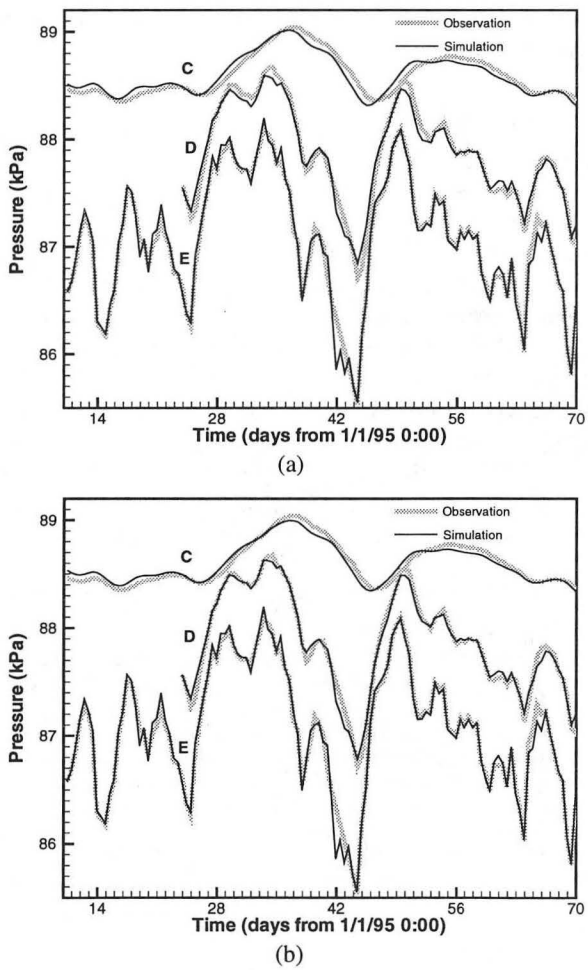

Figure 3. Simulated pressure response at stations C (upper TSw, D (PTn) and E (TCw) in borehole NRG-7a using diffusivity estimated by joint inversion of NRG-6 and NRG-7a data (a) and individual inversion of NRG-7a data (b).

observations for the individual data inversion is significant because the TSw data represents a large portion of the data being inverted. The improved match between simulation and observation means that the estimates of diffusivity between the lowest instrument station in the PTn and the highest in the TSw are more certain.

Prediction

Once the models are calibrated through data inversion, predictions of the subsurface response to barometric pumping are made for portions of the observed data not used in the calibration. The predictions allow evaluation of the models under different conditions than those of calibration, providing insight into possible conceptual model deficiencies.

Figure 5 shows the predicted pressures at instrument station D in the upper TSw. From day 196 (July 16, 1995) through day 270 (September 28, 1995), the simulation matches the observation reasonably well, indicating that the conceptual model and the calibration from the previous time period are valid.

However, after day 270, the simulation systematically over-predicts the amplitude attenuation at station D. Since we know that the model has not changed, we can assume that the real system has changed. In the original conceptual model, it was assumed that NRG-6 was too far from the ESF tunnel to be affected by the barometric signal introduced into the subsurface through the tunnel. This was confirmed because when the tunnel excavation passed closest to NRG-6 no change in the signal was observed. However, around the same time as the change in the observed data, excavation of the ESF tunnel intersected a fault (beyond the point of closest approach to NRG-6) that also passes near NRG-6. It seems very likely that the barometric signal is transmitted from the ESF, through the fault, which is assumed to have a high diffusivity, to instrument station D in NRG-6. This would account for the added amplitude in the observed signal after September 28.

Conclusions

Measurements of the subsurface response to barometric pumping of the unsaturated zone can be used to determine pneumatic diffusivity. In this study, we have used independently determined geology to define layering in two boreholes. Diffusivity of these layers is then estimated through inversion of observed time-series pressures from the subsurface. Using the data from two boreholes, we have compared the match between observation and simulation for a joint inversion and individual inversions and compared the uncertainty of the estimated parameters for the joint and individual inversions. In both cases, the matches between observation and simulation were reasonable though slightly better for the individual inversions. At the same time, the uncertainty of the estimated parameters increased for six of the nine individual inversion estimates with respect to the uncertainty of the joint inversion estimates. Because the match for the individual inversions is not overwhelmingly better or the uncertainty of the diffusivity estimate much less for the joint inversion, one technique does not seem to be clearly better than the other for this case. If the assumption of layer homogeneity were absolutely true, then the joint inversion should have been the better approach. If, however, the layers were strongly heterogeneous, then the individual inversion should have been clearly better. This would seem to indicate that the system is strongly heterogeneous between layers and homogeneous or weakly heterogeneous within layers.

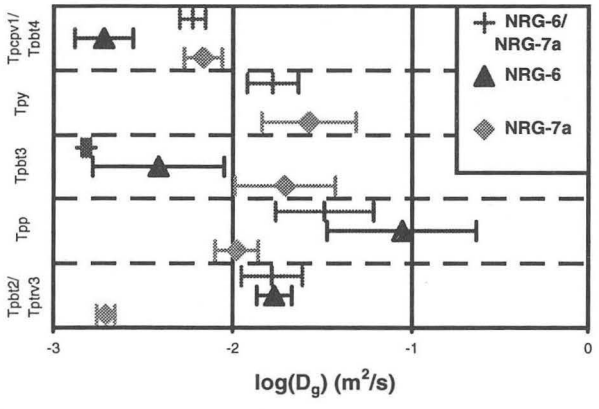

Figure 4. Estimated diffusivity and uncertainty of the estimates from joint and independent inversions of NRG-6 and NRG-7a data.

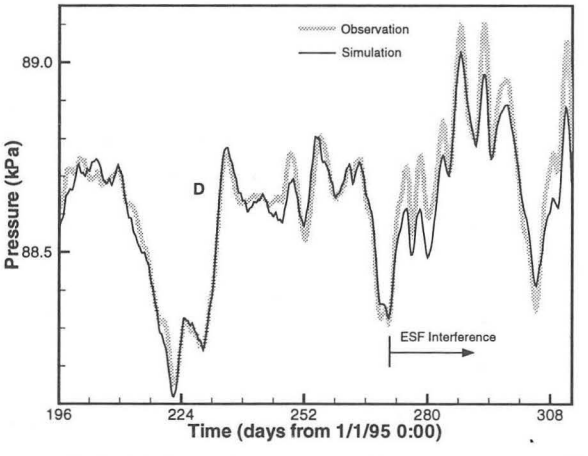

Figure 5. Prediction of pressures at instrument station D (upper TSw) in NRG-6.

Predictions of subsurface response, based on calibrated models, have helped to validate not only the estimated values but also the conceptual model of gas flow. The predictions have also pointed out where and when other factors, such as the introduction of the barometric signal into the subsurface by the ESF tunnel, are of importance to the models.

Acknowledgments

The authors would like to thank J. Rousseau (USGS) for the use of data that he and his colleagues collected. The authors would also like to thank all of our colleagues who reviewed this work and helped prepare it for publication. This work was supported by the Director, Office of Civilian Radioactive Waste Management, through Memorandum Purchase Order EA9013MC5X between TRW Environmental Safety Systems, Inc. and the Ernest Orlando Lawrence Berkeley National Laboratory, under Contract No. DE-AC03-76SF00098.

References

Buesch, D. C., R. W. Spengler, T. C. Moyer, and J. K. Geslin, Revised Stratigraphic Nomenclature and Macroscopic Identification of Lithostratigraphic Units of the Paintbrush Group Exposed at Yucca Mountain, Nevada, U. S. Geological Survey, Open File Report 94-469, 1995.

Buckingham, E., Contributions to our knowledge of the aeration of soils, Bureau of Soils—Bulletin No. 25, U. S. Department of Agriculture, 1904.

Finsterle, S., ITOUGH2 command reference, LBL-40041, Lawrence Berkeley National Laboratory, Berkeley, CA, 1997a.

Finsterle, S., ITOUGH2 sample problems, LBL-40042, Lawrence Berkeley National Laboratory, Berkeley, CA, 1997b.

Montazer, P. and W. E. Wilson, Conceptual hydrologic model of flow in the unsaturated zone, Yucca Mountain, Nevada, Water Resources Investigations Report 84-4355, U. S. Geological Survey, Denver, CO, 1984.

Moridis, G. J. and K. Pruess, TOUGH simulations of Updegraff's set of fluid and heat flow problems, LBL-32611, UC-800, Lawrence Berkeley Laboratory, Berkeley, CA, 1992.

Pruess, K., TOUGH2—a general purpose numerical simulator for multiphase fluid and heat flow, LBL-29400, Lawrence Berkeley Laboratory, Berkeley, CA, 1991.

Rozsa, R., D. Snoeberger, J. Baker, Permeability of a nuclear chimney and surface alluvium, area 2, ERDA NTS, UCID-16722, Lawrence Livermore Laboratory, Livermore, CA, March 10, 1975.

Scott, R. B. and J. Bonk, Preliminary geologic map of Yucca Mountain, Nye County, Nevada, with geologic sections, U. S. Geological Survey Report OFR-84-494, U. S. Geological Survey, Denver, CO, 1984.

Shan, C., Analytical solutions for determining vertical air permeability in unsaturated soils, *Water Resources Research*, vol. 31, no. 9, pp. 2193-2200, September, 1995.

Stallman, R. W., Flow in the zone of aeration, Ven Te Chow, ed., *Advances in Hydroscience*, vol. 4, pp. 151-195, 1967.

Stallman, R. W. and E. P. Weeks, The use of atmospherically induced gas-pressure fluctuations for computing hydraulic conductivity of the unsaturated zone (abs.), *Geol. Soc. America Abs. with Programs*, part 7, p. 213, 1969.

Weeks, E. P., Field determination of vertical permeability to air in the unsaturated zone, Geological Survey Professional Paper 1051, 1978.

MODELING OF ACID MINE DRAINAGE PHYSICAL PROCESSES IN THE NORDHALDE OF THE RONNENBURG MINING DISTRICT, GERMANY

René Lefebvre[1+], Jason Smolensky[2*], and Daryl Hockley[2]
+: Corresponding author, *: Presenter, 1: INRS-Géoressources, 2535 Laurier, Sainte-Foy, Quebec, Canada, G1V 4C7
2: Stefen, Robertson & Kirsten (Canada) Ltd., Suite 800, 580 Hornby St., Vancouver, B.C., Canada V6C 3B6

ABSTRACT

The Nordhalde is one of the largest waste rock piles in the Ronnenberg mining district, consisting of approximately 27,000,000 m^3 of material. The pile contains significant amounts of pyrite which is currently oxidizing, resulting in the generation of Acid Mine Drainage (AMD). The oxidation of pyrite is directly related to the consumption of oxygen and the production of heat. To better understand the rate and physical processes which govern pyrite oxidation in the Nordhalde, the pile was subject to extensive geochemical characterization and borehole instrumentation. A numerical model which integrates the physical parameters available and represents the coupled physical processes was developed for the Nordhalde using the program TOUGH AMD. This program has an equation of state for water, nitrogen and oxygen and a module representing the kinetics of the pyrite oxidation process. This module calculates the sinks of oxygen and the sources of heat related to pyrite oxidation. A vertical cross-section through the site which intersects the major waste rock types was used as the basis for a two-dimensional model. The relatively low permeability of the material makes diffusion an important oxygen transport mechanism. The global oxidation rate is thus relatively lower than in other waste rock piles where convection is dominant. However, the low heat conductivity of the material is responsible for a significant rise in temperature within the Nordhalde. This creates a temperature gradient within the pile causing advective gas flow despite the low permeability materials. Cyclic variations in surface boundary conditions can be modeled with TOUGH AMD. This feature was used to study the effect of yearly temperature variations and weekly barometric pressure changes on oxygen supply within the Nordhalde. Overall, the model allows a coherent representation of the conditions monitored within the waste rock pile and the confirmation of its physical properties. By being able to predict the longer term potential for AMD production at the site, the model contributes to the choice of the most appropriate approach to rehabilitation.

INTRODUCTION

The Ronnenberg mining district is located in the state of Thuringia in Germany (former German Democratic Republic). Extensive mining of Uranium, from open pit and underground workings, occurred there from 1950 through to 1990. This district is presently the object of a major environmental rehabilitation effort.

The Nordhalde is one of the largest waste rock piles in the area, consisting of approximately 27 million m^3 of material. The pile contains significant amounts of pyrite which is currently oxidizing, resulting in the generation of Acid Mine Drainage (AMD). The oxidation of pyrite is directly related to the consumption of oxygen and the production of heat. To better understand the rate and physical processes which govern pyrite oxidation in the Nordhalde, the pile was subject to extensive geochemical characterization and borehole instrumentation. The boreholes allow the monitoring of pore gas oxygen concentration, temperature and pressure through time.

The development of a numerical model for the Nordhalde was intended 1) to verify previous pyrite oxidation rate estimates from analytical solutions applied to temperature and oxygen profiles, 2) to get a better understanding of the physical mechanisms responsible for oxygen supply within the Nordhalde, and 3) to integrate and validate available information on physical properties of the material. The numerical model used was TOUGH AMD. That model represents the physical processes involved in AMD production in waste rock dumps (Lefebvre, 1994 and 1995). These capabilities were developed starting from the TOUGH2 simulator (Pruess, 1987 and 1991).

ACID MINE DRAINAGE (AMD) PROCESSES

Even though pyrite oxidation is a biochemical process, the generation of AMD in waste rock dumps involves much more than chemistry. Waste rock dumps comprise coarse mineral materials and are partially saturated media. A wide range of coupled physical processes are involved in these systems.

Within waste rock dumps, at the heart of all other processes is the oxidation of the pyrite present in the rocks. Oxidation involves oxygen consumption, even though the direct oxidant is often ferric iron (Fe^{3+}). A supply of oxygen is thus required to sustain pyrite oxidation. Heat production also occurs since pyrite (Py) oxidation is strongly exothermic (11,7 MJ/kg Py oxidized). The release of heat drives temperature up, as high as 70 °C in some places (Gélinas et al., 1994). This increase in temperature is important since it totally modifies the mechanisms responsible for oxygen transport to oxidation sites. Initially, in all systems, diffusion is the main process providing oxygen within waste rock accumulations. In materials of low permeability, such as in mine tailings, diffusion is believed to remain the only means of oxygen transport. However, in higher permeability materials, following an initial increase in temperature, temperature-driven convection currents are generated. The resulting advection is a much more efficient oxygen transport process than diffusion and sustains higher global oxidation rates. Finally, water infiltration occurs through the unsaturated porous material and picks up oxidation components to form an acidic leachate containing high concentrations of sulfate and metals.

In summary, waste rock dumps are complex systems posing an interesting problem of coupled physical processes: multiphase flow, heat transfer, and mass transfer in the liquid phase (advection) and in the gas phase (advection and diffusion). Numerical simulation is needed to handle all those processes and understand their interactions.

TOUGH AMD DESCRIPTION

The TOUGH AMD model is described elsewhere by Lefebvre (1994 and 1995). The model was developed in the context of a detailed study of a waste rock dump at Mine Doyon (Gélinas et al., 1994). Only the main features of the program are summarized here.

TOUGH AMD evolved from TOUGH2 (Pruess, 1987 and 1991) with the equation of state model for water and air (EOS3). Only the main changes made to TOUGH2 are mentionned. Three components are considered in TOUGH AMD: water and air subdivided in two components (oxygen and the other air gases). Oxygen has to be considered as a separate component because it is consumed by the oxidation reaction and its concentration affects the first-order kinetics. To define a system with three components and heat, four primary variables are required. The mass fraction of oxygen in air was thus added to the primary variables. As in TOUGH2, those variables differ depending on the number of phases present.

In waste rock dumps, pyrite is contained in rocks in which the pyrite grains are surrounded by other minerals. Pyrite oxidation proceeds from the surface of waste rock fragments. As pyrite near the surface is oxidized, the oxidant must penetrate within the blocks to reach unreacted pyrite. A zonation appears within waste rock fragments, showing an external zone in which pyrite is completely oxidized and an internal core where pyrite is unreacted.

Reaction core models provide a link between the pyrite oxidation surface reaction kinetics and the volumetric oxidation rate observed in waste rocks. They must account for the concentration and surface of pyrite exposed within waste rocks and consider the supply of oxidant within the blocks by diffusion. These models also establish a relationship between the reduction of pyrite fraction and its impact on the volumetric oxidation rate. A new reaction core model was developed and implemented in TOUGH AMD. The reaction core model computes the oxygen loss and heat production resulting from pyrite oxidation as a function of temperature, oxygen concentration and pyrite mass fraction.

New modifications were made to TOUGH AMD for the present study. The program was first migrated to Intel-based personal computers. New capabilities for representing sinusoidal variations in temperature and pressure in boundary elements were developed. This feature includes the internal calculation of static pressure profiles for boundary elements located at different elevations. Finally, output files were made compatible with the LBNL program EXT to allow the use of Tecplot for graphics.

PHYSICAL CONDITIONS AND PROPERTIES

The extensive monitoring and characterization program carried at the Nordhalde provides a unique opportunity to better understand physical processes in waste rock systems, especially the oxygen transport mechanisms.

The Nordhalde waste rock dump results from the extensive uranium mining operations which occurred in the area over a 40 year period. It contains pyritic slates covering an area of 100 ha at a height of more than 70 m. The dump consists primarily of Zone A, or strongly reactive, waste rock. Overlying this in part is an unintentional cover of Zone C material that is not producing AMD (Hockley et al., 199*).

Eight boreholes reaching depths between 8 and 75 m, were instrumented with transducers and sampling tubes at 2 m intervals. Downhole pressure and temperature were measured every hour. Oxygen concentration measurements daily. Monitoring began in July, 1996. This study considers a full year of data from the site. Figure 1 shows a monthly sampling of profiles measured in borehole 38. Temperature (Fig. 1a) is seen to increase well above the average surface temperature of 9 °C, indicating active heat production by pyrite oxidation. The oxygen profiles (Fig. 1b) are more telling of the processes active in the pile throughout the year. During summer months, oxygen patterns are typical of a diffusion process, showing an exponential decrease with depth. Short term barometric changes affect this pattern slightly, moving the profiles vertically upwards and downwards. During winter months, oxygen profiles become erratic, showing an overall increase in oxygen concentration at depth, especially near the edge of the pile. However, O_2 depletion occurs near the surface. This is indicative of thermal convection from the edge to the summit.

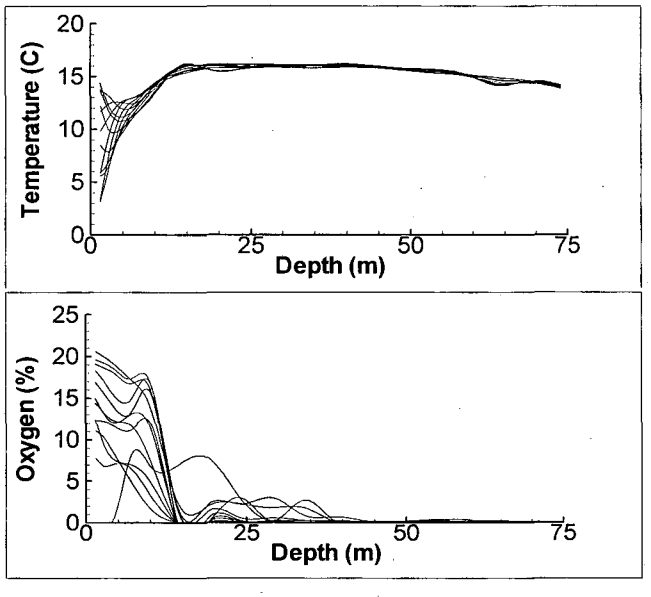

Figure 1. a) Temperature and b) oxygen profiles in Nordhalde borehole 38 in 1997

The monitoring program and numerous physical measurements in the field and laboratory allow a relatively precise evaluation of the global physical properties of materials in the Nordhalde. Table 1 summarizes the parameters required for the numerical model. These properties were determined from an hydrological evaluation of the infiltration rate, hydraulic conductivity tests, and measurements of grain sizes, global density and water content. Vertical air permeability was determined by matching pressure changes within the Nordhalde after barometric pressure variations with a SRK internal numerical model. Likewise, heat diffusivity was obtained by matching cyclic near-surface temperature variations with an internal SRK model. Initial values of the oxidation rate were derived from a diffusion and heat conduction analytical model of pyrite oxidation matched to temperature profiles.

Table 1. Physical properties of the Nordhalde

Property	Symbol and values
Global oxidation constant	$K_{ox} = 10^{-8}$ s^{-1}
Diffusive/Chemical times	$\tau_d/\tau_c = 0$
Pyrite mass fraction	$w_{py} = 0{,}031$
Horizontal permeability	$k_h = 8\text{x}10^{-11}$ m^2
Vertical permeability	$k_v = 8\text{x}10^{-12}$ m^2
Porosity	$n = 0{,}30$
Solids density	$\rho_s = 2751$ kg/m^3
Dry thermal conductivity	$K_{th,d} = 0{,}25$ W/m·°C
Wet thermal conductivity	$K_{th,w} = 1{,}2$ W/m·°C
Heat capacity of solids	$c_{ps} = 710$ J/kg·°C
Thermal conduct. of base	$K_{th} = 1{,}2$ W/m·°C
Global density of base	$\rho_b = 2106$ kg/m^3
Heat capacity of base	$c_p = 1021$ J/kg·°C
Standard diffusion coef.	$D_o = 4\text{x}10^{-5}$ m^2/s
Temperature diffusion coef.	$\theta = 1{,}8$
Tortuosity factor	$\tau = 0{,}85$
van Genuchten m factor	$m = 0{,}256$
van Genuchten α factor	$\alpha = 0{,}00036$ Pa^{-1}
Residual water saturation	$S_{wr} = 0{,}284$

THE NORDHALDE NUMERICAL MODEL

Figure 2 shows the numerical model grid used to represent the Nordhalde. TOUGH AMD considers gas convection and diffusion that affect oxygen supply, heat transfer by conduction, fluid advection and gas diffusion, and water infiltration from the surface by an imposed value of saturation. Infiltration affects heat transfer and leachate production – which is not

discussed here. Pyrite oxidation is represented by a reaction core model but no limiting effect of diffusion is considered. Since the material is relatively fine grained, pyrite is supposed mostly free in the wastes and exposed to oxygen.

A one-dimensional vertical model was used to verify initial model parameter values and boundary conditions. Since such a model cannot represent convection properly, the temperature reached in this model was below the observed values at the site. However, the results of the one-dimensional model was useful in developing the two-dimensional model.

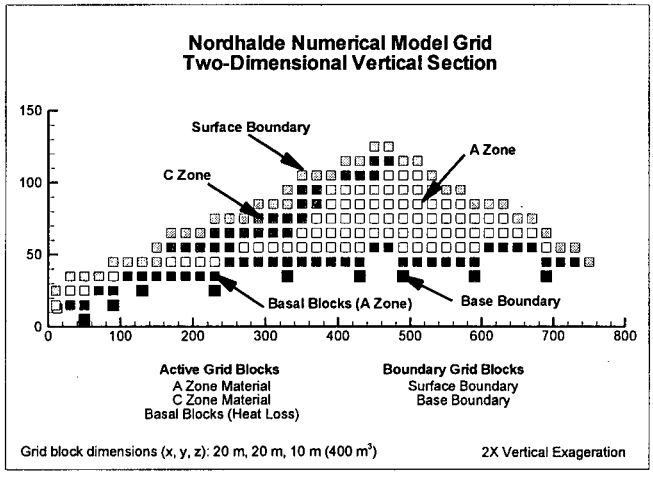

Figure 2. Numerical model grid located in a transverse cross section through the Nordhalde

Figure 2 shows the transverse vertical section used in the two-dimensional model. The grid blocks are uniform in dimensions: 10 m high with a 20x20 m base for a total of 135 active elements. A section is necessary to represent gas convection and diffusion processes. Since gas exchanges should be limited in the longitudinal direction of the heap, a three-dimensional model was not judged necessary to properly represent the most important oxygen transport features of the Nordhalde.

The surface boundary (41 non active elements) had imposed pressure, water saturation (sets infiltration rate), oxygen concentration and temperature. Yearly cyclic surface temperature were used for all runs. Variable pressure conditions were used only in special short term runs to study their general effect.

Active elements represented material with Zone A (reactive) and Zone C (low reactivity) properties. The bottom layer of the waste rock materials allowed heat loss to the base computed with a semi-analytical module adapted from TOUGH2. The base boundary is only made up of a few (9) saturated inactive elements allowing the drainage of the infiltrating water. These elements have a very low heat conductivity so that no heat is lost to them.

CONDITIONS AND GAS FLUX WITHIN THE NORDHALDE

Figure 3 shows the results obtained from the model after 30 years, corresponding to the period of operation of the Nordhalde. The model shows a significant increase in temperature, reaching nearly 20 °C, very similar to observed values. To get such an increase, some of the oxygen has to be supplied by advection. This advection occurs under the temperature gradient established between atmospheric and internal gas. However, convection is triggered only if permeability is sufficiently high. Initial runs with slightly lower values of permeability would not allow advection to start and temperatures remained well under observed values (at about 12 °C). The Nordhalde is thus at the limit between conditions that would imply a totally diffusive system and a convective system. This conclusion is supported by field indications of increased convection under winter conditions.

Even though convection occurs, diffusion is still an important oxygen supply mechanism. In Figure 3 (middle), oxygen fluxes are seen to be mostly perpendicular to oxygen concentration profiles, as would be expected from a diffusive process. The combination of oxygen transport processes cannot counteract oxygen depletion by pyrite oxidation. Oxygen concentrations are thus only important near the surface of the heap whereas the core is totally depleted in oxygen. Oxygen fluxes are seen to be higher on the edges of the heap than at the surface. This is explained by the upward advection of gas with a reduced oxygen content that counteracts downward diffusion.

The Zone C material has some impact on the global oxidation rate. This is seen on the lower part of Figure 3. Lower temperatures and lower oxidation rates are encountered where Zone C material is present. Low reaction kinetics were used to model this material. This is supported by observed oxygen and temperature profiles. In boreholes going through Zone C material, temperature profiles show straight line increases and oxygen remains high, indicating that oxidation is not significant. Uncertainties remain however about the exact reactivity of this material.

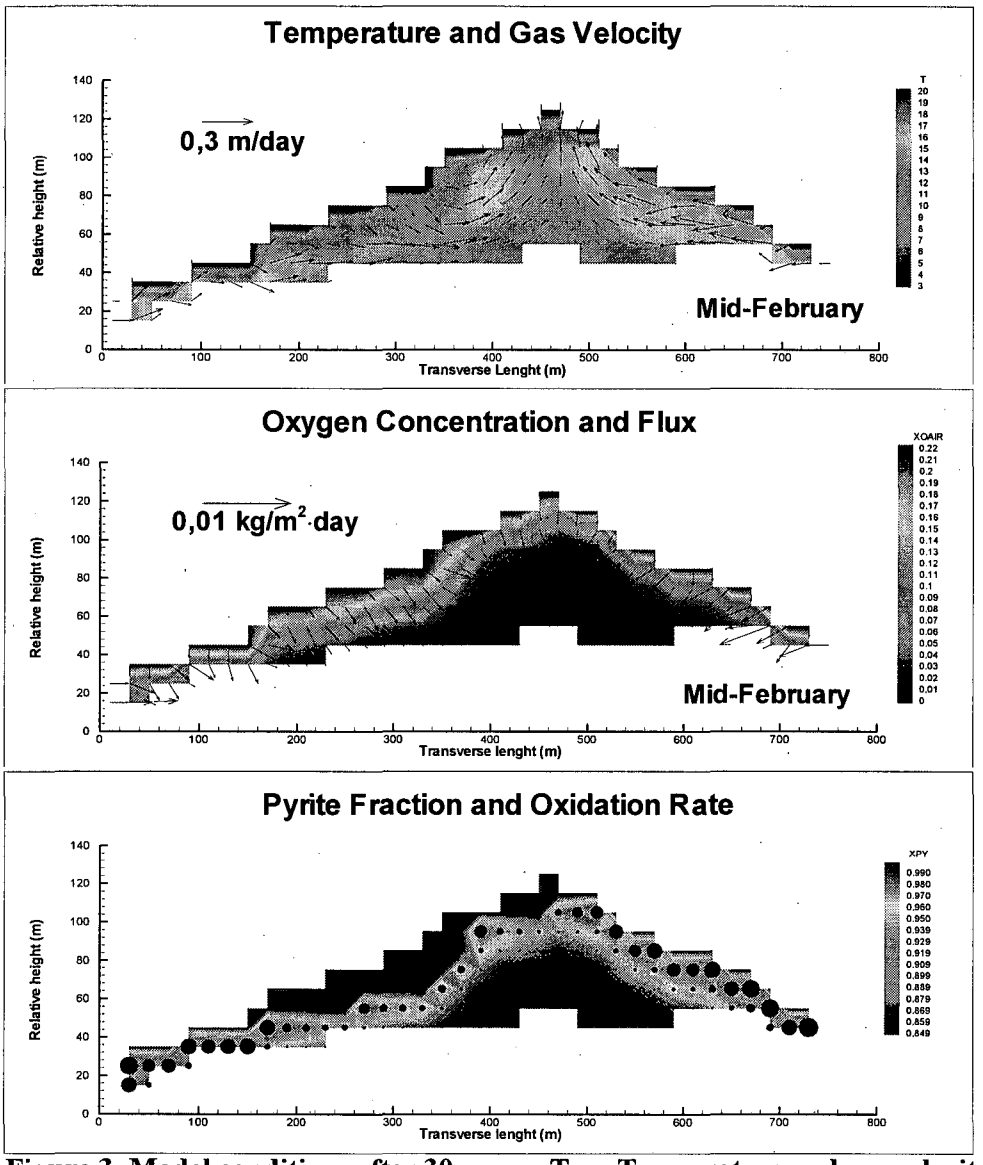

Figure 3. Model conditions after 30 years. Top: Temperature and gas velocity Middle: Oxygen concentration and flux. Bottom: Pyrite remaining and oxidation rate

CYCLIC BOUNDARY CONDITIONS

The fact that physical conditions predicted by the model are representative of observation would indicate that the physical processes operating in that system are globally well described, especially the ones responsible for oxygen supply. Since observations indicate that seasonal changes occur in oxygen concentrations, we were interested in modeling the effect of variable boundary conditions. This prompted the development of such capabilities for the model.

The first effect modeled was the yearly cyclic temperature variations. Since average temperature varies slowly, the use of cyclic surface temperature did not imply a high computational burden. However, barometric pressure changes are much more rapid and more erratic. Thus, variable boundary pressure was not included like temperature in the long term modeling runs. Instead, a short term run was used to study the effect of variable surface pressure. The conclusions from these modeling efforts are not yet definitive.

Figures 4 and 5 illustrate the modeled evolution of global average conditions within the Nordhalde using variable surface temperature. During the modeling period, there is a steady increase in temperature with indications of some leveling off at the end. Figure 4 is quite interesting because it indicates the onset of convection. The break in slope of the average oxygen concentration beyond 5 years occurs when the systems

goes from being dominated by diffusion to one in which convection plays a more important role, as revealed by graphs like figure 3 for this time. After this time, the more steady oxygen profile is related to well established convection.

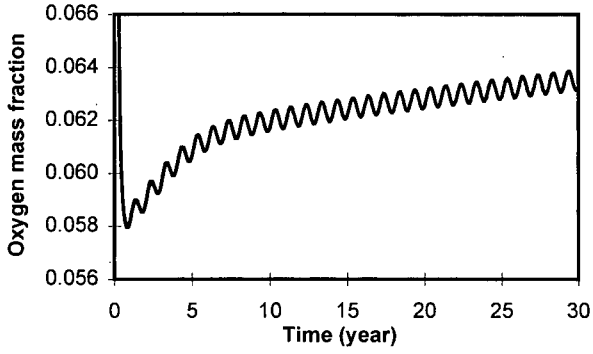

Figure 4. Evolution of average oxygen concentration in gas phase

The relatively steady increase in oxygen concentration shown in figure 4 does not equate to higher average oxidation rates. On the contrary, figure 5 shows that oxidation rates are globally decreasing. This is caused by the depletion of readily accessible pyrite. The reaction core model involves a reduction in the "reactivity" of the material as pyrite gets depleted. This counteracts the increase in oxygen.

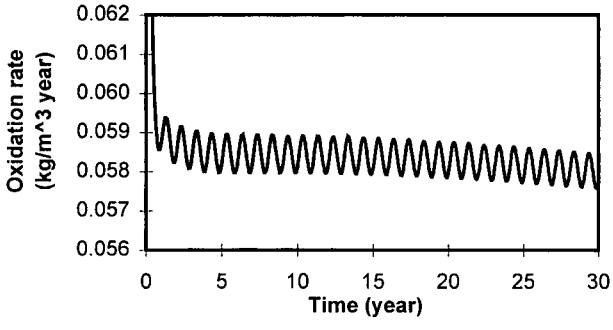

Figure 5. Evolution of the average volumetric oxidation rate (oxygen mass consumption)

Figure 6 shows the result of a short term modeling run with variable barometric pressure. Comparing figures 4 and 6, we see that important atmospheric pressure variations induce short term changes in average oxygen concentration. This effect is thus potentially important as an oxygen supply mechanism. Graphs similar to figure 3 show that convection patterns are actually modified quite significantly by variations in barometric pressure. More work needs to be done to fully understand the interaction between temperature and pressure fluctuations that influence convection patterns within the Nordhalde and its impact on oxygen supply and pyrite oxidation rate.

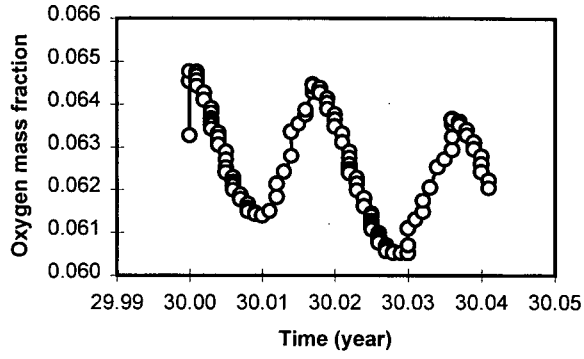

Figure 6. Variations in oxygen concentration in the gas phase during barometric pressure changes

CONCLUSION

The Nordhalde is an important site and can teach us a great deal about the oxygen supply mechanisms in AMD-producing mined materials. This site is exceptional by the quality of the characterization and monitoring program. Also, the low permeability of the material allow us to better understand the conditions necessary to trigger convection. This site actually shows evidence of convection under conditions that were previously believed to be unfavorable.

REFERENCES

Gélinas, Lefebvre, Choquette, Isabel, Locat, Guay, 1994: Monitoring and modeling of acid mine drainage from waste rock dumps - La Mine Doyon case study. MEND program, GREGI report 1994-12, to CANMET, 240 p.

Lefebvre, 1994: Caractérisation et modélisation numérique du drainage minier acide dans les haldes de stériles. Ph.D. Thesis, Université Laval, June 1994, 375 p.

Lefebvre, 1995: Modeling Acid Mine Drainage in Waste Rock Dumps. TOUGH Workshop '95, LBL-37200.

Pruess, 1987: TOUGH user's guide. LBNL.

Pruess, 1991: TOUGH2 - A general purpose numerical simulator for multiphase fluid and heat flow. LBNL.

Smolensky, Lefebvre, Hockley, 1998: Initial Numerical Modeling of Physical Processes Responsible for AMD Production in the Nordhalde - Ronneberg mining district, Thuringia, Germany. Steffen, Robertson & Kirsten report.

AKNOWLEDGEMENTS

This paper is presented by kind permission of WISMUT GmbH.

Introducing Reactive Chemical Transport to TOUGH2: Application to Supergene Copper Enrichment

Tianfu Xu[1], Karsten Pruess[1], and George Brimhall[2]

(1) Earth Sciences Division, Lawrence Berkeley National Laboratory
University of California, Berkeley, CA 94720

(2) Department of Geology and Geophysics
University of California, Berkeley, CA 94720

Introduction

Reactive chemical transport occurs in a vast variety of geochemical environments, and over a broad range of space and time scales. Different methods are available to model coupled processes of fluid flow, mass transport, and chemical reactions in subsurface systems [Yeh and Tripathi, 1989; Steefel et al., 1994; White, 1995; Lichtner et al., 1996]. These differ in their emphasis on accuracy and comprehensiveness of flow and transport modeling on the one hand, and chemical interactions between rocks and fluids on the other. Three major approaches have been used to couple mass transport and chemical reaction: (1) direct substitution approach (DSA) which substitutes the chemical reaction equations directly into the transport equations, (2) sequential iteration approach (SIA) which solves the transport and the chemical equations separately in a sequential manner with an iterative procedure, and (3) sequential non-iteration approach (SNIA) which is similar to the SIA but without the iterative procedure. The use of the DSA leads to a system of fully coupled highly nonlinear transport equations. Its advantage is high accuracy, but its main disadvantage is a very high demand on computing resources, which limits the number of species that can be handled. In the SIA and SNIA, since the sets of equations that are solved simultaneously are much smaller than in the DSA, larger systems with larger sets of chemical species can be handled. Owing to the enormous diversity of transport and chemical reaction pheneomena, no universally accepted methodology for modeling such processes has emerged, or is likely to emerge. Instead, simulation methodology must be carefully chosen and tailored to the specific physical and chemical properties of the system being investigated, and to the objectives of the modeling study.

The objectives of the present work are twofold: (1) develop a general, comprehensive capability for modeling coupled processes of flow, transport, and rock-fluid interactions, and (2) develop a practical simulation tool for the study of supergene enrichment, the oxidative weathering and acidification that causes mobilization of metals in the unsaturated zone, with subsequent formation of enriched ore deposits in the reducing conditions below water table. Such redox-driven processes have produced some of the world's largest copper deposits. Redox reactions pose difficult challenges for numerical modeling because they result in huge variations in the concentrations of aqueous species involved. For example, in systems where pyrite (FeS_2) is oxidized in the vadose zone through contact with atmospheric oxygen, aqueous oxygen concentrations may vary over 70 orders of magnitude. Similarly, between oxidizing and reducing conditions. the concentrations of sulfide and sulfite species may range over more than 90 orders of magnitude.

This paper summarizes the development for a general-purpose simulation capability for reactive chemical transport on the framework of TOUGH2 [Pruess, 1991], and its application to the one-dimensional model of supergene copper enrichment developed previously by Ague and Brimhall [1989]. This earlier effort was based on field and laboratory geochemical studies of supergene copper systems and their dynamics under conditions of climatic change [Brimhall, et al, 1985;Alpers and Brimhall, 1988 and 1989; Brimhall and Crerar, 1990] and has provided the geochemical focus for this work. By coupling the speciation and reaction path code EQ3/6 [Wolery, 1992] to TOUGH2, the code TOUGH2-EQ3/6 has comprehensive geochemical capabilities for aqueous species and secondary mineral products. TOUGH2-EQ3/6 keeps track of the full EQ3/6 chemical database for each grid block at each time step. The

process simulation capability of TOUGH2-EQ3/6 is very computationally intensive; it serves as a benchmark for the development of more efficient, approximate methods for solving field scale multi-dimensional problems of interest in hydrogeology, acid mine drainage remediation and mining engineering. For this purpose, TOUGHREACT has been developed as an alternative. This code is much more efficient (94 times faster than TOUGH2-EQ3/6 for the present problem). TOUGH2-EQ3/6 is used first for a few grid-blocks over a short time period. TOUGHREACT initially uses the speciation and secondary mineral products obtained from TOUGH2-EQ3/6. These two codes provide a comprehensive description of rock-fluid interactions during fully transient, multi-phase, nonisothermal flow and transport in hydrologically and geochemically heterogeneous media. We demonstrate application to a simplified problem of supergene enrichment of a typical copper protore that includes the sulfide minerals pyrite (FeS_2) and chalcopyrite ($CuFeS_2$).

Methodology

Our model of flow, transport, and chemical reactions in geologic media is based on space discretization by means of integral finite differences [Narasimhan and Witherspoon, 1976]. TOUGH2-EQ3/6 code uses a non-iterative, sequential solution scheme; TOUGHREACT uses a sequential iteration approach. Both codes have the same structure (see Figure 1); full details of the mathematical and numerical model are given in [Xu et al., 1997]. The non-isothermal multiphase flow equations are solved first, and the resultant fluid velocities and phase saturations are used for transport simulation. Transport in the liquid phase is treated in terms of total dissolved concentrations. In addition, if gaseous species are present, the transport is solved in terms of their partial pressures. The resulting concentrations and partial pressures from the transport calculation are substituted into the chemical reaction module. The temperature distribution obtained from the solution of the multiphase flow equations is used to update physical and chemical parameters. The transport equations are solved on a component basis, whereas the chemical equations are solved on a grid block basis. Two time stepping levels are used. The global time step, Δt_1, is controlled by the solution of flow equations. During a time interval of Δt_1, depending on convergence, multiple steps Δt_2, with $\sum \Delta t_2 = \Delta t_1$ can be used for solution of reactive transport.

Application

A number of test cases were run for which analytical solutions are available, to verify accuracy and convergence behavior of the TOUGH2-EQ3/6 and TOUGHREACT codes. We then proceeded to the process of supergene enrichment of primary copper ores, which are exposed to oxidizing conditions over geologic time as a consequence of tectonic and climatic changes. A schematic representation of the model system is shown in Figure 2. Oxygen is supplied to a protore containing pyrite and chalcopyrite (Table 1) as a dissolved species in infiltrating rainwaters as well as by gaseous diffusion from the land surface boundary.

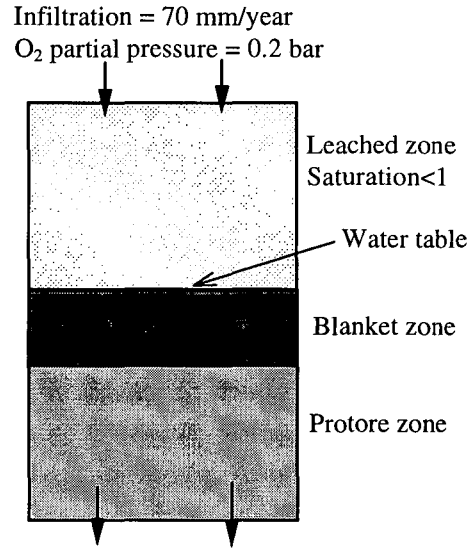

Figure 2. Schematic representation of a supergene enrichment system

A vertical column of 20 m thickness is used, which is discretized into 10 grid blocks with a constant spacing of 2 m. The top 5 blocks represent the unsaturated zone (water saturation: 0.43, 0.43, 0.44, 0.48 , 0.72 from the top to the bottom), while the bottom 5 blocks represent the water saturated zone. A steady-state water flow regime is assumed throughout the simulation. Mineral dissolution/precipitation effects on porosity are not considered in the current simulation. A diffusion coefficient of 4.38×10^{-5} m^2/s and a tortuosity of 0.1 are used for gaseous oxygen.

The column is initially filled entirely with a protore mineral assemblage as listed in Table 1. The

dissolution of the protore minerals is kinetically controlled. We use a rate expression given by Lasaga et al. [1994]:

$$r_m = k_m \sigma_m (1 - \Omega_m^{\theta})^{\eta} \qquad (1)$$

where m is the mineral index, r_m is the mineral dissolution rate (moles of mineral per unit volume of water and unit time, and negative values indicates precipitation), k_m is the rate constant (moles per unit mineral surface area and unit time) which is function of temperature, σ_m is the specific reactive surface area per unit fluid volume, Ω_m is the mineral saturation ratio (i.e. the ratio between the ion activity product and the equilibrium constant). The parameters θ and η must be determined from experiments; in this simulation, they are taken equal to one. The term $a_{H^+}^n$ accounts for the catalytic effect of H^+ where the value of n is determined experimentally; in this simulation, this term is not considered. The kinetic rate constants and specific surface area are listed in Table 1. The chemical formulae of the primary minerals are given in Table 2. The mineral abundances and specific surface areas in the input data are normalized to one dm^3. The interaction of O_2 gas with the aqueous solution is assumed at local equilibrium. The precipitation of secondary minerals (Table 3) during the simulation progress are considered instantaneously.

Table 1. Chemical properties of protore mineral reactants. Volume fraction, rate constant and specific surface area are based on Ague and Brimhall [1989] and Gerard et al. [1997]. Abundance is calculated from volume fraction (in this table) and mole volume presented in the EQ3/6 database [Wolery, 1992].

Mineral	Volume fraction (%)	Abundance (mol/dm^3 medium)	Rate constant ($mol/cm^2/s$)	Surface area (cm^2/dm^3 medium)
Pyrite	9.0	3.76	4.0×10^{-15}	5866.7
Chalcopyrite	4.5	1.05	4.0×10^{-15}	5866.7
Magnetite	4.5	1.01	2.0×10^{-15}	5866.7
K-feldspar	18.0	1.65	3.1×10^{-16}	58666.7
Albite	9.0	0.9	3.1×10^{-16}	69813.4
Anorthite	9.0	0.89	1.5×10^{-16}	29920.0
Annite	4.5	0.29	2.4×10^{-18}	29333.3
Muscovite	9.0	0.64	2.4×10^{-18}	17600.0
Quartz	18.0	7.93	4.3×10^{-18}	61600.1
Anhydrite	4.5	0.98	1.5×10^{-16}	5866.7
	Total=90			
	Void=10			

Table 2. Chemical reaction equations for oxygen gas and the primary mineral reactants. The thermodynamic equilibrium constants are from the EQ3/6 database [Wolery, 1992]

Mineral (or gas)	Reactions equation	log K (25°C)
Oxygen gas	$O_2(g) = O_2(aq)$	-2.898
Pyrite	$FeS_2 + H_2O + 3.5O_2(aq) = 2SO_4^{--} + Fe^{++} + 2H^+$	217.4
Chalcopyrite	$CuFeS_2 + 4O_2(aq) = 2SO_4^{--} + Fe^{++} + Cu^{++}$	244.07
Magnetite	$Fe_3O_4 + 8H^+ = Fe^{++} + 2Fe^{+++} + 4H_2O$	10.4724
K-feldspar	$KAlSi_3O_8 + 4H^+ = K^+ + Al^{+++} + 3\ SiO_2(aq) + 2H_2O$	-0.2753
Albite	$NaAlSi_3O_8 + 4H^+ = Na^+ + Al^{+++} + 3\ SiO_2(aq) + 2H_2O$	2.7645
Anorthite	$CaAl_2Si_2O_8 + 8H^+ = Ca^{++} + 2Al^{+++} + 2\ SiO_2(aq) + 4H_2O$	26.5780
Annite	$KFe_3AlSi_3O_{10}(OH)_2 + 10H^+ = K^+ + 3Fe^{++} + Al^{+++} + 3\ SiO_2(aq) + 6H_2O$	29.4693
Muscovite	$KAl_3Si_3O_{10}(OH)_2 + 10H^+ = K^+ + 3Al^{+++} + 3\ SiO_2(aq) + 6H_2O$	13.5858
Quartz	$SiO_2 = SiO_2(aq)$	-3.9993
Anhydrite	$CaSO_4 = Ca^{++} + SO_4^{--}$	-4.3064

Table 3. The chemical reaction equations for secondary minerals. the thermodynamic equilibrium constants are from the EQ3/6 database [Wolery, 1992]

Mineral	Reaction equation	log K (25°C)
Covellite	$CuS + H^+ = Cu^{++} + HS^-$	22.8310
Chalcocite	$Cu_2S + H^+ = 2Cu^+ + HS^-$	-34.7342
Bornite	$Cu_5FeS_4 + 4H^+ = Cu^{++} + 4Cu^+ + Fe^{++} + 4HS^-$	-102.44
Goethite	$FeOOH + 3H^+ = Fe^{+++} + 2H_2O$	-0.283
Hematite	$Fe_2O_3 + 6H^+ = 2Fe^{+++} + 3H_2O$	0.1086
Kaolinite	$Al_2Si_2O_5(OH)_4 + 6H^+ = 2Al^{+++} + 2\,SiO_2(aq) + 5H_2O$	6.8101
Alunite	$KAl_3(OH)_6(SO_4)_2 + 6H^+ = K^+ + 3Al^{+++} + 2SO_4^{--} + 6H_2O$	-0.3479
SiO_2(amorphous)	$SiO_2 = SiO_2(aq)$	-2.7136

A dilute oxidizing water with an oxygen fugacity (partial pressure) of 0.2 bar is initially placed in the five uppermost (unsaturated) grid blocks, while a reducing water with a fugacity of 1.0×10^{-70} is assumed for the remaining (saturated) grid blocks. The infiltration water composition is the same as the initial unsaturated water. TOUGH2-EQ3/6 is used first. The results of aqueous speciation and secondary mineral products are used for the subsequent TOUGHREACT simulation. A total of more than 100 species is automatically taken into account in TOUGH2-EQ3/6. However, in the TOUGHREACT simulation, only the 52 significant species are considered. The aqueous complexation is assumed at local equilibrium. Detailed results for the chemical evolution, simulated with TOUGHREACT, are given in Figures 3 and 4.

In the unsaturated zone, pyrite and chalcopyrite are oxidized and dissolved (Figure 3a). As aqueous phase oxygen is depleted through reaction with pyrite and chalcopyrite, it is replenished by dissolution from the gas phase, and diffusive transport from the atmospheric boundary at the land surface. The pH decreases downward (Figure 4a), and Cu and S concentrations increase (Figure 4d) due to pyrite and chalcopyrite oxidation. Maximum dissolved concentrations occur near the bottom of the unsaturated zone. When this water reaches the reducing saturated zone, the secondary copper bearing minerals chalcocite and covellite are precipitated (Figure 3b), forming the enrichment blanket immediately below the water table [Ague and Brimhall, 1989]. In addition, goethite precipitates in the unsaturated zone.

At the same time magnetite, K-feldspar, albite, anorthite, annite and muscovite dissolve throughout the column due to decrease of pH (Figures 3c and d). Magnetite dissolution (Figure 3a) creates additional Fe^{2+} and Fe^{3+}. Fe^{3+} acts as an oxidant, which contributes to pyrite and chalcopyrite oxidation. Dissolution of K-feldspar, albite, anorthite, annite and muscovite produces Na, K, Ca, Al and SiO_2(aq). As a result, amorphous silica or SiO_2(am) precipitates throughout the column (Figure 3e). Kaolinite occurs only in the bottom 3 grid blocks of the saturated zone (Figure 3b), while alunite appears only in the top 7 grid blocks of the column (Figure 3e). There is no quartz dissolution as this mineral is stable in our simulation, as it is in nature.

Discussion

Quasi-stationary state. After a brief transient evolution, the system settles into a "quasi-stationary state" (QSS; Lichtner, 1988), during which aqueous concentrations of all chemical species remain essentially constant. During QSS, dissolution of primary and precipitation of secondary minerals proceeds at constant rates. A relative concentration change and a relative dissolution (or precipitation) rate change are used to monitor attainment of QSS conditions,

$$\max_{\substack{\text{all components}\\ \text{all blocks}}} \left| \frac{C^{k+1} - C^k}{C^k} \right| < \varepsilon_C \qquad (2a)$$

$$\max_{\substack{\text{all minerals}\\ \text{all blocks}}} \left| \frac{r^{k+1} - r^k}{r^k} \right| < \varepsilon_r \qquad (2b)$$

where k is the transport time step index, C are dissolved component concentrations, r are dissolution or precipitation rates, and ε_C and ε_r are convergence tolerances (see Figure 5). After some 50 years relative concentration changes are reduced to 10^{-5}, while dissolution rates are not very stable. The maximum relative dissolution rate changes only for the unsaturated leaching zone are shown in Figure 6. After 15 years, the rates essentially remain constant in the unsaturated zone. The observed numerical sensitivities suggest that criteria for the quasi-stationary state need to be carefully specified. This is of considerable practical importance, because substantially larger time steps should be possible during periods where a QSS is present [Neretnieks, 1997].

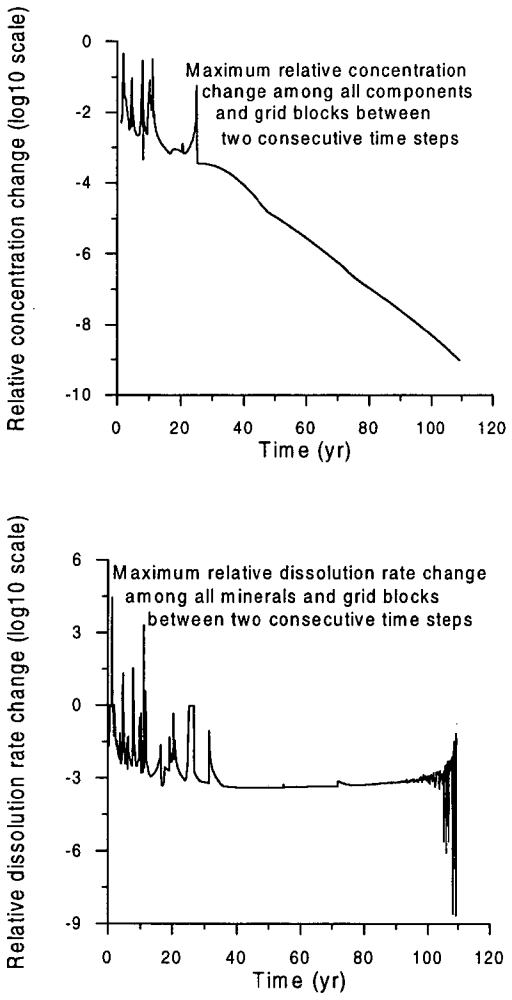

Figure 5. Maximum relative concentration and dissolution (precipitation) rate change for the TOUGHREACT simulation of supergene copper enrichment in a 1-D column.

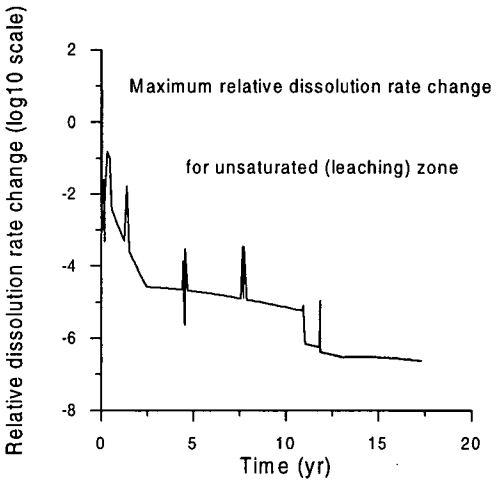

Figure 6. Maximum relative dissolution (precipitation) rate change for the unsaturated leaching zone.

Time step limitations. Mass balance considerations can provide useful insights into practical limitations for modeling the oxidative consumption of sulfide minerals in unsaturated flow systems. At ambient conditions of T = 25 °C, oxygen partial pressure P_{O2} = 0.2 bar, effective density of oxygen dissolved in water at the solubility limit is $\rho_{O2(l)} = 8.1\times10^{-3}$ kg/m^3, while oxygen density in atmospheric air is 32 times larger, namely, $\rho_{O2(g)}$= .258 kg/m^3. Oxidation of pyrite to Fe^{2+} and SO_4^{2-} nominally requires 3.5 moles of oxygen (112 g) per mole of pyrite (120 g). A porous medium with porosity ϕ = 10 % contains approximately 8.1×10^{-4} kg/m^3 of dissolved oxygen when the pore space is fully water-saturated, and 2.58×10^{-2} kg/m^3 of oxygen when completely unsaturated. The oxidation of 1 vol.% of pyrite (50 kg/m^3), requires 46.7 kg of oxygen per m^3 of medium, which corresponds to 1,845 PV (pore volumes) of gas, or 57,654 PV of aqueous phase. In an explicit time stepping scheme, the maximum stable time step for advective flow is $\Delta t_{adv} = \Delta x/v$, where Δx is the grid spacing, and v is the advective velocity, $v = u/\phi S$, with u the Darcy velocity (volumetric flux), and S saturation of the flowing phase. The amount of oxygen introduced into a grid block by advective flow during the maximum stable explicit time step is

$$M_{O_2,adv} = \Delta t_{adv} u \rho_{O_2} = \Delta x \phi S \rho_{O_2} \qquad (3)$$

which corresponds to the movement of 1 PV of fluid through the grid block. The maximum stable time step for diffusive transport is $\Delta t_{dif} = \Delta x^2/2D_{eff}$ [Peaceman, 1977], where D_{eff} is the total effective diffusion coefficient in a porous medium under multiphase conditions. The amount of oxygen introduced into a grid block by diffusive transport during the maximum stable explicit time step is

$$M_{O_2,dif} = \Delta t_{dif} F_{dif} = \frac{\Delta x^2}{2} \nabla C \qquad (4)$$

where $F_{dif} = - D_{eff} \nabla C$ is the diffusive flux, and ∇C is the concentration gradient driving diffusion. For the parameters used in our problem, we have $\Delta t_{adv} = 8.64 \times 10^8$ s, $\Delta t_{dif} = 4.56 \times 10^5$ s, $M_{adv} = 7.29 \times 10^{-4}$ kg/m^2 and $M_{dif} = 0.517$ kg/m^2. The amount of oxygen that can be supplied during an explicit time step is seen to be small, suggesting that for modeling of "substantial" reaction progress, an explicit time stepping approach is impractical for advectively dominated conditions, and may at best be marginally viable for diffusively dominated conditions. The fully implicit simultaneous solution is not an attractive alternative either, because of the large number of species conservation equations that need to be solved (of order of 100 per grid block in our problem). The most promising approach appears to be a "mixed explicit-implicit" or "adaptive implicit" scheme [Evans et al., 1954; Thomas, 1982], where grid blocks are dynamically "switched" from explicit to implicit time stepping in the course of a simulation, based on their intrinsic time step constraints. Such an approach would seem well suited for our problem: in regions where oxygen consumption is strong, many chemical species will be present, but time step constraints are relaxed so that an explicit approach should be effective; in regions where oxygen-consuming minerals have been depleted we have the opposite characteristics: explicit time step constraints are severe, implicit time stepping is favored and seems practical because only a limited number of chemical species is active.

Conclusions and future work

Oxidative weathering is an extremely difficult process to model numerically, because (1) it is driven by oxygen whose concentration in ambient soil gas, and dissolved in pore water in the unsaturated zone, is very small compared to the amounts of solid minerals which are to be reacted, and (2) the chemical activities and total elemental solubilities of key species vary over an enormous range of tens of orders of magnitude during redox processes. We have presented a sequential approach for modeling flow, transport, and chemical reactions, and have explored a non-iterative (TOUGH-EQ3/6) and an iterative (TOUGHREACT) solution scheme. Our model provides a comprehensive suite of process modeling capabilities. An application to a supergene copper enrichment system demonstrated results reasonably close to known geochemical behavior. Mass balance and time stepping considerations showed that explicit time-stepping approaches can only be used for modeling "incremental" evolution of redox-driven systems over brief time periods. In order to simulate substantial reaction process and mobilization and reprecipitation of large amounts of chemical species over geologic time, one should benefit from the quasi-stationary approximation. Alternatively it will be necessary to resort to mixed explicit-implicit or fully implicit methods.

Acknowledgement

The authors appreciate stimulating discussions with Tom Wolery, John Apps, and Frederic Gérard. We thank Eric Sonnenthal and Nicolas Spycher for their careful review of the manuscript. This work was supported by the Laboratory Directed Research and Development Program of the Ernest Orlando Lawrence Berkeley National Laboratory, under Contract No. DE-AC03-76SF00098 with the U.S. Department of Energy.

References

Ague, J. J., and Brimhall G. H., Geochemical modeling of steady state and chemical reaction during supergene enrichment of porphyry copper deposits, *Econ. Geol.*, 84, 506-528, 1989.

Alpers, C.N. and Brimhall, G.H., Middle Miocene climatic change in the Atacama Desert, northern Chile: Evidence from supergene mineralization at La Escondida: Geol. Soc. Amer. Bull., v. 100, p. 1640-1656, 1988.

Alpers, C.N. and Brimhall, G.H., Paleohydrologic evolution and geochemical dynamics of cumulative supergene metal enrichment at La Escondida, Atacama Desert, northern Chile: Econ. Geol., v. 84, p. 229-255, 1989.

Brimhall, G.H., Alpers, C.N. and Cunnigham, A.B., Analysis of supergene ore-forming processes and ground water solute transport using mass balance principles, Econ. Geol., v. 80, p. 1227-1256, 1985.

Brimhall, G.H. and Crerar, D.A., Ore fluids: Magmatic to supergene, in Thermodynamic Modeling of Geological Materials: Minerals, Fluids and Melts, I. Carmichael and H. Eugster, eds., Min. Soc. Amer. Reviews in Mineralogy, v. 17, ch. 10, p. 235-321, 1990.

Gérard, F., T. Xu, G. Brimhall and K. Pruess, Modeling reactive chemical transport problems with the codes EQ3/6 and TRANQUI, Lawrence Berkeley Laboratory Report LBL-40505, Berkeley, California, 1997.

Evans, G.W., R.J. Brousseau and R. Keirstead. Instability Considerations for Various Difference Equations Derived from the Diffusion Equation, Lawrence Livermore National Laboratory Report UCRL-4476, Livermore, CA, 1954.

Lasaga, A. C., Soler, J. M., Ganor, J., Burch, T. E., and K. L. Nagy, Chemical weathering rate laws and global geochemical cycles, *Geochim. Cosmochim. Acta*, 58, 2361-2386, 1994.

Lichtner, P.C. The Quasi-Stationary State Approximation to Coupled Mass Transport and Fluid-Rock Interaction in a Porous Medium, *Geochim. Cosmochim. Acta*, Vol. 52, pp. 143 - 165, 1988.

Lichtner, P.C., C.I. Steefel and E.H. Oelkers. Reactive Transport in Porous Media, *Rev. in Mineralogy*, Vol. 34, Mineralogical Society of America, Washington, DC, 1996.

Narasimhan, T. N. and P. A. Witherspoon. An Integrated Finite Difference Method for Analyzing Fluid Flow in Porous Media, *Water Res. Res.*, 12 (1), 57–64, 1976.

Neretnieks, I., J.W. Yu and J. Liu. An Efficient Time Scaling Technique for Coupled Geochemical and Transport Models, *J. Contam. Hydr.*, Vol. 26, pp. 269 - 277, 1997.

Peaceman, D. W. *Fundamentals of Numerical Reservoir Simulation*, Elsevier, Amsterdam, The Netherlands, 1977.

Pruess, K. TOUGH2 - A General Purpose Numerical Simulator for Multiphase Fluid and Heat Flow, Lawrence Berkeley Laboratory Report LBL-29400, Lawrence Berkeley Laboratory, Berkeley, CA, May 1991.

Steefel, C. I., and A. C. Lasaga, A coupled model for transport of multiple chemical species and kinetic precipitation / dissolution reactions with applications to reactive flow in single phase hydrothermal system, *Am. J. Sci.*, 294, 529-592, 1994.

Thomas, G.W. *Principles of Hydrocarbon Reservoir Simulation*. International Human Resources Development Corporation, Boston, 1982.

White, S.P. Multiphase Non-Isothermal Transport of Systems of Reacting Chemicals, *Water Resour. Res.*, Vol. 32, No. 7, pp. 1761-1772, 1995.

Wolery, T. EQ3/6, A Software Package for Geochemical Modeling of Aqueous Systems: Package Overview and Installation Guide (Version 7.0), Lawrence Livermore National Laboratory Report UCRL-MA-110662 PT1, Livermore, CA 94550, September 1992.

Xu, T., F. Gérard, K. Pruess and G. Brimhall, Modeling non-isothermal multiphase multi-species reactive chemical transport in geologic media, Lawrence Berkeley Laboratory Report LBL-40504, Berkeley, California, 1997.

Yeh, G.T. and V.S. Tripathi. A Critical Evaluation of Recent Developments in Hydrogeochemical Transport Models of Reactive Multichemical Components. *Water Resour. Res.*, Vol. 25, No. 1, pp. 93 - 108, 1989.

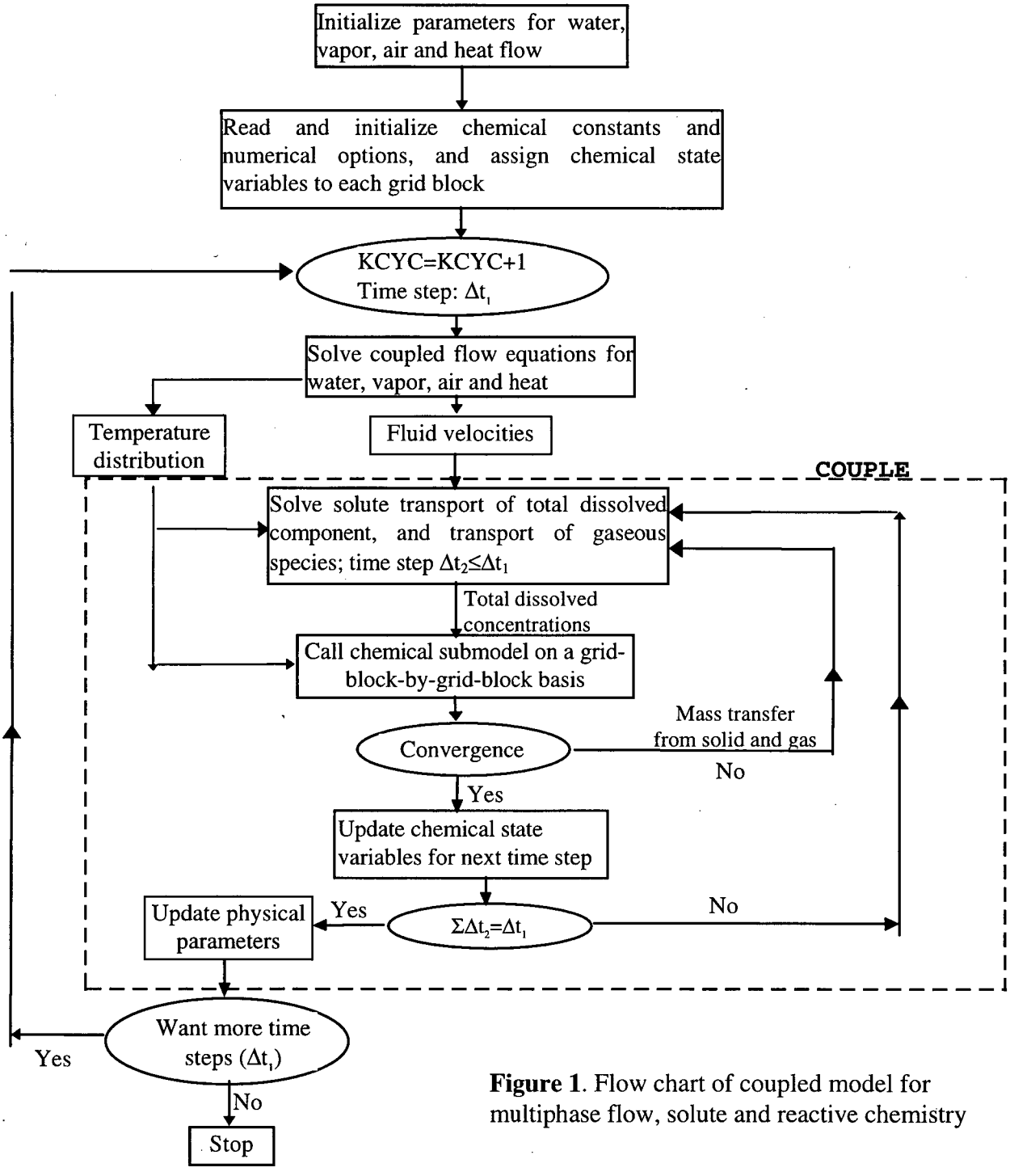

Figure 1. Flow chart of coupled model for multiphase flow, solute and reactive chemistry

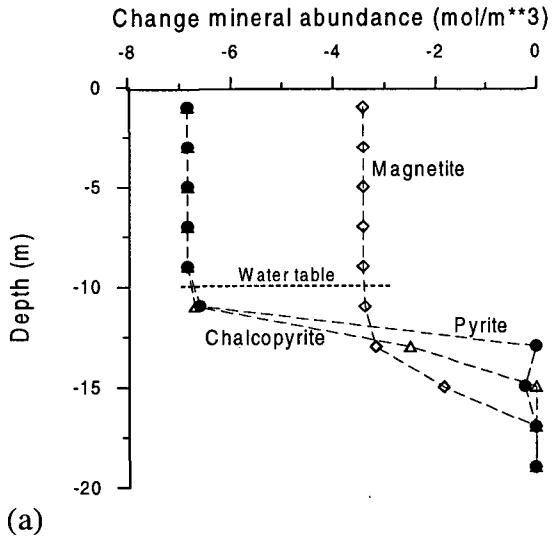

(a)

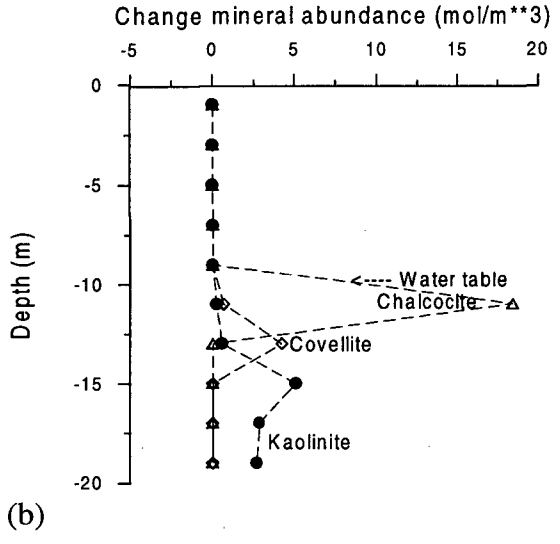

(b)

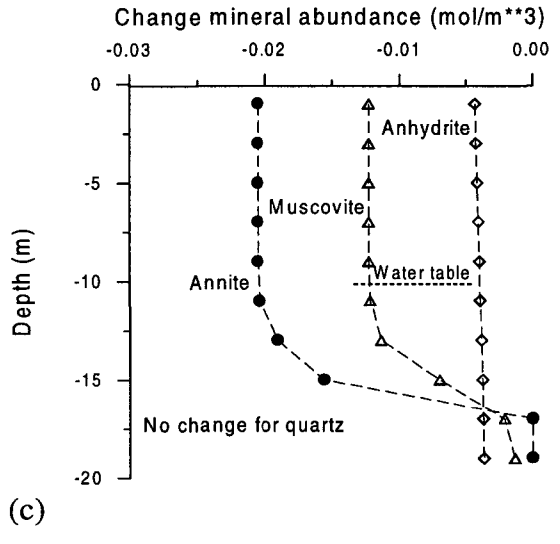

(c)

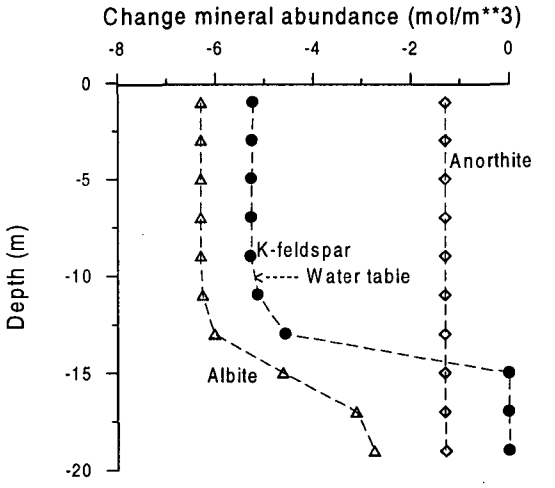

(d)

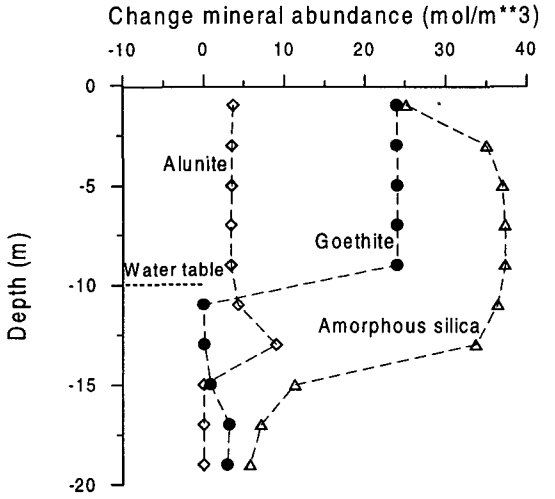

(e)

Figure 3. Change of mineral abundances (in moles per cubic meter medium) after 90 years. Negative values indicate dissolution, positive indicate precipitation.

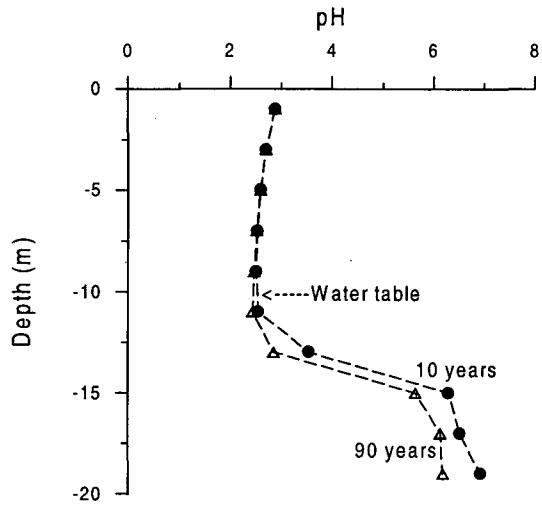

(a)

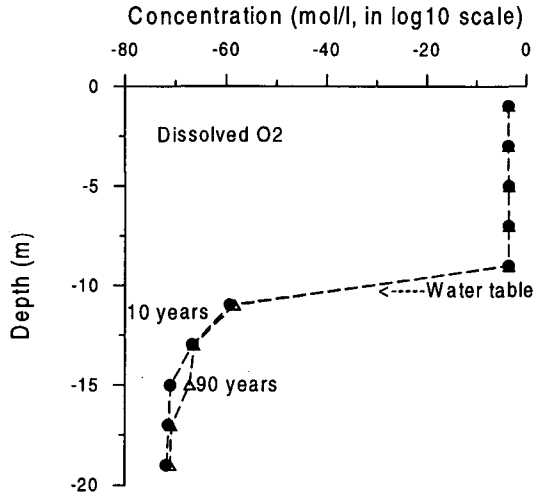

(b)

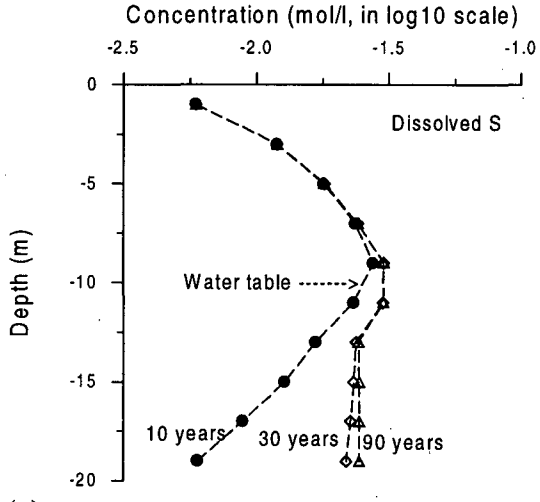

(c)

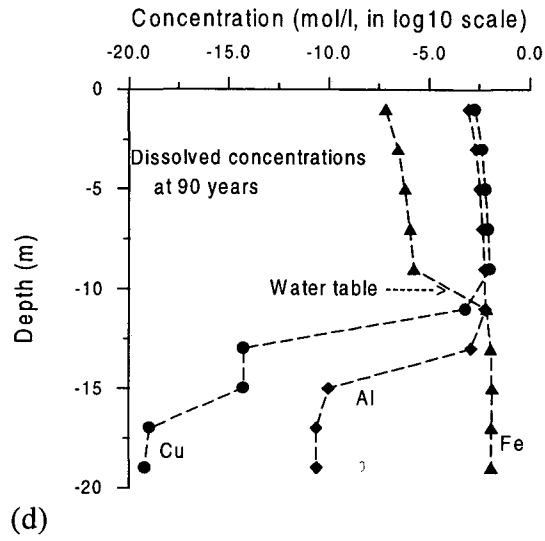

(d)

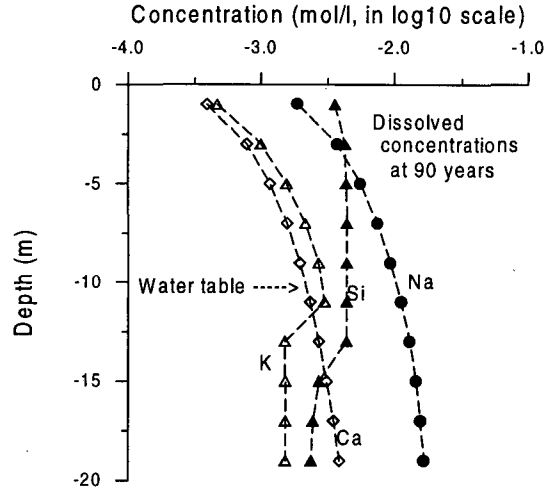

(e)

Figure 4. Total dissolved concentration distribution along the vertical column.

Reactive Chemical Transport

Stephen P White[1,2], Tianfu Xu[2], Karsten Pruess[2]

[1] Industrial Research Ltd, P.O. Box 31 310, Lower Hutt, New Zealand
[2] Lawrence Berkeley National Laboratory, University of California, Berkeley, California 94720

1. Introduction

Heat and mass transport and the interactions of fluid with the earth's crust are of interest for many reasons. For example economic geologists are interested in where conditions are appropriate for ore deposition, geothermal field developers are interested in the chemical composition of the fluid they plan to produce and how it may change. Contaminant transport is of interest to those charged with ensuring a potable water supply.

For many years it has been possible to compute the transport of heat and mass within the earth using simulators such as TOUGH2. Also speciation codes are well developed and used as a matter of course by geochemists to unravel the intricacies of the chemistry of fluids within the earth. Recently there has been a growing interest in combined these two disciplines to allow the modelling of reactive chemical transport in porous media. Some recent workers in the area are Lichtner (1992), Steffel and Lasaga (1995) Friedly (1989), Friedly and Rubin (1992), White (1995), Lichner and Seth (1996) and Bear and Niato (1995).

In this paper we will present an outline of modelling pyrite dissolution using Chem TOUGH2 (White 1995). Pyrite oxidation, dissolution and precipitation play an important role in the supergene enrichment of porphyry copper deposits. This process takes place when oxygen-rich water infiltrates into pyrite bearing geologic media. The pyrite is initially oxidised, with the oxidation products being in the aqueous phase. These products are transported in the aqueous phase and may precipitate when chemical or other conditions change. The importance of these processes has been known for some time (see, for example Emmons 1918, Locke 1926, Bateman 1950). Auge and Brimhall (1989) modelled the supergene enrichment of a porphyry copper deposit. Their work modelled the chemistry of the system in some detail, but the discretization of the domain used for transport calculations was quite coarse.

We consider a number of increasingly complex models of pyrite dissolution. All of these consider the reaction of oxygen-rich infiltration water with rock containing the mineral pyrite. Water in equilibrium with atmospheric oxygen has a dissolved oxygen concentration of 1.265×10^{-4} mol/l at 25° C, and we use this value for water entering the system.

2. Hydrodynamic and chemical parameters

In the first example we model a one-dimensional horizontal porous column 0.5 m long with a cross-sectional area of 1 m^2 which contains the mineral pyrite; at the left boundary infiltration water is injected at 2.31×10^{-4} kg/sec and is withdrawn from the right boundary at the same rate. Porosity of the column is 0.4 which, with the prescribed injection rate, leads to a pore velocity of 0.05 m/day. The column is discretized into 10 grid blocks, each with a length of 0.05 m.

The dissolved oxygen carried by infiltration water reacts with pyrite which dissolves. Oxidation and dissolution of pyrite results in redistribution of aqueous species. We considered that the system is made up of the following species: H^+, H_2O, $O_2(aq)$, SO_4^{2}, Fe^{+2}, OH^-, HSO_4^-, $FeSO_4(aq)$, HS^-, $H_2S(aq)$, Fe^{+3} and FeS_2 (Pyrite). For this example we force the system to contain single phase liquid only (i.e. no gas phase). The boundary infiltration solution has a dissolved oxygen concentration of 1.265×10^{-4} mol/l which is a strongly oxidising condition. This amount of oxygen is equivalent to a gaseous oxygen pressure of .1 bar (assuming a fugacity coefficient of 1.0). The reactions taking place between the species in solution are

$$
\begin{aligned}
&2\text{pyrite}(FeS_2) + 7O_2(aq) + 2H_2O = 4H^+ + 4SO_4^{-2} + 2Fe^{+2} \\
&HS^- + 2O_2(aq) = H^+ + SO_4^{-2} \\
&H_2S(aq) + 2O_2(aq) = 2H^+ + SO_4^{-2} \\
&4Fe^{+2} + O_2(aq) + 4H^+ = 4Fe^{+3} + 2H_2o \qquad (1) \\
&OH^- + H^+ = H_2O \\
&HSO_4^- = H^+ + SO_4^{-2} \\
&FeSO_4(aq) = SO_4^{-2} + Fe^{+2}
\end{aligned}
$$

2.1 Results

The infiltration water, having a large amount of dissolved oxygen, causes pyrite oxidation and dissolution. The O_2(aq) is consumed almost completely (the dissolved O_2 concentration after reaction is 6.763×10^{-69} mol/l). Dissolution of one mole of pyrite consumes 3.5 moles of aqueous O_2, and creates 2 moles of H^+, 2 moles of SO_4^{-2} and 1 mole of Fe^{+2}. Consequently, total dissolved S and Fe concentrations increase and pH decreases.

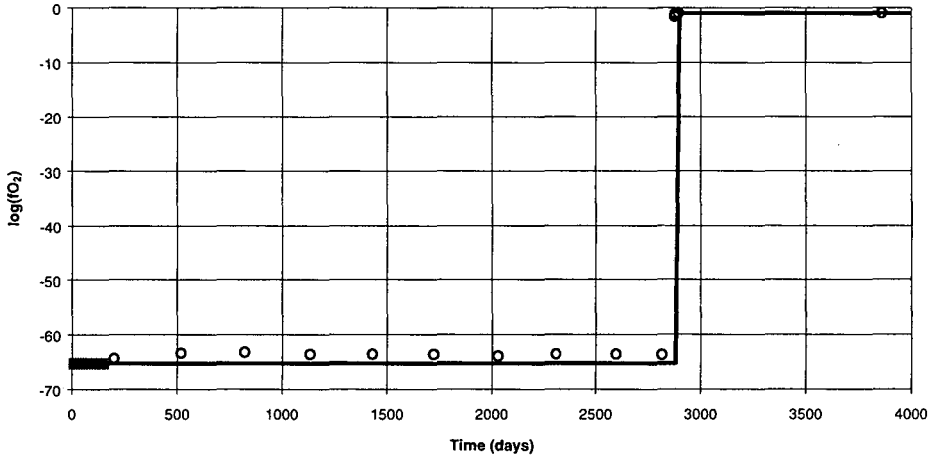

Figure 1: log of oxygen fugacity vrs grid pore volume (= time in days) at the center of the first grid block.

3. Two-phase simulations

The following two examples consider oxidation of pyrite in the vadose zone. Both examples use the same geometry shown in Figure 5. We model flows in a vertical column with a cross-sectional area of $1m^2$ and a length of 150 meters. At the top is air at 25° C and 1 bar, the bottom has a liquid saturation of 1.0 and a pressure of 10.5 bars.

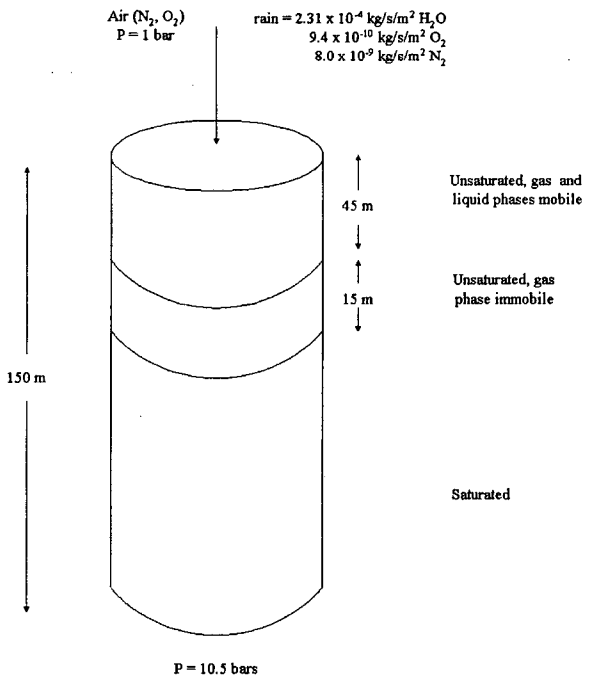

Figure 2: *Schematic representation of unsaturated column.*

The initial temperature is 25° C throughout the column. The initial conditions for pressure and saturation are the steady-state values calculated when chemical reactions are ignored. The column is unsaturated to a depth of 70 meters, below this the column is fully saturated. Water saturated in oxygen and nitrogen is injected into the block at the top of the column at a rate of 2.31×10^{-4} kg/s. We have used the relative permeability and capillary pressure functions of Van Genuchen (1980). With the parameters chosen for relative permeability the gas phase becomes immobile at a liquid saturation of about 0.8. This means that gas is mobile in the top three elements of the column, immobile in the fourth element and not present below that. For these examples involving transport in both the aqueous and gas phases, the chemistry is more complicated than given Equation 1 and we must include reactions between aqueous and gaseous oxygen and between aqueous and gaseous nitrogen.

$$O_2(aq) = O_2(gas)$$
$$N_2(aq) = N_2(gas)$$

While nitrogen does not react with any of the other species we must include it to obtain the correct pressures in the gas phase. As in the horizontal case we consider two examples, in the first all reactions are considered to be in equilibrium, in the second the pyrite oxidation reaction is treated as a kinetic reaction. Oxygen concentration as a function of depth for the equilibrium case is shown in Figure 11. This figure presents an interesting contrast to the fully saturated case shown in Figure 1b. In areas where the gas phase is mobile, the pyrite dissolves at an almost uniform rate, with oxygen flowing from the surface in the gas phase, dissolving in the oxygen depleted liquid and reacting with the pyrite. Figure 11 shows the top three elements with a high dissolved oxygen concentration as all the pyrite originally in these elements has been removed. This figure represents the situation after 5200 days which is insufficient time for the oxygen in the water injected into element 1 to have dissolved this volume of pyrite. Therefore transport of oxygen in the gas phase makes a significant difference to the rate at which pyrite is removed. In the fourth block, where the gas phase is not mobile, once the small amount of oxygen initially present has been consumed no further reaction takes place until all the pyrite has been consumed from the element above. Then the water flowing into element four will be saturated in oxygen, and the oxidation front will move through the saturated portion of the column as it did in the fully saturated horizontal example.

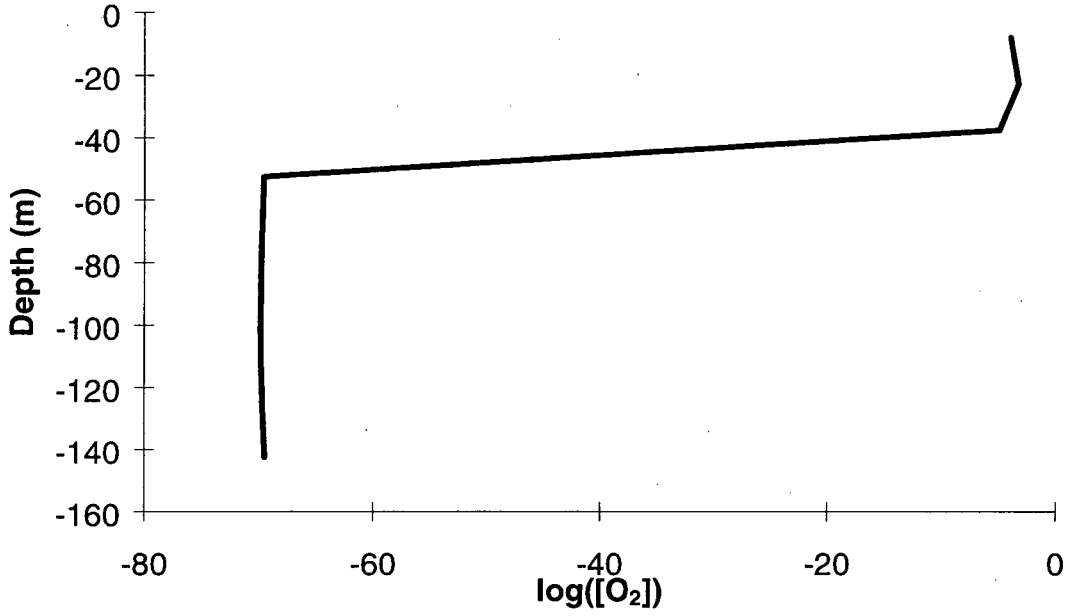

Figure 3: *Aqueous phase oxygen concentration in vertical column assuming equilibrium chemistry .*

3.1 Kinetic Reaction Rate

We assume a pyrite dissolution is described by a kinetic reaction of the form

$$\frac{dC_{pyrite}}{dt} = \alpha f(S) C_{pyrite} \tag{4}$$

From Welch *et al.* (1980) we estimate α=-1.8×10^{-5} sec^{-1} at a liquid saturation of 0.5. The reaction rate is a strong function of saturation (see Figure 16 of Welch *et al.*) and *f(S)* is a function of liquid saturation approximated from the data of Welch *et al.* (1980).

Obviously the reaction rate will also be modified by the amount of oxygen present in the aqueous phase. The expression given in Equation (4) is modified so that in a given time the reaction cannot consume more oxygen than is available at the beginning of that time plus any that is transported into an element during that time.

In Figure 12 we show the oxygen concentration as a function of depth assuming kinetic control for pyrite oxidation. Oxygen concentration is highest in the three elements nearest the surface. Once the gas phase is immobile or disappears, oxygen concentration drops approximately linearly with depth. It is interesting to note that only a small portion of the oxygen is consumed and the water flowing out the bottom of the model still contains about 90% of the oxygen that is present in the surface elements. This contrasts with the equilibrium case where all the oxygen is consumed in the unsaturated zone or when the pyrite there is depleted in the first element containing pyrite.

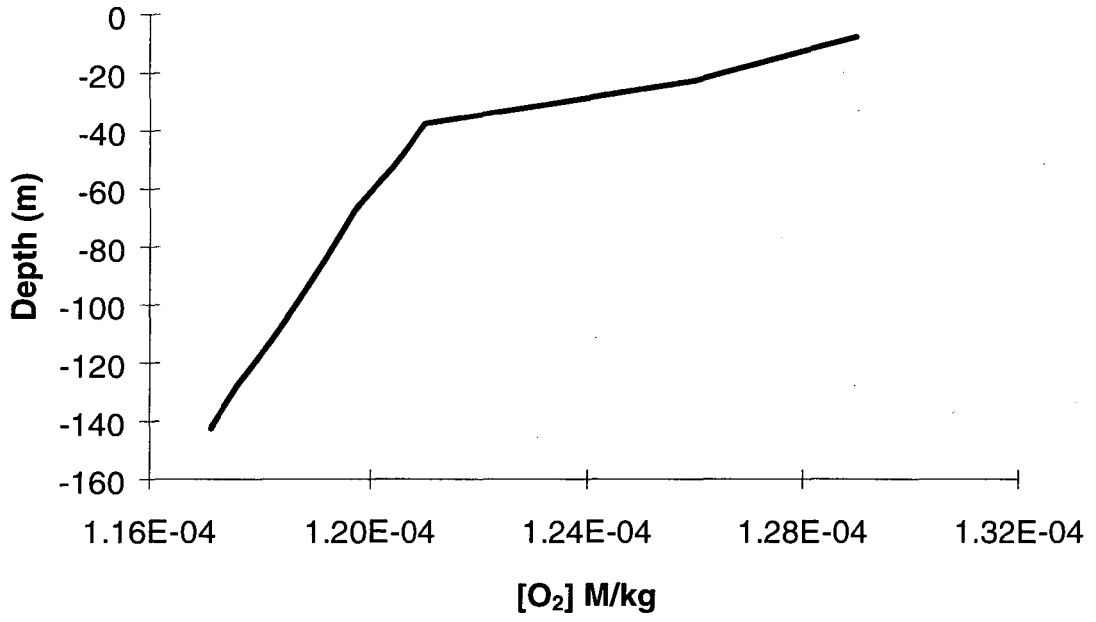

Figure 12: *Aqueous phase oxygen concentration in vertical column assuming non-equilibrium pyrite dissolution.*

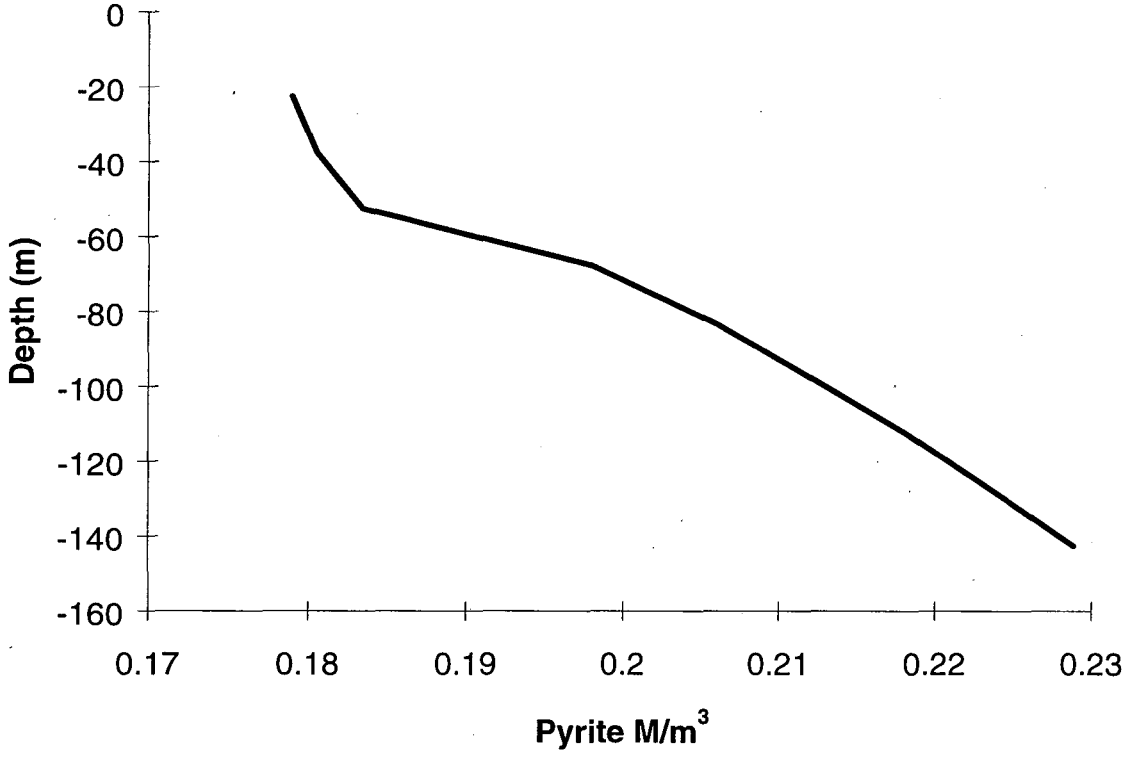

Figure 4: *Pyrite concentration in vertical column assuming non-equilibrium pyrite dissolution.*

4. Conclusions

We have modelled pyrite dissolution, where it is possible to calculate analytic properties of the modelled system (such as oxidation front speed), this has been done and compared with the numerical results. Good agreement with the numerical results was found.

Simulation of a vertical column containing a saturated zone confirms the importance of processes taking place in this zone to explaining the rate of pyrite removal. Pyrite will be oxidised from the rock over the whole of the vadose zone where the gas phase is mobile. This results in a much greater flux of pyrite oxidation products out of the column modelled than would be found for a fully saturated column.
When pyrite oxidation is treated as a kinetic reaction, the reaction may take place not only in the unsaturated zone but also to a considerable depth in the saturated zone. In the system modelled, only about 10% of the available oxygen was consumed by a depth of 160 meters. The kinetic reaction rate used in this modelling is an approximation to the true rate, and we have ignored the effect of pH on reaction rate and also treated the effect of oxygen concentration in a crude manner. However we believe sufficient detail has been included to reproduce the important effects of kinetic pyrite oxidation in a partially saturated column.

5. References

Ague, J.J., Brimhall, G.H. (1989) Geochemical Modeling of Steady State Fluid Flow and Chemical reaction during Supergene Enrichment of Porphyry Copper Deposits, *Economic Geology* 84, 506-528 (1989)

Bateman A. M (1950) Economic mineral deposit: New York, John Wiley, p245-287

Emmons W.H. (1918) The principles of echonomic geology. New York, McGraw-Hill 153 p

Lichtner, P.C. (1992) Time-space continuum description of fluid/rock interaction in permeable media. *Water Resour. Res.* 28:3135-3155 (1992)

Friedly, J.C. (1991), Extent of reaction for open systems with multiple heterogengeneous reactions. J. 37,687-693 (1991)

Friedly, J.C. and Rubin, J. (1992), Solute transport with multiple equilibrium controlled or kinetically controlled chemical reactions. Water Resour. Res., 28, 1935-1953 (1992)

Lichtner, P.C. and Seth, M.S. (1996) Multiphase-multicomponent nonisothermal reactive transport in partially saturated porous media. Presented at the International Conference on Geological Disposal of Radioactive Waste, Canadian Nuclear Society. Sept 16-19 Winnipeg Manitoba, Canada. (1996)

Locke, A. (1926) Leached outcrops as guides to copper ores. Baltimore, Williams, Wilkens Co., 166p

Steefel, C.I. and Lasaga, A.C., (1994). A coupled model for transport of multiple chemical species and kinetic precipitation/dissolution reactions with applications to reactive flow in single phase hydrothermal system, *Am. J. Sci.*, 294, 529-592. (1994)

Van Genuchten, M. T., and W. J. Alves, (1982) Analytical solutions of the one-dimensional convective-dispersive solute transport equation, *U. S. Department of Agriculture, Technical Bulletin No. 1661,* 151 pp., (1982).

Welch, V.S. II, Dann, M.W., Mehta, B. (1990) Predicting Oxygen Depletion in Reservoir Environments. *SPE 20721* (1990)

White, S. P., Multiphase non-isothermal transport of systems of reacting chemicals, *Water Resour. Res.*, 31, 1761-1772, (1995).

INVERSE MODELING OF A MULTISTEP OUTFLOW EXPERIMENT FOR DETERMINING HYSTERETIC HYDRAULIC PROPERTIES

S. Finsterle[1], T. O. Sonnenborg[2], and B. Faybishenko[1]

[1]Lawrence Berkeley National Laboratory
Earth Sciences Division, Mail Stop 90-1116
Berkeley, CA 94720

[2]Department of Hydrodynamics and Water Resources (ISVA)
Technical University of Denmark
2800 Lyngby, Denmark

ABSTRACT

A new, closed-form hysteretic model of the capillary pressure-saturation and relative permeability-saturation relationship has been implemented into ITOUGH2. The hysteretic capillary pressure function is based on the van Genuchten model, with a modified version of the dependent domain model of Mualem to describe the scanning curves. Hysteresis in the relative permeability relations is considered to be mainly a result of nonwetting fluid entrapment. The hysteresis model was used in combination with inverse modeling techniques to examine the potential of a simple drainage-imbibition experiment to determine hysteretic hydraulic properties.

INTRODUCTION

Hysteresis in the capillary pressure-saturation relationship, as well as entrapment of the nonwetting phase as a result of alternating drainage and imbibition events, has a significant impact on the distribution of moisture and contaminants in the subsurface [*Niemi and Bodvarsson*, 1988; *Essaid et al.*, 1993; *Deng and Pantazidou*, 1998]. Hysteresis in water retention properties of soils may be attributed to several factors, such as [*Hillel*, 1982]:

- Geometric nonuniformity of individual pores, resulting in the "inkbottle effect";
- Different spatial connectivity of pores during drying and wetting;
- Variations in liquid-solid contact angle;
- Air entrapment.

Some or all of these factors may act simultaneously, which makes it difficult to separate the individual effects based on observed hysteretic data. Furthermore, hysteresis depends on the velocity, with which the saturation changes occur.

While the presence of hysteresis in porous materials and its importance for predicting multiphase flow is well recognized, only a limited number of simulation studies using hysteretic capillary pressure functions have been performed [*Lenhard and Parker*, 1987; *Kool and Parker*, 1988]. Furthermore, most of these studies neglect hysteresis in the relative permeability functions, which may strongly influence the behavior of the nonwetting phase [*Sonnenborg et al.*, 1998].

Predicting hysteretic behavior by means of numerical simulation requires (1) selecting an appropriate parametric model describing the hysteretic hydraulic properties of the porous medium, and (2) estimating the parameters of the hysteretic capillary pressure and relative permeability functions. Both steps are complex and require handling strongly nonlinear effects, especially during saturation-path reversals.

The objectives of this study are (1) to implement a hysteretic capillary pressure and relative permeability model into TOUGH2, and (2) to evaluate the potential of inverse modeling techniques to derive soil hysteretic properties from a transient drainage-imbibition experiment.

HYSTERESIS MODEL

Hysteretic capillary pressure and relative permeabilities depend on the saturation-desaturation history. More specifically, the functional forms and their parameters change whenever a saturation reversal point is reached, i.e., when the saturation transient switches from imbibition to drainage or vice versa. Note that

at any given point in time, different volume elements of the porous material may undergo drainage or imbibition, which requires the numerical model to keep track of the saturation history in each individual gridblock.

In our model, the main branches of the hysteretic capillary pressure-saturation relation are described using the expression proposed by *van Genuchten* [1980]:

$$P_c = -\frac{1}{\alpha^\gamma}\left[\left(\frac{S_l - S_{lr}}{1 - S_{lr} - S_{gr}^\Delta}\right)^{-1/m^\gamma} - 1\right]^{1/n^\gamma} \quad (1)$$

where $P_c = P_l - P_g$ is the capillary pressure, S_l is the liquid saturation, S_{lr} and S_{gr}^Δ are the residual liquid and gas saturations, respectively, α, m and n are curve shape parameters with $m = 1 - 1/n$, and the superscript γ refers to drying (d) or wetting (w). The residual gas saturation S_{gr}^Δ is not considered to be a constant, but depends on the saturation at which reversal from drainage to imbibition occurs. The lower the liquid saturation at the reversal point, the more gas is entrapped because it is forced into progressively smaller pores during drainage; the amount of gas left behind as isolated islands during the imbibition process increases with decreasing reversal saturation S_l^Δ as follows:

$$S_{gr}^\Delta = \frac{1 - S_l^\Delta}{1 + R_{gl}(1 - S_l^\Delta)} \quad (2)$$

where

$$R_{gl} = \frac{1}{S_{gr}^{\max}} - \frac{1}{1 - S_{lr}} \quad (3)$$

The maximum amount of entrapped gas, $S_{gr}^{\max}$, which is an input parameter, is asymptotically reached when following the main wetting curve. This model describes the amount of air entrapped under both unsaturated and quasi-saturated conditions, accounting for the change in the volume fraction of air in a free, connected state, and air entrapped within the liquid phase [*Chahal*, 1969; *Faybishenko*, 1995].

The history-dependent entrapped gas saturation as well as its inclusion in the relative permeability curves are the new feature added to the hysteretic van Genuchten model described by *Niemi et al.* [1988].

The scanning curves are based on a modified version of the dependent domain model of *Mualem* [1984] as described in *Niemi and Bodvarsson* [1988]. The first-order wetting scanning curve is given by

$$S_l = S_l^d(P_c^\Delta) + \frac{[S_{lc} - S_l^d(P_c^\Delta)]}{[S_{lc} - S_l^w(P_c^\Delta)]}[S_l^w(P_c) - S_l^w(P_c^\Delta)] \quad (4)$$

where P_c^Δ is the capillary pressure at the reversal point from the main drying curve to the first-order wetting curve, S_l^d and S_l^w are the liquid saturations evaluated on the main drying and wetting curves, respectively, and $S_{lc} = 1 - S_{gr}^\Delta$ is the so-called critical liquid saturation. Equation (4) is used to solve for $S_l^w(P_c)$, which is the only unknown in the expression. Note that S_l is the primary variable known from the solution of the governing two-phase flow equations, the reversal capillary pressure P_c^Δ is saved when the reversal takes place, and $S_l^d(P_c^\Delta)$ and $S_l^w(P_c^\Delta)$ can be solved by inverting Equation (1). Once $S_l^w(P_c)$ is evaluated, the corresponding hysteretic capillary pressure P_c can be solved from the main wetting curve using (1).

Second-order drying curves are evaluated using

$$S_l = S_l^\Delta - \frac{[S_{lc} - S_l^d(P_c^+)]}{[S_{lc} - S_l^w(P_c^+)]^2} \cdot [S_{lc} - S_l^w(P_c)][S_l^w(P_c^\Delta) - S_l^w(P_c)] \quad (5)$$

where S_l^Δ is the liquid saturation at the reversal point from the first-order wetting scanning curve to the second-order drying scanning curve, and P_c^+ is the capillary pressure for which $S_l^d(P_c^+)$ equals S_l. Again, the only unknown in Equation (5) is $S_l^w(P_c)$; the capillary pressure P_c^+ can be found from the expression for the main drying curve. Solving (5) for $S_l^w(P_c)$ produces a parabolic equation with two solutions. *Niemi et al.* [1987] showed that the physically meaningful solution, $S_l^w(P_c) < S_l^w(P_c^\Delta)$ can be readily detected.

Higher-order scanning curves are approximated as semilog-straight lines between the last two reversal points, leading to hysteretic loops that become narrower with increasing order, and that meet at the appropriate reversal points.

Assuming that hysteresis in the relative permeability functions is mainly a result of nonwetting fluid entrapment, we adopt the approach described by *Lenhard and Parker* [1987]. They modified *Mualem*'s [1976] predictive model by including a term that accounts for the reduction in liquid relative permeability as a result of gas-phase entrapment. The amount of entrapped gas lies between zero and S_{gr}^{Δ}, and is assumed to be a linear function of the effective liquid saturation. The final expression for the hysteretic relative permeability includes a sum of terms representing the saturation history from the starting point to the current position. For details, the reader is referred to *Lenhard and Parker* [1987].

A total of six parameters (S_{lr}, $S_{gr}^{\max}$, α^d, α^w, n^d, n^w) have to be determined for this specific hysteresis model. The experimental, pointwise determination of hysteretic capillary pressure and relative permeability functions is very difficult and time consuming. We propose to use inverse modeling to estimate hysteretic hydraulic properties from transient laboratory experiments or field tests. In the following section, we summarize the elements of a formal parameter estimation procedure, and then apply the method to synthetically generated data that exhibit relatively strong hysteresis effects.

INVERSE MODELING

Solving the inverse problem is usually defined as the estimation of parameters by calibrating a model against observed data. We follow the standard procedure [*Beck and Arnold*, 1977] and minimize some measure of the differences between the observed and predicted system responses, which are assembled in the residual vector $\mathbf{r}$ with elements

$$r_i = y_i^* - y_i(\mathbf{p}) \tag{6}$$

Here, y_i^* is an observation at a given point in space and time, and y_i is the corresponding model prediction, which depends on the vector $\mathbf{p}$ of the unknown model parameters. In inverse modeling, the distribution of the final residuals is expected to be consistent with the distribution of the measurement errors, provided that the true system response is correctly identified by the model. If the error structure is assumed to be Gaussian, the objective function to be minimized can be inferred from maximum-likelihood considerations to be the sum of the squared residuals weighted by the inverse of the covariance matrix $\mathbf{C}_{yy}$:

$$Z(\mathbf{p}) = \mathbf{r}^T \mathbf{C}_{yy}^{-1} \mathbf{r} \tag{7}$$

An iterative procedure is needed to minimize Equation (7). The Levenberg-Marquardt modification of the Gauss-Newton algorithm [*Beck and Arnold*, 1977] was found to be suitable for our purposes [*Finsterle*, 1997b].

Under the assumption of normality and linearity, a detailed error analysis of the final residuals and the estimated parameters can be conducted. For example, the covariance matrix of the estimated parameter set is given by

$$\mathbf{C}_{pp} = s_0^2 (\mathbf{J}^T \mathbf{C}_{yy}^{-1} \mathbf{J})^{-1} \tag{8}$$

where $\mathbf{J}$ is the Jacobian matrix at the solution. Its elements are the sensitivity coefficients of the calculated system response with respect to the parameters:

$$J_{ij} = -\frac{\partial r_i}{\partial p_j} = \frac{\partial y_i}{\partial p_j} \tag{9}$$

In Equation (8), s_0^2 is the estimated error variance, a goodness-of-fit measure given by

$$s_0^2 = \frac{\mathbf{r}^T \mathbf{C}_{yy}^{-1} \mathbf{r}}{M - N} \tag{10}$$

where M is the number of observations and N is the number of parameters. The inverse modeling formulation outlined above is implemented in a computer program named ITOUGH2 [*Finsterle*, 1997a,b]. ITOUGH2 provides estimates of any TOUGH2 input parameter [*Pruess*, 1991] based on any type of observation, for which a corresponding TOUGH2 output variable can be calculated. We use ITOUGH2 to analyze synthetically generated data from a multistep drainage-imbibition experiment, and to examine the potential of this experiment for estimating hysteretic hydraulic properties.

APPLICATION

Model Development

Figure 1 shows a schematic of a flow cell designed for radial drainage-imbibition experiments on soil samples. A vacuum can be applied at the central ceramic cylinder for soil water extraction. The apparatus is instrumented with a vial to measure the cumulative water discharge through the central cylinder. Moreover, a tensiometer for water potential measurements is installed near the outer wall of the flow cell. A similar configuration is used for water injection.

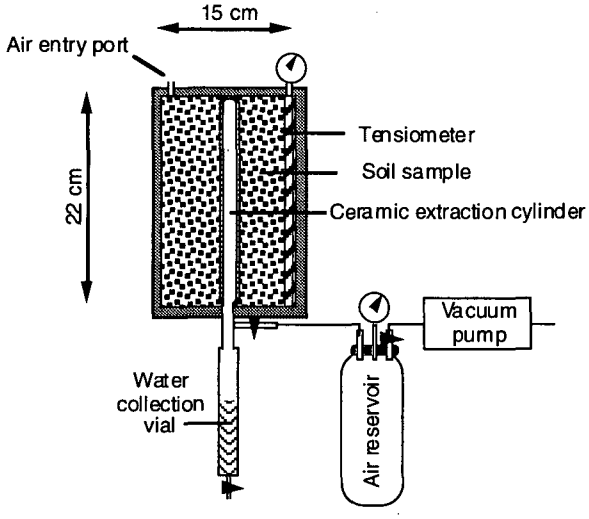

Figure 1. Schematic of apparatus for radial flow experiment.

Neglecting the minor effects of gravity, a one-dimensional radial model was developed, taking into account the impedance of the ceramic cylinder. A set of hysteretic hydraulic properties was assumed (see Table 1, Column 2), and synthetic cumulative outflow and capillary pressure data were generated for a multistep drainage-imbibition experiment, in which a suction pressure of -90 kPa was first applied at the extraction cylinder for 3 days. Subsequently, water was supplied without overpressure through the central cylinder for a 3-day period, leading to entrapment of air in the soil sample. Another drainage-imbibition cycle was simulated for time periods of 6 and 18 hours, respectively. Gaussian noise was added to the synthetic, true system response to simulate measurement errors. The standard deviations for the noise added to the capillary pressure and cumulative outflow data were 5 kPa and 25 ml, respectively.

The true hysteretic capillary pressure and relative permeabilities at the outer wall of the flow cell are visualized in Figures 2 and 3, respectively. Note that Figures 2 and 3 do not render the actual observed data; the measurements are shown as symbols in Figures 4 through 6. Nevertheless, an approximation of the hysteretic capillary pressure curve could be obtained by plotting the tensiometer data against the average soil saturation as calculated from the cumulative outflow data. Because of the averaging, this procedure would yield only an approximation of the curve shown in Figure 2, which represents the actual hysteretic loop encountered by the tensiometer. The hysteresis in the gas and liquid relative permeabilities cannot be directly observed during a transient experiment.

Inversions

Three different models have been calibrated against the synthetic data. The first model uses standard, non-hysteretic van Genuchten functions, i.e., $\alpha^d = \alpha^w = \alpha$, $n^d = n^w = n$, and $S_{gr}^{\max} = S_{gr}$. The second model allows for hysteresis, but neglects the effects of air entrapment by setting $S_{gr}^{\max} = 0$. Finally, the data are matched using the full hysteresis model. The matches to the capillary pressure and cumulative outflow data obtained with the three models are shown in Figures 4 through 6; the resulting parameter sets are summarized in Table 1.

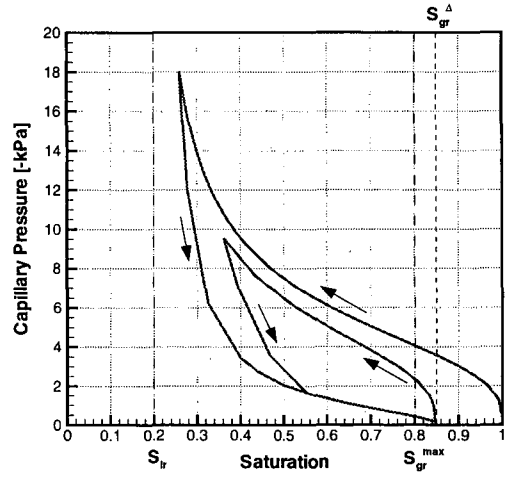

Figure 2. Computed hysteretic capillary pressure path at the outer wall of the flow cell.

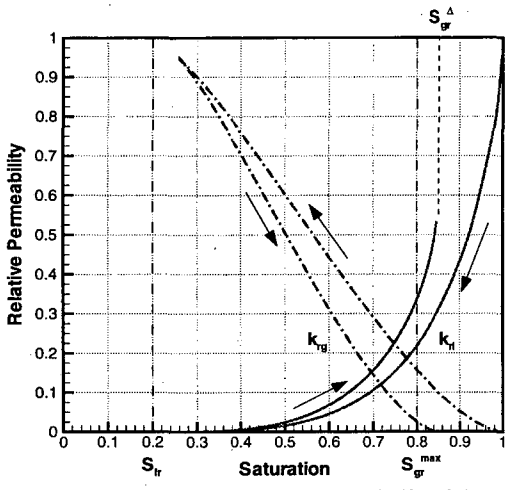

Figure 3. Computed gas and liquid relative permeability paths at the outer wall of the flow cell.

Table 1. True and Estimated Parameter Sets

Parameter	True	No hysteresis	No air entrapment	Hysteresis
$\log(k_{abs}$ [m^2])	-12.00	-11.64	-11.92	-11.97
$\log(1/\alpha^d$ [Pa])	3.69	3.41	3.71	3.70
$\log(1/\alpha^w$ [Pa])	3.00	-	2.43	2.98
n^d	3.00	2.13	3.14	3.01
n^w	2.00	-	1.33	1.97
S_{lr}	0.20	0.16	0.21	0.20
S_{gr}^{max}	0.20	0.40#	-	0.18

At specified upper boundary

Discussion

Matching data that exhibit hysteretic effects with a nonhysteretic model yields an imperfect match. While the estimated α and n parameters are within the bounds of the respective drying and wetting values of the hysteretic model, an unreasonably high residual gas saturation is required to obtain near-zero capillary pressures and reduced flow rates during imbibition. Furthermore, the absolute permeability is overestimated by more than a factor of 2, to partly compensate for the reduced effective liquid permeability and the reduced driving force during drainage, which stems from the lower capillary pressure gradient.

An almost perfect match to the observed data is obtained with the second model (see Figure 5). This result may be surprising given that the hysteretic model does not include the effect of air entrapment, which is believed to have a strong impact on system behavior [*Faybishenko*, 1995]. There are several explanations for this result First, while S_{gr}^{max}, which describes air entrapment, may be a sensitive parameter affecting forward predictions, its effect on the observed data, which are used during inverse modeling, may not be uniquely distinguishable. In other words, the lack of a formal inclusion of air entrapment in the model can be partly compensated for by adjusting other parameters, especially those describing the wetting curves. Since a reasonable match was obtained despite fixing S_{gr}^{max} at zero, it can be expected that it will be difficult to identify each of the parameters of the hysteretic model based on the available data.

Second, the impact of air entrapment becomes more important towards the end of a saturation period. While the cumulative outflow continuously declines during the imbibition periods (see Figure 5), the one obtained with the full hysteresis model (see Figure 6) asymptotically approaches a final, non-zero value representing the total amount of entrapped air. Therefore, it is likely that the experiment is inappropriate to identify S_{gr}^{max}. The design of the experiment could be improved by extending the imbibition periods, as suggested by the increase in the sensitivity coefficients $|\partial q(t)/\partial S_{gr}^{max}|$ for $t \rightarrow 6$ days. Furthermore, approaching the main wetting curve by extending the drainage period also help better identify S_{gr}^{max}.

Finally, neglecting air entrapment may not be significant for this soil and the prevailing test conditions. The main wetting branch of the capillary pressure curve is not strongly affected by S_{gr}^{max}, and the differences in the relative liquid permeabilities have only an impact during a small period of the entire test duration.

The hysteretic hydraulic properties are accurately identified when using the correct hysteresis model. Deviations from the true values are a result of the noise in the data. Note, however, that the relatively strong parameter correlations may lead to non-unique solutions when analyzing real data, i.e., when the assumed hysteresis model is unlikely to perfectly mimic the actual hysteretic behavior.

The discussion above emphasizes the importance of a careful test design, which should also be based on synthetic inversions rather

than on forward modeling alone [*Finsterle and Faybishenko*, 1997]. If S_{gr}^{max} is considered a key parameter for making model predictions, the experiment should be designed to maximize the sensitivity of the observed variables with respect to S_{gr}^{max}. The correlation of S_{gr}^{max} to the other parameters should be reduced to obtain an independent estimate of sufficiently low uncertainty.

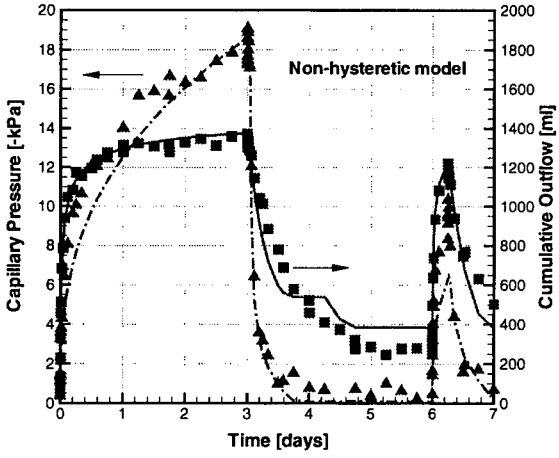

Figure 4. Comparison between observed (symbols) and calculated (lines) capillary pressure and cumulative outflow. Nonhysteretic model.

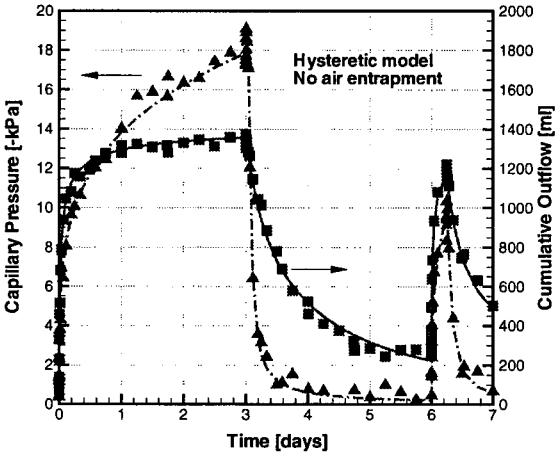

Figure 5. Comparison between observed (symbols) and calculated (lines) capillary pressure and cumulative outflow. Hysteretic model without air entrapment.

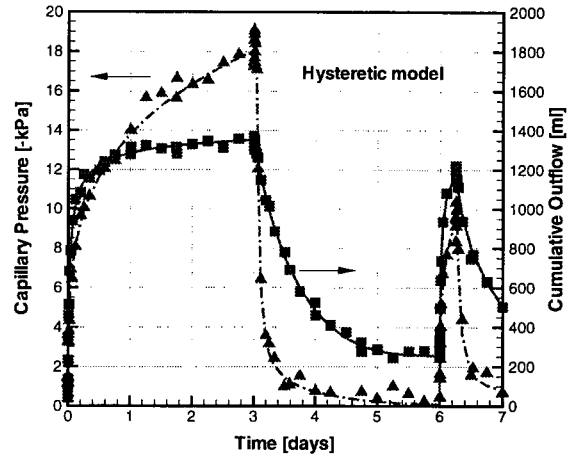

Figure 6. Comparison between observed (symbols) and calculated (lines) capillary pressure and cumulative outflow. Hysteretic model.

We proceed with a discussion of some of the statistical parameters calculated by ITOUGH2. First, the goodness-of-fit as measured by the estimated error variance (see Equation (10)) provides an overall assessment of the match obtained. Table 2 shows that while the correct hysteresis model realizes the best match according to the goodness-of-fit criterion (the differences are statistically significant on the 95% confidence level), it may not be justified to estimate all parameters of the full hysteresis model. The A-optimality criterion, which is the sum of the estimation variances scaled by the square of the parameter values, in fact favors the hysteresis model that does not include air entrapment. Estimating an additional parameter, i.e., S_{gr}^{max}, leads to higher overall correlations and thus larger estimation uncertainties, which cannot be fully compensated by the improvement of the fit.

Table 2. Estimated Error Variance and A-Optimality Criterion

Model	Number of parameters	Estimated error variance	A-optimality criterion[#]
No hysteresis	5	9.52	0.0081
Hysteresis no air entrapment	6	1.71	0.0008
Hysteresis	7	0.98	0.0014

[#] Trace of scaled estimation covariance matrix $\mathbf{C}_{pp}$

CONCLUDING REMARKS

A new hysteresis module has been developed for use with ITOUGH2. With a limited set of parameters, hysteresis in the capillary pressure curve as well as the gas and liquid relative permeability functions is modeled, taking into account history-dependent entrapment of the nonwetting phase. The module was used to generate synthetic data of a multistep drainage-imbibition experiment using radial flow geometry.

Parameter estimation using ITOUGH2 demonstrates the flexibility of inverse modeling concepts to extract information about hysteretic soil properties from a combined analysis of transient data, such as cumulative outflow and capillary pressure measurements. It becomes obvious, however, that the experiment has to be carefully designed to explore the full saturation range using alternating drying and resaturation events.

We are currently running a laboratory experiment to obtain hysteretic data that will be analyzed using the approach developed in this paper.

ACKNOWLEDGMENT

This work was supported, in part, by the Assistant Secretary for Energy Efficiency and Renewable Energy, Office of Geothermal Technologies, of the U.S. Department of Energy under Contract No. DE-AC03-76SF00098. We would like to thank C. Doughty and G. Moridis for thoughtful reviews.

REFERENCES

Beck, J. V. and K. J. Arnold, *Parameter Estimation in Engineering and Science*, John Wiley & Sons, New York, 1977.

Chahal, R. S., "Effect of Temperature and Trapped Air on Matric Suction," *Soil Sci., 100*(4), 262-266, 1965.

Deng, Y. and M. Pantazidou, "Effects of Hysteresis in Capillary Pressure-Saturation Relationships on Predicting LNAPL Mobility," *Proceedings*, XII International Conference on Computation Methods in Water Resources, Crete, Greece, June 15-19, 1998.

Essaid, H. I., W. N. Herkelrath and K. M. Hess, "Simulation of Fluid Distributions Observed at a Crude Oil Spill Site Incorporating Hysteresis, Oil Entrapment, and Spatial Variability of Hydraulic Properties," *Water Resour. Res., 29*(6), 1753-1770, 1993.

Faybishenko, B., "Hydraulic Behavior of Quasi-Saturated Soils in the Presence of Entrapped Air: Laboratory Experiments," *Water Resour. Res., 31*(10), 2421-2435, 1995.

Finsterle, S., *ITOUGH2 Command Reference, Version 3.1*, Report LBNL-40041, Lawrence Berkeley National Laboratory, Berkeley, Calif., 1997a.

Finsterle, S., *ITOUGH2 Sample Problems*, Report LBNL-40042, Lawrence Berkeley National Laboratory, Berkeley, Calif., 1997b.

Finsterle, S. and B. Faybishenko, "Design and Analysis of an Experiment to Determine Hydraulic Parameters of Variably Saturated Porous Media," Report LBNL-40245, Lawrence Berkeley National Laboratory, Berkeley, Calif., (submitted to *Advances in Water Resour.*), 1997.

Hillel, D., *Introduction to Soil Physics*, Academic Press, Inc., San Diego, Calif., 1982.

Kool, J. B. and J. C. Parker, "Analysis of the Inverse Problem for Transient Unsaturated Flow," *Water Resour. Res., 24*(6), 817-830, 1988.

Lenhard, R. J. and J. C. Parker, "A Model for Hysteretic Constitutive Relations Governing Multiphase Flow, 2. Permeability-Saturation Relations," *Water Resour. Res., 23*(12), 2197-2206, 1987.

Mualem, Y. "Hysteretical Models for Prediction of the Hydraulic Conductivity of Unsaturated Porous Media," *Water Resour. Res., 12*(6), 1248-1254, 1976.

Mualem, Y., "A Modified Dependent Domain Theory of Hysteresis," *Soil Sci., 137*(5), 283-291, 1984.

Niemi, A. and G. S. Bodvarsson, "Preliminary Capillary Hysteresis Simulation in Fractured Rocks, Yucca Mountain, Nevada," *J. Contam. Hydrol., 3*, 277-291, 1988.

Niemi, A., G. S. Bodvarsson and K. Pruess, *Incorporation of the Capillary Hysteresis Model HYSTR into the Numerical Code TOUGH*, Report LBL-23592, Lawrence Berkeley Laboratory, Berkeley, Calif., 1987.

Pruess, K., *TOUGH2—A General-Purpose Numerical Simulator for Multiphase Fluid and Heat Flow*, Report LBL-29400, Lawrence Berkeley Laboratory, Berkeley, Calif., 1991.

Sonnenborg, T. O., M. B. Butts, and S. Finsterle, "Estimation of Hysteretic Two-Phase Hydraulic Properties From Transient Flow Experiments," Report, Technical University of Denmark, 1998.

van Genuchten, M. Th., "A Closed-Form Equation for Predicting the Hydraulic Conductivity of Unsaturated Soils," *Soil Sci. Soc. Am. J., 44*(5), 892-898, 1980.

Review of Enhanced Vapor Diffusion in Porous Media

Stephen W. Webb and Clifford K. Ho
Sandia National Laboratories
Albuquerque, New Mexico 87185

ABSTRACT

Vapor diffusion in porous media in the presence of its own liquid has often been treated similar to gas diffusion. The gas diffusion rate in porous media is much lower than in free space due to the presence of the porous medium and any liquid present. However, enhanced vapor diffusion has also been postulated such that the diffusion rate may approach free-space values. Existing data and models for enhanced vapor diffusion, including those in TOUGH2, are reviewed in this paper.

INTRODUCTION

Gas diffusion in porous media is generally significantly smaller than in free space due to the presence of the porous medium. The flow area for gas-phase diffusion is reduced by the presence of the solid particles, by the presence of any liquid, and by the fact that the flow path for diffusion in a porous medium is more tortuous than in free space. Using Fick's law, gas diffusion in a porous media may be expressed as

$$F_i = -\tau\phi S_g D_{12}\rho_g \nabla\omega_i = -\beta D_{12}\rho_g \nabla\omega_i \qquad (1)$$

where D_{12} is the free-space diffusion coefficient at the pressure and temperature of interest. The product of the tortuosity coefficient, τ, the porosity, ϕ, and the gas saturation, S_g, is often referred to as the porous media factor, β. The porous media factor, β, is always less than 1, and gas diffusion in a porous medium is usually much lower than in free space.

In contrast, it has been postulated that diffusion of a condensible vapor in the presence of its liquid may be considerably enhanced compared to gas diffusion rates and may approach or exceed free-space values. (In the present discussion, *gas* refers to a non-condensible inert gas under the conditions of interest, or air. *Vapor* refers to the gas phase which may have a liquid phase present, or water vapor). The mechanisms for such an enhancement are postulated to occur at the pore scale and include local condensation and evaporation at isolated liquid "islands" within the porous medium, and an increased temperature gradient in the gas phase compared to the average temperature gradient in the equivalent porous medium. Enhanced vapor diffusion was first considered by Philip and deVries (1957) for soils. Jury and Letey (1979) estimated that the value of β is of the order 1.0 resulting in considerable enhancement of vapor diffusion compared to gas diffusion. When β equals 1.0, diffusion is not affected by the porous medium at all and is equal to the value for free-space diffusion. Enhanced vapor diffusion is commonly assumed in soil science but has seen limited use in engineering applications.

Ho and Webb (1998) reviewed enhanced vapor diffusion and came to the conclusion that, while enhanced vapor diffusion may exist, there is no direct evidence to support it. Only indirect evidence exists, where the enhancement has been inferred from other measurements such as moisture content or heat flux. As part of their review, Ho and Webb recommended additional modeling and experiments at multiple length scales. Subsequent to the review by Ho and Webb (1998), which was actually conducted in early 1996, a number of modeling and experimental studies have been conducted. The current status of enhanced vapor diffusion is considerably more advanced than in 1996 due to these investigations, which are continuing.

PORE-SCALE ANALYSIS

It is instructive to review the pore-scale analysis presented by Ho and Webb (1998). Ho and Webb used a pore-scale model, which is depicted in Figure 1, to estimate the steady-state mass flow of water vapor in various pore-scale transport paths. The first path considered (A-A) is flow through the liquid island due to water vapor condensation and evaporation, which is a postulated mechanism for enhanced vapor diffusion. The second path (B-B) in Figure 1 is due to Fickian diffusion around the liquid island. The mass flux for path (A-A) through the liquid island was based on an energy balance, which was performed on the surface of the liquid island exposed to the hotter side. The latent heat of condensation added to the liquid island was balanced by heat conduction through the liquid island. For path (B-B), Fick's law was used to evaluate the mass flux. Properties for

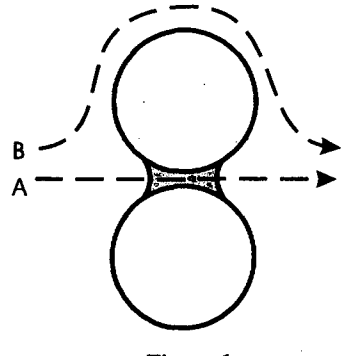

Figure 1
Pore-Scale Transport Paths
(A-A) Enhanced Vapor Diffusion
(B-B) Fickian Diffusion

water at 20°C were used.

The results from this simple pore-scale model indicate that net water vapor mass transfer through the liquid islands may be about an order of magnitude higher than water vapor transport around the liquid island by Fickian diffusion, or

$$\frac{m_{v,liquid\ island}}{m_{v.Fickian\ diffusion}} \sim 10 . \quad (2)$$

While the existence of these mechanisms remains to be experimentally demonstrated, the possibility exists based on this simple analysis.

ENHANCEMENT FACTORS

Before reviewing the various models and data, some terms need to be defined and clarified. There are a number of different enhancement factors and models. The two types of enhancement factors are a mechanistic enhancement factor, η, which is the enhancement of the vapor diffusion rate compared to the gas diffusion rate, and the porous media factor, β, which is relative to diffusion in free space. The two factors are simply related by the gas diffusion values of tortuosity, porosity, and gas saturation, or

$$\beta = \tau\phi S_g\eta \quad (3)$$

In addition, there are various vapor diffusion models which use the enhancement factors in different ways. As mentioned earlier, enhanced vapor diffusion was first considered by Philip and deVries (1957) for soils. Their vapor diffusion equation is

$$F_v = - D_{atm}\nu\tau\phi S_g\nabla\rho_v \quad (4)$$

which is essentially the same as equation (1) earlier. The term ν is a mass-flow factor term which is equal to the ratio of the total pressure to the air partial pressure. This term will be assumed equal to 1.0 and will not be included in the equations given below. Philip and deVries (1957) separated the vapor diffusion flux into temperature gradient and moisture gradient components by defining the vapor density gradient as a function of temperature and moisture content, or

$$\nabla\rho_v = h\frac{d\rho_0}{dT}\nabla T + \rho_0\frac{dh}{d\theta}\nabla\theta \quad (5)$$

where h is the relative humidity and ρ_0 is the saturated vapor density. The resulting equation is

$$F_v = - D_{T,v}\nabla T - D_{\theta,v}\nabla\theta \quad (6)$$

where

$$D_{T,v} = D_{atm}\tau\phi S_g h\frac{d\rho_0}{dT} \quad (7)$$

$$D_{\theta,v} = D_{atm}\tau\phi S_g\frac{g\rho_v}{RT}\frac{d\Psi}{d\theta} \quad (8)$$

and Ψ is the capillary pressure. (Note that Philip and deVries, 1957, ignored the dependence of h on temperature as corrected by Nakano and Miyazaki, 1979). Per Philip and deVries (1957), enhancement of the vapor diffusion rate is only attributed to the thermal gradient term, so

$$D_{T,v,enh} = \eta D_{atm}\tau\phi S_g h\frac{d\rho_0}{dT} \quad (9)$$

or

$$D_{T,v,enh} = \beta D_{atm} h\frac{d\rho_0}{dT} \quad (10)$$

If there is no temperature gradient, the model of Philip and deVries (1957) predicts that enhanced vapor diffusion will not occur. This model has been used by numerous investigators including Milly (1984), Shurbaji and Phillips (1995), and Nassar and Horton (1997) among others.

The question of only applying the enhancement factor to the thermal gradient term is due to the perceived dominance of the temperature gradient on the proposed mechanisms for enhanced vapor diffusion. Pore-scale modeling and some ongoing experiments, to be discussed later, contradict this temperature-only dependence as enhanced vapor diffusion is seen even if no temperature gradient is imposed. Milly (1997, personal communication) also speculated that the enhancement factor may apply to the other terms, although he only applied it to the thermal gradient in his analyses.

Gu et al. (1998) used another form of the vapor diffusion equation by including the Soret effect, or

$$F_v = - \tau\phi S_g(D_{12}\rho_g\nabla\omega_v + D_{Soret}\nabla T) \quad (11)$$

and any enhancement factor is applied to both terms, or

$$F_v = - \tau\phi S_g(\eta D_{12}\rho_g\nabla\omega_v + \eta D_{Soret}\nabla T) \quad (12)$$

This relationship was used to derive an enhancement factor for their data. Note that only about 5-8% of the vapor diffusion rate was attributed to the Soret effect (Gu et al., 1998).

Due to the different enhanced vapor diffusion equations, any values from the Gu et al. data can not be directly compared to data or models that are based on the Philip and deVries approach. It is anticipated that the values from Gu et al. (1998) should be smaller than those factors for the Philip and deVries model, simply because the equation used by Gu et al. (1998) applies the enhancement to the total vapor density gradient, not just the thermal component.

EXPERIMENTAL DATA

A large number of experiments related to enhanced vapor diffusion exist in the soil science and engineering literature; Ho and Webb (1998) list a number of them. However, vapor diffusion rates were not directly measured. In soil science experiments, the vapor diffusion rate was inferred from total water flow (liquid plus vapor) and/or the thermal conductivity - heat flux data. In the engineering literature, the drying rate is often of most interest, which is strongly influenced by the heat and mass transfer coefficients at the drying surface, which are unknown. A discussion of some of the problems with inferring vapor diffusion rates from these data is given by Ho and Webb (1998).

Most of the inferred values of enhanced vapor diffusion, such as Cary (1965) who deduced vapor movement from total water movement, are at discrete values for different average temperatures and moisture contents. No continuous variation of a parameter, such as the moisture content, was performed. The data from Cass et al. (1984) are significantly different. Their data, which inferred vapor diffusion rates from thermal conductivity information, give a continuous variation in the vapor diffusion rate, and the enhancement, as a function of moisture content at different temperatures. Their empirical fit, which is discussed later, is also important because it considers the behavior of the enhancement factor at various moisture content limits.

Cass et al. (1984) present their data as a mechanistic enhancement factor, η, and as a porous media factor, β, based on the Philip and deVries approach. Figure 2 gives the fits of η and β provided by Cass et al. (1984) for their two soils (lysimeter sand and Portneuf Silt Loam) at various temperatures. The mechanistic enhancement factor, η, increases rapidly from a value of around 1.0 for all-gas conditions (zero saturation), reaching a value of about 8-15 for a saturation of about 0.15 to 0.40; the value then slowly increases thereafter. The porous media factor, β, starts out at approximately the porous media factor for all-gas conditions, increases to a maximum of 2 to 4 at a saturation of about 0.15 to 0.40, and decreases thereafter to 0.0 at full liquid saturation.

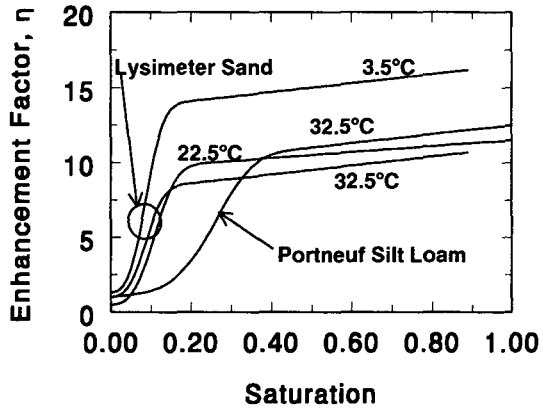

Figure 2a

Cass et al. (1984) Enhancement Factors, η

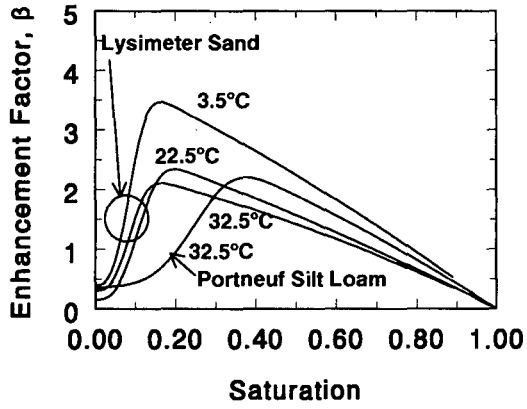

Figure b

Cass et al. (1984) Enhancement Factors, β

Other data, as tabulated by Jury and Letey (1979), consist of 38 values at various conditions from five different investigations. They based their enhancement factors on the Philip and deVries model. Water content information is given for less than half the data. The values of β range from 0.72 to 3.8, with an average value of 1.83 ± 0.79.

As noted earlier, all the above enhancement data are inferred. Recently, three different experimental investigations have been initiated to directly measure enhanced vapor diffusion at three different scales.

Experiments are underway at New Mexico Tech to measure vapor diffusion at the pore scale. The experimental setup consists of an individual pore, or two pores in parallel, with a concentration gradient across the pore(s); no temperature gradient is imposed. The concentration gradient is enforced by boundaries of pure water and a brine solution. The liquid in the pore is a mixture of the water and brine solutions. Mass changes in the reservoirs are used to evaluate the vapor diffusion rates. Preliminary results indicate significant enhancement of vapor diffusion rates if a liquid island is present in the pore (T. Silverman, personal communication, 1998).

At Sandia National Laboratories, enhanced vapor

diffusion is being studied in a rough-walled analog fracture using alcohol as the fluid. Light transmission methods are used to characterize the aperture field and measure liquid phase structure as a function of time within the fracture plane. Boundary conditions are imposed to yield constant vapor concentrations at the upstream (1.0) and downstream (0.0) edges of the fracture. These experiments are currently underway (R.J. Glass, Jr., personal communication, 1998).

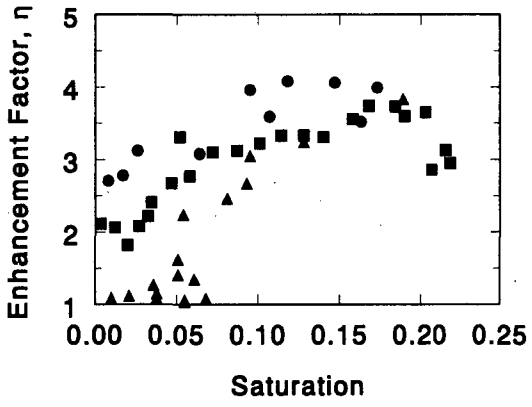

Figure 3a
Gu et al. (1998) Enhancement Factor (η) Data

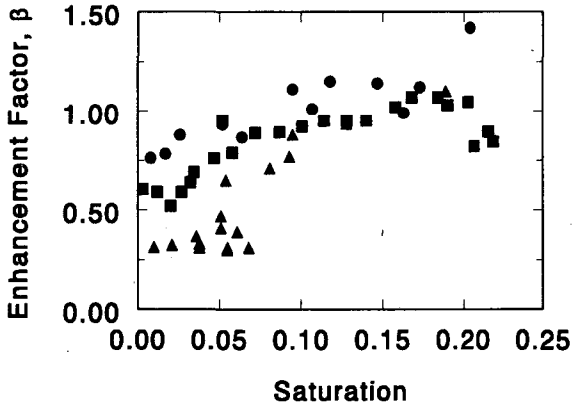

Figure 3b
Gu et al. (1998) Enhancement Factor (β) Data

Finally, at Washington State University, enhanced vapor diffusion has been measured in a packed bed of glass beads. The boundary conditions ranged from a concentration gradient under isothermal conditions, to combined concentration and temperature gradients, to drying conditions with only an imposed temperature gradient. Vapor fluxes are measured by a mass balance at the inlet and outlet reservoirs as well as the mass in the porous media packed bed. The data from the first series of experiments are given in Figure 3 (Gu et al, 1998); the various symbols represent different experiments. The mechanistic enhancement factor, η, increases from about 1.0 to a value approaching 4-5 at a saturation of 0.20; similarly, β increases from a value of about 0.5 at zero saturation to a value greater than 1.0 at higher saturations. The trends are in general agreement with the inferred data for Cass et al., although the values are typically lower. Differences are probably due to the different enhanced vapor diffusion equation used in each investigation as discussed above.

EMPIRICAL MODELS

There are a number of empirical models used to describe enhanced vapor diffusion. All the models, except that in TOUGH2 (Pruess, 1991), are based on the Philip and deVries (1957) assumption that enhanced vapor diffusion is only due to a thermal gradient.

The first empirical model for enhanced vapor diffusion was developed by Philip and deVries (1957) considering the difference in the temperature gradient in the gas phase compared to the average bulk temperature gradient, and the movement of vapor through isolated liquid islands. Jury and Letey (1979) modified the Philip and deVries (1957) model by considering the thermal conductivity of the vapor and liquid phases which changes the temperature gradient term. Cary (1979) developed another model, again based on the temperature gradient approach.

Cass et al. (1984) present curve fits to their data in the form

$$\eta = A + BS_l - (A-D)\exp[-(CS_l)^E] \quad (13)$$

and; β can be calculated from

$$\beta = \tau\phi S_g\eta \quad (14)$$

Their values of A, B, C, D, and E are given in Table 1.

Table 1. Cass et al. Curve Fit Coefficients

	A	B	C	D	E
Lysimeter Sand, 3.5°C	13.5	3	10	1.3	3
Lysimeter Sand, 22.5°C	9.5	2	8	0.5	3
Lysimeter Sand, 32.5°C	8.0	3	10	1.0	3
Portneuf Silt Loam, 32.5°C	9.5	3	3.5	1.0	4

As reported by Globus and Gee (1995), Campbell (1985) proposes a fit which is presumably based on the Cass et al. (1984) data, which is

$$\eta = 9.5 + 6\theta - 8.5\exp[-[(1 + 2.6f^{-1/2})\theta)]^4] \quad (15)$$

where θ is the moisture content (ϕS_g), and f is the clay fraction content.

Finally, TOUGH2 allows for the use of a constant

value of β as input. In this case,

$$\eta = \frac{\beta}{\tau \phi S_g} \qquad (16)$$

The factors in TOUGH2 are based on equation (1) and any enhancement is applied to the total diffusion rate.

The value of β from the various models are compared in Figure 4. Note that Cass et al. (1984) did a similar comparison for their correlation and the models of Cary (1979) and Jury and Letey (1979). The prediction of Cary (1979) is taken from the Cass et al. (1984) plots. Where needed, the tortuosity is set equal to 0.66 (Penman, 1940) as done by Philip and deVries (1957) and Cass et al. (1984). As can be seen, none of the models, other than the correlation of Cass et al. (1984) and the fit of Campbell (1985), adhere to the dramatic variation in the porous media factor at low liquid saturations, where enhanced vapor diffusion is most important. Equally disheartening, the models do not follow the appropriate behavior at low liquid saturations such that the value of β should go to the all-gas value at all-gas conditions.

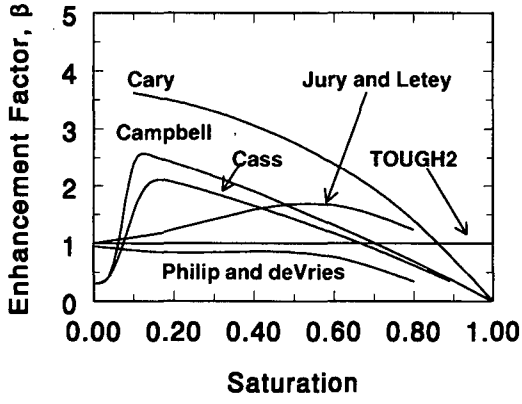

Figure 4
Model Comparison

MODELING STUDIES

As part of the enhanced vapor diffusion investigation being conducted at Sandia, pore-scale modeling has been performed using TOUGH2. Details of the model are discussed in more detail by Webb and Ho (1998). Significant enhancement of vapor diffusion up to an order of magnitude has been calculated under a concentration gradient (no temperature gradient) as shown by Webb and Ho (1997). These results indicate that enhancement may occur without a temperature gradient, contrary to the model of Philip and deVries (1957). Temperature gradient results for the pore-scale model are presented by Webb (in. prep) which indicate that the concentration gradient may dominate temperature gradient effects. In addition, Webb (1998) has shown that enhancement factors are equivalent for steady-state vapor diffusion and transient drying conditions, which has important modeling implications.

The original enhancement results of Webb and Ho (1997) were presented as enhancement as a function of liquid island length. These results are converted to enhancement as a function of model saturation for comparison to other information. The results from the single pore and the pore network are shown on Figure 5. The single pore results are considered to be the maximum enhancement factor because the liquid islands would be uniformly distributed among the pores. The pore network model with a single liquid island is the minimum enhancement factor. Note that the porosity of the model is 0.322.

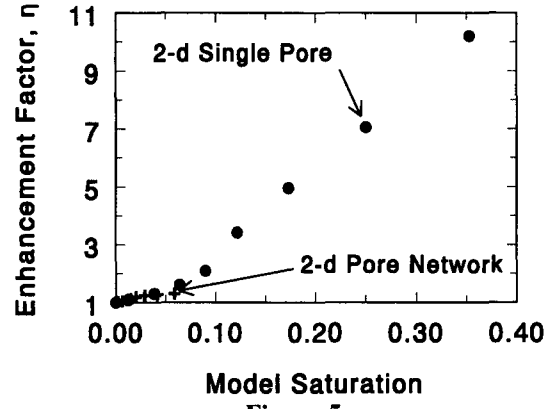

Figure 5
Pore-Scale Model Results (Webb and Ho, 1997)

The enhancement factor is applied to the total vapor diffusion rate similar to Gu et al. (1998). The calculated enhancement factor is in qualitative agreement with the data and model of Cass et al. (1984), and reasonable qualitative and quantitative agreement with Gu et al. (1998). The enhancement factor starts out as 1.0 which slowly increases until a saturation of about 0.05. The factor then increases rapidly, reaching a value of about 5.5 at a saturation of 0.20. This agreement may be fortuitous given the simplifications in the pore-scale model. As noted by Ewing and Gupta (1993), pore-scale modeling is a "useful concept rather than a physical reality". Further modeling studies should be conducted to investigate the effect of various model parameters on the results.

The above results indicate that if TOUGH2 were used at the pore scale, and individual liquid islands are included, enhanced vapor diffusion could be directly calculated. However, this amount of detail is impossible in practical applications, and continuum models with average enhancement factors must be used. The present enhanced vapor diffusion function in TOUGH2 does not agree with the expected variation as shown in Figure 4. A function similar to Cass et al. (1984) or Campbell (1985) would seem to be more appropriate.

DISCUSSION AND CONCLUSIONS

Enhanced vapor diffusion in the presence of its own liquid should be treated differently than air diffusion. Due to pore-level effects, vapor diffusion is enhanced relative to air diffusion rates. Even though this enhancement was inferred in previous studies, new information confirms the existence of enhanced vapor diffusion through direct measurements.

The existing models for enhanced vapor diffusion are based on the theory of Philip and deVries (1957), in which the enhancement is only due to temperature gradient effects. If there is no temperature gradient, there is no enhancement. Preliminary data and pore-scale modeling studies indicate that vapor diffusion is enhanced even if there is no temperature gradient, indicating that the theory and model of Philip and deVries may need to be revised.

Most of the existing models do not exhibit adequate behavior, especially at low liquid saturation. The exceptions to this behavior are the correlations of Cass et al. (1984) and Campbell (1985). Unfortunately, the enhancement factors are based on the model of Philip and deVries (1957), so the values may need to be revised. Nevertheless, these correlations are the best models to date. If the enhancement is applied to the entire vapor diffusion flux, as is tentatively recommended, the correlations of Cass et al. (1984) or Campbell (1985) should provide an upper bound of the enhancement factor, η.

NOMENCLATURE

D_{atm}	atmospheric diffusion coeffient
D_{soret}	Soret diffusion coeffcient
D_T	temperature diffusion coeffcient
D_{12}	binary diffusion coefficient
F	mass flux
h	relative humidity
m_v	vapor mass transfer rate
S	saturation
v	mass-flow factor
β	porous media factor
η	enhancement factor
ρ	density
τ	tortuosity coefficient
ϕ	porosity
ω	mass fraction
θ	moisture content
Ψ	capillary pressure

Subscripts

enh	enhanced
g	gas
i	gas i
l	liquid
v	vapor
0	saturated value

ACKNOWLEDGMENTS

This work was supported by the United States Department of Energy under Contract DE-AC04-94AL85000 as part of a Sandia LDRD Project on Enhanced Vapor-Phase Diffusion in Porous Media. Sandia is a multiprogram laboratory operated by Sandia Corporation, a Lockheed Martin Company, for the United States Department of Energy.

This study was stimulated by the paper by Y.W. Tsang and K. Pruess, "Modeling Studies of Gas Movement and Moisture Migration at Yucca Mountain, Nevada," presented at the TOUGH Workshop, September 13-14, 1990.

REFERENCES

Campbell, G,S., 1985, "Soil Physics with BASIC," Elsevier, Amsterdam, as refrenced by Globus and Gee.

Cary, J.W., 1965, "Water Flux in Moist Soil: Thermal Versus Suction Gradients," *Soil Science,* 100:168-175.

Cary, J.W., 1979, "Soil Heat Transducers and Water Vapor Flow," *Soil Sci. Soc. Am. J.,* 43:835-839.

Cass, A., Campbell, G.S., and Jones, T.L., 1984, "Enhancement of Thermal Water Vapor Diffusion in Soil," *Soil Sci. Soc. Am. J.,*48:25-32.

Ewing, R.P., and Gupta, S.C., 1993, "Modeling percolation properties of random media using a domain network," *Water Resourc. Res.*, 29:3169-3178.

Globus, A.M., and Gee, G.W., 1995, "Method to Estimate Water Diffusivity and Hydraulic Conductivity of Moderately Dry Soil," *Soil Sci. Soc. Am. J.,* 59:684-689.

Gu, L., Ho, C.K., Plumb, O.A., Webb, S.W., 1998, "Diffusion With Condensation and Evaporation in Porous Media," AIAA/ASME Joint Thermophysics and Heat Transfer Conference, Albuquerque, NM.

Ho, C.K., and Webb, S.W., 1998, "A Review of Porous Media Enhanced Vapor-Phase Diffusion Mechanisms, Models, and Data - Does Enhanced Vapor-Phase Diffusion Exist?" *J. Porous Media, 1:71-92..*

Jury, W.A., and Letey, Jr., J., 1979, "Water Vapor Movement in Soil: Reconciliation of Theory and Experiment," *Soil Sci. Soc. Am. J.,* 43:823-827.

Milly, P.C.D., 1984, "A Simulation Analysis of Thermal Effects on Evaporation From Soil," *Water Resour. Res.,* 20:1087-1098.

Nakano, M., and Miyazaki, T., 1979, "The Diffusion and Nonequilibrium Thermodynamic Equations of Water Vapor in Soils Under Temperature Gradients," *Soil Science,* 128:184-188.

Nassar, I.N., and Horton, R., 1997, "Heat, Water, and Solute Transfer in Unsaturated Porous Media:I-Theory Development and Transport Coefficient Evaluation," *Trans. in Porous Media,* 27:17-38.

Philip, J.R., and deVries, D.A., 1957, "Moisture Movement in Porous Materials under Temperature Gradients," *Trans., Am. Geophys. Union,* Vol. 38, No. 2, pp. 222-232, p. 594.

Penman, H.L., 1940, "Gas and Vapour Movements in Soil: I. The Diffusion of Vapours in Porous Solids," *J. Agric. Sci. (England),* 30:347-362.

Pruess, K., 1991, *TOUGH2 - A General-Purpose Numerical Simulator for Multiphase Fluid and Heat Flow,* LBL-29400, Lawrence Berkeley Laboratory.

Shurbaji, A.-R.M., and Phillips, F.M., 1995, "A numerical model for the movement of H_2O,$H_2{}^{18}O$, and ^2HHO in the unsaturated zone," *J. Hydrology,* 171:125-142.

Webb, S.W., and C.K. Ho, 1997, "Pore-Scale Modeling of Enhanced Vapor Diffusion in Porous Media," *Proceedings of the ASME Fluids Engineering Division,* FED-Vol. 244, pp. 457-468.

Webb, S.W., 1998, "Pore-Scale Modeling of Transient and Steady-State Vapor Diffusion in Partially-Saturated Porous Media," 1998 AIAA/ASME Joint Thermophysics and Heat Transfer Conference, Albuquerque, NM, June 15-18.

Webb, S.W., in prep., "Temperature Gradient Effects in Vapor Diffusion in Partially-Saturated Porous Media."

Webb, S.W. and C.K. Ho, 1998, "Pore-Scale Modeling Using TOUGH2," TOUGH Workshop '98, Lawrence Berkeley Laboratory, May 4-6, 1998.

FERROFLUID FLOW FOR TOUGH2

Curtis M. Oldenburg and George J. Moridis

Earth Sciences Division
Berkeley Lab
Berkeley, CA, 94720

ABSTRACT

Ferrofluids are suspensions of magnetite particles with average diameter of order 10 nm stabilized by surfactants in carrier liquids. The potential applicability of ferrofluids to subsurface environmental engineering has recently been recognized. In one potential environmental engineering application, externally applied magnetic fields are used to control and direct the flow of ferrofluids underground. In order to facilitate the design and experimentation of porous media ferrofluid applications, we have developed a TOUGH2 module called EOS7M for simulating the flow and transport of ferrofluid. In the presence of an external magnetic field, the ferromagnetic colloidal particles suspended in the carrier liquid of a ferrofluid become magnetized and produce attractive forces on each particle that produce a body force on the liquid. The steps involved in calculating ferrofluid flow are (1) calculation of the external magnetic field and its gradient, (2) calculation of the ferrofluid magnetization, (3) calculation of the magnetic force on the fluid, (4) addition of the magnetic force to the pressure gradient and gravitational body force terms, and (5) calculation of the resulting liquid phase fluxes. These methods along with simple density and viscosity relations for the aqueous phase as a function of the mass fraction of ferrofluid have been implemented in a module called EOS7M. Example calculations that model laboratory experiments have been carried out to validate the methods.

INTRODUCTION

Ferrofluids are suspensions of single domain magnetite particles with average diameters of approximately 10 nm stabilized by surfactants in carrier liquids (Rosenzweig, 1985; Berkowsky *et al.*, 1993). Ferrofluids have found applications in a variety of engineered devices and systems for, among other things, lubrication and sealing of bearings (Raj and Moskowitz, 1990). Recently, their potential utility in subsurface environmental engineering has been recognized (Moridis *et al.*, 1998). In one potential environmental engineering application, externally applied magnetic fields are used to control and direct the flow of ferrofluids underground. We call the driving force on the ferrofluid generated by the application of an external magnetic field magnetopressure. Carefully applied magnetopressure could be useful for creating and testing subsurface barriers, grouting rock for strength, and directing injected chemical agents and microbes toward particular contaminated zones.

In order to facilitate the design and experimentation of porous media ferrofluid applications, as well as to carry out numerical experiments of ferrofluid flow phenomena, we have developed simulation capability for ferrofluids. This simulation capability is being built upon the TOUGH2 framework (Pruess, 1987; 1991a) as an equation of state module called EOS7M (Oldenburg *et al.*, 1998a). The purpose of this paper is to summarize the equations and methods used to simulate the flow of ferrofluids in porous media and to present example simulations from EOS7M.

MATHEMATICAL DEVELOPMENT

Magnetic Force

In the presence of an external magnetic field, the single-domain colloidal magnetite particles suspended in the carrier liquid of a ferrofluid become magnetized (Fig. 1). The magnetization or polarization of the fluid interacts with the external magnetic field to produce attractive forces on each particle. By virtue of the suspension of ferrofluid particles in the liquid, the attractive magnetic force manifests itself as a body force on the liquid, analogous to the body force on a liquid due to gravity. The attractive force on ferrofluid per unit volume is given by

$$\boldsymbol{F} = \mu_o M \nabla H \qquad (1)$$

where μ_o is the magnetic permeability of free space (Tesla m/Ampere-turn), M is the magnetization (Ampere-turn/m), and H is the magnetic field strength of the external magnetic field (Ampere-turn/m). The units of Eq. 1 are thus

$$\frac{N}{m^3} [=] \frac{Tm}{A} \frac{A}{m} \frac{A}{m^2} [=] \frac{TAm}{m^3} \qquad (2).$$

Thus the calculation of the magnetopressure involves calculating H, ∇H, and M, along with the ferrofluid mass fraction at each gridblock. The remainder of this section outlines the methods for calculating these quantities.

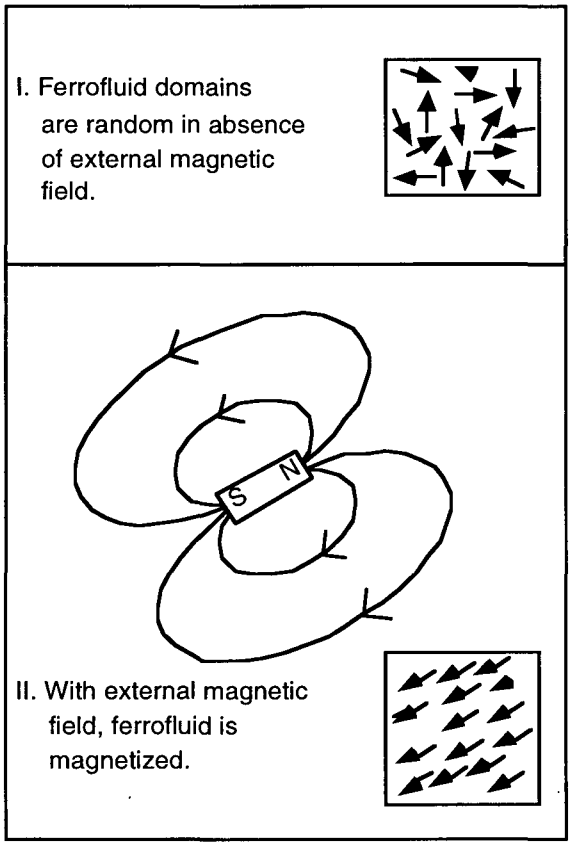

Fig. 1. Polarization of ferrofluid particles.

Magnetic Field Strength

The calculation of magnetic field strength is complicated for general systems with variable magnetic permeability. However, if the medium is free of ferromagnetic minerals and a permanent magnet is the source of the magnetic field, we can use some simple equations to calculate the components of H directly. These direct equations were presented with an error in McCaig (1977) and corrected in McCaig and Clegg (1987). In the direct equations, the poles of the magnet are a distance L apart, and the field at any location is the difference between the fields due to each pole. The full equations are too lengthy to include here, but are presented in full in Oldenburg *et al.* (1998b). Along the Z-axis assumed perpendicular to the face of either the North or South pole of a rectangular magnet (Fig. 2), the equation for the Z component of H simplifies to

$$H_z = \frac{B_r}{\pi\mu_0}\left[\tan^{-1}\left(\frac{ab}{z\left(a^2+b^2+z^2\right)^{1/2}}\right) - \tan^{-1}\left(\frac{ab}{(z+L)\left(a^2+b^2+(z+L)^2\right)^{1/2}}\right)\right] \quad (3)$$

where B_r is the residual flux density of the permanent magnet. The magnetic field strength (H) needs only to be calculated once at the beginning of the simulation for all gridblocks in the domain. The gradient of H is calculated by simple differencing at each gridblock interface.

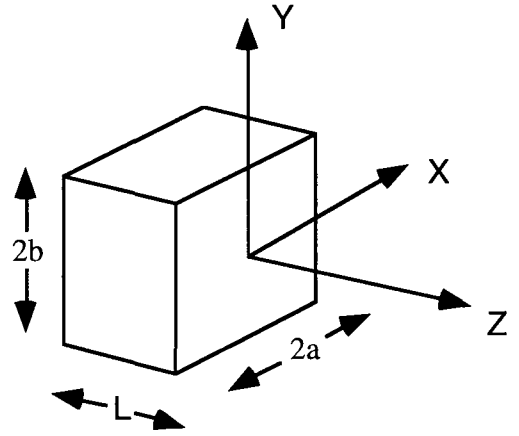

Fig. 2. Local coordinate system for the magnetic field produced by a permanent magnet.

Magnetization

As the strength of an external magnetic field is increased from zero A/m, pure ferrofluid will become magnetized to a degree controlled by the strength of the external field and the properties of the ferrofluid. The relationship between the magnetic induction (B), and magnetic field strength (H), and magnetization (M) is known as the B-H curve, where

$$\mathbf{B} = \mu_o(\mathbf{H}+\mathbf{M}) \quad (4).$$

Eq. 4 has been written in terms of the vectors **B, H,** and **M**, but can also be written as a scalar equation where B, H, and M are scalars representing the corresponding vector magnitudes. As the external magnetic field is increased, the ferrofluid reaches a maximum magnetization, or saturation magnetization. Thus the magnetization is a function (f) of H whose parameters depend on the particular type and size of the ferromagnetic material in the fluid:

$$\mathrm{M} = f(\mathrm{H}) \quad (5)$$

An example magnetization curve and an arctangent function model fit for the ferrofluid EMG 805 (Ferrofluidics, NH) is shown in Fig. 3.

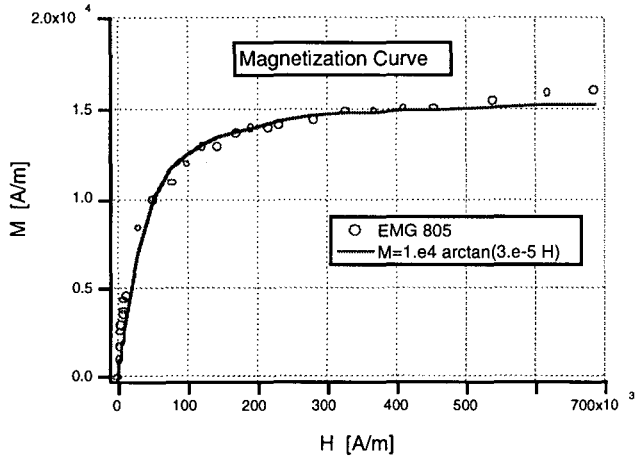

Fig. 3. Magnetization data and arctangent curves used to model ferrofluid magnetization. The arctangen functions are of the form $M = a1$ arctan $(b1*H)$.

Mixing Model

The ferrofluid in EOS7M is assumed to be miscible with water, giving rise to a single aqueous phase with components (1) water and (2) ferrofluid pseudo component. Following the work of Reeves *et al.* (1986) and Herbert *et al.* (1988) on brine-water mixtures, we use the simple mixing models as in EOS7 (Pruess, 1991b) where density and viscosity are given by

$$\frac{1}{\rho} = \frac{1 - X_{ff}}{\rho_w} + \frac{X_{ff}}{\rho_{ff}} \qquad (6)$$

$$f(X_{ff}) = 1 + \mu(1)X_{ff} + \mu(2){X_{ff}}^2 + \mu(3){X_{ff}}^3 \quad (7)$$

where the density of the two components are given by ρ_w and ρ_{ff}, and the last two terms in Eq. 7 have been neglected due to lack of data. The magnetization (M) of the water-ferrofluid mixture is assumed to be directly proportional to the ferrofluid mass fraction:

$$M = M_{(X_{ff}=1)}X_{ff} \qquad (8).$$

Transport parameters controlling processes such as dispersivity, diffusivity, adsorption, and straining are poorly known and are not currently included in EOS7M. Similarly, the non-isothermal behavior of magnetic materials is complicated and we currently restrict EOS7M to isothermal conditions at 20°C.

Solution Methodology

After the magnetic field strength and its gradient are calculated by the use of the direct equations, the magnetic body force must be included in a set of flow equations that includes conservation of ferrofluid component. We have used the TOUGH2 (Pruess, 1987; Pruess, 1991a) framework and developed a module called EOS7M (Oldenburg *et al.*, 1998a) for ferrofluid flow and transport for TOUGH2. The integral conservation equations solved by the integral finite difference method in TOUGH2 consist of balances between mass accumulation and flux and source terms over all grid blocks V_n into which the flow domain V has been partitioned:

$$\frac{d}{dt}\int_{V_n} M^{(\kappa)} dV = \int_{\Gamma_n} F^{(\kappa)} \cdot n \, d\Gamma + \int_{V_n} q^{(\kappa)} dV \qquad (9)$$

In Eq. 9, the index n = 1, ..., N corresponds to the grid blocks with volume V_n and surface area Γ_n. The index κ = 1, ..., NK+1 corresponds to the NK fluid components and heat. The mass accumulation term (M) in Eq. 9 is given by

$$M^{(\kappa)} = \phi \sum_{\beta=1}^{NPH} S_\beta \rho_\beta X_\beta^{(\kappa)} \qquad (10)$$

The flux term can be written

$$\boldsymbol{F}^{(\kappa)} = \sum_{\beta=1}^{NPH} X^{(\kappa)} \boldsymbol{F}_\beta \qquad (11)$$

where hydrodynamic dispersion and molecular diffusion have been neglected. Eq. 11 accounts for the flux of component κ arising from Darcy flux of the phases containing κ. With the inclusion of magnetic forces along with the usual pressure gradient and gravitational body forces, the phase flux term for a single phase (β subscript dropped) can be written

$$\boldsymbol{F} = \rho \mathbf{u} = -\frac{k}{\mu}\rho(\nabla P - \rho \mathbf{g} - \mu_o M \nabla H) \qquad (12).$$

As shown in Eqs. 6, 7, 8, and 12, the forces on ferrofluid depend on the ferrofluid mass fraction. Therefore, flow of ferrofluid is strongly coupled to ferrofluid transport. This type of strongly coupled flow problem is analogous to variable density flow problems with large density changes and requires strongly coupled solution techniques (Oldenburg and Pruess, 1995) such as those used in TOUGH2.

In EOS7M, we calculate the external magnetic field once at the beginning of each simulation. The coupling between ferrofluid flow and the external magnetic field occurs through the M and ∇H terms. Magnetization is modeled using the arctangent function (Fig. 3) and the assumption that magnetization is a linear function of ferrofluid mass fraction. Then the magnetic force at the interface between each gridblock is calculated and added to the pressure gradient and gravitational body force terms. A diagram showing the calculation procedure is presented in Fig. 4.

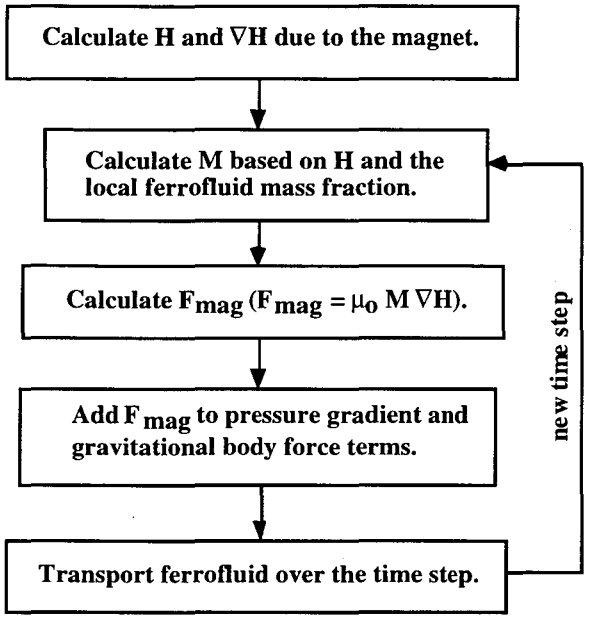

Fig. 4. Schematic of ferrofluid flow calculation implemented in EOS7M.

EXAMPLE SIMULATIONS

We present next two example simulations of (1) the magnetopressure generated, and (2) the two-dimensional flow of ferrofluid in response to an external magnetic field. The first simulation models a laboratory experiment in which five 2 inch x 2 inch x 1 inch NdFeB permanent magnets are moved toward a small horizontal tube that is open to atmospheric pressure on one end and connected to a pressure transducer (DP 15-26, Validyne Engineering Corp.) on the other end (Borglin *et al.*, 1998). The tube is aligned with the magnetic poles. The pressures are measured and recorded resulting in a plot of ferrofluid pressure *versus* distance where the pressure is due to the force on the ferrofluid as given by Eq. 1. Shown in Fig. 5 is the comparison between measured pressures and pressures calculated using EOS7M. The agreement is good. In the experiment it was observed that the ferrofluid develops spikes near the magnet at the interface with the oil in the tube connected to the pressure transducer. These spikes are analogous to the chains of dry magnetite particles that follow magnetic lines of flux in a strong magnetic field. These effects are not modeled in EOS7M and may have contributed to the smaller experimental pressures compared to the simulated pressures at high field strength near the magnet. We note that because the polarization of ferrofluid is caused by the external magnetic field, it does not matter whether the magnet is aligned with the north pole or the south pole closest to the pressure transducer end of the tube; the force on the ferrofluid is always attractive, and the pressure always increases at the end closer to a magnet regardless of its polarization.

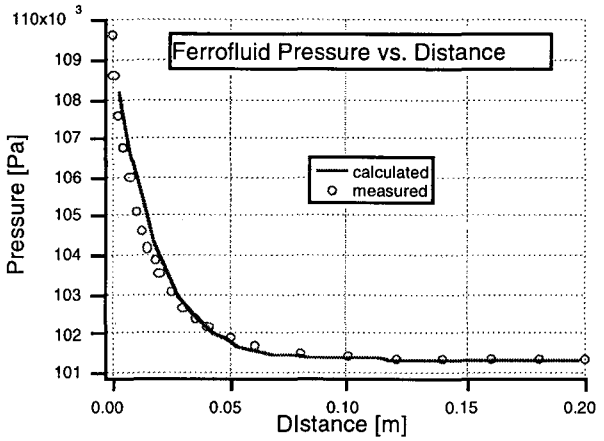

Fig. 5. Measured and calculated ferrofluid pressures versus distance from a permanent magnet.

In the second example simulation, we model the two-dimensional flow of ferrofluid in a narrow gap between two glass plates (a Hele-Shaw cell). This experiment was also carried out in the lab. We present first in Fig. 6 the external magnetic field calculated using EOS7M due to the magnet at the right-hand side of the domain. Properties of the system are presented in Table 1.

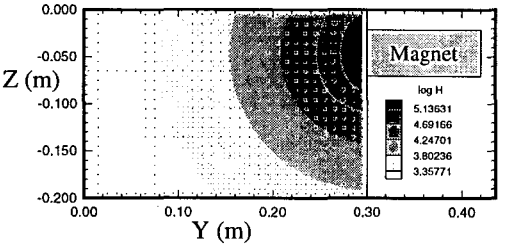

Fig. 6. Magnetic field (H) in units of log A/m around magnet in Hele-Shaw cell experiment.

Shown in Fig. 7 is the two-dimensional ferrofluid mass fraction field along with velocity vectors at three different times. The initial condition (upper left-hand frame of Fig. 7) has a small pool of pure ferrofluid in the lower left-hand corner and a magnet at the upper right-hand corner. The gap is filled with colloidal silica, a dense liquid chosen to minimize the density difference between ferrofluid and the background fluid (see Table 4). As such, the viscosity of the pure water aqueous phase in EOS7M was set specially for this simulation to 4.5 x 10^{-3} Pa s to model the laboratory experiment which used colloidal silica in the gap, while the viscosity of pure

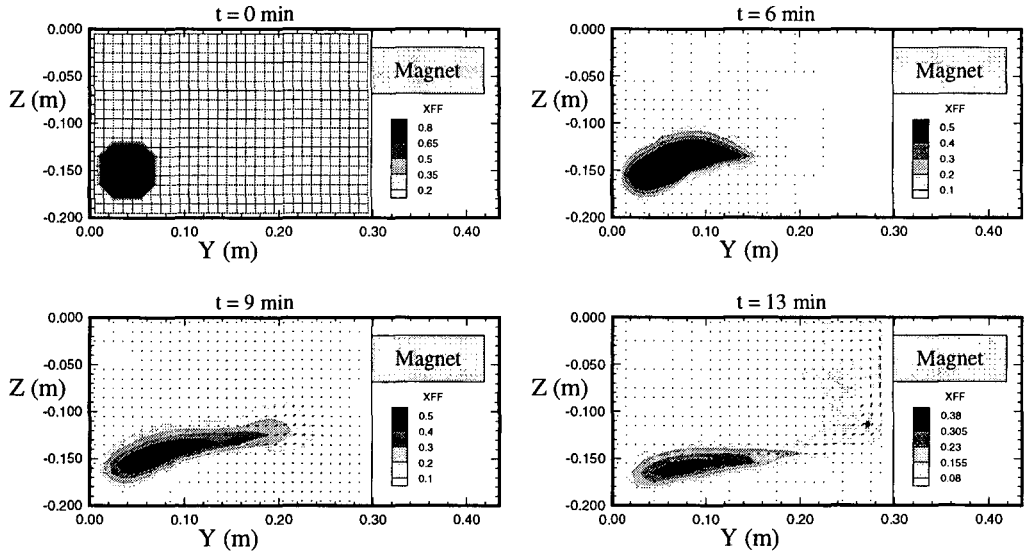

Fig. 7. Ferrofluid mass fraction and flow in Hele-Shaw cell simulation at t = 0 min, t = 6 min, t = 9 min, and t = 13 min.

Table 1. Properties of the Hele-Shaw cell flow simulation.

Domain	
Size (ΔY x ΔZ)	0.30 m x 0.20 m
Discretization for two-dimensional model	30 x 20 gridblocks of size 0.01 m square.
Permeability (k)	1.17×10^{-7} m^2
Porosity (ϕ)	0.999
Gravity (g)	0. m s^{-2}
Ferrofluid M-H curve fit:	
a1	1.00×10^4 A m^{-1}
b1	3×10^{-5} m A^{-1}
	[i.e., M= 1.00×10^4 A m^{-1} x arctan(3×10^{-5} m A^{-1} x H A m^{-1})]
Properties of the magnet (NdFeB)	
Residual flux density (B_r)	1.19 T
Size	5 x (2 in x 2 in x 1 in)
Properties of colloidal silica	
Viscosity of pure colloidal silica at T = 20 °C	4.5×10^{-3} kg m^{-1} s^{-1}
Density of pure colloidal silica at T = 20 °C	1200 kg m^{-3}
Properties of the ferrofluid (EMG 805)	
Viscosity of pure ferrofluid at T = 20 °C	2.35×10^{-3} kg m^{-1} s^{-1}
Density of pure ferrofluid at T = 20°C	1190 kg m^{-3}

ferrofluid is taken as 2.35 x 10^{-3} Pa s. The plates are horizontal and gravity effects are ignored. After 6 minutes (upper right-hand frame), the ferrofluid has been slightly deformed in response to the magnetic field and its gradient. At t = 9 minutes, the fluid has moved strongly toward the magnet. Note that in this closed Hele-Shaw cell, there are recirculations caused by ferrfofluid motion. In other words, as ferrofluid is drawn from left to right in the system, pure water is displaced from right to left. Thus the flow of ferrofluid is affected by the water fluxes that occur in response to the ferrofluid flow. At t = 13 minutes, the ferrofluid has been attracted to the magnet and begun to cluster and circulate around the magnet. These results broadly matched the actual laboratory experiment in terms of flow geometry and time scales (Borglin et al., 1998). Differences arise primarily from numerical dispersion and associated mixing and dilution that occurs in the simulation and not in the laboratory Hele-Shaw cell.

CONCLUSIONS

We have developed EOS7M, a ferrofluid flow and transport module for TOUGH2. EOS7M calculates the magnetic forces on ferrofluid caused by an external magnetic field and allows simulation of flow and advective transport of ferrofluid-water mixtures through porous media. Such flow problems are strongly coupled and well suited to the TOUGH2 framework. Preliminary applications of EOS7M to some simple pressure and flow problems for which experiments were carried out in the lab show good qualitative agreement with the laboratory results.

ACKNOWLEDGMENT

We thank Yu-Shu Wu and Karsten Pruess for reviews. This work was supported by the Laboratory Directed Research and Development Program of Lawrence Berkeley National Laboratory under the U.S. Department of Energy, contract No. DE–AC03–76SF00098.

REFERENCES

Berkowsky, B.M., V.F Medvedev, M.S. Krakov, *Magnetic Fluids Engineering Applications*, Oxford Univ. Press, New York, 243 pp., 1993.

Borglin, S. E., and G.J. Moridis, Experimental studies of magnetically driven flow of ferrofluids through porous media, *Lawrence Berkeley Laboratory Report, LBL-40126*, March 1998).

Herbert, A.W., Jackson, C.P., and Lever, D.A., Coupled groundwater flow and solute transport with fluid density strongly dependent on concentration, *Water Res. Res., 24* (10), 1781-1795, 1988.

McCaig, Malcolm, *Permanent Magnets in Theory and Practice*, John Wiley & Sons, New York, 374 pp., 1977. pg. 187-188.

McCaig, Malcolm, and Alan G. Clegg, *Permanent Magnets in Theory and Practice Second Edition*, Halsted Press, John Wiley & Sons, New York, 415 pp., 1987. pg. 199-200.

Moridis, G.J., S.E. Borglin, C.M. Oldenburg, and A. Becker, Theoretical and experimental investigations of ferrofluids for guiding and detecting liquids in the subsurface, *Lawrence Berkeley Laboratory Report, LBL-41069*, March 1998).

Oldenburg, C.M., G.J. Moridis, and K. Pruess, EOS7M: Ferrofluid Flow for TOUGH2, in prep., 1998a.

Oldenburg, C.M., S.E. Borglin, and G.J. Moridis, Numerical simulation of ferrofluid flow for subsurface environmental engineering applications, in prep., 1998b.

Oldenburg, C.M. and K. Pruess, Dispersive transport dynamics in a strongly coupled groundwater-brine flow system, *Water Resources Research, 31*(2), 289–302, 1995.

Pruess, K., TOUGH User's Guide, *Nuclear Regulatory Commission, Report NUREG/CR-4645*, June 1987 (also *Lawrence Berkeley Laboratory Report, LBL-20700*, June 1987).

Pruess, K., TOUGH2- A general-purpose numerical simulator for multiphase fluid and heat flow, *Lawrence Berkeley Laboratory Report LBL-29400*, May 1991a.

Pruess, K., EOS7, An equation-of-state module for the TOUGH2 simulator for two-phase flow of saline water and air, *Lawrence Berkeley Laboratory Report LBL-31114*, Berkeley, California, August 1991b.

Raj, K., and R. Moskowitz, Commercial applications of ferrofluids, J. *of Magnetism and Magnetic Materials, 85*, 233–245, 1990.

Reeves, M., Ward, D.S., Johns, N.D., and Cranwell, R.M., Theory and implementation of SWIFT II, the Sandia Waste-Isolation Flow and Transport Model for Fractured Media, *Report No. SAND83-1159*, Sandia National Laboratories, Albuquerque, N.M., 1986.

Rosenzweig, R.E., *Ferrohydrodynamics*, Cambridge University Press, 344 pp., 1985.

Gas-Phase Diffusion in Porous Media: Comparison of Models

Stephen W. Webb
Sandia National Laboratories
Albuquerque, New Mexico 87185

ABSTRACT

Two models are commonly used to analyze gas-phase diffusion in porous media in the presence of advection, the Advective-Dispersive Model (ADM) and the Dusty-gas Model (DGM). The ADM, which is used in TOUGH2, is based on a simple linear addition of advection calculated by Darcy's law and ordinary diffusion using Fick's law with a porosity-tortuosity-gas saturation multiplier to account for the porous medium. Another approach for gas-phase transport in porous media is the Dusty-Gas Model. This model applies the kinetic theory of gases to the gaseous components and the porous media (or "dust") to combine transport due to diffusion and advection that includes porous medium effects. The two approaches are compared in this paper.

INTRODUCTION

Gas-phase diffusion in porous media may be significant in the flow of multiphase fluids and the transport of contaminants in the subsurface. In many applications, such as removal of nonaqueous phase liquid (NAPL) contaminants from low-permeability layers in the subsurface, gas-phase diffusion may be the limiting transport mechanism. Gas-phase diffusion may also be important in the analysis of contaminant migration in potential nuclear waste repositories, evaporation and drying processes, and porous catalysts.

A number of different models for combined advection-diffusion of gases in porous media have been employed that are strongly correlated with the corresponding discipline. For example, in earth sciences and in many engineering fields, the most widely used model is the Advective-Dispersive Model, or ADM. In chemical engineering, the most common approach for gas-phase transport in porous media is the Dusty-Gas Model. These models are dramatically different in their treatment of gas-phase diffusion. The main objectives of the present paper are to compare the ADM and DGM models with Graham's laws, which are fundamental relationships for diffusion, and to evaluate both models against a number of comprehensive experimental data sets. In addition, the two approaches are applied to an air-water heat pipe that is encountered in earth science applications.

DIFFUSION MODELS

Advective-Dispersive Model

The Advective-Dispersive Model (ADM) is commonly used in earth sciences as exemplified by TOUGH2 (Pruess, 1991). The ADM is based on a simple *ad hoc* linear addition of advection calculated by Darcy's law and ordinary diffusion using Fick's law. Slip effects, or Knudsen diffusion, are included through a Klinkenberg parameter to define an effective permeability for the advective flux. Porous medium effects for ordinary diffusion are included through a porosity-tortuosity-gas saturation factor applied to the diffusive flux in free space. This simple additive approach, while intuitively appealing, ignores possible coupling between advection and diffusion.

The ADM mass flux for gas-phase component i, F_i, in a binary mixture is

$$F_i = -k\frac{k_{r,g}}{\mu_g}\rho_g\omega_i\left(\nabla P_g - \rho_g g_c\right) - D_{12}\rho_g\nabla\omega_i \quad (1)$$

where $D_{12}=D_{21}$ is assumed. Slip, or Knudsen diffusion, is simply incorporated into the model through the Klinkenberg factor, b, or

$$k = k_o\left(1 + b/P_g\right) \quad (2)$$

The effective diffusion coefficient is given by

$$D_{12} = \tau\phi S_g D_{12}^0 \frac{P_0}{P}\left(\frac{T+273.15}{273.15}\right)^{\theta} \quad (3)$$

where the exponent θ is typically 1.8 (Pruess, 1987).

In the case of pure ordinary diffusion (no advection), the ADM reduces to

$$F_{i=1} = -D_{12}\rho_g\nabla\omega_{i=1} \quad (4a)$$

$$F_{i=2} = -D_{12}\rho_g\nabla\omega_{i=2} \quad (4b)$$

For a binary mixture, $\nabla\omega_{i=1} = -\nabla\omega_{i=2}$, so

$$F_{i=1} = -F_{i=2} \quad (5)$$

and the mass fluxes of the two components are equal and opposite.

Dusty-Gas Model

The Dusty-Gas Model (DGM) was developed to describe gas transport through porous media including the coupling between the various transport mechanisms. The term dusty-gas is used because the porous medium consists of large "dust" molecules fixed in space that are treated as a component of the gas mixture. The kinetic theory of gases is applied to this dusty-gas mixture. The DGM, including numerous data-model comparisons, is discussed in detail by Mason and Malinauskas (1983) and by Cunningham and Williams (1980). The present discussion is limited to a binary gas mixture. In addition, temperature gradients and external forces such as gravity are ignored. The more complex nonisothermal and/or multicomponent system is treated in the DGM references given above.

Similar to the ADM, the DGM considers advection, Knudsen diffusion, and ordinary diffusion. One of the key aspects of the DGM is the combination of diffusion (ordinary and Knudsen) and advection. Ordinary and Knudsen diffusion are combined through addition of momentum transfer based on kinetic-theory arguments, and diffusive fluxes (ordinary plus Knudsen) are added to advective fluxes based on Chapman-Enskog kinetic theory.

There are many alternative forms of the DGM that can be derived by combining various forms of the equations. Thorstenson and Pollock (1989) present a number of useful forms for binary mixtures that are of special interest here. In particular, the total mole flux of component 1 in an isothermal binary system can be written as

$$J_1 = -\frac{\left[D_{1K}D_{12}\frac{P_g}{RT}\nabla x_1 + D_{1K}(D_{12}+D_{2K})x_1\frac{\nabla P_g}{RT}\right]}{(D_{12}+x_1D_{2K}+x_2D_{1K})} - x_1\frac{k_0P_g}{\mu_g}\frac{\nabla P_g}{RT} \qquad (6)$$

and the total mole flux is given by

$$J = J_1 + J_2 = -\frac{\left[D_{12}(D_{2K}-D_{1K})\frac{P_g}{RT}\nabla x_1 - (D_{12}(x_1D_{1K}+x_2D_{2K})+D_{1K}D_{2K})\frac{\nabla P_g}{RT}\right]}{(D_{12}+x_1D_{2K}+x_2D_{1K})} - \frac{k_0P_g}{\mu_g}\frac{\nabla P_g}{RT} \qquad (7)$$

In equation 6, the flux of component 1 consists of a diffusive flux (first term) and an advective flux (second term). The diffusive flux has ordinary diffusion (mole fraction gradient) and Knudsen diffusion (pressure gradient) components, similar to the ADM equation.

ADM - DGM COMPARISON

The predictions for both models were made by the TOUGH2 code (Pruess, 1991). The code was modified to use the DGM gas transport expressions.

Comparison to Fundamental Relationships and Experimental Data

Two important relationships were discovered by Thomas Graham in the 1800's for gas diffusion in a binary mixture (Mason and Malinauskas, 1983). For Knudsen diffusion, or free-molecule flow, Graham's law of effusion applies as experimentally discovered by Graham (1846). Similarly, for ordinary diffusion without advection, the ratio of the diffusive fluxes is given by Graham's law of diffusion as experimentally discovered by Graham (1833). The ratio of diffusive mole fluxes for **both** regimes is the same, or

$$-J_{1K}/J_{2K} = -J_{1D}/J_{2D} = (m_2/m_1)^{1/2} \qquad (8)$$

while the diffusive mass flux ratio is

$$-F_{1K}/F_{2K} = -F_{1D}/F_{2D} = (m_1/m_2)^{1/2} \qquad (9)$$

The above relationships are very important. Graham's laws were misunderstood and were independently rediscovered in the 1950's and 1960's (Mason and Malinauskas, 1983). Graham's laws are fundamental relationships for gas diffusion and were used in the development of the DGM. The data of Evans, Watson, and Truitt (1962, 1963) strongly support Graham's laws and show that the assumption of equimolar counterdiffusion is not correct.

Evans, Watson, and Truitt Data

Evans, Watson, and Truitt (1962, 1963) performed a number of experiments for flow and diffusion of helium and argon across low-permeability graphite. Pure helium was present on one side, while pure argon was present on the other. These data were obtained to support the DGM as summarized by Mason and Malinauskas (1983).

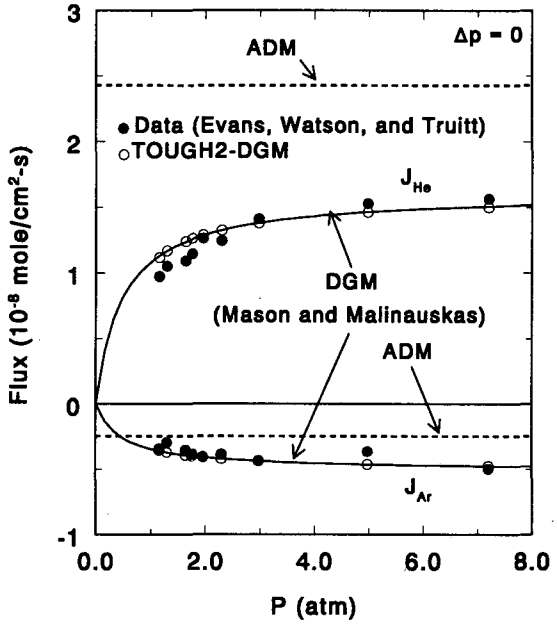

Figure 1
Mole Flux Data-Model Comparison for Zero Pressure Difference Conditions

Zero Pressure Difference

The first data-model comparison considers zero pressure difference such that there is only diffusion. From Graham's laws, if only diffusion is occurring, the ratio of the mole fluxes (not the magnitude) for Knudsen diffusion and for ordinary diffusion is the same. Based on the molecular weights of helium (m=4.00) and argon (m=39.944), Graham's Laws give a mole flux ratio of helium to argon of 3.2.

Figure 1 compares the data with the predictions from the ADM and the DGM as a function of the average pressure. Helium mole flux is positive, while argon mole flux is negative. The mole flux data for both gases increase with increasing pressure. The DGM predicts the variation of the data quite well. The ratio of the mole fluxes is consistent with the theoretical ratio given above. In contrast, the ADM predicts a constant mole flux value independent of pressure that is inconsistent with the data. As discussed earlier, for pure diffusion, the mass fluxes of the two components are equal in the current implementation of the ADM. The ADM mole flux ratio (helium/argon) is simply the inverse of the ratio of the molecular weights, or about 10; this ratio is much higher than the data. The ADM overpredicts the helium mole flux and underpredicts the argon mole flux. The ADM, which in this case is simply Fick's law, does not predict the correct gas diffusion values or trends for this simple diffusion-only case.

The constant flux prediction for the ADM can be explained by analyzing the formulation. In the ADM, only ordinary diffusion is important for zero pressure difference conditions; Knudsen diffusion is not invoked through the Klinkenberg factor because there is no pressure difference and no advective flow. For the ADM, the mass flux due to ordinary diffusion was given earlier where the diffusion coefficient, D_{12}, is inversely proportional to pressure. The gas density increases with pressure while the diffusion coefficient decreases with pressure. Therefore, for pure diffusion of perfect gases, the ADM will predict a constant mass and mole flux as a function of pressure.

Zero Net Mole Flux

The second case simulates what would occur in a closed volume, where the total mole fluxes of the helium and argon components are equal, $J_{He} = - J_{Ar}$. In this situation, diffusion and advection balance each other resulting in a zero net mole flux. The predicted flux corresponding to this condition, and the pressure difference across the low-permeability graphite associated with it, are compared to the experimental data.

Figure 2 shows the predicted mole flux for the ADM and the DGM along with the data as a function of the average pressure. The DGM predictions compare reasonably well with the experimental data including the variation of flux with pressure. In contrast, the ADM predicts a constant mole flux as a function of pressure similar to the zero pressure difference case. The ADM predictions are about 20% to 50% too high depending on the pressure; the higher error is for the lower pressures.

Figure 3 presents the data for the pressure difference across the low-permeability graphite sample and the model predictions. The pressure difference is the value required for equal and opposite mole fluxes across the graphite. The data are well predicted by the DGM. The DGM predicts a maximum pressure difference at an average pressure of about 1 atmosphere; the data are not sufficient to resolve the details of this behavior. The shape of the DGM pressure difference curve is due to the dominance of Knudsen diffusion pressure drop at low pressures and the dominance of advection pressure drop at higher pressures. The ADM consistently overpredicts the pressure difference by a factor of 2 or more and does not have the predicted shape of the DGM.

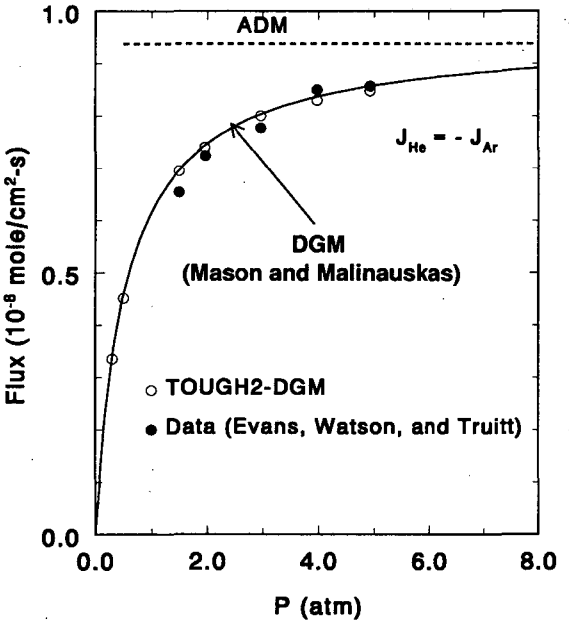

Figure 2
Mole Flux Data-Model Comparison for Zero Net Mole Flux Conditions

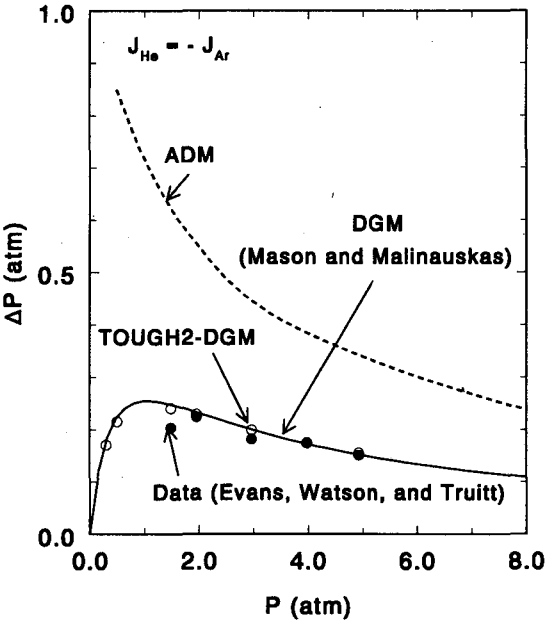

Figure 3
Pressure Difference Data-Model Comparison for Zero Net Mole Flux Conditions

Combined Advection and Diffusion

The next case is the most general situation of combined advection and diffusion. In this series of tests, the pressure difference across the test section was varied while maintaining the same average pressure. The individual fluxes of helium and argon across the low-permeability graphite test section were recorded at steady-state conditions. The predicted mole fluxes as a function of pressure difference are compared in Figures 4 and 5. Figure 4 presents the results for the ADM. The ADM predictions do not compare favorably with the data. Errors of a factor of 2 and greater are noted for the individual fluxes with corresponding differences in the net flux. While the general behavior is observed, the detailed variation is not reproduced by the ADM approach. In Figure 5, DGM predictions of the mole fluxes are shown. These results compare quite well with the data for the individual mole fluxes of helium and argon as well as with the net flux, including the variation with pressure difference.

Linear Air-Water Heat Pipe

On a practical basis, many multiphase advection-diffusion problems involve air and water vapor. For this combination of gases (assuming air is a single component), the molecular weight ratio is only about 1.6 compared to approximately 10 for the He-Ar system studied by Evans, Watson, and Truitt. In addition, the mole fraction differences for an air-water vapor system are considerably more limited for typical conditions. The problem chosen for comparison of the ADM and DGM for an air-water vapor system is a two-phase linear air-water porous media heat pipe. This problem was also selected because it was used for TOUGH code verification.

Figure 6 shows the thermodynamic results for the ADM and DGM. Note that the liquid saturation is scaled relative to the residual liquid saturation. The predictions from both models are very similar except for the liquid saturation near z=0, where the liquid saturation is higher for the DGM. Otherwise, the temperature, gas pressure, liquid saturation, and air mole fraction in the gas phase are practically the same. The linear heat pipe is driven by heat, and water evaporation/condensation is the dominant flow process. The total (advection plus diffusion) water vapor flow rates for the ADM and DGM are shown in Figure 7. Water vapor flows from the hot (right) end, where evaporation occurs, to the cold (left) end, where it condenses. The values for both models are practically identical due to the prescribed heat flux.

DISCUSSION

Two commonly used models for gas-phase diffusion and advection in porous media, the Advective-Dispersive Model (ADM) and the Dusty-Gas Model (DGM), have been compared. Evaluation of the models against Graham's laws and He-Ar data dramatizes the significant differences between the models. The DGM should, and does, agree very well with Graham's laws and the He-Ar

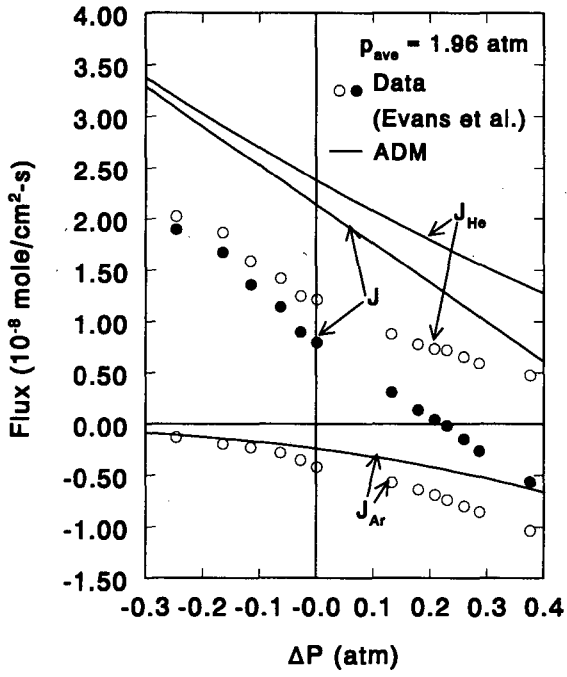

Figure 4
ADM Mole Flux Data-Model Comparison For Combined Advection and Diffusion

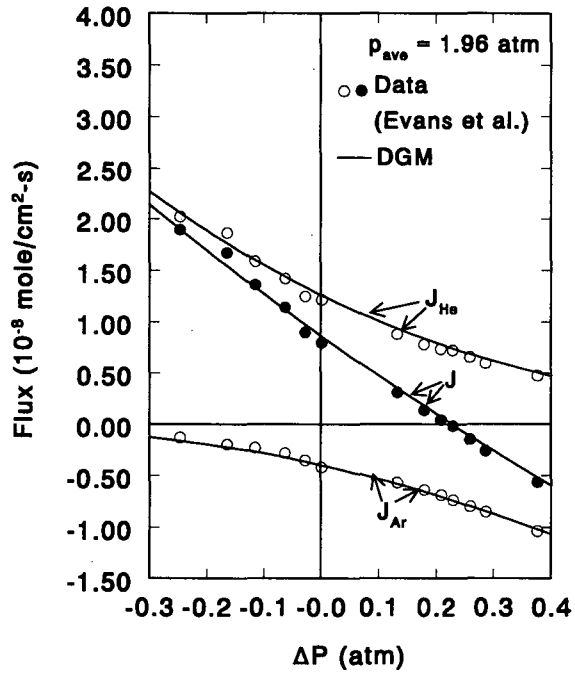

Figure 5
DGM Mole Flux Data-Model Comparison For Combined Advection and Diffusion

data because both were used in the model development and validation of the DGM. In contrast, the ADM does not agree well with either Graham's laws or the experimental data. The magnitude and the trend of the ADM predictions, such as the mole flux variation with pressure for pure diffusion, are significantly different than the data. In this case, the DGM is significantly better than the ADM, which may give incorrect trends and/or misleading results.

Model predictions for an air-water vapor system have also been compared. This system has similar molecular weights for the gas components, and the mole fraction difference is relatively small. The predicted difference between the two models is small in this case. Webb (1996, 1998) provides more details on the comparison on these two models, including parameter values and additional cases.

CONCLUSIONS

1. The ADM and DGM both consider advection, Knudsen diffusion, and ordinary diffusion. While the advective flow component can be shown to be the same for both models, significant differences may exist for the diffusion fluxes.

2. The DGM observes the fundamental relationships for diffusive fluxes given by Graham's laws. In contrast, the ADM violates these fundamental relationships.

3. DGM predictions are in excellent agreement with the comprehensive experimental He-Ar data of Evans, Watson, and Truitt (1962, 1963). ADM predictions are in disagreement with the magnitude and some of the trends of the data.

4. The common conception of equimolar counterdiffusion is not supported by Graham's laws or by the He-Ar data of Evans, Watson, and Truitt (1962, 1963).

5. If diffusion is an important transport mechanism, the DGM is significantly better than the ADM, although the ADM may give reasonable qualitative results. For quantitative analysis and the analysis of diffusion trends, the DGM should be used because the ADM may give incorrect trends and/or misleading results.

NOMENCLATURE

b	Klinkenberg factor
D_{iK}	Knudsen diffusion coefficient for gas i
D_{12}	effective binary diffusion coefficient
D^0_{12}	free space binary diffusion coefficient at 1 bar and 0°C
F	mass flux
g_c	gravitational constant
J	mole flux
J_{iD}	ordinary diffusion mole flux
J_{iK}	Knudsen diffusion mole flux
k	permeability

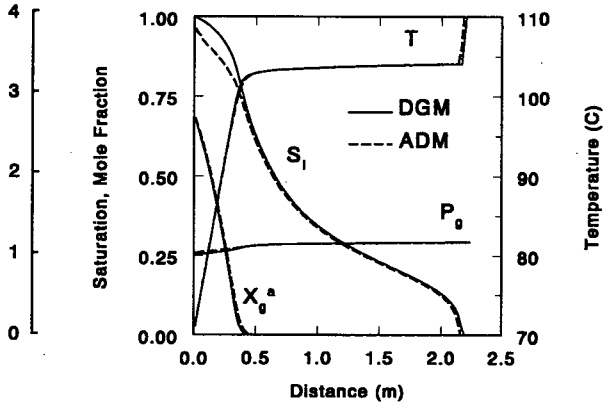

Figure 6
Linear Heat Pipe Thermodynamic Results

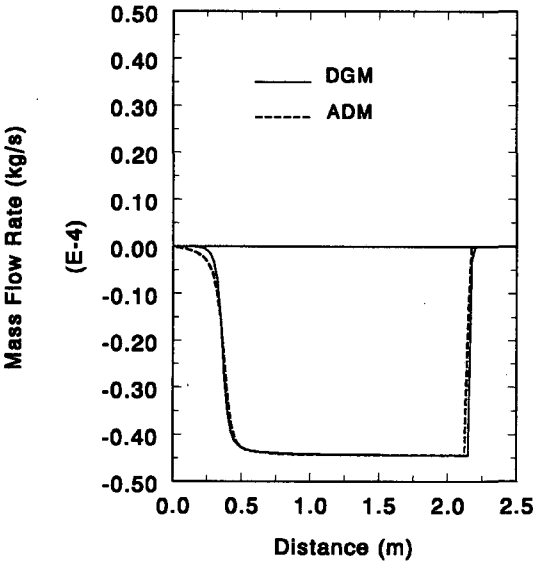

Figure 7
Linear Heat Pipe Vapor Flow Rates

P	pressure
P_0	pressure of 1 bar
R	universal gas constant
T	temperature
x	mole fraction

Greek symbols

μ	viscosity
ρ	density
τ	tortuosity
ϕ	porosity
ω	mass fraction
θ	exponent on diffusion coefficient

Subscripts

g	gas
r	relative
0	intrinsic
1,2	species or component number

ACKNOWLEDGMENTS

This work was supported by the United States Department of Energy under Contract DE-AC04-94AL85000 as part of a Sandia Laboratory Directed Research and Development Project on Enhanced Vapor-Phase Diffusion in Porous Media. Sandia is a multiprogram laboratory operated by Sandia Corporation, a Lockheed Martin Company, for the United States Department of Energy.

This work was stimulated by the paper by John M. Farr, "Gaseous Transport of Volatile Organics in Porous Media: Comparison of Mathematical Model," presented at the TOUGH Workshop, September 13-14, 1990.

REFERENCES

Cunningham, R.E., and Williams, R.J.J., 1980, Diffusion in Gases and Porous Media, Plenum Press, New York.

Evans, III, R.B., Watson, G.M., and Truitt, J., 1962, "Interdiffusion of gases in a low permeability graphite at uniform pressure," *J. Appl. Phys.*, 33:2682-2688.

Evans, III, R.B., Watson, G.M., and Truitt, J., 1963, "Interdiffusion of gases in a low permeability graphite. II. Influence of pressure gradients," *J. Appl. Phys.*, 34:2020-2026.

Graham, T., 1833, "On the law of the diffusion of gases," *Phil. Mag.*, 2:175, 269, 351, reprinted in "Chemical and Physical Researches," 44-70, Edinburgh Univ. Press, Edinburgh, 1876.

Graham, T., 1846, "On the motion of gases," *Phil. Trans. Roy. Soc.*, 136:573, reprinted in "Chemical and Physical Researches," 44-70, Edinburgh Univ. Press, Edinburgh, 1876.

Mason, E.A., and Malinauskas, A.P., 1983, Gas Transport in Porous Media: The Dusty-Gas Model, Chem Eng. Monograph 17, Elsevier, New York.

Pruess, K., 1987, *TOUGH User's Guide*, NUREG/CR-4645, SAND86-7104, LBL-20700, US Nuclear Regulatory Commission.

Pruess, K., 1991, *TOUGH2 - A General-Purpose Numerical Simulator for Multiphase Fluid and Heat Flow*, LBL-29400, Lawrence Berkeley Laboratory.

Thorstenson, D.C., and Pollock, D.W., 1989, "Gas Transport in Unsaturated Zones: Multicomponent Systems and the Adequacy of Fick's Laws," *Water Resour. Res.*, 25:477-507.

Webb, S.W., 1996, *Gas-Phase Diffusion in Porous Media - Evaluation of an Advective-Dispersive Formulation and the Dusty-Gas Model Including Comparison to Data for Binary Mixtures*, SAND96-1197, Sandia National Laboratories.

Webb, S.W., 1998, "Gas-Phase Diffusion in Porous Media – Evaluation of an Advective-Dispersive Formulation and the Dusty-Gas Model for Binary Mixtures," *J. Porous Media*, 1:187-199.

A computational study of some possible factors associated with Melt Eruption Events

Will Schreiber[1] and John Kuo[2]

ABSTRACT

The current paper describes a computer model designed to analyze the moisture transport in the unmelted, porous soil neighboring a convecting melt. The time-dependent fluid and heat flow in the soil melt is simulated implicitly using the SIMPLE method generalized to predict viscous fluid motion and heat transfer on boundary-fitted, non-orthogonal coordinates which adapt with time. TOUGH2, a general-purpose computer code for multiphase fluid and heat flow developed by K. Pruess at Lawrence Berkeley Laboratory, has been modified for use on time-adaptive, boundary-fitted coordinates to predict heat transfer, moisture and air transport, and pressure distribution in the porous, unmelted soil. The soil melt model is coupled with the modified TOUGH2 model via an interface (moving boundary) whose shape is determined implicitly with the progression of time.

The computer model's utility is demonstrated in the present study with a special two-dimensional study. A soil initially at 20°C and partially saturated with either a 0.2 or 0.5 relative liquid saturation is contained in a box two meters wide by ten meters high with impermeable bottom and sides. The upper surface of the soil is exposed to a 20°C atmosphere to which vapor and air can escape. Computation begins when the soil, which melts at 1700°C is heated from one side (maintained at constant temperatures ranging from 1700°C to 4000°C). Heat from the hot wall causes the melt to circulate in such a way that the melt interface grows more rapidly at the top of the box than at the bottom. As the upper portion of the melt approaches the impermeable wall it creates a bottleneck for moisture release from the soil's lower regions. The pressure history of the trapped moisture is examined as a means for predicting the potential for moisture penetration into the melt. The melt's interface movement and moisture transport in the unmelted, porous soil are also examined.

INTRODUCTION

The *In Situ* Vitrification (ISV) process offers an economical and relatively uncomplicated means of remediating buried contaminants such as nuclear and toxic chemical wastes. The ISV process consists of melting the contaminated soil with electrodes or plasma torches while capturing off-gases in a hood that covers the treatment site. After the designated volume of contaminated soil, up to ten meters in diameter, has been melted, it is subsequently allowed to solidify into an impervious glass. The glassified contaminated soil is, for all practical purposes, entirely impervious to ground water and can be safely left on site.

While the ISV process has been used successfully by both government and commercial interests to remediate numerous contaminated sites, there have been problems in several isolated instances in the form of Melt Eruption Events (MEE). During an MEE, the melt erupts to spatter equipment in the off-gas hood and to release pressurized gas products into the atmosphere. One likely scenario postulated for these problems is that soil moisture becomes trapped between the encroaching melt front and an impervious surface. Once the soil vapor has been effectively sealed off from any escape route, it pressurizes rapidly to the point where it is forced into the melt. Having broached the melt, the gas is energized and leads to an MEE. It is generally agreed that better site characterization in concert with an improved understanding of the interaction of melting soil with moisture transport in the native soil are needed to improve the safety of the ISV process. Conceptual models for this phenomenon have been formulated, and one of these models has been simulated previously using thermal hydraulic numerical codes (Roberts et al. 1992, Schreiber 1996a,b).

The current paper describes a computational method for examining the effect of melt movement on moisture transport and pressure build-up in the surrounding soil.

At its current stage of development, the model makes two major restricting assumptions.

1. Melt viscosity is considered constant.
2. Density difference between the porous soil and the melted soil is ignored; consequently, the fluid melt occupies the same volume as the porous soil it has displaced.

Both of these restrictions will admittedly affect the model's predictions but can be addressed in a more elaborate model.

---

[1] Associate Professor, Mechanical Engineering Department, The University of Alabama, PO Box 870276, Tuscaloosa, AL 35487

[2] Research Engineer, ADT Engineering, Inc., Flint Michigan

MATHEMATICAL MODELS

Three models are combined for the purposes of prediction described in the abstract and introduction sections. All three models are generalized for use on a non-orthogonal, boundary-fitted grid that adapts to a growing melt. A CFD model of the melt (Kuo and Schreiber, 1994) is coupled, via a moving interface model, to a general-purpose computer code, TOUGH2 developed by Pruess (1985,1986), for multiphase fluid and heat flow in a porous medium. The CFD model has been developed to predict fluid flow and heat transfer of a viscous fluid, the melt, on a non-orthogonal, boundary-fitted grid that adapts to a growing melt. The TOUGH2 code has been modified to enable its use for modeling moisture, air, and heat transport in the unmelted soil on a similar time-dependent grid system that is congruent with the melt region. (See Figure 1.) The interface that separates the melted and unmelted regions is calculated in terms of a heat balance including latent heat of phase change. The calculation procedure for the interface is implicit in time so as to allow a reasonably large time step.

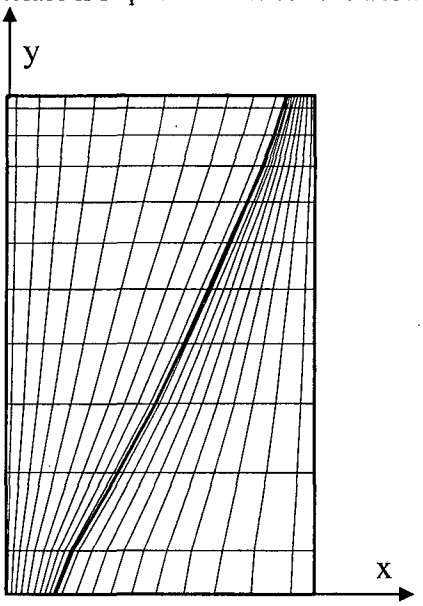

Figure 1. 20x10 grid used for computation. Grid to the left of the diagonally oriented, curved interface used by CFD melt code; grid to the right of the interface used by TOUGH2. Scale of picture is expanded by a factor of three in the horizontal (x) direction.

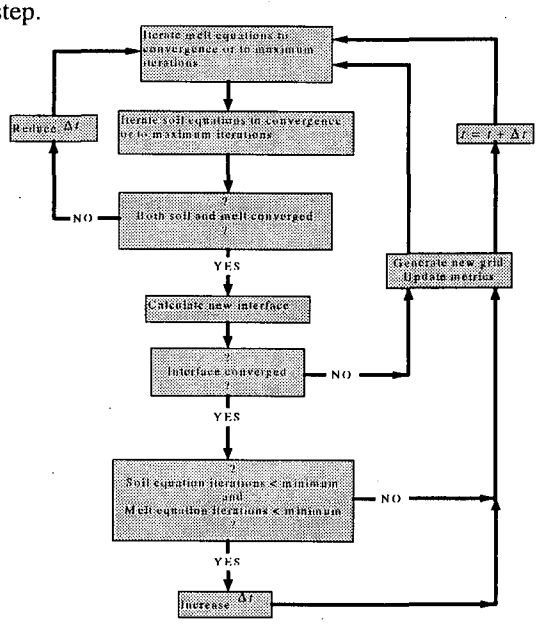

Figure 2. Flow chart for algorithm used to exact interface movement implicitly in time.

In TOUGH2, an integral equation describes the balance of M, the accumulation of internal energy or species, relative to a control volume, V_n.

$$\frac{d}{dt}\int_{V_n} M^{(\kappa)}\,dv = \oint (F^{(\kappa)}\cdot\hat{n}) + \int_{V_n} q^{(\kappa)}\,dv \qquad (1)$$

The term F is the flux of mass or heat, q is the source of mass or heat (per volume), t is time, and $\hat{n}$ is the direction normal and inward to a control volume surface. The superscript (κ) is the species index where: κ = 1: water, κ = 2: air, and κ = 3: heat.

Further formulas are described in reference 2 that define the storage, flux, and generation terms found in equation (1) for species transfer and for heat transfer as well as the constitutive equations needed to relate thermodynamic properties. The thermodynamic state of each control volume is described in the code in terms of the primary properties. Secondary properties are determined with constitutive equations as a function of the primary properties. After it is differenced implicitly in time, equation (1) may be expressed in terms of a residual

$$R_n^{(\kappa)k+1} = M_n^{(\kappa)k+1} - M_n^{(\kappa)k} - \frac{\Delta t}{V_n}\left(\sum_m A_{nm} F_{nm}^{(\kappa)k+1} + V_n q_n^{(\kappa)k+1}\right) = 0 \qquad (2)$$

where R is the numerical residual, A is the control volume interface area. The index n signifies the control volume, m indicated the neighboring control volume index, and k is the time step index.
The residual is minimized using the Newton-Raphson method to find the values at the k+1 time implicitly.

To predict transport in a static domain, TOUGH2 does not require that the control volumes be ordered in terms of a grid. Only the interface areas between the control volumes and the size of the control volumes need be provided as input data. In order to incorporate domain boundaries, which adapt with time; however, a grid system must be imposed since the time-dependent volume and interface areas of each control volume depend on the location of the moving interface boundary. In the current application of TOUGH2, the control volumes are mapped to an ordered two-dimensional coordinate system (referred to as the physical space, x-y) as pictured in figure 1. This non-orthogonal grid is further mapped to a rectangular grid (known as the computational space, $\xi - \eta$) through the use of geometric transformations (metrics). Thompson (1984) describes the grid generation and derives the geometric transformations needed to enact this mapping.

The TOUGH2 code has been modified to include the metrics needed to transform TOUGH2's differenced equations from physical to computational space. The input data for the code includes volumes and control volume interface areas of unit size plus the values of the metric coefficients needed to transform equations to conform to the boundary-fitted geometry. With each ensuing time step, the grid and metrics are recalculated to conform to the time-dependent interface boundary.

The equations that describe transport in the melt are also transformed to a computational space coordinate system in (ξ,η) where $\xi = \xi(x,y,t)$ and $\eta = \eta(x,y,t)$.

Transport of momentum (in which ϕ is the x or y component of velocity, U or V)

or **heat** (in which ϕ is the temperature, T)

$$\frac{\partial(\phi J)}{\partial t} + \frac{\partial}{\partial \xi}\left(U_r\phi - \alpha\Gamma\phi_\xi\right) + \frac{\partial}{\partial \eta}\left(V_r\phi - \gamma\Gamma\phi_\xi\right) = \frac{\partial}{\partial \xi}\left(-\beta\Gamma\phi_\eta\right) + \frac{\partial}{\partial \eta}\left(-\beta\Gamma\phi_\xi\right) + S_\phi \tag{3}$$

where: $$S_\phi = \frac{J}{\rho}\left[-\left(\frac{\partial p}{\partial n}\right)_\phi + B_\phi\right] \text{ for the momentum equations.} \tag{4}$$

The term B_ϕ is the body force, p is the dynamic pressure, Γ is the diffusivity, and ρ is the density. The term r indicates relative to grid velocity.

The geometric transformations found in the transport equation are:

$$J = x_\xi y_\eta - x_\eta y_\xi \tag{5}$$

$$\alpha = \left(x_\eta^2 + y_\eta^2\right)/J \tag{6}$$

$$\beta = \left(x_\xi x_\eta + y_\xi y_\eta\right)/J \tag{7}$$

$$\gamma = \left(x_\xi^2 + y_\xi^2\right)/J \tag{8}$$

Continuity

$$\frac{\partial U}{\partial \xi} + \frac{\partial V}{\partial \eta} = 0 \tag{9}$$

These equations are solved using a SIMPLE procedure modified to account for the non-orthogonal, time-dependent coordinate system. (Karki, 1986, and Kuo, 1994)

An equation is needed to determine the velocity $\tilde{U}_i$ of the isothermal interface. Latent heat, L_H, is required for melting the soil and is set equal to the difference of heat transferred from the melt to the interface and the heat transferred from the interface to the soil. This equation includes the assumption that the density of the porous soil is the same as that of the melt.

$$\frac{k_s\left(\alpha T_\xi\right)_s}{h_2} - \frac{k_{mt}\left(\alpha T_\xi\right)_{mt}}{h_2} = -J\rho L_H \tilde{U}_i \tag{10}$$

In this equation, the indices mt and s refer to the melt and the soil respectively, k is the conductivity, and L_H is the latent heat of soil matrix. The term, h_2, is a metric given by

$$h_2 = \sqrt{x_\eta^2 + y_\eta^2} \tag{11}$$

NUMERICAL PROCEDURE

The three computational models are all solved implicitly with time. A flow chart of the grand solution scheme is given in figure 2.

The TOUGH2 code was modified by including metrics for area and volume transformation as coefficients of the unit area and volume associated with each control volume. The effect of grid movement relative to the mass transport was included in the

computation. To account for the mass flow associated with grid movement, the volume metric for each control volume was modified in the residual equation (2) after each update of the grid and metrics. Including an advective heat flux proportional to the grid velocity modified heat conduction to include the effects of grid movement. While the characteristic time scales for the melt flow and porous flow codes were on the same order of magnitude, the time step size as depicted in figure 2 was mostly dictated by the melt flow equations.

RESULTS AND DISCUSSION

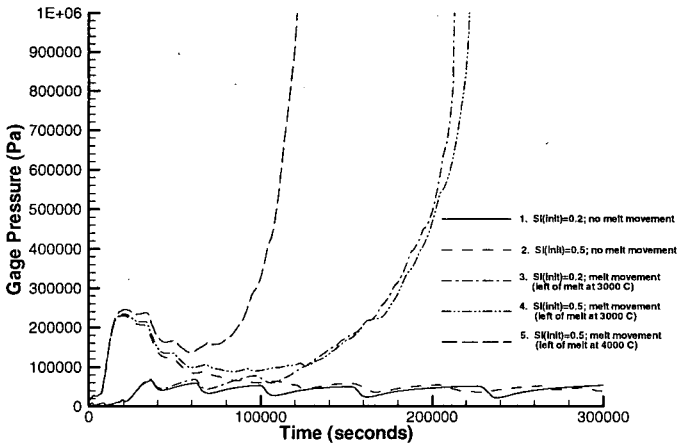

Figure 3. Pressure histories of porous soil at a point near bottom of melt.

The computer model's utility is demonstrated in the present study with a special two-dimensional case as described in the abstract. The soil simulated for this study has a soil grain density of $2900\,kg/m^3$, a porosity of 0.4, a permeability of 10^{-11} m^2, and a grain specific heat of $1.2\,kJ/kg\cdot K$. The soil's heat conductivity at saturation is $1.81\,W/m\cdot K$. The relative permeability function is described by the equations,

For the liquid water, $$k_{rl} = \sqrt{S^*}\left\{1-\left[1-(S^*)^{1/\lambda}\right]^{\lambda}\right\}^2 \tag{12}$$

For the water vapor, $$k_{rg} = 1 - k_{rl} \tag{13}$$

where $$S^* = \frac{S_l - 0.214}{1 - 0.214} \quad \text{and} \quad \lambda = 0.63.$$

The capillary pressure function is given by,

$$P_{cap} = -P_o\left[(S^*)^{-1/\lambda} - 1\right]^{1-\lambda} \tag{9}$$

where $$P_o = 18{,}250\,Pa.$$

Case #	Rayleigh Number	Stefan Number	Initial Soil Liquid Saturation (S_l)
1	0	0	0.2
2	0	0	0.5
3	1.215×10^6	10.6	0.2
4	1.215×10^6	10.6	0.5
5	2.149×10^6	18.8	0.5

Table 1. Soil and melt data plus description of the five cases.

The melt properties are those of SiO_2 @ 1700°C and are not temperature-dependant in the current model. For brevity, the properties given in table 1 are given as non-dimensional in terms of the Rayleigh number (with a characteristic length of 2

meters and temperature difference between the isothermal wall and the 1700°C interface), the Stefan number, and the Prandtl number (which is 9.87×10^4 for all cases).

Depicted in figure 3 are histories of the pressure at a point in the porous soil located adjacent to the melt and the cavity's bottom. The pressure history curves exhibit some waviness that can be explained in terms of the numerical procedure. As the heat from the 1700°C interface is transferred to an adjacent saturated cell, the pressure and temperature of the cell rise slowly along the saturation curve. After the cell has dried out, the heat transferred from the cell, with its finite size and thermal inertia, to the next saturated cell will initially be less than the heat transferred from the interface to the first saturated cell. Steam generation in the next saturated cell is initially lower and the pressure drops until the dried out cell can reach a high enough temperature to cause the pressure to rise again in the next cell out.

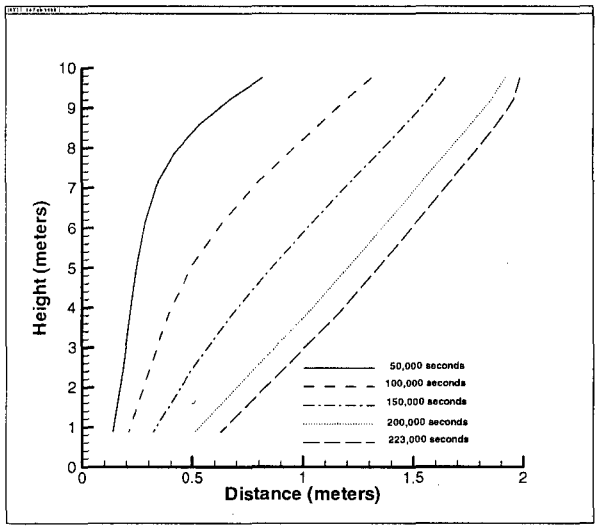

Figure 4: History of interface movement for case 4.

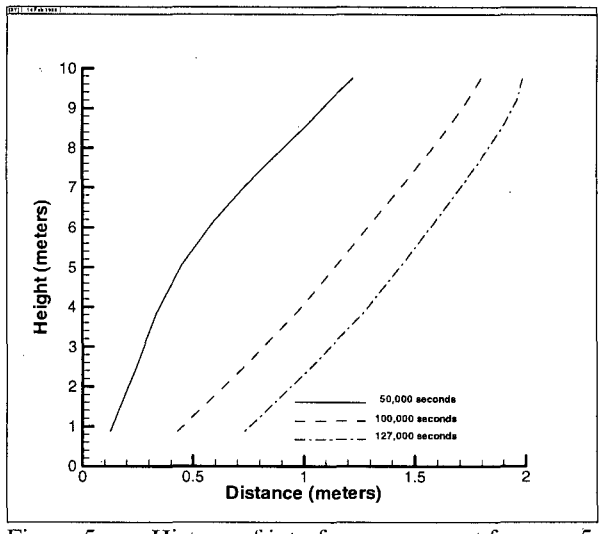

Figure 5: History of interface movement for case 5.

The pressure history curves for cases 1 and 2 remain well below one atmosphere. With no melt interface movement, the vapor path to the surface remains relatively unrestricted and pressure does not build up.

The pressure histories of cases 3 and 4 are similar. Initially, the pressures experience a rapid increase followed by a return to less than an atmosphere at about 100,000 seconds. Shortly after 100,000 seconds, the pressures for both cases experience a pronounced increase such that they exceed 10 atmospheres after a total time of 200,000 seconds. The pressure history curve for case 5 shows a similar pattern, except that the second pressure rise reaches 10 atmospheres shortly after 100,000 seconds.

The pressure histories can be explained by consideration of the melt interface histories seen in figures 4 and 5. Figure 4 illustrates the history of the interface movement for case 4. It is seen that the melt interface totally seals off the vapor release from the porous soil after 223,000 seconds. The initial increase in pressure for case 3 and 4 can be explained as result of the initial heat addition to the porous soil combined with melt movement. Until a dried out region is opened up for vapor to escape freely to the surface, the combination of rapid boil off near the interface and decreasing volume causes a temporary pressure surge.

After 100,000 seconds, the bottleneck created by the melt at the top of the soil region creates a critical block to vapor release. Interestingly, the pressure curves are not affected by the soil's initial liquid saturation. The history of the melt movement for case 3 (not shown) differs very slightly from that for case 4. The similarity in the two cases' melt growth can be explained in terms of the vapor history in the porous soil. Once a dry zone is established near the interface, the heat leaving the interface is not affected by the soil's overall saturation levels, therefore, the net heat entering the interface and consequent interface growth is the same for both cases.

The interface growth for case 5, depicted in figure 5, is increased because of the higher melt boundary temperature. This higher growth rate for case 5 causes the earlier development of a bottleneck accompanied by an earlier pressure rise as illustrated in figure 3.

CONCLUSIONS AND RECOMMENDATIONS

1. Coupling the three models to simulate the heat and mass transfer in the native soil adjacent to a growing melt yields some useful insights into the pressure history of the native soil. The basic model described in this paper could be enhanced to provide accurate simulations the ISV process.
2. The initial liquid saturation level was not found to have much affect on melt growth.
3. Higher melt growth rates are clearly associated with earlier MEE's.
4. Including the effect of density differences between the melt and the native soil would require a more sophisticated model but would yield better accuracy.
5. Properties for the melt are highly temperature dependent. Including temperature-dependent properties would affect the melt growth rate and, consequently, the native soil's pressure history.

REFERENCES

Karki, K. C. and H. C. Mongia, 1990, "Evaluation of a coupled solution approach for fluid flow and scalar transport in body-fitted coordinates", *Int. J. Numer. Methods in Fluids*, vol. 11, pp 1 - 20.

Kuo, C. H., 1994, "A Computational Study of Phase-Change Problems Using an Adaptive Grid in the Front-Tracking Method", Ph.D. Dissertation.

Kuo, C. H. and W. C. Schreiber, 1994, "An interface-tracking method for solving pure substance phase-change problems using nonsteady curvilinear coordinates", *Current Developments in Numerical Simulation of Flow and Heat Transfer* (HTD-vol. 275), pp. 57 - 64, Ed. K. Vafai and J. L. S. Chen.

Pruess, K. and T. N. Narasimhan, 1985, "A practical method for modeling fluid and heat flow in fractured porous media", *Society of Petroleum Engineers Journal*, vol. 25, pp 14 - 26.

Pruess, K., 1986, *TOUGH User's Guide*, Sandia National Laboratories research report (NUREG/CR-4645, SAND 86-7104, RW)

Roberts, J. S., S. L. Woosley, D. L. Lessor, and C. Strachan. 1992. Preliminary investigation for the potential for transient vapor release events during in situ vitrification based on thermal-hydraulic modeling, PNL-8170, Pacific Northwest National Laboratory, Richland, Washington.

Schreiber, W. C., 1996a, "A computer model for predicting two-phase ground water transport in the soil surrounding a growing melt in the *In Situ Vitrification* process", ASME Procedings of the 31st National Heat Transfer Conference (HTD-vol. 331), pp. 63-70, Ed. H. A. Hadim et al.

Schreiber, W. C., P. S. Lowery, and J. S. Roberts, 1996b, "A parameter study of the two-phase ground water transport in the soil surrounding a growing hemispherical In Situ Vitrification melt, HTD-vol 335, pp. 75-81, International Congress and Exposition (IMECE), Atlanta GA.

Thompson, J. F., Z. U. A. Warsi, and C. W. Mastin, 1985, *Numerical Grid Generation: Foundations and Applications*, North-Holland, New York.

ANALYSIS OF BOILING EXPERIMENTS USING INVERSE MODELING

S. Finsterle[1], C. Satik[2], and M. Guerrero[2]

[1]Earth Sciences Division
Lawrence Berkeley National Laboratory
University of California
Berkeley, CA 94720

[2]Stanford Geothermal Program
Stanford University
Stanford, CA 94305

ABSTRACT

Numerical predictions of geothermal reservoir behavior strongly depend on the assumed steam-water relative permeabilities, which are difficult and time-consuming to measure in the laboratory. This paper describes the estimation of the parameters of the relative permeability and capillary pressure functions by automatically matching simulation results to data from a transient boiling experiment performed on a Berea sandstone. A sensitivity analysis reveals the strong dependence of the observed system behavior on effects such as heat transfer from the heater to the core, as well as heat losses through the insulation. Parameters of three conceptual models were estimated by inverse modeling. Each calibration yields consistent effective steam permeabilities, but the shape of the liquid relative permeability remains ambiguous.

INTRODUCTION

The experimental determination of relative permeability and capillary pressure functions for nonisothermal, single-component, two-phase flow problems as encountered in geothermal reservoir engineering is very challenging, mainly because of the need to measure saturation, matric potentials, and flow rates under high temperatures and pressures. Moreover, the standard concept of characteristic curves as saturation-dependent material properties may be inappropriate in such systems, because interfacial tension, wetting characteristics, and pore-level condensation-evaporation mechanisms are affected by temperature changes. The need for steam-water relative permeability and capillary pressure functions in numerical simulations of geothermal reservoirs prompted several investigators to analyze enthalpy data from production wells [e.g., *Grant*, 1977; *Horne and Ramey*, 1978] or to conduct steam-injection and boiling experiments in the laboratory [e.g., *Ambusso et al.*, 1996; *Satik*, 1997]. In this paper, we describe the estimation of the parameters entering the relative permeability and capillary pressure functions, by automatically matching simulation results to data from a transient boiling experiment performed on a Berea sandstone. If we use inverse modeling for parameter estimation, the functional form of the characteristic curves is part of the conceptual model, i.e., it cannot be directly inferred from the data. However, by subjecting competing conceptual models to the estimation process, we can find the function that best matches the observed data. If the match was achieved without overparameterization, the most likely model is identified.

We first discuss the inverse modeling approach implemented in ITOUGH2 [*Finsterle*, 1997a,b] and describe the boiling experiment. Next, we analyze the temperature, saturation, pressure, and heat flow data using inverse modeling with ITOUGH2.

INVERSE MODELING

Inverse modeling is a technique to derive model-related parameters from a variety of observations made on a hydrogeologic system, from small-scale laboratory experiments to field tests to long-term geothermal reservoir responses. In this section, we briefly summarize the various steps involved in the iterative procedure of automatic model calibration. A detailed discussion of inverse modeling theory can be found elsewhere (e.g., *Carrera and Neuman* [1986]).

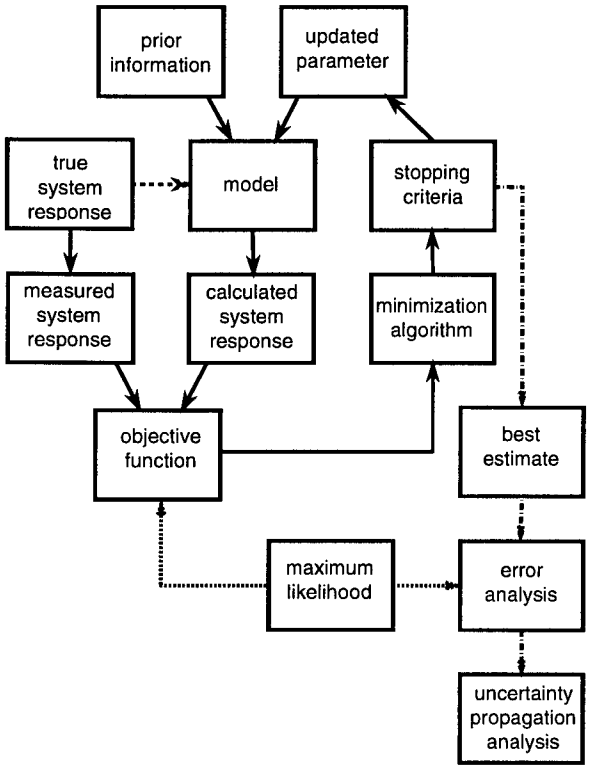

Figure 1. Inverse modeling flow chart showing main elements of automatic model calibration procedure.

The flow chart shown in Figure 1 illustrates the process and main elements of inverse modeling. The core of an inverse modeling code is an accurate, efficient, and robust simulation program such as TOUGH2 [*Pruess*, 1991] to solve the so-called forward problem. A problem- and site-specific conceptual model has to be developed, capable of simulating the flow and transport processes that govern the observed system behavior. Note that any error in the conceptual model leads to a bias in the parameter estimates, which is usually much larger than the uncertainty introduced by random measurement errors.

Next, an objective function has to be selected to obtain an aggregate measure of deviation between the observed and calculated system response. The choice of the objective function can be based on maximum likelihood considerations, which for normally distributed measurement errors leads to the standard weighted least-squares criterion:

$$S = \mathbf{r}^T \mathbf{C}_{zz}^{-1} \mathbf{r} \qquad (1)$$

Here, $\mathbf{r}$ is the residual vector with elements $r_i = z_i{}^* - z_i(\mathbf{p})$, where $z_i{}^*$ is an observation (e.g., pressure, temperature, flow rate, etc.) at a given point in space and time, and z_i is the corresponding simulator prediction, which depends on the vector $\mathbf{p}$ of the unknown parameters to be estimated. The i-th diagonal element of the covariance matrix $\mathbf{C}_{zz}$ is the variance representing the measurement error of observation $z_i{}^*$. Note that alternative objective functions are available to reduce the impact of outliers in the data or systematic modeling errors [*Finsterle and Najita* [1997].

The objective function S has to be minimized in order to maximize the probability of reproducing the observed system state. Due to strong nonlinearities in the functions $z_i(\mathbf{p})$, an iterative procedure is required to minimize the objective function S. A number of minimization algorithms are available in ITOUGH2. They reduce the objective function by iteratively updating the parameter vector $\mathbf{p}$ based on the sensitivity of z_i with respect to p_j. Details about the minimization algorithms implemented in ITOUGH2 can be found in *Finsterle* [1997a].

Finally, under the assumption of normality and linearity, a detailed error analysis of the final residuals and the estimated parameters is conducted. As demonstrated in *Finsterle and Pruess* [1995a,b], these analyses provide valuable information about the estimation uncertainty, the adequacy of the model structure, the quality of the data, and the relative importance of individual data points and parameters. Of special interest is the covariance matrix of the estimated parameter set, which is given by

$$\mathbf{C}_{pp} = s_0^2 (\mathbf{J}^T \mathbf{C}_{yy}^{-1} \mathbf{J})^{-1} \qquad (2)$$

where $\mathbf{J}$ is the Jacobian matrix, updated at the solution. Its elements are the sensitivity coefficients of the calculated system response with respect to the parameters:

$$J_{ij} = -\frac{\partial r_i}{\partial p_j} = \frac{\partial y_i}{\partial p_j} \qquad (3)$$

In Equation (2), s_0^2 is the estimated error variance, a goodness-of-fit measure given by

$$s_0^2 = \frac{\mathbf{r}^T \mathbf{C}_{yy}^{-1} \mathbf{r}}{M - N} \qquad (4)$$

where M is the number of observations and N is the number of parameters.

More than its efficiency, the formalized sensitivity, residual, and error analyses make inverse modeling superior to conventional trial-and-error model calibration.

BOILING EXPERIMENT

A vertical boiling experiment was performed at Stanford, taking advantage of the high-resolution X-ray computer tomography (CT) scanner, which measures porosity and steam saturation during the course of the experiment. A schematic of the experimental setup is shown in Figure 2. A 43-cm-long Berea sandstone core of radius 2.54 cm was sealed with epoxy and insulated with a ceramic fiber blanket. The core was saturated with water before being heated from the bottom. At the top, the core is open to atmospheric conditions. During the 7-day experiment, the heater power was increased stepwise, eventually reaching 10.4 Watts; boiling conditions were reached after about 5 days. Temperature, water pressure, and heat flux were measured at 41 points along the core, using thermocouples, pressure transducers and heat flux sensors, respectively; four CT scans were run at $t = 4$, 5, 6, and 7 days to measure steam saturation. The CT numbers depend on fluid density and thus temperature, which was evident during the first 5 days of heating. A simple linear correction was employed to avoid unreasonable steam saturation values in the first part of the experiment, when temperatures were below the boiling point. The differences between a CT scan of the fully liquid-saturated core and the dry core yielded a porosity estimate of 0.22. A detailed description of the experiment is given in *Satik* [1997]. Table 1 summarizes the assumed properties of the materials used in the experiment.

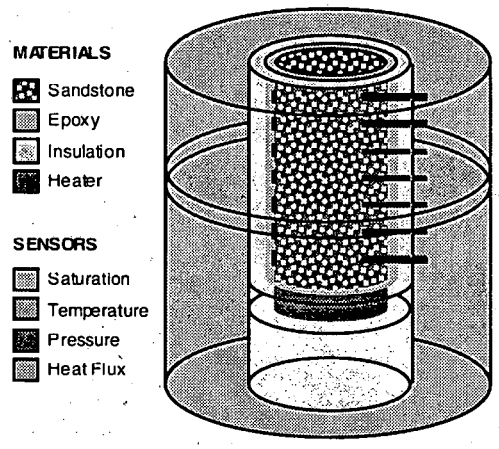

Figure 2. Schematic of experimental setup for boiling experiment.

Table 1. Thermal Properties of Materials Used in the Boiling Experiment

Material	Density [kg m^{-3}]	Heat cond. [W m^{-1} K^{-1}]	Spec. heat [J kg^{-1} K^{-1}]
Sandstone	2160	4.33 (4.93#)	858
Heater	2200	2.89	245
Heater insulator	530	0.13 (0.15#)	1047
Epoxy	1200	0.58	1047
Core insulator	192	0.09 (0.12#)	105

Determined by inverse modeling, see below

MODEL DEVELOPMENT

A two-dimensional, radial TOUGH2 model was developed for simulating the boiling experiment. It consists of 51 layers along the core axis, to discretize—from the bottom to the top—the heater insulation, the heater, the core, and the atmospheric boundary. In the radial direction, the model consists of 4 rings, the innermost representing the sandstone core, followed by two rings for the epoxy and the insulation material, and finally the outer boundary blocks. Material properties, nodal distances, and initial conditions for the heater and insulation materials were selected such that they were impermeable to fluid flow, but pervious to conductive heat transfer. The capillary pressure functions of *Brooks and Corey* [1964] and *van Genuchten* [1980] were modified (see *Finsterle* [1997a] for details) so that a finite value is obtained when saturation is at or below residual liquid saturation, conditions achieved as a result of boiling.

A number of forward simulations were performed to better understand the system behavior before inverse runs were initiated. During the first five days of the experiment, the temperature condition in the core depends exclusively on the heat source, the heat transfer from the heater to the core, and the thermal properties of the sandstone as well as the insulation materials, which determine heat losses. No hydrologic parameters affect the system behavior as long as single-phase liquid conditions prevail. A sensitivity analysis indicates that the heat loss from the heater as well as from the core to the environment have a significant impact on the initial steam development. Once the boiling point has been reached, the upward propagation of steam is influenced by the two-phase flow properties. Both steam and water relative permeabilities determine the pressure and temperature conditions, the steam front propagation, and saturation distribution within the core. Counterflow of liquid and steam by buoyancy

and capillarity is an important mechanism transporting water to the heater, affecting the instance when single-phase steam conditions are reached and temperatures start to rise beyond the boiling temperature.

INVERSIONS

While the objective of the inversions is to estimate parameters of the steam-water relative permeability and capillary pressure functions, the discussion above reveals that the system behavior is strongly affected by a number of additional, uncertain or variable parameters, such as the absolute permeability, the thermal properties, and the source terms. Since these parameters are correlated to the parameters of interest, any errors in the fixed values will lead to errors in the estimated parameters. This problem can only be solved (1) by obtaining accurate and independent measurements of these parameters, or (2) by considering them to be unknown, and including them into the estimation process. We follow the latter approach because it helps reduce estimation bias, allows examination of parameter correlations, and provides increased, more reasonable uncertainty estimates. Furthermore, if we select the first approach, very accurate measurements of the thermal properties would be required, in order for them to be sufficiently known so they can be fixed in the model. The requirement for high measurement accuracy of the thermal parameters is a consequence of heat losses—and thus the insulation material properties—strongly affecting the experiment.

In order to reduce the correlation between the thermal properties and the two-phase flow parameters of interest, we perform the inversion in two steps. First, we estimate the thermal properties from the data obtained during the first 5 days of heating, when the temperatures were below the boiling point. In the second inversion, we fix the thermal properties and estimate hydrogeologic parameters from the remainder of the data that exhibit two-phase flow effects.

The matches to the temperature and heat flow data during the single-phase period are visualized in Figures 3 and 4, respectively. The vertical distance of the symbol to the diagonal line represents the residual. The numbers indicate the sensor locations, where Sensor 1 is closest to the heater, Sensor 2 is 3 cm higher, etc. The random scattering of the points around the diagonal line indicates that the average behavior is identified as intended by minimizing the least-squares objective function (1). Note, however, that the matches to the individual sensors are not optimal in the least-squares sense. Specifically, the heat flow rates show a systematic under- or overprediction of the heat losses at different points along the core. Since this pattern is not reflected in the temperature data, we suspect that the heat flux sensors exhibit systematic trends. Nevertheless, we believe that by estimating the heat conductivity of the insulation material from all available heat flow data, the average heat loss is well captured. The estimates are shown in Table 1.

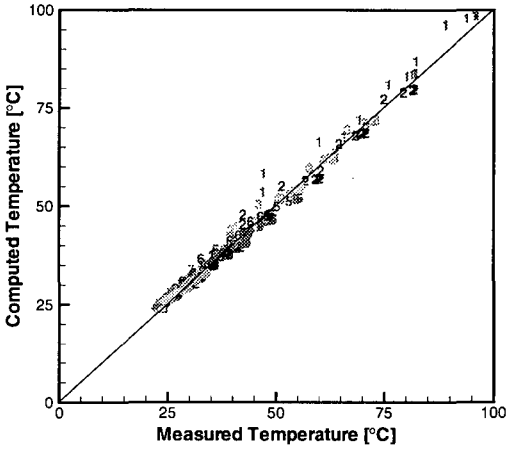

Figure 3. Measured versus calculated temperatures after calibration of single-phase period.

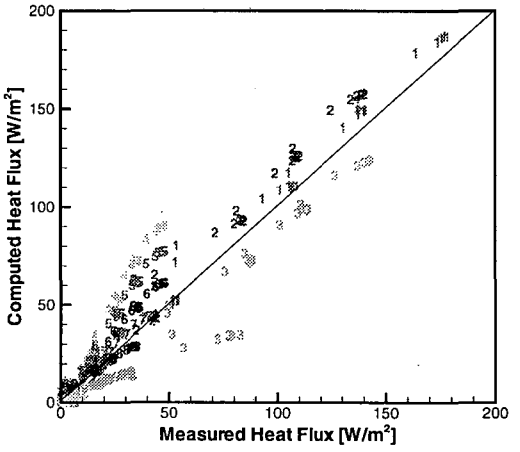

Figure 4. Measured versus calculated heat flow rates after calibration of single-phase period.

Three different relative-permeability and capillary-pressure models were calibrated against the available temperature, saturation, pressure, and heat-flow data from the boiling period. The first model consists of linear (LI) functions, the second is the Brooks-Corey (BC), and the third is the van Genuchten (VG) model as modified by *Finsterle* [1997a].

The distribution of the residuals obtained with the BC model is visualized in Figures 5 and 6; the *a priori* assumed measurement error and the *a posteriori* standard deviations of the final residuals are given in Table 2, along with the contribution of each observation type to the final value of the objective function. The assumed accuracy of the attainable match was overestimated, especially for the saturation data, which may include a systematic measurement error. The estimated error variance $s_0^2 = 5.5$, which is significantly greater than one, reflects the fact that the match is not as good as expected. Nevertheless, the contributions of each observation type to the objective function are relatively well balanced.

Using the estimated error variance as a goodness-of-fit criterion, none of the three models performs significantly better than the competing alternatives, indicating that the data do not contain sufficient information for us to distinguish among different conceptual models. This result is unfortunate, because the three models are believed to be sufficiently different from one another, such that key questions regarding the nature of steam-water relative permeabilities could have been answered by a clear preference of a specific model. For example, while the BC and VG model exhibit strong phase interference, the linear relative permeability functions suggest that steam flow is not greatly affected by the presence of liquid water. The BC and VG models also differ in regard to the presence or absence of a finite gas entry pressure, leading to a sharper or more diffuse saturation front.

Table 2. Assumed Measurement Error, Standard Error of Final Residuals, and Contribution to Objective Function (COF)

Observation type	Measurement error	Std. dev. of residuals	COF [%]
Temperature [°C]	1.0	1.9	17.2
Pressure [kPa]	1.0	1.4	12.7
Saturation [%]	1.0	0.9	33.7
Heat flux [W/m^2]	10.0	27.7	36.4

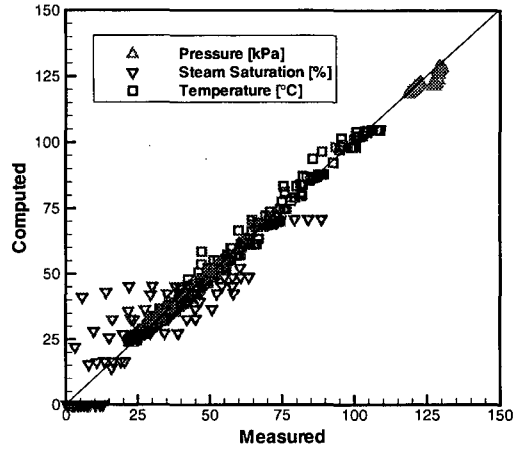

Figure 5. Measured versus calculated temperatures, pressures and steam saturations.

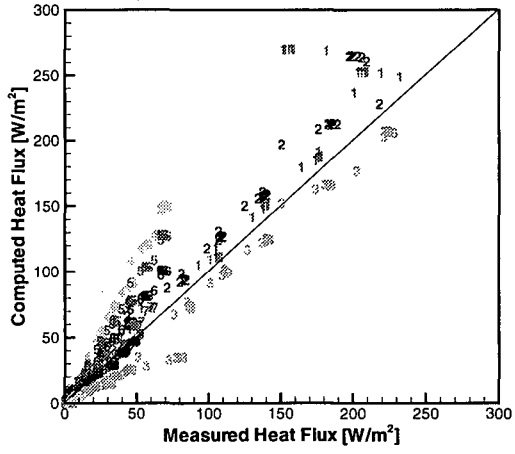

Figure 6. Measured versus calculated heat fluxes.

The relative permeability functions as obtained with the best estimate parameter sets are shown in Figure 7. The linear functions estimated by inverse modeling are in good agreement with the data obtained by *Ambusso et al.* [1996], who determined relative permeabilities by concurrently injecting steam and water into a Berea sandstone core. The VG steam relative permeability also coincides with the latter two functions. The BC function is somewhat lower, which is partly compensated for by a 50% higher absolute permeability estimate. In conclusion, the effective steam permeabilities as obtained with all three models are consistent and in agreement with the results of *Ambusso et al.* [1996]. The relative liquid permeability, however, is significantly lower in the BC and VG model as compared to LI and Ambusso et al. Since the observations made during the

boiling experiment are more sensitive to steam than to liquid relative permeability, inverse modeling makes the former consistent, and allows the latter to deviate according to the restrictions imposed by the individual models. Note that unlike the BC and VG model, the linear steam and liquid relative permeability functions are independent from one another, allowing the water relative permeability to vary more easily, which eventually came to agree with the data of Ambusso et al.

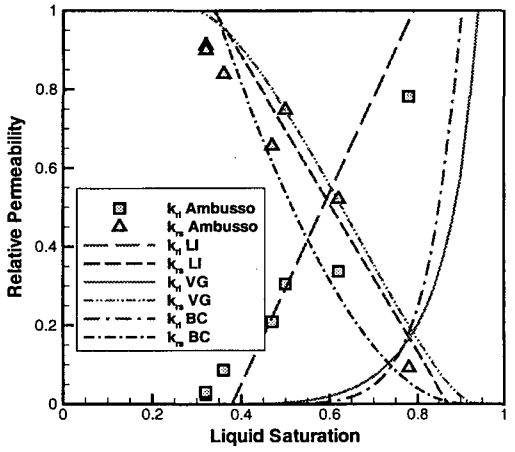

Figure 7. Relative permeability functions estimated by inverse modeling. Independent data obtained by *Ambusso et al.* [1996] are shown as symbols.

One might argue that the inverse problem as formulated here, with 6 parameters estimated for each model, is ill-posed due to over-parameterization. This is certainly true given the apparent nonuniqueness of the solution. The situation can be improved only if independent estimates for some of the key parameters can be obtained. The difficulties encountered here are also a result of the overall test design, in which two-phase flow conditions are initiated not by steam injection, but by boiling. This scheme makes the heat source the main driving force, which becomes dependent on the thermal properties of the core and the laboratory equipment, possibly introducing additional uncertainties. While the experiment provided interesting insights into the boiling process in porous media [*Satik*, 1997], a quantitative analysis of the data for the determination of steam-water relative permeability proved difficult and ambiguous.

CONCLUDING REMARKS

Temperature, steam saturation, pressure, and heat flux data from a vertical boiling experiment were used to estimate thermal and hydrogeologic properties of a Berea sandstone core. Since heating was the only driving force in this experiment, the development of a two-phase flow field was strongly coupled to the temperature conditions in the core. Consequently, the thermal properties, not only of the sandstone, but also of the insulation material, became a major factor in understanding the system behavior. From an inverse perspective, the high sensitivity of the insulation and heater properties, as well as the strong correlation of these properties to the parameters of interest, make it difficult to obtain accurate estimates.

All three conceptual models used for calibration yield similar matches to the data, i.e., no conclusive statement about the appropriate form of the relative permeability functions can be made. However, all three models produce consistent effective permeabilities for the steam phase, which is a major factor governing the propagation of the boiling front.

The comprehensive analysis of all available data from a nonisothermal multiphase flow experiment provided insight into the coupling of processes and the correlation of parameters. This information is useful for the design of future experiments.

ACKNOWLEDGMENT

This work was supported, in part, by the Assistant Secretary for Energy Efficiency and Renewable Energy, Office of Geothermal Technologies, of the U.S. Department of Energy under Contract No. DE-AC03-76SF00098. We would like to thank C. Oldenburg and E. Sonnenthal for thoughtful reviews.

REFERENCES

Ambusso, W. J., C. Satik and R. N. Horne, " A Study of Relative Permeability for Steam-Water Flow in Porous Media," *Proceedings*, 21st Stanford Workshop on Geothermal Reservoir Engineering. Stanford, Calif., 305-311, 1996.

Brooks, R. H. and A. T. Corey, "Hydraulic Properties of Porous Media," *Hydrol. Pap., 3*, 1-27, Colorado State Univ., Fort Collins, 1964.

Carrera, J. and S. P. Neuman, "Estimation of Aquifer Parameters Under Transient and Steady-State Conditions, 1, Maximum Likelihood Method Incorporating Prior Information," *Water Resour. Res. 22*(2), 199-210, 1986.

Finsterle, S., "ITOUGH2 Command Reference, Version 3.1," Report LBNL-40041, Lawrence Berkeley National Laboratory, Berkeley, Calif., 1997a.

Finsterle, S., "ITOUGH2 Sample Problems," Report LBNL-40042, Lawrence Berkeley National Laboratory, Berkeley, Calif., 1997b.

Finsterle, S. and J. Najita, *Robust Estimation of Hydrogeologic Model Parameters*, Report LBNL-40684, Lawrence Berkeley National Laboratory, Berkeley, Calif., (submitted to *Water Resour. Res.*), 1997.

Finsterle, S. and K. Pruess, "Solving the Estimation-Identification Problem in Two-Phase Flow Modeling," *Water Resour. Res., 31*(4), 913-924, 1995a.

Finsterle, S. and K. Pruess, "Automatic History Matching of Geothermal Field Performance," *Proceedings*, 17th New Zealand Geothermal Workshop, p. 193-198, Auckland, New Zealand, November 8-10, 1995b.

Grant, M. A., "Permeability Reduction Factors at Wairakei," *Proceedings*, ASME/AIChE Heat Transfer Conference, Salt Lake City, Utah, paper 77-HT-52, 15-17, August, 1997.

Horne, R. N. and H. J. Ramey, "Steam/Water Relative Permeabilities From Production Data," *GRC Trans. (2)*, 291, 1978.

Pruess, K., "TOUGH2—A General-Purpose Numerical Simulator for Multiphase Fluid and Heat Flow," Report LBL-29400, Lawrence Berkeley Laboratory, Berkeley, Calif., 1991.

Satik, C., "A Study of Boiling in Porous Media," *Proceedings*, 19th New Zealand Geothermal Workshop, Auckland, New Zealand, 205-209, 1997.

van Genuchten, M. Th., "A Closed-Form Equation for Predicting the Hydraulic Conductivity of Unsaturated Soils," *Soil Sci. Soc. Am. J., 44*(5), 892-898, 1980.

Pore-Scale Modeling Using TOUGH2

Stephen W. Webb and Clifford K. Ho
Sandia National Laboratories
Albuquerque, New Mexico 87185

ABSTRACT

TOUGH2 is a porous media code which is widely-used for simulating flow and transport in fractured and porous media. TOUGH2 is generally employed using REV(Representative Elementary Volume)-size elements or larger volumes. However, because TOUGH2 solves mass, momentum, and energy conservation equations, it can also be used for any size volumes as long as the proper constitutive relationships are included. The present paper discusses application of TOUGH2 to pore-scale modeling of enhanced vapor diffusion in porous media, and the changes and approximations that were employed.

INTRODUCTION

Gas diffusion in porous media is generally significantly smaller than in free space due to the presence of the porous medium. The flow area for gas-phase diffusion is reduced by the presence of the solid particles, by the presence of any liquid, and by the fact that the flow path for diffusion in a porous medium is more tortuous than in free space. Using Fick's law, gas diffusion in a porous media may be expressed as

$$F_i = -\tau\phi S_g D_{12}\rho_g \nabla\omega_i = -\beta D_{12}\rho_g \nabla\omega_i \qquad (1)$$

where D_{12} is the free-space diffusion coefficient at the pressure and temperature of interest. The product of the tortuosity coefficient, τ, the porosity, ϕ, and the gas saturation, S_g, is often referred to as the porous media factor, β. The porous media factor, β, is always much less than 1, and gas diffusion in a porous medium is usually much lower than in free space.

In contrast, it has been postulated that diffusion of a condensible vapor in the presence of its liquid may be considerably enhanced compared to gas diffusion rates and may approach or even exceed free-space values. Enhanced vapor diffusion is discussed in more detail by Ho and Webb (1998) and Webb and Ho (1998). The mechanisms for such an enhancement are postulated occur at the pore scale and include local condensation and evaporation at isolated liquid "islands" within the porous medium, and an increased temperature gradient in the gas phase compared to the average temperature gradient in the equivalent porous medium. As part of their review, Ho and Webb (1998) recommended additional modeling and experiments at multiple length scales, including the pore scale.

MODEL DESCRIPTION

TOUGH2 (Pruess, 1991a) is used to develop a numerical model to investigate the pore-scale processes in enhanced vapor diffusion. The model is described below. More details are given by Webb and Ho (1997).

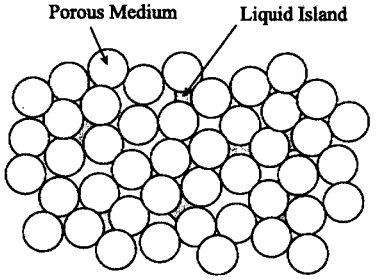

Figure 1
Porous Medium Conceptual Model

Conceptual Model. The conceptual model is depicted in Figure 1. The porous media is a series of randomly-arranged spheres. Heat transfer occurs between the spheres due to particle-to-particle contact, while flow of gas occurs around the spheres and around any liquid islands present. The liquid saturation is assumed to be low such that the liquid is confined to pendular rings, or "liquid islands", and no global flow of liquid occurs. Gas and vapor flow occur due to pressure, temperature, and/or concentration gradients.

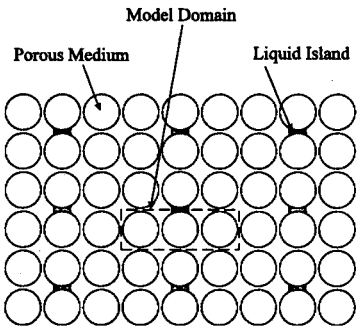

Figure 2
Porous Medium Simplified Representation

Simplified Representation. Figure 2 shows the simplified representation based on the conceptual model. The particles are arranged in rows, and the liquid islands occur on a regular basis. Symmetry is invoked as indicated by the dashed-line box in the figure. A two-dimensional representation has been used, and the solid particles are represented as cylinders.

Numerical Method. TOUGH2 has been slightly modified for the present analysis as discussed below.

1. The flux term for the gas phase is based on the Dusty Gas Model (DGM). Note that the original version of TOUGH2 uses an advective-dispersive formulation. The difference between these two formulations is discussed by Webb (1998a).

2. Some of the phase parameters in the connections have been modified. The standard version assumes that if more than one phase is present in an element, the phases are completely mixed. In the present model, the only elements which contain more than one phase are the elements at the ends of the liquid island, or the interface volumes. For simplicity, the liquid island length is defined so the interface is exactly in the middle of an interface element, and the element is half liquid and half gas. Due to capillary forces and the pore-scale nature of the present model, the phases will be separate, not mixed. The flow path from the interface volume to the gas phase will be entirely gas. Similarly, the flow path between the interface element and the liquid island will be all liquid. The flow path transport parameters used in the code, such as the saturation and fluid transport properties, were modified to reflect separate, rather than mixed, phases.

Model Geometry. Three different geometries were studied:

1) one-dimensional linear system;
2) two-dimension single pore; and
3) two-dimensional pore network.

The use of the one-dimensional linear system allows for a simple evaluation of the effect of the liquid island on the vapor diffusion rate, while the two-dimensional single pore includes the variation in cross-sectional area in a pore. Finally, the two-dimensional pore network considers the competition between vapor diffusion through open pores and through liquid islands. The model parameters, including the nodalization, are discussed in the next section.

MODEL PARAMETERS

The model parameters are summarized in Table 1.

Pore-Scale Dimensions The dimensions for the pore-scale model are consistent with the enhanced vapor diffusion data given by Jury and Letey (1979). For the average value of the capillary head of 300 cm, and using Young-Laplace's equation for the pressure difference across a curved surface, the minimum pore radius is 5 μm.

The cylinders are represented by an octagon (rather than a square) in order to approximate some of the variation of the pore cross-sectional area. A non-symmetrical octagon was employed such that the faces

Table 1
Pore-Scale Model Parameters

Dimensions	
Pore Radius	5 μm
Equivalent Permeability	2×10^{-12} m^2
Particle Radius	50 μm
Model Porosity	0.322
Diffusion	
Binary Diffusion Coefficient	2.42×10^{-5} m^2/s
Knudsen Diffusion Coefficient - Air	1.54×10^{-3} m^2/s
Knudsen Diffusion Coefficient - Vapor	1.96×10^{-3} m^2/s

parallel to the x- and y- directions have a slightly different length than the diagonal faces. This shape allows for the use of a regular grid consisting of square elements except at the diagonal faces of the solid; square elements are desirable when using the 9-point differencing scheme as discussed below. On the diagonal faces, the square elements are divided into two equal triangles, one which is solid and one which is fluid. The particle diameter is 50 μm, which supports the use of square elements, and gives a reasonable model porosity value of 0.322.

The standard version of TOUGH2 employs a 5-point stencil to connect the elements in the x- and y-directions. This numerical scheme is not appropriate for flow along the diagonal surfaces in the model or for flow between the square and triangular elements. Therefore, a 9-point differencing scheme has been used which adds diagonal connections between elements. The main advantage of the 9-point scheme is connections parallel to the diagonal surfaces of the solid particles. As shown by Pruess and Bodvarsson (1983) and Pruess (1991b), grid orientation effects can be significant for the 5-point scheme, especially when a diagonal surface is present; these effects are greatly reduced when a 9-point scheme is employed.

The nodalization of the three models is shown in Figure 3. For simplicity, the boundary elements are not shown. For the one-dimensional linear system, 24 square elements were used including boundary elements on either end of the model; the effective model length is 110 μm (22 active elements x 5 μm). Making use of symmetry, the two-dimensional single-pore model is 24 elements long and 11 elements wide, and the effective model dimensions are 110 μm long by 55 μm wide. Finally, the two-dimensional pore network is 68 elements long and 22 elements wide. The two end columns represent boundary conditions, so the effective dimensions are 330 μm long and 110 μm wide.

Permeability. The analogy between Darcy's law and laminar flow between parallel plates has been used, and the equivalent permeability for the minimum pore dimension of 5 μm is 2×10^{-12} m^2. This analogy

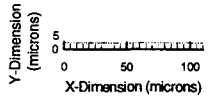

(a) One-Dimensional Linear Model

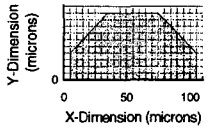

(b) Two-Dimensional Single Pore

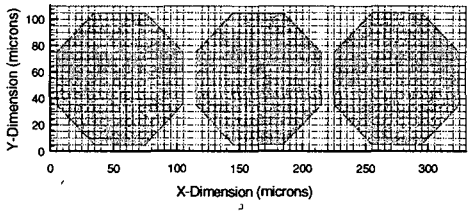

© Two-Dimensional Pore Network

Figure 3
Pore-Scale Models

assumes a parabolic velocity profile between the parallel plates, which is questionable due to the large variation in flow area. This problem has been at least partially addressed by Brown et al. (1995), who calculated velocity profiles between undulating surfaces of a hypothetical fracture. For the present geometry, the results from Brown et al. (1995) indicate that, under steady flow conditions, the fluid velocity profile will be nearly parabolic at the pore throat and "Gaussian" at the wider part of the channel. The fluid velocity is also dependent on the shape of the channel which is not captured in the analogy. Nevertheless, for simplicity, locally parabolic velocity profiles will be implicitly assumed in the present model by relying on the parallel plate analogy. Because the flow modeling is primarily concerned with diffusion, the error introduced through the use of this analogy should be small.

Accepting the parallel plate analogy, the effective permeability must vary normal to the flow direction in order to produce the desired parabolic velocity profile. The effective permeability for a given element can be derived by integrating the velocity profile over the respective coordinates. For an element with coordinates h_1 and h_2 from the center of the channel to the edges of the element, the effective permeability is given by

$$k = \frac{1}{2}\left(\frac{r^2}{4} - \frac{1}{12}\left(h_2^2 + h_1 h_2 + h_1^2\right)\right) \qquad (2)$$

where r is the distance from the centerline of the channel to the solid surface. For any given element, there may be different radii in the horizontal and vertical directions as indicated in Figure 4. Assuming parabolic profiles in both the horizontal and vertical directions, these radii result in different horizontal (h) and vertical (v) effective permeabilities according to the above relationship.

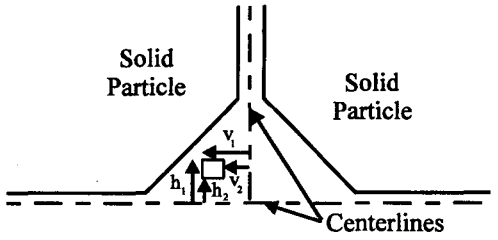

Figure 4
Horizontal and Vertical Effective Permeabilities

Diffusion. The binary diffusion coefficient for the present study is 2.42 x 10^{-5} m^2/s at the analysis conditions of 10^5 Pa and 20° C (Pruess, 1991a). The Knudsen diffusion coefficient is calculated by the following formula from Cunningham and Williams (1980) for perfectly diffuse molecule-wall collisions, or

$$D_\kappa^K = \frac{2}{3} r v \qquad (3)$$

where v is the mean molecular speed

$$v = \left(\frac{8 k_B T}{\pi M_\kappa} \right)^{1/2} \qquad (4)$$

and k_B is Boltzmann's constant. For the minimum pore dimension of 5 μm, the Knudsen diffusion coefficient is 1.54 x 10^{-3} m^2/s for air at 20°C. For water vapor, the value for air is scaled by the inverse of the square root of the ratio of molecular weights, or 1.96 x 10^{-3} m^2/s. No modifications are made to account for the presence of the porous medium.

Similar to the effective permeability, any given element may have different radii in the horizontal and vertical directions. However, as discussed by Cunningham and Williams (1980), the velocity profile due to Knudsen diffusion is independent of distance from the wall. Therefore, the Knudsen diffusion coefficient is simply a function of the horizontal and vertical radii and, unlike the effective permeability, is *not* a function of the local coordinates.

Liquid Island The model for the liquid island is one of the major pieces of the current pore-scale analysis. Capillary pressure across the gas-liquid interface and vapor pressure lowering is included. Capillary pressure is a function of position, or length, of the liquid island; the capillary pressure for a short liquid island is much higher than for a longer liquid island due to the decrease in interface curvature as shown in Figure 5. By geometry, the radius of curvature for a given contact angle can be calculated as a function of liquid island length. For a contact angle of 0°, the capillary pressure as a function of liquid island length is shown in Figure 6, where the coordinate (x) is zero at the minimum pore dimension. A maximum x/R value of 0.75, where R is the particle radius, was used in the development of the capillary pressure function.

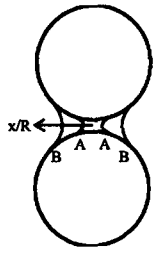

Figure 5
Liquid Island

The capillary pressure due to the gas-liquid interface results in local vapor pressure lowering due to the curvature. For a temperature of 20°C, the saturated water vapor pressure is 2337 Pa. For the maximum capillary pressure of about 30 kPa, the vapor pressure lowering factor is 0.99978, which gives a maximum vapor pressure lowering of only about 0.5 Pa. Even though the magnitude of vapor pressure lowering is small, it can have a large influence on enhanced vapor diffusion as shown by Webb (1998b).

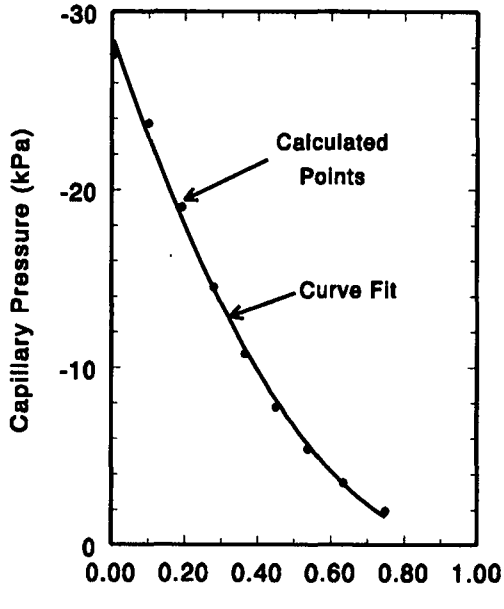

Figure 6
Liquid Island Caoillary Pressure Function

Thermal Conductivity. The thermal conductivity of the gas, liquid, and solid phases are assumed to be 0.025, 0.6, and 2.0 W/m-K, respectively.

Boundary Conditions. The boundary conditions for the problem depend on the gradient imposed. In the results shown in this paper, only a concentration gradient was imposed; the pressure and temperature at both boundaries are the same. These boundary conditions do *not* imply uniform pressure or temperature in the model, rather that a zero gradient was imposed. Webb (in prep.) shows some results including a temperature gradient.

RESULTS

Two-dimensional Pore Network. The two-dimensional pore network is the most general of the three models described in this study. Mass flow vectors for gas-only diffusion, or diffusion without liquid islands, are shown in Figure 7. Because there is no boundary pressure gradient, all flow is due to diffusion. Vapor diffuses from right-to-left, while air diffuses from left-to-right. The mass flux of air is higher than that of water vapor consistent with Graham's law of diffusion as discussed by Webb (1998a).

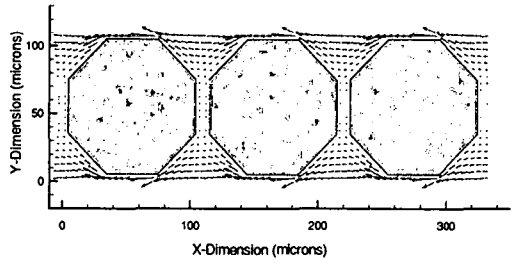

(a) Water Vapor Total Mass Flow Vectors

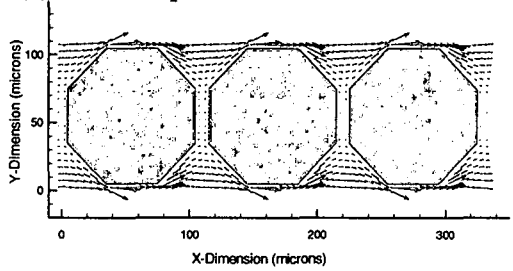

(b) Air Total Mass Flow Vectors

Figure 7
Mass Flow Vectors For All Gas Conditions

A value of the porous media factor, β, can be calculated for the two-dimensional pore model for all-gas conditions. The calculated porous media factor for water vapor is 0.147 compared to Fick's law value in free space, while the porous media factor for air is

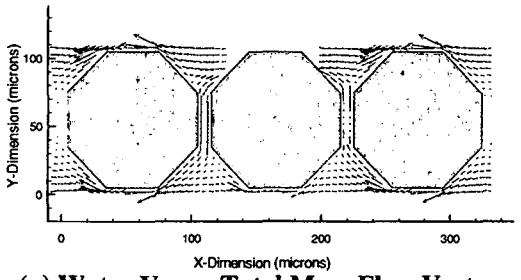

(a) Water Vapor Total Mass Flow Vectors

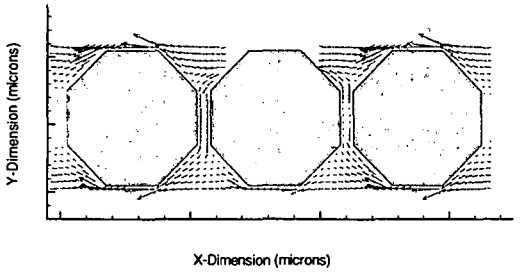

(b) Water Vapor Diffusion Mass Flow Vectors

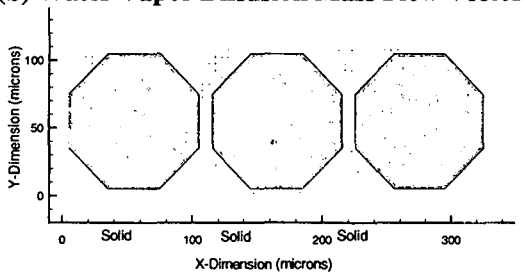

(c) Water Vapor Advection Mass Flow Vectors

Figure 8
Water Vapor Mass Flow Vectors
for the Two-Dimensional Pore Network Model
For a Liquid Island Length of x/R=0.75

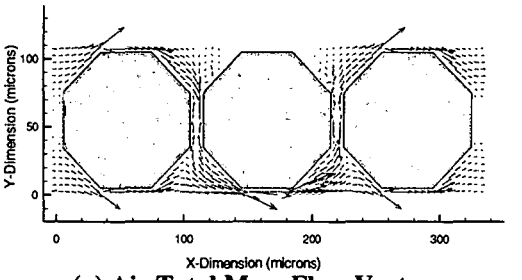

(a) Air Total Mass Flow Vectors

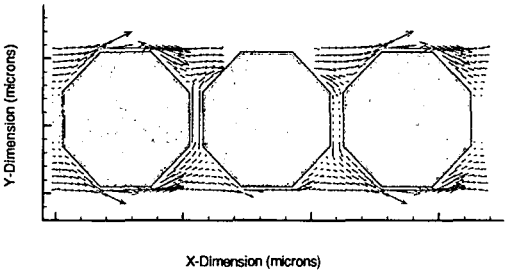

(b) Air Diffusion Mass Flow Vectors

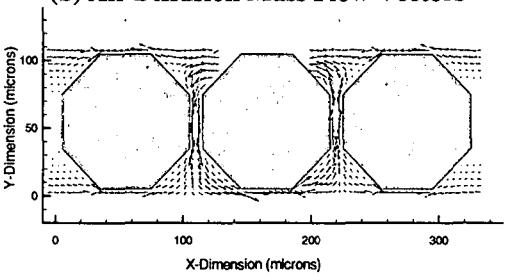

(c) Air Advection Mass Flow Vectors

Figure 9
Air Mass Flow Vectors
for the Two-Dimensional Pore Network Model
For a Liquid Island Length of x/R=0.75

0.186. The value are different because the present model satisfies Graham's Laws, and the mass flux of air and water vapor are different by the square root of the molecular weights, or a factor of 1.27 (Webb, 1998a). These porous media factors (air and water vapor) are reasonably consistent with the theoretical value predicted by Ryan et al. (1981) of approximately 0.17 and with the experimental data shown by them.

For cases with a liquid island, even though the boundaries have the same total pressure, advection and Knudsen diffusion occur. While vapor essentially flows "through" the liquid island, gas (air) is effectively blocked by the liquid island and builds up on the upstream end of the island. Because air is stagnant at the liquid island, diffusion away from the liquid island caused by the buildup of air must be balanced by advection towards the liquid island. Therefore, there are diffusion, advection, and Knudsen diffusion contributions to vapor and air flow.

Figures 8 and 9 show the mass flow vectors for water vapor and air in the case of the longest liquid island, respectively. The liquid island is assumed to be in the top pore throat of the center particle. Three velocity vectors plots are shown for the total, diffusive, and advective mass velocity contributions using the same scale. Knudsen mass velocity fluxes are not shown since their contribution is small in the present simulations. Vapor essentially diffuses "through" the liquid island via condensation/evaporation mechanisms as indicated by the vector plots. The total vapor mass flow is dominated by diffusive fluxes; the advective contribution is small as indicated by the vector plots. The vapor mass velocity vectors are slightly larger than for the all-gas case indicating enhanced vapor diffusion. For the air, the flow pattern is just about the opposite of the vapor. Since the liquid island effectively blocks air flow, the air must go around the liquid island, and air is stagnant next to the interface. At the right end of the liquid island, vapor diffuses toward the gas-liquid interface; therefore, air diffusion will be opposite and away from the interface. Because air is stagnant, a small pressure gradient will be established to balance

the air diffusive flow rate. This pattern is seen in the velocity vectors. There is a significant advective air flow rate in the middle of the model, especially near the liquid island.

DISCUSSION

The results shown above make qualitative and quantitative sense. For the all-gas case, all the flow is due to diffusion, and the air mass flow rate is slightly greater than the water vapor mass flow rate, consistent with Graham's Law. With a liquid island, vapor pressure lowering causes condensation/evaporation at the liquid island. Air is blocked from flowing through the island, which sets up local counterdiffusion and advection. Overall, the behavior is consistent with gas diffusion principles from the Dusty-Gas Model. It can therefore be concluded that the results make sense and seem reasonable.

CONCLUSIONS

Pore-scale models of enhanced vapor diffusion in porous media have been developed. The detailed results, such as the various mass flow rates and directions, make physical sense. It can therefore be concluded that the pore-scale model developed using TOUGH2 is a reasonable representation of the processes modeled.

One BIG caveat is in order. As noted by Ewing and Gupta (1993), pore-scale modeling is a "useful concept rather than a physical reality". The present authors support this notion.

NOMENCLATURE

D_{12} binary diffusion coefficient for water vapor and air
D^K Knudsen diffusion coefficient
F mass flux
h coordinate measured from the center of the channel
k permeability
k_B Boltzmann's constant
M molecular weight
r pore radius
S saturation
T temperature
v mean molecular speed

Greek

β porous media factor
ρ density
τ tortuosity coefficient
ϕ porosity
ω mass fraction

Subscripts

g gas
κ component

ACKNOWLEDGMENTS

The authors wish to thank Karsten Pruess of Lawrence Berkeley National Laboratory for providing a routine to implement the 9-point differencing scheme used in this analysis. This work was supported by the United States Department of Energy under Contract DE-AC04-94AL85000 as part of a Sandia Laboratory Directed Research and Development Project on Enhanced Vapor-Phase Diffusion in Porous Media. Sandia is a multiprogram laboratory operated by Sandia Corporation, a Lockheed Martin Company, for the United States Department of Energy.

REFERENCES

Brown, S.R., Stockman, H.W. and Reeves, S.J., 1995, "Applicability of the Reynolds equation for modeling fluid flow between rough surfaces," *Geo. Res. Let.*, 22:2537-2540.

Cunningham, R.E., and Williams, R.J.J., 1980, Diffusion in Gases and Porous Media, Plenum Press, New York.

Ewing, R.P., and Gupta, S.C., 1993, "Modeling percolation properties of random media using a domain network," *Water Resourc. Res.*, 29:3169-3178.

Ho, C.K., and Webb, S.W., 1998, "A Review of Porous Media Enhanced Vapor-Phase Diffusion Mechanisms, Models, and Data - Does Enhanced Vapor-Phase Diffusion Exist?" *J. Porous Media*, 1:71-92.

Jury, W.A., and Letey, Jr., J., 1979, "Water Vapor Movement in Soil: Reconciliation of Theory and Experiment," *Soil Sci. Soc. Am. J.*, 43:823-827.

Pruess, K., and G.S. Bodvarsson, 1983, "A Seven-Point Finite Difference Method for Improved Grid Orientation Performance in Pattern Steamfloods," Paper SPE-12252, Seventh Society of Petroleum Engineers Symposium on Reservoir Simulation, San Francisco, CA.

Pruess, K., 1991a, *TOUGH2 - A General-Purpose Numerical Simulator for Multiphase Fluid and Heat Flow*, LBL-29400, Lawrence Berkeley Laboratory.

Pruess, K., 1991b, "Grid Orientation and Capillary Pressure Effects in the Simulation of Water Injection into Depleted Vapor Zones," *Geothermics*, 20:257-277.

Ryan, D., Carbonell, R.G., and Whitaker, S., 1981, "A Theory of Diffusion and Reaction in Porous Media," *AIChE Symposium Series*, 202(77), pp. 46-62.

Webb, S.W., and C.K. Ho, 1997, "Pore-Scale Modeling of Enhanced Vapor Diffusion in Porous Media," *Proceedings of the ASME Fluids Engineering Division*, FED-Vol. 244, pp. 457-468.

Webb, S.W., 1998a, "Gas-Phase Diffusion in Porous Media: Comparison of Models," TOUGH Workshop '98, Lawrence Berkeley Laboratory, May 4-6, 1998.

Webb, S.W., 1998b, "Pore-Scale Modeling of Transient and Steady-State Vapor Diffusion in Partially-Saturated Porous Media," 1998 AIAA/ASME Joint Thermophysics and Heat Transfer Conference, Albuquerque, NM, June 15-18.

Webb, S.W., in prep., "Temperature Gradient Effects in Vapor Diffusion in Partially-Saturated Porous Media."

Webb, S.W. and C.K. Ho, 1998, "Enhanced Vapor Diffusion in Porous Media," TOUGH Workshop '98, Lawrence Berkeley Laboratory, May 4-6, 1998.

The use of an adaptive grid with TOUGH2 to track a moving phase front

Will Schreiber
Department of Mechanical Engineering
PO Box 870276
The University of Alabama Tuscaloosa, AL

ABSTRACT

Two different computer models, Computational Grid I (CGI) and Computational Grid II (CGII), are tested for their usefulness in predicting the water balance and pressure field in a porous soil surrounding a growing hemispherical melt with a surface temperature of 1700°C. The hemispherical annulus of soil is bounded on the inner radius by the melt, on the outer radius by an impervious wall, and on the planar surface by the atmosphere at 20°C and 1 atm. The motion of liquid and vapor water in the porous soil is modeled using Darcy's equation. Both computer models employ grids, which adapt to the boundary of the growing melt. CGI adapts with the melt boundary by contracting uniformly in the radial direction. In addition to adapting to the melt boundary, CGII also adapts to track the liquid-vapor interface, which moves outward from the 1700°C melt. CGII has been devised in order to attempt to reduce, at a reasonable CPU cost, numerical pressure oscillations, which arises when the grid is too coarse. A very fine CGI is used as a benchmark to test CGII and a coarser version of CGI. Results from the two CGI and the one CGII cases are presented graphically to illustrate the mass flux of liquid and vapor water and the build-up in pressure as the melt boundary approaches the impermeable wall.

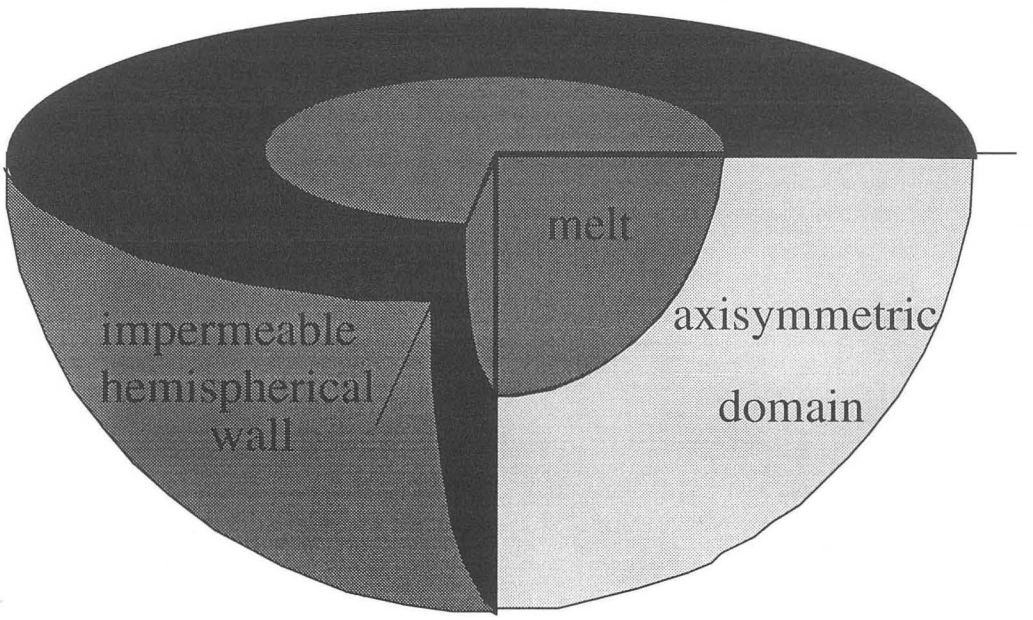

Figure 1 Illustration of the hemispherical annulus of soil bounded by the isothermal, impermeable melt interface; the impermeable outer containing wall, and the atmosphere.

INTRODUCTION

The *In Situ* Vitrification (ISV) process is currently being studied as a means for remediating soils which have been contaminated with nuclear or chemically-toxic wastes. The basic premise of the ISV process is fairly simple. Large electrodes are initially planted in the soil surrounding the contamination. Enough current is passed through the soil to raise its temperature to above melting. During the ISV process, the electrodes are continuously gravity-fed far enough into the melt to ensure that the melt reaches the depth of the contamination. After the soil containing the contaminants has been melted, it is allowed to solidify into a glass. Organic material and volatile chemical wastes are destroyed, while all other material is captured in a glass which is impervious to ground water. The necessity of handling and of transporting the wastes is virtually eliminated since they remain *in situ*. While the underlying theory behind ISV is fairly elementary, many of the details required for actually implementing the process are complicated and require thoughtful analysis for their understanding. The complications include handling the off-gas generated during the ISV process and understanding the water balance surrounding the growing melt.

The water balance in the surrounding soil is important for at least two reasons. If the object of the ISV process is to capture chemical contaminants, then one needs to know whether these contaminants, which may be carried by the water movement, will be overtaken by the melt. A second important reason for studying the water balance surrounding the melt is to be able to predict sudden pressure increases near the melt that may allow water vapor to penetrate the melt and bubble up to pressurize the off-gas containment system. The problem of sudden pressure spikes is particularly relevant in the processes when liquid water may be trapped between the growing melt front and the pit's walls.

One way to analyze the effect of a moving melt on the surrounding ground water is with computational simulation. A computer code, TOUGH2, developed by Pruess (1985, 1986) can predict the transport of heat, liquid and vapor water, air, and other species, including the effect of phase change, in a porous soil. Integral equations that describe the balance of heat and species transport relative to a control volume, V_n, are of the form,

$$\frac{d}{dt}\int_{V_n} M^{(\kappa)}\, dv = \oint (F^{(\kappa)} \cdot \hat{n}) + \int_{V_n} q^{(\kappa)}\, dv \tag{1}$$

where: $\kappa = 1$: water, $\kappa = 2$: air, and $\kappa = 3$: heat.

The finite difference formulation and solution of equation (1) as well as the equations that define $M^{(\kappa)}$, the accumulation of mass (or heat), $F^{(\kappa)}$, the transfer of mass or heat, $q^{(\kappa)}$, the source of mass or heat, and constitutive equations are described by Pruess (1985, 1986).

Equation (1) may be expressed as in implicit finite difference in time in terms of a residual, which is set equal to zero,

$$R_n^{(\kappa)k+1} = M_n^{(\kappa)k+1} - M_n^{(\kappa)k} - \frac{\Delta t}{V_n}\left(\sum_m A_{nm} F_{nm}^{(\kappa)k+1} + V_n q_n^{(\kappa)k+1}\right) = 0. \tag{2}$$

The Newton-Raphson method is used to update all unknown variables implicitly in equation (2) as well as the ancillary equations.

For the present project, two modified versions of the TOUGH2 code are considered and tested on a problem whose geometry is illustrated in figure 1. The parameters for the test case are given in table 1. The first version of TOUGH2 has been modified to solve the transport equations on a relatively fine grid (CGI) which is uniform in the radial direction and adapts uniformly to the growing melt boundary. (See figure 2.) The second version of TOUGH2 uses a doubly adaptive grid (CGII) which moves with both the external boundary (the melt front) and internal boundary (the liquid/vapor phase front). (See figure 3.) As the melt front progresses, CGII is continuously reconfigured to fit the changing external and internal boundaries. A thin line of small cells captures the liquid/vapor phase front and "ferry" it across the domain that represents the drying soil.

Kuo and Schreiber (1994), Haywood et al (1994), Lee and Yeh (1994), Gottardi and Venutelli (1994), and Zhang and Moallemi (1995) have recently published articles describing the use of adaptive grids with transport problems. Thompson (1985) describes many of the general considerations for this type of problem.

NUMERICAL METHOD

Both CGI and CGII have in common the ability to adapt to an inner spherical boundary whose radius increases with time. Both grids are constructed from lines (spokes) which increase in the radial direction along fixed angular coordinates and lines which increase in the angular direction. The two sets of grid lines intersect at nodes, which can slide along the spokes to fit the changing inner boundary. The melt front moves continuously throughout the computation and the grid has to be regenerated at every time step to keep pace with the changing boundary. The amount that the spokes' lengths shorten with every time step is determined as the product of the melt front velocity and the length of the time step.

The grid is updated and the lengths between cells, the interface areas, and the cell volumes are recalculated to suit the new grid location. New node locations are determined as a simple interpolation along the spokes since only one boundary, the melt interface, changes location. In order to maintain constant relative radial distances between the nodes, the distances between nodes are divided by the ratio of the total spoke length before and after the melt movement.

The original TOUGH2 code has an adaptable time step length. If the Newton-Raphson iteration cannot converge for a given time step, that time step is decreased prior to another attempt at convergence. To accommodate the adaptive time step, the grid values prior to the time step are saved in order to recalculate the new grid in the event that a reduced time step is necessary for convergence.

Melt radius	Initial: 1.0 m; Final: 1.9 m	Soil:	Density: 2600 kg/m^3: Sp. heat of grain: 700 J/kg·K
Melt Boundary:	Isothermal @ 1700°C; impermeable		Initial Temp.: 20°C; Initial liquid sat. 0.2; Porosity: 0.4
	Hemispherical growth: 4.4 x 10^{-5} m^3/s		Conductivity (fully saturated) 1.13 W/m K;
Outer Boundary:	Solid impermeable wall; radius: 2.0 m		Permeability: 10^{-12} m2; Saturation of immobile water: 0.15
	mass: 15,250 kg; specific heat: 700 J/kg·K		Reference pressure: 632 kPa
	initial temperature 20°C		Capillary Pressure Model: Leverett's (1941) function
Upper Boundary:	Permeable; Atmospheric pressure; 20°C		Relative Permeability: Fatt and Klikoff (1959)

Table 1 Parameters and boundary conditions for test problem.

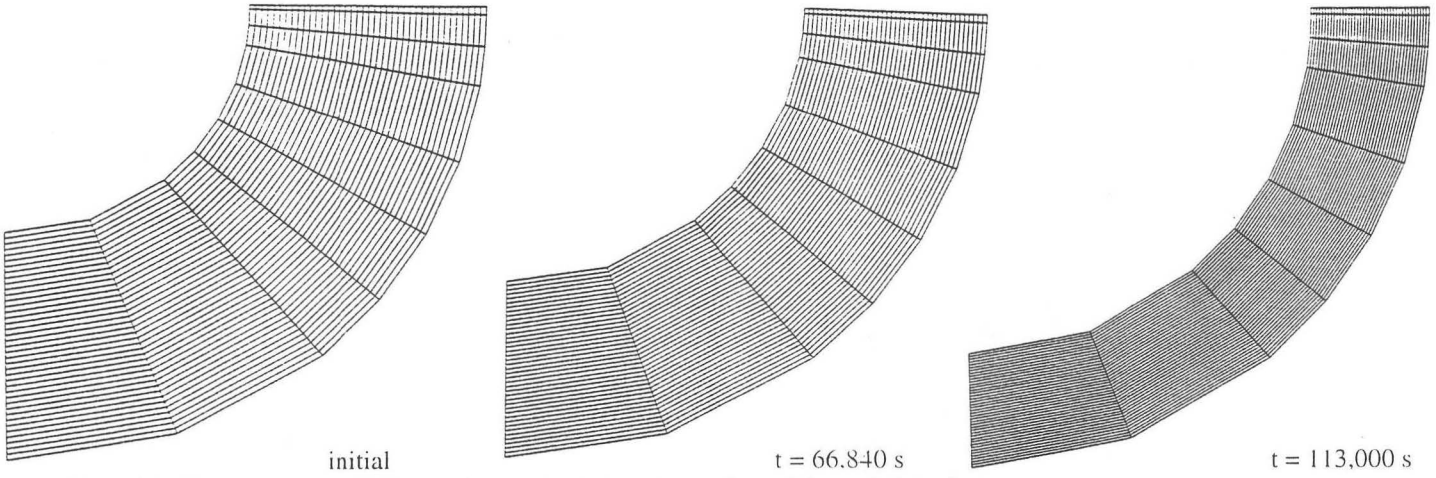

Figure 2 CGI contracts radially to adapt to the increasing radius of the melt interface.

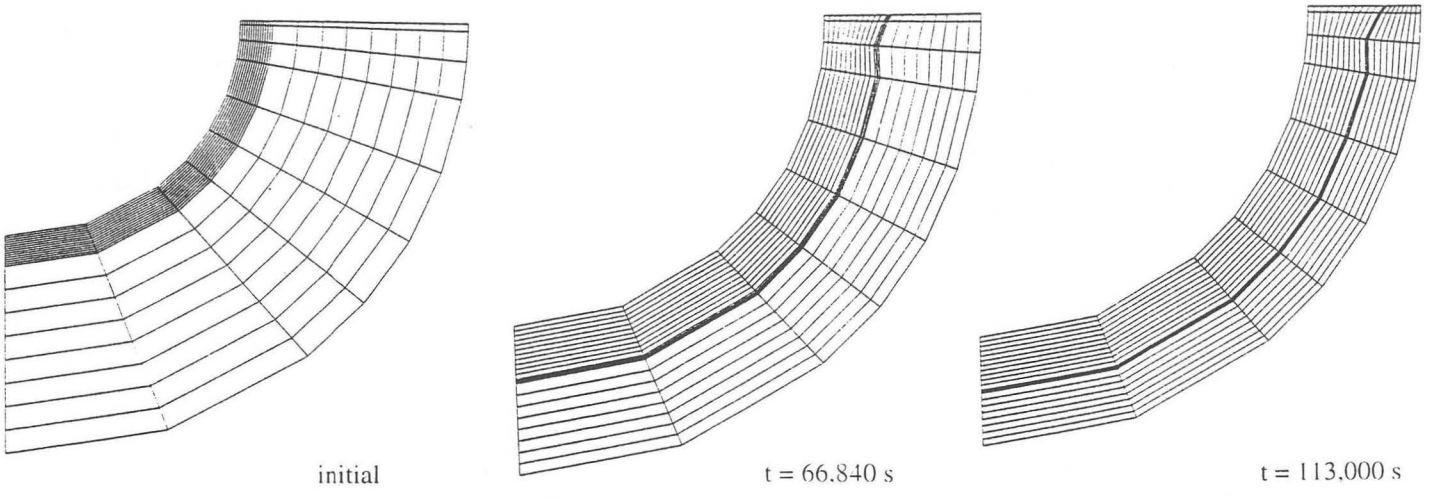

Figure 3 CGII adapts to the increasing radius of the inner boundary and to the moving vapor-liquid interface. Three narrow cells move with and contain the vapor-liquid interface.

Thompson (1985) has demonstrated that the cell interface moving with an adaptive grid effectively experiences an advective flow due to the Lagrangian grid movement. The advective flow due to the Lagrangian grid movement is added to the advection due to fluid motion relative to the Eulearian grid. For the static grid, the flux of heat or mass is a combination of diffusive and advective transport modes. In the case of flow in a porous media, the conduction mode is mainly confined to heat conducted in the rock matrix. The advection transport consists of fluid motion through the matrix. Including the effect of a moving grid as an advective term causes the flux for conduction in the radial direction, to be modified as,

$$q_{conduction} = \left[-K_{nm} \frac{T_m - T_n}{r_m - r_n} - \rho \, c_p \, v_{grid} \left(1 - \Phi\right) T_m \right] A_{nm} \tag{3}$$

The time-dependency of a cell's volume must also be included in the solution procedure to correctly account for mass and enthalpy conservation. The Newton-Raphson solution technique is used for solving the nonlinear equations. To account for the cell volume change over the course of the time step, the variable at the old time value is multiplied by the ratio of the old cell volume by the new cell volume. This variation of volume with time accounts for the effect of grid movement on the mass advection.

The grid CGII has been devised in an effort to eliminate the pressure oscillation problem associated with the boiling and subsequent dry-out of the cells. In addition to adapting like CGI, CGII can also adapt to track the interface between the saturation region and the vapor region. Using an adaptive grid, the interface can be held within three special narrow cells which move prior to drying out and ferry the interface across the domain. In the initial grid, the seven cell layers closest to the hub are very fine. Fifteen large cell layers extend between the finely packed layer of cells and the outer boundary. As the grid adapts to the changing solution, the grid nodes are allowed to move along the rigid spokes. Since the nodes along a given spoke move independently of the nodes of the other spokes, the grid is flexible enough to adapt to a time-dependent vapor phase front whose radial growth rate varies with angle.

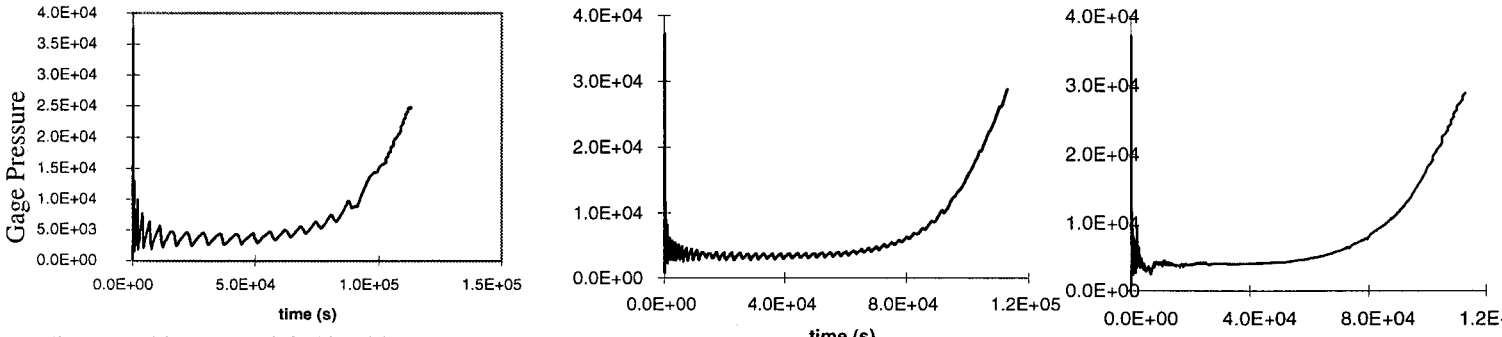

Pressure history on GCI40 grid

Pressure history using CGI100

Pressure history using CGII

Figure 4. Pressure history on melt surface at $\phi = \pi$. Illustration on the left shows pressure oscillation problem experienced when CGI is too coarse. Two illustrations on the right compare pressure histories as predicted by CGI with 100 uniform cell divisions in the radial direction and CGII with 22 cell divisions with adapting lengths in the radial direction.

For the grid's adaptation to the movement of the vapor phase front, several issues had to be considered. A means had to be devised for maintaining the vapor front within two narrow cells while the cells in the direction toward the inner hub had to expand and the cells toward the outer rim had to compress as the special cell moved. With each time step, a decision is made whether a node should move along its spoke and, if so, how far the cell's nodes should move to capture the vapor interface within the narrow cell. To effect the cell moves, the value of vapor saturation at the nodes is determined as well as moving the grid without disturbing the spatial distribution of thermodynamic properties within the problem domain. In order not to interfere with the calculation of the grid generation due to melt front movement, a special short time step is used whenever the grid is required to adapt to the vapor-liquid front. During this shortened time step, the melt movement is turned off and the primary properties are allowed to come to equilibrium (through numerical iterations within the time step). After the special time step, the length of the time step is subtracted from the sum total time of the computation. It was found that moving the cells at every angular value all at once is better than allowing the different sets of constant angle cells to move higgledy-piggledy. Whenever the criteria for moving is met for any group of special cells, the required movement is determined for every set of constant-angle special cells. The one-for-all, all-for-one cell movement approach ensures better convergence and fewer disruptions in the program's time stepping.

When the thickness of the cell layers located between the special cells and the outer rim are less than a specified minimum value, the grid ceases to adapt to follow the vapor phase front and the outer cells are allowed to dry out.

RESULTS

As discussed in the "numerical methods" section above, figure 1 illustrates the problem geometry. Table 1 lists the parameters and boundary conditions of the problem. The saturated water in the soil is vaporized as heat is transferred

from the melt interface to raise the temperature of the surrounding soil above the boiling point. The pressure surrounding the melt rises due to the creation of vapor at a rate which is larger than the rate the vapor escapes from the soil into the atmosphere as well as due to the decreasing volume of the soil region in which the vapor is confined.

Two CGI grids and one CGII grid are compared for their ability to simulate the water-vapor balance and pressure distribution for the problem described above. A CGI grid with 100 radial cell divisions (CGI100) was used as a benchmark by which to compare a coarser CGI grid, with 40 radial cell divisions (CGI40), and an adaptive CGII with 22 radial cell divisions. CGI40 was the coarsest grid used that allowed convergence of the solution to 295,000s. For all three grid configurations, the angular direction was divided into 9 divisions as illustrated in figures 2 and 3.

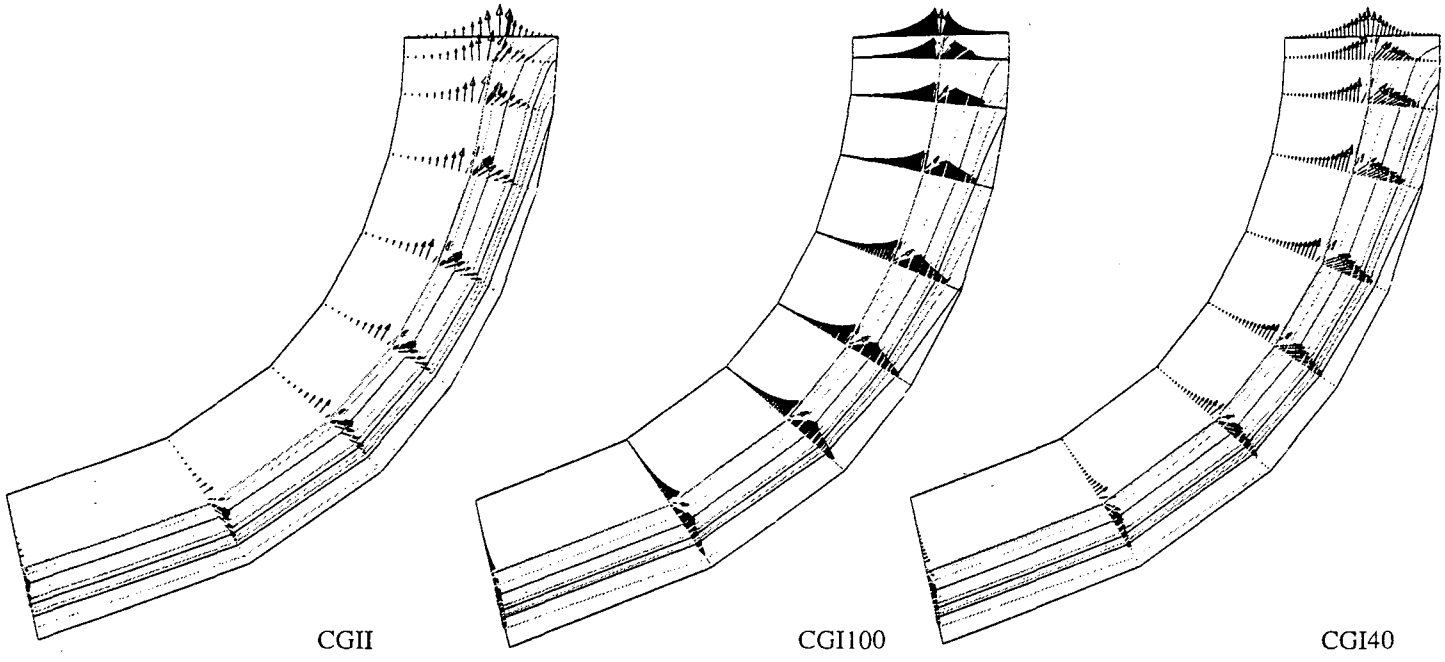

Figure 5 Comparison of vapor mass flux, $\dot{m}_g$, and liquid saturation, s_l, distribution at 113,000s when melt radius is at 1.5 m. Maximum $\dot{m}_g$ (kg/m^{2}s) / s_l: CGII: 1.05x10^{-3} / 0.80, CGI40: 7.77x10^{-4} / 0.87, CGI100: 9.02x10^{-4} / 0.78

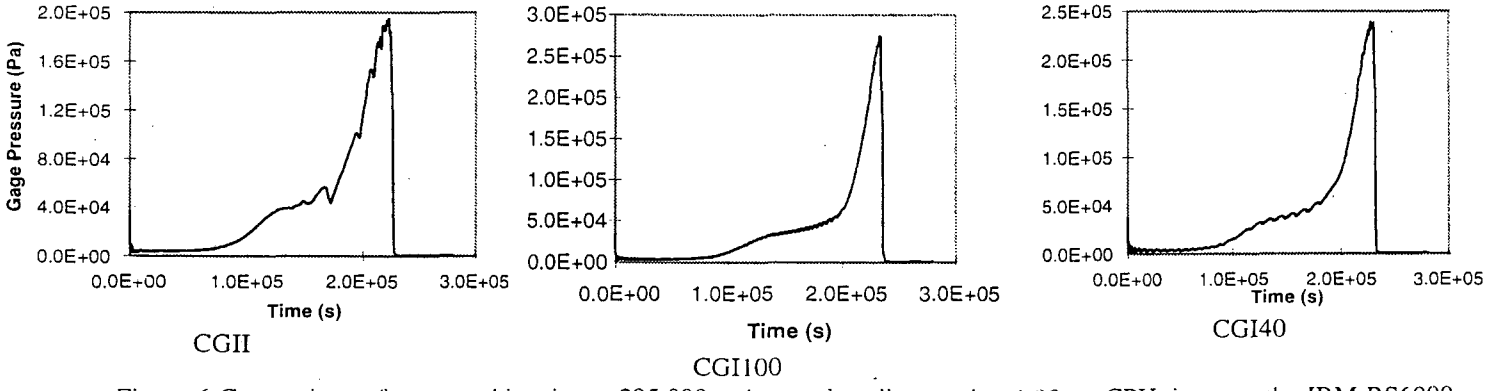

Figure 6 Comparison of pressure histories to 295,000s when melt radius reaches 1.90 m. CPU times on the IBM RS6000 model 520: CGII - 86,500 s; CGI100 - 660,700 s; CGI40 - 88,600 s.

In figure 4, it is seen that the use of CGII is effective for virtually eliminating the pressure oscillations. Even with 100 radial cell divisions, CGI still exhibits noticeable pressure oscillations over the time period of 113,000 s. In figure 5, the mass flux of vapor and the liquid saturation is depicted. The soil is dried out (containing only water vapor) to a radial location approximately halfway between the melt and outer wall. The mass of vapor being transported toward the soil surface in the dried out region is approximately the same as that in the wet region. The vapor mass flux just outboard of

the dry out region exhibits a strong component of radial velocity because of the vapor generation at this interface. Some of the outward flow of vapor recondenses when it reaches the cooler soil to cause the highest liquid saturation to exist near the outer wall. At 41,000 s, this recondensed vapor forms a layer between two drier regions of soil. By 113,000 s, this layer has reached the outer wall.

As the average liquid saturation in the soil between the melt and the outer wall increases, a higher rate of boiling occurs at the vapor-liquid interface. The increased generation rate of vapor combined with the narrowing of the soil channel between the melt and the outer wall cause the pressure level at the lowest point of the melt's surface to rise. Figure 6 illustrates the gage pressure history of the point at the line of symmetry on the melt's surface. At about 200,000 s, the pressure is seen to spike. The maximum gage pressure peak is predicted by CGI100 to reach 2.74 bar at 234,000 s, by CGI40 to reach 2.39 bar at 228,000 s, and by CGII to reach 1.95 bar at 223,000 s. CGI40 and CGII require about the same amount of CPU on the IBM RS6000 model 320 workstation. CGI40's spurious pressure oscillation illustrated in figure 4 does not seem to have adversely affected the prediction of the pressure history. The radial grid separation decreases as the simulation progresses; consequently, pressure oscillation diminishes. On the other hand, CGII's overprediction of liquid water loss through the soil's surface and the subsequent decreased fraction of water that remains before the pressure spike causes a pressure spike of somewhat lower magnitude than CGI100.

CONCLUSIONS

1. Computational prediction of the water-vapor transport around an ISV melt growing in soil confined by an impermeable wall can be useful for predicting pressure spikes.
2. The CGI model needs to be verified using experimental or analytical data for comparison but seems to offer a viable means to model heat and mass transport in the soil around an ISV melt.
3. The CGII does not currently offer any advantage over the CGI.
4. The CGII may be useful for modeling other ISV water balance problems in which a computational grid does not contract with the progression of time.

REFERENCES

Fatt, I. and Klikoff, W. A., 1959, "Effect of Fractional Wettability on Multiphase Flow through Porous Media" AIME Transactions, vol. 216, p. 246.

Fredlund, D. G. and Rahardjo, H., 1993, *Soil Mechanics for Unsaturated Soils*, Wiley-Interscience Publication.

Gottardi, G. and Venutelli, M., 1994, "One-Dimensional Moving Finite-Element Model of solute Transport", *Ground Water*, vol. 32, pp. 645 - 649.

Haywood, R. J., Renkisbulut, M., and Raithby, G. D., 1994, "Numerical Solution of Deforming Droplets at Intermediate Reynolds Numbers", *Numerical Heat Transfer, Part A*, vol. 26, pp. 253 - 272.

Kuo, C. H. and Schreiber, W. C., 1994, "An Interface Tracking Method for Solving Pure Substance Phase change Problems Using Nonsteady Curvilinear Coordinates", *Current Developments in Numerical Simulation of flow and Heat Transfer* (HTD-Vol. 275), pp. 57 - 64, ed. K. Vafai and J. L. S. Chen.

Lee, D. and Yeh, C. L., 1994, "Computation of Turbulent Recirculating Flows Using a Hybrid Adaptive Grid", ", *Numerical Heat Transfer, Part A*, vol. 26, pp. 415 - 430.

Leverett, M. C., 1941, "Capillary Behavior in Porous solids, AIME Trans., vol. 142, p. 152.

Pruess, K. and Narasimhan, T. N., 1985, "A practical Method for Modeling Fluid and Heat Flow in Fractured Porous Media", Society of Petroleum Engineers Journal, vol. 25, pp 14 - 26.

Pruess, K., 1986, *TOUGH User's Guide*, Sandia National Laboratories research report (NUREG/CR-4645, SAND 86-7104, RW)

Thompson, J. F., Warsi, Z. U. A., and Mastin, C. W., 1985, *Numerical Grid Generation: Foundations and Applications*, North-Holland, New York.

Udell, K. S. and Fitch, J. S., 1985, Heat and Mass Transfer in Capillary Porous Media Considering Evaporation, condensation, and Non-Condensible Gas Effects, 23rd ASME/AIChE National Heat Transfer Conference, Denver, Co..

Zhang, Hui and Moallemi, M. K., 1995, "Numerical Simulation of Hot-Dip Metallic Coating Process", *Int. J. Heat Mass Transfer*, vol. 38, pp. 241 - 257.

TOUGH90: A FORTRAN90 Implementation of TOUGH2

George J. Moridis

Earth Sciences Division, Lawrence Berkeley National Laboratory
University of California, Berkeley, CA 94720

Abstract
TOUGH90 is a FORTRAN90 implementation of TOUGH2, and represents a major change in syntax and architecture over TOUGH2, while maintaining full backward compatibility with existing input data files. The main features of TOUGH90 include dynamic memory management, the use of modules, derived types, array operations, matrix manipulation, and new and very powerful intrinsic procedures. These result in a faster, more efficient and compact code, which is conceptually simpler, and significantly easier to modify and upgrade.

1. Introduction

The TOUGH2 [*Pruess*, 1991] family of codes is a descendant of the earlier MULKOM code [*Pruess*, 1983], and provides multi-dimensional numerical models for simulating the coupled transport of water, vapor, non-condensible gas and heat in porous and fractured subsurface media. These models describe the processes and interactions involved in the flow of fluids in the subsurface, including the appearance and disappearance of liquid and vapor phases, boiling and condensation, multiphase flow due to pressure, gravity, and capillary forces, vapor adsorption with vapor pressure lowering, heat conduction, and heat exchange between rocks and fluids. TOUGH2 offers the flexibility of handling different fluid mixtures, e.g., water, water with tracer; water and CO_2; water and air; water and air with vapor pressure lowering, water and hydrogen; water, gas and an organic liquid phase. Additional information is available in a number of reports [*Pruess*, 1991, 1995; *Pruess et al.*, 1996; *Wu et al.*, 1996], and on the web at URL http://ccs.lbl.gov/TOUGH/.

The code in all the members of the TOUGH2 family is written in FORTRAN, the most widely used scientific programming language. Each FORTRAN version is a superset of all previous versions, which therefore allows the seamless integration of code segments developed at different times since the first release of the MULKOM [*Pruess*, 1983] parent to TOUGH2. In that respect, the current version of TOUGH2 can be compiled and run without any problem using a FORTRAN90 compiler.

FORTRAN90 is the latest version of FORTRAN, and was released as an international standard language in 1991 [*Ellis et al.*, 1994]. It has many new features and capabilities (based on experience gained with similar concepts in other languages) which extend the functionality of the language and broaden its applicability, in addition to providing its own contributions to the development of new programming concepts. TOUGH90 is a FORTRAN90 implementation of TOUGH2, written to take advantage of the unique capabilities of the language. As such, it does not represent an incremental change over TOUGH2 but is rather a completely rewritten code with different syntax and architecture, although full backward compatibility with existing input data files is maintained.

In this paper, the most important features of TOUGH90 are discussed, i.e., the use of modules, dynamic memory management, derived types, array operations, matrix manipulation, and new intrinsic procedures. For demonstration purpose, code segments of TOUGH90 are compared to equivalent TOUGH2 code.

2. The Use of Modules

Modules are new program units of FORTRAN 90, which provide a simple but highly adaptable method to compartmentalize code. They are defined as a collection of declarations and subprograms, and they make some or all of the entities declared within them accessible to the program units that invoke them.

Modules in TOUGH90 replace all uses of INCLUDE statements, COMMON blocks, and statement functions. The power of modules is in the collection of these basic concepts, i.e., shared declarations, globally accessible data, inline code expansion, etc., and generalization in the more flexible and powerful object of a module [*Kerrigan*, 1993]. This enables highly adaptable and easy to compartmentalize code, provides protection of data and of important source code of major data specifications or subprograms, and makes code upgrading an extremely easy task. In TOUGH90, all subprograms related to fluid properties are included in appropriate modules.

A simple TOUGH90 module is:

```
MODULE T90_Arithmetic
   IMPLICIT NONE
   SAVE
!Integer Parameters
   INTEGER, PARAMETER :: kind_n = SELECTED_REAL_KIND(P=14) !Set the required accuracy
END MODULE T90_Arithmetic
```

The T90_Arithmetic module demonstrates both the concept of the module and the power of the new intrinsic functions of FORTRAN90. In addition to REAL and REAL*8 variables, FORTRAN90 introduces the REAL(KIND=n) declaration. Setting n=4,8,16 yields single-, double- and quad-precision arithmetic. The intrinsic function SELECTED_REAL_KIND(P=14) returns the KIND parameter of a real data type with decimal precision of 14 digits. Thus, inclusion of the module in the various TOUGH90 program units allows the automatic setting of the arithmetic of real variables regardless of machine and compiler specificities. In the module

```
MODULE T90_Constants
   USE T90_Arithmetic
   IMPLICIT NONE
   SAVE
!Real Parameters
   REAL(KIND = kind_n), PARAMETER :: pi    = 3.1415926536e0
   REAL(KIND = kind_n), PARAMETER :: t_0   = 2.7316e2
   REAL(KIND = kind_n), PARAMETER :: zero  = 0.0
   REAL(KIND = kind_n), PARAMETER :: one   = 1.0
   REAL(KIND = kind_n), PARAMETER :: large = 1.0e50
END MODULE T90_Constants
```

which defines some basic parameters used in TOUGH90, the T90_Arithmetic module is invoked (thus making its contents accessible) by using the command USE T90_Arithmetic. Compared to a module, the concepts of COMMON and INCLUDE are limited.

3. Dynamic Memory Allocation

Memory allocation in TOUGH2 involves fixed-size arrays, and recompilation is required if the array size is increased. The need to recompile is eliminated in TOUGH90 by exploiting the dynamic memory management capabilities of FORTRAN90 through the use of allocatable arrays. These afford complete control over the array size, which is specified during the program execution. Moreover, memory occupied by arrays no longer needed is released, and made available to other arrays, thus increasing the size of tractable problems. This represents an important capability for creation and handling of internal work arrays in subprograms. An example of dynamic memory allocation is demonstrated in the Water_properties module below:

```
MODULE Water_properties
   USE T90_Arithmetic
   IMPLICIT NONE
!
   PRIVATE
   PUBLIC :: SAT_PRESSURE
!
   CONTAINS
      SUBROUTINE SAT_PRESSURE(tempr,sat_p,unit_n)
         IMPLICIT NONE
!
         INTEGER :: unit_n        !  Number of printout unit
         INTEGER :: nnn           !  size of "tmpr"
         INTEGER :: n_out         !  # of cells where "tmpr" is outside the range
         INTEGER :: i             !  counter
         INTEGER :: alloc_er1,alloc_er2,alloc_er3,dealloc_er1,dealloc_er2,dealloc_er3
! Integer arays
         INTEGER, DIMENSION(:), ALLOCATABLE :: igood_sat_p   !  flag for saturation pressure
! Real arays
         REAL(KIND = kind_n), DIMENSION(:), INTENT(IN)  :: tempr   ! temperature vector
         REAL(KIND = kind_n), DIMENSION(:)              :: sat_p   ! saturation pressure vector
         REAL(KIND = kind_n), DIMENSION(:), ALLOCATABLE :: tc,sc   ! intermediate arrays
! Constant coefficients for Psat = Psat(tempr)
```

```
      REAL(KIND = kind_n), DIMENSION(5) :: a_sat = (/-7.691234564e0,-2.608023696e1,-1.681706546e2,&
                                                    & 6.423285504e1,-1.189646225e2/)
      REAL(KIND = kind_n), DIMENSION(4) :: b_sat = (/4.167117320e0,  2.097506760e1,1.0e9,6.0e0/)
!
      nnn = SIZE(tempr)
      ALLOCATE (tc(nnn),          STAT = alloc_er1)          ! Allocate space for the work arrays
      ALLOCATE (sc(nnn),          STAT = alloc_er2)
      ALLOCATE (igood_sat_p(nnn), STAT = alloc_er3)

       IF(alloc_er1 /= 0 .OR. alloc_er2 /= 0 .OR. alloc_er3 /= 0) THEN
         WRITE(UNIT = unit_n, FMT = 6001)
          STOP
       END IF
!
      sc          = 0
      igood_sat_p = 0
!
      WHERE(tempr >= 1.0e0 .AND. tempr <= 5.0e2)        !  If the temperature is within range, ...
         tc = (tempr+2.7315e2)/6.473e2                  !  ... calculate sat_p
         sc = a_sat(1)*(1.0e0-tc) + a_sat(2)*(1.0e0-tc)**2 + a_sat(2)*(1.0e0-tc)**3 &
            &                     + a_sat(4)*(1.0e0-tc)**4 + a_sat(5)*(1.0e0-tc)**5
         sat_p = 2.212e7*exp(sc/(tc*(1.0+b_sat(1)*(1.0-tc)+b_sat(2)*(1.0-tc)*(1.0-tc))) &
               &             -(1.0-tc)/(b_sat(3)*(1.0-tc)*(1.0-tc)+b_sat(4)))
      ELSEWHERE                                         !  Otherwise, ...
         igood_sat_p = 2                                !  ... set the flag and
      END WHERE
!
      n_out = COUNT(igood_sat_p .EQ. 2)
      IF(n_out > 0) THEN
         WRITE(UNIT = unit_n, FMT = 6002) n_out         !  ... write the info out ...
         STOP
      END IF
!
      DEALLOCATE (tc,          STAT = dealloc_er1)
      DEALLOCATE (sc,          STAT = dealloc_er2)
      DEALLOCATE (igood_sat_p, STAT = dealloc_er3)
      IF(dealloc_er1 /= 0 .OR. dealloc_er2 /= 0 .OR. dealloc_er3 /= 0) THEN
         WRITE(UNIT = unit_n, FMT = 6003)
         STOP
      END IF
...
    END SUBROUTINE SAT_PRESSURE
!
END MODULE Water_properties
```

In its entirety, the `Water_properties` module includes all the variables and subprograms which compute the properties of the water substance in the liquid and vapor state. The portion shown above includes only the subprogram which calculates the saturation pressure of water as a function of temperature. Regarding dynamic memory allocation, the three temporary arrays `tc`, `sc` and `igood_sat_p` are first declared as allocatable arrays (1st and 2nd underlined statements). The size of the assumed-shape array `tempr` (containing the input temperature vector) is determined using the `SIZE` intrinsic function (3rd underlined statement), and then memory for the `tc`, `sc` and `igood_sat_p` arrays is allocated (4th through 6th underlined statements). After the computation of the saturation pressures (assumed-shape array `sat_p`), memory no longer needed is deallocated (last three underlined statements).

This module provides an opportunity to discuss some additional features of TOUGH90. `Water_properties` as shown above includes only a subprogram, but no variable declarations. It controls data access and protection through the use of the PRIVATE and PUBLIC statements. If these are missing, all contents in a module are public (i.e., accessible) to the program unit that invokes it. In the case of `Water_properties`, the contents of the module are all private (i.e., protected and inaccessible), with the exception of the subroutine declaration which is explicitly declared as public. Therefore, all the data in `Water_properties` (e.g., the values of the parameter arrays `a_sat` and `b_sat`) are protected and cannot be accessed and/or altered during execution.

The other very important feature of FORTRAN90 in the `Water_properties` module is the use of whole array operations. The statement `sc=0` involves such an operation by setting the whole `sc` array equal to 0. This is entirely equivalent to using a `DO` loop, but is simpler, less error-prone, and usually faster. The masked array assignment of the `WHERE` construct in the module is directly related to array processing. The assignment statements following it are executed for only those array elements for which the mask expression (i.e., `tempr>=1.0e0.AND.tempr<=5.0e2`, the range of acceptable temperatures) is true. Conversely, the statements following the `ELSEWHERE` statement are executed for those elements for which the mask is false. It must be clearly pointed out that although the `WHERE` construct has a certain syntactic similarity to the block `IF` construct, the former

does not involve sequential operations. Its effect is the simultaneous assignment of all the array elements, with the mask either preventing some of the assignment taking place, or causing different ones to take place.

4. Derived Types

FORTRAN77 in TOUGH2 requires that an array contain information of a single data type, leading to arrays which hold either numbers of characters, but not both. FORTRAN90 in TOUGH90 allows the creation of new data types to supplement the intrinsic types provided by the language. These derived types are powerful tools for the creation of data structures which contain elements of any data type mixed freely in any proportion. Gridblock names, connections and properties can thus be grouped in derived-type arrays, allowing easier handling as well as programming. The use of derived types is illustrated in the module `T90_grid`.

```
MODULE T90_Grid
   USE T90_Arithmetic
!
   IMPLICIT NONE
   SAVE
!Type Declaration
   TYPE element_attributes
      CHARACTER (LEN = 5) :: name      ! element name
      INTEGER             :: mat_n     ! element rock number
      REAL(KIND = kind_n) :: vol       ! element volume
      REAL(KIND = kind_n) :: phi       ! element porosity
      REAL(KIND = kind_n) :: p         ! element pressure
      REAL(KIND = kind_n) :: tempr     ! element temperature
   END TYPE element_attributes
!
   TYPE connection_attributes
      CHARACTER (LEN = 5) :: name_1,name_2    ! element names in a connection
      INTEGER             :: nex_1,nex_2      ! element numbers in a connection
      INTEGER             :: isox             ! specifies pemeability as k = k(isox); isox=1,2,3 for x,y,z
      REAL(KIND = kind_n) :: del_1,del_2      ! element distances from interface
      REAL(KIND = kind_n) :: area             ! connection area
      REAL(KIND = kind_n) :: beta             ! angle between the g vector and the element line
   END TYPE connection_attributes
!Dimensioning
   TYPE (element_attributes),    DIMENSION(:), ALLOCATABLE :: element
   TYPE (connection_attributes), DIMENSION(:), ALLOCATABLE :: connection
!
END MODULE T90_Grid
```

The derived types `element_attributes` and `connection_attributes` which are defined in the module include character, integer and real data types. Note that two allocatable arrays are defined: `element` of type `element_attributes` and `connection` of type `connection_attributes`, respectively. Memory for these arrays is allocated dynamically immediately after determining the number of elements (`nel`) and connections (`ncon`), i.e.,

```
ALLOCATE (element(nel),     STAT = alloc_er1)
ALLOCATE (connection(ncon), STAT = alloc_er2)
```

Array operations can be used to assign values to the various components of the derived types. For example, an initial temperature distribution of 20 ^{0}C is assigned by the statement

```
element%tempr = 20.
```

Thus the set of TOUGH2 statements

```
PARAMETER(MNEL=800,MNCON=2400,MNEQ=3,MNK=2,MNPH=2,MNB=6)
PARAMETER(MNOGN=50,MGTAB=2000)
...
COMMON/NN/NEL,NCON,NOGN,NK,NEQ,NPH,NB,NK1,NEQ1,NBK,NSEC,NFLUX
...
COMMON/E1/ELEM(MNEL)
COMMON/E2/MATX(MNEL)
COMMON/E3/EVOL(MNEL)
COMMON/E4/PHI(MNEL)
COMMON/E5/P(MNEL)
COMMON/E6/T(MNEL)
...
COMMON/C1/NEX1(MNCON)
COMMON/C2/NEX2(MNCON)
COMMON/C3/DEL1(MNCON)
COMMON/C4/DEL2(MNCON)
COMMON/C5/AREA(MNCON)
COMMON/C6/BETA(MNCON)
COMMON/C7/ISOX(MNCON)
COMMON/C9/ELEM1(MNCON)
COMMON/C10/ELEM2(MNCON)
```

is replaced by the T90_grid module and the following T90_Dimensions module

```
MODULE T90_Dimensions
   IMPLICIT NONE
   SAVE
!Integer Parameters
   INTEGER :: nel       ! # of elements/gridblocks
   INTEGER :: nela      ! # of active elements
   INTEGER :: ncon      ! # of connections
   INTEGER :: neq       ! # of equations per element
   INTEGER :: nph       ! # of phases
   INTEGER :: nk        ! # of components
   INTEGER :: nogn      ! # of sources and/or sinks
   INTEGER :: neq_tot   ! # of total equations ( = order of the Jacobian)
   INTEGER :: n_zero    ! # of non-zero elements of the Jacobian
END MODULE T90_Dimensions
```

The information contained therein is accessible to all the program that invoke the modules. Note that there is no explicit declaration of the values of the variables in T90_Dimensions. This is because the array sizes in TOUGH90 are allocated dynamically. The use of the derived types allows a simpler and more intuitive handling of the grid-related properties.

5. Array Operations, Matrix Manipulation and Expanded Set of Intrinsic Functions

An indication of the power and convenience of whole array operations has already been shown in Section 3. In this section we discuss some additional features of array operations and related intrinsic procedures. This is illustrated by an example involving the following code segment from the DBCG subroutine of the T2CG1 module [*Moridis and Pruess*, 1995]:

```
         IF(ITER .EQ. 1) THEN
            DO 18 I = 1,N
              P(I) = Z(I)
              PP(I) = ZZ(I)
   18       CONTINUE
         ELSE
            BK = BKNUM/BKDEN
            DO 20 I = 1, N
               P(I)  = Z(I) + BK*P(I)
               PP(I) = ZZ(I) + BK*PP(I)
 20         CONTINUE
         ENDIF
         BKDEN = BKNUM
C
         CALL MATVEC(N, P, Z, NELT, IA, JA, A, ISYM)

         DDOT = 0.D0
         DO 25 I = 1,N
           DDOT = DDOT + PP(I)*Z(I)
   25    CONTINUE
         AKDEN = DDOT
```

In the same routine of TOUGH90 this segment is replaced by the much easier and more compact

```
IF(ITER .EQ. 1) THEN
   p  = z
   pp = zz
ELSE
   BK = BKNUM/BKDEN
   p  = z + bk*p
   pp = zz + bk*pp
ENDIF
   BKDEN = BKNUM
!
CALL MATVEC(N, P, Z, NELT, IA, JA, A, ISYM)
!
AKDEN = DOT_PRODUCT(pp,z)
```

It is evident that the code in TOUGH90 is more intuitive and much easier to develop and follow, as the code is quite similar to the descriptive pseudocode. The above example also illustrates the use of the DOT_PRODUCT array intrinsic function, which returns the dot product of the two vectors in its argument list and can be significantly faster than the equivalent DO loop, in addition to being simpler and less error-prone. Similarly, the determination of the maximum residual and its location in the MULTI subroutine changes from

```
C
C
C-----TEST FOR CONVERGENCE----------------------------------------------
C
      RERM=0.D0
      DO10 N=1,NELA
         NLOC=(N-1)*NEQ
```

```
      DO10 K=1,NEQ
         NLM=NLOC+K
         DOA=ABS(DOLD(NLM))
         IF(DOA.LT.RE2) RER=R(NLM)/RE2
         IF(DOA.GE.RE2) RER=R(NLM)/DOLD(NLM)
         IF(ABS(RER).LE.RERM) GOTO 10
         RERM=ABS(RER)
         NER=N
         KER=K
   10 CONTINUE
```

to the following array-based syntax in TOUGH90.

```
WHERE(abs(dold).LT.RE2)
   rerm = MAXVAL(abs(r/RE2))
   merm = MAXLOC((abs(r/RE2)))
ELSEWHERE
   rerm = MAXVAL(abs(r/dold))
   merm = MAXLOC((abs(r/dold)))
END WHERE
nnn = SIZE(r,DIM=2)
ner = merm(1)
ker = merm(nnn)
```

The above segment uses the WHERE construct, and obtains the maximum values and their locations using the MAXVAL and MAXLOC intrinsic procedures. The array merm contains the indices of the location of the maximum residual, from which the corresponding element and equation numbers are determined.

The matrix manipulation capabilities of FORTRAN90 greatly reduce the coding complexity in the handling of linear algebra. All the matrix-vector multiplication routines (e.g., DSMV, DSMTV, DSLUI, DSLUTI) in the T2CG1 package [*Moridis and Pruess*, 1995] have been replaced by the very efficient (in terms of speed and storage) procedure

```
MATMUL(matrix_A,matrix_B)
```

where matrix_A and matrix_A are arrays of rank 1 or 2. The replacement of whole TOUGH2 subroutines by the simple and powerful new intrinsic functions available to the FORTRAN90 is quite common in TOUGH90. For example, the FLOP subroutine in TOUGH2 determines the number of significant decimal digits and the default increment for the calculation of derivatives based on machine-specific values.

```
SUBROUTINE FLOP
...
      A = SQRT(.99D0)
      B = A
      DO 1 N=1,260
         B = B/2.D0
         C = A+B
         D = C-A
         IF(D.EQ.0.D0) GO TO 2
    1 CONTINUE
C
    2 B2=B*2.D0
      N10=-INT(LOG10(B2))
      DF=SQRT(B2)
...
END
```

FLOP is replaced in TOUGH90 by the statements

```
n10 = PRECISION(one)
df  = SQRT(EPSILON(one))
```

which use the intrinsic FORTRAN90 functions PRECISION (determining the decimal precision of a variable of the same type as one) and EPSILON (returning the smallest possible number ε such that $1.0+\varepsilon$ is numerically different than 1). Similarly, the subroutine SECONDS (which provides timing information in TOUGH2 by using system- and machine-specific subroutines) is replaced in TOUGH90 by::

```
CALL SYSTEM_CLOCK(COUNT=itime, COUNT_RATE=irate)
```

This is a FORTRAN90 generic statement, and is compiler- and machine-independent, thus eliminating the need for adjustments which TOUGH2 requires when moving between computing platforms and compilers.

6. Summary

TOUGH90 is a FORTRAN90 implementation of TOUGH2, and represents a major change in syntax and architecture over TOUGH2, while maintaining full backward compatibility with existing input data files. The main features of TOUGH90 include dynamic memory management, the use of modules, derived types, array operations, matrix manipulation, and new and very powerful intrinsic procedures. These result in a faster, more efficient and compact code, which is conceptually simpler, and significantly easier to modify and upgrade.

Modules in TOUGH90 replace all uses of INCLUDE statements, COMMON blocks, and statement functions. Additionally, all subprograms related to fluid properties are included in the appropriate modules. The power of modules is in the collection of the basic concepts represented in the standard FORTRAN features, i.e., shared declarations, globally accessible data, inline code expansion, etc., and generalization in the more flexible and powerful object of a module. This enables highly adaptable and easy to compartmentalize code, provides protection of data and of important source code of major data specifications or subprograms, and makes code upgrading an extremely easy task.

The need to recompile TOUGH90 with an increasing problem size is eliminated by exploiting the dynamic memory management capabilities of FORTRAN90. Allocatable arrays allow the total size of the arrays to be specified through the input files during the program execution. Moreover, memory occupied by arrays no longer needed is released, and made available to other arrays. This represents an important capability for creation and handling of internal work arrays in subprograms, and increases the size of tractable problems.

Derived types are powerful tools for the creation of data structures which contain elements of any data type mixed freely in any proportion. Gridblock names, connections and properties can thus be grouped in derived-type arrays, allowing easier handling as well as programming. TOUGH90 uses the array operations of FORTRAN90 for a code that is more transparent, faster and easier to program. Extensive use of array and matrix manipulation operations is made in the linear algebra of the solvers in TOUGH90. This leads to a sizable reduction in the memory requirements and improvements in the execution speed.

7. Acknowledgments

This work was supported by the Assistant Secretary for Energy Efficiency and Renewable Energy, Office of Geothermal Technologies, of the U.S. Department of Energy, under contract No. DE-AC03-76SF00098. Drs. J. Apps and C. Oldenburg are thanked for their helpful review comments.

8. References

Ellis, T.M.R., I.R. Philips and T.M. Lahey, *FORTRAN90 Programming*, Addison-Wesley, New York, NY. 1994.

Kerrigan, J.F., *Migrating to FORTRAN90*, O'Reilly and Associates, Sebastopol, CA, 1993.

Moridis, G.J. and K. Pruess, Flow and transport simulations usingT2CG1, a package of preconditioned conjugate gradient solvers for the TOUGH2 family of codes, *Rep. LBL-36235*, Lawrence Berkeley National Laboratory, Berkeley, CA, 1995.

Pruess, K, Development of the general purpose simulator MULKOM, *Rep. LBL-15500*, Lawrence Berkeley Laboratory, Berkeley, CA, 1983.

Pruess, K., TOUGH2 - A general-purpose numerical simulator for multiphase fluid and heat flow, , *Rep. LBL-29400*, Lawrence Berkeley Laboratory, Berkeley, CA, 1991.

Pruess, K (ed), Proceedings of the TOUGH2 Workshop '95, *Rep. LBL-37200*, Lawrence Berkeley Laboratory, Berkeley, CA, 1995.

Pruess, K., A. Simmons, Y.S. Wu and G. Moridis, TOUGH2 software qualification, *Rep. LBNL-38383*, Lawrence Berkeley National Laboratory, Berkeley, CA, 1996.

Wu, Y.S., C.F. Ahlers, P. Fraser, A. Simmons and K. Pruess, Software qualification of selected TOUGH2 modules, *Rep. LBNL-39490*, Lawrence Berkeley Laboratory, Berkeley, CA, 1996.

Presented at TOUGH Workshop '98
Lawrence Berkeley National Laboratory, May 4-6, 1998

Overview of TOUGH2, Version 2.0

Karsten Pruess, Curt Oldenburg, and George Moridis

Earth Sciences Division, Lawrence Berkeley National Laboratory
University of California, Berkeley, CA 94720

Introduction

TOUGH2 is a general-purpose numerical simulation program for multiphase, multicomponent fluid and heat flows in porous and fractured media (Pruess, 1991). Chief application areas are in geothermal reservoir engineering, nuclear waste isolation studies, environmental assessment and remediation, oil and gas production and storage, and flow under variably saturated conditions in the vadose zone (Pruess, 1995).

The governing equations for multiphase fluid and heat flow have the same mathematical form, regardless of the nature and number of fluid phases and components present. This suggests setting up a simulation code with a modular architecture, in which the main flow and transport module can interface with different fluid property modules, allowing for a flexible description of different types of flow systems. Such an architecture was first implemented at Berkeley in a research code known as "MULKOM" in the early 80s and later formed the basis of TOUGH, a more specialized multiphase code for water-air-heat (Pruess, 1987). We now use the term "MULKOM" to denote the general architecture or "blueprint" of the code, while the specific FORTRAN77 implementation is called "TOUGH2."

Since TOUGH2 was first released to the public in 1991, the only change in the "official," publicly available version occurred in 1994, when a set of preconditioned conjugate gradient solvers replaced the previous exclusive reliance on the direct solver MA28 (Moridis and Pruess, 1995). In the intervening years, considerable development of process simulation capabilites and user features has occurred at Berkeley and elsewhere. As had been true for previous versions of the TOUGH/MULKOM codes, work at Berkeley was primarily driven by specific application needs, rather than by a desire for comprehensive process simulation capabilities as such.

Version 2.0 of TOUGH2 includes enhanced versions of the earlier program modules, as well as a selection of newly developed modules for more comprehensive process simulation capabilities. Some of the criteria and objectives used in assembling the new TOUGH2-version were as follows:

- add significant capabilities for simulating flow and transport processes, that will be useful for engineering and geoscience applications;
- add features to improve useability of the code, but avoid encumbering users with "feature creep;"
- keep code changes to the minimum required to achieve desired capabilities;
- remain as much as possible upward compatible with the earlier version;
- stay with FORTRAN77 and publish source code;
- facilitate code maintenance by minimizing the number of independent modules and "minor" variations among them;
- increasingly emphasize solved problems and internal documentation as a way of communicating code features and use.

This paper summarizes the main features and advances of Version 2.0 relative to the earlier release, including (1) several new EOS modules for different fluid mixtures, (2) enhanced capabilities for previously released fluid property modules, (3) description of diffusion and dispersion in multiphase systems, (4) strongly coupled flow and transport processes, (5) coupling between flow in geothermal reservoir and wellbores in two-phase conditions, (6) tracer transport with sorption and radioactive decay, and (7) flow in media with "strong" heterogeneity. In addition, numerous enhancements were made to facilitate applications to more diverse and demanding flow problems.

Full documentation and user instructions for these new modules will be available in a self-contained user's guide (in preparation).

Here we highlight the scope of major enhancements in modeling capabilities for flow and transport of multiphase, multicomponent fluids, and for a coupled treatment of flow in reservoirs and wellbores.

Fluid property modules

The original TOUGH2 released in 1991 provided five different fluid property or "EOS" (equation-of-state) modules. Labeled "EOS1" - "EOS5," these included the main modules for geothermal and nuclear waste applications. The new Version 2.0 release of TOUGH2 includes improved versions of these five EOS modules, as well as several new fluid property modules (Table 1). The subroutines for water properties (COWAT, SUPST, SAT) were replaced with faster routines written by M. O'Sullivan (University of Auckland, New Zealand). In EOS2, an improved correlation for the temperature dependence of CO_2 solubility in water was implemented that remains accurate for temperatures down to 5 °C (see Fig. 1; Battistelli et al., 1997).

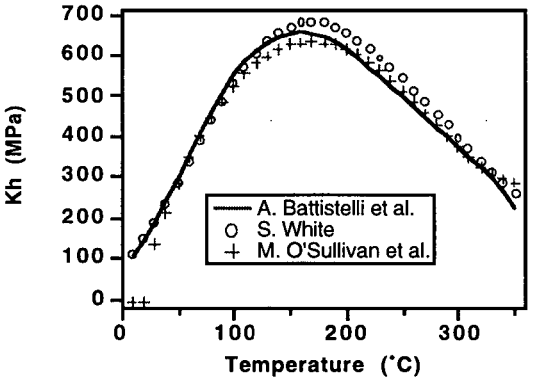

Figure 1. Henry's law coefficient for CO_2 solubility in water. EOS2 initially used a correlation developed by O'Sullivan et al. (1985) for geothermal applications. This was recently replaced with a correlation developed by Battistelli et al. (1997). Another correlation due to S. White (private communication) is also shown for comparison.

EOS4 now has an optional single-component (water only) capability, and initialization of two-phase conditions can be made either by specifying saturation, or relative humidity. We proceed to briefly summarize the new EOS modules.

EOS7

EOS7 is an extension of the EOS3 module. The aqueous phase is described as a mixture of brine (mass fraction X^b) and water (mass fraction $X^w=1-X^b$). Following Reeves et al. (1986) and Herbert et al. (1988), simple mixing models are used for viscosity and density of the aqueous phase. EOS7 does not explicitly describe the solid salt, and does not represent physical constraints on solubility. This type of approach is most suitable for isothermal or moderately non-isothermal flow systems that do not involve strong phase change effects. It is applicable to single-phase and two-phase (water-gas) flow systems with variable salinity, ranging from pure water to saturated NaCl brines.

Table 1. New fluid property modules for TOUGH2

Module	Capabilities
EOS7	water, brine, air
EOS7R	water, brine, air, parent-daughter radionuclides
EOS8	water, "dead" oil, non-condensible gas
EOS9	variably-saturated flow according to Richards' equation
EWASG	water, salt (NaCl), non-condensible gas (includes precipitation and dissolution, with porosity and permeability change)

EOS7R

This is an extension of EOS7 which includes a parent-daughter pair of radionuclide tracers for a total of five mass components. The tracers may partition between aqueous and gas phases, and may sorb on the solid grains. A detailed description is available in a laboratory report (Oldenburg and Pruess, 1995a).

EOS8

This module provides a basic three-phase flow modeling capability for fluid mixtures consisting of water, a non-condensible gas, and a "dead" oil. Most fluid properties are defined through user-supplied parameters. EOS8 contains extensive comments that document the fluid property model and user inputs. This

module is primarily intended as a platform for the development of research applications.

EOS9

EOS9 was designed for applications in vadose zone hydrology. It considers isothermal, saturated-unsaturated flow of water, with air a passive bystander. For these conditions, the general multiphase flow equations solved in TOUGH2 reduce to Richards' (1931) equation (Oldenburg and Pruess, 1993).

EWASG for H_2O-NaCl-CO_2 mixtures

Thermophysical properties

The EWASG fluid property module (Battistelli et al., 1997) features an accurate description of three-phase (aqueous, solid, gas) mixtures of three components (water, sodium chloride, non-condensible gas). The dependence of brine density, enthalpy, viscosity, and vapor pressure on salinity is taken into account, as are effects of salinity on gas solubility ("salting out") and heat of solution. TOUGH2/EWASG includes a capability for modeling precipitation and dissolution of salt, and associated porosity and permeability changes. It also models vapor pressure-lowering effects from suction pressures (capillary and vapor adsorption effects). The thermophysical property correlations used in EWASG are accurate for most conditions of interest in geothermal reservoir studies: temperatures in the range from 100 to 350 °C, fluid pressures up to 80 MPa, CO_2 partial pressures up to 10 MPa, and salt mass fraction up to halite saturation. With the exception of brine enthalpy, thermophysical property correlations are accurate to below 10 °C. Several choices are available for the non-condensible gas (CO_2, air, CH_4, H_2, N_2).

TOUGH2/EWASG considers the rock matrix as inert, except for a single active mineral, NaCl, which may be present in both aqueous solution and as a solid precipitate. Solid precipitated salt is treated in complete analogy to fluid phases (aqueous, gas), except that, being immobile, its relative permeability is identically zero. From mass balances on salt in liquid and solid phases we calculate the volume fraction of precipitated salt in the original pore space ϕ_0, which is termed "solid saturation," and denoted by S_S. A fraction $\phi_0 S_S$ of reservoir volume is occupied by precipitate, while the remaining void space $\phi(S_s) = \phi_0(1-S_s)$ is available for fluid phases. The reduction in pore space reduces the permeability of the medium.

Production from a reservoir with hypersaline brine and CO_2

TOUGH2/EWASG was used to simulate geothermal production from a hypothetical reservoir with high salinity and CO_2. A difficulty in applications is the need to specify the relationship between porosity and permeability change. Laboratory experiments have shown that modest reductions in porosity from chemical precipitation can cause large reductions in permeability (Vaughan, 1987). This is explained by the convergent-divergent nature of natural pore channels, where pore throats can become clogged by precipitation while disconnected void spaces remain in the pore bodies (Verma and Pruess, 1988). The effects depend on pore geometry, and are expected to be quite different for different porous media (Weir and White, 1995). In the simulation presented here, we use a relationship derived by Verma and Pruess (1988) for a tube-in-series pore channel model. We specify a single well that produces at a constant rate of 65 kg/s from an infinite-acting reservoir in 1-D radial flow geometry. Other parameters are given in Table 2.

Table 2. Parameters for production from a saline reservoir with CO_2

Reservoir thickness	500 m
Permeability	50×10^{-15} m^2
Porosity	0.05
Relative permeability Corey curves S_{lr} = S_{gr} =	 0.30 0.05
Rock grain density	2600 kg/m^3
Specific heat	1000 J/kg °C
Thermal conductivity	2.1 W/m °C
Initial conditions	
Temperature	275.55 °C
Gas saturation	0.45
Pressure	60.0 bar
NaCl mass fraction in liquid phase	0.30
CO_2 partial pressure	14.79 bar
Wellblock radius	5 m

Fluid withdrawal causes pressures to drop near the production well. Boiling of reservoir

fluid gives rise to dilution of CO_2 in the gas phase and to increased concentrations of dissolved NaCl, which begins to precipitate when the aqueous solubility limit is reached. As the boiling front recedes from the well, solid precipitate fills approximately 10 % of the original void space (see Fig. 2), causing permeability to decline to approximately 28 % of its original value.

Specifications of this problem (1-D radial geometry, homogeneous medium, uniform initial conditions, constant well rate) were chosen so that a "similarity solution" should be applicable, which should depend on radial distance R and time t only through the similarity variable $x = R^2/t$ (O'Sullivan, 1981). This similarity property should hold even when all complexities of two-phase flow with non-linear relative permeabilities, CO_2 exsolution effects, salt precipitation, and associated porosity and permeability effects are taken into account. Simulated results for two different times ($5x10^5$ and $2x10^6$ seconds) are plotted as a function of the similarity variable in Fig. 2. It is seen that the similarity property holds very accurately for all thermodynamic variables.

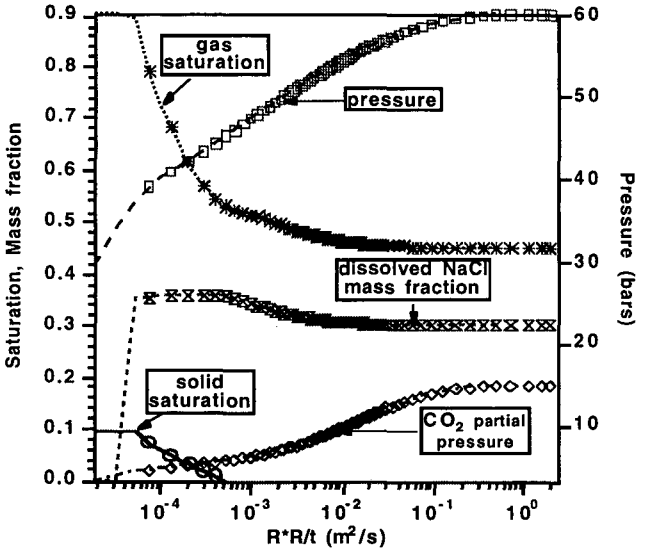

Figure 2. Simulated thermodynamic conditions for 1-D radial flow problem with salinity and non-condensible gas, plotted as a function of the similarity variable $x = R^2/t$. Results at $2x10^6$ seconds are shown as lines, while the data at $t = 5x10^5$ seconds are given as symbols.

Coupled wellbore flow

Geothermal production wells typically operate at (nearly) constant wellhead pressures. As flow rate and flowing enthalpy change with time, wellbore pressure gradients and flowing bottomhole pressures will also change. From a conceptual point of view, the most straightforward way to describe production from geothermal wells is to set up and solve equations for flow in the reservoir and flow in the wellbore in a fully coupled manner. This approach was taken by Hadgu et al. (1995) who coupled the reservoir simulator TOUGH with the wellbore simulator WFSA (Hadgu and Freeston, 1990).

From a practical viewpoint, an alternative approach may be preferable in which the wellbore and reservoir simulations are performed separately. Flowing wellbore pressures may be represented by tables which can be generated through repeated running of a wellbore simulator ahead of the reservoir simulation. As discussed by Murray and Gunn (1993), this offers a number of advantages, including increased robustness and calculational efficiency. It also makes it possible to use different wellbore simulators and two-phase flow correlations without any programming changes in the reservoir simulation code.

We have incorporated a tabular interpolation scheme for dynamic changes of flowing bottomhole pressure into TOUGH2. Flowing enthalpy h at the downhole well feed is known from phase mobilities and enthalpies calculated by the reservoir simulator. The unknown well flow rate q and flowing bottomhole pressure P_{wb} are then obtained by Newton-Raphson iteration on

$$R(q) \equiv q - \left(\sum \frac{k_{r\beta}}{\mu_\beta} \rho_\beta \right) \cdot PI \cdot \left(P - P_{wb}(q,h) \right) = 0 \qquad (1)$$

where $P_{wb}(q,h)$ is interpolated from tables, see Fig. 3. The iterative solution of Eq. (1) was embedded in the "outer" (Newtonian) iteration performed by TOUGH2 on the coupled mass and heat balance equations. Additional computational work in comparison to conventional simulations with constant downhole pressure is insignificant.

Application

As an application example we have considered a reservoir-wellbore system similar to Problem 1 of Hadgu et al. (1995). An exact replication of their test problem is not possible because they did not give complete specifica-

tions in their paper. A well of 0.2 m inside diameter produces from a 500 m thick two-phase reservoir containing water at initial conditions of P = 60 bars, T = $T_{sat}(P)$ = 275.5 °C, S_g = 0.1. Wellhead pressure is 7 bars, and feed zone depth is 1000 m. Fig. 3 shows a contour diagram of flowing bottomhole pressures obtained by running the HOLA wellbore simulator (Aunzo et al., 1991) for a range of flow rates and enthalpies.

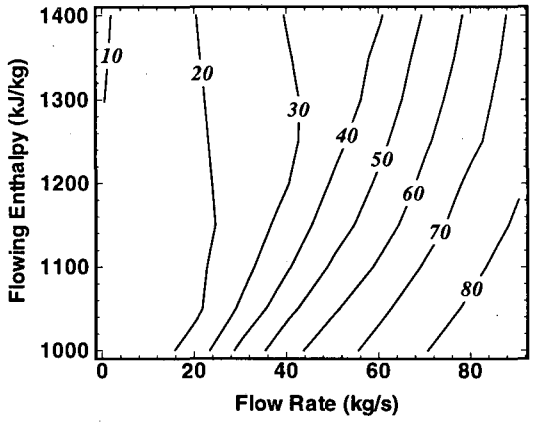

Figure 3. Flowing bottomhole pressures (in bars) at 1000 m feed zone depth for a well of 20 cm (≈ 8 inch) inside diameter, producing at 7 bar wellhead pressure (calculated from HOLA; Aunzo et al., 1991).

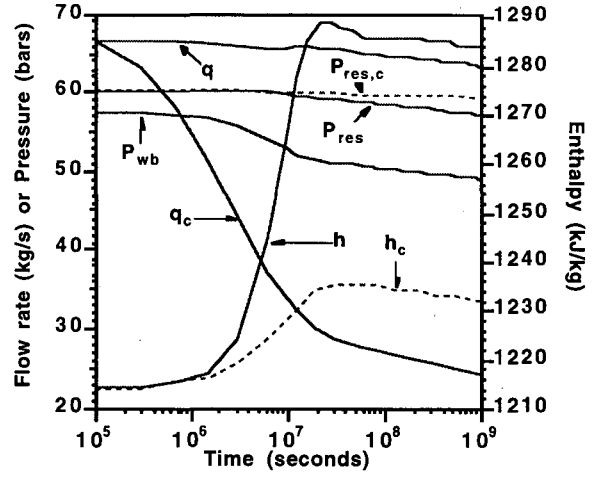

Figure 4. Simulated flow rate (q), flowing enthalpy (h), flowing bottomhole pressure (P_{wb}) and reservoir pressure in well grid block (P_{res}) for a problem adapted from Hadgu et al. (1995). Results obtained for constant bottomhole pressure of P_{wb} = 57.37 bars, labeled q_c, h_c, and $P_{res,c}$, are also shown.

Our coupled reservoir-wellbore flow simulation uses the well pressure data shown in Fig. 3. Results are given in Fig. 4, along with a comparison case in which flowing wellbore pressure was kept constant at the early-time value obtained in the coupled calculation (P_{wb} = 57.37 bars). Our results are similar to those of Hadgu et al. (1995). Flow rates and flowing enthalpies for the coupled model are a few percent higher than those obtained by Hadgu et al., while flowing bottomhole pressures are slightly lower. The simulation with constant bottomhole pressure gives a rapidly declining production rate that agrees well with Hadgu et al. (1995).

Multiphase diffusion and dispersion

Molecular diffusion

All fluid property modules now optionally include diffusive fluxes of all components in all phases. In multiphase conditions, the diffusive flux of mass component κ in phase β is customarily written as

$$\mathbf{f}_\beta^\kappa = -\phi S_\beta \rho_\beta \tau_0 d_\beta^\kappa \nabla X_\beta^\kappa \qquad (2)$$

where ∇X is the mass fraction gradient. The accumulation term in the mass balance equation for component κ includes the same group $\phi S_\beta \rho_\beta$ as appears in Eq. (2), so that the effective diffusion coefficient, $\tau_0 d_\beta^\kappa$, is saturation-independent in this formulation. This does not appear to be realistic.

TOUGH2 offers an alternative, more general expression for multiphase diffusive flux, as follows

$$\mathbf{f}_\beta^\kappa = -\phi \tau_\beta \rho_\beta \tau_0 d_\beta^\kappa \nabla X_\beta^\kappa \qquad (3)$$

$\tau_\beta = \tau_\beta(S_\beta)$ is a saturation-dependent tortuosity which is poorly known at present. In the spirit of conceptual consistency, we currently use the assignment $\tau_\beta(S_\beta) = k_{r\beta}(S_\beta)$.

Hydrodynamic dispersion

Following Scheidegger's seminal paper (1954), the spreading of solute plumes due to "small-scale" randomness of permeable media has traditionally been described in analogy to Fickian diffusion. Much hydrogeological research during the last twenty years has shown this analogy to be of limited validity and usefulness for field problems; yet for

many applications there are no practical alternatives.

We have incorporated a "standard" approach to hydrodynamic dispersion, with appropriate generalization to multiphase flow systems, in a specialized TOUGH2 module known as "T2DM" (Oldenburg and Pruess, 1993, 1995b). Dispersive mass flux is given by

$$\mathbf{F}^{\kappa}\Big|_{dis} = -\sum_{\beta} \rho_{\beta} \overline{\mathbf{D}}_{\beta}^{\kappa} \nabla X_{\beta}^{\kappa} \qquad (4)$$

where

$$\overline{\mathbf{D}}_{\beta}^{\kappa} = D_{\beta,T}^{\kappa} \overline{\mathbf{I}} + \frac{\left(D_{\beta,L}^{\kappa} - D_{\beta,T}^{\kappa}\right)}{u_{\beta}^{2}} \mathbf{u}_{\beta} \mathbf{u}_{\beta} \qquad (5)$$

is the dispersion tensor, with $\mathbf{u}_{\beta}$ the Darcy velocity, and $D_{L,T}$ the longitudinal and transverse dispersion coefficients. Evaluation of dispersive fluxes requires knowledge of the full velocity and concentration gradient vectors at grid block interfaces. These depend not only on conditions in the two grid blocks between which dispersive mass transport occurs, and hence require interpolation using data from several additional grid blocks. T2DM is designed for two-dimensional rectangular grids, which greatly facilitates such interpolation. A fully three-dimensional implementation for general irregular grids is in an earlier stage of development (Wu and Pruess, 1998), and is not included in Version 2.0 of TOUGH2.

Inclusion of dispersive fluxes automatically provides a capability for modeling strongly coupled flow and transport. This is because TOUGH2 fully accounts for all thermophysical property dependencies on primary thermodynamic variables, and all mass and energy balances are solved completely simultaneously. An example where dispersive spreading of salinity has a strong impact on fluid density, and subsequently alters buoyancy effects in advective flow, is given in (Oldenburg and Pruess, 1995b).

Linear equation solvers

Most of the computational work in the numerical simulation of fluid and heat flow arises in the solution of large systems of linear equations. TOUGH2, Version 2.0, features a new solver package "T2SOLV" (Moridis and Pruess, 1998). In addition to the algorithms previously included in T2CG1, T2SOLV includes the BiCGSTAB method (van der Vorst, 1992; Sleijpen and Fokkema, 1993), and a banded direct solver. It also features a choice of different preconditioners for poorly conditioned matrices, such as matrices with mostly zeros in the main diagonal. Test calculations have shown that T2SOLV can handle difficult flow problems for which T2CG1 failed. Full details have been presented in (Moridis and Pruess, 1998).

Miscellaneous code enhancements

We briefly summarize various enhancements made in the new Version 2.0 of TOUGH2. In order to allow for coupled reservoir-wellbore flow simulations, as discussed above, subroutine QU was completely re-written in modular structure. It now features a "rigorous step-rate capability:" for a user-specified table of time-dependent rates, production rate during time stepping can be automatically adjusted in such a manner that the total cumulative mass exchange $\sum q_i (t_{i+1} - t_i)$ is rigorously conserved. An analogous capability is available for flowing enthalpy.

Subroutine MULTI now includes a capability for radiative heat transfer between grid blocks. For strongly heterogeneous media, permeability modifiers ζ can be applied to each grid block, so that $k_n \rightarrow k_n' = \zeta_n \times k_n$. Strength of capillary pressure is scaled consistently with permeability on a grid-block-by-grid-block basis according to $P_{c,n} \rightarrow P_{c,n}' = P_{c,n}/\sqrt{(\zeta_n)}$ (Leverett, 1941). Random permeability modifiers can be internally generated in TOUGH2; for spatially-correlated permeability distributions geostatistical techniques can be used to derive appropriate fields of ζ_n-coefficients (Tompson, 1989; Pruess, 1997).

Discussion and Conclusions

TOUGH2, Version 2.0, consists of a set of program modules that were developed in response to specific types of flow and transport problems. It includes a considerably enhanced set of fluid property modules and additional process simulation capabilities, such as multiphase diffusion and hydrodynamic dispersion, dissolution and precipitation of solids, radiative heat transfer, and coupling between reservoir and wellbore flow. It includes many improvements and new user features, such as generating graphics files, tabulating thermodynamic data, and block-by-block permeability modification for strongly heterogeneous

media. Changes in existing TOUGH2 modules were kept to a minimum, and were only made as needed to achieve the additional functionalities desired. Data inputs are upward compatible with the previous version, so that existing TOUGH2 input files should produce identical results when run with Version 2.0. Additional data inputs are needed to use new, enhanced process simulation capabilities. Coding continues to be in FORTRAN77 for maximum portability.

Even though the Version 2.0 program modules were thoroughly tested individually, their integration into a single program structure is a difficult and potentially "hazardous" task. Many different options can be selected in different program modules. It is not practically possible to exhaustively cross-check the mutual compatibility and proper performance of all options. There is no finite process by which all program bugs that may be present can be identified and corrected. Fixing a bug may cause unanticipated problems elsewhere. Continuing vigilance and application testing are needed. The Version 2.0 program package is currently (April 1998) being readied for "beta-testing" by a small group of experienced users. Public release is expected for early 1999.

Acknowledgement

We wish to acknowledge many valuable contributions from our collaborators inside and outside LBNL, especially Alfredo Battistelli, Ron Falta, Stefan Finsterle, Michael O'Sullivan, Steve Webb, and Yu-Shu Wu. Review of the manuscript by Marcelo Lippmann and Stefan Finsterle is gratefully acknowledged. This work was supported by the Assistant Secretary for Energy Efficiency and Renewable Energy, Office of Geothermal Technologies, U.S. Department of Energy under Contract No. DE-AC03-76SF00098.

Notation

d_β^κ diffusion coefficient for component κ in phase β, m^2/s.

$\overline{\mathbf{D}}_\beta^\kappa$ dispersion tensor for component κ in phase β, m^2/s.

$D_{\beta,L}^\kappa$ longitudinal dispersions coefficient for component κ in phase β, m^2/s.

$D_{\beta,T}^\kappa$ transverse dispersions coefficient for component κ in phase β, m^2/s.

$\mathbf{f}_\beta^\kappa$ diffusive mass flux of component κ in phase β, kg/s m^2.

$\mathbf{F}^\kappa\big|_{dis}$ diffusive mass flux of component κ in phase β, kg/s m^2.

h specific enthalpy, J/kg.

$\bar{\mathbf{I}}$ identity tensor.

k_n permeability of grid block n, m^2.

$k_{r\beta}$ relative permeability of the β phase.

P pressure, Pa.

$P_{c,n}$ capillary pressure in grid block n, Pa.

PI productivity index, m^3.

P_{wb} wellbore pressure, Pa.

q well flow rate, kg/s.

R residual function for well rate, kg/s.

S_s saturation of solid precipitate.

S_β saturation of phase β.

$\mathbf{u}_\beta$ Darcy velocity, m/s.

X_β^κ component κ mass fraction in phase β.

ζ permeability modification coefficient.

μ_β β phase viscosity, kg/m s.

ρ_β density of phase β, kg/m^3.

τ_0 tortuosity.

τ_β tortuosity factor in phase β.

ϕ porosity.

References

Aunzo, Z.P., G. Bjornsson and G.S. Bodvarsson. Wellbore Models GWELL, GWNACL, and HOLA. Lawrence Berkeley National Laboratory Report LBL-31428, Berkeley, CA, 1991.

Battistelli, A., C. Calore and K. Pruess. The Simulator TOUGH2/EWASG for Modeling Geothermal Reservoirs with Brines and a Non-Condensible Gas, *Geothermics*, Vol. 26, No. 4, pp. 437 - 464, 1997.

Hadgu, T. and D. H. Freeston. A Multi-Purpose Wellbore Simulator. *Geothermal Resources Council Transactions*, Vol. 14, pp. 1279 - 1286, 1990.

Hadgu, T., R.W. Zimmerman and G.S. Bodvarsson. Coupled Reservoir-Wellbore Simulation of Geothermal Reservoir Behavior. *Geothermics*, Vol. 24, No. 2, pp. 145-166, 1995.

Herbert, A. W., C. P. Jackson and D. A. Lever. Coupled Groundwater Flow and Solute Transport with Fluid Density Strongly Dependent on Concentration, *Water Resour. Res.*, 24 (10), 1781-1795, 1988.

Leverett, M. C. Capillary Behavior in Porous Solids, *Trans. Soc. Pet. Eng. AIME*, 142, 152-169, 1941.

Moridis, G. and K. Pruess. T2SOLV: An Enhanced Package of Solvers for the TOUGH2 Family of Reservoir Simulation Codes, Geothermics, in press, 1998.

Moridis, G. and K. Pruess. Flow and Transport Simulations Using T2CG1, a Package of Conjugate Gradient Solvers for the TOUGH2 Family of Codes, Lawrence Berkeley National Laboratory Report LBL-36235, Berkeley, CA, 1995.

Murray, L. and C. Gunn. Toward Integrating Geothermal Reservoir and Wellbore Simulation: TETRAD and WELLSIM, Proc. 15th NZ Geothermal Workshop, pp. 279 - 284, Auckland, New Zealand, 1993.

Oldenburg, C.M. and K. Pruess. A Two-Dimensional Dispersion Module for the TOUGH2 Simulator, Lawrence Berkeley National Laboratory Report LBL-32505, Berkeley, CA, September 1993.

Oldenburg, C.M. and K. Pruess. EOS7R: Radionuclide Transport for TOUGH2. Lawrence Berkeley National Laboratory Report LBL-34868, Berkeley, CA, 1995a.

Oldenburg, C.M. and K. Pruess. Dispersive Transport Dynamics in a Strongly Coupled Groundwater-Brine Flow System. *Water Resour. Res.*, Vol. 31, No. 2, pp. 289-302, 1995b.

O'Sullivan, M. J. A Similarity Method for Geothermal Well Test Analysis, *Water Resour. Res.*, Vol. 17, No. 2, pp. 390-398, 1981.

O'Sullivan, M. J., G. S. Bodvarsson, K. Pruess and M. R. Blakeley. Fluid and Heat Flow in Gas-Rich Geothermal Reservoirs, *Society of Petroleum Engineers Journal*, 25 (2), 215-226, April 1985.

Pruess, K. TOUGH User's Guide, Nuclear Regulatory Commission Report NUREG/CR-4645; also Lawrence Berkeley National Laboratory Report LBL-20700, Berkeley, CA, 1987.

Pruess, K. TOUGH2 - A General Purpose Numerical Simulator for Multiphase Fluid and Heat Flow, Lawrence Berkeley National Laboratory Report LBL-29400, Berkeley, CA, 1991.

Pruess, K. (ed.). Proceedings of the TOUGH Workshop '95, Lawrence Berkeley National Laboratory Report LBL-37200, Berkeley, CA, 1995.

Pruess, K. On Vaporizing Water Flow in Hot Sub-Vertical Rock Fractures, *Transport in Porous Media*, Vol. 28, pp. 335 - 372, 1997.

Reeves, M., D. S. Ward, N. D. Johns and R. M. Cranwell. Theory and Implementation of Swift II, The Sandia Waste-Isolation Flow and Transport Model for Fractured Media, Report No. SAND83-1159, Sandia National Laboratory, Albuquerque, NM, 1986.

Richards, L. A. Capillary Conduction of Liquids Through Porous Mediums, *Physics*, 1, 318-333, 1931.

Scheidegger, A. E. Statistical Hydrodynamics in Porous Media, *J. Appl. Phys.*, 25 (8), 994-1001, 1954.

Sleijpen, G.L.G. and D. Fokkema. BiCGSTAB(m) for Linear Equations Involving Unsymmetric Matrices with Complex Spectrum, *Electronic Transactions on Numerical Analysis*, Vol. 1, pp. 11 - 32, 1993.

Tompson, A.F.B. Implementation of the Three-Dimensional Turning Bands Random Field Generator, *Water Resour. Res.*, Vol. 25, No. 10, pp. 2227 - 2243, 1989.

van der Vorst, H.A. Bi-CGSTAB: A Fast and Smoothly Converging Variant of BiCG in the Presence of Rounding Errors, *SIAM J. Sci. Statist. Comput.*, Vol. 13, pp. 631 - 644, 1992.

Vaughan, P.J. Analysis of Permeability Reduction During Flow of Heated, Aqueous Fluid Through Westerly Granite, in C.F. Tsang (ed.), *Coupled Processes Associated with Nuclear Waste Repositories*, pp. 529 - 539, Academic Press, New York, 1997.

Verma, A. and K. Pruess. Thermohydrologic Conditions and Silica Redistribution Near High-Level Nuclear Wastes Emplaced in Saturated Geological Formations, *Journal of Geophysical Res.*, 93 (B2), pp. 1159-1173, 1988.

Weir, G. and S.W. White. A Permeability-Porosity Relationship for Surface Deposition, Proc. 17th NZ Geothermal Workshop, pp. 205 - 210, Auckland, New Zealand, 1995.

Wu, Y.S. and K. Pruess. A 3-D Hydrodynamic Dispersion Model for Modeling Tracer Transport in Geothermal Reservoirs, Proc., Twenty-Third Workshop on Geothermal Reservoir Engineering, Stanford University, January 1998.

Acknowledgement

This work was supported by the Assistant Secretary for Energy Efficiency and Renewable Energy, Geothermal Division, of the U.S. Department of Energy under Contract No. DE-AC03-76SF00098.

Appendix A. Author Index

Ahlers, C.F. **222**
Battistelli, A. **160**
Birkholzer, J.T. **118**
Bodvarsson, G.S. **222**
Brimhall, G. **234**
Brown, K.W. **130, 172**
Bühler, C. **83**
Bullivant, D.P. **1, 36, 53**
Burnell, J. **47**
Chersicla, A. **160**
Cohen, A.J.B. **95**
Christian-Frear, T.L. **101**
Doughty, C. **210**
Falta, R.W. **136, 148, 186**
Faybishenko, B. **250**
Ferragina, C. **160**
Finsterle, S. **124, 136, 205, 222, 250, 281**
Follows, S. **1**
Freeze, G.A. **101**
Fryar, D.G. **71**
Garcia-Estrada, G. **59**
Gélinas, P.J. **154**
Gierke, J.S. **186**
Gribi, P. **112**
Guerrero, M. **281**
Hein, G.L. **186**
Ho, C.K. **216, 257, 288**
Hockley, D. **228**
Hodges, R.A. **136**
James, A.L. **205**
Javeri, V. **77**
Jobman, M. **106**
Kalacheva, E.G. **65**
Kiryukhin, A.V. **65**
Kissling, W.M. **25**
Knowles, M.K. **71**
Kroopnick, P. **166**
Kuo, J. **275**
Lefebvre, R. **154, 228**
Lesnykh, M.D. **65**
Liou, T.S. **198**
Lupo, M.J. **130, 172**
Mannington, W.I. **1**
Marschall, P. **83**
Matarrese, G. **160**
Miller, E.C. **178**
Moridis, G.J. **142, 172, 263, 300, 307**
Nastev, M. **154**
Niemeyer, M. **112**
Oldenburg, C.M. **13, 95, 205, 263, 307**
Osato, K. **41, 47**
O'Sullivan, M.J. **1, 36, 53**
Polyakov, A.Y. **65**
Phelan, J.M. **124**
Pieroni, M. **160**
Pruess, K. **13, 89, 124, 142, 198, 234, 244, 307**
Quijano, J. **30**
Reeves, M. **71**
Rossabi, J. **148**
Rubin, Y. **198**
Ruskauff, G.J. **101**
Samaniego, F. **19**
Satik, C. **281**
Sato, T. **41, 47**
Schreiber, W. **275, 294**
Schwind, P.J. **178**
Senger, R.K. **83, 112**
Sigurdsson, O. **7**
Smolensky, J. **228**
Sonnenborg, T.O. **250**
Statham, W.H. **71**
Stefansson, V. **7**
Suárez, M.C. **19**
Therrien, R. **154**
Tsang, Y.W. **118**
Webb, S.W. **101, 124, 192, 216, 257, 269, 288**
White, S.P. **25, 47, 244**
Wu, Y.S. **89, 142**
Xu, T. **234, 244**
Yokomoto, S. **41, 47**
Young, R.M. **25**
Zuidema, P. **112**

Appendix B. Registered Participants

Jorge A. Acuna
Unocal
1300 N. Dutton Ave.
Santa Rosa, CA 95401
707-521-7616
Fax: 707-521-7604
jacuna@unocal.com

Rick Ahlers
Lawrence Berkeley National Lab.
1 Cyclotron Road, MS 90-1116
Berkeley, CA 94720
510-486-7341
Fax: 510-486-6115
rick_Ahlers@lbl.gov

Richard Allis
University of Utah
423 Wakara Way
Salt Lake City, UT 84108
801-581-7849
Fax: 801-585-3540
rallis@egi.utah.edu

Brian G. Barnett
Kingston Morrison Ltd.
P.O. Box 9806
Newmarket
Auckland, New Zealand
649-521-6069
Fax: 649-520-4695
bgb@auck.km.co.nz

Alfredo Battistelli
Aquater, S.p.A.
61047 S. Lorenzo in Campo (Pesaro)
Italy
39-721-731326
Fax: 39-721-731308
ambid@aquater-sl.aquater.it

Jens T. Birkholzer
Lawrence Berkeley National Lab.
1 Cyclotron Road, MS 90-1116
Berkeley, CA 94720
510-486-7118
Fax: 510-486-5686
Jens_Birkholzer@lbl.gov

Grimur Björnsson
Orkustofnun
Grensasvegur 9
Reykjavik, Iceland IS-108
354-569-6000
Fax: 354-569-8896
omar@OS.IS

Edward W. Bolton
Yale University
Dept. of Geology & Geophysics
P.O. Box 208109
New Haven, CT 06520

Tatjana Brombach
Institut de Mineralogie et Petrographie
Universite de Lausanne
Lausanne, Switzerland
41-21-6924446
tatjana.brombach@imp.unil.ch

David P. Bullivant
University of Auckland
Engineering Science
Private Bag 92019
Auckland, New Zealand
649-373-7599 ext. 5807
Fax: 649-373-7468
d.bullivant@auckland.ac.nz

Steven J. Butler
GeothermEX, Inc.
5221 Central Ave.
Suite 201
Richmond, CA 94804
510-527-1876
Fax: 510-527-8164
geothermex@compuserve.com

Claudio Calore
Intl. Inst. for Geothermal Res. - CNR
Piazza Solferino 2
Pisa 56126
Italy
39-50-41503
Fax: 39-50-47055
calore@ccrisc.IIRG.PI.CNR.IT

Bruce W. Christenson
Inst. of Geological & Nuclear Sciences
Private Bag 2000
Taupo, New Zealand
64 7 374 8211
Fax: 64 7 374 8199
B.Christenson@GNS.CRI.NZ

Stefan Finsterle
Lawrence Berkeley National Lab.
1 Cyclotron Road, MS 90-1116
Berkeley, CA 94720
510-486-5205
Fax: 510-486-5686
SAFinsterle@lbl.gov

Andrew J.B. Cohen
Lawrence Berkeley National Lab.
1 Cyclotron Road, MS 90-1116
Berkeley, CA 94720
510-486-6950
Fax: 510-486-5686
ajbc@lbl.gov

Sabodh K.Garg
Maxwell Technologies
8888 Balboa Ave.
San Diego, CA 92123
619-576-7752
Fax: 619-637-7411
garg@maxwell.com

Robin N. Datta
CRWMS M&O
1140 Town Center Drive
Las Vegas, NV 89134
702-295-5741
Fax: 702-295-3554
robin_datta@notes.ymp.gov

Jil T. Geller
Lawrence Berkeley National Lab.
1 Cyclotron Road, MS 90-1116
Berkeley, CA 94720
510-486-7313
jtgeller@lbl.gov

Chris Doughty
Lawrence Berkeley National Lab.
1 Cyclotron Road, MS 90-1116
Berkeley, CA 94720
510-486-6453
Fax: 510-486-4159
cadoughty@lbl.gov

Peter Gribi
Colenco Power Engineering Ltd.
Mellingerstrasse 207
5405 Baden-Dättwil
Switzerland
41 56 483 12 12
Fax: 41 56 493 73 57
gri@colenco.ch

Kathy M. Economy
Applied Physics Inc.
8100 Mountain Road
Albuquerque, NM 87110
505-299-1282
Fax: 505--296-3289
kmecono@sandia.gov

Asgrimur Gudmundsson
National Energy Authority
Grensasvegur 9
108 Reykjavik
Iceland
530-752-9779
Fax: 530-752-0951
gudmundsson@geology.ucdavis.edu

Ronald W. Falta
Clemson University
Brackett Hall, Room 340C
Clemson, SC 29634
864-656-0125
Fax: 864-656-1041
faltar@clemson.edu

Teklu Hadgu
Applied Physics Inc.
6948 Forest Hills Dr., NE
Albuquerque, NM 87109
505-797-2762
Fax: 505-265-2237
thadgu@nwer.sandia.gov

Clifford K. Ho
Sandia National Labs
P.O. Box 5800
Albuquerque, NM 87185
505-844-0712
Fax: 505-848-0605
ckho@sandia.gov

Rex A. Hodges
Clemson University
340 Brackett Hall
Box 341908
Clemson, SC 29634
864-656-1051
Fax: 864-656-1041
rhodges@clemson.edu

Kuo-Chin Hsu
Daniel B. Stephens & Associates
6020 Academy NE, Suite 100
Albuquerque, NM 87109
505-822-9400
Fax: 505-822-8877
khsu@dbstephens.com

Motomu Ibaraki
Ohio State University
125 S. Oval Mall
Columbus, OH 43210
614-292-7528
Fax: 614-292-7688
ibaraki@geology.ohio-state.edu

April L. James
Lawrence Berkeley National Lab.
1 Cyclotron Road, MS 90-1116
Berkeley, CA 94720
510-486-6251
Fax: 510-486-4159
april@telos.lbl.gov

Vijen Javeri
GRS
Schwertnergasse 1
50667 Köln
Germany
49-221-2068-794
Fax: 49-221-2068-888

Michael Jobmann
DBE
Woltorfer Strasse 74
D-31224 Peine
Germany
49-5171 91 7747
Fax: 49 5171 91 7740
jobmann@DBE.de

James T. Kam
M&O/M-K
1180 Town Center Drive
c/o Yucca Mtn. Project
Las Vegas, NV 89134
702-295-4495
Fax: 702-295-4435
jim_kam@mk.com

Ali M. Khan
State of California
50 "D" Street, #300
Santa Rosa, CA 95404
707-576-2385
Fax: 707-576-2611
oilreport@aol.com

Alexey Kiryukhin
Institute of Volcanology
Petropavlovsk-Kamchatsky, 683006
RUSSIA
7-41522-59543
Fax: 7-41522-54723
volcan@svyaz.kamchatka.su

Kathy Knowles
Sandia National Labs
115 N. Main
Carlsbad, NM 88220
505-234-0058
Fax: 505-234-0061
kknowles@nm.net

Juhani A. Korkealaakso
Technical Research Centre of Finland
P.O. Box 19041
Espoo, FIN-02044
Finland
358 9 456 4852
Fax: 358 9 456 7927
juhani.Korkealaakso@vtt.fl

Peter Kroopnick
Fluor Daniel GTI
555 S. Renton Village Place
Suite 700
Renton, WA 98055
426-228-9645
Fax: 426-228-9793
pkroopnick@gtionline.com

René Lefebvre
INRS-Géoressources
Université du Québec
2700, rue Einstein
Case postale 7500
Sainte-Foy, G1V 4C7
Canada
418-654 2651
Fax: 418-654 2615
rlefebvre@gsc.emr.ca

Jianhua Li
Lawrence Berkeley National Lab.
1 Cyclotron Road, MS 90-1116
Berkeley, CA 94720
510-486-5625
Fax: 510-486-5686
JHLi@lbl.gov

Tai-Sheng Liou
University of California, Berkeley
Berkeley, CA 94720
510-486-7083
tsliou@alpha-2.ce.berkeley.edu

Marcelo J. Lippmann
Lawrence Berkeley National Lab.
1 Cyclotron Road, MS 90-1116
Berkeley, CA 94720
510-486-5035
Fax: 510-486-5686
MJLippmann@lbl.gov

Stephan Lorenz
GRS
Schwertnergasse 1
50667 Köln
Germany
49-221-2068-712
Fax: 49-221-2068-866

Ning Lu
Colorado School of Mines
Brown Building
Golden, CO 80401
303-273-3654
Fax: 303-273-3602
ninglu@mines.edu

Mark J. Lupo
KW Brown
13101 NW Freeway, Suite 314
Houston, TX 77040
713-895-9393
Fax: 713-895-7328
mlupo@kwbes.com

Manuel Ernesto Monterrosa
Comisión Ejecutiva Hidroeléctrica
del Rio Lempa (CEL)
El Salvador

George J. Moridis
Lawrence Berkeley National Lab.
1 Cyclotron Road, MS 90-1116
Berkeley, CA 94720
510-486-4746
Fax: 510-486-5686
gjmoridis@lbl.gov

Kazunaga Murakami
Kaihatsu Computing Service Center Ltd.
2-18, kukagawa 2-chome, Koto-ku
Tokyo 135-0002
Japan
81-3-3642-9771
Fax: 81-3-3642-9796
kcc09172@kcc.co.jp

Shigetaka Nakanishi
Electric Power Development Co., Ltd.
15-1 Ginza 6-Chome, Chuo-ku
Tokyo, 104-8165
Japan
81-3-3546-2211
Fax: 81-3-3546-9482
den09222@opdc.co.jp

Christopher J. Neville
Conestoga-Rovers & Associates
651 Colby Drive
Waterloo, N2V 1C2
Canada
519-725-3313
Fax: 519-725-1736
cneville@rovers.com

Purna C. Patnaik
Maxwell Technologies
8888 Balboa Ave.
San Diego, CA 92123
619-576-7763
Fax: 619-637-7411
patnaik@maxwell.com

Michael J. O'Sullivan
University of Auckland
Private Bag 92019
Auckland, New Zealand
64-9-3737599 ext. 8393
Fax: 64-9-3737468
m.osullivan@auckland.ac.nz

Mel G. Piepho
Math & Physics Applications, Inc.
2451 Pershing Ave.
Richland, WA 99352
509-375-1619
Fax: 509-375-3381
piepho@owt.com

Phil L. Oberlander
Lawrence Berkeley National Lab.
1180 Town Center Dr., MS 822
Las Vegas, NV 89134
702-295-3402
Fax: 702-295-3554
phil_Oberlander@crwms.ymp.gov

Karsten Pruess
Lawrence Berkeley National Lab.
1 Cyclotron Road, MS 90-1116
Berkeley, CA 94720
510-486-6732
Fax: 510-486-5686
K_Pruess@lbl.gov

Curtis M. Oldenburg
Lawrence Berkeley National Lab.
1 Cyclotron Road, MS 90-1116
Berkeley, CA 94720
510-486-7419
Fax: 510-486-5686
cmoldenburg@lbl.gov

Julio Quijano
Comisión Ejecutiva Hidroeléctrica
del Rio Lempa (CEL)
Km 11 1/2 Carretera al Puerto La Libertad
Santa Tecla
El Salvador

Kazumi Osato
Geothermal Energy Research
& Development Co.
Nihonbashi, Chuo-ku
Kyodo Bldg., 1107
Kabuto-cho, Tokyo, 103-0026
Japan
81-3-3666-5822
Fax: 81-3-3666-5389

Mark Reeves
Duke Engineering & Services
9111 Research Blvd.
Austin, TX 78758
512-425-2000
Fax: 512-425-2099
MReeves@duke-energy.com

Mauro A. Parini
Unocal
1300 North Dutton Ave.
Santa Rosa, CA 95401
707-521-7619
Fax: 707-521-7604
mparini@unocal.com

Anne Ritcey
Lawrence Berkeley National Lab.
1 Cyclotron Road, MS 90-1116
Berkeley, CA 94720
510-486-6085
Fax: 510-486-5686
acritcey@lbl.gov

Peter E. Rose
University of Utah
423 Wakara Way
Salt Lake City, UT 84108
801-581-7705
Fax: 801-585-3540
prose@egi.utah.edu

Rainer K. Senger
Duke Engineering & Services
9111 Research Blvd.
Austin, TX 78758
512-425-2000
Fax: 512-425-2099
rksenger@duke-energy.com

Joe Rossabi
Westinghouse Savannah River Co.
Bldg. 773-42A, Rm. 249
Aiken, SC 29808

Mike Shook
INEEL
P.O. Box 1625
Idaho Falls, ID 83415
208-526-6945
Fax: 208-526-0875
ook@inel.gov

Steven F. Saterlie
TRW Environmental Safety Systems Inc.
1180 Town Center Dr.
Las Vegas, NV 89134
702-295-4026
Fax: 702-295-4230
Steven_Saterlie@ymp.gov

Omar Sigurdsson
Orkustofnun
Grensasvegur 9
Reykjavik, IS-108
Iceland
354-569-6000
Fax: 354-568-8896
omar@OS.IS

Tatsuya Sato
Geothermal Energy Research
& Development Co.
Nihonbashi, Chuo-ku
Kyodo Bldg., 1107, Kabuto-cho
Tokyo 103-0026 Japan
81-3-3666-5822
Fax: 81-3-3666-5289

Eric L. Sonnenthal
Lawrence Berkeley National Lab.
1 Cyclotron Road, MS 90-1116
Berkeley, CA 94720
510-486-6115
Fax: 510-486-5686
elsonnenthal@lbl.gov

Michael Schnarr
Harding-Lawson Assoc.

Will C. Schreiber
University of Alabama
P.O. Box 870276
Tuscaloosa, AL 35401
205-348-1650
Fax: 205-348-6419
wschreiber@coe.eng.ua.edu

Nicolas Spycher
Lawrence Berkeley National Lab.
1 Cyclotron Road, MS 90-1116
Berkeley, CA 94720
510-495-2388
NSpycher@lbl.gov

Patrick J. Schwind
Parsons Infrastructure & Technology
175 Tri-County Parkway
Cincinnati, OH 45246
513-648-6811
Fax: 513-648-6892
pat_schwind@fernald.gov

Mario-César Suarez Arriaga
UNAM/UMSNH/CFE
Patzimba 438, Vista Bella
Morelia, Mich. 58090
Mexico
43 15 05 56
Fax: 43 14 47 35
msuarez@zeus.ccu.umich.mx

Daniel V. Swenson
Kansas State University
Nuclear Engineering
Manhattan, KS 66506
785-532-1210
Fax: 785-532-7057
swenson@ksu.edu

Paul Witherspoon
Witherspoon, Inc.
1824 Monterey Ave.
Berkeley, CA 94707

Scott Versluis
Parsons Infrastructure & Technology
260 S. Woodruff Ave., #313
Idaho Falls, ID 83401
208-526-1186
Fax: 208-526-8426
scott_versluis@parsons.com

Yu-Shu Wu
Lawrence Berkeley National Lab.
1 Cyclotron Road
Berkeley, CA 94720
510-486-7291
Fax: 510-486-5686
yswu@lbl.gov

Stephen W. Webb
Sandia National Labs
P.O. Box 5800, MS-0977
Albuquerque, NM 87185
505-844-3931
Fax: 505-844-2057
swwebb@sandia.gov

Tianfu Xu
Lawrence Berkeley National Lab.
1 Cyclotron Road, MS 90-1116
Berkeley, CA 94720
510-486-7057
Fax: 510-486-5686
Tianfu_Xu@lbl.gov

Mark D. White
PNNL
3200 Q Street
Richland, WA 99352
509-372-6070
Fax: 509-372-6089
mark.white@pnl.gov

Wei Zhou
QuantiSci, Inc.
3900 S. Wadsworth Blvd., Suite 555
Denver, CO 80235
303-985-0005
Fax: 303-980-5900
wzhou@quantisci.com

Stephen P. White
Industrial Research Ltd.
P.O. Box 31310
Lower Hutt, New Zealand
64 4 5690 000
Fax: 64 4 5690 003
s.white@irl.cri.nz

Appendix C. Technical Program

TOUGH Workshop '98

May 4 - 6, 1998

Lawrence Berkeley National Laboratory (LBNL)
Berkeley, California 94720, USA

FINAL TECHNICAL PROGRAM (as presented)

Monday, May 4, 1998

A.M.

7:30 Registration: Lobby, Auditorium, Building 50

8:30 Welcome and Introduction (Karsten Pruess, LBNL)

8:45 **Session 1: *Geothermal Reservoir Engineering* I**
(chairman: Alfredo Battistelli, Aquater S.p.A., Italy)

M.J. O'Sullivan, D.P. Bullivant, S. Follows, and W.I. Mannington, Dept. of Engineering Science, U. of Auckland, NEW ZEALAND. "Modelling of the Wairakei-Tauhara Geothermal System"

Omar Sigurdsson and Valgardur Stefansson, Orkustofnun, Reykjavik, ICELAND. "Use of TOUGH2 in Studying Reinjection Strategies"

C.M. Oldenburg and K. Pruess, LBNL. "Higher-Order Differencing for Front Propagation in Geothermal Systems"

M.C. Suárez A. and F. Samaniego V, CFE/PEMEX, Morelia, MEXICO. "FITH2 - A Set of FORTRAN Interfaces to Process TOUGH2 Information, Data and Results"

10:25 Coffee Break

10:55 **Session 2: *Nuclear Waste Isolation* I**
(chairman: Ron Falta, Clemson University, South Carolina)

M. Reeves, D.G. Fryar, W.H. Statham, and M.K. Knowles, Duke Engineering & Services, Austin, TX. "Assessing Seal Performance and Parameter Sensitivity with a Full-Shaft Model"

V. Javeri, GRS, Köln, GERMANY. "Combined Gas and Nuclide Transport in a Two-Dimensional Repository Considering Variable Rock Convergence"

R. Senger, P. Marschall, and C. Bühler, Duke Engineering/NAGRA/Solexperts, SWITZERLAND. "Gas Tracer Transport in Two-Phase Flow Field: Numerical Simulations and Field Experiments at the Grimsel Test Site (GTS), Switzerland"

P.M.

12:10 Lunch Break

1:30 **Session 3: *Recent TOUGH2 Enhancements at Berkeley***
(chairman: René Lefebvre, INRS-Géoressources, Quebec, Canada)

Y.S. Wu and K. Pruess, LBNL. "Several TOUGH2 Modules Developed for Site Characterization Studies of Yucca Mountain"

G.J. Moridis, LBNL. "TOUGH90: A FORTRAN90 Implementation of TOUGH2"

K. Pruess, LBNL. "Overview of TOUGH2 , Version 2.0"

Monday, May 4, 1998 (continued)

P.M.

2:45 Adjourn for Poster Setup

4:00 **Session 4: Posters** (LBNL Cafeteria)

S.W. Webb, S.A. Finsterle, K. Pruess, and J.M. Phelan, Sandia/LBNL, Albuquerque, NM. "Prediction of the TNT Signature from Buried Landmines"

M.J. Lupo and K.W. Brown, KW Brown Environmental, College Station, TX. "Distinguishing the Contributions of Multiple Sources from a Gasoline Release"

R.A. Hodges, R.W. Falta, and S. Finsterle, Clemson University/LBNL, Clemson, SC. "Three-Dimensional Simulation of DNAPL Transport at the Savannah River Site"

M.C. Suárez A., CFE, Morelia, MEXICO. "Some Historical Aspects of the Influence of Volcanoes and Geothermal Energy in the Mesoamerican Cultures"

S.P. White, R.M. Young, and W.M. Kissling, IRL, Wellington, NEW ZEALAND. "Using ITOUGH2 to Improve Geothermal Reservoir Models"

J. Quijano, Comisión Ejecutiva Hidroeléctrica del Rio Lempa (CEL), El Salvador. "Transmissivity Distribution at the Ahuachapán-Chipilapa Geothermal Field in El Salvador"

S.W. Webb, Sandia, Albuquerque, NM. "Using TOUGH2 to Model Capillary Barriers"

G.J. Moridis, Y.S. Wu, and K. Pruess, LBNL. "EOS9nT: A TOUGH2 Module for the Simulation of Flow and Solute/Colloid Transport"

A.J.B. Cohen and C.M. Oldenburg, LBNL. "Effects of Faulted Stratigraphy on Saturated Zone Flow Beneath Yucca Mountain, Nevada"

G.A. Freeze, G.J. Ruskauff, T.L. Christian-Frear, and S.W. Webb, Duke Engineering & Services /Sandia, Albuquerque, NM. "Modeling the Effect of Excavation-Disturbed Zone Porosity Increase on Groundwater Inflow to an Underground Repository"

W. Schreiber, University of Alabama, Tuscaloosa, AL. "The Use of an Adaptive Grid with TOUGH2 to Track a Moving Phase Front"

D. Bullivant and M.J. O'Sullivan, Dept. of Engineering Science, U. of Auckland, NEW ZEALAND. "Graphics and TOUGH2"

T.S. Liou, K. Pruess, and Y. Rubin, LBNL/UC Berkeley. "Numerical Simulation Experiments on Water Seepage in Unsaturated, Heterogeneous Fractures"

S. Finsterle, T.O. Sonnenborg and B. Faybishenko, LBNL/Technical University of Denmark. "Inverse Modeling of a Multistep Outflow Experiment for Determining Hysteretic Hydraulic Properties"

S.W. Webb and C.K. Ho, Sandia, Albuquerque, NM. "Enhanced Vapor Diffusion in Porous Media"

C.M. Oldenburg and G.J. Moridis, LBNL. "Ferrofluid Flow for TOUGH2"

A.L. James, C.M. Oldenburg, and S. Finsterle, LBNL. "Analysis of Uncertainty for 2-D Fracture Flow and Seepage into an Excavated Drift"

K. Osato, T. Sato, and S. Yokomoto, GERD, Ltd., Tokyo, JAPAN. "The Modeling Study Using TOUGH2 and the Micro-Gravity Change in Yanaizu-Nishiyama Geothermal Field"

T. Sato, K. Osato, S. White, J. Burnell, and S. Yokomoto, GERD/IRL, Ltd., Tokyo, JAPAN. "Development of an Integrated Reservoir Modeling System for the Modeling Study Using TOUGH2"

6:00 Buffet Dinner (LBNL Cafeteria)

7:30 Adjourn

Tuesday, May 5, 1998

A.M.

8:30 **Session 5: *Environmental Remediation* I**
(chairman: Steve White, IRL, Wellington, New Zealand)

J. Rossabi and R.W. Falta, Savannah River/Clemson University, SC. "The Behavior of Volatile Organic Contaminants in the Vadose Zone with Respect to Barometric Pumping and the Estimate of Residual Mass and Mass Removal Using T2VOC"

S.W. Webb, Sandia, Albuquerque, NM. "Gas-Phase Diffusion in Porous Media: Comparison of Models"

M. Nastev, R. Lefebvre, R. Therrien, and P.J. Gélinas, Soprin-ADS/NRS, Quebec, CANADA. "Numerical Modeling of Landfill Gas Production and Migration with a N2-CO2-CH4-H2O System and a Production Function"

A. Battistelli, A. Chersicla, C. Ferragina, G. Matarrese, and M. Pieroni, Aquater S.p.A., S. Lorenzo in Campo, ITALY. "Simulation of the Transport of Aromatic Amines in the Unsaturated Zone for the Evaluation of an Environmental Remediation Project"

10:10 Coffee Break

10:40 **Session 6: *Vadose Zone Hydrology***
(chairman: Stefan Finsterle, LBNL)

C. Doughty, LBNL. "Numerical Modeling of Field Tests in Unsaturated Fractured Basalt at the Box Canyon Site"

C.K. Ho and S.W. Webb, Sandia, Albuquerque, NM. "The Effects of Heterogeneities and Wavy Interfaces on Capillary Barrier Performance"

C.F. Ahlers, S. Finsterle, and G.S. Bodvarsson, LBNL. "Characterization and Prediction of Subsurface Pneumatic Pressure Variations at Yucca Mountain, Nevada"

11:55 Lunch Break

P.M.

2:00 **Session 7: *Process Modeling Applications***
(chairman: Curt Oldenburg, LBNL)

W. Schreiber and J. Kuo, University of Alabama, Tuscaloosa, AL. "A Computational Study of some Possible Factors Associated with Melt Eruption Events"

S. Finsterle, C. Satik, and M. Guerrero, LBNL/Stanford University. "Analysis of Boiling Experiments Using Inverse Modeling"

S.W. Webb and C.K. Ho, Sandia, Albuquerque, NM. "Pore-Scale Modeling Using TOUGH2"

3:15 Coffee Break

3:45 **Session 8: *Mining Engineering***
(chairman: Karsten Pruess, LBNL)

R. Lefebvre, J. Smolensky, and D. Hockley, INRS/SRK Inc., Quebec, CANADA. "Modeling of Acid Mine Drainage Physical Processes in the Nordhalde of the Ronnenburg Mining District, Germany"

T. Xu, K. Pruess, and G. Brimhall, LBNL/UCB, Berkeley, CA. "Introducing Reactive Chemical Transport to TOUGH2: Application to Supergene Copper Enrichment"

S.P. White, T. Xu, and K. Pruess, IRL/LBNL, Wellington, NEW ZEALAND. "Reactive Chemical Transport"

5:00 Adjourn

7:00 Banquet

Speaker: Dr. Sabodh Garg, Maxwell Technologies, San Diego, California

Wednesday, May 6, 1998

A.M.

8:30 **Session 9: *Environmental Remediation* II**
(chairman: Rainer Senger, Duke Engineering, Austin, Texas)

P. Kroopnick, Fluor-Daniel, Kent, WA. "Numerical Modeling of JP-8 Remediation by Steam Injection into Artificial Fractures in a Clay Matrix"

M.J. Lupo, G.J. Moridis, and K.W. Brown, KW Brown Environmental/LBNL, College Station, TX. "Predicting the Fate of Trichloroethylene and its Daughters in a Heterogeneous Environment"

P.J. Schwind and E.C. Miller, Parsons Engineering/Lockheed Martin, Cincinnati, OH. "T2VOC Simulation and Optimization of SVE System Pulse Pumping of Vadose Zone Carbon Tetrachloride Contamination at the Idaho National Engineering and Environmental Laboratory"

R.W. Falta, J.S. Gierke, and G.L. Hein, Clemson University/Michigan Tech, Clemson, SC. "Using T2VOC to Model Kinetic Interphase Mass Transfer During Air Sparging"

10:10 Coffee Break

10:40 **Session 10: *Nuclear Waste Isolation* II**
(chairman: George Moridis, LBNL)

M. Jobmann, DBE, Peine, GERMANY. "Modification and Application of the TOUGH2 Code for Modeling of Water Flow Through Swelling Unsaturated Sealing Constructions"

P. Gribi, M. Niemeyer, R. Senger, and P. Zuidema, Colenco/Duke Engineering/NAGRA, Baden, SWITZERLAND. "Preliminary Investigation of Radionuclide Release under Two-Phase Conditions from a Proposed L/ILW Repository in Switzerland"

J.T. Birkholzer and Y.W. Tsang, LBNL. "Numerical Analysis of Thermal-Hydrological Conditions in the Single Heater Test at Yucca Mountain"

11:55 Lunch Break

P.M.

1:20 **Session 11: *Geothermal Reservoir Engineering* II**
(chairman: Yu-Shu Wu, LBNL)

D. Bullivant and M.J. O'Sullivan, Dept. of Engineering Science, U. of Auckland, NEW ZEALAND. "Inverse Modelling of the Wairakei Geothermal Field"

C. Calore, A. Battistelli, and K. Pruess, IIRG, Pisa, ITALY. "Analysis of Injection and Falloff Testing in High-Salinity Reservoirs Using TOUGH2/EWASG"

A.V. Kiryukhin, M.D. Lesnykh, A.Y. Polyakov, and E.G. Kalacheva, Institute of Volcanology, Petropavlovsk-Kamchatsky, RUSSIA. "TOUGH Applications to Analysis of the Pressure Transient Data of Verkhne-Mutnovsky Site, Mutnovsky Geothermal Field, Kamchatka"

3:00 Coffee Break

3:30 **Session 12: Open Discussion: Future Developments and Exchanges of the TOUGH/MULKOM Codes**
(chairman and moderator: Michael O'Sullivan, University of Auckland, New Zealand)

5:00 Workshop ends

Appendix D. TOUGH Questions

Here we present a questionnaire that was handed out to workshop participants, along with the responses received.

TOUGH Questions

(Please check all that apply)

Your area(s) of interest

O geothermal energy
O nuclear waste disposal
O vadose zone hydrology
O environmental contamination
O mining engineering
O design/analysis of experiments
O other (specify: .....)

Your reasons for attending the workshop

O present a paper
O find out about new TOUGH2 modules
O exchange ideas for simulator applications and development
O find out about current directions in multiphase flow simulation
O other (specify: .....)

What TOUGH codes have you used or are you using?

O MULKOM
O TOUGH
O TOUGH2
O T2VOC
O M2NOTS
O ITOUGH2

What is your mode of useage?

O R&D application
O engineering
O educational
O used code as delivered
O made minor modifications (changed printout, added capillary pressure functions, ...)
O made major modifications (re-wrote or added subroutines)

What computing platform(s) are you using?

O PC
O Macintosh
O workstation
O workstation cluster
O mainframe
O massively parallel

What kind of organization do you work for?

O governmental (such as national laboratories)
O university
O engineering firm
O self-employed consultant

Your wish list for future code enhancements

O run faster
O run bigger problems (more grid blocks)
O facilitate mesh design
O graphical user interface
O more comprehensive process descriptions
O solute transport
O reactive chemistry
O microbial interactions
O coupling with rock mechanics
O other (specify: .....)

In the future, would you attend O another TOUGH workshop O an (I)TOUGH2 short course

Comments and suggestions: .....

.....

TOUGH Question – Results
(47 responses)

Area of interest:

Geothermal energy: **23**
Environmental contamination: **22**
Vadose zone hydrology: **19**
Nuclear waste disposal: **20**
Mining engineering: **4**
Design/analysis of experiments: **12**

Other:

Applied mathematics and rock mechanics
General modeling of reactive transport in crustal fluid flows
Moisture movement in green sand casting
Earthquake precursors mechanism, volcanology
Volcanic hydrothermal environments/processes

Reason for attending:

Present a paper: **23**
Exchange ideas for simulator applications and development: **30**
Find out about new TOUGH2 modules: **33**
Find out about current directions in multiphase flow simulation: **31**

Other:

Learn about possible applications of TOUGH
To see authors and ask questions
Discuss special problems
To determine whether it will be feasible to use TOUGH2/T2VOC for consulting applications; exploratory trip for me
Meshmakers for fracture dominated systems
Get introduced to various applications

What TOUGH codes have you used or are you using?

MULKOM: **7**
TOUGH: **11**
TOUGH2: **33**
T2VOC: **14**
M2NOTS: **3**
ITOUGH2: **12**

What is your mode of usage?

R&D application: **24**
Engineering: **18**
Educational: **4**
Used code as delivered: **8**
Made minor modifications (changed printout, added capillary pressure functions, ...): **12**
Made major modifications (re-wrote or added subroutines): **15**

What computing platform(s) are you using?

PC: **31**
Macintosh: **2**
Workstation: **24**
Workstation cluster: **4**
Mainframe: **3**
Massively parallel: **1**

What kind of organization do you work for?

Government (such as national laboratories): **36**
University: **13**
Engineering firm: **15**
Self-employed consultant: **2**

Your wish list for future code enhancements:

Run faster: **21**
Run bigger problems (more grid blocks): **13**
Facilitate mesh design: **23**
Graphical user interface: **22**
More comprehensive process descriptions: **14**
Solute transport: **24**
Reactive chemistry: **16**
Microbial interactions: **3**
Coupling with rock mechanics: **15**

Other:

Benchmark comparisons with other codes on similar problems
Coupling with gravity/subsidence
Must have TVD scheme for advection and full dispersion tensor
Robustness is my major concern. Before I acquire TOUGH2/T2VOC I must know that my model may converge with a minimum of tweaking.
Qualification and validation to use for license application

In the future, would you attend:
Another TOUGH workshop: **45** An (I)TOUGH2 short course: **17**

Comments and suggestions:

- This workshop was interesting. I would suggest that in future TOUGH workshops there also be short intensive courses on TOUGHX uses with examples.
- Excellent workshop! Well organized. Good presentations.
- Monitored WWW discussion group.
- An increase in the length of element names (from 5 to say 10) will be needed for larger and larger problems, multiple perm. elements.
- Very productive workshop!
- I would like to know more about (I)TOUGH2.
- It would be nice to be able to get the new improved modules as soon as possible.
- This has been very educational; interesting problems being solved using the TOUGH code. Have learned this code has a lot of flexibility due to the multiple eyes, minds, problems it has been used for.
- I am hearing lots of anecdotal evidence of modeling difficulties, but those difficulties and suggestions for resolving them (and generally improving model performance) are not being presented in the talks. I am somewhat disappointed that the "workshop" is really just a "mini-conference."
- I am excited about variable array sizes in the FORTRAN 90 version. This would make QA easier because only one executable file is needed.
- Give a short introduction of field and problems for every session. For example, I'm involved in nuclear waste and not common with environmental problems, so sometimes a brief introduction makes it easier to follow.
- A separate session to discuss the difficulties of users in using TOUGH2 in different applications could be helpful.
- I hope we receive a list of attendees.
- To extend possible applications in earth sciences problems.
- I learned a lot about the possibilities and applications of TOUGH, and I enjoyed talking to other members of the TOUGH community. Why not meet every two years?
- Please provide a complete and comprehensive users guide for TOUGH2.

Ernest Orlando Lawrence Berkeley National Laboratory
One Cyclotron Road | Berkeley, California 94720

Prepared for the U.S. Department of Energy under Contract No. DE-AC03-76SF00098